Journal of Experimental and Theoretical Physics, Vol. 100, No. 5, 2005, pp. 1005–1017.
Translated from Zhurnal Éksperimental'noĭ i Teoreticheskoĭ Fiziki, Vol. 127, No. 5, 2005, pp. 1138–1152.

ELECTRONIC PROPERTIES OF SOLIDS

Current-Induced Spin Injection and Surface Torque in Ferromagnetic Metallic Junctions

Yu. V. Gulyaev[a], **P. E. Zil'berman**[a,*], **E. M. Epshtein**[a], **and R. J. Elliott**[b]
[a]*Institute of Radio Engineering and Electronics, Russian Academy of Sciences (Fryazino Branch),*
pl. Vvedenskogo 1, Fryazino, Moscow oblast, 141190 Russia
[b]*University of Oxford, Department of Physics, Theoretical Physics, Oxford OX1, UK*
**e-mail: zil@ms.ire.rssi.ru*

Received November 29, 2004

Abstract—The joint influence of two current-induced effects, namely, longitudinal nonequilibrium spin injection and surface torque, on spin-valve-type ferromagnetic metallic junctions is considered theoretically. The current flows normally to layer boundaries. The analysis is based on solving a system of coupled equations of motion for mobile electron and lattice magnetizations. The boundary conditions for the equations of motion are derived from the continuity condition for the total magnetization flux in these subsystems. A dispersion relation is derived for spin wave fluctuations depending on the current through the junction. The fluctuations become unstable at currents exceeding some threshold value (usually, 10^6–3×10^7 A/cm^2). The joint action of longitudinal spin injection and torque lowers the instability threshold. Current-induced spin injection decreases spin wave frequencies near the threshold and can strengthen magnetization pinning at the injecting contact. © *2005 Pleiades Publishing, Inc.*

1. INTRODUCTION

In recent years, considerable attention has been given to the special features of current flowing through so-called ferromagnetic junctions, that is, layered structures with contacting thin ferromagnetic layers. Experiments showed that current can influence the magnetic state of layers in these junctions substantially. This leads to characteristic resistance jumps [1–3] and microwave radiation emission [4–6].

The mechanism of the influence of current on the junction magnetic state still remains incompletely understood. The mechanism suggested in [7] explains the effect of current on the ferromagnetic layer magnetization **M** by the injection of nonequilibrium longitudinal (i.e., collinear with **M**) spins into the layer. The corresponding theory was formulated in [8–10]. Injection creates nonequilibrium carrier spin polarization in the layer. This polarization in turn contributes to the s–d exchange energy $U_{s-d}(\mathbf{j})$ and the corresponding effective s–d exchange field $\mathbf{H}_{s-d}(\mathbf{j})$, which depend on the electric current density **j**. Above some threshold current density, a first-order reorientation phase transition in the field $\mathbf{H}_{s-d}(\mathbf{j})$ occurs and the magnetization vector **M** direction changes jumpwise. This current-induced magnetization reversal (or current-induced magnetization switching) leads to electrical resistance jumps, in close agreement with the experimental data [1–3].

Another mechanism was suggested in [11, 12] to describe current effects on the state of ferromagnetic layers long before the experimental data [1–6] appeared. According to this mechanism, the flux of transverse (with respect to **M**) electron spins must disappear near the interface between two noncollinear ferromagnets. Because of the interaction of mobile electrons with the magnetic lattice (s–d exchange interaction), a torque appears at the interface. This torque acts on the lattice and turns the disappearing spin current to it. As a result, the total spin flux of mobile electrons and the lattice remains continuous at the interface.

In addition to this torque proportional to the current, a dissipation-induced moment acts on the **M** vector to restore magnetic equilibrium. The dissipation effect should eventually be outbalanced by the torque moment as the current density **j** increases. Equilibrium then becomes unstable, and the reorientation of the magnetization vector occurs. Estimates show that such a magnetization switching mechanism is also in agreement with the experimental data [1–6].

It was assumed in original works [11, 12] that the transverse electron spin flux disappeared under ballistic transport conditions. The opposite limiting case, that of the predominance of diffusion transport, was considered in [13, 14]. In this work, we, however, follow the approach suggested in [11, 12] and assume that transport in the immediate vicinity of the interface can be considered ballistic. The quantitative criteria of the validity of this assumption are presented in Section 2.

An important question arises concerning the situation with real experiments when both effects coexist, namely, longitudinal spin injection and the corresponding current-dependent effective field on the one hand and current-dependent torque at the interface in a mag-

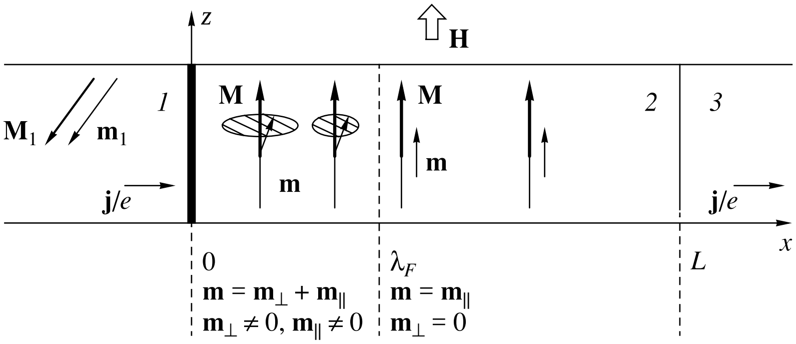

Fig. 1. Scheme of the magnetic junction under consideration illustrating processes in layer *2*. *1*, *2*, and *3* are the contacting layers. The arrows show the directions of the vectors $\mathbf{M}_1$ and $\mathbf{m}_1$ (magnetizations in layer *1*), **M** and **m** (magnetizations in layer *2*), **H** (external magnetic field in the $x = 0$ junction plane), and $\mathbf{j}/e$ (electron flux density). The vertical dashed lines are the boundaries of two sublayers in layer *2*. In the $0 \le x \le \lambda_F$ sublayer, there is precession conventionally shown by ovals. The **m** vector then has both the longitudinal $\mathbf{m}_\parallel$ and transverse $\mathbf{m}_\perp$ components. The precession angle decreases as x increases. In the $x > \lambda_F$ sublayer, precession stops and only one of the **m** vector components specified above (the longitudinal component) remains.

netic junction on the other. Previously, these effects were always studied separately. They, however, not only coexist but influence each other. Therefore, to understand the experimental situation better, the two effects must be taken into consideration simultaneously within the scope of a unified theory. This is the approach taken in the present paper.

Two points should be mentioned. First, a theoretical description of the “anatomy” of the torque is a rather difficult microscopic quantum problem, as follows from original [11, 12] and other works, including paper [15], specially concerned with such a description. Undoubtedly, a solution to this problem would be of great interest in itself. In our view, applying this approach to construct the desired unified theory would, however, be an excessive complication. We think it more reasonable to take advantage of the difference between the spatial scales of the action of the two factors under consideration (spin injection and torque). The torque is a purely surface effect. According to [11, 12], it acts near the interface at distances d from the interface between ferromagnetic layers. These distances are of the same order of magnitude as the electron quantum wave length on the Fermi surface, $\lambda_F \sim 1$ nm. On the other hand, nonequilibrium longitudinal spins are injected inside a film much more deeply, by the spin diffusion length l ($l \approx 10$–100 nm for ferromagnetic metals at room temperature). It follows that spin injection is to a much greater degree a volume effect than the torque. Spin injection is therefore described below by solving a system of coupled equations for mobile electrons and the lattice magnetization vector **M** in the bulk of the ferromagnetic layer, while the torque is included as a boundary condition for these equations. We show that such a boundary condition can be obtained rather easily from the condition of total spin flux conservation.

Next, some comments should be made concerning the methodology of this work. Earlier (e.g., see [8–10]), we used the variational principle of minimum magnetic energy. In this work, the problem is solved purely dynamically on the basis of the linearized Landau–Lifshitz–Gilbert equations. In [8–10], we described a spin injection-induced reorientation phase transition which corresponded to the energy minimum disappearance without taking the surface torque into account. We show below that torque-induced instability has no bearing on phase transitions and energy minima. Rather, it is caused by the energy generation mechanism that exceeds dissipative loss. We must therefore use the most general approach based on the equations of motion to describe both types of instability simultaneously. The approaches mentioned above are equivalent when applied to the purely injection mechanism [9]. This conclusion is substantiated by the calculations performed in the present work.

2. A MAGNETIC JUNCTION MODEL

Let us consider a spin-valve-type magnetic junction with current flowing normally to layer interfaces (see Fig. 1). The junction contains ferromagnetic layer *1* with a fixed orientation of the lattice and free electron spins. This orientation is attained most effectively if there is fairly strong induced magnetic anisotropy in layer *1* and layer *1* is made of a semimetal in which only one of the two spin subbands participates in conduction [16]. Another ferromagnetic metal layer *2* with magnetization **M** is assumed to contain free spins, and the magnetization direction can change in it under the action of external magnetic field **H** or spin-polarized current **j**. There is a very thin nonmagnetic spacer between layers *1* and *2* (shown by a thick line in Fig. 1). The electric circuit is closed by nonmagnetic metal layer *3*.

The plane $x = 0$ is the interface between layers *1* and *2*. Within layer *1*, the lattice $\mathbf{M}_1$ and mobile electron $\mathbf{m}_1$ magnetization vectors are collinear, and it is assumed that $\mathbf{M}_1$ is parallel to the $x = 0$ plane. The angle between the $\mathbf{M}_1$ and $\mathbf{M}$ vectors can be nonzero, $\chi \neq 0$. The electrons transferred by the current into layer *2* are therefore in a nonstationary quantum state near the $x = 0$ boundary and "migrate" between the spin subbands. This corresponds to precession of the mobile electron $\mathbf{m}$ and lattice $\mathbf{M}$ magnetizations (Fig. 1). According to [11, 12], the spin of every electron precesses with its own initial phase

$$\varphi(d) = [k_{x\uparrow} - k_{x\downarrow}]d, \tag{1}$$

which depends on the distance d between the electron and the interface. In (1), the $k_{x\uparrow}$ and $k_{x\downarrow}$ values are the electron wave vector $\mathbf{k}$ components in the spin-up (along $\mathbf{M}$) and spin-down subbands. Because of the statistical spread of electron velocities, the term in square brackets in (1) changes in magnitude from 0 to $2\pi/\lambda_F$, where λ_F is the wavelength on the Fermi surface. Phase (1) is therefore distributed within the interval $0 \leq \varphi \leq 2\pi$ at $d = \lambda_F$. Since the transverse (with respect to $\mathbf{M}$) component $\mathbf{m}_\perp$ of the $\mathbf{m}$ vector is the sum of the transverse components of individual electrons $\delta\mathbf{m}_\perp$, the terms of this sum almost exactly cancel each other, and we have

$$\mathbf{m}_\perp = \sum \delta\mathbf{m}_\perp \longrightarrow 0. \tag{2}$$

We stress that $l \gg \lambda_F$, and spin relaxation therefore has no influence on the fulfillment of condition (2). In addition, this condition was derived on the assumption of ballistic electron motion conditions in the $0 \leq x \leq \lambda_F$ layer. The $\mathbf{k}$ vector therefore does not change as a result of collisions. This is valid if $l_p > \lambda_F$, where l_p is the momentum mean free path. Typically, $l_p \sim 1$–10 nm and $\lambda_F \sim 1$ nm. The ballistic motion conditions can therefore be well satisfied. Layer *2* is further assumed to be rather extended and have thickness $L \gg \lambda_F, l_p$.

Corollaries to (2) are two conclusions important for what follows.

(1) Precession in layer *2* stops at a small distance $d \sim \lambda_F \sim 1$ nm from the interface separating layers *1* and *2*. As a result, the transverse component of mobile electron magnetization and the related spin flux disappear. According to [11, 12], this is the reason for the appearance of a torque, which acts on the lattice and ensures continuity of the flux of the transverse component of the total magnetization ($\mathbf{M}_\perp + \mathbf{m}_\perp$).

2) At $x > d \sim \lambda_F$, the mobile electrons adapt themselves to the new quantization axis direction (vector $\mathbf{M}$ direction) and occupy spin subbands new for them. The subband populations, however, depend on the current and are far from equilibrium. They are determined by the continuity condition for the longitudinal component of the mobile electron magnetization flux (vector $\mathbf{m}_\parallel$ flux) across the interface. The longitudinal flux component does not change at distances $x \ll l$ from the interface. This is the spin injection effect considered for the first time, we believe, in [17]. In essence, it is similar to the well-known charge injection effect in semiconductors [18].[1] According to typical parameter estimates, $l \gg l_p$, and the motion of injected electrons deep in layer *2* occurs under diffusion conditions.

3. BASIC EQUATIONS

Let us consider processes in layer *2*. They are described by a system of dynamical equations for the magnetization vectors $\mathbf{M}$ and $\mathbf{m}$. The lattice magnetization[2] $\mathbf{M}$ obeys the Landau–Lifshitz–Gilbert equation

$$\frac{\partial \mathbf{M}}{\partial t} = -\gamma[\mathbf{M} \times \mathbf{H}_{\text{eff}}] + \frac{\kappa}{M}\left[\mathbf{M} \times \frac{\partial \mathbf{M}}{\partial t}\right], \tag{3}$$

where γ is the gyromagnetic ratio, κ is the dimensionless damping constant ($0 < \kappa \ll 1$), t is the time, and $\mathbf{H}_{\text{eff}}$ is the effective field

$$\mathbf{H}_{\text{eff}} = \mathbf{H} + \beta(\mathbf{M} \cdot \mathbf{n}) \cdot \mathbf{n} + A\frac{\partial^2 \mathbf{M}}{\partial x^2} + \mathbf{H}_{s-d} + \mathbf{H}_d. \tag{4}$$

Here, β is the dimensionless anisotropy constant, $\mathbf{n}$ is the unit vector along the anisotropy axis, A is the inhomogeneous exchange constant, $\mathbf{H}_d$ is the demagnetizing field, and $\mathbf{H}_{s–d}$ is the effective s–d exchange field. According to the definitions given in [20], $\mathbf{H}_{s–d}$ has the form

$$\mathbf{H}_{s-d}(x, t) = -\frac{\delta U_{s-d}}{\delta \mathbf{M}(x, t)}, \tag{5}$$

where $\delta/\delta\mathbf{M}(x, t)$ is the variational derivative. The s–d exchange energy is given by

$$U_{s-d} = -\alpha\int_0^L dx'\mathbf{m}(x', t)\mathbf{M}(x', t), \tag{6}$$

where α is the dimensionless s–d exchange interaction constant (typically, $\alpha \sim 10^4$–10^6 [8]). Term (5) in (4) couples the oscillations of the $\mathbf{M}$ and $\mathbf{m}$ vectors.

The magnetization $\mathbf{m}$ of mobile electrons obeys the general continuity equation [17, 21]

$$\frac{\partial \mathbf{m}}{\partial t} + \frac{\partial \mathbf{J}}{\partial x} + \gamma\alpha[\mathbf{m} \times \mathbf{M}] + \frac{\mathbf{m} - \bar{\mathbf{m}}}{\tau} = 0, \tag{7}$$

where τ is the time of relaxation to the locally equilibrium $\bar{\mathbf{m}} = \bar{m} \cdot \hat{\mathbf{M}}$ value, $\hat{\mathbf{M}} \equiv \mathbf{M}/M$ is the unit vector,

---

[1] Spin injection can be induced not only by current, as in [17] or the present work, but also by polarized light (e.g., see review [19]). It appears that the spin injection concept can acquire great significance in the future, comparable to that of charge injection in semiconductor devices.

[2] We mean the lattice of magnetic ions described in the continuous medium approximation.

and **J** is the magnetization flux density. For subsequent estimations, let us substitute $\partial\mathbf{m}/\partial t = \omega\Delta\mathbf{m}$, where $\Delta\mathbf{m} \equiv \mathbf{m} - \overline{\mathbf{m}}$ and ω is the effective frequency of vector **m** oscillations in time, into (7).

According to Section 2, the vector **m** precesses at a high rate in the *s–d* exchange field. Therefore, $\omega \sim \gamma\alpha M \equiv \omega_{s-d}$. At the typical parameter values $\alpha \sim 2 \times 10^4$, $M \sim 10^3$ G, and $\tau \sim 3 \times 10^{-13}$ s, we have $\omega_{s-d}\tau \sim 10^2 \gg 1$. The last relaxation term in (7) can therefore be ignored. We can then calculate the products $(\Delta\mathbf{m} \cdot \mathbf{M})$ and $[\Delta\mathbf{m} \times \mathbf{M}]$ using (7). Solving (7) with respect to $\Delta\mathbf{m}$, now explicitly present in it, yields

$$\Delta\mathbf{m} = -\omega^{-1} \times \frac{\partial\mathbf{J}/\partial x + \zeta[\hat{\mathbf{M}} \times \partial\mathbf{J}/\partial x] + \zeta^2\hat{\mathbf{M}}(\hat{\mathbf{M}} \cdot \partial\mathbf{J}/\partial x)}{1 + \zeta^2}. \tag{8}$$

Here, we introduced the parameter $\zeta = \omega_{s-d}\omega^{-1} \sim 1$. It follows from (8) and an estimate for this parameter that the longitudinal and transverse (with respect to **M**) $\Delta\mathbf{m}$ components can be comparable in magnitude, which is in agreement with the picture of electronic spin precession in the boundary sublayer (see Section 2).

A detailed analysis of the motion of spins in this sublayer is, however, impeded, because it involves calculations of the flux **J** expressing it via the **m** vector. In the sublayer $0 \le x < \lambda_F$, this would require additionally solving an equation for the spin density matrix, because the electrons are in a quantum nonstationary and inhomogeneous state. We shall circumvent this difficulty and show (see Section 4) that solving such a quantum problem is not necessary for our purposes and can be replaced by the introduction of some new boundary condition.

We must perform a detailed analysis of motions for the $x > \lambda_F$ sublayer. The **m** and **M** vectors in this sublayer should be almost collinear. Accordingly, the effective frequency ω should be determined by the precession of the **M** vector in comparatively low fields H, βM, $H_d \ll \alpha M$. We suggest the fulfillment of the condition

$$\omega\tau \ll 1. \tag{9}$$

This allows us to ignore the derivative with respect to time compared with the relaxation term (Eq. (7)). The representation of $\Delta\mathbf{m}$ in form (8) then remains valid, but we must replace ω^{-1} with τ and ζ with $\omega_{s-d}\tau \gg 1$. As a result, the estimates of the terms in (8) change. The last term in the numerator of (8) becomes predominant, and we can write

$$\Delta\mathbf{m} = -\tau\hat{\mathbf{M}}(\hat{\mathbf{M}} \cdot \pi\partial/\partial x). \tag{10}$$

This substantiates the validity of the suggestion that the $\Delta\mathbf{m}$ (therefore, the whole **m**) and **M** vectors are collinear. The transverse **m** components nevertheless exist, but they are small with respect to the $(\omega_{s-d}\tau)^{-1} \sim 10^{-2} \ll 1$ parameter and will be ignored below.

The mobile electrons occupy two spin subbands in the $x > \lambda_F$ sublayer, with spins up (parallel to **M**) and down (antiparallel to **M**). The magnetization **m** contains contributions from these two subbands and can be represented as

$$\mathbf{m} = \mu_B(n_\uparrow - n_\downarrow)\hat{\mathbf{M}} \equiv m\hat{\mathbf{M}}, \tag{11}$$

where μ_B is the Bohr magneton and $n_{\uparrow,\downarrow}$ are the partial electron densities in the spin subbands. The total electron density $n = n_\uparrow + n_\downarrow$ is independent of x and t by virtue of the local metal neutrality condition. The magnetization flux **J** in (10) can also be related to the partial electric current densities in the subbands, $j_\uparrow$ and $j_\downarrow$. Clearly, the corresponding equation has the form

$$\mathbf{J} = \frac{\mu_B}{e}(j_\uparrow - j_\downarrow)\hat{\mathbf{M}}. \tag{12}$$

The total current $j = j_\uparrow + j_\downarrow$ is also independent of x and t because of the one-dimensional character of our model.

Let us consider a simple situation when the *s–d* exchange gap in layer *2* is independent of x and t and, therefore, the $\hat{\mathbf{M}}$ vector direction. In addition, the transport relaxation times in metals are rather short at room temperatures, and the current can therefore be represented by the drift and diffusion terms. Spin current (12) calculations were performed in [9] on these assumptions. Substituting the well-known equations for the partial currents into (12) and following the procedure for calculations described in [9], we obtain

$$\mathbf{J} = \left(\frac{\mu_B}{e}Qj - \tilde{D}\frac{\partial m}{\partial x}\right)\hat{\mathbf{M}}, \tag{13}$$

where $Q = (\sigma_\uparrow - \sigma_\downarrow)/(\sigma_\uparrow + \sigma_\downarrow)$ is the current spin polarization and $\tilde{D} = (\sigma_\uparrow D_\downarrow + \sigma_\downarrow D_\uparrow)/(\sigma_\uparrow + \sigma_\downarrow)$ is the spin diffusion coefficient. Here, $\sigma_\uparrow$, $\sigma_\downarrow$ and $D_\uparrow$, $D_\downarrow$ are the specific partial conductivities and diffusion coefficients, respectively, for the electrons with spins up and down. To obtain (13), we in addition assumed that

$$\frac{j}{j_D} \ll 1, \tag{14}$$

where $j_D \equiv enl/\tau$ is the characteristic current density in layer *2*. Condition (14) means that the current disturbs subband populations comparatively weakly, and the level of spin injection is low. Substituting the typical parameter values $n \sim 10^{22}$ cm^{-3}, $l \sim 3 \times 10^{-6}$ cm and $\tau \sim 3 \times 10^{-13}$ s into (14) yields $j_D \sim 1.6 \times 10^{10}$ A/cm^2. Below, our concern will be much lower currents $j \le 10^7$–10^8 A/cm^2, because such is the order of magnitude of the instability thresholds obtained in this study. Therefore, condition (14) is more than well satisfied in our calculations.

It remains to substitute flux (13) into representation (10) of equation of motion (7). This yields

$$\frac{\partial^2 m}{\partial x^2} - \frac{m - \bar{m}}{l^2} = 0, \tag{15}$$

where the $m(x, t)$ function is defined in (11) and its locally equilibrium value $\bar{m}$ is defined in the comments to (7). As the *s–d* exchange gap is fixed, $\bar{m}$ should be considered independent of x and t. The spin diffusion length is $l = \sqrt{\tilde{D}\tau}$.

4. BOUNDARY CONDITIONS

We must now determine what solutions to basic dynamic equations (3) and (15) should be sought. This will be done by deriving boundary conditions for these equations. The derivation will be based on the continuity condition for the total magnetization flux (mobile electron plus lattice magnetization fluxes) at interlayer boundaries.

Since the lattice in layer *1* is pinned, the magnetization flux $\mathbf{J}_1$ in this layer is only caused by the transfer of mobile electron spins induced by the electric current $\mathbf{j}$. The magnetization flux is then given by an equation similar to (13) but without the second term containing the derivative with respect to the coordinate. Indeed, the magnetization vector of mobile electrons is fixed in layer *1* and cannot change depending on x. The flux $\mathbf{J}_1$ therefore takes the form

$$\mathbf{J}_1 = \frac{\mu_B}{e} Q_1 j \hat{\mathbf{M}}_1, \tag{16}$$

where $\hat{\mathbf{M}}_1 = \mathbf{M}_1/|\mathbf{M}_1|$ and Q_1 is defined as Q in (13) but with the partial conductivities and diffusion coefficients for layer *1*. Flux (16) has longitudinal and transverse components with respect to the $\hat{\mathbf{M}}$ vector; these are

$$\mathbf{J}_{1\parallel} = \frac{\mu_B}{e} Q_1 j (\hat{\mathbf{M}}_1 \cdot \hat{\mathbf{M}}) \hat{\mathbf{M}}, \tag{17}$$

$$\mathbf{J}_{1\perp} = \frac{\mu_B}{e} Q_1 j [\hat{\mathbf{M}} \times [\hat{\mathbf{M}}_1 \times \hat{\mathbf{M}}]]. \tag{18}$$

Longitudinal spin relaxation is absent in the $0 \le x < \lambda_F$ sublayer. The longitudinal flux (16) component should therefore coincide with flux (13) close to the $x = 0$ interface. Let us write this equality of fluxes explicitly and find the scalar products of its both sides by $\hat{\mathbf{M}}$ taking into account that $\hat{\mathbf{M}}_1 = -\hat{\mathbf{y}} \sin\chi + \hat{\mathbf{z}} \cos\chi$, where $\hat{\mathbf{x}}$, $\hat{\mathbf{y}}$, and $\hat{\mathbf{z}}$ are the unit vectors along the coordinate axes. We then find that the equality

$$\begin{aligned} &\frac{\mu_B}{e} Q_1 j (-\hat{M}_y \sin\chi + \hat{M}_z \cos\chi) \\ &\qquad = \frac{\mu_B}{e} Q j - \tilde{D} \frac{\partial m}{\partial x} \end{aligned} \tag{19}$$

should be satisfied at $x = 0$. This is the first boundary condition for our problem.

The second boundary condition is obtained taking into account that the transverse component of the mobile electron magnetization flux disappears in the sublayer $0 \le x < \lambda_F$ (see (2) and comments to it). The condition of the total (mobile electron and lattice) flux continuity therefore requires that flux (18) continue in layer *2* as a lattice magnetization flux. The equation for this flux is derived in Appendix I (see (I.4)). Equating it to (18) at $x = 0$ yields

$$\frac{\mu_B}{e} Q_1 j [\hat{\mathbf{M}} \times [\hat{\mathbf{M}}_1 \times \hat{\mathbf{M}}]] = aM \left[\hat{\mathbf{M}} \times \frac{\partial \hat{\mathbf{M}}}{\partial x}\right], \tag{20}$$

where $a = \gamma MA$ according to Appendix I. Condition (19) in a slightly different form was discussed and applied earlier (e.g., see [9]). As concerns condition (20), it is likely new. In the selected coordinate system (see Fig. 1), condition (20) gives two independent equations valid at $x = 0$,

$$\begin{aligned} \frac{\partial \hat{M}_x}{\partial x} + k\hat{M}_y \cos\chi + k\hat{M}_z \sin\chi &= 0, \\ \frac{\partial \hat{M}_y}{\partial x} - k\hat{M}_x \cos\chi &= 0, \end{aligned} \tag{21}$$

where $k = \mu_B Q_1 j / eaM$ and the component $\hat{M}_z$ can be found from the equality $|\hat{\mathbf{M}}| = 1$.

Next, let us consider the interface between layers *2* and *3* at $x = L$. Layer *3* is nonmagnetic, and $Q_3 = 0$. The continuity condition for the longitudinal flux therefore gives

$$\frac{\mu_B}{e} Q j - \tilde{D} \frac{\partial m}{\partial x} = -\tilde{D}_3 \frac{\partial m_3}{\partial x} \tag{22}$$

at $x = L$. Since lattice magnetization is absent in layer *3*, the lattice magnetization flux should disappear at this interface; that is, $aM[\hat{\mathbf{M}} \times (\partial \hat{\mathbf{M}}/\partial x)] = 0$, or, in terms of the vector components,

$$\frac{\partial \hat{M}_x}{\partial x} = 0, \quad \frac{\partial \hat{M}_y}{\partial x} = 0 \tag{23}$$

at $x = L$.

Several other important conditions are related to the exchange of mobile electrons through interlayer boundaries. This exchange should ensure continuity of the differences in the chemical potentials of spin subbands on the two sides of the interfaces. We ignore the thermal spread of the Fermi distribution for electrons in both subbands. Direct calculations then give the following equation for the difference of the chemical potentials:

$$\begin{aligned}&\zeta_\uparrow - \zeta_\downarrow \\ &= (2\mu_B)^{-1}\left(\frac{1}{g_\uparrow(\bar{\zeta})} + \frac{1}{g_\downarrow(\bar{\zeta})}\right)\Delta m \equiv N\Delta m,\end{aligned} \tag{24}$$

where $g_{\uparrow,\downarrow}$ are the energy-dependent partial densities of electron states in the subbands and $\bar{\zeta}$ is the equilibrium chemical potential value. The continuity condition for (24) at the interface between layers *2* and *3* is

$$\Delta m N = \Delta m_3 N_3. \tag{25}$$

The chemical potential difference has a discontinuity at the interface between layers *1* and *2*. This discontinuity appears because our model idealizes layer *1*. Recall that we assume all spins to be strictly fixed in this layer.

Let us find the solution to (15) that satisfies boundary conditions (19), (22), and (25). This yields the following injected magnetization distribution $\Delta m(x)$ in layer *2*:

$$\begin{aligned}\Delta m(x) &= \left(\frac{j}{j_D}\right)\frac{\mu_B n}{\sinh\lambda + \nu\cosh\lambda} \\ &\times \{Q\cosh\xi + [Q_1(-\hat{M}_y\sin\chi + \hat{M}_z\cos\chi) - Q] \\ &\times [\cosh(\lambda - \xi) + \nu\sinh(\lambda - \xi)]\}.\end{aligned} \tag{26}$$

Equation (26) contains dimensionless lengths $\lambda = L/l$ and $\xi = x/l$. The parameter

$$\nu = \frac{nN}{n_3N_3}\frac{j_{D3}}{j_D} \tag{27}$$

describes the influence of layer *3*.

5. THE STATIC STATE AND FLUCTUATIONS

Let an external field **H** be applied in the positive direction of axis **z** and the anisotropy field be also parallel to this axis. Then clearly, magnetization in layer *2* is aligned with **z** in the absence of current, when the layers in our model are not coupled.

With current switched on, spins flow through the interfaces $x = 0, L$. This creates a connection between layers *1*, *2* and *3* and can change the magnetization direction in layer *2*. To describe this process, let us calculate the U_{s-d} energy by substituting (26) into (6). This yields

$$\begin{aligned}U_{s-d} &= -\alpha\bar{m}ML - \alpha(\hat{\mathbf{M}}_1\cdot\mathbf{M}(+0))l \\ &\times \mu_B n Q_1\left(\frac{j}{j_D}\right)\left(1 - \frac{\nu}{\sinh\lambda + \nu\cosh\lambda}\right).\end{aligned} \tag{28}$$

Here, we ignore corrections on the order of the j/j_D ratio, which is small (see (14)), in the first term proportional to M. Calculations of variational derivative (5) require representing (28) as a functional of the $\mathbf{M}(x)$ vector. We then obtain

$$\begin{aligned}\frac{\delta}{\delta\mathbf{M}(x)}(ML) &= \frac{\delta}{\delta\mathbf{M}(x)}\int_0^L M dx' \\ &= \int_0^L \hat{\mathbf{M}}(x')\delta(x' - x)dx' = \hat{\mathbf{M}}(x),\end{aligned} \tag{29}$$

$$\frac{\delta}{\delta\mathbf{M}(x)}(\hat{\mathbf{M}}_1\cdot\mathbf{M}(+0)) = \hat{\mathbf{M}}_1\delta(x - \varepsilon)$$

as $\varepsilon \longrightarrow +0$. Equations (28) and (29) can be used to calculate the *s–d* exchange field according to (5),

$$\begin{aligned}\mathbf{H}_{s-d}(x) &= \alpha\bar{m}\hat{\mathbf{M}}(x) + \alpha\hat{\mathbf{M}}_1\mu_B n Q_1\left(\frac{j}{j_D}\right) \\ &\times \left(1 - \frac{\nu}{\sinh\lambda + \nu\cosh\lambda}\right) l\delta(x - \varepsilon).\end{aligned} \tag{30}$$

The first term in (30) is directed along **M** and therefore drops out of equation of motion (3). The second term is directed along $\mathbf{M}_1$. If the angle χ is arbitrary, this term and, on the whole, the $\mathbf{H}_{s-d}$ and effective $\mathbf{H}_{\text{eff}}$ (4) fields can be not aligned with axis **z**. Clearly, the magnetization $\bar{\mathbf{M}}$ in the static state, which is found from the equation $\bar{\mathbf{M}} \times \mathbf{H}_{\text{eff}} = 0$, can also deviate from **z**. In addition, by virtue of boundary conditions (21), the magnetization $\bar{\mathbf{M}}$ is inhomogeneous within layer *2*. Moreover, the Landau–Lifshitz–Gilbert equation for $\bar{\mathbf{M}}$ is nonlinear, which creates serious difficulties.

However, fortunately, there are two definite angles χ ($\chi = 0, \pi$) for which the vector $\bar{\mathbf{M}}$ can easily be found. Indeed, at these angles, (21) and (23) are satisfied for the *x*-independent vector $\bar{\mathbf{M}}$, whose components are $\bar{M}_x = 0$ and $\bar{M}_y = 0$. In addition, the vector $\mathbf{M}_1$ is parallel to the **z** axis, and equation of motion (3) is therefore also satisfied in the static state. At $\chi = 0, \pi$, we obtain

$$\bar{M}_x = \bar{M}_y = 0 \text{ and } \bar{M}_z = M > 0. \tag{31}$$

Our further analysis will be limited to consideration of the specified angles only; that is, we will study the stability of static state (31). In particular, we have $\mathbf{M}_1 = M_1\mathbf{z}$ at $\chi = \pi$, where $M_1 = \cos\pi|\mathbf{M}_1| = -|\mathbf{M}_1| < 0$.

For calculation purposes, the δ function in (30) can conveniently be replaced by the finite function

$$\delta(x-\varepsilon) \longrightarrow \frac{1}{r}\exp\left(-\frac{x}{r}\right), \tag{32}$$

bearing in mind the subsequent passage to the limit $r \longrightarrow +0$. The right-hand side of (32) is then nonzero only at $x = 0$. In addition, the integral of (32) in x over the interval $0 \le x < \infty$ is 1. Let us introduce fluctuations $\Delta\mathbf{M}$ as

$$\mathbf{M} = M\hat{\mathbf{z}} + \Delta\mathbf{M}. \tag{33}$$

The linearization of Landau–Lifshitz–Gilbert equations (3) with respect to $\Delta\mathbf{M}$ and the substitution of exchange field (30) and the demagnetization field $\mathbf{H}_d = -4\pi\Delta M_x \cdot \hat{\mathbf{x}}$ into these equations yields

$$\begin{gathered}\frac{\partial\Delta M_x}{\partial t} + \kappa\frac{\partial\Delta M_y}{\partial t} = a\frac{\partial^2\Delta M_y}{\partial x^2} \\ -\left(\Omega_y - \gamma B\frac{l}{r}\exp\left(-\frac{x}{r}\right)\right)\Delta M_y, \\ \frac{\partial\Delta M_y}{\partial t} - \kappa\frac{\partial\Delta M_x}{\partial t} = -a\frac{\partial^2\Delta M_x}{\partial x^2} \\ +\left(\Omega_x - \gamma B\frac{l}{r}\exp\left(-\frac{x}{r}\right)\right)\Delta M_x.\end{gathered} \tag{34}$$

Here, we use the notation

$$\begin{aligned}\Omega_x &= \gamma(H + \beta M + 4\pi M), \\ \Omega_y &= \gamma(H + \beta M),\end{aligned} \tag{35}$$

$$B = \alpha\frac{\mu_B jl}{e\tilde{D}}Q_1\left(1 - \frac{\nu}{\sinh\lambda + \nu\cosh\lambda}\right). \tag{36}$$

The coefficients of (34) contain x as an independent variable. It can conveniently be replaced with the use of the equalities

$$y = b\exp\left(-\frac{x}{2r}\right), \quad b = 2\sqrt{\frac{\gamma Blr}{a}}. \tag{37}$$

For the temporal Fourier components ΔM_x, $\Delta M_y \sim \exp(-i\omega t)$, we obtain

$$\begin{gathered}y^2\frac{\partial^2\Delta M_x}{\partial y^2} + y\frac{\partial\Delta M_x}{\partial y} \\ +\left(y^2 - \frac{4r^2\Omega_x}{a} + \frac{4r^2}{a}i\kappa\omega\right)\Delta M_x = \frac{4r^2}{a}i\omega\Delta M_y, \\ y^2\frac{\partial^2\Delta M_y}{\partial y^2} + y\frac{\partial\Delta M_y}{\partial y} \\ +\left(y^2 - \frac{4r^2\Omega_y}{a} + \frac{4r^2}{a}i\kappa\omega\right)\Delta M_y = -\frac{4r^2}{a}i\omega\Delta M_x.\end{gathered} \tag{38}$$

Equations (38) are close in structure to the equations for the Bessel function. The ΔM_x and ΔM_y components are, however, coupled with each other in both equations (38). To uncouple them, consider the system

$$\begin{aligned}\left[s^2 - \frac{4r^2}{a}(\Omega_x - i\kappa\omega)\right]\Delta M_x - \frac{4r^2}{a}i\omega\Delta M_y &= 0, \\ \left[s^2 - \frac{4r^2}{a}(\Omega_y - i\kappa\omega)\right]\Delta M_y + \frac{4r^2}{a}i\omega\Delta M_x &= 0.\end{aligned} \tag{39}$$

The solvability condition for (39) yields the s^2 parameter in the form

$$s^2 = \frac{2r^2}{a}\left[\Omega_x + \Omega_y - 2i\kappa\omega \pm \sqrt{(\Omega_x - \Omega_y)^2 + 4\omega^2}\right]. \tag{40}$$

It follows from (40) that there are two different s^2 values. Each of them corresponds to a certain type of fluctuation and should therefore be included in stability analysis. Let us take some solution to (40), substitute it into (39), and use these equations to exclude the ΔM_y component from the first and ΔM_x from the second equation in (38). As a result, both equations in (38) transform into the standard equation for Bessel functions with index s. The general solution to (38) can therefore be written as

$$\Delta M_{x,y}(y) = A_{x,y}J_s(y) + B_{x,y}Y_s(y), \tag{41}$$

where J_s and Y_s are the Bessel functions of the first and second kind, respectively [22], and $A_{x,y}$ and $B_{x,y}$ are constants that must be found from boundary conditions (21) and (23) at $\chi = \pi$. The solvability condition for the equations for the four constants $A_{x,y}$ and $B_{x,y}$ is given in Appendix II. The passage to the limit $r \longrightarrow +0$ (its possibility is provided by substitution (32)) is also performed in Appendix II. As a result, we obtain the following dispersion equation for fluctuations:

$$qL\tan qL = \Phi, \tag{42}$$

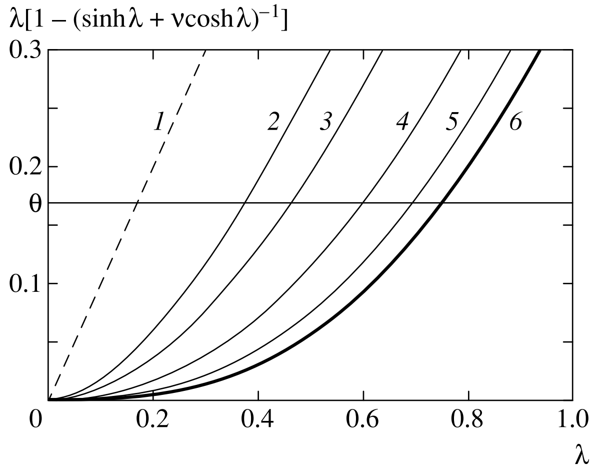

Fig. 2. Diagram for determining junction parameters corresponding to various values of the effective lattice spin pinning parameter $|\Phi|$. We have $|\Phi| = 1$ at the $\theta(j)$ level, $|\Phi| < 1$ below this level, and $|\Phi| > 1$ above this level; ν parameter values: (*1*) 0, (*2*) 0.5, (*3*) 1.0, (*4*) 3.0, (*5*) 10, and (*6*) ∞.

where

$$\Phi = -\frac{\gamma B L^2}{a\lambda} \pm ikL, \tag{43}$$

and the $q \equiv is/2r$ parameter determined by (40) further plays the role of the wavenumber. Equation (42) coincides in form with the well-known dispersion equation for standing spin waves in layer *2* [20, 23]. The right-hand side (Φ) has the meaning of the effective lattice spin pinning parameter at the end layer surfaces (at the $x = 0$ plane of our model). We stress that, in our model, there is spin pinning at the boundaries in the absence of a current, as directly follows from boundary conditions (21) and (23). Effective pinning nevertheless occurs under the action of the current *j*. According to (43), the real part of Φ describes pinning caused by the effective exchange field, and the imaginary part describes effective pinning caused by the torque. Note that experimental studies of spin wave resonance absorption in magnetic junctions could give important information about the character of surface spin pinning.

We will use dispersion equation (42) to calculate the complex eigenfrequency ω of fluctuations under consideration and determine instability conditions, that is, the conditions under which $\mathrm{Im}\,\omega \geq 0$.

6. INSTABILITY OF FLUCTUATIONS

Let us analyze solutions to (42). The simplest situation corresponds to the absence of a current. By definition of *B* and *k* in (36) and (21), it follows from (43) that the right-hand side $\Phi = 0$ at $j = 0$. This corresponds to spin wave resonance when spins at the end surfaces are not pinned. The solutions to (42) are then

$$qL = n\pi \quad \text{and} \quad \omega = \sqrt{\left(\Omega_x + a\frac{n^2\pi^2}{L^2}\right)\left(\Omega_y + a\frac{n^2\pi^2}{L^2}\right)} - \frac{i\kappa}{2}\left(\Omega_x + \Omega_y + 2a\frac{n^2\pi^2}{L^2}\right), \tag{44}$$

where $n = 0, \pm 1, \pm 2, \ldots$. Expressions (44) are obtained using the definition $q \equiv is/2r$ and Eq. (40). Since $\mathrm{Im}\,\omega < 0$ in (44), fluctuations are stable because of dissipation in the absence of a current.

Next, let a current be turned on and j/e be larger than 0. According to (43), we then have

$$\mathrm{Im}\Phi/\mathrm{Re}\Phi = \kappa\eta \ll 1, \tag{45}$$

where

$$\eta \equiv \left[a\gamma M\tau\kappa\left(1 - \frac{\nu}{\sinh\lambda + \nu\cosh\lambda}\right)\right]^{-1}. \tag{46}$$

Parameter (46) can be smaller than, on the order of, or larger than one. We show below that it is this parameter that describes the relation between the torque and spin injection contributions to the current-induced instability threshold and increment. As dissipation is weak, that is, $\kappa \ll 1$, the strong inequality in (45) is, as a rule, fulfilled.

Bearing in mind (45), let us estimate the right-hand side of (42). We have

$$|\Phi| \approx \mathrm{Re}\Phi = \lambda\left(1 - \frac{\nu}{\sinh\lambda + \nu\cosh\lambda}\right)\theta^{-1}(j). \tag{47}$$

Here, the $\theta(j) \equiv eAM/a\mu_B j\tau Q_1 l$ value is, in particular, determined by the current. By way of example, let us use the typical parameters $\alpha \sim 2 \times 10^4$, $Q_1 \sim 0.3$, $\tau \sim 3 \times 10^{-13}$ s, $l \sim 17$ nm, $A \sim 10^{-12}$ cm^2, and $M \sim 10^3$ G. This gives $\theta(j) \approx 0.17$ at the current $j \sim 3.3 \times 10^7$ A/cm^2, which corresponds to the instability threshold (e.g., see [1–3]). Figure 2 allows us to determine those $\lambda = \lambda'$ values for which $|\Phi| = 1$ at several ν parameter values. We see that $0.4 < \lambda' < 0.7$, which corresponds to $7 \leq L \leq 12$ nm. As far as we know, only thicknesses *L* of 2 to 10 nm have been studied thus far [1]. According to the estimates above, the inequality $|\Phi| \ll 1$ or $|\Phi| \leq 1$ should then be satisfied. At somewhat larger thicknesses of $L \approx 20$–80 nm (or $\lambda \approx 1$–5), however, we may have $|\Phi| \gg 1$. For this reason, we consider both large and small $|\Phi|$ values (more exactly, the limiting cases $|\Phi| \ll 1$ and $|\Phi| \gg 1$).

6.1. Let us consider instability at $|\Phi| \ll 1$. The solutions to (42) are then close to spin wave resonance modes (44). First, consider the solution that is close to homogeneous resonance with the number $n = 0$. We only retain the main term $q^2L^2 \ll 1$ in the left-hand side of (42) and use the definition $q = is/2r$ and Eqs. (40) and (43). The frequency ω is then given by the quadratic equation

$$\omega^2 = \left[\Omega_x - \frac{\gamma B}{\lambda} - i\left(\kappa\omega \pm \frac{ak}{L}\right)\right] \times \left[\Omega_y - \frac{\gamma B}{\lambda} - i\left(\kappa\omega \pm \frac{ak}{L}\right)\right]. \tag{48}$$

This equation has complex roots. Separate equations for the real and imaginary parts of these roots will be necessary. Direct calculations yield

$$(1+\kappa^2)\mathrm{Re}\,\omega = \pm\frac{\kappa ak}{L} \pm \frac{1}{\sqrt{2}}\sqrt{W + \sqrt{W^2 + V^2}}, \tag{49}$$

$$(1+\kappa^2)\mathrm{Im}\,\omega = -\frac{\kappa}{2}\left(\Omega_x + \Omega_y - \frac{2\gamma B}{\lambda}\right) \pm \frac{1}{\sqrt{2}}\sqrt{-W + \sqrt{W^2 + V^2}}. \tag{50}$$

In (49), we can use arbitrary sign combinations. In addition,

$$W = \left(\Omega_x - \frac{\gamma B}{\lambda}\right)\left(\Omega_y - \frac{\gamma B}{\lambda}\right) - \frac{(ak)^2}{L^2} - \frac{\kappa^2}{4}(\Omega_x - \Omega_y)^2, \tag{51}$$

$$V = \frac{ak}{L}\left(\Omega_x + \Omega_y - \frac{2\gamma B}{\lambda}\right).$$

In (50), we only retain the upper sign, which admits instability. The instability condition then takes the form

$$\kappa^2\left(\Omega_x - \frac{\gamma B}{\lambda}\right)\left(\Omega_y - \frac{\gamma B}{\lambda}\right) - \left(\frac{ak}{L}\right)^2 \le 0. \tag{52}$$

Condition (52) clearly shows that there are two sources of instability. One of these is the current-injected longitudinal spin contribution to effective field (30). This contribution is described by the terms proportional to the B parameter (see (36)). The other source of instability is the torque contribution at the $x = 0$ boundary. This contribution appears because of boundary conditions (21); it is described by the term proportional to k^2.

According to (52), dissipation influences these two contributions quite differently. Dissipation is inessential to the appearance of the injection-type instability because it is then sufficient that $\gamma B/\lambda$ be larger than Ω_y. However, if the torque only remains ($B \longrightarrow 0$), overcoming some threshold caused by dissipation is necessary. At the same time, the joint action of both mechanisms always decreases the left-hand side of (52) and therefore facilitates the appearance of instability.

Since B and k are proportional to j, we can obtain a quadratic equation for the threshold current density j_{th} by setting the left-hand side of (52) equal to zero. Solving this equation yields

$$\frac{j_{\mathrm{th}}}{j_\perp} = \eta\frac{(f + f^{-1}) - \sqrt{(f - f^{-1})^2 + 4\eta^2}}{2(1-\eta^2)}, \tag{53}$$

where

$$j_\perp = \frac{\kappa e M \omega_0 L}{\mu_B Q_1}, \tag{54}$$

$\omega_0 = \sqrt{\Omega_x\Omega_y}$ is the spin wave resonance frequency at the number $n = 0$ (cf. (44)), and $f = \sqrt{\Omega_y/\Omega_x}$. The $j_\perp$ value (54) is nothing but the threshold current density under the torque action only (at $B = 0$). It follows from general equation (53) for the threshold that $j_{\mathrm{th}} \longrightarrow j_\perp$ if $\eta \gg 1$. However, if $\eta \ll 1$, the spin-injection instability mechanism predominates. The threshold is then given by

$$j_{\mathrm{th}} \longrightarrow j_\perp f\eta = j_D\frac{(H + H_a)\lambda(\sinh\lambda + \nu\cosh\lambda)}{\alpha\mu_B n Q_1[\sinh\lambda + \nu(\cosh\lambda - 1)]}. \tag{55}$$

This coincides with the equation obtained earlier [9] by another method, namely, from the requirement of minimum magnetic energy (recall that the current j_D is defined in (14) and $H_a = \beta M$). As in [9], threshold (55) is for homogeneous fluctuations because of the use of the spin wave resonance mode with $qL \ll 1$.

Note an important relation between threshold currents and spin wave resonance frequencies. It follows from (49) and (50) that

$$\frac{(\mathrm{Re}\,\omega)_{\mathrm{th}}}{\omega_0} = \frac{j_{\mathrm{th}}}{j_\perp}. \tag{56}$$

Ratio (56) tends to zero as $\eta \longrightarrow 0$ and to 1 as $\eta \longrightarrow \infty$, because the torque only influences spin wave resonance damping and changes its sign at the instability threshold. The resonance frequency remains constant. Conversely, injection in addition influences the real part of the frequency and makes it vanish at the threshold. The eigenfrequency then softens; that is, it behaves as under the conditions of a reorientation phase transition in an external magnetic field. This opens up an interesting possibility of experimentally identifying the injection mechanism by measuring the resonance frequency at current densities close to the threshold value.

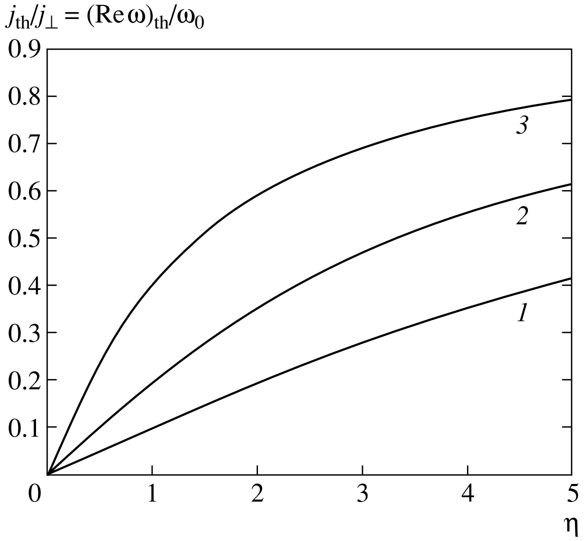

Fig. 3. Threshold current and spin wave eigenfrequency at the threshold as functions of the η parameter characterizing the relative torque and spin injection contributions. The curves correspond to different $f = \sqrt{\Omega_y/\Omega_x}$ parameter values: f = (*1*) 0.1, (*2*) 0.2, and (*3*) 0.5.

Ratio (56) as a function of the η parameter at various f values is shown in Fig. 3. Interestingly, the instability threshold is always lower than threshold (54). Let us estimate threshold (54) using the set of typical parameters specified for (47) with the dissipation parameter $\kappa = 3 \times 10^{-2}$, frequency $\omega_0 = 2.3 \times 10^{10}$ s^{-1}, and $\lambda = 0.4$ added to it. This yields $j_\perp \approx 2.7 \times 10^7$ A/cm^2. Approximate equation (55) gives a similar estimate within the range of its applicability. We find that, on the whole, threshold current density estimates are in agreement with the experimental data.

6.2. Let us consider instability of inhomogeneous spin wave modes with $n \neq 0$ at $|\Phi| \ll 1$. Solutions to (42) are then close to the zeros of $\tan qL$; that is,

$$q \approx \frac{n\pi}{L} - \frac{\Phi}{n\pi L}. \qquad (57)$$

Again applying (40) and using the definitions $q = is/2r$ and (43), we obtain a quadratic equation for the frequency ω. Let us separate the real and imaginary parts of the roots of this equation, as with (48) above. The instability condition $\mathrm{Im}\,\omega > 0$ then takes the form

$$\kappa^2\left[\Omega_x + a\left(\frac{n\pi}{L}\right)^2 - \frac{2\gamma B}{\lambda}\right] \times \left[\Omega_y + a\left(\frac{n\pi}{L}\right)^2 - \frac{2\gamma B}{\lambda}\right] - \left(\frac{2ak}{L}\right)^2 < 0. \qquad (58)$$

Condition (58) has the structure of (52). The conclusions about the effective field and torque contributions therefore remain valid.

The threshold current density j^n_{th} for $n \neq 0$ is calculated the same way as previously. We obtain

$$j^n_{th} = \frac{1}{2} j_\perp \frac{\eta}{2(1-\eta^2)}\Big[2n^2 g + f + f^{-1} - \sqrt{(f^{-1} - f)^2 + 4(1 + n^2 g f)(1 + n^2 g f^{-1})\eta^2}\Big], \qquad (59)$$

where we introduced the new parameter $g = \pi^2 a/\omega_0 L^2$. It follows from (59) that the instability threshold sharply increases as the number n grows.

6.3. Let us consider instability at $|\Phi| \gg 1$. Dispersion relation (42) is then substantially modified by current. As strong inequality (45) is fulfilled in our model, direct substitution shows that there is a solution in which the imaginary part of q predominates. For this solution,

$$q^2 \approx -(\Phi/L)^2. \qquad (60)$$

The definitions $q = is/2r$ and (43) allow (42) to be transformed into the quadratic equation for the frequency

$$\omega^2 = \left[\Omega_x - \frac{(\gamma Bl)^2}{a} + ak^2 - i(\kappa\omega \pm 2\gamma Blk)\right] \times \left[\Omega_y - \frac{(\gamma Bl)^2}{a} + ak^2 - i(\kappa\omega \pm 2\gamma Blk)\right]. \qquad (61)$$

Equation (61) is qualitatively different from (48) in two respects. First, the current-induced corrections to the frequencies $\Omega_{x,y}$ are quadratic rather than linear in the current. Secondly, both factors, the injection field ($\sim B$) and torque ($\sim k^2$), contribute simultaneously to both the real and imaginary parts of the multipliers on the right-hand side of (61).

Equation (61) yields the instability condition $\mathrm{Im}\,\omega > 0$ in the form

$$\kappa^2\left[\Omega_x - \frac{(\gamma Bl)^2}{a} + ak^2\right] \times \left[\Omega_y - \frac{(\gamma Bl)^2}{a} + ak^2\right] - (2\gamma Blk)^2 < 0. \qquad (62)$$

As distinct from condition (52), the appearance of instability is now impossible in the absence of an effective injection field, that is, if $B = 0$. If there is no surface torque ($k^2 = 0$), instability nevertheless appears at $(\gamma Bl)^2/a > \Omega_y$.

Since $B \sim j$ and $k \sim j$, setting the left-hand side of (62) equal to zero yields a biquadratic equation for the threshold current density. The solution to this equation has the form

$$j_{\mathrm{th}} = \frac{e}{\mu_B\alpha\gamma\tau Q_1}\sqrt{\frac{a}{2(1-4\eta^2)}} \times\sqrt{\Omega_x+\Omega_y-\sqrt{(\Omega_x-\Omega_y)^2+16\eta^2\Omega_x\Omega_y}}. \qquad (63)$$

Equation (63) is valid if the condition $|\Phi| \gg 1$ is met. The region in Fig. 2 that corresponds to this inequality lies much higher than the θ level. All curves in this region increase linearly as λ grows. According to (46), the η parameter is then virtually independent of λ, that is, layer thickness L. It is therefore clear that threshold (63) is also independent of L. This property sharply contrasts with a linear increase in the threshold in (54) and (55) at $|\Phi| \ll 1$. This difference appears because inhomogeneous fluctuations with $|qL| \gg 1$ (see (60)) are most unstable in the case under consideration. A still more interesting result is obtained when we numerically estimate threshold (63). Substituting the standard set of parameters into it, we find that the condition $|\Phi| \gg 1$ can only be satisfied for layers of thickness $L \geq 20$ nm. The threshold current density then equals $j_{\mathrm{th}} \approx 3 \times 10^6$ A/cm^2 at the frequencies $\Omega_x \approx 2.3 \times 10^{11}$ s^{-1} and $\Omega_y \approx 1.8 \times 10^9$ s^{-1}. This value is an order of magnitude smaller than the estimates obtained by (54) and (55).

7. THE ELECTRIC CURRENT EFFECT ON THE SPECTRUM OF SPIN WAVES

Current through a junction influences not only the spin wave decrement Imω but also the spin wave spectrum Reω. Let us discuss this influence in more detail for the example of two effects: (1) spin mode eigenfrequency softening near the instability threshold, and (2) the appearance of current-induced new spin modes.

7.1. The softening effect will be considered for the $n = 0$ mode ignoring dissipation, that is, on the assumption that $\kappa \ll 1$. For definiteness, put $|\Phi| \ll 1$. Equation (48) directly yields

$$\frac{\mathrm{Re}\,\omega}{\omega_0} = \sqrt{\left(1-\frac{f}{\eta}\frac{j}{j_\perp}\right)\left(1-\frac{1}{f\eta}\frac{j}{j_\perp}\right)}. \qquad (64)$$

Let us substitute the equality $j/j_\perp = (j/j_{\mathrm{th}})(j_{\mathrm{th}}/j_\perp)$ into (64) and use (53). We eventually obtain

$$\frac{\mathrm{Re}\,\omega}{\omega_0} = \left\{\left[1-\frac{f[f^{-1}+f-\sqrt{(f^{-1}-f)^2+4\eta^2}]}{2(1-\eta^2)}\frac{j}{j_{\mathrm{th}}}\right] \times\left[1-\frac{f^{-1}+f-\sqrt{(f^{-1}-f)^2+4\eta^2}}{2f(1-\eta^2)}\frac{j}{j_{\mathrm{th}}}\right]\right\}^{1/2}. \qquad (65)$$

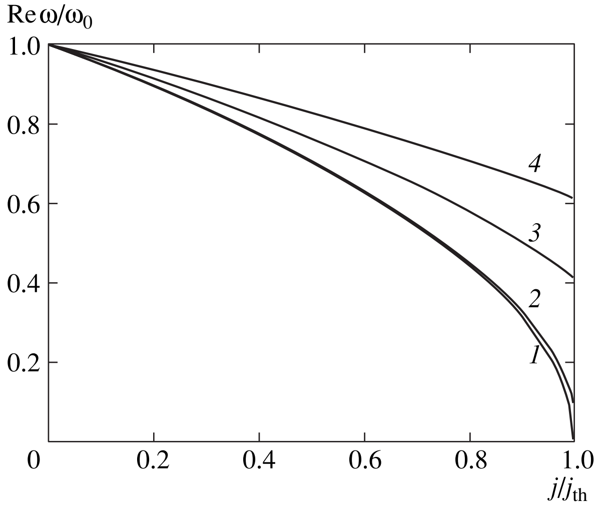

Fig. 4. Spin wave eigenfrequency as a function of current density. The frequency softens as the current approaches the threshold value. The calculations were performed for the $n = 0$ mode at $|\Phi| \ll 1$ and $f = 0.1$. The curves correspond to different η parameter values: (*1*) 0.1, (*2*) 1.0, (*3*) 5, and (*4*) 10.

Several curves constructed according to (65) are shown in Fig. 4. For each of then, the threshold j_{th} was calculated with the corresponding η parameter value. We see that Reω decreases as the current approaches the instability threshold. The decrease becomes steeper and steeper as η decreases, that is, as the system approaches the conditions under which the effective injection field plays a key role.

If $|\Phi| \gg 1$, we obtain curves similar to (65) but with a steeper frequency drop as the threshold is approached.

7.2. The effect of current-induced new spin modes is observed if $|\Phi| \gg 1$. In this limit, several solutions to dispersion equation (42) additional to that considered in Section 6.3 appear. The real part of q in these solutions is much larger than imaginary. Since condition (45) is always satisfied, (42) takes the form

$$qL\tan qL \approx \mathrm{Re}\,\Phi \gg 1, \qquad (66)$$

and the solutions are close to

$$q \approx \frac{\pi}{L}\left(n+\frac{1}{2}\right). \qquad (67)$$

According to spin wave resonance theory [20, 23], solutions (67) with half-integer "numbers" (in parentheses) correspond to natural oscillations of a layer with tightly pinned surface magnetization. In the model under consideration, magnetization pinning is caused by large ReΦ values, that is, by a high effective injection field. It appears that, because current-injected spins participate in *s*–*d* exchange, they create unidirectional magnetic anisotropy near the $x = 0$ surface, and it is this anisotropy that pins magnetization.

8. CONCLUSIONS

We for the first time considered the joint action of two electric current-induced effects, namely, (1) nonequilibrium spin injection and (2) surface torque. These effects influence the state of ferromagnetic layers in spin-valve-type metallic junctions.

At current densities exceeding a certain threshold (usually 10^6–3×10^7 A/cm^2), spin wave fluctuations in junctions become unstable. The joint action of the effects specified above lowers the instability threshold.

The surface torque determines the instability threshold in junctions with a comparatively small free ferromagnetic layer thickness ($L \sim 2$–7 nm) and a small Landau–Lifshitz–Gilbert dissipation parameter ($\kappa < 10^{-2}$). The instability threshold linearly increases as L grows and corresponds to virtually homogeneous ferromagnetic layer excitation.

Current-induced nonequilibrium spin injection determines the instability threshold at comparatively large thicknesses and dissipation parameters of the free ferromagnetic layer, for instance, at $L > 20$ nm and $\kappa \sim 3 \times 10^{-2}$. As the thickness increases, the instability threshold begins to correspond to essentially inhomogeneous layer excitation. The current density at the threshold is then comparatively low, of about 10^6 A/cm^2.

Current-induced injection of nonequilibrium spins results in instability because of an orientation phase transition in the effective exchange field created by these spins. Injection therefore influences not only the fluctuation decrement but also the spectrum of fluctuations. The eigenfrequencies of spin fluctuations decrease to zero (“soften”) as the current increases and approaches the threshold value.

Conversely, surface torque only influences the decrement and not the spin fluctuation spectrum. This circumstance allows the mechanism of instability to be identified experimentally.

Strong current-induced spin injection into a ferromagnetic metallic layer causes effective pinning of layer lattice magnetization near the surface of injection. According to calculations, such pinning should result in the appearance of new spin wave resonance lines as the current increases.

ACKNOWLEDGMENTS

The authors thank A.I. Krikunov, A.V. Medved’, and V.A. Sablikov for interesting discussions. This work was financially supported by the Russian Foundation for Basic Research (project nos. 03-02-17540 and 04-02-08248).

APPENDIX I

The Lattice Magnetization Flux Density

Let us explicitly separate the exchange terms (intralattice exchange and *s–d* exchange) in Landau–Lifshitz–Gilbert equation (3). We obtain

$$\begin{aligned}\frac{\partial \mathbf{M}}{\partial t} &= -\gamma A\left[\mathbf{M} \times \frac{\partial^2 \mathbf{M}}{\partial x^2}\right] \\ &- \gamma[\mathbf{M} \times \mathbf{H}_{s-d}] - \gamma[\mathbf{M} \times \mathbf{H}'] + \kappa\left[\hat{\mathbf{M}} \times \frac{\partial \mathbf{M}}{\partial t}\right],\end{aligned} \tag{I.1}$$

where $\mathbf{H}' \equiv \mathbf{H} + \beta(\mathbf{M} \cdot \mathbf{n})\mathbf{n} + \mathbf{H}_d$. Suppose that the estimates $\kappa \ll 1$ and $|\mathbf{M} \times \mathbf{H}'| \ll |\mathbf{M} \times \mathbf{H}_{s-d}|$ are valid within the $0 \le x < \lambda_F$ sublayer. These estimates allow the last two terms in the right-hand side of (I.1) to be eliminated. Let us transform the vector product in (I.1) containing the second derivative as follows:

$$\begin{aligned}\left[\mathbf{M} \times \frac{\partial^2 \mathbf{M}}{\partial x^2}\right] &= \frac{\partial}{\partial x}\left[\mathbf{M} \times \frac{\partial \mathbf{M}}{\partial x}\right] \\ -\left[\frac{\partial \mathbf{M}}{\partial x} \times \frac{\partial \mathbf{M}}{\partial x}\right] &= \frac{\partial}{\partial x}\left[\mathbf{M} \times \frac{\partial \mathbf{M}}{\partial x}\right].\end{aligned} \tag{I.2}$$

The simplifications introduced and Eq. (I.2) allow (I.1) to be written in the form

$$\frac{\partial \mathbf{M}}{\partial t} + \gamma[\mathbf{M} \times \mathbf{H}_{s-d}] + \frac{\partial}{\partial x}\left\{a\left[\hat{\mathbf{M}} \times \frac{\partial \mathbf{M}}{\partial x}\right]\right\} = 0, \tag{I.3}$$

where $a = \gamma AM$.

The first term in (I.3) describes time-dependent magnetization changes, and the second term is proportional to the moment of forces that appear because of the action of mobile electrons on the lattice. The last term is therefore the divergence of the lattice magnetization flux. It follows that the value

$$\mathbf{J}_\perp = a\left[\hat{\mathbf{M}} \times \frac{\partial \mathbf{M}}{\partial x}\right] \tag{I.4}$$

has the meaning of the lattice magnetization flux, and the a parameter is the magnetization diffusion constant.

APPENDIX II

The Derivation of the Dispersion Equation for Fluctuations

The substitution of general solution (41) into boundary conditions (21) and (23) yields the solvability condition

$$I_1^2 + 4k^2 I_2^2 = 0, \tag{II.1}$$

where

$$\begin{aligned} I_1 &= J_s'(b)Y_s'(be^{-L/2r}) - Y_s'(b)J_s'(be^{-L/2r}), \\ I_2 &= \frac{r}{b}[J_s(b)Y_s'(be^{-L/2r}) - Y_s(b)J_s'(be^{-L/2r})]. \end{aligned} \tag{II.2}$$

Here, primes denote differentiation with respect to the argument. According to (32), we must take the limit as $r \longrightarrow +0$. This, in particular, implies the transition to the limiting case of small Bessel function indices and arguments, because, according to (37) and (40), $b \sim \sqrt{r}$ and $s \sim r$. We will use the following representations of the Bessel functions of the first and second kind [22]:

$$J_s(y) \approx \frac{y^s}{2^s\Gamma(s+1)}\left[1 - \frac{y^2}{4(s+1)}\right], \tag{II.3}$$

$$\begin{aligned} Y_s(y) &\approx \frac{1}{\pi s} \\ &\times \left[\frac{y^s}{2^s\Gamma(s+1)} - \frac{y^{-s}}{2^{-s}\Gamma(-s+1)}\right]\left(1 - \frac{y^2}{4}\right). \end{aligned} \tag{II.4}$$

Let us differentiate (II.3) and (II.4) with respect to the argument and calculate these functions and their derivatives at $y = b$ and $y = be^{-L/2r}$. Substituting the results into (II.2) while retaining the main terms as $r \longrightarrow 0$ yields

$$\begin{aligned} I_1 &\approx \frac{2}{\pi}e^{L/2r}\frac{s}{b^2}\left(\sinh\frac{Ls}{2r} - \frac{b^2}{2r}\cosh\frac{Ls}{2r}\right), \\ I_2 &\approx \frac{2}{\pi}e^{L/2r}\frac{r}{b^2}\cosh\frac{Ls}{2r}. \end{aligned} \tag{II.5}$$

Here, it is taken into account that $\Gamma(s + 1) = s\Gamma(s)$ and $\Gamma(s)\Gamma(-s) = -\pi/s\sin\pi s \approx -1/s^2$.

Substituting (II.5) into (II.1) yields

$$\left(\tanh\frac{Ls}{2r} - \frac{b^2}{2s}\right)^2 + \left(\frac{2kr}{s}\right)^2 = 0. \tag{II.6}$$

The s/r and b^2/s values tend to finite limits as $r \longrightarrow 0$. Using the denotation $q = is/2r$ and the definition of b (Eq. (37)), we obtain the dispersion equation in form (42).

REFERENCES

1. J. A. Katine, F. J. Albert, R. A. Buhrman, *et al.*, Phys. Rev. Lett. **84**, 3149 (2000).
2. J. Grollier, V. Cross, A. Hamzic, *et al.*, Appl. Phys. Lett. **78**, 3663 (2001).
3. J.-E. Wegrowe, A. Fabian, Ph. Guittienne, *et al.*, Appl. Phys. Lett. **80**, 3361 (2002).
4. M. Tsoi, A. G. M. Jansen, J. Bass, *et al.*, Phys. Rev. Lett. **80**, 4281 (1998); **81**, 493(E) (1998).
5. S. I. Kiselev, J. C. Sankey, I. N. Krivorotov, *et al.*, Nature **425**, 380 (2003).
6. J. Bass, S. Urazhdin, N. O. Birge, and W. P. Pratt, Jr., Phys. Status Solidi A **201**, 1379 (2004).
7. C. Heide, P. E. Zilberman, and R. J. Elliott, Phys. Rev. B **63**, 064424 (2001).
8. Yu. V. Gulyaev, P. E. Zil'berman, É. M. Épshteĭn, and R. J. Elliott, Pis'ma Zh. Éksp. Teor. Fiz. **76**, 189 (2002) [JETP Lett. **76**, 155 (2002)].
9. R. J. Elliott, E. M. Epshtein, Y. V. Gulyaev, and P. E. Zilberman, J. Magn. Magn. Mater. **271**, 88 (2004).
10. Yu. V. Gulyaev, P. E. Zil'berman, É. M. Épshteĭn, and R. J. Elliott, Pis'ma Zh. Éksp. Teor. Fiz. **79**, 507 (2004) [JETP Lett. **79**, 402 (2004)].
11. J. C. Slonczewski, J. Magn. Magn. Mater. **159**, L1 (1996).
12. L. Berger, Phys. Rev. B **54**, 9353 (1996).
13. S. Zhang, P. M. Levy, and A. Fert, Phys. Rev. Lett. **88**, 236601 (2002).
14. A. Shpiro, P. M. Levy, and S. Zhang, Phys. Rev. B **67**, 104430 (2003).
15. M. D. Stiles and A. Zangwill, Phys. Rev. B **66**, 014407 (2002).
16. A. M. Haghiri-Gosnet, T. Arnal, R. Soulimane, *et al.*, Phys. Status Solidi A **201**, 1392 (2004).
17. A. G. Aronov and G. E. Pikus, Fiz. Tekh. Poluprovodn. (Leningrad) **10**, 1177 (1976) [Sov. Phys. Semicond. **10**, 698 (1976)].
18. V. L. Bonch-Bruevich and S. G. Kalashnikov, *Physics of Semiconductors*, 2nd ed. (Nauka, Moscow, 1990) [in Russian].
19. B. P. Zakharchenya, D. N. Mirlin, V. I. Perel', and I. I. Reshina, Usp. Fiz. Nauk **136**, 459 (1982) [Sov. Phys. Usp. **25**, 143 (1982)].
20. A. I. Akhiezer, V. G. Bar'yakhtar, and S. V. Peletminskiĭ, *Spin Waves* (Nauka, Moscow, 1967; North-Holland, Amsterdam, 1968).
21. M. I. Dyakonov and V. I. Perel, Phys. Lett. A **35A**, 459 (1971).
22. *Handbook of Mathematical Functions*, Ed. by M. Abramowitz and I. A. Stegun (Dover, New York, 1971; Nauka, Moscow, 1979).
23. A. G. Gurevich, *Magnetic Resonance in Ferrites and Antiferromagnets* (Nauka, Moscow, 1973) [in Russian].

Translated by V. Sipachev

Journal of Experimental and Theoretical Physics, Vol. 100, No. 5, 2005, pp. 1018–1028.
Translated from Zhurnal Éksperimental'noĭ i Teoreticheskoĭ Fiziki, Vol. 127, No. 5, 2005, pp. 1153–1165.
Original Russian Text Copyright © 2005 by Vaulina, Petrov, Fortov.

STATISTICAL, NONLINEAR, AND SOFT MATTER PHYSICS

Simulations of Mass-Transport Processes on Short Observation Time Scales in Nonideal Dissipative Systems

O. S. Vaulina*, O. F. Petrov, and V. E. Fortov
Institute of Thermal Physics of Extreme States, Russian Academy of Sciences,
ul. Izhorskaya 13/19, Moscow, 127412 Russia
**e-mail: vaul@ihed.ras.ru*

Received August 11, 2004

Abstract—We present the results of our numerical simulations of mass-transport processes on short observation time scales for extended quasi-two-dimensional and three-dimensional nonideal dissipative systems of macroparticles interacting through a screened Coulomb potential. The simulations were performed for the parameters corresponding to the experimental conditions in laboratory dusty plasmas. The evolution of the rms macroparticle displacement on short observation time scales in nonideal liquid systems is shown to be similar to the evolution of the thermal particle oscillations at lattice sites. *© 2005 Pleiades Publishing, Inc.*

1. INTRODUCTION

Problems related to mass-transport processes in dissipative systems of interacting particles are of considerable interest in various fields of science and technology (hydrodynamics, plasma physics, medical industry, polymer physics and chemistry, etc.) [1–9]. The main problem in studying the physical properties of such systems is associated with the absence of an analytical theory for a liquid that could explain its thermodynamic properties, give an equation of state, describe the heat- and mass-transport phenomena, etc. [7–10]. The development of approximate models to describe the liquid state of a substance is based on two main approaches. The first approach is a semiempirical method for determining the relationship of the liquid parameters to one another and to the properties of the original crystals that relies on analogies between the crystalline and liquid states of a substance [7–10]. The second approach is based on a complete statistical calculation of the properties of nonideal media by means of molecular dynamics using model data on the particle interaction energy [11, 12]. Such simulations allow various physical phenomena (phase transitions, thermal macroparticle diffusion, the dynamics of the approach of a system to an equilibrium state, etc.) to be studied. Numerical simulations of the dynamics of nonideal systems are of great importance in the theory of a liquid, because there is no small parameter in such systems that could be used to analytically describe its state and thermodynamic properties, as can be done for a gas, due to strong interparticle interaction.

A laboratory dusty plasma, a weakly ionized gas with disperse-phase micron-sized macroparticles (dust particles), is a good experimental model for studying the properties of nonideal systems [13–17]. A dusty plasma is a widespread natural object, and it is often produced through various technological processes. The micron-sized dust particles in plasma can acquire a significant electric charge and form quasi-stationary dust structures similar to liquids or solids. Depending on the experimental conditions, such structures can be similar to homogeneous three-dimensional systems or have a highly anisotropic one-dimensional or quasi-two-dimensional pattern, such as the chains of macroparticles observed in a direct-current glow discharge plasma [16, 17] or the separate dust layers (usually from one to ten) in the near-electrode region of a high-frequency discharge [13–15]. In contrast to real liquids, the macroparticles in plasma can be recorded by a video camera. This simplifies significantly the use of direct nonintrusive diagnostic techniques and makes it possible to study the physical properties of nonideal systems at the kinetic level. Such studies could play a significant rule both in testing existing analytical models for the structure of a liquid and in developing new ones.

Most of the numerical studies of dusty plasmas are based on the model of a screened Coulomb potential:

$$U = (eZ)^2 \exp(-l/\lambda)/l, \qquad (1)$$

where l is the interparticle distance, λ is the screening length, and eZ is the macroparticle charge in elementary electron charges e. The properties of nonideal systems of macroparticles interacting with a screened potential are also of considerable interest in analyzing the various kinetic processes in molecular biology, polymer chemistry, etc. [2, 5]. The two dimensionless parameters responsible for the mass-transport processes and the phase state in systems with a screened

Coulomb potential for screening parameters $\kappa = l_p/\lambda < 6–7$ were determined in [18–20]. (Here, l_p is the mean interparticle distance, which is equal to the inverse square root of the particle surface density for two-dimensional systems and to the inverse cubic root of the particle volume density for three-dimensional systems). The first is the effective coupling parameter responsible for the phase state of a system of interacting particles:

$$\Gamma^* = \frac{a(Ze)^2}{Tl_p}\left\{\left(1 + \kappa + \frac{\kappa^2}{2}\right)\exp(-\kappa)\right\}^{1/2}. \qquad (2)$$

The second is the scale parameter responsible for the scaling of the dynamical processes in dissipative systems and is the ratio of the characteristic energy scattering frequency ω^* (as the charged macroparticles move toward the displacement of the system's center of mass) to the effective frequency ν_{fr} of their collisions with neutrals of the ambient gas (which characterizes the rate of energy exchange between the neutrals and the dust particle [2, 5, 21, 22]):

$$\xi \equiv \frac{\omega^*}{\nu_{fr}} = \frac{eZ}{\nu_{fr}}\left\{b\left(1 + \kappa + \frac{\kappa^2}{2}\right)\frac{\exp(-\kappa)}{l_p^3\pi M}\right\}^{1/2}. \qquad (3)$$

Here, M and T are the mass and temperature of the dust particle, and the coefficients a and b depend on the dimensionality of the problem: $a \equiv b = 1$ for a homogeneous three-dimensional system and $a = 1.5$, $b = 2$ for the solution of the quasi-two-dimensional problem that models an extended dust layer. These coefficients were introduced for convenience to describe the transport characteristics of liquid systems (such as the diffusion coefficient D and the pair correlation functions $g(l)$), which, given the proposed normalization, have similar values at the same parameters Γ^* and ξ. As Γ^* increases to $\Gamma_m^* \approx 106$ ($\kappa < 6$), a body-centered crystal structure is formed in a three-dimensional system, while a two-dimensional system crystallizes into a hexagonal lattice structure.

The diffusion of macroparticles is the main mass-transport process that determines the energy losses (dissipation) in plasma–dust systems and their dynamical properties, such as the phase state and the conditions for the propagation of waves and for the formation of dust instabilities. The theory of diffusion in liquids has been developed in two directions, one of which (more fundamental) is based on the general principles of statistical physics. The other approach (the theory of jumps) is based on analogies between liquids and solids. The essence of this theory is that the molecules of such a liquid are in an equilibrium (settled) state for the time it takes for an (activation) energy high enough for the potential bonds to be broken between the neighboring molecules and for the transition into the surroundings of other molecules to a new settled state to be imparted to them. Thus, a diffusing (active) particle may be assumed to be capable of occupying the energetically equivalent locations at the sites of an imaginary lattice and migrating by jumping to one of the equivalent locations. The random motion of an active particle over the lattice sites after a large number of jumps is described by macroscopic diffusion equations (with a constant time-independent coefficient D); i.e., Fick's laws are applicable [2, 5]. However, the current state of the art of experimental physics necessitates going outside the scope of the diffusion approximation, and the currently available simulation methods based on the theory of stochastic processes make this possible. In particular, the description in terms of macroscopic (Fick) kinetics may prove to be inadequate for analyzing the transport processes on physically short time scales. Investigating the mass-transport processes on short observation time scales is of particular importance in studying fast processes (such as the propagation of shock waves, impulsive actions, or the motion of the front of chemical conversions in condensed media [5, 23]) and in analyzing the transport properties of weakly dispersive ($\xi \gg 1$) nonideal media (such as colloidal solutions, combustion-product plasmas, atmospheric-pressure nuclear-induced dusty plasmas [2, 24, 25]), where the proper measurement of the macroparticle diffusion coefficients requires carrying out prolonged experiments.

2. PARTICLE MASS-TRANSPORT PROCESSES IN NONIDEAL MEDIA

Using the hydrodynamic approaches allows the mass-transport processes to be successfully described only in the case of short-range interactions. When the forces of interparticle interaction are not as weak as those in gases, the construction of a proper kinetic equation fails. The fundamental theories of diffusion in liquids are based on the fact that the particle number density for each component of the system under consideration is a hydrodynamic variable that slowly varies in space and time. Such systems are in a statistical equilibrium state, and they can be characterized by a certain set of physical parameters, for example, the density, kinetic temperature, and pressure, which can fluctuate only slightly about their mean equilibrium values. In statistical physics, such a state is described by using various Gibbs distributions, depending on the type of contact between the system and the ambient medium (a thermostat) that forbids or permits the energy or particle exchange with it, and Nyquist's formulas, Green's functions, and the fluctuational–dissipative theorem are used to analyze the equilibrium fluctuations and the transport coefficients [21, 26].

In the case of small deviations of the system under study from a statistical equilibrium, the particle diffusion coefficient D is described by a relation that is a special case of the Green–Kubo formulas [2]:

$$D = \int_0^{\infty} \langle V(0)V(t)\rangle dt/m, \qquad (4)$$

where $\langle V(0)V(t)\rangle$ is the autocorrelation function of the particle velocities V, t is the time, and $m = 2$ or $m = 3$ are for two-dimensional or three-dimensional systems, respectively. To investigate the evolution of the mass transport with time, $D(t)$, the autocorrelation function of the particle velocities in Eq. (4) is integrated over a finite time interval:

$$D(t) = \int_0^{t} \langle V(0)V(t)\rangle dt/m.$$

The diffusion coefficient for interacting particles can also be determined by analyzing the particle heat transport through a unit area in a homogeneous medium for $t \longrightarrow \infty$:

$$D = \lim_{t \to \infty} D(t), \qquad (5)$$

where the evolution of the mass transport with time, $D(t)$, is defined by the relation [5]

$$D(t) = \frac{\langle\langle(\Delta l)^2\rangle_N\rangle_t}{2mt}. \qquad (6)$$

Here, $\Delta l = \Delta l(t)$ is the displacement of an individual particle in time t, $\langle\ \rangle_N$ is the averaging over an ensemble of N particles, and $\langle\ \rangle_t$ is the averaging over all time intervals of duration t in the total measurement time. The latter is necessitated by the requirement that the mean characteristics be properly determined for liquid systems in accordance with the theory of jumps. Thus, for example, it was shown in [18] that the dynamical behavior of strongly nonideal systems is not ergodic, and the ensemble averaging

$$\langle\{\Delta l(t)\}^2\rangle_N \approx \langle\langle\{\Delta l(t)\}^2\rangle_N\rangle_t$$

is only for $\Gamma^* < 40$–50.

Since no assumptions about the pattern of thermal motion are made when deriving relations (4)–(6), they are valid both for gases and for liquids and solids. In most cases, however, the calculation of the diffusion coefficient using these relations admits no analytical solutions. The simple solution $D \equiv D_0 = T_p/\nu_{fr}M$, which is known as Einstein's relation, can be obtained only for noninteracting (Brownian) particles. Here, it should be noted that the quantity $f = \nu_{fr}M$ (usually called the coefficient of macroparticle friction) does not depend on the density of the dust particle material, but is determined by the particle size and relative velocity, the conditions for the accommodation of neutrals on the particle surface, and the Knudsen number (Kn); for a spherical particle, the latter is equal to the ratio of the neutral mean free path l_n to its radius a_p [2, 5, 21, 22]. In the hydrodynamic regime (Kn $\ll 1$), $f = 6\pi\eta a_p$, where η is the viscosity of the ambient gas.

In the semiempirical theory of jumps, the analytical relation for the diffusion coefficient of molecules can be represented as [1, 9]

$$D = \frac{d^2}{2m\tau_0}\exp\left(-\frac{W}{T}\right), \qquad (7)$$

where d is the mean distance between the molecules, τ_0 is the characteristic time that determines the frequency of their transitions from one settled state to another, and W is the energy barrier overcome during these transitions. The exponential dependence of D on the temperature T of molecular liquids is confirmed experimentally. A similar temperature dependence for the thermal diffusion coefficient D of macroparticles was found for dissipative systems with a screened potential in [18, 27]. In these papers, it was shown that the diffusion coefficient for strongly nonideal liquid structures could be represented as

$$D \approx \frac{T\Gamma^*}{12\pi(\xi + 1)\nu_{fr}M}\exp\left(-3\frac{\Gamma^*}{\Gamma_c^*}\right), \qquad (8)$$

where $\Gamma_c^* = 102$ is the crystallization point. For Γ^* in the range from 50 to 102, the error with which the calculated D is fitted by formula (8) does not exceed 5–10% for both three- and two-dimensional systems.

As was said above, no exact analytical relation for the function $D(t)$ that would describe the evolution of the mass-transport processes with time can be obtained in the case of liquids. Disregarding the interparticle interaction, the mean square of the displacement of the jth particle per degree of freedom under the action of a random force F_{run} can be determined from Langevin's equation, represented as [18]

$$M\frac{d^2x_j^2}{dt^2} = -M\nu_{fr}\frac{dx_j^2}{dt} + 2M\left(\frac{dx_j}{dt}\right)^2 + 2x_jF_{\text{run}}. \qquad (9)$$

In the absence of a correlation between the slow particle displacement and the fast stochastic action ($\langle F_{\text{run}}x_j\rangle = 0$), the simultaneous solution of Eqs. (6) and (9) for a homogeneous medium ($M\langle(dx_i/dt)^2\rangle \equiv T$, $\langle(\Delta l)^2\rangle = m\langle x_j^2\rangle$) can then be written as [5]

$$\frac{D(t)}{D_0} = 1 - \frac{1 - \exp(-\nu_{fr}t)}{\nu_{fr}t}. \qquad (10)$$

Thus, the function $D(t) = D_0$ for noninteracting particles on long time scales compared to the reciprocal of the friction frequency ($\nu_{fr}t \gg 1$), while the ballistic pattern of particle motion manifests itself on short time scales ($\nu_{fr}t \ll 1$): $\langle x_j^2 \rangle \approx Tt^2/M$ and $D(t) = \langle x_j^2 \rangle/2t \propto t$.

Let us consider the motion of a macroparticle at a site of an imaginary crystal lattice. If the restoring force $F_r = -M\omega_c^2 x_j$ acting on the particle in this lattice can be described by one characteristic frequency ω_c, the equation of motion in the field of this force can be transformed to

$$M\frac{d^2x_j^2}{dt^2} - M\nu_{fr}\frac{dx_j^2}{dt} - 2M\omega_c^2x_j^2 + 2M\left(\frac{dx_j}{dt}\right)^2 + 2x_jF_{\text{run}}. \tag{11}$$

In the absence of a correlation between the displacement x_j and the random force ($\langle F_{\text{run}}x_j\rangle = 0$), the simultaneous solution of Eqs. (6) and (11) for a homogeneous medium ($M\langle (dx_i/dt)^2\rangle \equiv T$, $\langle(\Delta l)^2\rangle = m\langle x_j^2 \rangle$) can be written as

$$\frac{D(t)}{D_0} = \frac{1}{2\xi^{*2}\nu_{fr}t}\left\{1 - \exp\left(-\frac{\nu_{fr}t}{2}\right)\left(\cosh\frac{\nu_{fr}t\sqrt{1-8\xi^{*2}}}{2} + \sinh\frac{\nu_{fr}t\sqrt{1-8\xi^{*2}}}{2}\frac{1}{\sqrt{1-8\xi^{*2}}}\right)\right\} \tag{12a}$$

$$\text{at } \xi^* = \frac{\omega_c}{\nu_{fr}} < \frac{\sqrt{2}}{4},$$

$$\frac{D(t)}{D_0} = \frac{1}{2\xi^{*2}\nu_{fr}t}\left\{1 - \exp\left(-\frac{\nu_{fr}t}{2}\right)\left(\cos\frac{\nu_{fr}t\sqrt{8\xi^{*2}-1}}{2} + \sin\frac{\nu_{fr}t\sqrt{8\xi^{*2}-1}}{2}\frac{1}{\sqrt{8\xi^{*2}-1}}\right)\right\} \tag{12b}$$

$$\text{at } \xi^* = \frac{\omega_c}{\nu_{fr}} > \frac{\sqrt{2}}{4}.$$

It is easy to see that the ballistic regime of motion ($\langle x_j^2 \rangle \approx Tt^2/M$, $D(t) = \langle x_j^2 \rangle/2t \propto t$) is also characteristic of the particle at a lattice site on short observation time scales ($\nu_{fr}t \ll 1 + \xi^*$), as in the case of noninteracting particles. The mass-transport processes on short observation time scales for various parameters ξ^* (solutions (10), (12a), and (12b)) are illustrated in Fig. 1.

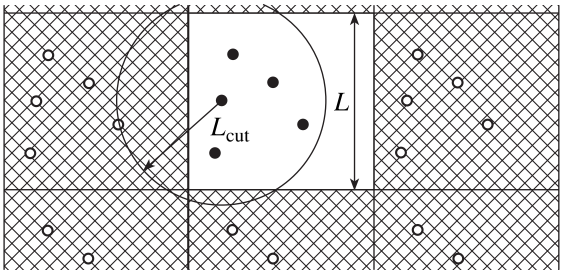

Fig. 1. Illustration of our numerical simulation using periodic boundary conditions

The function $D(t) = \langle(\Delta l)^2\rangle/2t \longrightarrow 0$ for a particle at a lattice site as the observation time increases ($\nu_{fr}t \gg 1$), since the rms deviation $\langle(\Delta l)^2\rangle$ of this particle from its equilibrium position is constant and corresponds to the deviation of a harmonic oscillator

$$\langle(\Delta l)^2\rangle = mT/M\omega_c^2. \tag{13}$$

Either the quasi-harmonic approximation or Einstein's approximation [28, 29] is used most commonly to determine the frequency ω_c, which characterizes the deviation of a particle from its equilibrium position in crystal lattices of various types. These approximations are based on the calculations of the oscillation frequency for an individual particle when the positions of the remaining particles are fixed. The frequencies obtained by these methods have no analytical dependence on the parameters of the interparticle interaction potential (Z and λ) and need additional fitting to describe the results of the existing numerical calculations of phase diagrams for systems with a screened pair interaction. For this purpose, the numerical data are fitted by linear, quadratic, or cubic functions on different (short) segments of the phase diagram [19, 28, 29]. A simple relation for the characteristic particle oscillation frequency $\omega_c = \omega_{bcc}$ that defines the melting line of a body-centered cubic lattice (according to Lindemann's criterion) and that requires no empirical fitting of the numerical data was suggested in [19]:

$$\omega_{bcc}^2 \approx \frac{(2eZ)^2\exp(-\kappa)}{l_p^3M\pi}\left(1 + \kappa + \frac{\kappa^2}{2}\right). \tag{14}$$

The interparticle collision probability $\sim N_{cn}/4\pi$, where N_{cn} is the number of pairs of the closest neighbors of an individual particle (located along with it on the same straight line) that ensure its stable position at the lattice site, was taken into account in this paper. (For a body-centered cubic lattice, $N_{cn} = 4$.) It was also assumed in the above paper that the restoring force F_r acting on the particle at the center of a cubic cell is proportional to twice the second derivative of the interparticle interaction potential at $l = l_p$. No such relation has been suggested previously for the characteristic macroparticle oscillation frequency $\omega_c = \omega_h$ in a quasi-two-dimensional hexagonal lattice. If we followed the reasoning of [19], then, given the interparticle collision probability in a plane hexagonal cell ~3/2π, we could assume that $\omega_h^2 \approx 1.5\omega_{bcc}^2$. This assumption agrees well with the calculated value of $\langle(\Delta l)^2/l_p^2\rangle$ on the melting line of two-dimensional structures [30]. In a quasi-two-dimensional structure, however, the particles have an additional degree of freedom that allows them to be displaced perpendicularly to the lattice plane. Such fluctuations do not activate the restoring forces in the crystal plane, but reduce the probability of effective collisions by a value of $\sim 3N_t/(2\pi)^3$, where $N_t = 4$ is the number of possible combinations for the simultaneous displacement of three particles (located on the same straight line) orthogonally to the lattice plane. Thus, the following fit may be suggested to estimate the characteristic macroparticle oscillation frequency in a quasi-two-dimensional hexagonal lattice:

$$\begin{aligned}\omega_h^2 &\approx 6(1-\pi^{-2})\frac{(eZ)^2\exp(-\kappa)}{l_p^3 M\pi}\left(1+\kappa+\frac{\kappa^2}{2}\right)\\ &\approx 5.4\frac{(eZ)^2\exp(-\kappa)}{l_p^3 M\pi}\left(1+\kappa+\frac{\kappa^2}{2}\right).\end{aligned} \tag{15}$$

3. USING THE METHOD OF MOLECULAR DYNAMICS TO MODEL THE TRANSPORT PROCESSES IN A DUSTY PLASMA

Two well-known numerical algorithms, the Monte Carlo method and the method of molecular dynamics, are commonly used to analyze the transport properties of systems of interacting macroparticles. In contrast to the Monte Carlo method, which was developed to calculate equilibrium quantities, the method of molecular dynamics allows the approach of the system under study to an equilibrium state to be described. Therefore, it is an irreplaceable tool for studying the heat- and mass-transport processes, the propagation of waves, and the formation dynamics of instabilities.

The method of molecular dynamics is based on the solution of a system of ordinary differential equations, the equations of particle motion in the field of various forces. Within the framework of this approach, we can separate the method of molecular dynamics that is based on the integration of reversible equations of particle motion (MRD) and the method of Brownian (or Langevin) dynamics that is based on the solution of Langevin's equations and that includes the irreversibility of the processes under study (MBD). In the first case (MRD), only the elastic interactions between particles are taken into consideration, while the dissipation (friction) and other processes of energy exchange between the particles and the ambient medium (a thermostat) are disregarded. The motion of particles in such a system is unstable (in Lyapunov's sense), and the computational data are renormalized after a certain number of integration steps to maintain their equilibrium temperature. This approach allows the processes in atomic systems to be properly modeled and is unsuitable for analyzing the motion of macroparticles in laboratory plasmas, where the dissipation due to collisions with atoms or molecules of the gas plays a significant role. In contrast to the MRD, the method of Brownian dynamics incorporates the particle kinetic energy losses through friction, and the equilibrium state of a system with a constant temperature is maintained through its energy exchange with the thermostat. This exchange is specified by the random force $F_{\rm run}$ reconciled with the forces of friction in the system under consideration by using the fluctuational–dissipative theorem [26]. The particular significance of the MBD in modeling the dynamics of macroparticles in dusty plasmas lies in the fact that Langevin's equations allow the interaction of dust particles with the thermostat particles that maintain a statistical equilibrium in the system under consideration to be taken into account. Such an equilibrium is observed in many experimental situations where the Maxwellian dust particle velocity distributions are recorded. In this case, the MBD allows one to take into account the energy exchange between the macroparticles and the ambient medium not only through their collisions with molecules of the ambient gas, but also through other stochastic processes, for example, through the macroparticle charge fluctuations that cause their kinetic temperature T to rise relative to the gas temperature [31, 32].

To model the equilibrium microscopic processes in extended homogeneous clouds of interacting macroparticles, apart from the random forces $F_{\rm run}$, which are the source of thermal particle motion, the forces of pair interparticle interaction $F_{\rm int}$ are included in the system of N_p equations of motion (N_p is the number of particles):

$$\begin{aligned}M\frac{d^2\mathbf{l}_k}{dt^2} &= \sum_j F_{\rm int}(l)\big|_{l=|\mathbf{l}_k-\mathbf{l}_j|}\frac{\mathbf{l}_k-\mathbf{l}_j}{|\mathbf{l}_k-\mathbf{l}_j|}\\ &\quad - M\nu_{fr}\frac{d\mathbf{l}_k}{dt}+\mathbf{F}_{\rm run}.\end{aligned} \tag{16}$$

Here, $F_{\rm int}(l) = \partial U/\partial l$, and $l = |\mathbf{l}_k - \mathbf{l}_j|$ is the interparticle distance. Under local thermodynamic equilibrium conditions, the mean value of the random force is $\langle F_{\rm run}\rangle = 0$, while the autocorrelation function

$$\langle F_{\rm run}(0)F_{\rm run}(t)\rangle = 6TM\nu_{fr}\delta(t)$$

describes a delta-correlated Gaussian process [2, 5]. Here, $\delta(t)$ is the delta-function. The random increments in macroparticle momentum can be used to model such stochastic processes,

$$p_{\rm run}^{x} = (2T\nu_{fr}\Delta tM)^{1/2}\psi,$$

where $p_{\rm run}^{x}$ is the momentum increment per degree of freedom, ψ is a random variable with a normal distribution with an rms deviation of 1, and Δt is the time integration step for the equations of motion (16). For the random forces to be properly modeled, the integration step Δt must satisfy the condition $\Delta t \ll \max(\nu_{fr}, \omega^*)$.

Periodic boundary conditions along the x, y, and z axes are commonly used to study the equilibrium processes in extended three-dimensional dust systems; these conditions allow the number of particles and their mean kinetic energy to be kept constant. Such boundary conditions can be realized by modeling 27 identical cubic cells the spatial arrangement of particles in which is kept similar to their arrangement in the central cell at each time of the computation (see Fig. 2). When crossing any boundary of the central cell, a particle returns with the velocity of its escape from the cell, but on the diametrically opposite side. In this case, what should be studied is the microscopic particle transport produced by the random forces that are balanced by the dissipation processes and the forces of interparticle interaction. To model the dynamics of macroparticles in extended dust layers, which are formed, for example, in the near-electrode plasma layer of a high-frequency capacitive discharge, periodic boundary conditions only in two selected directions (nine computational cells) are used, while the action of the balanced external forces is commonly considered along the remaining axis.

The numerical simulation procedure is as follows. The particles are arranged randomly within the central cell at the initial time of the computation, and a self-organization then begins via the interaction between them. Once an equilibrium configuration of the particle system for the specified parameters of the problem has been reached, data on the successive particle positions are written to the computer memory for their subsequent analysis. The dynamical characteristics (particle velocities and displacements) are analyzed only for the central cell.

All the particles of the full system of 27 (or 9, for the solution of the two-dimensional problem) cells that fall within the range of action of the pair potential are taken into account when calculating the forces of interparticle interaction. In this case, the interparticle interaction is often cut off at a certain distance $l = L_{\rm cut}$ determined by the condition for weak disturbance of the system's electroneutrality. For systems with a screened Coulomb potential, this condition can be represented as

$$\frac{Z_{L_{\rm cut}}}{Z} \sim \left(\frac{L_{\rm cut}}{l_p}\right)^3 \exp\left(-\frac{L_{\rm cut}}{\lambda}\right) \ll 1,$$

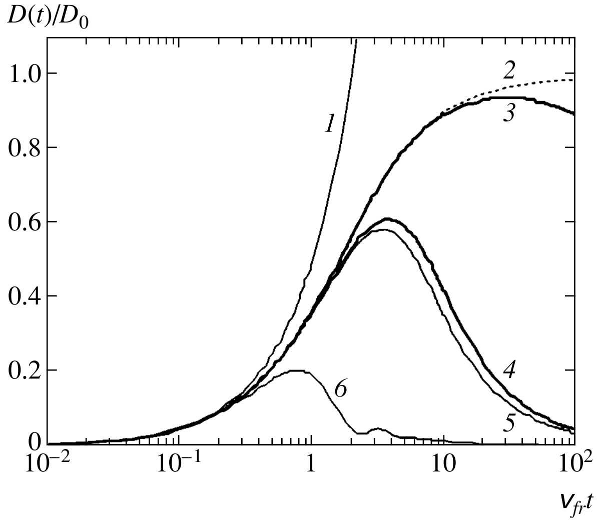

Fig. 2. Illustration of the mass-transport processes on short observation time scales. The function $D(t)/D_0$ is plotted against $t\nu_{fr}$: *1*—the ballistic regime ($D(t) \propto t$), *2*—noninteracting particles (10), and the solution of the problem for a harmonic oscillator at various parameters ξ^*: *3*—0.033 (12a), *4*—0.33 (12a), *5*—0.38 (12b), and *6*—2 (12b).

where $Z_{L_{\rm cut}}$ is the uncompensated charge in the modeled system. Hence, the size L of the computational cell for the proper modeling of the macroparticle dynamics in systems with a screened potential is specified by the condition $L \gg \lambda$ [33]. The parameters of the problem at which the length $L_{\rm cut}$ does not exceed $(4–8)l_p$, which corresponds to the number of independent particles (in the central cell) from 64 to 512, are used to perform most of the computations. In this case, cutting off the interaction potential does not lead to any significant error for screening parameters $\kappa = l_p/\lambda > 1$. When modeling systems with $\kappa < 1$, the longer-range interactions should also be taken into account. This can be done by using an appropriate algorithm whose essence consists in modeling an infinite system by constructing a large number of translational cells [29]. This method was developed to study the properties of crystals and is by no means always suitable for modeling the dynamics of liquid systems without any long-range order in the particle arrangement.

It should be emphasized that cutting off the potential at $L_{\rm cut}$ is a necessary condition for a stable state of the modeled system containing a large, but finite number of particles. Otherwise, such a point that more particles on one side than on the other side can always be found in this system. Thus, the action of electric forces is uncompensated at this point, and the system of particles under consideration is unstable. Since the cutoff length of the potential is finite, the modeled systems have an excess positive energy (due to the uncompensated charge) [33]. In this case, the problem under consideration is equivalent to the problem of particle confinement in the trap produced by external electric forces or

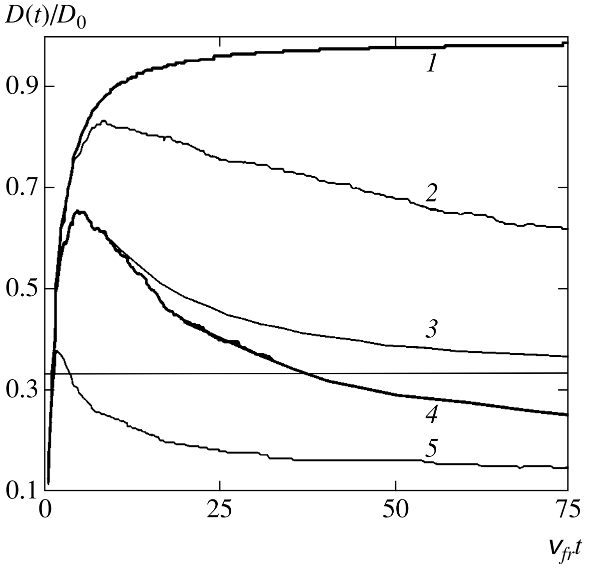

Fig. 3. $D(t)/D_0$ versus $t\nu_{fr}$ for noninteracting particles (*1*) and for three-dimensional systems ($\kappa = 4.8$) at various values of ξ and Γ^*: *2*—$\xi = 0.04$, $\Gamma^* = 77$; *3*—$\xi = 0.14$, $\Gamma^* = 30$; *4*—$\xi = 0.14$, $\Gamma^* = 77$; and *5*—$\xi = 0.41$, $\Gamma^* = 77$.

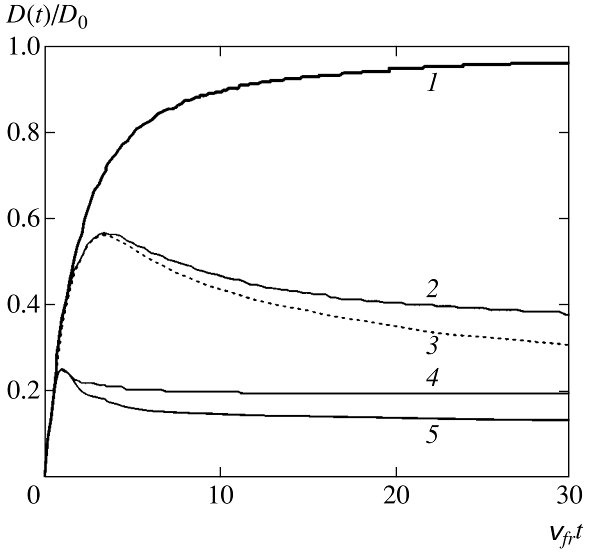

Fig. 4. $D(t)/D_0$ versus $t\nu_{fr}$ for noninteracting particles (*1*) and for quasi-two-dimensional systems ($\kappa = 2$) at various values of ξ and Γ^*: *2*—$\xi = 0.93$, $\Gamma^* = 27$; *3*—$\xi = 0.93$, $\Gamma^* = 56$; *4*—$\xi = 0.23$, $\Gamma^* = 27$; and *5*—$\xi = 0.23$, $\Gamma^* = 56$.

other potential forces, which ensure that a constant number of particles N_p is within a vessel of volume V and which maintain a pressure P in it.

4. NUMERICAL SIMULATIONS OF THE EVOLUTION OF MACROPARTICLE MASS-TRANSPORT PROCESSES ON SHORT OBSERVATION TIME SCALES IN TWO-DIMENSIONAL AND THREE-DIMENSIONAL SYSTEMS

We investigated the mass-transport processes for two cases: a homogeneous three-dimensional system and a quasi-two-dimensional system modeling an extended dust layer. The scale parameter was varied over the range $\xi \approx 0.04$ to $\xi \approx 3.6$, typical of the experimental conditions in gas discharge plasmas. The effective coupling parameter Γ^* was varied between 10 and 120.

For the three-dimensional problem, the main computations were performed for 125 independent particles in the central computational cell; the total number of particles in the computation of the pair interaction reached 3000. The screening parameter was set equal to $\kappa = 2.4$ and 4.8. The choice of λ was dictated by the condition for the proper modeling of the dynamics of such systems ($L \gg \lambda$). The interparticle interaction potential was cut off at $L_{\text{cut}} = 4l_p$. To check whether the computational results were independent of the number of particles and the cutoff length of the potential, we performed additional test computations for 512 independent particles at $L_{\text{cut}} = 7l_p$ in systems with $\Gamma^* = 1.5$, 17.5, 25, 49, and 92. The discrepancy between the results of these computations did not exceed the numerical error and was within ±(1–3)%.

To model an extended homogeneous layer of macroparticles, we specified periodic boundary conditions in two selected directions (x and y) and took into account the action of the gravity Mg compensated by the linear electric field $E_z = \beta z$, where β is the electric field gradient ($eZ_pE_z = Mg$), along the z axis. We varied the number N_p of independent particles in the computational cell between 50 and 1000 and set the screening parameter κ equal to 2 and 4. Depending on the number of particles, the cutoff length of the potential L_{cut} varied between $5l_p$ and $25l_p$. The gradient β of the electric field E_z, which bounds the dust layer along the z axis, was varied between ~100 to 10^{-2} V cm^{-2}. Our simulations revealed no tangible dependence of the macroparticle dynamics on the field gradient β and the number of independent particles N_p adopted for the computations.

The time dependences of $D(t)/D_0$ (in reciprocal braking times ν_{fr}^{-1}) derived by numerical simulations for three-dimensional and two-dimensional systems are shown in Figs. 3 and 4 for various parameters ξ and Γ^*. Curve *1* in these figures represents the exact solution of Langevin's equation for noninteracting particles (10). It is easy to see that the behavior of the function $D(t)$ for interacting particles on observation time scales $t\nu_{fr} \ll 1$ corresponds to the ballistic regime of particle motion. Subsequently, $D(t)$ reaches its maximum, whose value can be used to analyze the mass-transport processes on short observation time scales. In this case, neither the ratio $D_{\max}/D_0$ nor the position $t_{\max}\nu_{fr}$ of the $D(t)/D_0$ maximum depend on the parameter Γ^* and are deter-

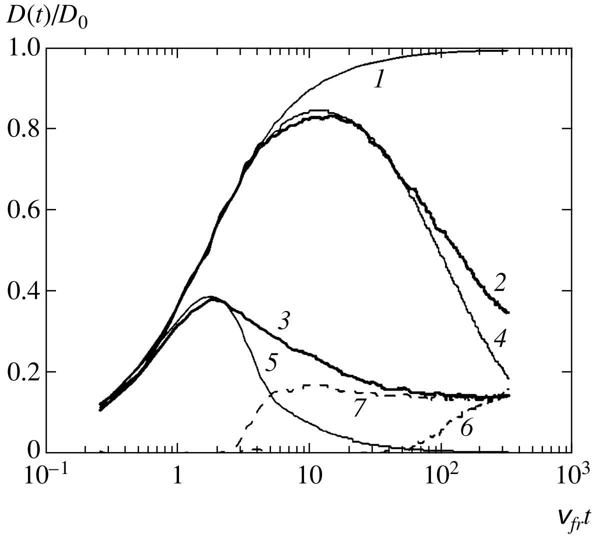

Fig. 5. $D(t)/D_0$ versus $t\nu_{fr}$ for noninteracting particles (*1*), for three-dimensional systems ($\kappa = 4.8$) at $\Gamma^* = 80$, $\xi = 0.04$ (*2*), 0.41 (*3*), and for a harmonic oscillator with $\xi^* = 0.08$ (*4*), 0.82 (*5*). Curves *6* and *7* represent the difference between the numerical solution of the three-dimensional problem (curves *2* and *3*) and the solution for a harmonic oscillator with the corresponding ξ^* (curves *4* and *5*, respectively).

mined by the parameter ξ for both the three-dimensional problem and the modeled two-dimensional system. This was pointed out previously in [18, 20]. As $t \longrightarrow \infty$, the function $D(t)$ tends to its constant value, $D = \lim_{t \to \infty} D(t)$, which corresponds to the standard definition of the particle diffusion coefficient as one of the main transport coefficients.

The evolution of the mass-transport processes in the analyzed liquid ($\Gamma^* < 102$) three-dimensional and quasi-two-dimensional extended systems is compared with the behavior of the function $D(t)/D_0$ for a harmonic oscillator at lattice sites in Figs. 5–7. The ratio of the scale parameter $\xi = \omega^*/\nu_{fr}$ to $\xi^* = \omega_c/\nu_{fr}$ presented in the captions to these figures is defined as $\xi^*/\xi = 2$ for three-dimensional problems and $\xi^*/\xi \approx 1.63$ for quasi-two-dimensional systems. In analyzing the three-dimensional problem, we used $\omega_c = \omega_{bcc}$ (14), which corresponds to the macroparticle oscillation frequency in a body-centered cubic lattice, as the characteristic particle oscillation frequency. The characteristic particle oscillation frequency in a two-dimensional hexagonal lattice, $\omega_c = \omega_h \approx 1.15\omega_{bcc}$, was determined by fitting the results of the numerical solution of the quasi-two-dimensional problem and the analytical solutions (12a) and (12b). This frequency closely corresponds to fit (15), which yields $\omega_h \approx 1.16\omega_{bcc}$.

We found that the functions $D(t)$ computed for extended systems closely corresponded to solutions (12a) and (12b) for a harmonic oscillator in all the analyzed systems on observation time scales $t\nu_{fr} \le 2/\xi^*$. Thus, the jump activation time t_a (the mean settled lifetime of the particles between the jumps) in the modeled systems was virtually independent of the temperature and was determined by the particle oscillation frequency in the settled state: $t_a \approx 2/\omega_c$.

The differences between the harmonic solution (curve *4*) and the computational results for an extended crystalline quasi-two-dimensional system (curve *2*) with $\xi = 1.3$ and $\Gamma^* = 115$ are shown in Fig. 7. It is easy to see that the numerical solution for an extended crystalline system approaches zero much more slowly than

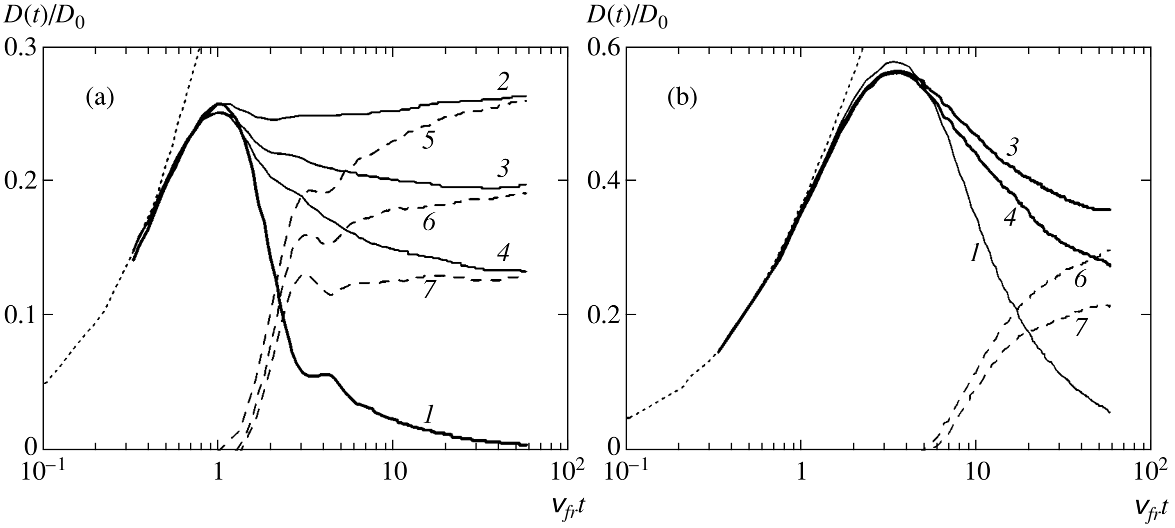

Fig. 6. $D(t)/D_0$ versus $t\nu_{fr}$ for quasi-two-dimensional systems ($\kappa = 4$) at $\xi = 0.93$ (a) and 0.23 (b) for $\Gamma^* = 12$ (*2*), 27 (*3*), and 56 (*4*). Curves *5*, *6*, and *7* represent the difference between the numerical solution for the quasi-two-dimensional problem (curves *2*, *3*, and *4*) and the solution for a harmonic oscillator (curve *1*). The ratio $D(t)/D_0$ for noninteracting particles is indicated by the dotted line.

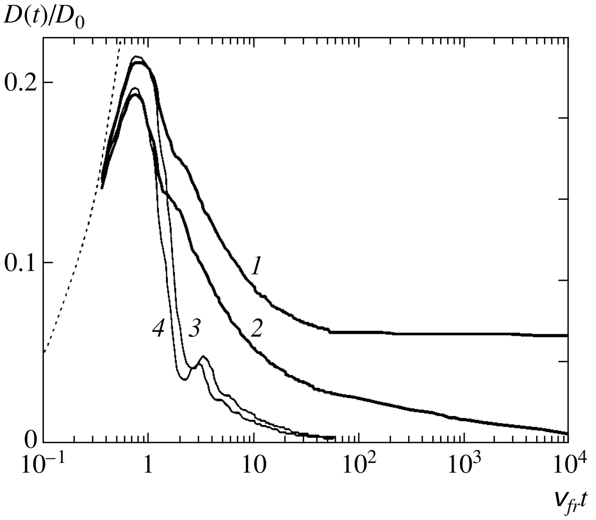

Fig. 7. $D(t)/D_0$ versus $t\nu_{fr}$ for quasi-two-dimensional systems ($\kappa = 4$) at $\xi = 1.14$, $\Gamma^* = 100$ (*1*) and $\xi = 1.3$, $\Gamma^* = 115$ (*2*). Curves *3* and *4* were obtained for a harmonic oscillator with the corresponding ξ^*. The ratio $D(t)/D_0$ for noninteracting particles is indicated by the dotted line.

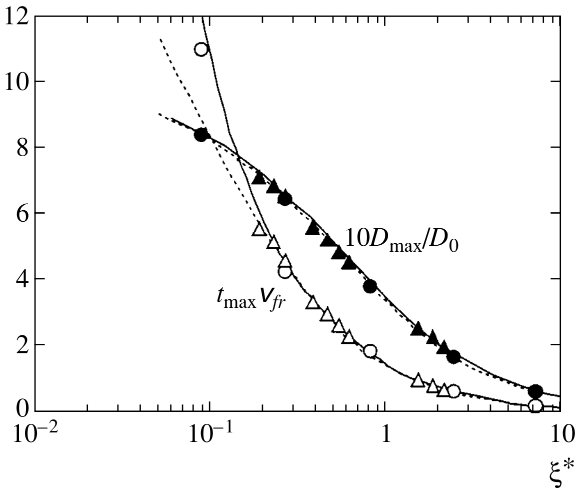

Fig. 8. $D_{\max}/D_0$ (●, ▲) and $t_{\max}\nu_{fr}$ (○, △) versus ξ^* for the quasi-two-dimensional (△, ▲) and three-dimensional (○, ●) problems. The solid lines represent the solution of the problem for a harmonic oscillator; the dotted lines represent fits (17) and (18) for $D_{\max}/D_0$ and $t_{\max}\nu_{fr}$, respectively.

the analytical solution for an ideal harmonic oscillator. This may be attributable to the excitation of lower lattice vibration modes under the influence of far neighbors in the extended system.

The maximum $D_{\max}$ of the function $D(t)$ and its position $t_{\max}\nu_{fr}$ are plotted against ξ^* in Fig. 8 for extended systems of macroparticles and for a one-dimensional oscillator. Since Eqs. (12a) and (12b) cannot be solved analytically, we solved these equations by the method of simple iterations. Empirical fitting of the numerical data by convenient analytic functions yields

$$D_{\max} \approx D_0/(1+2\xi^*) \tag{17}$$

for the ξ^* dependence of the maximum $D_{\max}$ and

$$t_{\max}\nu_{fr} \approx \frac{4\sqrt{2}}{\pi(1+8\sqrt{2}\xi^*)} \tag{18}$$

for the position $t_{\max}$ of this maximum. The suggested relations describe the numerical data (see Fig. 7), with an accuracy of 5%, for two-dimensional and three-dimensional systems, as well as the numerical solution for the problem of the motion of a one-dimensional oscillator in the ξ^* range 0.2 to 10. Thus, our numerical studies have revealed that the mass-transport processes on short observation time scales are determined by the parameter $\xi^* = \omega_c/\nu_{fr}$ (the value and position of the maximum of the function $D(t)/D_0$ depend only on ξ^* and are the same at equal ξ^* for both two-dimensional and three-dimensional systems). In contrast, the macroparticle diffusion coefficient $D = \lim_{t\to\infty} D(t)$ depends on $\xi = \omega^*/\nu_{fr}$ and Γ^* (see (8)). Accordingly, as the time increases, the dynamical characteristics of the system (the function $D(t)/D_0 \longrightarrow D/D_0$) cease to be determined by the characteristic macroparticle oscillation frequency ω_c at the lattice sites of this system in its solid state.

The evolution of the functions $D(t)$ under study illustrates the dynamics of the approach of the modeled system to a statistical equilibrium state in the case of its small deviations from this state. Our computations show that, in contrast to a system of Brownian particles, for which $D(t) \longrightarrow D_0$ at $t \gg \nu_{fr}^{-1}$, a system of interacting particles can be described by constant transport coefficients only on time scales $t \gg 2\omega_c^{-1}$. An analysis of the behavior of $D(t)$ on short observation time scales can be of use both in independently estimating ξ or ξ^*, which contain information about the interparticle interaction potential, and in restoring the macroparticle temperature T if the resolution of the measuring instrument is too low for their velocity spectrum to be properly determined.

In conclusion, note that the difference in the ratios ξ^*/ξ found for two-dimensional and three-dimensional systems allows us to explain the underestimated (by about 40–50%) scale parameters $\xi \sim 0.4$–0.5 that were obtained by comparing the simulations for the three-dimensional problem and the experimental measurements of the maximum $D_{\max}$ of the function $D(t)$ for the only dust layer formed in the near-electrode region of a high-frequency discharge in [34]. The parameter ξ measured by two other methods (by analyzing the pair correlation functions $g(l)$ and the diffusion coefficients D of macroparticles) corresponded to 0.66, to within

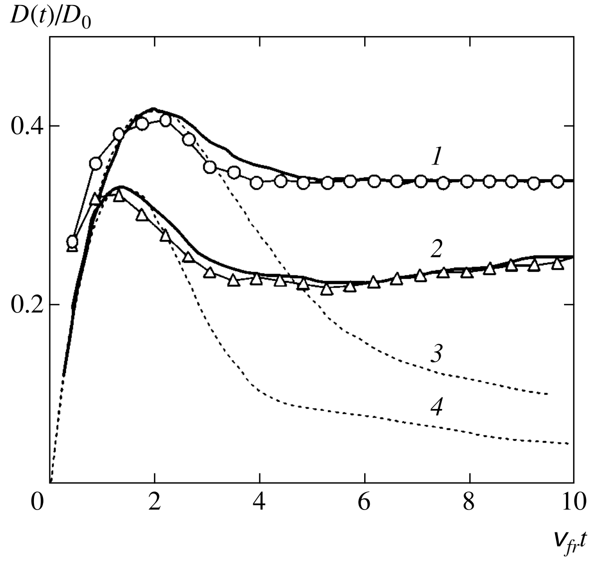

Fig. 9. Measurements of the function $D(t)/D_0$ for the three-dimensional dust structures in a direct-current discharge, $\xi \approx 0.36$, $\Gamma^* \approx 20$ (*1*), and for the dust layer, $\xi \approx 0.66$, $\Gamma^* \approx 35$, in the near-electrode region of a high-frequency discharge (*2*) [34]. The solution of the problem for a harmonic oscillator at $\xi^* = 2\xi$ for a three-dimensional cloud of macroparticles (*3*) and at $\xi^* \approx 1.63\xi$ for a quasi-two-dimensional dust layer (*4*). The results of our numerical simulations of the function $D(t)/D_0$ for two-dimensional ($\xi = 0.66$, $\Gamma^* = 35$) and three-dimensional ($\xi = 0.36$, $\Gamma^* = 20$) liquid systems are indicated by the heavy lines.

5%. The error lay in the fact that, when reversing the results of the measurements ($D_{\max}$ and $t_{\max}$), we assumed that the ratio ξ^*/ξ for a dust layer was equal to 2, as in the case of three-dimensional systems (accordingly, the characteristic frequency ω_h in a two-dimensional hexagonal lattice was assumed to be approximately equal to $\sqrt{2}\,\omega_{bcc}$). Figure 9 illustrates the $D(t)/D_0$ measurements for the three-dimensional dust structures in a direct-current glow discharge (curve *1*) and for the dust layer formed in the near-electrode region of a high-frequency discharge (curve *2*) presented in [34]. The values of ξ and Γ^* restored in this paper from the $g(l)$ and D measurements for the experimental conditions are given in the caption to the figure. It is easy to see that the behavior of the experimental $D(t)/D_0$ curves on observation time scales $t\nu_{\rm fr} \le 2/\xi^*$ is in good agreement with solutions (12a) for a harmonic oscillator at $\xi^* = 2\xi$ (for a three-dimensional cloud of macroparticles) and $\xi^* \approx 1.63\xi$ (for a quasi-two-dimensional dust layer). Figure 9 also shows the functions $D(t)/D_0$ obtained by numerically simulating a quasi-two-dimensional structure (with $\xi = 0.66$, $\Gamma^* = 35$) and a three-dimensional liquid system (with $\xi = 0.36$, $\Gamma^* = 20$). The differences on the initial segment of the curves are attributable to the noise introduced by the measuring procedure [34].

5. CONCLUSIONS

We presented the results of our numerical simulations of mass-transport processes on short observation time scales for extended quasi-two-dimensional and three-dimensional nonideal dissipative systems of macroparticles interacting via a screened Coulomb potential. The simulations were performed for the parameters corresponding to the experimental conditions in laboratory dusty plasmas. The evolution of the rms particle displacement on short observation time scales was found to correspond to lattice vibrations with a frequency proportional to the second derivative of the pair interparticle interaction potential. These results closely agree with the theory of jumps constructed by using analogies between the liquid and solid states of the medium. We provided estimates for the characteristic particle oscillation frequencies (ω_c) in three-dimensional face-centered cubic lattices and two-dimensional hexagonal crystal structures. These frequencies were shown to be responsible for the mean settled particle lifetime ($t_a \approx 2/\omega_c$) in nonideal liquid systems and to determine the pattern of mass-transport processes on observation time scales $t < t_a$.

The results can be used for passive diagnostics of parameters of the interparticle interaction potential in weakly dispersive plasma–dust structures and to numerically analyze the pattern of fast processes on physically short time scales that are not large enough for them to be described in terms of macroscopic kinetics.

ACKNOWLEDGMENTS

This work was supported in part by the Russian Foundation for Basic Research (project no. 04-02-16362), INTAS (grant no. 01-0391), the CRDF (grant no. RU-P2-2593-MO-04), the Program of the Presidium of the Russian Academy of Sciences, and the Foundation for Support of Russian Science.

REFERENCES

1. Ya. I. Frenkel', *Kinetic Theory of Liquids* (Nauka, Leningrad, 1975; Oxford Univ. Press, Oxford, 1976).
2. *Photon Correlation and Light Beating Spectroscopy,* Ed. by H. Z. Cummins and E. R. Pike (Plenum, New York, 1974).
3. R. Balescu, *Equilibrium and Nonequilibrium Statistical Mechanics* (Wiley, New York, 1975; Mir, Moscow, 1978).
4. N. K. Ailawadi, Phys. Rep. **57**, 241 (1980).
5. A. A. Ovchinnikov, S. F. Timashev, and A. A. Belyĭ, *Kinetics of Diffusely-Controlled Chemical Processes* (Khimiya, Moscow, 1986) [in Russian].
6. H. M. Thomas and G. E. Morfill, Nature **379**, 806 (1996).
7. A. A. Zhukhovitskiĭ and L. A. Shvatsman, *Physical Chemistry* (Metallurgiya, Moscow, 1987) [in Russian].

8. D. K. Belashchenko, *Transport Phenomena in Liquid Metals and Semiconductors* (Atomizdat, Moscow, 1970) [in Russian].
9. Ya. I. Frenkel', *Introduction to the Theory of Metals* (Nauka, Moscow, 1958) [in Russian].
10. A. V. Gorshkov, Prikl. Fiz., No. 6, 65 (1999).
11. G. G. Petrik, Z. R. Gadzhieva, and B. E. Todorovskiĭ, *Chemistry and Computer Simulation. Butlerov Lectures*, Supplement to Special Issue No. 10, 301 (2002).
12. D. A. Young and B. J. Alder, Phys. Rev. A **3**, 364 (1971).
13. J. Chu and L. I. Lin, Phys. Rev. Lett. **72**, 4009 (1994).
14. H. Thomas, G. Morfill, V. Demmel, *et al.*, Phys. Rev. Lett. **73**, 652 (1994).
15. A. Melzer, T. Trottenberg, and A. Piel, Phys. Lett. A **191**, 301 (1994).
16. A. P. Nefedov, O. F. Petrov, V. I. Molotkov, and V. E. Fortov, Pis'ma Zh. Éksp. Teor. Fiz. **72**, 313 (2000) [JETP Lett. **72**, 218 (2000)].
17. A. M. Lipaev, V. I. Molotkov, A. P. Nefedov, *et al.*, Zh. Éksp. Teor. Fiz. **112**, 2030 (1997) [JETP **85**, 1110 (1997)].
18. O. S. Vaulina and S. V. Vladimirov, Plasma Phys. **9**, 835 (2002).
19. O. S. Vaulina, S. V. Vladimirov, O. F. Petrov, *et al.*, Phys. Rev. Lett. **88**, 245002 (2002).
20. O. S. Vaulina, I. E. Dranzhevsky, and O. F. Petrov, in *Contributions of the 31st EPS Conf. Plasma Phys.* (London, 2004), Vol. 28G, p. 1.039.
21. E. M. Lifshitz and L. P. Pitaevskiĭ, *Physical Kinetics* (Nauka, Moscow, 1979; Pergamon, Oxford, 1981).
22. N. A. Fuchs, *The Mechanics of Aerosols* (Dover, New York, 1964).
23. R. K. Dodd, J. C. Eilbeck, J. Gibbon, and H. C. Morris, *Solitons and Nonlinear Wave Equations* (Academic, New York, 1982; Mir, Moscow, 1988).
24. A. P. Nefedov, O. F. Petrov, S. A. Khrapak, *et al.*, Teplofiz. Vys. Temp. **36**, 141 (1998) [High Temp. **36**, 137 (1998)].
25. V. Fortov, A. Nefedov, V. Vladimirov, *et al.*, Phys. Lett. A **258**, 305 (1999).
26. E. M. Lifshitz and L. P. Pitaevskiĭ, *Course of Theoretical Physics*, Vol. 5: *Statistical Physics*, Part 2 (Nauka, Moscow, 1978; Pergamon, New York, 1980).
27. O. S. Vaulina and S. A. Khrapak, Zh. Éksp. Teor. Fiz. **119**, 264 (2001) [JETP **92**, 228 (2001)].
28. M. O. Robbins, K. Kremer, and G. S. Grest, J. Chem. Phys. **88**, 3286 (1988).
29. S. Hamaguchi, R. T. Farouki, and D. H. E. Dubin, Phys. Rev. E **56**, 4671 (1997).
30. X. H. Zheng and J. C. Earnshaw, *Advances in Dusty Plasma*, Ed. by P. K. Shukla, D. A. Mendis, and T. Desai (World Sci., Singapore, 1997).
31. V. V. Zhakhovskiĭ, V. I. Molotkov, A. P. Nefedov, *et al.*, Pis'ma Zh. Éksp. Teor. Fiz. **66**, 392 (1997) [JETP Lett. **66**, 419 (1997)].
32. O. S. Vaulina, S. A. Khrapak, O. F. Petrov, and A. P. Nefedov, Phys. Rev. E **60**, 5959 (1999).
33. R. T. Farouki and S. Hamaguchi, Appl. Phys. Lett. **61**, 2973 (1992).
34. O. S. Vaulina, O. F. Petrov, V. E. Fortov, *et al.*, Fiz. Plazmy (Moscow) **29**, 698 (2003) [Plasma Phys. Rep. **29**, 642 (2003)].

Translated by V. Astakhov

Journal of Experimental and Theoretical Physics, Vol. 100, No. 5, 2005, pp. 1029–1034.
Translated from Zhurnal Éksperimental'noĭ i Teoreticheskoĭ Fiziki, Vol. 127, No. 5, 2005, pp. 1166–1172.
Original Russian Text Copyright © 2005 by Vasilyak, Vetchinin, Polyakov, Fortov.

STATISTICAL, NONLINEAR, AND SOFT MATTER PHYSICS

Formation of Complex Structures in Dusty Plasmas under Temperature Gradients

L. M. Vasilyak, S. P. Vetchinin, D. N. Polyakov, and V. E. Fortov

Institute for High Energy Densities, Joint Institute for High Temperatures, Russian Academy of Sciences, Moscow, 125412 Russia

e-mail: lab852@ihed.ras.ru

Received November 3, 2004

Abstract—Thermophoretic effects on dust structures under temperature gradients in glow and radio-frequency discharge plasmas are studied experimentally. The geometry of dust structures consisting of micrometer-sized polydisperse grains depends on heat release in the plasma. Thermophoretic forces associated with heat release can control the formation of dust structures of different geometries. A theoretical model is proposed to describe dust separation with respect to grain size caused by the effects of radial electrostatic and thermophoretic forces. The glow discharge currents under critical conditions for grain separation predicted by the model agree with those observed experimentally. *© 2005 Pleiades Publishing, Inc.*

1. INTRODUCTION

The geometry of plasma-dust structures consisting of micrometer-sized grains depends on heat release in the plasma [1, 2]. It was found that this geometry depends on discharge current in glow discharges [3]. It was shown in [2] that nonuniform distribution of discharge current gives rise to temperature gradients and thermophoretic forces acting on dust grains. The effect of thermophoretic forces associated with heat release on dust grains can lead to the formation of dust structures having various geometries, such as annular structures [3] or more complicated ones consisting of two dust clouds [1]. The geometry of a dust cloud is determined by the parameters of the potential well resulting from the balance of different forces. The existence of various plasma-dust geometries and structures mainly depends on the balance of forces in the radial direction, because the radial well depth is much smaller than the longitudinal well depth [2]. While the ambipolar radial electric field acting on charged dust grains is directed inwards, dust grains are pushed outwards by ion friction and thermophoretic force. The latter force is proportional to the temperature gradient, and its direction is parallel to the conductive heat flux in neutral gas. In most experiments where dust grains are trapped in charged layers, ion friction is much weaker than thermophoretic forces. Thermophoretic force can be used to change the position and geometry of a dust cloud, remove dust grains from the discharge, and create thermophoretic traps in plasmas, for example, at cryogenic temperatures [1, 4]. In this study, we experimentally examine thermophoretic effects on dust structures associated with variations of heat release in glow and radio frequency (RF) discharge plasmas caused by variations of current and power input and determine conditions for formation of complex polydisperse dust structures.

2. EXPERIMENTAL

We studied plasma-dust structures that develop in the first striation in a glow discharge sustained in a 2-cm diameter discharge tube and in the electrical double layer in 13.56 MHz RF discharges sustained in 2- and 5-cm diameter discharge tubes (see Fig. 1). The anode was a grounded cylindrical electrode in the case of glow discharge and a grid placed outside the discharge tube in the case of RF discharge. The experiments were conducted in air at pressures of 0.1 to 0.2 Torr. Plasma-dust structures were created by using 5- to 20-μm-diameter magnesium oxide particles and

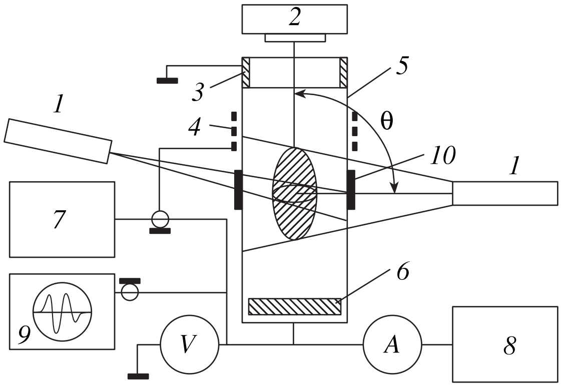

Fig. 1. Experimental setup: (*1*) solid-state laser; (*2*) camera; (*3*) annular anode; (*4*) grid electrode; (*5*) glass discharge tube; (*6*) cathode; (*7*) RF generator; (*8*) dc voltage source; (*9*) oscilloscope; (10) Peltier cooler; θ = shooting angle; *A* = ammeter; *V* = voltmeter.

1063-7761/05/10005-1029$26.00 © 2005 Pleiades Publishing, Inc.

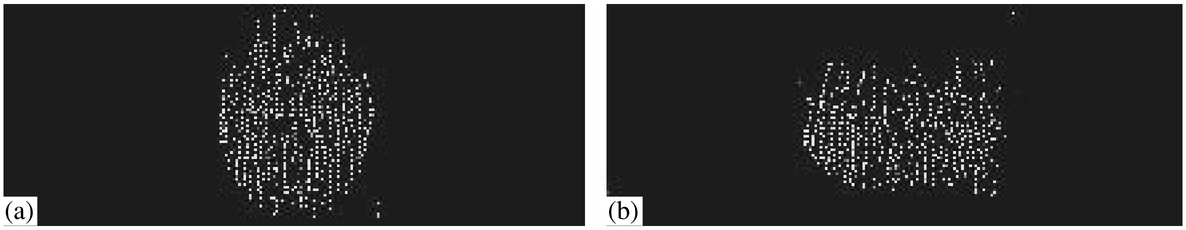

Fig. 2. Longitudinal cross-sectional images of aluminum dust structures obtained at $\theta = 0$: (a) $I = 0.4$ mA; (b) $I = 0.8$ mA. The lateral dimensions of the images correspond to the outer diameter of the discharge tube.

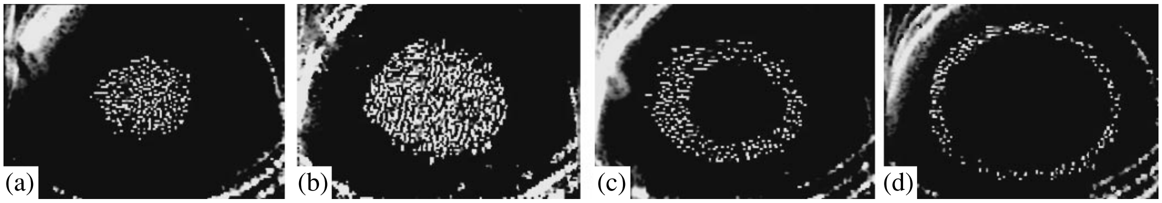

Fig. 3. Transverse cross-sectional images of aluminum dust structures obtained at $\theta = 45°$: (a) $I = 0.4$ mA; (b) $I = 1.2$ mA; (c) $I = 1.6$ mA; (d) $I = 3$ mA. The lateral dimensions of the images correspond to the inner diameter of the discharge tube.

1- to 5-μm-diameter aluminum particles. The properties of the structures were examined by varying the glow discharge current between 0.4 and 4 mA and the RF discharge voltage between 100 and 150 V. We measured the glow discharge voltage and current and the potential at the active electrode of the RF discharge by means of a Tektronix TDS 3032 oscilloscope. The plasma-dust structures were studied by using a Watec LCL-187 CCD camera (at a shutter speed of 1/1000) set at various angles θ to capture the light reflected from a dust structure illuminated by mutually perpendicular laser sheets with a waist diameter of 150 μm. The camera had an imaging system with 22× optical zoom. Transverse and longitudinal cross-sectional video images were taken through a window in the end wall of the tube, digitized, and computer-processed to enhance contrast. An external gradient of the temperature field in the 5-cm-diameter discharge tube was created by using two 2.5-cm-long Peltier coolers mounted on the side wall of the tube.

3. RESULTS

3.1. Glow Discharge

In glow discharge plasmas, dust structures consisting of microscopic grains form in striations. We examined the central part of the cross section of the first striation. The geometry of a dust structure depends on the discharge current (see [2, 3]). When the discharge current was $I = 0.4$–1 mA, we observed the formation of an ellipsoidal structure having a diameter of about one-third or one-fourth of the tube diameter (see Fig. 2). The diameter of the structure increased with the current, reaching the size of the bright part of the striation at a current of 4 mA. The longitudinal size of the structure decreased with increasing current (see Fig. 2). An annular structure developed at $I > 1.6$ mA, and its diameter increased with the current while its width decreased (see Fig. 3). No grains were observed near the axis, and the longitudinal size of the annular structure varied weakly with increasing current. The values of the current corresponding to transitions between different geometries of dust structures depend on the gas pressure in the tube and the dust grain size. It was found in [2] that the change from disk to annulus in the cross-section of a dust structure with increasing discharge current is controlled by the radial temperature gradient associated with joule heating of the gas in the tube.

Figure 4 demonstrates that the presence of dust in a glow discharge plasma changes ambient plasma properties, shifting the current–voltage characteristic of the discharge. The discharge voltage corresponding to a particular current can increase [5] or decrease (Fig. 4) in the presence of a plasma-dust structure. The increase in voltage depends on the additional loss of electrons and ions on grain surface, grain charging, and the relative number of the electrons that are attached to the grains and do not contribute to current and ionization in the bulk plasma. The decrease in voltage can be explained by the electron emission from the grain surface induced by incident photons and ions accelerated by the fields of charged grains to the energy corresponding to the electron temperature T_e.

At a high degree of dust polydispersity in a glow discharge, a decrease in gas pressure leads to the formation of a complex dust structure with geometry depending on the discharge current, and radial separation of grains is observed in the cross section of the structure. For example, in the case of MgO particles characterized by a size distribution with peaks at about 5 and 15–20 μm,

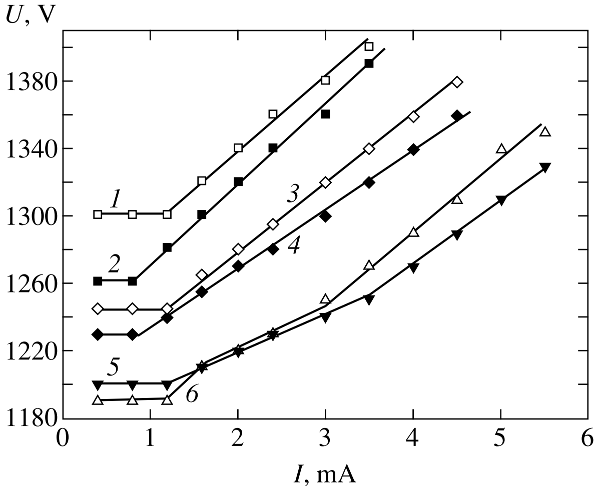

Fig. 4. Effect of aluminum dust structures on discharge current–voltage characteristics at several air pressures: (*1*, *2*) $P = 0.1$ Torr; (*3*, *4*) $P = 0.15$ Torr; (*5*, *6*) $P = 0.2$ Torr. Closed symbols correspond to dusty plasmas.

an almost uniform dust structure is observed at the tube axis at a discharge current of 0.4 mA. As the current increases to 1.6 mA, a fraction of the dust remains at the axis, while the rest moves to the wall, which leads to the formation of two dust clouds (see Fig. 5). At a current of 2.4 mA, all dust grains concentrate at the walls, making up an annular structure. The formation of dust clouds having this complex geometry takes place in narrow ranges of discharge current, gas composition, and pressure and depends on the grain size distribution.

Analysis of results. Our experimental results can be described by the following model of dust separation with respect to grain size caused by the effects of radial electrostatic and thermophoretic forces. At a low gas pressure, the thermophoretic force is

$$F_T = -4PLa^2\nabla T/T,$$

where P is the neutral-gas pressure, T is the gas temperature, L is the mean free path of molecules, and a is the grain radius ($L \gg a$). In a glow discharge plasma, the ambipolar radial electrostatic field that sustains charged dust grains is

$$F_E = ZkT_e\nabla n/n,$$

where n is the electron density and eZ is the grain charge. The balanced state of dust grains is determined by their potential energy, which depends on grain size. Since both forces exerted by an ambipolar radial electrostatic field and thermophoretic forces are proportional to the corresponding gradients, the potential energy can be expressed as follows [2]:

$$U(r) = -\alpha[1 - J_0(2.4r/R)] - \beta \ln J_0(2.4r/R),$$

where $\alpha = PLa^2IE/(2\lambda T_w)$ $\beta = ZT_e$, λ denotes the thermal conductivity of the gas, E is the longitudinal electric field strength in the striation, and T_w is the wall temperature. In the model of a discharge plasma controlled by ionization and diffusion, the electron-density distributions in the positive column and striation are described by the Bessel function $J_0(2.4r/R)$, where R is the tube radius. Therefore, the force F_E scales with radius near the axis and increases more rapidly toward the tube wall. If the heat release in the plasma is axially symmetric, then the thermophoretic force is also proportional to radius near the axis. The formation of two radially separated structures is explained by the difference in the electrostatic and thermophoretic forces acting on grains of different size. Since the thermophoretic force scales with grain cross section, whereas the electrostatic force is proportional to grain charge or radius, the potential-energy distribution may have a minimum. The minimum is located closer to the tube wall for larger grains. At particular gas pressure and discharge current, dust grains larger than certain size make up an annulus, while smaller grains are localized near the tube axis. (Larger particles are pushed out of a finite-depth potential well toward the wall by the thermophoretic force.) The conditions under which the minimum appears are the threshold conditions for transition to annular structure of dust clouds in a glow-discharge

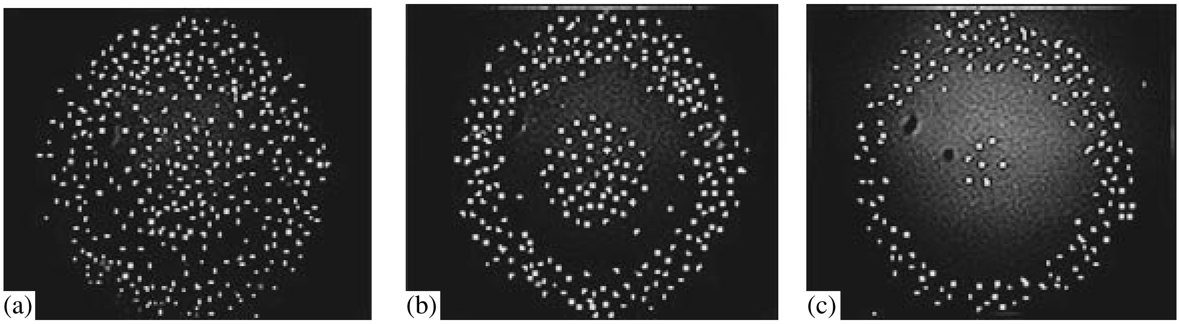

Fig. 5. Cross-sectional images of MgO dust structures in glow discharge plasmas obtained at $\theta = 90°$: (a) $I = 1$ mA; (b) $I = 1.4$ mA; (c) $I = 1.8$ mA.

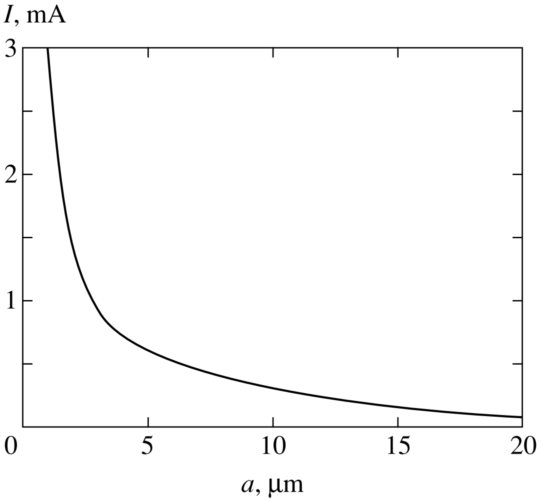

Fig. 6. Transition to annular structure in a glow-discharge cross section.

cross section. Figure 6 shows the transition current calculated for glow discharge in air as a function of grain size by using measured electric field strengths. Annular structure is observed at currents lying above the curve. Conditions below the curve correspond to dust grains localized near the tube axis. This model describes dust separation with respect to grain size in experiments on polydisperse dust in glow discharge. The values of current calculated by using the model agree with experimental results. Note that larger (15–20 μm) grains are additionally driven toward the wall by ion friction, which is ignored here. Thermophoretic forces can be used to change the position and geometry of a dust cloud and remove dust grains from the discharge.

3.2. RF Discharge

An analogous dependence of the geometry of a plasma-dust structure on heat release is observed for RF discharge. At relatively low voltages, the structure is localized in the space-charge layer at the active electrode surface. With increasing RF discharge voltage, a dust-free zone develops in the central region of the plasma-dust structure (see Figs. 7–9). This is explained by an increase in the axially symmetric power input, which manifests itself by higher emission from the zone. We found that the average interparticle spacing increases with RF discharge voltage when the spacing is smaller than 0.2 mm. Analogous behavior was observed in glow discharge as the discharge current was increased [3]. Further increase in power input leads to transition to annular structure (see Fig. 9). When the initial average interparticle spacing is larger than 0.2 mm, it does not increase and annular structure develops at lower rates of power input. The bright area in Fig. 9 corresponds to a zone of higher power input (higher total intensity of light emitted by the plasma).

When the temperature of the RF-discharge tube wall is reduced by 20 K, the dust structure located between the Peltier coolers is stretched in the radial direction by thermophoretic forces (see Fig. 10). Its cross section becomes an ellipse stretched toward the cooled walls. Eventually, the dust cloud splits into two parts, which are attracted to the cooled walls. (An analogous effect was revealed in glow-discharge striations when the discharge tube was cooled on opposite sides [1].) Dust grains are trapped in a new balanced state sustained by superposition of the longitudinal electric field and the thermophoretic forces due to radial temperature gradients. The temperature field can be adjusted to create dust clouds of different geometries. Experimental results on splitting dust clouds can be used to estimate the binding energy for grains in the structure. Consider an initially spherical charged dust cloud that splits into two equal spherical parts, which move apart in an ambipolar radial electrostatic field. The binding energy can be estimated by using the difference between the potential energies of the charged clouds and the work done by thermophoretic forces to displace the clouds in the electric field. Suppose that the potentials of both fragments are equal to the floating potential φ of the plasma. The change in electrostatic energy is

$$\Delta W = 0.5\Delta C\varphi^2 + 0.4R_C\varphi^2,$$

where ΔC is the change in the capacitance of the spheres and R_C is the initial cloud radius. According to experimental observations, the initial cloud diameter is 5 mm, the number of grains in the cloud is $N \approx 6000$, and the distance between the spheres is approximately

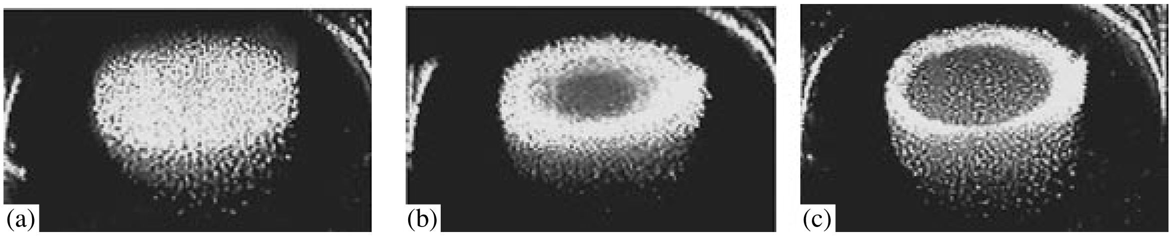

Fig. 7. Images of dust structure in an RF-discharge cross section in a 2-cm diameter tube obtained at θ = 45° for voltage amplitudes of (a) 100, (b) 110, and (c) 120 V.

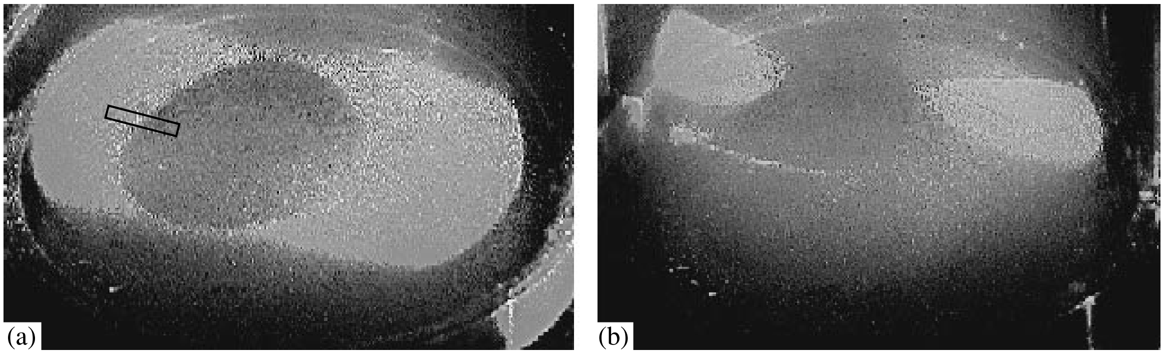

Fig. 8. Images of dust structure with a dust-free central zone in RF discharge in a 5-cm diameter tube obtained at θ = 45° and a voltage of 150 V: (a) transverse cross section; (b) longitudinal cross section. The lateral frame size corresponds to the discharge tube diameter.

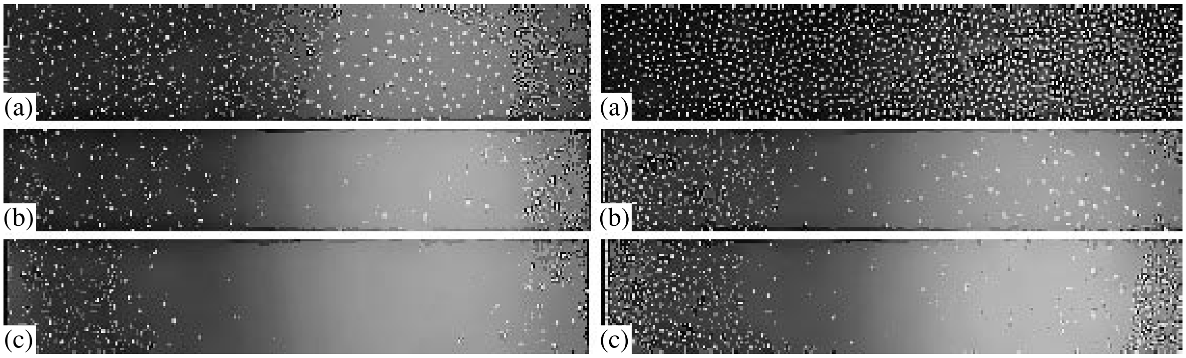

Fig. 9. Fragments of images of aluminum dust structures in RF discharge obtained at θ = 90° for (a) 100, (b) 105, and (c) 110 V. The lateral frame size is approximately equal to the framed area in Fig. 8a. The right and left columns correspond to different dust densities.

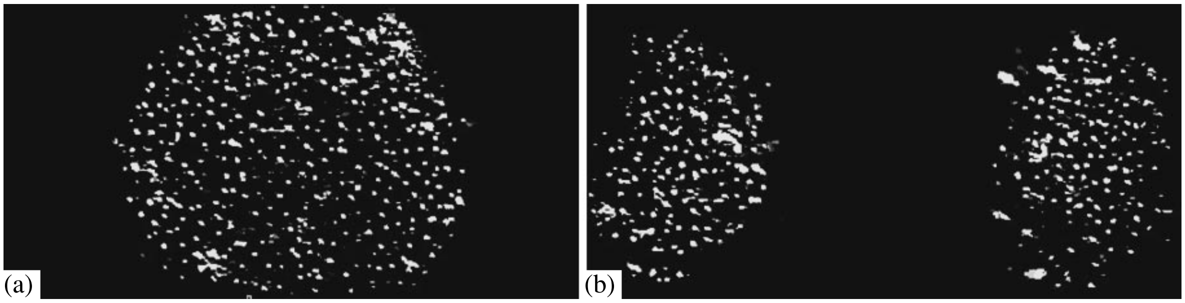

Fig. 10. Splitting of a dust structure in RF discharge caused by cooling of the discharge tube on opposite sides: (a) before cooling; (b) after cooling.

equal to their diameter d. The number of broken bonds, $\Delta N \approx 400$, is approximately equal to the number of grains in the cross section of the splitting. The total work is the sum of the work $\Delta C\varphi^2$ done by electrostatic field to displace the excess charge on the two spheres and the work A done by thermophoretic forces,

$$A + \frac{N\alpha\Delta T d^2}{4T_w\Lambda^2},$$

where $\Lambda = R/2.4$. The total work produces a change ΔW in electrostatic energy and a change $\Delta N\varepsilon$ in binding energy:

$$\Delta C\varphi^2 + A = \Delta W + \Delta N\varepsilon.$$

The evaluated binding energy, $\varepsilon \approx 3$ keV, is comparable to the binding energy of a dust molecule calculated in [6].

4. CONCLUSIONS

Thermophoretic forces associated with heat release in electric discharge control the formation of complex dust structures. Thermophoretic traps can be created to produce plasma-dust clouds having various geometries. The measured current–voltage characteristics demonstrate that the properties of glow discharge change in the presence of dust grains. Thermophoretic forces induce separation with respect to grain size, which can be used in practical applications.

REFERENCES

1. L. M. Vasilyak, S. P. Vetchinin, V. S. Zemnukhov, *et al.*, Zh. Éksp. Teor. Fiz. **123**, 493 (2003) [JETP **96**, 436 (2003)].
2. V. V. Balabanov, L. M. Vasilyak, S. P. Vetchinin, *et al.*, Zh. Éksp. Teor. Fiz. **119**, 99 (2001) [JETP **92**, 86 (2001)].
3. L. M. Vasilyak, S. P. Vetchinin, A. P. Nefedov, and D. N. Polyakov, Teplofiz. Vys. Temp. **38**, 701 (2000) [High Temp. **38**, 675 (2000)].
4. V. E. Fortov, L. M. Vasilyak, S. P. Vetchinin, *et al.*, Dokl. Akad. Nauk **382**, 50 (2002) [Dokl. Phys. **47**, 21 (2002)].
5. L. M. Vasilyak, S. P. Vetchinin, D. N. Polyakov, and V. E. Fortov, Zh. Éksp. Teor. Fiz. **121**, 609 (2002) [JETP **94**, 521 (2002)].
6. G. E. Morfill, V. N. Tsytovich, and H. Thomas, Fiz. Plazmy (Moscow) **29**, 3 (2003) [Plasma Phys. Rep. **29**, 1 (2003)].

Translated by A. Betev

Journal of Experimental and Theoretical Physics, Vol. 100, No. 5, 2005, pp. 1035–1041.
Translated from Zhurnal Éksperimental'noĭ i Teoreticheskoĭ Fiziki, Vol. 127, No. 5, 2005, pp. 1173–1180.
Original Russian Text Copyright © 2005 by Kuz'min.

**STATISTICAL, NONLINEAR,
AND SOFT MATTER PHYSICS**

Contribution of Multiple Scattering to the Dielectric Constant of a Randomly Inhomogeneous Medium

V. L. Kuz'min
St. Petersburg Institute of Trade and Economics, ul. Novorossiiskaya 50, St. Petersburg, 194021 Russia
e-mail: Vladimir.Kuzmin@paloma.spbu.ru

Received November 17, 2003; in final form, September 2, 2004

Abstract—Within the statistical theory of multiple scattering of light in random media, the dielectric constant of a suspension is represented as a diagram series in scattering orders and concentration of particles. The contributions of double and triple scattering events are determined. The extinction length and the transport mean free path in highly concentrated suspensions calculated with the use of the optical theorem are in good agreement with the available data. It is shown that the two-particle Born approximation, combined with the Mie form factor and the Percus–Yevick structure factor, is not adequate for systems with a high concentration of scatterers. A contribution to the optical parameters is found that is missing in the above approximation. © *2005 Pleiades Publishing, Inc.*

1. INTRODUCTION

The wide application [1] of coherent and correlation effects of multiple scattering of light in strongly inhomogeneous opaque colloidal systems (suspensions, emulsions, gels, foams, and biological tissues [2–10]) made the problem of calculating the optical parameters of these systems topical.

The main parameters that characterize radiation transfer in the multiple scattering regime are the photon mean free path l (or the extinction length) and the transport mean free path $l^* = l(1 - \overline{\cos\theta})$, where $\overline{\cos\theta}$ is the average cosine of the scattering angle—the basic parameter that characterizes the anisotropy of the scattering cross section. The optical theorem in the Born approximation relates the parameters l and l^* to the scattering cross section of electromagnetic radiation in the second, the lowest nonvanishing, order with respect to the difference $\Delta\varepsilon = \varepsilon_p - \varepsilon_0$ of the dielectric constants of a particle ε_p and the medium ε_0 in which the particles are dispersed. In this case, the differential cross section, or the scattering indicatrix, is represented as a product of a form factor, which characterizes the scattering by an individual particle, and a structure factor. To describe the structure factor of a suspension, one widely uses the Percus–Yevick approximation [11], which proved to be quite successful for describing the model of solid spheres. For most systems, the parameter $\Delta\varepsilon$ is not small. Therefore, one replaces the Rayleigh–Gans form factor by the Mie form factor [2, 4–6], while remaining within the Born approximation. However, for condensed suspensions, the application of the Mie form factor is not consistent with the Percus–Yevick structure factor because the latter factor takes into account the correlation in the positions of particles in all orders in concentration, whereas the Mie form factor involves an expression for the field near an isolated particle. The discrepancy between the measured values of the parameters and those calculated according to the above scheme amounts to 30% for condensed suspensions [5, 6].

In the present paper, we apply the diagram technique developed earlier [12–14] in the theory of propagation and scattering of light in random media to describe the dielectric constant of a suspension as a series in the parameter $\Delta\varepsilon$ and the concentration. This allows us to calculate the optical parameters of a suspension beyond the framework of Born approximation. It is obvious that the standard approach does not take into account multiparticle correlations of order greater than 2. However, we show that the standard approach, based on the multiplicative representation of the scattering cross section as a product of the Mie form factor and the structure factor [2, 4–6] when the latter factor takes into account the terms of any order in the concentration, completely ignores the processes of multiple rescattering among a given number of particles; it does not even completely take into account the second-order terms in the concentration. We find an explicit expression for the correction to the dielectric constant that comes from the rescattering between two particles. This correction is of second order in the concentration and of third order in the parameter $\Delta\varepsilon$. This additional term improves the agreement between theoretical and the available experimental results [5] in the range of high concentrations.

In this paper, we consider systems without intrinsic absorption, i.e., absorption associated with inelastic

1063-7761/05/10005-1035$26.00 © 2005 Pleiades Publishing, Inc.

$$\hat{\Pi}(\mathbf{r}_1 - \mathbf{r}_2) = \frac{\Delta\varepsilon}{4\pi\varepsilon_0}\delta(\mathbf{r}_1 - \mathbf{r}_2)$$

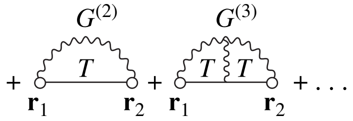

Fig. 1. Contributions of the first-, second-, and third-order terms in Δε in the diagram series to the dielectric constant.

interaction between light and matter. Thus, the damping in this case is attributed to the phase shifts of the field. In systems of this type, the attenuation of light is associated with the processes of multiple elastic scattering by random configurations of dielectric scatterers with a size on the order of the wavelength.

The paper is organized as follows. In the Section 2, we present a general expression for the dielectric constant of a suspension in the form of a diagram series in powers of Δε and concentration. Section 3 is devoted to the calculation of the optical parameters of a suspension in the Born approximation and to the comparison of the results with the available experimental data. In Section 4, we derive corrections to the Born approximation that are associated with the processes of multiple rescattering between the particles of a suspension. Conclusions are devoted to the discussion of the results.

2. DIAGRAM SERIES FOR THE DIELECTRIC CONSTANT

Consider the system as an ensemble of spherical particles that are randomly distributed in a solvent. We will neglect the intrinsic absorption associated with inelastic scattering processes.

Let a plane monochromatic electromagnetic wave of frequency ω be incident on the system. The Green function of the electromagnetic field in a random medium satisfies the Dyson equation (see, for example, [13])

$$\begin{aligned}\hat{T}(\mathbf{r}_1 - \mathbf{r}_2) &= \hat{T}_0(\mathbf{r}_1 - \mathbf{r}_2) \\ &+ \int d\mathbf{r}' d\mathbf{r}'' \hat{T}_0(\mathbf{r}_1 - \mathbf{r}')\hat{\Pi}(\mathbf{r}' - \mathbf{r}'')\hat{T}(\mathbf{r}'' - \mathbf{r}_2).\end{aligned} \tag{2.1}$$

The tensor

$$\hat{T}_0(\mathbf{r}) = 4\pi(k_0^2\hat{I} + \nabla \times \nabla)\int \frac{d\mathbf{q}}{(2\pi)^3}\frac{e^{i\mathbf{q}\cdot\mathbf{r}}}{q^2 - (k_0 + i\eta)^2} \tag{2.2}$$

represents the Green function of the wave equation in a pure solvent with dielectric constant ε_0, $\mathbf{k}_0$ is the wavevector in this medium, $k_0 = 2\pi n_0 \lambda^{-1}$, $n_0 = \sqrt{\varepsilon_0}$ is the real refractive index of the dispersion medium, and $\lambda = \omega/c$ is the wavelength in vacuum. For short, we omit the exponential factor $\exp(i\omega t)$ that describes the time dependence of the monochromatic wave.

The kernel of the Dyson equation, or a polarization operator $\hat{\Pi}(\mathbf{r}_1 - \mathbf{r}_2)$, is represented as a series of irreducible diagrams (Fig. 1). All segments in these diagrams represent dressed Green functions. Each vertex is assigned a factor $\Delta\varepsilon/4\pi\varepsilon_0$. A multitail vertex or a star of n wavy lines denotes a crossed correlator

$$\begin{aligned}G^{(n)}(\mathbf{r}_1, \ldots, \mathbf{r}_n) &= \prod_{i=1}^{n}\int d\mathbf{R}_i \Theta\left(\frac{D}{2} - |\mathbf{r}_i - \mathbf{R}_i|\right) \\ &\times F^{(n)}(\mathbf{R}_1, \ldots, \mathbf{R}_n),\end{aligned} \tag{2.3}$$

where D is the diameter of a particle; the Heaviside function $\Theta(D/2 - |\mathbf{r}_i - \mathbf{R}_i|)$ in this equation guarantees that the scattering occurs inside a particle. The correlation functions $F^{(n)}(\mathbf{R}_1, \ldots, \mathbf{R}_n)$ are defined as connected, or cumulative, parts of n-particle distribution functions in the system of solid spheres centered at $\mathbf{R}_1, \ldots, \mathbf{R}_n$. The one-particle distribution function represents the mean density of the number of particles,

$$F^{(1)}(\mathbf{R}) = \rho = \bar{N}/V,$$

where V is the volume of the system and $\bar{N}$ is the mean particle number,

$$F^{(2)}(\mathbf{R}_1, \mathbf{R}_2) = \rho\delta(\mathbf{R}_1 - \mathbf{R}_2) + g^{(2)}(\mathbf{R}_1, \mathbf{R}_2), \tag{2.4}$$

$$\begin{aligned}F^{(3)}(\mathbf{R}_1, \mathbf{R}_2, \mathbf{R}_3) &= \rho\delta(\mathbf{R}_1 - \mathbf{R}_2)\delta(\mathbf{R}_1 - \mathbf{R}_3) \\ &+ \delta(\mathbf{R}_1 - \mathbf{R}_2)g^{(2)}(\mathbf{R}_2, \mathbf{R}_3) \\ &+ \delta(\mathbf{R}_2 - \mathbf{R}_3)g^{(2)}(\mathbf{R}_3, \mathbf{R}_2) \\ &+ \delta(\mathbf{R}_3 - \mathbf{R}_1)g^{(2)}(\mathbf{R}_1, \mathbf{R}_2) + g^{(3)}(\mathbf{R}_1, \mathbf{R}_2, \mathbf{R}_3),\end{aligned} \tag{2.5}$$

where $g^{(n)}(\mathbf{R}_1, \ldots, \mathbf{R}_n)$ are the well-known Ursell correlation functions [11, 15]. The δ functions indicate that a lesser number of particles take part in the scattering process; thus, the terms with δ functions describe contributions of lower order to the concentration than those that do not contain δ functions.

In the general case, the terms of the diagram series represent integral convolutions of the Green functions and multiparticle correlation functions for a system of solid spheres.

The Fourier image of the polarization operator,

$$\tilde{\hat{\Pi}}(\mathbf{k}) = \int d\mathbf{r}\hat{\Pi}(\mathbf{r})e^{-i\mathbf{k}\cdot\mathbf{r}}$$

defines the dielectric constant ε of the suspension,

$$\frac{\varepsilon - \varepsilon_0}{4\pi\varepsilon_0} = \tilde{\Pi}_\perp(\mathbf{k}), \tag{2.6}$$

where $\mathbf{k} = \sqrt{\varepsilon'/\varepsilon_0}\,\mathbf{k}_0$ is the wavevector of a field in the suspension, the index "⊥" denotes the transverse (with respect to $\mathbf{k}$) component of the tensor $\hat{\tilde{\Pi}}(\mathbf{k})$, and $\varepsilon' = \operatorname{Re}\varepsilon$. The dependence of the dielectric constant on the wavevector points out that the system of finite-size scatterers is characterized by spatial dispersion.

The imaginary part of the polarization operator defines the photon mean free path,

$$\frac{1}{l} = \sqrt{\frac{\varepsilon'}{\varepsilon_0}}4\pi k_0 \operatorname{Im}\tilde{\Pi}_\perp(k), \tag{2.7}$$

under the condition that $\operatorname{Im}\tilde{\Pi}_\perp \ll \operatorname{Re}\tilde{\Pi}_\perp$.

3. DIELECTRIC CONSTANT IN THE BORN APPROXIMATION

The diagram series for the polarization operator is ordered with respect to the number of vertices, i.e., with respect to the parameter $\Delta\varepsilon$ (hats in the symbols denoting operators are omitted in what follows). At the same time, it contains another expansion parameter—the concentration $c = \rho v$, where $v = \pi D^3/6$ is the volume of a particle in the suspension. Physically, the terms of order c^n describe the scattering by a system of n mutually impermeable particles.

In Fig. 2, the polarization operator is represented as the series

$$\Pi = \Pi_{\mathrm{Mie}} + \Pi_{\mathrm{PY}} + \Pi_{\mathrm{R}} + \Pi_{\mathrm{M}} + \ldots, \tag{3.1}$$

which is ordered with respect to both the number of scatterers and the parameter $\Delta\varepsilon$.

The first sum of diagrams, Π_{Mie}, represents the processes of multiple scattering in the bulk of a single isolated particle. The summation over all orders n gives rise to a field that is described by the Mie formulas; the integration of this expression over the volume of the sphere yields the Mie form factor. This is a contribution of maximally connected diagrams, in which all arguments of the correlation functions are related by δ functions,

$$F^{(n)}(\mathbf{R}_1, \ldots, \mathbf{R}_n) \sim \rho\delta(\mathbf{R}_1 - \mathbf{R}_2)\ldots\delta(\mathbf{R}_1 - \mathbf{R}_n).$$

The second sum of diagrams, Π_{PY}, describes successive events of scattering by two particles; the wavy line represents the correlation function of the position of particles; as a rule, one uses the Percus–Yevick approximation for this function. It is these two terms, Π_{Mie} and Π_{PY}, owing to which the representation of the scattering cross section as a product of the Mie form factor by the structure factor has found wide application.

The third group of the diagrams, Π_{R}, describes the scattering by a single particle with regard to a single intermediate rescattering by another particle that correlates with the first particle; this type of scattering is disregarded in the standard approach. However, one can see that the diagrams contained in Π_{R} are of the same order of magnitude as the diagrams in Π_{PY}, which are described as a convolution of the form factor and the structure factor.

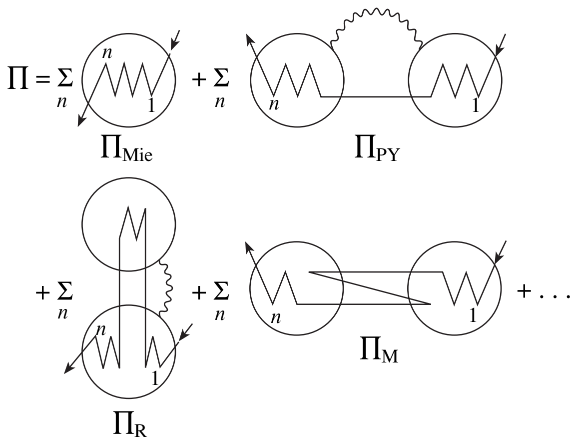

Fig. 2. Diagrams of the first and second order in the concentration of scatterers. The spheres bound the domain of integration over the coordinates of vertices.

These diagrams do not exhaust the contribution of two-particle correlations. The diagrams Π_{M} represent the contributions of multiple rescattering processes between a given pair of particles.

In the absence of the intrinsic absorption, formula (2.7) with regard to the diagrams of the second order in $\Delta\varepsilon$ leads to the well-known optical theorem that relates the scattering cross section and the photon mean free path:

$$\frac{1}{l} = \frac{\pi k_0^4}{4}\left(\frac{\Delta\varepsilon}{\varepsilon_0}\right)^2\int\frac{d\Omega}{(2\pi)^3}\tilde{\Theta}^2(\mathbf{k}-\mathbf{k}_s)(1+\cos^2\theta) \times[\rho+\tilde{g}^{(2)}(\mathbf{k}-\mathbf{k}_s)], \tag{3.2}$$

where

$$\tilde{\Theta}(q) = \frac{4\pi}{q^3}\left(\sin\frac{qD}{2} - \frac{qD}{2}\cos\frac{qD}{2}\right)$$

is the Fourier image of the Heaviside function and θ is the angle between the vectors $\mathbf{k}$ and $\mathbf{k}_s$; the integration is performed over the orientations of the wavevector $\mathbf{k}_s$ of the scattered wave.

Up to a factor, the integrand in (3.2) represents the differential cross section $\tilde{G}(q)$ of single scattering in the Born approximation:

$$\tilde{G}(q) = \rho F(q)S(q), \tag{3.3}$$

where $F(q) = (\Delta\varepsilon/\varepsilon_0)^2\tilde{\Theta}^2(q)$ is the Rayleigh–Gans form factor and $S(q) = 1 + g^{(2)}(q)/\rho$ is the structure factor.

Table 1. Comparison of the experimental values of the photon mean free path l (column 2) and the transport mean free path l^* calculated within the Percus–Yevick approximation: with the Mie form factor (column 4) and with the Rayleigh–Gans form factor (columns 3 and 5); columns 6 and 7 present experimental and calculated values of $\overline{\cos\theta}$, respectively, for suspensions of particles of different diameters D. The concentration is $c = 0.1$, and $\Delta\varepsilon = 0.759$

D/λ	l/λ		l^*/λ		$\overline{\cos\theta}$	
	exp.	PY + RG	PY + Mie	PY + RG	exp.	PY + RG
0.14	197 [18]	280	210 [18]	284		0.01
0.21	64 [17]	87		90		0.04
0.47	14 [18]	17	41 [18]	35		0.51
0.68	9.7 [17]	10		39		0.74
0.73	7.6 [18]	9.1	36 [18]	38		0.57
0.89	5.4 [17]	6.9	37 [19]	39	0.85 [19]	0.83
0.95	5.7 [18]	6.5	39.5 [18]	42	0.86	0.85
1.55	3.9 [17]	3.6		50		0.93
1.72	4.1 [16]	3.2	59 [16]	55	0.93 [16]	0.94

Formula (3.2) represents the contribution of the sum of the first two diagrams to Π_{Mie} and Π_{PY}, a vertex in each sphere in the diagrams. The replacement of the Rayleigh–Gans form factor by the Mie form factor is equivalent to taking into account all the diagrams in Π_{Mie} and Π_{PY}.

The transport mean free path l^* in this approximation is defined as

$$\frac{1}{l^*} = \frac{\pi k_0^4\rho}{4}\int\frac{d\Omega}{(2\pi)^3}(1+\cos^2\theta) \tag{3.4}$$
$$\times(1-\cos\theta)F(\mathbf{k}-\mathbf{k}_s)S(\mathbf{k}-\mathbf{k}_s).$$

In the case of a low concentration, the structure factor becomes equal to unity, $S(q) \longrightarrow 1$ as $c \longrightarrow 0$. For finite concentrations, one applies the Percus–Yevick approximation for the two-particle function $g^{(2)}(\mathbf{k}-\mathbf{k}_s)$.

In [4], it was pointed out that, for highly concentrated suspensions, the results of calculation of the scattering cross sections with the use of the Rayleigh–Gans form factor only slightly differ from a similar results obtained with the use of the Mie form factor. To assess the possibility of applying the expansion in the parameter $\Delta\varepsilon$, we carried out calculations by formula (3.2) with the use of the Rayleigh–Gans form factor and compared the results with the available results, both with the experimental data and the numerical results obtained with the use of the Mie form factor.

Choosing the wavelength as a reasonable spatial scale, we compared the values of the mean free path and the transport mean free path obtained in [16–18] for water suspensions of latex particles with different values of the parameter D/λ and the same concentration $c = 0.1$ with the results of our calculations performed with the use of the Rayleigh–Gans form factor. For given values of $\Delta\varepsilon$ and concentration, the dielectric constant is a homogeneous function of the ratio D/λ; this fact allows us to compare the results obtained for different wavelengths of light.

In [18], the authors experimentally determined the mean free path l with the use of a He–Ne laser with a wavelength of $\lambda = 0.633$ μm and calculated the transport mean free path l^* with the use of the Mie form factor for particles of different diameters. In [16, 17], experimental values of l for latex water solutions were obtained with the use of light with wavelengths of $\lambda = 0.633$ μm [16] and $\lambda = 0.515$ μm [17]. In Table 1, the results obtained in [16–18] are compared with the values of l and l^* obtained in our calculations in the Percus–Yevick approximation with the use of the Rayleigh–Gans form factor. One can see that the experimental and numerical results for the mean free path of photons agree to within 10–20% for different systems; the same degree of agreement is observed for the transport mean free path l^* calculated with the Mie formula and the Rayleigh–Gans formula. This means that the parameter $\Delta\varepsilon(kD)^2$ can be assumed small for the major part of investigated systems; therefore, one may calculate only the main diagram in Π_R and neglect the diagrams Π_M that describe the contribution of multiple rescattering processes. The greatest discrepancy in the results is observed for small particles; in this case, when $\lambda^{-1}D \gg 1$, the main contribution is made by the long-wavelength part of the structure factor $S(q)$, which significantly differs from unity even for concentrations of $c \sim 0.1$.

Note that calculations in the “gas” approximation with the structure factor equal to unity give lower values of the spatial parameters *l* and *l** compared with the calculations using the Mie form factor, while the calculations with the Percus–Yevick structure factor give higher values of these parameters.

The quantities $\overline{\cos\theta}$ calculated by the formula $l^* = l(1 - \overline{\cos\theta})^{-1}$ are in good agreement with the results of [16, 19].

In [5], the authors determined the transport mean free path experimentally, by measuring the attenuation of light transmitted through a latex suspension in a wide spectral range; they investigated three condensed and three diluted latex suspensions consisting of particles with the diameters $D = 0.205$, 0.299, and 0.460 μm. Then, they compared the measured values of l^* with the values calculated with the use of the Mie form factor. They point out that, for suspensions with concentrations of $c \approx 0.3$, the calculation yields underestimated values for the transport mean free path l^* compared with the measured values; this is especially manifest for a suspension with the size of particles $D = 0.460$ μm. We calculated l^* for the same values of parameters using the Percus–Yevick structure factor (Table 2). Note that, in this case of very high concentrations of suspensions, calculations performed within the Born approximation with the use of the Rayleigh–Gans form factor (i.e., in the principal order in the parameter $\Delta\varepsilon$) and with the use of the Mie form factor (i.e., with regard to all orders in $\Delta\varepsilon$) agree to within a few percent.

4. CONTRIBUTION OF MULTIPLE RESCATTERING BETWEEN SCATTERERS

Consider a contribution of order $\Delta\varepsilon^3$ to the diagram term Π_R (see Fig. 2), which describes the scattering from a single particle with regard to the field distortion due to the presence of another particle:

$$\Pi_R^{(3)} = \left(\frac{\Delta\varepsilon}{4\pi\varepsilon_0}\right)^3 \int \frac{d\mathbf{q}_1 d\mathbf{q}_2}{(2\pi)^6} \tilde{T}(\mathbf{q}_1)\tilde{T}(\mathbf{q}_2) \times \tilde{\Theta}(\mathbf{k}-\mathbf{q}_1)\tilde{\Theta}(\mathbf{q}_2-\mathbf{k})\tilde{\Theta}(\mathbf{q}_2-\mathbf{q}_1)\tilde{g}^{(2)}(\mathbf{q}_2-\mathbf{q}_1). \tag{4.1}$$

For approximate numerical estimates, we use a linear approximation of the form

$$\tilde{g}^{(2)}(\mathbf{q}_2-\mathbf{q}_1) \approx \lambda_1\tilde{g}^{(2)}(\mathbf{k}-\mathbf{q}_2) + \lambda_2\tilde{g}^{(2)}(\mathbf{k}-\mathbf{q}_1),$$

and a similar approximation for $\tilde{\Theta}(\mathbf{q}_2 - \mathbf{q}_1)$, where the weights $\lambda_1 > 0$ and $\lambda_2 > 0$ satisfy the condition $\lambda_1 + \lambda_2 = 1$. This approximation is justified in the case of a strongly anisotropic scattering cross section, when the main contribution to the integrand is made by the domain $\mathbf{q}_1 \sim \mathbf{q}_2 \sim \mathbf{k}$. Numerical results for different weight factors coincide to within a few percent.

Table 2. The transport mean free path *l** calculated by using the Percus–Yevick structure factor and the Mie form factor (column 3), the Rayleigh–Gans form factor (column 4), and the Mie form factor allowing for the contribution of $\Pi_R^{(3)}$ (column 5). $\lambda = 0.5$ μm

D, μm	*c*	*l**, μm		
		PY + Mie	PY + RG	PY + Mie + $\Pi_R^{(3)}$
0.205	0.349	9.8 [5]	8.5	12
0.299	0.354	9.2 [5]	10	13.5
0.460	0.299	9.2 [5]	8.1	11

We calculated the contribution of the correction $\Pi_R^{(3)}$ for the mean free path of a photon using the parameters of the three highly concentrated systems investigated in [5]. The contributions of individual terms of the polarization operator are additive with respect to the inverse of the mean free path. Data for the transport mean free path were obtained in [5] in an approximation equivalent to taking into account all terms of the form Π_{Mie} and Π_{PY} (Fig. 2). This allows one to determine a correction to the transport mean free path by adding $4\pi k_0(1 - \overline{\cos\theta})\Pi_R^{(3)}$ to the values of the inverse transport mean free path $(l^*)^{-1}$ calculated with the use of the Mie form factor [5]; the parameter $\overline{\cos\theta}$ was calculated in the Born approximation,

$$\overline{\cos\theta} = \frac{\int d\Omega G(\mathbf{k}-\mathbf{k}_s)\cos\theta}{\int d\Omega G(\mathbf{k}-\mathbf{k}_s)}.$$

The results of calculations are presented in Table 2 (column 5). One can see that the values of the transport mean free path obtained with the use of the correction $\Pi_R^{(3)}$ are greater than the values calculated in [5] with the use of the Mie form factor by about 20% and are in better agreement with the experimental results.

CONCLUSIONS

The dielectric constant of a suspension depends on three parameters: the difference $\Delta\varepsilon$ between the dielectric constants of the particles and the medium, the concentration *c*, and the ratio of the particle size to the wavelength, k_0D. The standard Born approximation is formally applicable only in the range of $\Delta\varepsilon \ll 1$ and finite values of k_0D for diluted solutions with a structural factor close to unity, $S(q) \approx 1$. In order to describe systems with finite values of $(k_0D)^2\Delta\varepsilon$, one applies the Mie form factor instead of the Rayleigh–Gans form factor. In the range of small concentrations, such a replacement is justified and leads to excellent agreement with experiment. We have shown that the conventional representation of the scattering cross section as a product of the Mie form factor and the Percus–Yevick structure factor is not justified for highly concentrated suspensions because it does not take into account multiparticle correlations. We have shown that this multiplicative representation of the indicatrix is not valid even when terms of order $\Delta\varepsilon^3c^2$ are taken into account. Our estimates of the contribution of order $\Delta\varepsilon^3c^2$ improve the agreement with the available experimental data. The approach developed in this paper can be generalized to the case of polydisperse colloidal systems.

The dielectric constant is usually defined as a coefficient in the linear relation between the displacement and field vectors. However, according to (2.1) and (2.6), the same quantity normalizes the pole of the Fourier image of the dressed Green function (for a given frequency) and thus defines the damping law for the Green function in the asymptotic domain of large distances $r \gg \lambda$. The intensity, i.e., a quantity quadratic in the amplitude of the incident field is measured in the experiment. Radiation transfer is described by the radiation transfer equation, or the Bethe–Salpeter equation, in which a complex-conjugate product of dressed Green functions serves as a priming propagator. Thus, in a domain where the contribution of the product of mean fields to the intensity is negligible due to the exponential damping and there is only scattered diffuse radiation with a different, power, damping law, the behavior of this diffuse radiation is still determined by the photon mean free path l and the transport mean free path l^*, which, in turn, are determined by the imaginary part of the dielectric constant.

The radiation transfer problem is usually considered in the approximation of weak scattering $\lambda/l \ll 1$. According to the optical theorem, the corrections obtained in this paper imply that the multiple scattering cross section takes into account the next terms after the weak scattering approximation. In the optics of strongly inhomogeneous media, this is the first step from weak localization to strong localization. Corrections of the same order are taken into account when passing from the Rayleigh–Gans form factor to the Mie form factor; we point to some disregarded corrections of the same order. The Mie form factor takes into account the contribution of multiple rescattering processes within a single particle; the diagrams considered here describe multiple rescattering between two particles.

From the viewpoint of field theory, the optical theorem plays the role of the Ward identity. The two-tail diagrams shown in Fig. 2 turn into four-tail diagrams that describe the multiple scattering cross section when each element representing a dressed Green is broken in succession, which corresponds to the calculation of the imaginary part.

Corrections of the same order as those obtained in the present paper also arise in the kernel of the Bethe–Salpeter equation. In the present paper, we did not consider these corrections. However, by virtue of the above-mentioned Ward identity and the conservation of the optical theorem, these corrections are equivalent to the corrections to the polarization operator, at least in the diffusion approximation within which the experimental results of [5] are interpreted.

To calculate the optical parameters of colloidal suspensions, it is desirable that one experimentally investigate extinction in highly concentrated suspension with particles of different sizes and in a wide spectral range. Both theoretical and experimental investigations of hydrodynamic interaction in highly concentrated colloidal suspensions are desirable. A system of solid spheres is the simplest model of a strongly inhomogeneous system. Taking into account the nonsphericity, inhomogeneity, hydrodynamic interaction between particles and a medium, and nonadequate description of the structure factor in the Percus–Yevick approximation may also prove very important in applications.

ACKNOWLEDGMENTS

This work was supported by the Russian Foundation for Basic Research (project no. 02-02-16577) and the Royal Society (grant no. 15298).

The author is grateful to V.P. Romanov for fruitful discussions.

REFERENCES

1. *Wave Scattering in Complex Media: From Theory to Applications*, Ed. by B. van Tiggelen and S. Skipetrov (Kluwer Academic, Dordrecht, 2003).
2. M. H. Kao, A. G. Yodh, and D. J. Pine, Phys. Rev. Lett. **70**, 242 (1993).
3. J. Z. Xue, E. Herbolzheimer, M. A. Rutgers, *et al.*, Phys. Rev. Lett. **69**, 1715 (1992).
4. Hu Gand, A. H. Krall, and D. A. Weitz, Phys. Rev. Lett. **73**, 3435 (1994).
5. P. D. Kaplan, A. D. Dinsmore, A. G. Yodh, and D. J. Pine, Phys. Rev. E **50**, 4827 (1994).
6. A. J. C. Ladd, Hu Gang, J. X. Zhu, and D. A. Weitz, Phys. Rev. E **52**, 6550 (1995).
7. A. D. Dinsmore and A. G. Yodh, Phys. Rev. E **52**, 4045 (1995).
8. Hu Gang, A. G. Krall, H. Z. Cummins, and D. A. Weitz, Phys. Rev. E **59**, 715 (1999).

9. V. V. Berdnik and V. A. Loiko, J. Quant. Spectrosc. Radiat. Transf. **63**, 369 (1999).
10. V. L. Kuz'min, V. P. Romanov, and E. P. Obraztsov, Opt. Spektrosk. **93**, 1000 (2002) [Opt. Spectrosc. **93**, 923 (2002)].
11. C. Croxton, *Liquid State Physics: A Statistical Mechanical Introduction* (Cambridge Univ. Press, Cambridge, 1974; Mir, Moscow, 1978).
12. H. M. L. Boots, D. Bedeaux, and P. Mazur, Physica A (Amsterdam) **79**, 397 (1975).
13. S. M. Rytov, Yu. M. Kravtsov, and V. I. Tatarskiĭ, *Introduction to Statistical Radio Physics* (Nauka, Moscow, 1978), Part 2 [in Russian].
14. V. L. Kuzmin, Phys. Rep. **123**, 365 (1985).
15. J. S. Rowlinson and B. Widom, *Molecular Theory of Capillarity* (Clarendon, Oxford, 1982).
16. M. P. van Albada and A. Lagendijk, Phys. Rev. Lett. **55**, 2692 (1985).
17. P. E. Wolf and G. Maret, Phys. Rev. Lett. **55**, 2696 (1985).
18. K. Ishii, T. Iwai, and T. Asakura, J. Opt. Soc. Am. A **14**, 179 (1997).
19. E. Akkermans, P. E. Wolf, and R. Maynard, Phys. Rev. Lett. **56**, 1471 (1986).

Translated by I. Nikitin

Journal of Experimental and Theoretical Physics, Vol. 100, No. 5, 2005, pp. 821–832.
Translated from Zhurnal Éksperimental'noĭ i Teoreticheskoĭ Fiziki, Vol. 127, No. 5, 2005, pp. 931–944.
Original Russian Text Copyright © 2005 by Bezverbnyĭ.

ATOMS, MOLECULES, OPTICS

Evolution of an Optically Pumped Ensemble of Cold Ground-State Atoms in Weak Light Fields

A. V. Bezverbnyĭ
Admiral Nevelskii Maritime State University, Vladivostok, 690059 Russia
Tomsk State University, Tomsk, 634050 Russia
e-mail: alexb@mail.vntc.ru, alexb@msun.ru

Received July 26, 2004

Abstract—The evolution of multipole moments is analyzed for optically pumped cold ground-state atoms in the limit of low saturation of a closed $j_0 \longrightarrow j_1$ dipole transition. The longest multipole-moment relaxation times are analyzed as functions of ellipticity and frequency detuning from resonance for transitions with $j_0 \lesssim 5$. The qualitative difference between the evolution toward steady-state Zeeman sublevel populations and dynamics of transient spontaneous emission is demonstrated for transitions of the following types: $j \longrightarrow j-1$, $j \longrightarrow j$ with integer j, $j \longrightarrow j$ with half-integer j, and $j \longrightarrow j+1$. *© 2005 Pleiades Publishing, Inc.*

1. INTRODUCTION

Evolution of Zeeman-sublevel populations $\rho_{\mu\mu}(t)$ and coherences $\rho_{\mu\mu'}(t)$ $(\mu \neq \mu')$ for ground-state atoms interacting with optical fields are of interest in various branches of atomic physics and spectroscopy. In low-density atomic ensembles, collisional relaxation is negligible and the evolution is controlled by stimulated emission and absorption of photons and by spontaneous emission from excited states. In [1], a two-level model of steady-state resonant interaction between slowly moving atoms and a monochromatic field was analyzed. In the case when both ground and excited energy levels (E_0 and E_1) are degenerate with respect to the respective projections j_0 and j_1 of total angular momentum, the atomic density matrix $\hat{\rho}(\infty)$ was found for an arbitrary closed $j_0 \longrightarrow j_1$ dipole transition and an arbitrary saturation parameter S. However, the evolution of systems with $j_0 > 1$ toward this regime of interaction is slow when $S \ll 1$. For example, the average number of optical pumping cycles required for the $2 \longrightarrow 3$ transition in a one-dimensional field configuration to reach a steady-state regime was estimated at about ten in [2] by using $\tau_0 = (\gamma S)^{-1}$ as an estimate for cycle duration, where γ is the decay rate of the excited state. Therefore, both the radiative force and momentum diffusion tensor calculated in semiclassical approximation by using $\hat{\rho}(\infty)$ [3] are generally overestimated as compared to experimental results [4]. On the other hand, the time-dependent distribution $\rho_{\mu\mu'}(t)$ is of special interest for studies of various transient regimes of optical pumping employed in laser cooling schemes [5].

When recoil effects are neglected for an atom at rest, the time-dependent ground-state density matrix $\hat{\rho}(t)$ obeys a system of ordinary differential equations (ODEs), which are a special case of the generalized optical Bloch equations [1, 6] and can be written as

$$\frac{\partial \hat{\rho}}{\partial t} = \hat{\mathscr{L}}\hat{\rho}, \qquad (1)$$

where $\hat{\mathscr{L}}$ is a Liouville operator. However, their solutions are extremely cumbersome even for $j_0 = 1$ and $3/2$, because the dimension of (1) is $(2j_0+1)^2 - 1$ in the general case of elliptically polarized field. In the limit of $j_0 \gg 1$, the dynamics of atomic angular momentum can be described by using the expansion of the Bloch equations in terms of the small parameter $1/j_0$ [7]. This semiclassical approach was applied to analyze, up to contributions of order $1/j_0^2$, the evolution toward a steady-state angular-momentum distribution for atoms with $j_0 \gtrsim 10$ pumped by arbitrary elliptically polarized fields [6]. A similar analysis of angular-momentum evolution in a constant magnetic field was presented in [8]. Qualitatively different regimes of evolution toward a steady state were identified for transitions of three types: $j \longrightarrow j-1$, $j \longrightarrow j$, and $j \longrightarrow j+1$. As an alternative to system (1), a time-dependent model describing the populations of certain Zeeman sublevels in some specific field configurations can be developed in terms of the matrix of ensemble-averaged relaxation times [9],

$$\hat{\tau}_{\text{stat}} = \int_0^\infty [\hat{\rho}(t) - \hat{\rho}(0)]\,dt, \qquad (2)$$

which satisfies simpler algebraic equations of the form

$$\hat{\mathscr{L}}\hat{\tau}_{\text{stat}} = \hat{\rho}(\infty) - \hat{\rho}(0).$$

In this paper, the evolution toward the steady-state distribution $\hat\rho(\infty)$ is examined by analyzing system (1) in the general case of arbitrary elliptically polarized electromagnetic field. The starting point is an analysis of the evolution of the multipole moments ρ^κ of cold ground-state atoms (κ is the multipole rank), rather than $\rho_{\mu\mu}(t)$ and $\rho_{\mu\mu'}(t)$ (whose interpretation depends on the choice of a quantization axis). Intermediate values of angular momentum are considered ($1 \le j_0 \le 5$), for which the semiclassical approximation employed in [7] is not effective.[1] The values of j_0 in question include those characteristic of alkali and rare-earth metals widely used in atomic physics: $j_0 = 2$ for ^{23}Na, $j_0 = 5/2$ for ^{173}Yb, $j_0 = 3$ for ^{85}Rb, $j_0 = 4$ for ^{133}Cs, etc. The analysis is focused on the dependence of the longest relaxation time $\tau_{\max}$ on the degree $\mathcal{A}$ of circular polarization of a monochromatic field and on its detuning from atomic resonance, $\delta = \omega - \omega_0$, in the limit of low saturation of the dipole transition ($S \ll 1$), when the rate of evolution toward a steady state is particularly slow.

In Sections 2 and 3, the function $\tau_{\max}(\mathcal{A}, \delta)$ is shown to exhibit certain unexpected trends for j_0 between 1 and 10. Four qualitatively different types of $\tau_{\max}(\mathcal{A}, \delta)$ are identified for $j \longrightarrow j$ with integer j, $j \longrightarrow j$ with half-integer j, $j \longrightarrow j + 1$, and $j \longrightarrow j - 1$, respectively. A rough estimate for $\langle\tau_{\max}\rangle$ is found to agree in order of magnitude ($\sim j_0^2\tau_0$) with an estimate for the relaxation time obtained for ground-state atoms with $j_0 \gg 1$ [6]. However, the interval $0 \le |\mathcal{A}| \le 1$ corresponds to a wide range of $\tau_{\max}$ for a dipole transition of any type. The evolution of $\hat\rho_{\max}$ corresponding to $\tau_{\max}$ toward a steady state is described both for resonant and detuned elliptically polarized fields (with $|\delta| > 2\gamma$).

In Section 4, the method of minimal bipolar harmonics is used to show that even the evolution of a dynamical system (1) with dimension as large as $(2j_0 + 1)^2 - 1$ can be described in terms of only four variables if $j_0 \lesssim 5$ and the first- and second-rank multipole moments play a dominant role in the kinetics or spectroscopy problem under analysis. These variables are the coefficients $a_1^1(t)$, $a_2^2(t)$, $a_2^0(t)$, and $b_2^1(t)$ in the expansion in the minimal bipolar harmonics corresponding to the directions parallel to the major axis of the polarization ellipse and perpendicular to the polarization-ellipse plane. The variable a_1^1 is associated with the rank one atomic moment; the remaining three (a_2^0, a_2^2, b_2^1), with the rank two moment. The time scales of their evolution are shown to be related to $\tau_{\max}(\mathcal{A}, \delta)$: when the evolution starts from an equilibrium state $\rho_{\mu\mu'}(0)$, at least one of these variables is characterized by a relaxation time comparable to $\tau_{\max}$ for a dipole transition of any type.

Section 5 presents an analysis of dynamics of transient spontaneous emission: estimates are obtained for the average number N_{ph} of optical pumping cycles required to reach a steady state and the average cycle duration $\tau_{\text{opt}} \sim \tau_{\max}/N_{\text{ph}}$. Transitions with $j_0 = 2$ and $3/2 \longrightarrow 3/2$ transitions are analyzed to show that $\tau_{\text{opt}} = 1/\gamma\tilde S \sim \tau_0$ for $j \longrightarrow j + 1$ transitions. (Here, the effective saturation parameter $\tilde S(l)$ introduced in [1] is a function of the degree l of linear polarization of the field). However, this estimate is not valid for transitions of the remaining three types, because τ_{opt} strongly depends on $\hat\rho(0)$ and is generally larger than a rough estimate for τ_0.

2. OPTICAL PUMPING OF A GROUND-STATE ATOM: EXPANSION IN MINIMAL BIPOLAR HARMONICS

Consider interaction of an atomic ensemble characterized by ground- and excited-state total angular momenta j_0 and j_1 with resonant monochromatic field

$$\mathbf{E}(\mathbf{r}, t) = e^{-i\omega t}\mathcal{E}(\mathbf{r})\mathbf{e}(\mathbf{r}) + \text{c.c.}, \tag{3}$$

where $\mathcal{E}(\mathbf{r}) = |\mathcal{E}|e^{i\phi(\mathbf{r})}$ is the total complex amplitude (including the spatial phase ϕ), and $\mathbf{e}(\mathbf{r})$ is a polarization vector of unit magnitude ($\mathbf{e}\cdot\mathbf{e}^* = 1$).

In the limit of

$$S = \frac{|\Omega|^2}{\gamma^2/4 + \delta^2} \ll 1 \tag{4}$$

a closed master equation for the density operator $\hat\rho$ for an ensemble of slowly moving ground-state atoms can be written in the zeroth-order approximation with respect to recoil as follows (see [10]):

$$\begin{aligned}(\partial_t + \mathbf{v}\nabla)\hat\rho &= \hat\gamma\{S\hat V\hat\rho\hat V^\dagger\}\\ -\gamma S(\Delta^*\hat V^\dagger\hat V\hat\rho + \Delta\hat\rho\hat V^\dagger\hat V) &= \hat{\mathcal{L}}_s\hat\rho + \hat{\mathcal{L}}_c\hat\rho.\end{aligned} \tag{5}$$

Here, $\Delta = 1/2 - i\delta/\gamma$; $\Omega = -\mathcal{E}d/\hbar$ is the Rabi frequency; d is the reduced dipole matrix element for the optical transition in question; $\delta = \omega - \omega_0$ is the detuning from resonance; and $\hat V$ and $\hat V^\dagger$ denote the projections of the lowering and raising operators for reduced dipole moment on the polarization direction, respectively [1, 10]. The local saturation parameter defined in (4) is 1/2 for $\delta = 0$ and light intensity I equal to the saturation intensity $I_{\text{sat}} = 2\pi^2\hbar\gamma c/3\lambda^3$ [11]:

$$S = \frac{I/I_{\text{sat}}}{2 + 8(\delta/\gamma)^2}. \tag{4'}$$

---

[1] Note that a numerical analysis performed for higher $j_0 \lesssim 10$ revealed similar qualitative trends in the evolution of the atomic parameters considered here.

When represented in terms of the excited- and ground-state angular-momentum eigenvectors ($|j_1, \mu_1\rangle$ and $|j_0, \mu_0\rangle$), the density matrix elements $\rho_{\mu\mu'}$ characterize the Zeeman sublevel populations ($-j_0 \le \mu, \mu' \le j_0$) and the matrix elements of $\hat{V}$ are

$$V_{\mu_1\mu_0} = \sum_q C^{j_1\mu_1}_{j_0\mu_0 1q} e^q, \tag{6}$$

where $C^{j_1\mu_1}_{j_0\mu_0 1q}$ denotes the Clebsch–Gordan coefficients [12] and e^q are the components of the polarization vector in (3) in a cyclic basis.

Equation (5) describes the evolution of the ground state of an atomic ensemble driven by optical pumping. The first (repopulation) term on its right-hand side represents the increase in the ground-state population due to spontaneous decay of the excited state, i.e., the incoherent contribution to the evolution of the ensemble. The remaining terms (subsumed under the operator $\hat{\mathcal{L}}_c$) represent depopulation and light-induced shifts of ground-state energy levels, i.e., the coherent contribution to evolution of the ensemble. The operator $\hat{\gamma}$ on an arbitrary excited-state Zeeman sublevel population $X_{\mu_1\mu_1'}$ is expressed as follows [10]:

$$(\hat{\gamma}\{\hat{X}\})_{\mu_0\mu_0'} = \gamma \sum_{q, \mu_1, \mu_1'} C^{j_1\mu_1}_{j_0\mu_0 1q} C^{j_1\mu_1'}_{j_0\mu_0' 1q} X_{\mu_1\mu_1'}. \tag{7}$$

To analyze the spectrum of relaxation times $\{\tau_i\}$, consider the ground-state multipole moments and the corresponding projections ($-\kappa \le q \le \kappa$):

$$\begin{aligned} \rho^\kappa_q &= \sum_{\mu, \mu'} (-1)^{j_0 - \mu'} C^{\kappa q}_{j_0\mu j_0 - \mu'} \rho_{\mu\mu'}, \\ \rho_{\mu\mu'} &= \sum_{\kappa, q} (-1)^{j_0 - \mu'} C^{\kappa q}_{j_0\mu j_0 - \mu'} \rho^\kappa_q. \end{aligned} \tag{8}$$

For an ensemble of cold atoms driven by a monochromatic field, the evolution of the multipole moments is described by the following equations derived from (5) [13]:

$$\tau_0 \partial_t \rho^\kappa = \sum_{\kappa_1, \kappa_2} \mathcal{F}^{\kappa_1\kappa_2}_\kappa(\delta, j_0, j_1)\{\varrho^{\kappa_1} \otimes \rho^{\kappa_2}\}_\kappa. \tag{9}$$

Here, the summation is performed over the possible values of the multipole moments of the photon density matrix ($\kappa_1 = (0, 1, 2\}$) and the atomic density matrix ($\max(0, \kappa - \kappa_1) \le \kappa_2 \le \min(2j_0, \kappa + \kappa_1)$), and $\{\varrho^{\kappa_1} \otimes \rho^{\kappa_2}\}_\kappa$ is the tensor product of the photon and atomic multipole moments. The coefficients $\mathcal{F}$ are expressed in terms of the 6*j* and 9*j* symbols as

$$\begin{aligned} \mathcal{F}^{\kappa_1\kappa_2}_\kappa(\delta, j_0, j_1) &= \Pi(\kappa_1, \kappa_2)\Pi^2(j_1)(-1)^{j_1 - j_0 + \kappa} \\ &\times \left[(-1)^{2j_1}\Pi^2(j_1) \begin{Bmatrix} j_0 & j_0 & \kappa \\ j_1 & j_1 & 1 \end{Bmatrix} \begin{Bmatrix} 1 & 1 & \kappa_1 \\ j_0 & j_0 & \kappa_2 \\ j_1 & j_1 & \kappa \end{Bmatrix} \right. \\ &- [\Delta^* + (-1)^{\kappa + \kappa_1 + \kappa_2}\Delta] \begin{Bmatrix} \kappa & \kappa_1 & \kappa_2 \\ j_0 & j_0 & j_0 \end{Bmatrix} \\ &\left. \times \begin{Bmatrix} 1 & \kappa_1 & 1 \\ j_0 & j_1 & j_0 \end{Bmatrix} \right] = \mathcal{F}^{\kappa_1\kappa_2}_{\kappa;\,s} + \mathcal{F}^{\kappa_1\kappa_2}_{\kappa;\,c}, \end{aligned} \tag{10}$$

where $\Pi(x, y, \ldots) = \sqrt{(2x + 1)(2y + 1)\ldots}$. The multipole moments of the photon density matrix can be defined in terms of unit vectors $\boldsymbol{\nu}$ and $\boldsymbol{\epsilon}$ directed, respectively, along the normal to the polarization plane and the major axis of the polarization ellipse associated with the vector **e** [14]:

$$\begin{aligned} \varrho^0 &= -1/\sqrt{3}, \quad \varrho^1 = \mathcal{A}\boldsymbol{\nu}/\sqrt{2}, \\ \varrho^2 &= \ell\{\boldsymbol{\epsilon} \otimes \boldsymbol{\epsilon}\}_2 + [(\ell - 1)/2]\{\boldsymbol{\nu} \otimes \boldsymbol{\nu}\}_2. \end{aligned} \tag{11}$$

Here, $\ell = \mathbf{e} \cdot \mathbf{e} = \cos 2\varepsilon$ and $\mathcal{A} = \sin 2\varepsilon$ for a field in the pure state of polarization with ellipticity angle ε. These coefficients are the degrees of linear and circular polarization of the field, respectively.

In the method of minimal bipolar harmonics [15], minimal harmonics are defined as tensor direct products of spherical harmonics:

$$\mathcal{Y}^{k,\,p}_\kappa(\boldsymbol{\nu}, \boldsymbol{\epsilon}) = \{Y_k(\boldsymbol{\nu}) \otimes Y_{\kappa - k + p}(\boldsymbol{\epsilon})\}_\kappa,$$

where $k = p, p + 1, \ldots, \kappa$ ($p = 0, 1$). In particular, $\mathcal{Y}^{0,\,0}_1 \sim \boldsymbol{\epsilon}$, $\mathcal{Y}^{1,\,0}_1 \sim \boldsymbol{\nu}$, $\mathcal{Y}^{1,\,1}_1 \sim \boldsymbol{\nu} \times \boldsymbol{\epsilon}$, $\mathcal{Y}^{0,\,0}_2 \sim \{\boldsymbol{\epsilon} \otimes \boldsymbol{\epsilon}\}_2$, $\mathcal{Y}^{2,\,0}_2 \sim \{\boldsymbol{\nu} \otimes \boldsymbol{\nu}\}_2$, $\mathcal{Y}^{1,\,1}_2 \sim \{\boldsymbol{\nu} \otimes \{\boldsymbol{\epsilon} \otimes \boldsymbol{\epsilon}\}_2\}_2$, and so on. The method relies on the applicability of bipolar harmonics as basis functions in unique expansions of the form

$$\rho^\kappa = \sum_{l = 0}^{\kappa} a^l_\kappa \mathcal{Y}^{l,\,0}_\kappa + \sum_{m = 1}^{\kappa} b^m_\kappa \mathcal{Y}^{m,\,1}_\kappa. \tag{12}$$

By using a procedure for reducing the tensor product of bipolar harmonics of different ranks [15] and the normalization condition $\rho^0 = 1/\Pi(j_0)$, Eqs. (9) can

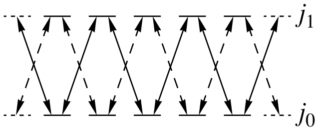

Fig. 1. Stimulated transitions between Zeeman sublevels of ground-state and excited atoms when ν is the quantization axis: solid and dashed lines represent transitions within mutually incoherent families of sublevels.

readily be reduced to ODEs for a_κ^l and b_κ^m with $0 \le l \le \kappa$, $1 \le m \le \kappa$, and $0 \le \kappa \le 2j_0$. The utility of minimal bipolar harmonics lies in the fact that two independent systems of ODEs are naturally obtained:

$$\tau_0 \frac{d\hat{\mathbb{X}}^{(1)}}{dt} = \hat{\mathbb{L}}_1 \cdot \hat{\mathbb{X}}^{(1)} - \hat{\mathbb{C}}, \tag{13a}$$

$$\tau_0 \frac{d\hat{\mathbb{X}}^{(2)}}{dt} = \hat{\mathbb{L}}_2 \cdot \hat{\mathbb{X}}^{(2)}. \tag{13b}$$

For example, for the 1 ⟶ 2 transition,

$$\hat{\mathbb{X}}^{(1)} = \begin{pmatrix} a_1^1 \\ a_2^0 \\ b_2^1 \\ a_2^2 \end{pmatrix},$$

$$\hat{\mathbb{L}}_1 = \begin{pmatrix} -\frac{1}{12} & -\frac{\sqrt{5}\mathscr{A}}{36} & \frac{\sqrt{5}i\tilde{\delta}\ell}{6\sqrt{2}} & \frac{\sqrt{5}\mathscr{A}}{18} \\ 0 & -\frac{15+2\ell}{36} & -\frac{5i\tilde{\delta}\mathscr{A}}{3\sqrt{2}} & \frac{\ell}{9} \\ \frac{i\tilde{\delta}\ell}{3\sqrt{10}} & -\frac{5i\tilde{\delta}\mathscr{A}}{6\sqrt{2}} & -\frac{5}{12} & 0 \\ -\frac{\mathscr{A}}{6\sqrt{5}} & \frac{\ell-1}{18} & -\frac{5i\tilde{\delta}\mathscr{A}}{6\sqrt{2}} & \frac{2\ell-11}{36} \end{pmatrix}, \tag{14}$$

$$\hat{\mathbb{C}} = \begin{pmatrix} \frac{5\mathscr{A}}{36\sqrt{6}} \\ \frac{\sqrt{5}\ell}{18\sqrt{6}} \\ 0 \\ \frac{\sqrt{5}(\ell-1)}{36\sqrt{6}} \end{pmatrix},$$

$$\hat{\mathbb{X}}^{(2)} = \begin{pmatrix} a_1^0 \\ b_1^1 \\ a_2^1 \\ b_2^2 \end{pmatrix}, \tag{15}$$

$$\hat{\mathbb{L}}_2 = \begin{pmatrix} -\frac{2+\ell}{12} & -\frac{5i\tilde{\delta}\mathscr{A}}{4\sqrt{6}} & \frac{\mathscr{A}}{4\sqrt{6}} & \frac{\sqrt{5}i\tilde{\delta}(1-\ell)}{12\sqrt{2}} \\ -\frac{5i\tilde{\delta}\mathscr{A}}{6\sqrt{6}} & -\frac{\ell-2}{12} & \frac{i\tilde{\delta}(1+\ell)}{12} & \frac{\sqrt{5}\mathscr{A}}{12\sqrt{3}} \\ -\frac{\mathscr{A}}{6\sqrt{6}} & -\frac{i\tilde{\delta}(1+\ell)}{12} & -\frac{(4+\ell)}{12} & -\frac{5\sqrt{5}i\tilde{\delta}\mathscr{A}}{12\sqrt{3}} \\ \frac{i\tilde{\delta}(1-\ell)}{6\sqrt{10}} & -\frac{\mathscr{A}}{4\sqrt{15}} & -\frac{\sqrt{5}i\tilde{\delta}\mathscr{A}}{4\sqrt{3}} & \frac{\ell-4}{12} \end{pmatrix},$$

where $\tilde{\delta} = \delta/\gamma$. Systems (13a) and (13b) describe the evolution of the multipole moments containing even and odd number of tensor direct products of $\boldsymbol{\epsilon}$, respectively. A comparison with the expression for $\rho_{\mu\mu'}$ (when $\boldsymbol{\nu}$ is the quantization axis) shows that inhomogeneous system (13a) describes the evolution of the Zeeman-sublevel states with …, $\mu - 2$, μ, $\mu + 2$, … considered in [16] toward the steady state represented by $\hat{\mathbb{X}}^{(1)}(\infty) = \hat{\mathbb{L}}_1^{-1} \cdot \hat{\mathbb{C}}$. In the general case, the sublevel states are coupled via light-induced coherence (see Fig. 1), making up two mutually incoherent families (for example, with even and odd μ). Homogeneous system (13b) describes the relaxation of the initial coherence between these families of states ($\hat{\mathbb{X}}^{(2)} \longrightarrow 0$). No coherence of this kind is induced by field (3) when an atom is at rest. However, coherence arises in slowly moving atoms in a two- or three-dimensional field configuration with polarization gradients because of a delay in optically driven Zeeman splitting [13].

3. THE LONGEST TIME OF EVOLUTION TOWARD A STEADY STATE

The real parts $\lambda_i^{(1,2)}$ of the eigenvalues of the matrices $\hat{\mathbb{L}}_{1,2}$ determine the spectrum of relaxation times $\tau_i^{(1,2)} = -(\lambda_i^{(1,2)}\gamma S)^{-1}$ for the states represented by $\hat{\mathbb{X}}_i^{(1,2)}$. Let us analyze the longest relaxation time $\tau_{\max} = \max \tau_i^{(1,2)}$ and the corresponding states $\mathbb{X}_{\max}^{(1,2)}$. When j_0 is small, $\xi = \tau_{\max}/\tau_0$ is independent of ellipticity and normalized detuning $\tilde{\delta}$: its value is 9/2 for the 1/2 ⟶ 1/2 and 1/2 ⟶ 3/2 transitions and 6 for the 1 ⟶ 0

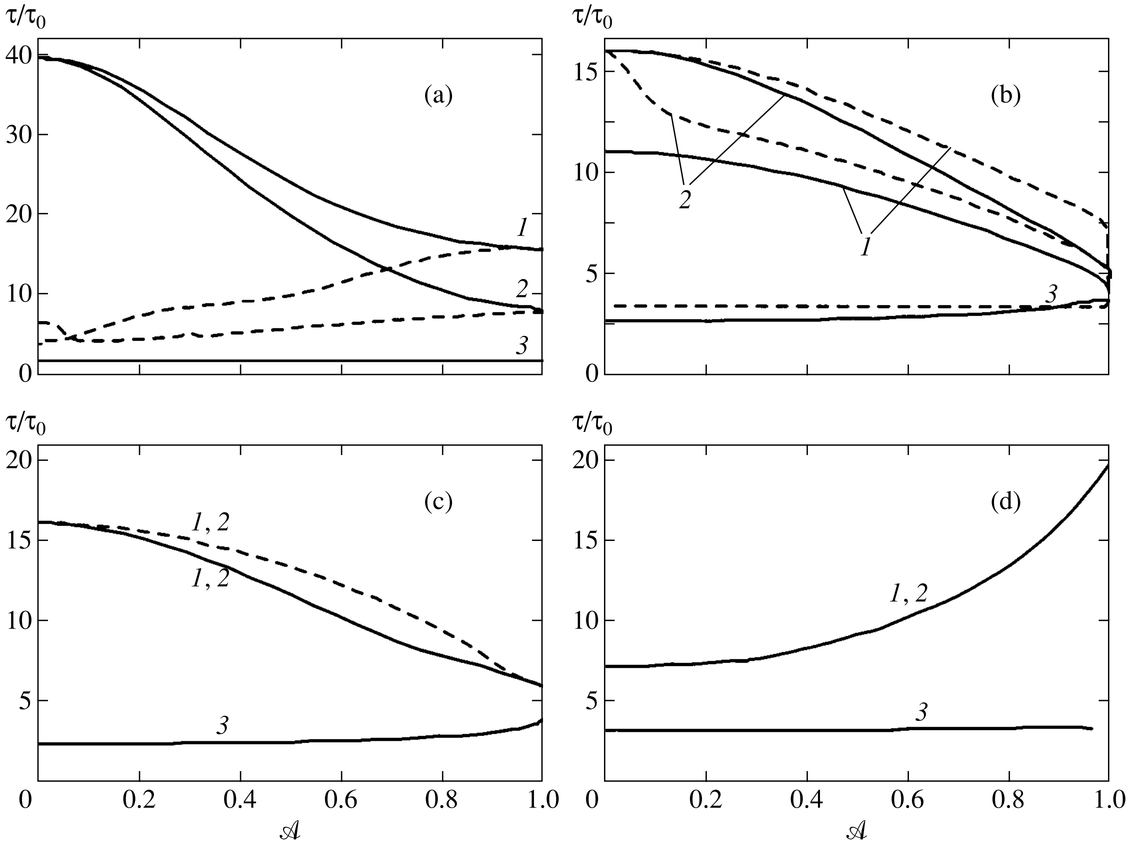

Fig. 2. Different behavior of $\tau^{(1)}_{\max}(\mathcal{A})$ (*1*), $\tau^{(2)}_{\max}(\mathcal{A})$ (*2*), and $\tau_{\min}(\mathcal{A})$ (*3*) for (a) 2 ⟶ 3, (b) 3/2 ⟶ 3/2, (c) 2 ⟶ 2, and (d) 2 ⟶ 1 transitions. Solid and dashed curves correspond to resonance and $|\tilde{\delta}| = 10$; $\tau_0 = (\gamma S)^{-1}$.

transitions,[2] and 4 for the 1 ⟶ 1 transitions. However, ξ strongly depends on ellipticity even for the 1 ⟶ 2 and 3/2 ⟶ 3/2 transitions, and its values corresponding to resonant ($|\tilde{\delta}| \ll 1$) and detuned ($|\tilde{\delta}| > 1$) fields are different in the general case. The transitions can be grouped into the following types characterized by different form of this dependence: (I) $j \longrightarrow j + 1$, (II) $j \longrightarrow j$ with half-integer j, (III) $j \longrightarrow j$ with integer j, and (IV) $j \longrightarrow j - 1$. Figure 2 illustrates the behavior of $\tau_{\max}$ as a function of the degree of circular polarization for the 2 ⟶ 3, 3/2 ⟶ 3/2, 2 ⟶ 2, and 2 ⟶ 1 transitions in regimes with $|\tilde{\delta}| \ll 1$ and $|\tilde{\delta}| = 10$. The curves representing $\tau^{(1)}_{\max}(\mathcal{A})$ and $\tau^{(2)}_{\max}(\mathcal{A})$ are identical for type III and IV transitions. Note that the dependence $\xi(\tilde{\delta})$ is very weak for type I, III, and IV transitions when $|\tilde{\delta}| \gtrsim 2$ and substantial for type II transitions. The curves of $\tau_{\min}$ corresponding to the states $\mathbb{X}_{\min}$ characterized by the fastest relaxation are also shown for comparison. The results shown in Fig. 1 suggest that $\tau_{\min} \approx (2\text{–}3)\tau_0$ for each type of transition. For $j_0 > 2$, this estimate holds, while the dependence on ellipticity is negligible. The lower estimates for $\tau_0 = (\gamma S)^{-1}$ obtained for several specific atoms are as follows:

(i) for $j_0 = 2$ in ^{23}Na atoms, $\lambda = 589.0$ nm, $\gamma/2\pi = 10$ MHz, $I_{\text{sat}} = 6.44$ mW/cm^2, and the value of τ_0 at $I = I_{\text{sat}}$ ($S = 1/2$) is $\tau_{0,\min} = 3.2 \times 10^{-8}$ s;

(ii) for $j_0 = 5/2$ in ^{173}Yb atoms, $\lambda = 555.8$ nm, $\gamma/2\pi = 0.187$ MHz, $I_{\text{sat}} = 0.14$ mW/cm^2 [17], and $\tau_{0,\min} = 1.7 \times 10^{-6}$ s;

(iii) for $j_0 = 3$ in ^{85}Rb and ^{52}Cr atoms, $\lambda = 795.0$ and 425.4 nm, $\gamma/2\pi = 6.1$ and 4.9 MHz, $I_{\text{sat}} = 1.6$ and 8.4 mW/cm^2, and $\tau_{0,\min} = 5.2 \times 10^{-8}$ and 6.5×10^{-8} s, respectively;

(iv) for $j_0 = 4$ in ^{133}Cs atoms, $\lambda = 852.1$ nm, $\gamma/2\pi = 5.2$ MHz, $I_{\text{sat}} = 1.1$ mW/cm^2, and $\tau_{0,\min} = 6.1 \times 10^{-8}$ s.

For different values of light intensity and detuning, the saturation parameter can be calculated by using expression (4').

---

[2] This value is the highest of those for decaying states, whereas the eigenvalues $\lambda^{(1)}_1 = 0$ and $\lambda^{(2)}_{1,2} = 0$ correspond to the two distinct coherent states not coupled to the field in $j \longrightarrow j - 1$ transitions [16].

Even for the values of j_0 specified above, the longest relaxation time is greater than τ_0 by an order of magnitude. Moreover, the value of ξ increases with j_0, because the 6j and 9j symbols in (10) are small at $j_0 \gtrsim 1$, and so are the corresponding matrix elements in $\hat{\mathbb{L}}_{1,2}$. A rough estimate for the mean value $\langle\xi\rangle$ is $\sqrt{3}/[(2j_1+1)\mathcal{F}_1^{1,0}]$. This quantity characterizes relaxation of the rank one multipole moments ρ^1 when the contributions of the multipole moments of rank $\kappa_2 > 1$ and rank $\kappa_1 > 0$ to the atomic and photon density matrices, respectively, are neglected in (9). The corresponding averages are

$$\langle\xi\rangle_{\mathrm{I}} \approx \sqrt{3}(j_0+1)^2(2j_0+1)/(2j_0+3),$$

$$\langle\xi\rangle_{\mathrm{II,\,III}} \approx \sqrt{3}j_0(j_0+1)/2,$$

$$\langle\xi\rangle_{\mathrm{IV}} \approx \sqrt{3}(j_0)^2(2j_0+1)/(2j_0-1).$$

The estimate $\tau \propto j_0^2/\gamma S$ is valid for large values of j_0 [6].[3]

Normally, the time $\tau_{\max}$ corresponding to linearly polarized field ($\mathcal{A} \approx 0$) is longer than that corresponding to circular polarized field ($|\mathcal{A}| \approx 1$), except for the type IV transitions and the type I transitions for $|\tilde{\delta}| > 1$. The function $\xi(\tilde{\delta})$ for cyclic (type I and II) transitions is qualitatively different from that for the bleached (type III and IV) ones (for which $\hat{\rho}(\infty)$ describes coherent states not coupled to the light field [16]). In the latter case, $\xi(\tilde{\delta})$ is a slowly varying function, whereas type I and II transitions corresponding to $|\tilde{\delta}| > 1$ are characterized by relaxation times much shorter and longer (when $|\mathcal{A}| \approx 0.5$), respectively, than those under resonance conditions. The analysis that follows is focused on the states represented by the slowest varying "eigenvectors" $\mathbb{X}_{\max}$ of the matrices $\hat{\mathbb{L}}_{1,2}$.

3.1. Exact Resonance

When $\delta = 0$, the systems in (13) split into blocks of equations describing the evolution of a_κ^l and b_κ^m separately. To be specific, let us consider the inhomogeneous system of ODEs. To improve description of $\mathbb{X}_{\max}^{(1,2)}$, let us compare these vectors with the populations and coherences represented by $\rho_{\mu\mu'}$ (when $\mathbf{v}$ is the quantization axis). According to (8) and (12), the equations for a_κ^l determine the evolution of the populations $N_\mu = \rho_{\mu\mu}$ and the real (symmetric) parts $P_{\mu\mu'} = (\rho_{\mu\mu'} + \rho_{\mu'\mu})/2$ of coherences (with $\mu \neq \mu'$ and even $|\mu - \mu'|$). The homogeneous equations for b_κ^m describe the evolution of the complex parts, $Q_{\mu\mu'} = (\rho_{\mu\mu'} - \rho_{\mu'\mu})/2i \longrightarrow 0$. For a cyclic transition, $Q_{\mu\mu'}$ varies much faster than N_μ and $P_{\mu\mu'}$: $2\tau_Q \approx \tau_N$ or τ_P. Consider the case of a field that is not linearly polarized. In type I transitions, the slowest varying characteristics are N_μ, i.e., the multipole moments having the form

$$\tilde{\rho}^\kappa = a_\kappa^\kappa\{\ldots\{\{\mathbf{v}\otimes\mathbf{v}\}_2\otimes\mathbf{v}\}_3\ldots\otimes\mathbf{v}\}_\kappa.$$

The corresponding $\tau_{\max}$ is nondegenerate and is separated from the remaining τ_i ($\tau_{\max} \gtrsim 2\tau_i$). Therefore, the function $\xi(\ell)$ can be accurately determined by analyzing only the reduced matrix $\hat{\mathbb{L}}_1$ characterizing the evolution of the transpose $(a_1^1;\ a_2^2;\ \ldots)^{\mathrm{T}}$. For example, a good approximation of $\xi(\ell)$ can be obtained for the $4 \longrightarrow 5$ transition by retaining only the first four coefficients. For the $1 \longrightarrow 2$ transition, (14) yields

$$\xi(\ell) \approx 36/(7 - \ell - \sqrt{4 - 8\ell + 13\ell^2}).$$

For type II transitions, the time $\tau_{\max}^{(1)} = \tau_N \approx \tau_P$ is such that $\tau_{\max} - \tau_i \ll \tau_{\max}$. Furthermore, type II transitions are characterized by slower evolution of the coherence $\rho_{\mu\mu'}$ between the families of states (with odd $|\mu - \mu'|$), because $\tau_{\max}^{(2)} > \tau_{\max}^{(1)}$ (see Fig. 2b). These include the coherences that correspond to the highest rank multipole moments proportional to $\mathcal{Y}_{2j_0}^{2m,0}$ ($m = 0, 1, \ldots$). In type III transitions, the slowest varying characteristics are the "highest rank" coherences (rather than populations), such as $\rho^8 \sim \mathcal{Y}_8^{m,p}$ with $m = 0, \ldots, 4$ for the $4 \longrightarrow 4$ transition. The corresponding $\tau_{\max}$ is doubly degenerate. In type IV transitions, the slowest varying characteristics are the populations and coherences $\rho_{\mu\mu'}$ with $|\mu - \mu'| \leq 4$, and $\tau_{\max}$ is doubly degenerate.

3.2. Detuned Pumping with $|\tilde{\delta}| > 1$

In this regime, the evolution of N_μ and $P_{\mu\mu'}$ is strongly related to that of $Q_{\mu\mu'}$, as can be shown by analyzing expressions (14) and (15) in the relatively simple case of the $1 \longrightarrow 2$ transition. Accordingly, very different $\mathbb{X}_{\max}^{(1,2)}$ and $\tau_{\max}(\mathcal{A})$ are obtained for transitions of certain types. Analysis shows that the dependence of ξ on detuning is negligible even for $|\tilde{\delta}| \approx 2$. Therefore, the limit value of $\tau_{\max}$ corresponding to $|\tilde{\delta}| \gg 1$ is a good

---

[3] The reduced dipole matrix element in the definition of the saturation parameter also depends on j_0. Note that the quantity d contained in (5) is defined in terms of the Clebsch–Gordan coefficients (see also [1, 3]), whereas a definition of $\tilde{d}$ in terms of Wigner 3jm symbols was used in [2, 6, 13]. These quantities satisfy the relation $\tilde{d} = \Pi(j_1)d$.

approximation. It can be found by setting to zero the coefficient of highest power of $\tilde{\delta}$ in the characteristic polynomial of the matrix $\hat{\mathbb{L}}_1$ or $\hat{\mathbb{L}}_2$. For the 1 ⟶ 2 transition, the resulting approximation is

$$\tau_{\max} \approx \frac{12(75 - 72\ell^2)\tau_0}{175 - 162\ell^2 - 2\sqrt{625 + 450\ell^2 - 2799\ell^4 + 728\ell^6}},$$

$$\ell^2 = 1 - \mathcal{A}^2.$$

This detuned regime is also characterized by a negligible $Q_{\mu\mu'}$ for $\mathbb{X}_{\max}$ corresponding to type I, II, and III transitions, despite the coupling between the components N_μ, $P_{\mu\mu'}$, and $Q_{\mu\mu'}$ in the dynamical system describing their evolution. Thus, the structure of $\mathbb{X}_{\max}$ is determined by N_μ and $P_{\mu\mu'}$ (mainly by those with $|\mu - \mu'| = 2$), while the corresponding $\tau_{\max}$ is nondegenerate and $\tau_{\max} \gtrsim 1.5\tau_i$. For type IV transitions, both structures of $\mathbb{X}_{\max}$ and $\tau_{\max}(\mathcal{A})$ are similar to those in the under resonant conditions.

3.3. Linearly Polarized Pumping

The limit cases of circular and linear field polarization (when $|\mathcal{A}| = 1$ and 0, respectively) are degenerate in the sense that the aforementioned families of Zeeman sublevels coupled via light-induced coherence break down into separate sublevels. In the former case, this is clear from Fig. 1. To analyze the latter case, the quantization axis is taken parallel to $\boldsymbol{\epsilon}$. Then, stimulated transitions are depicted by vertical arrows; i.e., they do not couple sublevels with different μ, while the sublevel populations are characterized by multipole moments of the form

$$\tilde{\tilde{\rho}}^{\kappa} \sim \mathcal{Y}_{\kappa}^{0,\,p} \sim \{\dots\{\{\boldsymbol{\epsilon} \otimes \boldsymbol{\epsilon}\}_2 \otimes \boldsymbol{\epsilon}\}_3 \dots \otimes \boldsymbol{\epsilon}\}_{\kappa}.$$

Note that the structure of $\mathbb{X}_{\max}$ corresponding to $\mathcal{A} \approx 0$ changes substantially even under weak variation of $\mathcal{A}$. The behavior of $\mathbb{X}_{\max}^{(1,\,2)}$ at $\mathcal{A} = 0$ can be characterized as follows. In type III transitions, the slowest varying characteristics are the populations of (new) sublevels, and ξ can easily be found by analyzing the reduced ODEs for $(a_2^0;\, a_4^0;\, \dots)^{\mathrm{T}}$. Analogous behavior is characteristic of type IV transitions when $|\tilde{\delta}| > 1$, but slow evolution under resonant conditions is exhibited not only by populations, but also by the coherences $\rho_{\mu,\,\mu \pm 1}$, i.e., the multipole moments proportional to $\mathcal{Y}_{\kappa}^{1,\,p}$. The eigenvalues that determine the corresponding $\tau_{\max}$ are nondegenerate for transitions of both types. The slowest varying characteristics in cyclic transitions under resonant conditions are the coherences $\rho_{\mu,\,\mu \pm 1}$ (i.e., $a_{\kappa}^1\mathcal{Y}_{\kappa}^{1,\,0}$), but not populations. The times $\tau_{\max}^{(1)}$ and $\tau_{\max}^{(2)}$ can be found from the reduced equations for $(a_1^1;\, a_3^1;\, \dots)^{\mathrm{T}}$ and $(a_2^1;\; a_4^1;\; \dots)^{\mathrm{T}}$, respectively. For example, $\xi = 12$ for the 1 ⟶ 2 transition. Totally different behavior of type I transitions is obtained for $|\tilde{\delta}| > 1$. In transitions with $j_0 \geq 5/2$, the slowest varying are the populations characterized by $\mathcal{Y}_{\kappa}^{0,\,p}$, and $\tau_{\max}^{(1)}$ can be evaluated by analyzing the reduced system of ODEs for $(a_2^0;\, a_4^0;\, \dots)^{\mathrm{T}}$. The resulting ξ substantially differs from that predicted resonant conditions. In transitions with lower j_0, the time $\tau_{\max}$ can be associated with several eigenvalues τ_i, which are equal or nearly equal. In particular, there exist three such values for the 1 ⟶ 2 transition, one of which corresponds to evolution of population and coherence proportional to $\mathcal{Y}_2^{2,\,0}$. As a result, $\xi = 4$ is obtained for this transition. Note that the corresponding $\xi(\tilde{\delta})$ is

$$\xi = \mathrm{Re}\left(\frac{12}{3 - 2\sqrt{1 - \tilde{\delta}^2}}\right);$$

i.e., the values of ξ rapidly varies in the neighborhood of $|\tilde{\delta}| \approx 1$. A similar dependence holds for type I transitions with $j_0 > 1$, while the difference between $\xi(|\tilde{\delta}| > 1)$ and $\xi(0)$ is even larger. For example, $\xi(0) \approx 145$ and $\xi(|\tilde{\delta}| \geq 2) \approx 7.36$ for $j = 4$.

4. EVOLUTION OF MULTIPOLE MOMENTS UNDER DIFFERENT INITIAL CONDITIONS

The evolution of ground-state multipole moments is determined not only by the spectrum of the operator $\hat{\mathcal{L}}$, but also by $\hat{\rho}(0)$. The dependence on the initial state is analyzed here for two examples: $\rho_{\mu\mu'}(0) = \delta_{\mu\mu'}/(2j_0 + 1)$ (case A) and $\rho_{\mu\mu'}(0) = \delta_{\mu\mu_0}\delta_{\mu'\mu_0}$ (case B, pure state in which only the Zeeman sublevel μ_0 is populated). It should be noted that both have been considered in analyses of specific models of atom–field interaction. Case A was examined in [9] to determine cooling dynamics for a j ⟶ j transition in a three-beam optical lattice. Case B was invoked in [2, 4] to calculate the cooling force and diffusion tensor for 1 ⟶ 2 and 2 ⟶ 3 transitions in certain one-dimensional field configurations. In case B, of particular interest is the initial state for which $|\mu_0| = j_0$ and $\mathbf{v}$ is the quantization axis, obtained when an atom is pumped by a circularly polarized field.

In these cases, $\hat{\mathbb{X}}^{(2)}(t) = 0$.[4] The evolution toward a steady state is determined by $a_\kappa^l(t)$ and $b_\kappa^m(t)$ in $\hat{\mathbb{X}}^{(1)}(t)$; i.e., the number of state variables is smaller by half than that in the problem of dimension $(2j_0 + 1)^2 - 1$. Furthermore, knowledge of $\hat{\rho}(t)$ is generally required to analyze kinetics or spectroscopy problems for systems of the type considered here. For example, only the multipole moments ρ^1 and ρ^2 are required to calculate cooling forces [13], because $\rho^0 = 1/\Pi(j_0)$ is determined by a normalization condition. The multipole moments of ranks $\kappa \le 2$ also play a key role in spectroscopy problems that do not involve higher rank multipole moments [18]. Therefore, the variation of a_1^1, a_2^2, a_2^0, and b_2^1 is of primary interest in these problems, irrespective of the complexity of a dipole transition. Recall that a_1^1 and a_2^2 characterize the Zeeman sublevel populations (when $\mathbf{v}$ is the quantization axis), while a_2^0 and b_2^1 characterize the real and imaginary components of the coherence between adjacent sublevels with μ and $\mu \pm 2$, respectively (see Fig. 1). In the degenerate case of linearly polarized driving field, when $\boldsymbol{\epsilon}$ is the quantization axis, a_2^0 characterizes the populations of new sublevels; a_1^1 and b_2^1 characterize, respectively, the real and imaginary components of the coherence between a sublevel μ and the adjacent sublevels with $\mu \pm 1$; and a_2^2 characterizes the population and coherence distributions between the sublevel μ and the sublevels with $\mu \pm 2$.

A numerical analysis of several transitions with j_0 up to 5 shows that the evolution of $\langle a_1^1\rangle$ driven by fields with arbitrary $\mathscr{A}$ in cases A and B is described by a monotonic function characterized by a relaxation time $\tau_1^1(\mathscr{A})$:

$$\langle a_1^1\rangle(t) = a_1^1(\infty) + [\tilde{a}_1^1 - a_1^1(\infty)]\exp(-t/\tau_1^1), \quad (16)$$

where $\tilde{a}_1^1$ corresponds to $\langle a_1^1\rangle(0)$, which differs from $a_1^1(0)$ in the general case. The angle brackets denote quantities obtained by averaging over oscillations (see Fig. 3a) with frequencies proportional to $\tilde{\delta}$, which are due to the dynamic Stark shifts of Zeeman sublevels in a detuned field. Even though the oscillations can have considerable amplitudes, their characteristics are not considered in this paper.

The evolution of $\langle a_2^2\rangle(t)$ and $\langle a_2^0\rangle(t)$ may not admit approximation by (16) with relaxation times τ_2^2 and τ_0^2. The cases when these variables exhibit nonmonotonic behavior are of special interest (see Figs. 3b and 3c). Figure 3b shows the evolution of $a_2^0(t)$ from an equilibrium state in a field with $\mathscr{A} \ne 0$ predicted for $\delta = 0$, which is characteristic of type I transitions only. Here, the coherence is obviously higher as compared to its steady-state value, which should be mainly attributed to higher intensities of stimulated emission and absorption of photons.[5] Recall that the qualitative pattern is different when $|\tilde{\delta}| \ne 0$ because of the contribution of the imaginary coherence represented by b_2^1. Figure 3c shows the evolution of $a_2^2(t)$ from the state $\mu_0 = -j_0$ in a field with $\mathscr{A} > 0$ predicted for $\delta = 0$. In this case, atoms are transferred from states dominated by $\mu < 0$ to those populated levels with $\mu > 0$, because $a_1^1(t)$ changes sign (as in Fig. 3a, but without oscillation) in the neighborhood of the minimum in $a_2^2(t)$. Note also that the sublevels tend to be uniformly populated during an intermediate stage of the evolution, retaining a high degree of mutual coherence (characterized by $a_2^0(t)$), as in the state that develops under linearly polarized pumping. In type I transitions, the coherence reaches peak values, as in Fig. 3b. In other regimes, $\langle a_2^0\rangle$ and $\langle a_2^2\rangle$ are accurately approximated by functions similar to (16).

The typical examples of evolution of b_2^1 presented in Fig. 3d for $\tilde{\delta} = 10$ illustrate the transient dynamics of stimulated emission and absorption, because $b_2^1(0) = b_2^1(\infty) = 0$. One of these demonstrates the oscillation of b_2^1 in case B from the state $\mu_0 = -j_0$, which is characterized by amplitudes of b_2^1 comparable to those considered above. The curve shown in the inset to Fig. 3d illustrated evolution from an equilibrium state toward a steady state. In this regime, the amplitude of $b_2^1(\mathscr{A})$ is smaller than the remaining coefficients by an order of magnitude.

A numerical analysis shows that the behavior of $\tau_1^1(\mathscr{A})$ for transitions with $j_0 \lesssim 5$ is qualitatively similar to $\tau_{\max}(\mathscr{A})$ (Fig. 2) for various regimes of detuning. For cyclic transitions from an equilibrium initial state,

---

[4] Note that the coherences represented by $\hat{\mathbb{X}}^{(2)}$ can be neglected when the pumping field configuration is one-dimensional. However, they must be taken into consideration in higher dimensional configurations with polarization gradients [13].

[5] The intensities of spontaneous transitions also increase, but monotonically (see next section).

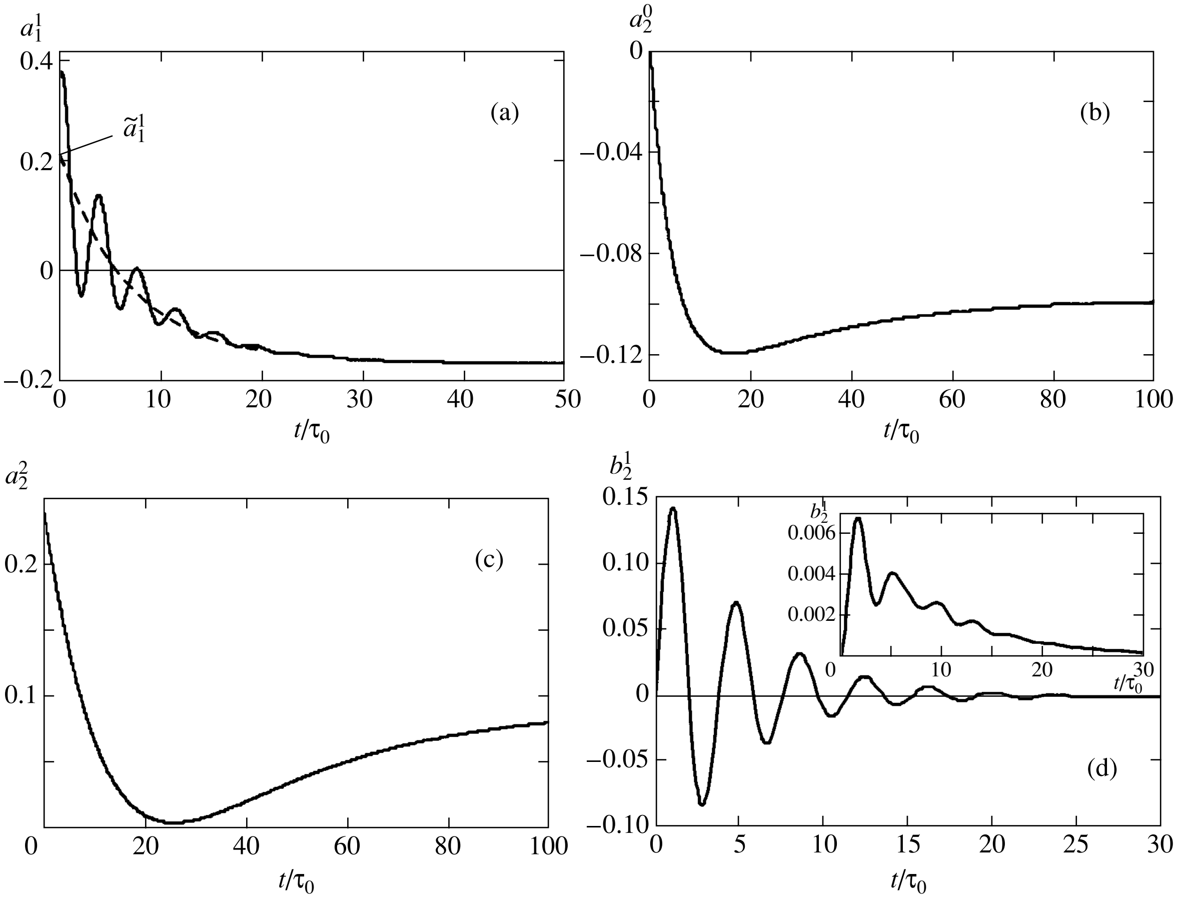

Fig. 3. Evolution of (a) a_1^1 (solid curve) and $\langle a_1^1 \rangle$ (dashed curve) for the $2 \longrightarrow 3$ transition from the state $\mu_0 = -2$ at $\mathcal{A} = 0.2$ and $\tilde{\delta} = 10$, (b) a_2^0 for the $2 \longrightarrow 3$ transition from an equilibrium state at $\tilde{\delta} = 0$ and $\mathcal{A} = 0.4$, (c) a_2^2 for the $2 \longrightarrow 3$ transition from the state $\mu_0 = -2$ at $\tilde{\delta} = 0$ and $\mathcal{A} = 0.4$, and (d) b_2^1 for the $2 \longrightarrow 3$ transition from an equilibrium state (inset) and from the state with $\mu_0 = -2$ at $\tilde{\delta} = 10$ and $\mathcal{A} = 0.4$; $\tau_0 = (\gamma S)^{-1}$.

quantitative agreement between τ_1^1 and $\tau_{\max}$ is obtained. The dependence of τ_2^0 and τ_2^2 on $\mathcal{A}$ is also qualitatively similar to $\tau_{\max}(\mathcal{A})$ when the corresponding averaged coefficients exhibit monotonic behavior: these times are much larger for type I, II, and III transitions under resonant pumping with small $|\mathcal{A}|$ as compared to an almost circularly polarized field ($|\mathcal{A}| \approx 1$), whereas the converse is true for type IV transitions. When $|\tilde{\delta}| > 2$, the behavior of $\tau_{\max}(\mathcal{A})$ for cyclic transitions is consistent with Figs. 2a and 2b. The time $\tau_{\max}(\mathcal{A})$ is quantitatively similar to at least one of the times τ_1^1, τ_2^0, and τ_2^2 if the evolution starts from an equilibrium state. Even though the evolution characterized by τ_1^1, τ_2^0, and τ_2^2 in case B with $\mu_0 = -j_0$ differs in certain aspects from that from an equilibrium state, the following characteristics are in qualitative similar: the relaxation times for $j \longrightarrow j$ transitions (for any δ) and $j \longrightarrow j + 1$ transitions (under resonant pumping) increase with decreasing $\mathcal{A}$, whereas the converse is true for $j \longrightarrow j - 1$ transitions (for any δ) and $j \longrightarrow j + 1$ (for $|\delta| > \gamma$).

5. DYNAMICS OF SPONTANEOUS EMISSION

The coherent and incoherent contributions to the evolution of optically pumped ground-state atoms are represented in Eq. (5) by the components $\hat{\mathcal{L}}_c$ and $\hat{\mathcal{L}}_s$ of the Liouville operator, respectively. Let us analyze the evolution of the intensity of spontaneous emission for transitions of different types in cases A and B. In a statistical treatment of the number of photons emitted by an atom [19], as well as in the description of atomic dynamics based on the quantum-jump approach [20], the quantity

$$P(t) = \mathrm{Tr}\{\hat{\mathcal{L}}_s \hat{\rho}(t)\} \qquad (17)$$

is the number of spontaneously emitted photons per unit time at an instant t. It can also be interpreted as the time distribution of quantum jumps that occur after periods of coherent evolution described by the operator $\hat{\mathcal{L}}_c$.

Let us use (17) to estimate the number N_{opt} of spontaneously emitted photons (or optical pumping cycles) required to reach a steady state $\hat{\rho}(\infty)$. In the general case, it can be shown that the function $P(t)$ calculated by applying the method of minimal bipolar harmonics is completely determined by a_1^1, a_2^2, and a_2^0. In case A, $a_n^m(0) = b_n^m(0) = 0$, and

$$P(0) = \gamma S \mathcal{F}^{00}_{0,s} \varrho^0 \rho^0 = \frac{(2j_1+1)\gamma S}{3(2j_0+1)}$$

for any transition [1]. In case B with $\mu_0 = -j_0$ (when $\mathbf{v}$ is the quantization axis),

$$a_n^n(0) = \frac{(2j_0)!}{\sqrt{(2j_0-n)!(2j_0+n+1)!}},\qquad (18)$$

$$a_n^{m\neq n}(0) = b_n^m(0) = 0.$$

According to a numerical analysis, the results presented below for transitions with $j_0 = 2$ and the $3/2 \longrightarrow 3/2$ transition hold for more complicated transitions with $j_0 \lesssim 5$.

For the transitions in question, $P(t)$ is expressed in terms of $\mathcal{A}$ and ℓ as

$$P_{3/2\to 3/2} = \frac{\gamma S}{15} \qquad (19)$$
$$\times[5 + 2\sqrt{15}\mathcal{A}a_1^1 - 4\sqrt{5}a_2^2 + 2\sqrt{5}(1+3\ell)a_2^0],$$

$$P_{2\to 1} = \frac{\gamma S}{40} \qquad (20)$$
$$\times[8 + 6\sqrt{30}\mathcal{A}a_1^1 + 2\sqrt{70}a_2^2 - \sqrt{70}(1+3\ell)a_2^0],$$

$$P_{2\to 2} = \frac{\gamma S}{24} \qquad (21)$$
$$\times[8 + 2\sqrt{30}\mathcal{A}a_1^1 - 2\sqrt{70}a_2^2 + \sqrt{70}(1+3\ell)a_2^0],$$

$$P_{2\to 3} = \frac{\gamma S}{60} \qquad (22)$$
$$\times[28 - 14\sqrt{30}\mathcal{A}a_1^1 + 2\sqrt{70}a_2^2 - \sqrt{70}(1+3\ell)a_2^0].$$

In the general case, the coefficients $a_n^m(t)$ are oscillating functions (see Fig. 3a). However, $P(t)$ is a monotonic function for arbitrary $\tilde{\delta}$ and $\mathcal{A}$.[6] It can be approximated by (16) with a relaxation time τ_{spont} similar to the time $\tau_{\max}$ characteristic of type I and III transitions in evolution from an equilibrium state for different detunings. In the remaining cases, $\tau_{\text{spont}} < \tau_{\max}$, and the behavior of $\tau_{\text{spont}}(\mathcal{A})$ is analogous to that of $\tau_1^1(\mathcal{A})$. Moreover, the variations of P corresponding to transitions of different types are very informative. It is an increasing function for type I transitions and a decreasing one for the remaining ones. Bleaching corresponds to $P_{\text{III}}(\infty) = P_{\text{IV}}(\infty) = 0$, while $P_{\text{II}}(\infty)$ corresponds to a very low intensity of spontaneous emission, which decreases with increasing j_0 (see [1]). In the limit of $j_0 \gg 1$, this intensity is negligible, and so is the difference between $j \longrightarrow j$ transitions with large integer and half-integer $j \sim 10$ [6, 8]. Compare the expressions for $P(\infty)$ corresponding to the $3/2 \longrightarrow 3/2$ and $3/2 \longrightarrow 5/2$ transitions:

$$P_{3/2\to 3/2}(\infty) = \gamma S\frac{3(1-\mathcal{A}^2)^2}{5(5+3\mathcal{A}^2)},$$
$$P_{3/2\to 5/2}(\infty) = \gamma S\frac{7[8+3\mathcal{A}^2(8+\mathcal{A}^2)]}{5(20+29\mathcal{A}^2)}. \qquad (23)$$

For the former transition, the highest intensity of spontaneous emission (in a linearly polarized field) is $3\gamma S/25$, and the lowest intensity corresponds to bleaching in circularly polarized field. The converse is true for the latter transition: the highest and lowest intensities, γS and $14\gamma S/25$, correspond to circularly and linearly polarized fields. An expression for $P(\infty)$ for arbitrary j_0 can be obtained by using the results reported in [1].

Define

$$N_{\text{opt}} = \int_0^\infty dt[P(t) - P(\infty)] \qquad (24)$$

for the bleaching transitions and the nearly bleached type II transitions and

$$N_{\text{opt}} = \int_0^{\tau_{\text{spont}}} dtP(t) \qquad (25)$$

for type I transitions. For example, $N_{\text{ph}}(\mathcal{A}) \lesssim 5$ for transitions with $j_0 = 2$ and the $3/2 \longrightarrow 3/2$ transition, except for the case of resonantly excited $2 \longrightarrow 3$ transition, when $N_{\text{opt}} \approx 15$.

An analysis of the functions $N_{\text{opt}}(\mathcal{A})$ and $\tau_{\text{spont}}(\mathcal{A})$ under the initial conditions considered above shows that the estimated optical cycle duration, $\tau_{\text{opt}} = \tau_{\text{spont}}/N_{\text{opt}}(\mathcal{A})$, cannot be equal for transitions of all types. The quantity $\tau_0 = (\gamma S)^{-1}$ used in [1, 3] and numerous other studies may widely differ from τ_{opt} and, a fortiori, from the characteristic time required to reach a

---

[6] As before, only pure polarization states (with $\ell^2 + \mathcal{A}^2 = 1$) are considered here.

steady state. A numerical analysis shows that τ_{opt} is virtually independent of δ.[7] However, its dependence on $\hat{\rho}(0)$ and ellipticity is different for transitions of different types.

For $j \longrightarrow j + 1$ transitions, the following estimate provides a good approximation irrespective of the form of $\hat{\rho}(0)$:

$$\tau_{\text{opt}} \approx 1/P(\infty) = 1/\gamma\tilde{S},$$

where the effective saturation parameter $\tilde{S}$ introduced in [1] can be approximated by the expression

$$\tilde{S}(\ell) \approx \frac{(2j+1)\ell P_{2j+1}(1/\ell)}{(4j+1)P_{2j}(1/\ell)}S \tag{26}$$

for $j_0 \lesssim 2$, with maximum and minimum values $\tilde{S}(0) = S$ and $\tilde{S}(1) = (2j+1)S/(4j+1) \approx S/2$, respectively ($P_n(x)$ denotes Legendre polynomials).

For transitions of other types, $\tau_{\text{opt}} \approx (2j_1 + 1)\tau_0$ for evolution from an equilibrium state. For evolution from the state $\mu_0 = -j_0$ (when $\mathbf{v}$ is the quantization axis),

$$\tau_{\text{opt}}(\mathcal{A}) \approx 1/P(0) = k\tau_0/(1+\mathcal{A}),$$

where $k_{3/2 \to 3/2} = 5$, $k_{2 \to 2} = 6$, and $k_{2 \to 1} = 10/3$ according to (18)–(21). The longest time τ_{opt} corresponds to $\mathcal{A} \approx -1$; i.e., the coherent stage of atom–field interaction lasts for a very long time, while the field parameters weakly deviate from the values corresponding to an initially noninteracting atom. However, N_{opt} is obviously proportional to the deviation of the initial atom from a steady state. For example, the maximum value $N_{\text{opt}}^{\max} \approx 2j_0 + 1$ is characteristic of an atom driven by a circularly polarized field ($\mathcal{A} = 1$), which induces transitions from the sublevel $\mu_0 = -2$ to the most distant sublevel $\mu = 2$ ($2 \longrightarrow 2$ transitions) or to the coherent superposition of states with $\mu = 1$ and 2 ($2 \longrightarrow 1$ transitions). Spontaneous emission plays a much more substantial role in this case: an increase in the number of spontaneously emitted photons sharply reduces the cycle duration ($\tau_{\text{opt}} \approx 2\tau_0$).

6. CONCLUSIONS

Evolution of ground-state atoms with angular momenta $j_0 \lesssim 5$ driven by weak elliptically polarized monochromatic light fields is a complicated phenomenon in the general case. On the one hand, this is explained by the large number, $(2j_0 + 1)^2 - 1$, of the variables that characterize (depending on the representation employed) the Zeeman sublevel populations or the atomic multipole moments. On the other hand, the semiclassical expansion in terms of $1/j_0$ employed in [7] is not effective for j_0 in this range. For example, it cannot be used to describe the difference between the unsteady and steady regimes for $j \longrightarrow j$ transitions with integer and half-integer j. The present analysis shows that an effective description of evolution toward a steady state can be developed for a wide variety of problems in which states with $j_0 \lesssim 5$ are of key importance by using a small number of characteristic times and state variables. Problems of this kind include the calculation of kinetics of an atomic ensemble in semiclassical approximation for translational degrees of freedom [3, 21], the calculation of the susceptibility of an atomic ensemble, and the related problem of interaction between a probe beam and a cold system of this kind [22].

A characteristic of particular interest is the longest time $\tau_{\max}$ of evolution toward a steady state for an atomic ensemble pumped by a field with arbitrary ellipticity. It is shown here that transitions can be grouped into the four types characterized by qualitatively different dependence of $\tau_{\max}$ on the degree $\mathcal{A}$ of circular polarization and detuning δ: (I) $j \longrightarrow j + 1$, (II) $j \longrightarrow j$ with half-integer j, (III) $j \longrightarrow j$ with integer j, and (IV) $j \longrightarrow j - 1$. For each transition type, the function $\tau_{\max}(\mathcal{A})$ exhibits specific qualitative behavior under resonant pumping ($|\delta| \ll \gamma$), whereas the dependence of $\tau_{\max}$ on detuning is negligible when $|\tilde{\delta}| > 2\gamma$. First, $\tau_{\max}(\mathcal{A})$ is generally larger for $\mathcal{A} \approx 0$ as compared to $|\mathcal{A}| \approx 1$, with the exception of $j \longrightarrow j - 1$ transitions at any detuning and $j \longrightarrow j + 1$ transitions for $|\delta| > 2\gamma$, for which the converse is true. Second, the change in $\tau_{\max}(\delta)$ caused by detuning from resonance to $|\tilde{\delta}| > 2\gamma$ is qualitatively different for cyclic (type I and II) and bleaching (type III and IV) transitions. For the bleach transitions, $\tau_{\max}$ weakly depends on δ, whereas the relaxation time is sharply reduced by detuning from resonance to $|\delta| > 2\gamma$ for type I transitions and considerably increases for $|\mathcal{A}| \approx 0.5$ for type II transitions.

The importance of $\tau_{\max}$ lies in the fact that it characterizes evolution toward a steady state from an initial state of equilibrium with respect to internal degrees of freedom. The transient process is also characterized by the number N_{opt} of optical pumping cycles and the average cycle duration τ_{opt}. The present analysis shows that the estimated τ_{opt} cannot be equal for transitions of all types and the estimate $\tau_0 = (\gamma S)^{-1}$ may widely differ from τ_{opt}. When S is held constant, τ_{opt} is virtually independent of detuning, whereas its dependence on ellipticity is different for transitions of different types. For $j \longrightarrow j + 1$, it can be represented as $\tau_{\text{opt}} = 1/\gamma\tilde{S}$, where $\tilde{S}(\ell)$ is an effective saturation parameter. For the three

---

[7] Henceforth, it is assumed that the parameter S is held constant when δ is varied by adjusting the Rabi frequency in expression (4).

remaining transitions, this estimate is generally not valid, and τ_{opt} strongly depends on $\hat{\rho}(0)$ and is generally greater than τ_0.

These characteristics of evolution toward a steady state correspond to optical pumping regimes with negligible collisional relaxation. When collisions substantially contribute to the evolution of multipole moments of both ground-state and excited atoms, the overall scenario of the evolution is different from that analyzed above. Suppose that the rate of nonradiative decay of multipole moments is γ_0^κ and γ_1^κ for the ground and excited states. Since the optical pumping time τ for a ground-state atom is greater than $\tau_0 = 1/\gamma S$ by an order of magnitude if $j_0 > 1$, the condition $\gamma_0^\kappa < 1/\tau$ implies that the largest value of γ_0^κ for which this mechanism of decay can be neglected must be corrected. An analysis of specific models characterized by γ_1^κ shows that the function $\tau(\mathcal{A}, \delta)$ is essentially different when relaxation of the excited atom is important: the value of τ is smaller, and there is no difference between pumping by resonant and widely detuned fields ($|\tilde{\delta}| > 1$).

Different transient behavior is also characteristic of the cases when the light polarization cannot be represented as a pure state. An analysis performed for $\mathcal{A}^2 + \ell^2 < 1$ shows that $\tau_{\max}$ strongly depends on $\tilde{\delta}$ when $|\tilde{\delta}| > 1$ for certain mixed states.

ACKNOWLEDGMENTS

I thank A.V. Taichenachev for helpful remarks and useful reference. This work was supported, in part, by the Russian Foundation for Basic Research, project no. 04-02-16488a.

REFERENCES

1. A. V. Taichenachev, A. M. Tumaikin, V. I. Yudin, and G. Nienhuis, Phys. Rev. A **69**, 033410 (2004).
2. P. J. Ungar, D. S. Weiss, E. Riis, and S. Chu, J. Opt. Soc. Am. B **6**, 2058 (1989).
3. A. V. Bezverbnyĭ, O. N. Prudnikov, A. V. Taĭchenachev, *et al.*, Zh. Éksp. Teor. Fiz. **123**, 437 (2003) [JETP **96**, 383 (2003)].
4. M. D. Hoogerland, H. P. de Bie, H. C. W. Beijerinck, *et al.*, Phys. Rev. A **54**, 3206 (1996).
5. S. Padua, C. Xie, R. Gupta, *et al.*, Phys. Rev. Lett. **70**, 3217 (1993).
6. K. A. Nasyrov, Phys. Rev. A **63**, 043406 (2001).
7. K. A. Nasyrov, J. Phys. A: Math. Gen. **32**, 6663 (1999).
8. K. A. Nasyrov, Zh. Éksp. Teor. Fiz. **125**, 556 (2004) [JETP **98**, 489 (2004)].
9. A. V. Taichenachev, A. M. Tumaikin, V. I. Yudin, and L. Hollberg, Phys. Rev. A **63**, 033402 (2001).
10. A. V. Taĭchenachev, A. M. Tumaĭkin, and V. I. Yudin, Zh. Éksp. Teor. Fiz. **110**, 1727 (1996) [JETP **83**, 949 (1996)].
11. C. S. Adams and E. Riis, Prog. Quantum Electron. **21**, 1 (1997).
12. D. A. Varshalovich, A. N. Moskalev, and V. K. Khersonskiĭ, *Quantum Theory of Angular Momentum* (Nauka, Leningrad, 1975; World Sci., Singapore, 1988).
13. A. V. Bezverbnyĭ, Zh. Éksp. Teor. Fiz. **118**, 1066 (2000) [JETP **91**, 921 (2000)].
14. N. L. Manakov, A. V. Meremianin, and A. F. Starace, Phys. Rev. A **57**, 3233 (1998).
15. N. L. Manakov, S. I. Marmo, and A. V. Meremianin, J. Phys. B **29**, 2711 (1996).
16. V. S. Smirnov, A. M. Tumaĭkin, and V. I. Yudin, Zh. Éksp. Teor. Fiz. **96**, 1613 (1989) [Sov. Phys. JETP **69**, 913 (1989)].
17. R. Maruyama, R. H. Wynar, M. V. Romalis, *et al.*, Phys. Rev. A **68**, 011403(R) (2003).
18. V. V. Yashchuk, D. Budker, W. Gawlik, *et al.*, Phys. Rev. Lett. **90**, 253001 (2003).
19. G. Nienhuis, J. Stat. Phys. **53**, 417 (1988).
20. M. B. Plenio and P. L. Knight, Rev. Mod. Phys. **70**, 101 (1998).
21. J. Javaninen, Phys. Rev. A **44**, 5857 (1991).
22. J. Guo, P. R. Berman, B. Dubetsky, and G. Grynberg, Phys. Rev. A **46**, 1426 (1992); A. V. Bezverbnyĭ, V. S. Smirnov, and A. M. Tumaĭkin, Zh. Éksp. Teor. Fiz. **105**, 62 (1994) [JETP **78**, 33 (1994)].

Translated by A. Betev

Journal of Experimental and Theoretical Physics, Vol. 100, No. 5, 2005, pp. 833–843.
Translated from Zhurnal Éksperimental'noĭ i Teoreticheskoĭ Fiziki, Vol. 127, No. 5, 2005, pp. 945–956.
Original Russian Text Copyright © 2005 by Zheltikov.

Limiting Temporal and Spectral Resolution in Spectroscopy and Microscopy of Coherent Raman Scattering with Chirped Ultrashort Laser Pulses

A. M. Zheltikov
International Laser Center, Physics Department, Moscow State University,
Vorob'evy gory, Moscow, 119992 Russia
e-mail: zheltikov@phys.msu.ru

Received August 26, 2004

Abstract—Chirped ultrashort light pulses offer new options for coherent nonlinear spectroscopy and microscopy. We show here that the temporal resolution of spectroscopy and microscopy based on coherent anti-Stokes Raman scattering (CARS) can be smoothly tuned within a broad range, with upper and lower bounds of this range controlled by the pump and probe pulse durations. The spectral resolution of CARS spectroscopy and microscopy is analyzed as a function of the duration and chirp of the pump pulses. Pulses with a periodic phase modulation can provide the limiting spectral resolution of the CARS technique, corresponding to the lower bound of uncertainty in spectral measurements, dictated by the uncertainty principle. *© 2005 Pleiades Publishing, Inc.*

1. INTRODUCTION

Generation of ultrabroadband pulses of coherent electromagnetic radiation is one of the most significant recent achievements of optical science. Optical-harmonic generation in high-intensity laser fields culminated in the breakthrough to the domain of attosecond pulse durations [1–3]. Novel types of waveguides—microstructure and photonic-crystal fibers (PCFs) [4–6]—can provide maximum confinement of electromagnetic radiation in guided modes of the light field [7, 8] and allow a nearly arbitrary tailoring of dispersion profiles of guided modes [9, 10]. Due to this unique combination of properties, PCFs can efficiently generate emission with a bandwidth exceeding an octave (supercontinuum) [11, 12] and offer ways of generating short light pulses with a shifted carrier frequency and controlled chirp [8, 13–15].

Attosecond pulses and supercontinuum sources open new horizons in laser spectroscopy and optical metrology, allowing measurements with an unprecedented time resolution [3, 16] and making it possible to coherently excite and probe physical, chemical, and biological objects within remarkably broad spectral ranges. Attosecond tomography [17–19]—tracking the dynamics of electrons in atoms and molecules from diffraction patterns of electrons ejected under the action of attosecond pulses—is one of the most impressive recent achievements of attosecond science. Photonic-crystal-fiber supercontinuum sources [11, 12] have led to revolutionary breakthroughs in optical metrology [20–22] and are widely employed in nonlinear laser spectroscopy [23, 24], optical coherence tomography [25], photochemistry [14], and ultrafast photonics [26]. Recent experiments have demonstrated that PCFs can provide high efficiencies of nonlinear-optical frequency conversion of ultrashort laser pulses, allowing generation of frequency-shifted pulses with a controlled chirp ideally suited for the spectroscopy [27, 28] and microscopy [29] of coherent anti-Stokes Raman scattering (CARS).

In this paper, we show that ultrashort light pulses with a controlled chirp offer new options for coherent nonlinear spectroscopy and for the rapidly growing field of CARS microscopy [30]. Linearly chirped pulses can scan the instantaneous frequency difference through Raman resonances in the CARS scheme. We will find analytic solutions for the temporal envelope of the CARS signal for different relations between the laser pulse durations and characteristic nonlinear response time. We will also explore the ways of using chirped pulses in coherent four-wave mixing (FWM) for high-resolution spectroscopy and microscopy, as well as for studying ultrafast processes in gas- and condensed-phase media.

2. CHIRPED-PULSE CARS SPECTROSCOPY

Chirped ultrashort pulses are a convenient tool for laser spectroscopy and quantum control [31–40]. In this section, we dwell upon using chirped pulses for measuring the nonlinear response of a Raman-active medium. Physically, the possibility of applying chirped pulses for spectral measurements using time-resolved methods is based on a linear frequency–time mapping defined by linearly chirped pulses (Fig. 1). The spec-

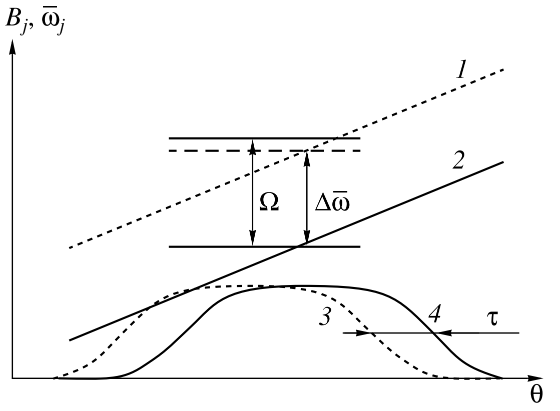

Fig. 1. The instantaneous frequencies $\bar{\omega}_j = \omega_j - \partial \arg A_j/\partial\theta$ and the amplitudes B_j of the first (curves *1* and *3*) and second (curves *2* and *4*) pump pulses as functions of the retarded time in CARS spectroscopy using chirped pulses (10)–(12). The difference of instantaneous frequencies of the first and second pump pulses, $\Delta\bar{\omega} = \bar{\omega}_1 - \bar{\omega}_2$, is scanned through the frequency of the Raman resonance Ω by varying the delay time τ between the pump pulses.

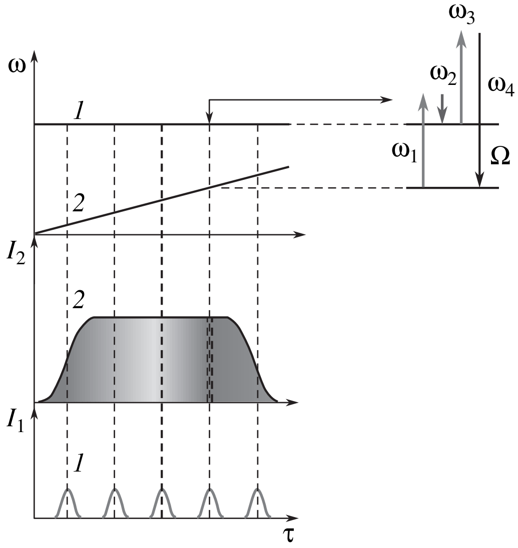

Fig. 2. Femtosecond CARS spectroscopy using chirped pulses.

trum of the nonlinear susceptibility can be thus recorded by measuring the nonlinear response signal as a function of the delay time between the pump and probe pulses [40, 41].

Consider a generic case when a nonlinear signal is produced through the CARS process $\omega_4 = \omega_1 - \omega_2 + \omega_3$ (Fig. 2) involving light pulses propagating along the z axis,

$$E_i = A_i\left(t - \frac{z}{v_i}, z\right)\exp[i(k_i z - \omega_i t)] + \text{c.c.}, \qquad (1)$$

where A_i, ω_i, k_i, and v_i are the slowly varying envelope, frequency, wavenumber, and the group velocity of the ith pulse ($i = 1, 2, 3, 4$).

Slowly varying envelope and phase approximation will be used to describe nonlinear-optical phenomena throughout this paper. This approximation limits the length of the nonlinear medium, which should not exceed the dispersion length $l_d = \tau_0^2/|k_2|$ for the duration τ_0 of the shortest of the light pulses and given group-velocity dispersion k_2. Neglecting dispersion effects beyond the first-order dispersion terms, we arrive at the following expression for the slowly varying envelope of the CARS signal [42]:

$$\left(\frac{\partial}{\partial z} - \frac{1}{v_4}\frac{\partial}{\partial t}\right)A_4\left(t - \frac{z}{v_4}, z\right) = -\frac{2\pi\omega_4^2}{ik_4c^2}P^{NL}\exp[-i(k_4 z - \omega_4 t)]. \qquad (2)$$

Here, the third-order nonlinear polarization of the medium is given by

$$P^{NL}(t, z) = \int_0^\infty\int_0^\infty\int_0^\infty \chi(t_1, t_2, t_3, z)E_1(t - t_1, z) \times E_2(t - t_2, z)E_3(t - t_3, z)dt_3dt_2dt_1, \qquad (3)$$

where $\chi(t_1, t_2, t_3, z)$ is the time-domain CARS susceptibility.

Provided that the frequency difference $\omega_1 - \omega_2$ is tuned to a resonance with a Raman-active transition in the medium under study, the CARS susceptibility can be written as

$$\chi(t_1, t_2, t_3, z) = \chi(t_1, z)\delta(t_1 - t_2)\delta(t_3). \qquad (4)$$

In the spectral domain, the nonlinear susceptibility (4) depends only on the frequency difference $\omega_1 - \omega_2$, thus corresponding to the case of a Raman resonance in a situation when the frequencies of the optical fields are detuned far off the remaining resonances in the quantum system (including resonances with one-photon and non-Raman multiphoton transitions). Physically, the approximation of Eq. (4) implies that the time of the nonresonant optical response is much less than the response time related to the resonant part of optical susceptibility. Such a relation between the resonant and nonresonant response times is a direct consequence of the uncertainty principle (see, e.g., [43]). More quantitatively, the ratio of the resonant and nonresonant response times is controlled by the detuning of optical radiation frequencies from the frequencies of eigenmodes in the quantum system. For most of the commonly used Raman-active media, this ratio may vary from 2–3 up to 6–8 orders of magnitude. Time delay on the order of ultrashort pulse duration, $\tau_d \sim 10$ fs, would typically suppress the nonresonant component of the coherent Raman signal by several orders of magnitude [37, 38].

Importantly, Eq. (4) implies no limitation on the relaxation times of Raman modes or the line shapes of Raman resonances in spectra of cubic susceptibilities. To verify this, we use Eq. (4) to calculate the frequency-domain nonlinear susceptibility corresponding to the CARS process $\omega_a = \omega_1 - \omega_2 + \omega_3$:

$$\chi(\omega_a;\, \omega_1, -\omega_2, \omega_3) \propto \int_0^\infty\int_0^\infty\int_0^\infty \chi(t_1, z)\delta(t_1 - t_2)\delta(t_3)$$

$$\times \exp(i\omega_1 t_1)\exp(-i\omega_2 t_2)\exp(i\omega_3 t_3)dt_1 dt_2 dt_3$$

$$= \int_0^\infty \chi(t_1, z)\exp[i(\omega_1 - \omega_2)t_1]dt_1 \equiv \chi_{\text{Raman}}(\omega_1 - \omega_2).$$

The shape of the spectrum of the nonlinear susceptibility and its parameters (including the line width and the response time) remain arbitrary as long as the function $\chi(t_1)$ is not specified. In particular, an exponential function $\chi(t_1)$ would correspond to a Lorentzian shape of a Raman resonance (see also Section 3).

Substituting Eq. (4) into Eq. (3) and performing integration in t_1 and t_3, we derive the following expression for the nonlinear polarization:

$$P^{NL}(t, z) = \int_0^\infty \chi(t_1, z)E_1(t - t_1, z) \times E_2(t - t_1, z)dt_1 E_3(t, z). \tag{5}$$

Expression (5) describes, jointly with Eq. (2), the CARS process in a plane-wave three-color pump field neglecting dispersion pulse spreading. In a spatially uniform medium, the energy of the CARS signal is given by

$$W(\tau) \propto \left|\int_{-\infty}^{\infty} E_3(t - \tau)Q(t)dt\right|^2, \tag{6}$$

where τ is the delay time of the third (probe) pulse,

$$Q(t) = \int_0^\infty F(t - \theta)\chi(\theta)d\theta, \tag{7}$$

and $F(t)$ is the driving force, determined by the type of interaction between the pump-field components.

For a methodologically important case of a biharmonic pump, the driving force is defined as $F(t) = F_0\exp(i\omega t)$, where $\omega = \omega_1 - \omega_2$ is the difference of the pump-field frequencies. Integration in Eq. (7) then yields

$$Q(t) = F_0\vartheta(\omega)\exp(i\omega t), \tag{8}$$

where

$$\vartheta(\omega) = \int_0^\infty \chi(\theta)\exp(-i\omega\theta)d\theta \tag{9}$$

is the frequency-domain nonlinear-optical susceptibility.

In the following sections, we will apply Eqs. (5)–(9) to analyze the temporal and spectral resolution of chirped-pulse CARS spectroscopy and microscopy.

3. COHERENT ANTI-STOKES RAMAN SCATTERING WITH TIME-ORDERED CHIRPED PULSES

In this section, we consider one of the possible schemes of high-resolution coherent four-photon spectroscopy with chirped pulses used for the Raman excitation of a nonlinear medium. In this scheme, the detuning of the instantaneous frequency difference of chirped pump pulses from the frequency of the Raman resonance is a linear function of the delay time between the pump pulses (Fig. 1). The spectrum of nonlinear susceptibility is then accessed by measuring the intensity of the CARS signal as a function of the delay time between the pump pulses.

Suppose that pump pulses with frequencies ω_1 and ω_2 are linearly chirped and have equal constant chirps (Fig. 1), while the third (probe) pulse is transform-limited. Then, neglecting group-velocity dispersion, we can represent the amplitudes of the pump pulses as

$$A_1(\theta, z) = B_1(\theta)\exp(-i\alpha\theta^2), \tag{10}$$

$$A_2(\theta, z) = B_2(\theta - \tau)\exp[-i\alpha(\theta - \tau)^2], \tag{11}$$

$$A_3(\theta, z) = B_3(\theta), \tag{12}$$

where $\theta = t - z/v_j$ is the retarded time, B_j is the envelope of the jth pulse ($j = 1, 2, 3$), α is the chirp, and τ is the delay time between the first and second pulses.

We need to assume in our analysis that only the third pulse [Eq. (12)] is short. The durations of the pulses defined by Eqs. (10) and (11) are assumed to be large as compared with the response time of the nonlinear polarization of the medium. The spectra of these two pulses, however, can (and must) be sufficiently broad due to their chirp. In experiments, such pulses are routinely produced by chirping ultrashort laser pulses. The pulses described by Eqs. (10) and (11) can be also compressed to very short durations through the compensation of their chirp.

Since the instantaneous frequency difference of the linearly chirped pulses (10) and (11) is a linear function of τ,

$$\Delta\bar{\omega} = \bar{\omega}_1 - \bar{\omega}_2 = \omega_1 - \omega_2 + 2\alpha\tau,$$

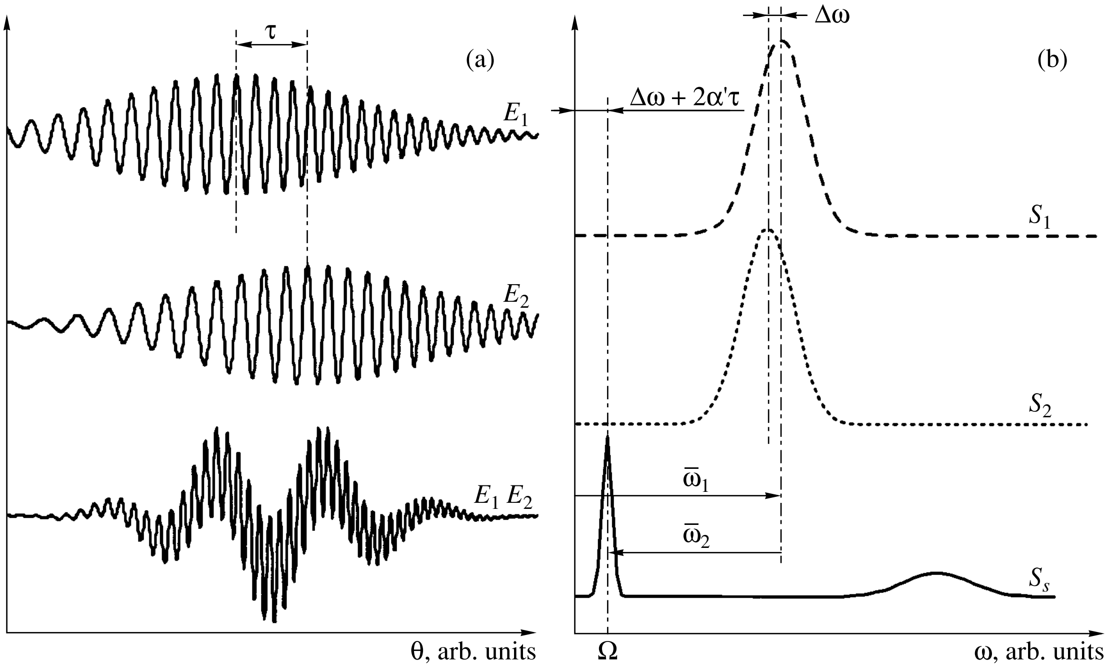

Fig. 3. Probing Raman modes with chirped pump pulses: (a) electric fields E_1 and E_2 of the first and second pulses and their product E_1E_2 as functions of the retarded time θ and (b) spectra $S_1 = \left|\int E_1 e^{i\omega\theta} d\theta\right|^2$ and $S_2 = \left|\int E_2 e^{i\omega\theta} d\theta\right|^2$ of the first and second pulses and the spectrum $S_s = \left|\int E_1 E_2 e^{i\omega\theta} d\theta\right|^2$ of the product of the pulse fields. For linearly chirped pulses with equal chirp rates, the product of the fields E_1E_2 involves a narrow spectral component with a frequency Ω depending on the delay time between the pulses τ and the width controlled by the bandwidth of the product of the pump-pulse envelopes.

it can be tuned around the Raman resonance under study by varying the delay time between the pump pulses (Fig. 1). In the frequency domain, this strategy of high-resolution spectroscopy can be understood in the following way. For linearly chirped pump pulses with equal chirps, the product of the fields E_1E_2 features a narrow spectral component (Fig. 3) whose frequency depends on the delay time between the pump pulses and whose bandwidth is controlled by the bandwidth of the product $B_1 B_2^*$ of pump pulse envelopes.

Using Eqs. (1), (2), (5), and (10)–(12) in the retarded frame of reference θ, *z*, we derive the following equation for the amplitude of the CARS signal:

$$\frac{\partial A_4(\theta, z)}{\partial z} = \frac{2i\pi\omega_4^3}{k_4c^2} \times \int_0^\infty \chi(t_1, z) B_1(\theta - t_1) B_2^*(\theta - t_1 - \tau) \quad (13)$$

$$\times \exp(i\Delta\bar{\omega}t_1)dt_1 B_3(\theta)\exp(i\alpha\tau^2 - i\Delta kz),$$

where $\Delta k = k_4 - k_1 + k_2 - k_3$ is the phase mismatch and $\omega_4 = \omega_1 - \omega_2 + \omega_3 + 2\alpha\tau$ is the central frequency of the signal.

If the envelopes of the pump pulses do not vary significantly within the characteristic decay time *T* of the nonlinear polarization, we can set $B_1(\theta - t_1) \approx B_1(\theta)$ and $B_2(\theta - \tau - t_1) \approx B_2(\theta - \tau)$ for $t_1 \le T$. With these assumptions, Eq. (13) can be rewritten as

$$\frac{\partial A_4(\theta, z)}{\partial z} = \frac{2i\pi\omega_4^2}{k_4c^2}\chi'(\Delta\bar{\omega}, z)B_1(\theta)B_2^*(\theta - \tau)B_3(\theta) \quad (14)$$

$$\times \exp(i\alpha\tau^2 - i\Delta kz),$$

where

$$\chi'(\omega, z) = \int_0^\infty \chi(t, z)\exp(i\omega t)dt$$

is the Fourier transform of the cubic susceptibility.

For a spatially uniform medium, where the nonlinear susceptibility is independent of *z*, the integration of Eq. (14) yields

$$A_4(\theta, \tau, z) = \frac{2i\pi\omega_4^2}{k_4c^2}\chi'(\Delta\bar{\omega})B_1(\theta)B_2^*(\theta - \tau)B_3(\theta) \quad (15)$$

$$\times \exp(i\alpha\tau^2)\frac{\exp(-i\Delta kz) - 1}{-i\Delta k}.$$

Thus, the amplitude of the CARS signal measured as a function of the delay time between linearly chirped pump pulses with equal chirps recovers the spectral dependence of the nonlinear-optical cubic susceptibility.

In the regime of phase matching, $\Delta k = 0$, Eq. (15) can be reduced to

$$A_4(\theta, \tau, z) = \frac{2i\pi\omega_4^2}{k_4c^2}\chi'(\Delta\bar{\omega})B_1(\theta)B_2^*(\theta-\tau)B_3(\theta) \times \exp(i\alpha\tau^2)z^2. \tag{16}$$

The power of the CARS signal is then given by

$$W(\tau) \propto \left|\int_{-\infty}^{\infty} A_4(\theta, \tau, z)d\theta\right|^2. \tag{17}$$

For pulses with Gaussian envelopes, $B_j(\theta) = B_{0j}\exp(-\theta^2/\tau_j^2)$, $j = 1, 2, 3$, integration in Eq. (17) for the case of two-color CARS with $\omega_1 = \omega_2$ and $\tau_1 = \tau_2$ gives

$$W(\tau) \propto |\chi'(\Delta\bar{\omega})|^2\exp\left(-\frac{2\tau^2}{\tau_1^2+2\tau_2^2}\right). \tag{18}$$

Consider now in greater detail a methodologically important case of a homogeneously broadened Raman resonance:

$$\chi(t, z) = \chi_0\exp(-i\Omega t - t/T), \tag{19}$$

where χ_0 is a constant and Ω is the frequency of the Raman resonance. The parameter T in this case is understood as the transverse relaxation time, which controls the spectral line width.

The Fourier transform of the nonlinear cubic susceptibility (19) yields a Lorentzian spectral contour:

$$\chi'(\omega) = \frac{T}{i(\Omega-\omega)T+1}. \tag{20}$$

Expression (18) can then be rewritten as

$$W(\tau) \propto \frac{1}{(\Omega-\omega_1+\omega_2-2\alpha\tau)^2+T^{-2}} \times \exp\left(-\frac{\tau^2}{\tau_1^2+2\tau_2^2}\right). \tag{21}$$

The considered technique thus allows the frequency dependence of the nonlinear-optical susceptibility to be measured with a high spectral resolution around a homogeneously broadened Raman resonance.

4. SPECTRAL RESOLUTION OF CHIRPED-PULSE FOUR-PHOTON TECHNIQUES

In this section, we focus on the spectral resolution of chirped-pulse CARS spectroscopy and microscopy. These techniques have been gaining powerful momentum over the past few years due to the development of novel light sources based on PCFs [4–6], providing high efficiencies of nonlinear-optical frequency conversion of ultrashort laser pulses and allowing the generation of field waveforms with a controlled chirp, ideally suited for spectroscopic and microscopic applications [6, 27, 28].

We start by using Eqs. (5)–(9) for calculating the temporal envelope of the CARS signal generated by light pulses (10)–(12) (Fig. 1). The driving force for the considered regime of nonlinear-optical interaction can be represented as

$$F(t-\theta) = F_0f(t-\theta) \times \exp[2i\alpha\tau(t-\theta) - i\alpha\tau^2]\exp[i\omega(t-\theta)], \tag{22}$$

where $f(t)$ is the temporal envelope of the driving force (determined by the shortest among the pump pulses) and τ is the delay time between the chirped pump pulses.

We assume first that the variation of the temporal envelope of the driving force can be neglected on the time scale of the nonlinear response time T (regime of long pulses). Then, substituting Eq. (22) into Eq. (7), we find that

$$Q(t) = F_0\exp(i\omega t)\exp(-i\alpha\tau^2) \times \exp(2i\alpha\tau t)f(t)\vartheta(\omega+2\alpha\tau). \tag{23}$$

The temporal profile of the CARS signal measured as a function of the delay time τ in this regime recovers the spectrum of the nonlinear-optical susceptibility:

$$W_{\mathrm{CARS}}(\tau, \eta) \propto |\vartheta(\omega+2\alpha\tau)|^2 \times \left|\int_{-\infty}^{\infty} E_3(t-\eta)f(t)\exp[i(\omega+2\alpha\tau)t]dt\right|^2. \tag{24}$$

To analyze the influence of finite pump-pulse widths on the spectral resolution of this CARS technique, we assume that the laser pulse has a rectangular shape with a duration τ_1, while the nonlinear response has a standard form,

$$\chi(\theta) = \chi_0\exp\left(-\frac{\theta}{T}\right)\exp(i\omega_0\theta), \tag{25}$$

corresponding to a Lorentzian spectral profile with the central frequency ω_0 and the line width $\gamma = 1/T$.

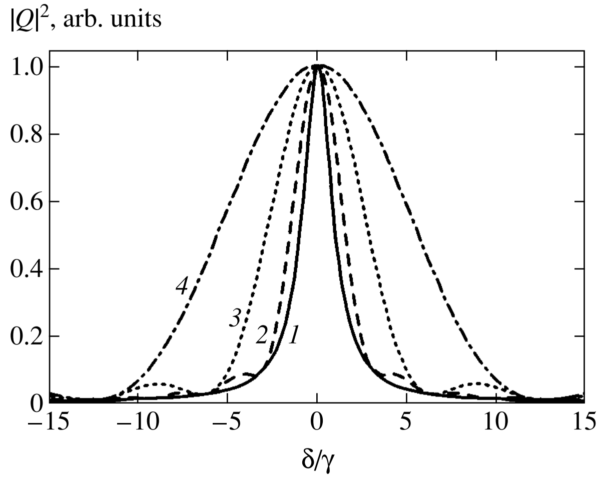

Fig. 4. Lorentzian spectral profile with a width γ (*1*) and the nonlinear response $|Q|^2$ (*2–4*) calculated with Eq. (26) as a function of the detuning $\delta = \omega_0 - \omega - 2\alpha\tau$ of the instantaneous frequency difference of the pump fields from the frequency of the Raman resonance normalized to the line width γ; $\gamma\tau_1 = 2$ (*2*), 1 (*3*), and 0.5 (*4*).

Integration in Eq. (7) yields

$$Q(t, \tau_1) \propto \frac{F_0 \exp(i\omega t)\exp[i\alpha\tau(2t-\tau)]}{\gamma - i\delta} \times \{1 - \exp[(-\gamma + i\delta)\tau_1]\}, \tag{26}$$

where $\delta = \omega_0 - \omega - 2\alpha\tau$.

The limiting transition $\tau_1 \longrightarrow \infty$ recovers Eq. (23) with a Lorentzian spectral profile:

$$|Q(t, \tau_1 \longrightarrow \infty)|^2 \propto \frac{1}{\gamma^2 + (\omega_0 - \omega - 2\alpha\tau)^2}. \tag{27}$$

In the general case, a finite pulse width limits the spectral resolution. Figure 4 compares a Lorentzian spectral profile with a width γ (solid line *1*) with the nonlinear response $|Q|^2$ (curves *2–4*) calculated with the use of Eq. (26) as a function of the detuning $\delta = \omega_0 - \omega - 2\alpha\tau$ of the instantaneous frequency difference of the pump fields from the Raman resonance normalized to the line width γ. As can be seen from this figure, the spectral resolution of CARS lowers as the pump-pulse duration τ_1 becomes smaller.

In the limiting case of $\gamma \longrightarrow 0$, we arrive at

$$|Q(t, \tau_1)| \propto \frac{2\left|\sin\left[(\omega_0 - \omega - 2\alpha\tau)\frac{\tau_1}{2}\right]\right|}{|\omega_0 - \omega - 2\alpha\tau|}. \tag{28}$$

Expression (28) gives the following estimate for the spectral resolution of the considered method (see also Fig. 4):

$$\delta\omega_{\mathrm{CARS}} \approx 1/\tau_1. \tag{29}$$

To derive a more general expression for the spectral resolution of chirped-pulse CARS, we use the frequency-domain representation for the nonlinear polarization $P(\omega_4)$ induced in a medium with a cubic nonlinearity at the anti-Stokes frequency $\omega_4 = \omega_1 - \omega_2 + \omega_3$ (Fig. 2):

$$P(\omega_4) \propto \int_{-\infty}^{\infty}\int_{-\infty}^{\infty} g(\Omega - \omega'')E_1(\omega')E_2^*(\omega' - \omega'') \times E_3(\omega_4 - \omega'')d\omega' d\omega'', \tag{30}$$

where $E_i(\omega)$ are the Fourier transforms of the laser fields ($i = 1, 2, 3$) and $g(\omega - \Omega)$ is the spectral line profile corresponding to the probed Raman mode with the frequency Ω (Fig. 2).

For a Raman mode with an infinitely narrow spectral line, $g(\omega - \Omega) = g_0\delta(\omega - \Omega)$, we find

$$P(\omega_4) \propto E_3(\omega_4 - \Omega)Q(\omega_1 - \omega_2 - \Omega), \tag{31}$$

$$Q(\omega_1 - \omega_2 - \Omega) = \int_{-\infty}^{\infty} E_1(\omega')E_2^*(\omega' - \Omega)d\omega'. \tag{32}$$

We search now for the spectral width of the nonlinear polarization (31), which is the measure of the spectral resolution of chirped-pulse CARS. To this end, we assume that one of the pump pulses is transform-limited, while the phase modulation of the second pulse is quadratic in time, corresponding to a linear chirp with a chirp rate α (Fig. 2). For pump fields with Gaussian spectra,

$$E_1(\omega) \propto \tau_1\sqrt{2\pi}\exp\left[-\frac{\tau_1^2(\omega - \omega_1)^2}{2}\right], \tag{33}$$

$$E_2(\omega) \propto \tau_2\sqrt{\frac{2\pi}{1 - 2i\alpha\tau_2^2}}\exp\left[-\frac{\tau_2^2(\omega - \omega_2)^2}{2(1 - 2i\alpha\tau_2^2)}\right], \tag{34}$$

integration in Eq. (32) gives

$$|Q(\omega_1 - \omega_2 - \Omega)| \propto \exp\left[-\frac{(\omega_1 - \omega_2 - \Omega)^2}{2\left(\tau_1^{-2} + \tau_2^{-2} + \dfrac{4\alpha^2}{\tau_1^{-2} + \tau_2^{-2}}\right)}\right]. \tag{35}$$

Using Eq. (35), we can find the spectral resolution of the method:

$$\delta\omega_{\mathrm{CARS}} = \left(\frac{1}{\tau_1^2} + \frac{1}{\tau_2^2} + \frac{4\alpha^2}{\tau_1^{-2} + \tau_2^{-2}}\right)^{1/2}. \tag{36}$$

As can be seen from Eq. (36), the spectral resolution of chirped-pulse CARS spectroscopy and microscopy is controlled by the durations and the chirp of the pump pulses (Fig. 5). With $\tau_1 \ll \tau_2$, Eq. (36) can be reduced to

$$\delta\omega_{\mathrm{CARS}} \approx \left(\frac{1}{\tau_1^2} + 4\alpha^2\tau_1^2\right)^{1/2}. \qquad (37)$$

In the case of $\tau_1^{-2} \ll 4\alpha^2\tau_1^2$, the spectral resolution of the CARS technique,

$$\delta\omega_{\mathrm{CARS}} \approx 2|\alpha|\tau_1 \qquad (38)$$

is determined by the deviation of the instantaneous frequency difference of the pump fields within the shortest of the laser pulses (Fig. 2).

We now interpret Eqs. (36)–(38) in terms of the Heisenberg uncertainty principle [44]. To this end, we represent Eq. (36) as

$$\delta\omega_{\mathrm{CARS}} = \left(\frac{1}{\tau_{\mathrm{eff}}^2} + 4\alpha^2\tau_{\mathrm{eff}}^2\right)^{1/2}, \qquad (39)$$

where

$$\tau_{\mathrm{eff}} = \left(\frac{1}{\tau_1^2} + \frac{1}{\tau_2^2}\right)^{-1/2} \qquad (40)$$

is the effective time of measurement made on the system. According to the Heisenberg uncertainty principle, the lower bound for the uncertainty of energy measurement, δE_H, is related to the maximum time Δt of measurements performed on a system by the expression $\delta E_H \Delta_t = \hbar$, where $\hbar$ is the Planck constant. In view of Eq. (39), we write

$$\delta\omega_{\mathrm{CARS}}\tau_{\mathrm{eff}} = (1 + 4\alpha^2\tau_{\mathrm{eff}}^4)^{1/2}. \qquad (41)$$

Setting $\Delta t = \tau_{\mathrm{eff}}$, we arrive at

$$\delta\omega_{\mathrm{CARS}} = \frac{1}{\tau_{\mathrm{eff}}}(1 + 4\alpha^2\tau_{\mathrm{eff}}^4)^{1/2} \geq \frac{\delta E_H}{\hbar}. \qquad (42)$$

As can be seen from relations of Eq. (42), the uncertainty of spectral measurements in CARS spectroscopy and microscopy using linearly chirped laser pulses (Fig. 5) always exceeds the lower bound dictated by the uncertainty principle. In the considered regime, the lower bound of uncertainty in spectral measurements is achieved with $\alpha = 0$ (the solid line in Fig. 5).

5. PULSES WITH A PERIODIC MODULATION OF PHASE AND THE LIMITING SPECTRAL RESOLUTION OF CARS

In this section, we will show that the lower bound of uncertainty in CARS spectral measurements dictated by the uncertainty principle can be achieved by using pump pulses with a periodic modulation of phase. Consider the pump field of the following form:

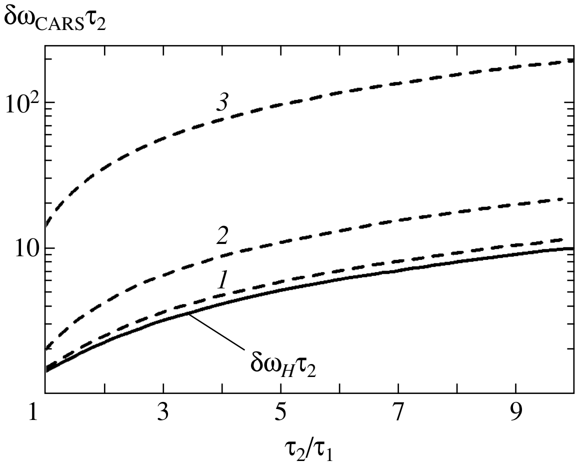

Fig. 5. Parameter $\delta\omega_{\mathrm{CARS}}\tau_2$ as a function of the ratio of pump-pulse durations τ_2/τ_1 for $\alpha\tau_1^2 = 0.3$ (*1*), 1 (*2*), and 10 (*3*). The solid curve shows the product $\delta\omega_H\tau_2$ corresponding to the lower bound of spectral uncertainty dictated by the uncertainty principle.

$$E(t) = B(t)\exp[i\Phi(t)]\exp(i\omega_0 t), \qquad (43)$$

where $\Phi(t)$ is a periodic function. In view of the periodicity of its argument, the phase factor $\exp[i\Phi(t)]$ can be expanded as a Fourier series:

$$\exp[i\Phi(t)] = \sum_n q_n \exp(in\sigma t), \qquad (44)$$

where σ is the period of the function $\Phi(t)$ and q_n are the expansion coefficients in the Fourier series.

In the case of a Gaussian envelope in (43),

$$B(t) = B_0\exp\left(-\frac{t^2}{2\tau_1^2}\right), \qquad (45)$$

we arrive at the following expression for the spectrum of the pump field:

$$E(\omega) \propto \sum_n q_n \exp\left[-\frac{(\omega - \omega_0 - n\sigma)^2\tau_1^2}{2}\right]. \qquad (46)$$

We now assume that measurements are performed with a single broadband pump pulse, which serves as a source of photons for the resonant excitation of Raman-active modes. Such a technique of femtosecond CARS spectroscopy is widely used for the investigation of ultrafast processes in molecular systems and dynamics of vibrational wave packets [38, 45–48]. Special phase profiles of ultrashort pulses, as shown in [49, 50], can

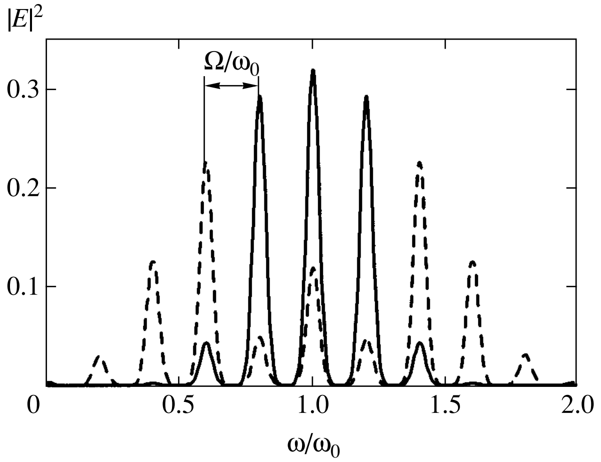

Fig. 6. The spectrum of a pulse with a harmonic modulation of the phase (48) for $(\omega_0\tau_1)^2 = 1000$, $\sigma/\omega_0 = 0.2$, and $a = 1.3$ (solid curve) and 3.3 (dashed curve).

suppress a coherent background in CARS spectra, thus improving the selectivity of CARS spectroscopy.

Integration in Eq. (32) then leads to

$$|Q(\sigma)| \propto \sum_{n,\,m} q_n q_m \exp\left\{-\frac{[(n-m)\sigma - \Omega]^2\tau_1^2}{4}\right\}. \tag{47}$$

Ultrashort pulses with a periodic modulation of phase can be synthesized in experiments with the use of spatial light modulators [51–53]. In particular, a harmonic phase mask [54] gives laser pulses of the following form:

$$E(t) = B(t)\exp[i(a\sin\sigma t + \omega_0 t)], \tag{48}$$

where a and σ are the amplitude and the frequency of phase modulation.

The spectrum of such pulses is given by

$$E(\omega) \propto \sum_n J_n(a)\exp\left[-\frac{(\omega - \omega_0 - n\sigma)^2\tau_1^2}{2}\right], \tag{49}$$

where $J_n(x)$ is the nth-order Bessel function.

Performing integration in Eq. (32) for the spectrum of the pump field (49), we derive

$$|Q(\sigma)| \propto \sum_{n,\,m} J_n(a)J_m(a) \times \exp\left\{-\frac{[(n-m)\sigma - \Omega]^2\tau_1^2}{4}\right\}. \tag{50}$$

The spectrum of the pump pulse with a periodic modulation of phase, as can be seen from Eqs. (46) and (49), has the form of a frequency comb consisting of equidistant components separated by the spectral interval σ (Fig. 6). The central frequency of the nth spectral component is equal to $\omega_0 + n\sigma$. The bandwidth of each spectral component in the frequency comb is controlled by the pulse duration τ_1. We assume that

$$\tau_1 > \sigma^{-1}. \tag{51}$$

When this inequality is satisfied, the spectral interval between the components of the frequency comb is larger than the bandwidth of each component (Fig. 6). The frequency comb can be then employed as a ruler for spectral measurements (see also [22]). In the limiting case of $\tau_1 \longrightarrow \infty$, the spectrum of the pump pulse has the form of a frequency comb consisting of infinitely narrow equidistant spectral components:

$$E(\omega) \propto \sum_n q_n \delta(\omega - \omega_0 - n\sigma). \tag{52}$$

The equality

$$(n-m)\sigma = \Omega \tag{53}$$

expresses the condition of a resonant excitation of Raman modes with the frequency Ω. The spectral resolution of the CARS technique, as can be seen from Eqs. (47) and (50), is then controlled by the inverse of the pump pulse duration. Comparison of Eqs. (35) and (47) shows that the spectral resolution of CARS spectroscopy and microscopy based on the use of a single pump pulse with a periodic modulation of phase coincides with the lower-bound limiting spectral resolution $\delta E_H \hbar^{-1}$ for the standard CARS technique, which involves two pump pulses with the difference of their central frequencies equal to $\omega_1 - \omega_2 \approx \Omega$.

The condition of Eq. (53) also provides the maximum selectivity of Raman-mode excitation with a broadband field of an ultrashort laser pulse. All the energy of the pump field under conditions of Eqs. (52) and (53) is concentrated (Fig. 6) in spectral components of laser radiation resonant to Raman modes of the system under study (see also [55]).

6. TEMPORAL RESOLUTION OF CHIRPED-PULSE CARS

In this section, we examine the temporal resolution of chirped-pulse CARS spectroscopy and microscopy. Assuming that chirped pump pulses employed in the CARS scheme have Gaussian envelopes, we represent the driving force in Eq. (7) as

$$F(t-\theta) = F_0\exp\left[-\frac{(t-\theta)^2}{\tau_1^2}\right] \times \exp[i\alpha(t-\theta)^2]\exp[i\omega(t-\theta)], \tag{54}$$

where τ_1 is the characteristic duration of the pump pulses (or the minimum among the pulse durations in the case of pump pulses with radically different pulse widths), and $\omega = \omega_1 - \omega_2$ is the difference of the central frequencies of the pump fields.

To determine the temporal resolution of the CARS technique, we consider a medium with an instantaneous nonlinear-optical response and set $\chi(\theta) = h_0\delta(\theta)$. Integration in Eqs. (6) and (7) then leads to the following dependence of the CARS signal on the delay time η of the probe laser pulse with a characteristic pulse duration τ_3:

$$W_{\mathrm{CARS}}(\eta, \alpha) \propto W_0 \exp\left\{-\frac{\eta^2}{\xi^2(\alpha, \tau_1, \tau_3)}\right\}, \qquad (55)$$

where

$$\xi^2(\alpha, \tau_1, \tau_3) = \frac{\tau_3^2[(\tau_1^2+\tau_3^2)^2 + \alpha^2\tau_1^4\tau_3^4]}{\tau_1^2(\tau_1^2+\tau_3^2) - (\tau_1^2+\tau_3^2)^2 - \alpha^2\tau_1^4\tau_3^4}. \qquad (56)$$

Figure 7 presents the ratio $\xi^2(\alpha, \tau_1, \tau_3)/\tau_3^2$, used as a measure of the temporal resolution of the CARS technique, calculated with Eq. (56) as a function of the chirp parameter of the pump pulse for $\tau_3/\tau_1 = 0.3$ (curve *1*) and 0.1 (curve *2*). In a particular case of transform-limited pump pulses, $\alpha = 0$, Eq. (56) yields the following physically instructive relationship:

$$W_{\mathrm{CARS}}(\eta, \alpha = 0) \propto W_0 \exp\left(-\frac{\eta^2}{\tau_1^2 + \tau_3^2}\right). \qquad (57)$$

The temporal resolution of the CARS technique in this regime (dashed lines *4* and *5* in Fig. 7) is given by the intuitively clear expression

$$\delta t \approx (\tau_1^2 + \tau_3^2)^{1/2}. \qquad (58)$$

The case of large α corresponds to broadband chirped pump pulses. The temporal resolution of CARS in this situation is determined by the duration of the probe pulse (dashed line *3* in Fig. 7):

$$W_{\mathrm{CARS}}(\eta, |\alpha|\tau_1^2\tau_3^2 > \tau_1^2, \tau_3^2) \propto W_0 \exp\left(-\frac{\eta^2}{\tau_3^2}\right). \qquad (59)$$

Thus, the temporal and spectral resolution of CARS measurements performed with an ultrashort probe pulse ($\tau_3 \ll \tau_1$) can be smoothly tuned by varying the chirp parameter (Fig. 7). The temporal resolution can range from $\delta t \approx (\tau_1^2 + \tau_3^2)^{1/2} \approx \tau_1$ in the regime of small α to $\delta t \approx \tau_3 \ll \tau_1$ in the case of strongly chirped pump pulses. This property of chirped-pulse CARS makes this technique an ideal tool for the spectroscopy and microscopy of ultrafast processes and nonstationary objects in the gas and condensed phases. Of special interest is to extend the methodology of chirped-pulse CARS spectroscopy and microscopy to attosecond metrology and tomography. Analysis presented in this section shows that, to provide a subfemtosecond time resolution in CARS spectroscopy or microscopy, only one of the pulses involved in the nonlinear-optical process has to be attosecond.

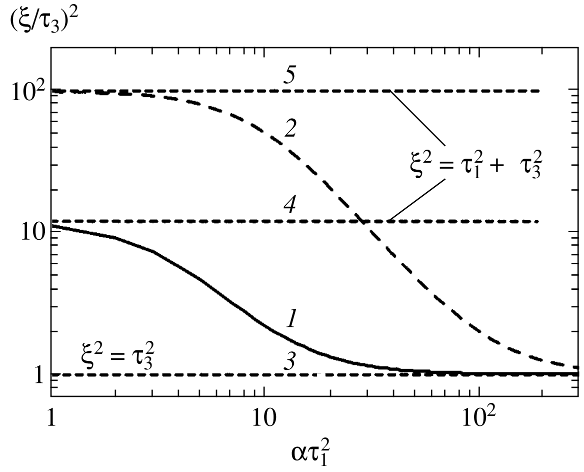

Fig. 7. The ratio $\xi^2(\alpha, \tau_1, \tau_3)/\tau_3^2$, used as a measure of the temporal resolution of the CARS technique, as a function of the chirp parameter of the pump pulse for $\tau_3/\tau_1 = 0.3$ (*1*) and 0.1 (*2*). The horizontal lines show the limiting temporal resolution of the CARS technique corresponding to $\xi^2(\alpha, \tau_1, \tau_3) = \tau_3^2$ (*3*) and $\xi^2(\alpha, \tau_1, \tau_3) = \tau_1^2 + \tau_3^2$ with $\tau_3/\tau_1 = 0.3$ (*4*) and 0.1 (*5*).

7. CONCLUSIONS

We have shown that ultrashort light pulses with controlled chirp offer new solutions for coherent nonlinear spectroscopy and microscopy. Pulses with a quadratic modulation of phase in time (corresponding to a linear chirp) define a simple one-to-one mapping between the delay time and the detuning of the frequency difference of the pump fields from the frequency of the Raman mode under study. We found analytical solutions for the temporal envelope of the CARS signal produced by chirped pulses and examined the ways of using chirped pulses for high-resolution nonlinear spectroscopy and microscopy, as well as for studying ultrafast processes in the gas and condensed phases. Our analysis shows that the temporal resolution of CARS measurements performed with an ultrashort probe pulse can be smoothly tuned by varying the chirp parameter. The upper and lower boundaries of this resolution tunability interval are controlled by the durations of the pump and probe pulses. This property of chirped-pulse CARS makes this technique an ideal tool for the spectroscopy and microscopy of ultrafast processes and nonstationary objects in the gas and condensed phases, including measurements on the subfemtosecond time scale. The spectral resolution of chirped-pulse CARS spectroscopy and microscopy is determined by the durations of the pump pulses and the chirp parameter. The uncertainty of spectral measurements for CARS techniques using linearly chirped laser pulses always exceeds the lower bound dictated by the uncertainty principle. This lower bound of uncertainty in CARS spectral measurements can be achieved by using pulses with a periodic phase modulation.

ACKNOWLEDGMENTS

Illuminating and interesting discussions with A.N. Naumov are gratefully acknowledged.

This study was supported in part by the President of the Russian Federation grant MD-42.2003.02, the Russian Foundation for Basic Research (project nos. 03-02-16929, 03-02-20002-BNTS, 04-02-39002-GFEN2004, and 04-02-81036-Bel2004), and INTAS (project nos. 03-51-5037 and 03-51-5288). The research described in this publication was made possible in part by award no. RP2-2558 of the US Civilian Research and Development Foundation for the Independent States of the Former Soviet Union (CRDF). This material is also based upon work supported by the European Research Office of the US Army under Contract no. 62558-04-P-6043.

REFERENCES

1. P. M. Paul, E. S. Toma, P. Breger, *et al.*, Science **292**, 1689 (2001).
2. M. Drescher, M. Hentschel, R. Kienberger, *et al.*, Science **291**, 1923 (2001).
3. M. Hentschel, R. Kienberger, Ch. Spielmann, *et al.*, Nature **414**, 509 (2001).
4. R. F. Cregan, B. J. Mangan, J. C. Knight, *et al.*, Science **285**, 1537 (1999).
5. P. St. J. Russell, Science **299**, 358 (2003).
6. A. M. Zheltikov, *Optics of Microstructured Fibers* (Nauka, Moscow, 2004) [in Russian].
7. A. B. Fedotov, A. M. Zheltikov, A. P. Tarasevitch, and D. von der Linde, Appl. Phys. B **73**, 181 (2001).
8. A. M. Zheltikov, Usp. Fiz. Nauk **174**, 73 (2004) [Phys. Usp. **47**, 69 (2004)].
9. W. H. Reeves, D. V. Skryabin, F. Biancalana, *et al.*, Nature **424**, 511 (2003).
10. D. V. Skryabin, F. Luan, J. C. Knight, and P. St. J. Russell, Science **301**, 1705 (2003).
11. *Nonlinear Optics of Photonic Crystals*, Feature issue of J. Opt. Soc. Am. B **19** (9) (2002), Ed. by C. M. Bowden and A. M. Zheltikov.
12. *Supercontinuum Generation*, Special issue of Appl. Phys. B **77** (2/3) (2003), Ed. by A. M. Zheltikov.
13. D. A. Akimov, E. E. Serebryannikov, A. M. Zheltikov, *et al.*, Opt. Lett. **28**, 1948 (2003).
14. S. O. Konorov and A. M. Zheltikov, Opt. Express **11**, 2440 (2003).
15. S. O. Konorov, E. E. Serebryannikov, A. M. Zheltikov, *et al.*, Opt. Lett. **29**, 1545 (2004).
16. M. Drescher, M. Hentschel, R. Kienberger, *et al.*, Nature **419**, 803 (2002).
17. H. Niikura, F. Legare, R. Hasbani, *et al.*, Nature **421**, 826 (2003).
18. H. Niikura, F. Legare, R. Hasbani, *et al.*, Nature **417**, 917 (2002).
19. R. Kienberger, E. Goulielmakis, M. Uiberacker, *et al.*, Nature **427**, 817 (2004).
20. D. J. Jones, S. A. Diddams, J. K. Ranka, *et al.*, Science **288**, 635 (2000).
21. R. Holzwarth, T. Udem, T. W. Hänsch, *et al.*, Phys. Rev. Lett. **85**, 2264 (2000).
22. Th. Udem, R. Holzwarth, and T. W. Hänsch, Nature **416**, 233 (2002).
23. S. O. Konorov, D. A. Sidorov-Biryukov, I. Bugar, *et al.*, Appl. Phys. B **78**, 547 (2004).
24. A. B. Fedotov, Ping Zhou, A. P. Tarasevitch, *et al.*, J. Raman Spectrosc. **33**, 888 (2002).
25. I. Hartl, X. D. Li, C. Chudoba, *et al.*, Opt. Lett. **26**, 608 (2001).
26. A. Baltuska, T. Fuji, and T. Kobayashi, Opt. Lett. **27**, 1241 (2002).
27. S. O. Konorov, D. A. Akimov, A. A. Ivanov, *et al.*, Zh. Éksp. Teor. Fiz. **126**, 26 (2004) [JETP **99**, 19 (2004)].
28. S. O. Konorov, D. A. Akimov, E. E. Serebryannikov, *et al.*, Phys. Rev. E **70**, 057601 (2004).
29. H. N. Paulsen, K. M. Hilligse, J. Thogersen, *et al.*, Opt. Lett. **28**, 1123 (2003).
30. A. Zumbusch, G. R. Holtom, and X. Sunney Xie, Phys. Rev. Lett. **82**, 4142 (1999).
31. E. T. J. Nibbering, D. A. Wiersma, and K. Duppen, Phys. Rev. Lett. **68**, 514 (1992).
32. W. S. Warren, H. Rabitz, and M. Dahleh, Science **259**, 1581 (1993).
33. B. Kohler, V. V. Yakovlev, J. Che, *et al.*, Phys. Rev. Lett. **74**, 3360 (1995).
34. T. Lang and M. Motzkus, J. Opt. Soc. Am. B **19**, 340 (2002).
35. C. J. Bardeen, Q. Wang, and C. V. Shank, Phys. Rev. Lett. **75**, 3410 (1995).
36. A. Assion, T. Baumert, M. Bergt, *et al.*, Science **282**, 919 (1998).
37. J. L. Herek, W. Wohlleben, R. J. Cogdell, *et al.*, Nature **417**, 533 (2002).
38. D. Zeidler, S. Frey, W. Wohlleben, *et al.*, J. Chem. Phys. **116**, 5231 (2002).
39. S. O. Konorov, D. A. Sidorov-Biryukov, I. Bugar, *et al.*, Chem. Phys. Lett. **381**, 572 (2003).

40. A. M. Zheltikov and A. N. Naumov, Quantum Electron. **30**, 606 (2000); A. N. Naumov and A. M. Zheltikov, J. Raman Spectrosc. **32**, 960 (2001).
41. A. N. Naumov and A. M. Zheltikov, Appl. Phys. B **77**, 369 (2003).
42. Y. R. Shen, *The Principles of Nonlinear Optics* (Wiley, New York, 1984; Nauka, Moscow, 1989).
43. P. N. Butcher and D. Cotter, *The Elements of Nonlinear Optics* (Cambridge Univ. Press, Cambridge, 1991).
44. W. Heisenberg, Z. Phys. **43**, 172 (1927).
45. *Femtosecond Coherent Raman Spectroscopy,* Special Issue of the J. Raman Spectrosc. **31** (1/2) (2000), Ed. by W. Kiefer.
46. M. Schmitt, G. Knopp, A. Materny, and W. Kiefer, J. Phys. Chem. A **102**, 4059 (1998).
47. A. Materny, T. Chen, M. Schmitt, *et al.*, Appl. Phys. B **71**, 299 (2000).
48. T. Hornung, R. Meier, and M. Motzkus, Chem. Phys. Lett. **326**, 445 (2000).
49. N. Dudovich, D. Oron, and Y. Silberberg, Nature **418**, 512 (2002).
50. D. Oron, N. Dudovich, D. Yelin, and Y. Silberberg, Phys. Rev. A **65**, 043408 (2002).
51. A. M. Weiner, D. E. Leaird, J. S. Patel, and J. R. Wullert, Opt. Lett. **15**, 326 (1990).
52. C. W. Hillegas, J. X. Tull, D. Goswami, *et al.*, Opt. Lett. **19**, 737 (1994).
53. A. M. Weiner, Prog. Quantum Electron. **19**, 161 (1995).
54. T. Hornung, R. Meier, D. Zeidler, *et al.*, Appl. Phys. B **71**, 277 (2000).
55. A. M. Zheltikov, J. Raman Spectrosc. **33**, 112 (2002).

Translated by A. Zheltikov

Journal of Experimental and Theoretical Physics, Vol. 100, No. 5, 2005, pp. 844–856.
Translated from Zhurnal Éksperimental'noĭ i Teoreticheskoĭ Fiziki, Vol. 127, No. 5, 2005, pp. 957–972.
Original Russian Text Copyright © 2005 by Ivanova, Ivanov.

ATOMS, MOLECULES, OPTICS

A Superpowerful Source of Far-Ultraviolet Monochromatic Radiation

E. P. Ivanova[a] **and A. L. Ivanov**[b]
[a]Institute of Spectroscopy, Russian Academy of Sciences, Troitsk, Moscow oblast, 142190 Russia
[b]Avesta-Project Limited-Liability Company, Troitsk, Moscow oblast, 142190 Russia
e-mail: eivanova@isan.troitsk.ru

Received September 29, 2004

Abstract—In several independent experiments investigating the interaction between the optical field of an intense laser pulse and a xenon cluster beam, we recorded an anomalously high quantum yield of the plasma radiation in the region 10–15 nm. In several cases, the conversion efficiency into the hemisphere reached 10% of the pumping pulse energy. The nature of this phenomenon has not yet been adequately explained. A high conversion efficiency is shown to be possible when producing a plasma with optimal parameters for the amplification of spontaneous radiation on Ni-like xenon transitions to be generated. In a collisional–radiative model, we performed detailed atomic–kinetic calculations of the gains and radiation spectra on the transitions with $\lambda \approx 4$, 10, and 11.3 nm and in the region 13–13.9 nm. For each transition, we determined the time dependences of the gains on plasma parameters. The theoretical and experimental values of the optimal plasma parameters and energy yields of the radiation are in close agreement. Using a theoretical model, we propose possible plasma pumping schemes to achieve the maximum yield of the intense, narrowly beamed soft X-ray radiation. At a pumping pulse repetition rate of 10^4 Hz, the output power for various Ni-like xenon transitions ranges from 100 to 5×10^3 W. *© 2005 Pleiades Publishing, Inc.*

1. INTRODUCTION

The experiments [1–4] carried out in the mid-1990s showed that the interaction of an intense ultrashort laser pulse with a cluster target could give rise to a plasma whose temperature is several orders of magnitude higher than the temperature of the plasma produced through the interaction of the same source with a gaseous or solid target. Highly charged ions of rare gases with energies above 1 MeV and electrons with energies of several keV were detected in [3, 4]. An almost 100% absorption of the pulse energy is possible during the interaction of a cluster beam with an optical laser field. This is mainly attributable to two factors: the density of the atoms in an individual cluster is comparable in order of magnitude to the density of the solid; there is virtually no reflection of the electromagnetic wave from the surface.

At present, there exist several models that interpret the ionization and decay of cluster targets [5–7]. External ionization, the escape of the produced photoelectrons from the cluster outward, takes place at the beginning of laser-pulse action. During the interaction of the laser pulse with the cluster, the ionized cluster expands and the electrons heat up to a temperature of several keV; the cluster is ionized and decays. As a result, immediately after the termination of an ultrashort laser pulse, the material at the focus of the laser beam is a high-temperature plasma composed of free electrons and multiply charged atomic ions. The charge composition, temperature, density, and radiative properties of the produced plasma depend significantly on how the cluster beam was formed as well as on the laser-pulse parameters and interaction conditions. The results presented in [1–7] can affect profoundly the trends in the physics of intense X-ray and EUV radiation sources.

Reliable methods for producing cluster beams of such rare gases as argon, krypton, and xenon have been developed in the last decade. A conical valve is commonly used. The gas pressure in the valve can vary over a wide range, up to 100 atm. Clusters are formed as a liquefied gas expands from the valve through a 10–400 μm hole into a vacuum chamber. Subsequently, a cluster beam is formed at the exit from the chamber hole, which is usually in the shape of a circle up to several millimeters in diameter. Both the mean size of the forming clusters and the pattern of spatial distribution of their concentration in the interaction region can be varied over a wide range by using various pressures and nozzle designs. The pressure dependences of the cluster sizes in the original chamber were analyzed in [8–10]. Experimental data on the formation of metal cluster beams are also available [5, 11].

At present, the energy distributions of the electrons and ions escaping from plasma are experimentally studied by means of time-of-flight spectroscopy. In these studies, the laser pulse is focused on a more rarefied part of the cluster beam at a distance of several centimeters from the nozzle. Thus, for example, the dependences of the energies of the escaping krypton and xenon ions on the cluster size (10^2–10^5 at. per cluster) as well as on the laser intensity ($I = 10^{14}$–10^{16} W cm^{-2}) and wavelength (780 and 390 nm) were determined in the experiment described in [12]. The mean and maximum ion energies were shown to increase with cluster size up to a certain optimal size. A further increase in the cluster size causes the ion energy to decrease. In this paper, it was also established that the ion and electron energies increase sharply at intensities from $I \approx 6 \times 10^{14}$ W cm^{-2} to $I \approx 10^{15}$ W cm^{-2}; a further increase in the intensity causes the temperature to rise only slightly. The experimental dependences are in good agreement with the numerical calculations of the nanoplasma dynamics, whose model was suggested in [1].

Investigating the spectra and quantum yields of the X-ray and EUV radiation from the plasma produced through the interaction of a laser pulse with a cluster is another direction of research. In these experiments, the laser pulse is focused on the cluster beam in the immediate vicinity of the chamber hole, at a distance of 0–2 mm where the beam density is at a maximum. Intense radiation from the high-temperature plasma produced through the interaction of a femtosecond pulse ($I \sim 10^{16}$–10^{17} W cm^{-2}) with He, Ne, Ar, and Kr clusters (the cluster size is ~100 Å) was detected in [13]. It was established in [13] that the resonant absorption of the laser-pulse energy plays a crucial role in the dynamics of the plasma formation and decay. It was also found that the quantum yield of the cluster plasma radiation is of the same order of magnitude as that for the plasma of a solid target; in this paper, the quantum yield depended significantly on the laser-pulse duration. The energy yield E_{out} of the X-ray radiation from the plasma formed from krypton clusters under the action of a femtosecond pulse ($I \approx 5 \times 10^{17}$ W cm^{-2}) was studied in the experiment described in [10]. The observed spectrum in [10] corresponded to the radiation of krypton ions with a degree of ionization of 24–27. The plasma radiation was isotropic, and E_{out} depended on the laser intensity and the mean cluster size; E_{out} for photons with an energy of 55 keV did not exceed 1.7×10^{-8} in 4π steradians, and E_{out} for photons with an energy of 1.25 keV was an order of magnitude higher.

The large number of parameters that characterize the target + laser pulse system is a fundamental problem of the experimental studies. For a given beam geometry, the main parameters include the mean cluster density in the beam, the mean cluster size and the cluster distribution in size (number of atoms in the cluster), and the gas fraction in the beam; the spatial inhomogeneity of the cluster beam also plays an important role. The characteristics of the emergent radiation are strongly affected by the parameters of the control pulse: its intensity, contrast, duration, wavelength, polarization, and focusing [14, 15]. A theory for the evolution of large atomic clusters when irradiated by a femtosecond laser pulse producing a superatomic field in the cluster was developed in [16, 17]. It is based on the above-barrier successive multiple internal ionization of atomic ions inside the cluster accompanied by the field ionization of external atoms. The ionization through electron–ion collisions was also taken into account in the calculations. As a result, the authors obtained the time dependences of the cluster radius, the electron and ion densities, and temperatures and described the dynamics of the internal and external ionization of a large (~10^6 atoms) xenon cluster irradiated by a laser pulse with a peak intensity of 10^{18} W cm^{-2} and a duration of 50 fs. The electron–cluster or ion–cluster interactions are also of great importance for a high-density cluster beam. An important role of the collisional interaction between free electrons and a cluster was demonstrated in [18]: free electrons are accelerated in the field of positively charged clusters, which contributes to faster cluster destruction.

The spectra and energy yields of the radiation from the plasma produced through the interaction between the optical field of various lasers and a xenon cluster beam were studied in detail at the Tsukuba [19, 20] and Max-Born [21, 22] Universities. In several cases, a 10% conversion of the pumping pulse energy into the plasma radiation in the spectral region 9–15 nm in 2π steradians was recorded. The time-integrated spectra corresponding to the Xe^{9+}–Xe^{29+} radiation were recorded in [19–22]. The most intense lines were observed in the regions $\lambda = 10.3$–10.7, 11.4, and 13–13.8 nm. A Ti-sapphire laser with an intensity of 10^{18} W cm^{-2} and a duration of 50 fs (0.2 J per pulse) was used in [21]; the radiation with $\lambda = 13.4$ nm along the plasma axis was found to be approximately threefold more intense than that across the axis. In this case, the conversion efficiency of the radiation with $\lambda = 11.4$ and 13.4 nm into the hemisphere was 2 and 0.5%, respectively. The dependence of the conversion efficiency on the polarization of the Ti-sapphire laser beam and on the pressure in the valve was also investigated in this paper. We have found no adequate explanation of the anomalously high quantum yield in the literature; the absence of time scans for the radiation spectra makes it difficult to interpret the results. In particular, there is no clear idea of precisely which xenon ions provide the maximum yield of the radiation in the spectral range under study. A theoretical study of the physical nature of this phenomenon is of current interest.

In our previous paper [23], based on atomic-kinetic calculations, we predicted several efficient lasing transitions in the region 10–15 nm in Ni-like xenon. In [23], a theoretical study was performed for the plasma of fairly low temperature ($T_e = 500$–1000 eV) produced by a long ($\tau_{\text{pump}} \gg 100$ ps) pumping pulse. Under such conditions, the amplification on several $3p^53d^{10}4f$–$3p^53d^{10}4d$ transitions between highly excited levels in the region of 13–14 nm and on the commonly studied $3d^94d$ $[J = 0]$–$3d^94p$ $[J = 1]$ transition with $\lambda \approx 10$ nm in Ni-like ions is of greatest interest. In recent years, we

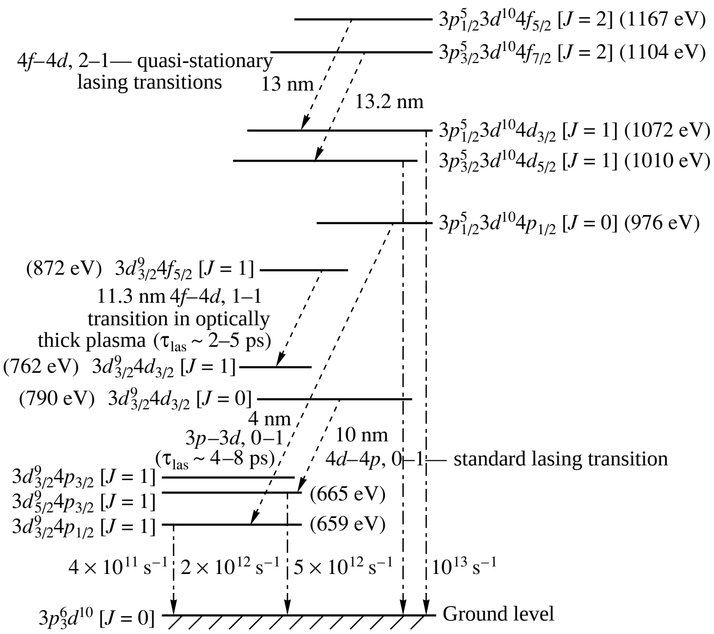

Fig. 1. Level diagram for Xe XXVII showing the strongest lasing transitions.

have calculated the gains in various Ne- and Ni-like ions by using our method [24, 25] for a detailed comparison with available experimental data. In [26], we tested our atomic–kinetic calculations of the gains on the Pd-like xenon ($\lambda = 41.8$ nm) transition in the plasma produced through the interaction between the optical field of a femtosecond pulse and gaseous xenon. Based on our calculations, we determined optimal parameters for the experiment to achieve the maximum yield of the radiation with $\lambda = 41.8$ nm.

In this work, we performed atomic-kinetic calculations of the radiation spectra for Ni-like xenon; the theoretical and experimental radiation spectra in the region of the resonance Xe XXVII transitions are compared in Section 2. The time dependences of the gains in a high-temperature plasma for the most promising lasing transitions of Ni-like xenon are considered in Section 3. In Section 4, our atomic–kinetic calculations are used to determine the plasma parameters in the experiments [20–22] that recorded an anomalously high energy yield of the plasma radiation in the region 10–15 nm. In conclusion, based on our calculations and using the experimental results from [20–22], we propose an experimental pumping setup that provides the maximum energy yield of the narrowly beamed radiation with $\lambda = 4$, 9.9, 11.4, and 13–14 nm.

2. SPECTRAL CHARACTERISTICS OF Ni-LIKE XENON

Figure 1 shows the working levels and wavelengths in Xe XXVII for the strongest lasing transitions. The lasing transitions are indicated by the inclined dotted lines; the radiative decays of the lower working levels are indicated by the vertical dash–dotted lines, with their rates being given near them. We calculated the wavelengths, the rates of the radiative transitions, and the rates of the transitions induced by collisions with electrons using the relativistic perturbation theory with the zeroth-approximation model potential [27, 28]. The results of our calculations are presented in the table. The error in the calculated wavelengths is within ±2 Å for the transitions between the lower $3d^94l$ configurations. For the transitions between the high-lying $3p^53d^{10}4l$ configurations, where the effect of the ignored correlation corrections is stronger, the error can be slightly larger.

The gains are usually measured experimentally for the $3d^44d$–$3d^44p$, 0–1 transition with $\lambda = 10$ nm, whose empirical wavelengths for the Ni-like sequence of ions with $Z = 46$–92 are presented in [29]. There are other, two less intense lines near 10 nm that correspond to the transitions from the same upper $3d^44d$ [$J = 0$] level to the other two states, $3d^44p$ [$J = 1$]. There are five strong lasing transitions in the region 13–13.9 nm between the highly excited $3p^53d^{10}4f$–$3p^53d^{10}4d$ configurations. Four of them were considered in [23]. The level population inversion for these four transitions, as for the $4d$–$4p$, 0–1 transitions, is quasi-stationary; it is stable if the plasma parameters are maintained. The inversion mechanism on these transitions is attributable to ordinary collisional–radiative processes; it is similar to the inversion mechanism for the $3p$–$3s$, 2–1 and $3p$–$3s$, 0–1 transitions in Ne-like ions. For simplicity, Fig. 1 shows only the two possible lasing transitions in the region 13–13.9 nm. Note that the lasing transition between the analogous highly excited levels in Ne-like ions, The transitions in Ni-like xenon on which the spontaneous radiation can be amplified

Upper level	J	Lower level	J	Transition level nos.	λ, Å	A_{ul}, s^{-1}	R_{col}, $\mathrm{cm}^{-3}\,\mathrm{s}^{-1}$	E_{tr}, eV	$\Delta\nu$, s^{-1}	$\check{N}_{\mathrm{u}}$, 3×10^{16} cm^{-3}	$\check{N}_{\mathrm{l}}$, 3×10^{16} cm^{-3}	I_0, 10^{23} $\mathrm{eV\,s}^{-1}$	$\hat{g}$, cm^{-1}	$\exp(\hat{g}L)$	$E_{\mathrm{las}}^{\mathrm{out}}$, 10^{15} eV
$3d_{3/2}4d_{3/2}$	0			35	9.5	4.5×10^{10}	1.3×10^{-10}	131	8.3×10^{12}	6.0		1.8	25	33	0.03
		$3d_{3/2}4p_{1/2}$	1	–9			4.1×10^{-12}				6.8				
		$3d_{5/2}4p_{3/2}$	1	–12	10.0	1.0×10^{11}	2.0×10^{-11}	125	1.1×10^{13}		5.9	3.8	45	544	1.0
		$3d_{3/2}4p_{3/2}$	1	–16	10.9	1.5×10^{10}	2.8×10^{-12}	113	8.1×10^{12}		5.0	3.4	15	8	0.02
*$3d_{3/2}4f_{5/2}$	1			57	10.3	1.5×10^{10}	3.3×10^{-10}	120	1.3×10^{13}	10.0		0.9	10	3	0.002
		$3d_{5/2}4d_{5/2}$	1	–22			2.8×10^{-13}				4.5				
		$3d_{3/2}4d_{3/2}$	1	–28	11.3	4.4×10^{10}	2.8×10^{-13}	110	9.6×10^{12}		4.8	2.4	65	8950	10
*$3p_{1/2}4p_{1/2}$	0			67	3.9	8.9×10^{11}	5.4×10^{-11}	317	9.0×10^{12}	7.0		100	50	1000	50
		$3d_{3/2}4p_{1/2}$	1	–9			4.1×10^{-12}				6.7				
$3p_{1/2}4d_{5/2}$	2			80	13.8	1.1×10^{11}	3.5×10^{-13}	89	4.3×10^{12}	3.0		1.5	26	37	0.03
		$3p_{1/2}4p_{3/2}$	1	–68			3.4×10^{-13}				2.0				
$3p_{1/2}4d_{5/2}$	3			81	13.9	1.2×10^{11}	1.2×10^{-12}	89	4.6×10^{12}	6.7		3.5	32	90	0.14
		$3p_{3/2}4p_{5/2}$	2	–69			1.8×10^{-12}				4.4				
$3p_{3/2}4f_{7/2}$	2			89	13.2	9.6×10^{10}	2.9×10^{-11}	94	9.8×10^{12}	5.9		2.7	37	180	0.2
		$3p_{3/2}4d_{5/2}$	1	–76			1.3×10^{-11}				2.5				
*$3p_{1/2}4f_{7/2}$	4			92	13.6	1.2×10^{11}	2.4×10^{-11}	91	5.5×10^{12}	4.5		2.5	50	1096	1.2
		$3p_{1/2}4d_{5/2}$	3	–81			1.2×10^{-12}				2.2				
$3p_{1/2}4f_{5/2}$	2			93	13.0	1.1×10^{11}	1.5×10^{-11}	95	6.1×10^{12}	4.5		2.3	57	2980	3.2
		$3p_{1/2}4d_{3/2}$	1	–79			4.2×10^{-12}				2.7				

Note: The table gives the transition wavelengths λ, radiative transition probabilities A_{ul}, and transition energies E_{tr}. The rates of level excitation by an electron collision from the ground state per unit volume R_{col}, the Voigt line width Δν, the time-averaged level populations $\check{N}_{\mathrm{u}}$ and $\check{N}_{\mathrm{l}}$, and the gain $\hat{g}$ were calculated for $n_e = 8\times10^{20}$ cm^{-3}, $T_e = 1800$ eV, and $d = 12.5$ μm. I_0 is the transition emissive power from a volume of 1.7×10^{-7} cm^3, and $E_{\mathrm{las}}^{\mathrm{out}}$ is the energy yield including the amplification for $\tau_{\mathrm{las}} = 4.6$ ps. The transitions with a short-lived inversion are denoted by an asterisk (*).

$2s2p^63d$ [$J = 2$]–$2s2p^63p$ [$J = 1$], was observed experimentally [30]. In Ni-like ions, the spectral density of the above highly excited states is very high. In addition to them, several more promising lasing transitions, whose wavelengths may overlap, lie in the region 13–15 nm.

The inversion of the remaining strongest transitions, denoted by an asterisk in the table, is possible only for an ultrashort plasma production time, when the Ni-like ions dominate at the initial time. The $3p_{1/2}^5 4d^{10}4p_{1/2}$ [$J = 0$]–$3p^63d_{3/2}^9 4p_{1/2}$ [$J = 1$] lasing transition with λ = 4 nm is of particular interest; unfortunately, this spectral region has not been studied experimentally. This is the so-called inner-shell transition between the $3p_{1/2}$–$3d_{3/2}$ vacancy states in the presence of a $4p_{1/2}$ "observer electron." In [25], we predicted a similar amplification mechanism on the short-wavelength inner-shell $2s$–$2p$, 0–1 transition in Ne-like ions. This result was confirmed for Ne-like ions in the calculations performed by other theoretical methods [31].

The reabsorption of photons to the upper working $3d_{3/2}^9 4f_{5/2}$ [$J = 1$] level is responsible for the inversion on the $4f$–$4d$, 1–1 transition with λ = 11.3 nm. In an optically thin plasma, the resonant decay of this level to the ground state occurs with a probability of 6×10^{13} s^{-1}. Because of the large oscillator strength, this level is intensively populated by an electron collision from the ground state (see table). In an optically thick plasma, including the reabsorption decreases the radiative decay probability for this level by a factor of

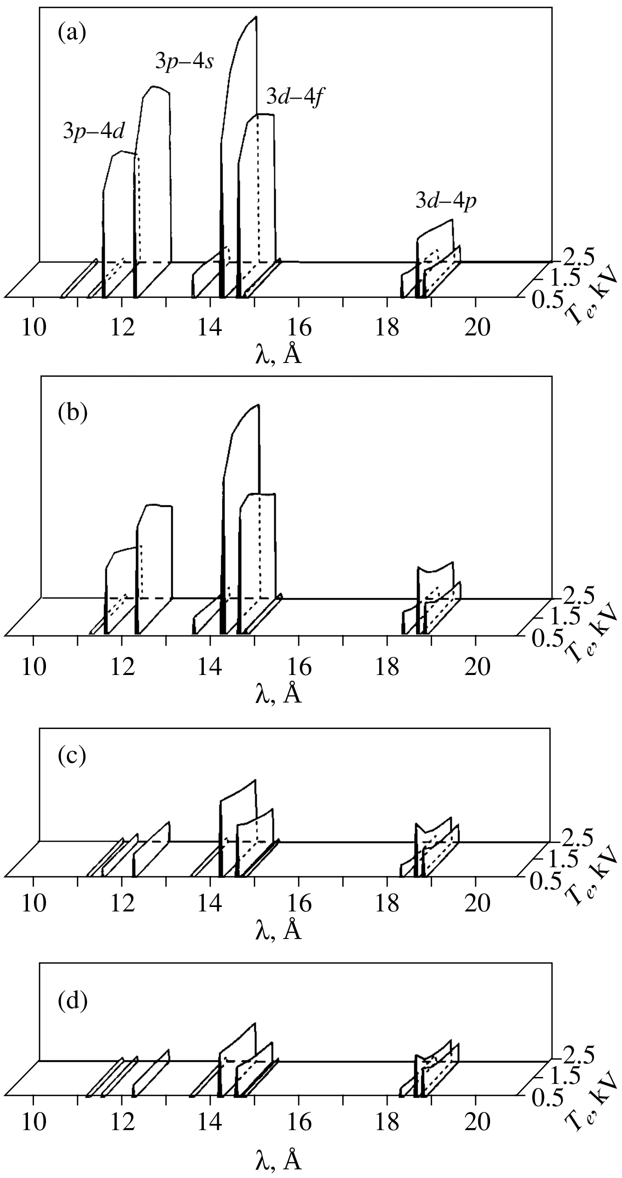

Fig. 2. Model Xe XXVII radiation spectrum in arbitrary units in the region 10–20 Å as a function of T_e and $n_e = 10^{21}$ (a), 5×10^{20} (b), 10^{20} (c), and 5×10^{19} cm^{-3} (d).

10 to 100. Given the reabsorption, the radiative transition rate A_{ij}^{eff} is determined by the escape factor ε: in our model, the photon reabsorption is taken into account for all transitions in the approximation presented in [32, 33], $A_{ij}^{\text{eff}} = \varepsilon_{ij} A_{ij}$, where $\varepsilon = 1.22[\ln(k_0 d)]^{1/2}/(k_0 d) < 1$ is the ratio of the radiative transition probability of an ion in plasma to the probability in an isolated ion, and k_0 is the photoabsorption coefficient. An increase in the population of the $3d_{3/2}^9 4f_{5/2}$ [$J = 1$] level through the reabsorption leads to an inverted state relative to the lower levels. The term "optical self-pumping" is used in the literature for this inversion mechanism. The amplification on this transition in Ni-like silver was first observed in [34]. Figure 1 shows the strongest possible lasing transition from the $3d_{3/2}^9 4f_{5/2}$ [$J = 1$] level with λ = 11.3 nm.

The model Xe XXVII radiation spectrum in the region 10–20 Å, where the line intensities were calculated at four values of n_e in the range 5×10^{19}–10^{21} cm^{-3}, is shown as a function of n_e and T_e in Fig. 2. T_e in the range 0.5–2.5 keV lies along the second horizontal axis. The relative line intensities are along the vertical axis on a linear scale. The Xe XXVII resonance transitions are located within the specified wavelength range; the line intensities are shown without including the satellite structure. The intensities of the strongest resonance transitions in ions with the filled shell of the ground state are known to be much higher than those of the transitions between excited states. The number of resonance lines in such ions is small; the most intense of them are known even for the heavy ions of the nickel isoelectronic sequence. The experimental wavelengths λ_{exp} for the five resonance transitions in Xe XXVII can be found in the review [35]. These lines can be seen in Fig. 2: three lines belong to the $4p$–$3d$ transitions with λ = 18.804 Å (λ_{exp} = 18.826 Å), λ = 18.641 Å (λ_{exp} = 18.667 Å), and λ = 18.301 Å (λ_{exp} = 18.326 Å); two lines belong to the $4f$–$3d$ transitions with λ = 14.222 Å (λ_{exp} = 14.247 Å) and λ = 14.602 Å (λ_{exp} = 14.618 Å). A comparison indicates that the wavelengths of the resonance transitions were calculated with an accuracy of about 0.1%. The presence of these resonance lines in the xenon plasma spectra directly points to the existence of Ni-like ions. Figure 2 shows the five lines that correspond to the transitions from the $3p^5 3d^{10} 4d$ [$J = 1$] states with λ = 12.340, 12.270, 11.570 Å and the $3p^5 3d^{10} 4s$ states with λ = 14.585 and 13.575 Å. We conclude from Fig. 2 that the highly excited $3p^5 3d^{10} 4l$ states are efficiently populated at $n_e \geq 5 \times 10^{20}$ cm^{-3}. The intensities of these transitions increase as the temperature changes from 500 to 2000 eV. One of the transitions, $3p^5 3d^{10} 4d$–$3p^6 3d^{10}$ (λ_{exp} = 11.57 Å), was identified by means of precision spectroscopy in [36]; this result closely agrees with our values calculated for the $3p_{1/2}^5 4d^{10} 4d_{3/2}$ [$J = 1$]–$3p^6 3d^{10}$ [$J = 0$] transition. The spectra of xenon ions at high ionization stages were not studied by means of precision experimental spectroscopy. Their shells are much more complex; in general, there are no distinct resonances in the spectra of complex shells.

The spectral characteristics of the radiation near the Xe XXVII resonance transitions in the plasma produced through the interaction of an optical laser field with a xenon cluster beam were studied in [19, 37, 38]. In actual spectra, many satellite lines that broaden the resonances lie near the resonance transitions; as a result, the experimental lines have smeared profiles. Nevertheless, the spectral resolution in these experiments is high enough for the positions and intensities of the resonances to be reliably judged. A laser with a pulse duration of ~300 fs and an intensity of ~10^{19} W cm^{-2} was used in [37]. The strong lines between 14 and 15 Å that correspond to the transitions to the 3*d* shell from the 4*f* state are clearly distinguishable in the radiation spectrum. In addition, there are intense lines in the region 10.5–12.5 Å, some of which are in satisfactory agreement with the model spectrum shown in Fig. 2; these lines correspond to the transitions to the 3*p* state from the 4*d* and 4*s* states. The xenon plasma radiation spectra in the region 12.5–15.5 Å were investigated in [38] by using a neodymium glass laser pulse with a duration of 2 ps, an intensity of 10^{15}–10^{17} W cm^{-2}, and an energy of 0.5 J. Here, a resolution higher than that in [37] was achieved. As a result, the two 4*f*–3*d* resonance transitions with $\lambda = 14.247$ and 14.618 Å were clearly identified. The third, fairly intense line lies between these two lines. According to our calculations, it corresponds to the $3p^5_{3/2}3d^{10}4s_{1/2}$ [$J = 1$]–$3d^{10}$ [$J = 0$] transition with $\lambda = 14.585$ Å. Another transition from this configuration, $3p^5_{1/2}3d^{10}4s_{1/2}$ [$J = 1$]–$3d^{10}$ [$J = 0$] with $\lambda = 13.575$ Å, was observed in [38] in the form of a weaker and smeared line.

An almost 100% absorption of the pumping pulse energy at pulse intensities within the range 5×10^{15}–5×10^{17} W cm^{-2} was demonstrated in [37]. The energy yield of the radiation near 1 keV (~12 Å) was measured in this paper; at the peak intensity, it was 5–12 μJ (~10^{-5}), depending on the cluster size. The resonance spectra of the xenon plasma radiation in the region 5–18 nm were also observed in [19] using a KrF laser, where the previously known $3d^94f$–$3d^{10}$ transitions were identified. In addition, the ~13.5, ~12.2, and ~11.5 nm lines were clearly observed here.

The time dependences of the gains $g(\tau|n_e, T_e, d)$ on Ni-like xenon transitions under long pumping pulse conditions were theoretically analyzed in [23]. The Ni-like state was assumed to be formed through one- or two-stage plasma heating in a gas-puff facility. An optimal density within the range $3 \times 10^{20} \le n_e \le 10^{21}$ cm^{-3} was found for each of the lasing transitions. In this paper, it was shown how sensitive the time it takes to reach the Ni-like stage ($\tau^{\mathrm{Cu}}_{\mathrm{ioniz}}$) and the ionization time of a Ni-like ion ($\tau^{\mathrm{Ni}}_{\mathrm{ioniz}}$) into the next Co-like state are to the plasma parameters. Thus, for example, $\tau^{\mathrm{Cu}}_{\mathrm{ioniz}}$ is several dozen nanoseconds at T_e ~ 150–200 eV and n_e ~ 10^{19} cm^{-3} and several picoseconds at T_e ~ 450–500 eV and n_e ~ 10^{21} cm^{-3}. The ionization balance, the ion fraction in the Ni-like state, is determined by T_e; the dependence on n_e is not so significant.

The plasma state at T_e ~ 450–550 eV is a “thermal trap” for Ni-like xenon, because the Xe^{26+} ionization processes under these conditions are balanced by the recombination processes to Xe^{26+}. According to our calculations [23], the fraction of Ni-like ions is ~0.4 at such T_e. This is confirmed by recent experiments [36], where the Xe XXVI–Xe XXVIII radiation spectra as well as the electron density, temperature, and ionization balance in a xenon plasma were investigated with a time resolution of 30 ps. The plasma was produced by irradiating an atomic xenon beam by a neodymium glass laser pulse with a duration of 650 ps. The time dependences of the radiation spectra were indicative of a steady state of the plasma ionization composition during the pulse action. The pulse energy and duration were chosen so as to compensate for the radiative plasma cooling by maintaining a steady value of T_e, which was estimated in [36] to be about 450 eV.

When ultrashort pumping pulses are used, the highly efficient lasing transitions on picosecond and subpicosecond time scales are of great interest. Such short-lived lasing transitions are attributable to the high population rate of some of the Ni-like xenon levels by an electron collision: during a short time interval, the populations of these levels exceed significantly those of the remaining slowly populated levels. The inversion duration depends on the level population rates, which are sensitive to the plasma density and temperature. This type of inversion is characterized by a very steep rise in the gain on a subpicosecond time scale. Depending on the initial plasma parameters, two inversion disappearance mechanisms are possible: ionization of the working ion into the next stage and collisional level mixing. For various lasing transitions in Xe XXVII, the lifetime of the transition inversion can be 1–10 pc, depending on plasma parameters.

3. TIME DEPENDENCES OF THE GAINS IN A HIGH-TEMPERATURE XENON PLASMA

In this section, we determine optimal conditions in plasma for the maximum quantum yield of the radiation on promising Xe XXVII lasing transitions to be achieved. These results will be used to interpret the experimental data presented in [19–22]. In our calculations, we made the following assumptions:

(1) Plasma is produced in the shape of a cylinder with diameter *d* and length *L* via the propagation of a laser pulse through a cluster beam with thickness *L;*

(2) The pumping pulse parameters are such that plasma with an initial temperature T_e ($\tau = 0$), in which the Xe^{26+} ions constitute 90% of the plasma and are in the ground state, is produced immediately after the interaction of the optical laser field with clusters;

(3) During approximately 10 ps, the plasma parameters (n_e, $T_e(\tau)$, d) are uniform along the propagation of the pumping laser beam;

(4) The electron and ion energy distribution is assumed to be Maxwellian, and the shape of the distribution plays no significant role in calculating the rates of the transitions induced by electron–ion collisions;

(5) The ion temperature $T_i = T_e$.

In our calculations, we average the gain $g(\tau)$ over the space and time coordinates. To this end, we break down the cylinder target into segments smaller than the pumping pulse scale length; the elementary processes in each segment then proceed in an identical way, but with a time delay. In this case, it will suffice to perform only a time averaging for the function $g(\tau)$. We calculate $g(\tau)$ at the line center from the commonly used formula (see, e.g., [39])

$$g(\tau) = \frac{A_{ul}\lambda^2}{8\pi\Delta\nu}\left[N_u(\tau) - \frac{g_u}{g_l}N_l(\tau)\right],$$

where A_{ul} is the radiative transition probability; λ is the wavelength; $N_u(\tau)$ and $N_l(\tau)$ are the time-varying number densities of atoms in the upper and lower states; and g_u and g_l are the statistical weights of the upper and lower levels, respectively. The shape of the transition line is determined by the convolution of the Doppler and intrinsic profiles. The latter is attributable to the radiative transitions and collisional processes that couple each level of the working ion with all the remaining levels of this ion and with the ions of the adjacent ionization stages. The line width (Voigt profile) $\Delta\nu$ can be determined by a simplified method suggested in [39]. We disregard the line broadening due to the Stark effect produced by quasi-static microfields in the plasma. For all the lasing transitions under consideration, $\Delta n = 0$ (n is the principal quantum number). In [40], it was shown for the $2p^53p$ [$J = 0, 2$]–$2p^53s$ [$J = 1$] transitions in Ne-like germanium that the line broadening due to microfields is negligible. Similar calculations were performed in [41] for the $4d^95d$ [$J = 0$]–$4d^95p$ [$J = 1$] in Pd-like xenon.

Once the pulse action has terminated, collisional–radiative processes, which lead to the population of excited Xe XXVII levels, take place in the plasma. Several elementary processes involving electrons and ions of the adjacent ionization stages also take place. All the significant elementary processes between the Xe XXVII states as well as between the Xe XXVII and Xe XXVI states were taken into account in the kinetic calculations. Our method for calculating the rate coefficients of the kinetic equations for the level populations is presented in [42–44]. The method for calculating the probabilities of radiative transitions between the levels of the ions whose ground state is the filled shell is described in [42, 44]. The method for calculating the cross sections and strengths of the lines of the transitions induced by collisions with electrons is described in detail for such ions in [43]. Our method for solving the kinetic equations to calculate the level populations is presented in [45]. The gain $g(\tau|n_e, T_e, d)$ is calculated for a set of parameters n_e, T_e, and d. The populations of the lower 93 levels of Ni-like xenon are calculated by using precise rate coefficients for the transitions between the levels of this ion. The rate coefficients for the transitions involving ions of the adjacent ionization stages are calculated by quasi-classical methods [45].

The calculations of the level populations are based on the solution of a system of differential equations including a large number of rate coefficients. The rate coefficients for different processes differ by several orders of magnitude. In addition, the rate coefficients and escape factors of photons vary with time due to the variations in plasma parameters, level populations, and radiation field. The proper populations on asymptotically long time scales are determined by solving the differential equations in conjunction with the method of iterations. To this end, the differential equations are integrated on fairly short time intervals $\Delta\tau_i$, on which the variations in rate coefficients, radiation field, and escape factors may be ignored. The rate coefficients and escape factors are calculated at the beginning of each time interval. The stability of the final results for the chosen time intervals $\Delta\tau_i$ is tested numerically.

Figure 3 shows the time dependences of the gains for the $4d$–$4p$, 0–1 (λ = 10 nm) and $3p$–$3d$, 0–1 (λ = 4 nm) transitions. The gains are given for three values of T_e and $n_e = 10^{21}$ cm^{-3}; the optimal values of n_e for these transitions lie within the range 5×10^{20}–10^{21} cm^{-3}. The plasma thickness was assumed to be d = 20 μm. Similar plots are shown in Fig. 4 for the transitions in the region 13–13.9 nm: $4f$–$4d$, 2–1 (λ = 13.0 nm) and $4f$–$4d$, 4–3 (λ = 13.6 nm). The value of $g(\tau)$ for the transitions shown in Figs. 3 and 4 varies only slightly when the diameter varies within the range 10–100 μm. The decay of the amplification on the transitions in the region 13–13.9 nm is attributable to the Xe XXVII ionization into higher stages, except one transition with λ = 13.6 nm (Fig. 4a). The decay of the amplification on this transition (just as on the transition with λ = 4 nm (Fig. 3b)) is caused mainly by collisional level mixing; as a result, the inversion disappears on a shorter time interval than it does on the remaining transitions in the region 13–13.9 nm (Figs. 4a and 4b). The temperature saturation occurs at $1500 < T_e < 2000$ eV, except the standard transition with λ = 10 nm. As was shown in [23], the time dependence $g(\tau)$ for the commonly studied $4d$–$4p$, 0–1 transition with λ = 10 nm also has a maximum near $\tau = 0$, but here collisional mixing leads only to a reduction in the inversion with increasing τ. At $n_e \approx 5 \times 10^{20}$ cm^{-3}, the lasing duration is $\tau_{\text{las}} \approx 8$ ps. However, under these conditions, the values of $g(\tau)$ are much lower for all transitions. At $n_e = 10^{21}$ cm^{-3}, $\tau_{\text{las}} \le 5$ ps.

Figure 5 shows the time dependences $g(\tau)$ for the $4f$–$4d$, 1–1 (λ = 11.3 nm) transition at an optimal value of $n_e = 10^{21}$ cm^{-3} and three value of T_e. For this transition, the temperature saturation occurs at $T_e \ge 5$ keV. It is important to note that the maximum possible values of $g(\tau)$ for this transition are much higher than those for other transitions; the maximum values are reached at τ = 0.3–0.4 ps. Figure 5 shows the dependences for two

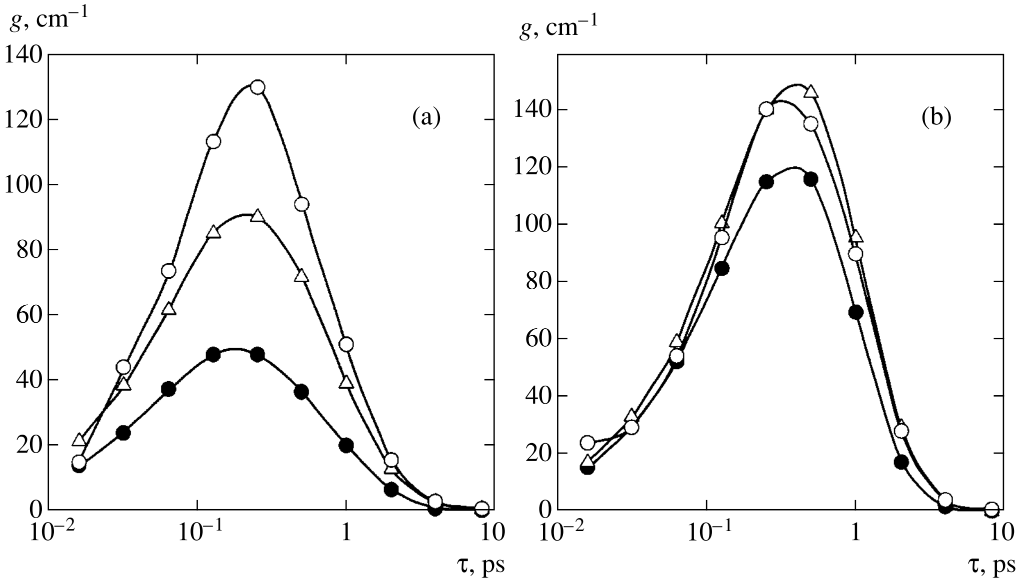

Fig. 3. Time evolution of the gain g in Xe XXVII for two 0–1 transitions; T_e = 1 (●), 2 (△), and 3 (○) keV; $n_e = 10^{21}$ cm^{-3}, d = 20 μm, λ = 10 (a) and 4 nm (b).

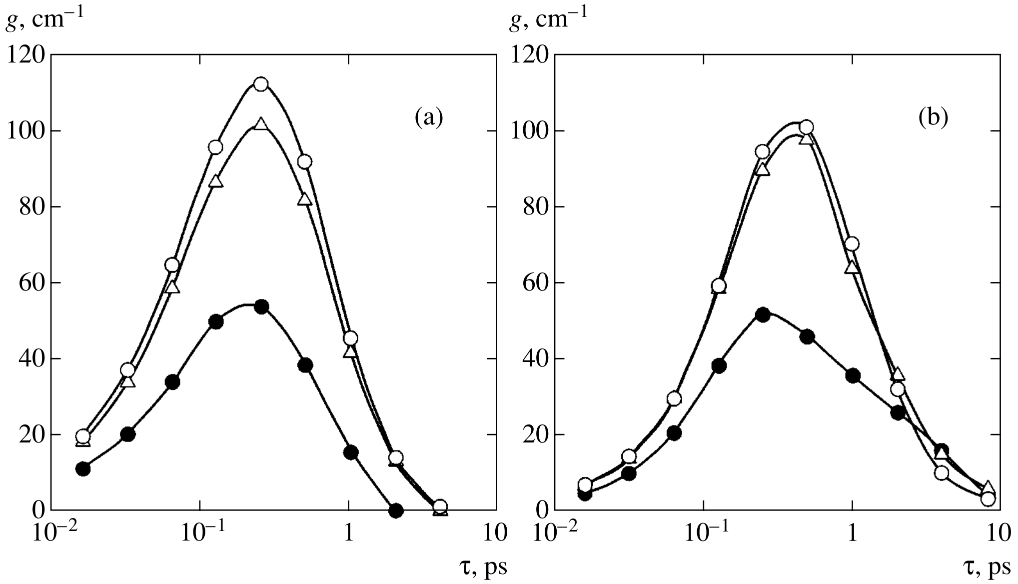

Fig. 4. Time evolution of the gain g for two transitions between highly excited levels in Xe XXVII: $3p^53d^{10}4f$–$3p^53d^{10}4d$ for λ = 136 (a) and 130 Å (b); T_e = 1 (●), 2 (△), and 3 (○) keV, $n_e = 10^{21}$ cm^{-3}, and d = 20 μm.

plasma diameters: d = 20 (a) and 60 μm (b). The gain increases significantly with plasma diameter; the amplification duration also increases.

The model spectra in the region 3.5–15.5 nm with amplification are shown in Fig. 6. We used the time-averaged values of $g(\tau)$ to compute the spectra. In Fig. 6a, the calculation was performed for $n_e = 5 \times 10^{20}$ cm^{-3}, T_e = 2000 eV, and d = 20 μm at a plasma length of L = 0.25 cm. The lines with λ = 4 and 10 nm and several lines in the region 13–13.9 nm dominate here. The three lines in the region 9.4–10.9 nm correspond to the transitions from the $3d_{3/2}4d_{3/2}$ [J = 0] state to the three lower $3d4p$ [J = 1] states. Figure 6b shows the model spectrum for an optically thick plasma with a higher temperature: $n_e = 10^{21}$ cm^{-3}, T_e = 3000 eV, d = 150 μm, and L = 0.12 cm. In this case, the line that corresponds to the λ = 11.3 nm transition attributable to the reabsorption of photons to the upper $3d_{3/2}4f_{5/2}$ [J = 1] level has the highest intensity. At the plasma parameters in Fig. 6b, this level is inverted relative to several lower-lying states; another two intense transitions with λ = 10.3 and 15.3 nm can be seen in Fig. 6b. The width of

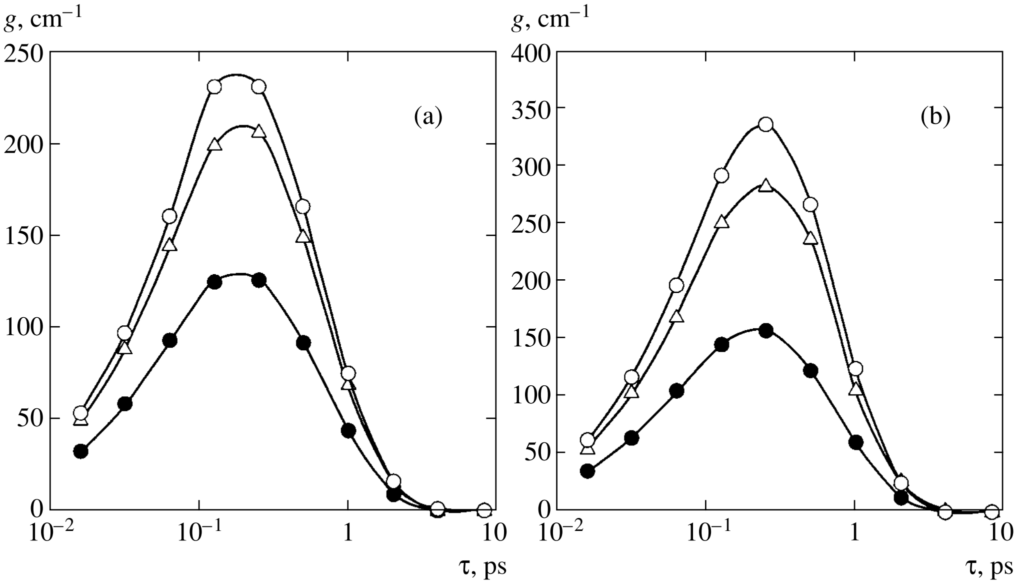

Fig. 5. Time evolution of g on the $3d^94f$–$3d^94d$, 1–1 transition with λ = 113.4 Å attributable to the reabsorption of photons in an optically thick plasma at T_e = 1 (●), 2 (△), and 3 keV (○), $n_e = 10^{21}$ cm^{-3}; d = 20 (a) and 60 μm (b).

these lines is attributable to the large radiative width of the upper level; the width of the remaining transitions is determined mainly by collisional processes. In addition to the transitions listed in the table, there are many slightly enhanced transitions in the region 11–15 nm whose wavelengths overlap.

4. INTERPRETATION OF THE RESULTS OF THE EXPERIMENTS THAT RECORDED ANOMALOUSLY HIGH CONVERSION EFFICIENCIES OF THE PUMPING PULSE ENERGY INTO THE PLASMA RADIATION

We use the results of the above calculations to estimate the energy yield of the radiation of the strongest lines in the experiment described in [21]. The radiation spectra of the plasma with λ = 7–15 nm produced by irradiating a beam of xenon clusters with a size of 10^5–10^6 at. per cluster by a Ti-sapphire laser pulse with an intensity of ~2×10^{18} W cm^{-2}, a duration of 50 fs, a wavelength of 800 nm, and an energy of about 200 mJ were recorded in this work. The pulse was focused to the beam center in the immediate vicinity of the exit from the chamber, $h = 0$. The diameter of the plasma produced along the laser beam is $d \approx 10$ μm; its length is equal to the thickness of the cluster beam, L = 1.4 mm. The spectra were measured along the plasma axis and at an angle of 45°. The time-integrated Xe^{9+}–Xe^{29+} spectra were recorded in [21]; the energy yield of the radiation depended on the xenon pressure in the valve, which was smoothly varied between 1 and 55 bar. The measurements along the plasma axis showed that an extreme dependence of the quantum yield on the xenon pressure in the chamber was observed only for the lines with $\lambda \approx 11$ and 13 nm. The maximum yield for these lines was observed at a pressure of 5–15 bar. Similar studies of the quantum yield at an angle to the plasma axis showed, first, a much lower quantum yield than that along the plasma axis and, second, the absence of any extreme pressure dependences. The anisotropy in the emergent radiation was investigated in detail for λ = 13.5 ± 2% nm: the intensity along the plasma axis was approximately three times as high as that recorded at an angle to the axis. The resulting radiation into the hemisphere was

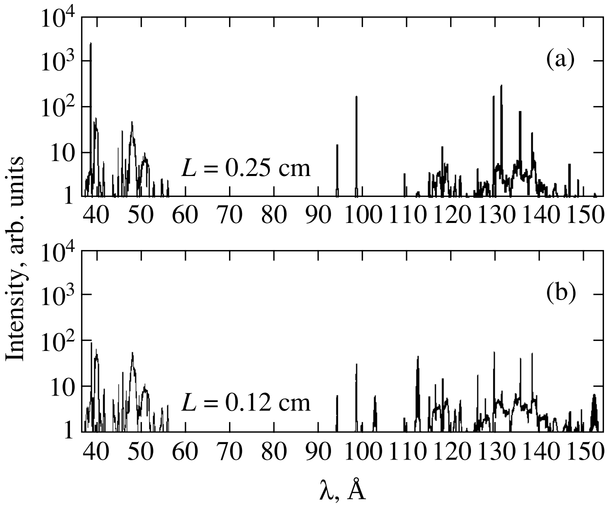

Fig. 6. Model Xe XXVII spectra computed with amplification. The plasma parameters are: (a) $n_e = 5 \times 10^{20}$ cm^{-3}, T_e = 2000 eV, d = 20 μm; (b) $n_e = 10^{21}$ cm^{-3}, T_e = 3000 eV, d = 150 μm.

determined by interpolating the intensities recorded in various directions away from the axis. The conversion efficiency was 0.5% in 2π steradians at 13 nm and reached 2% at 11 nm.

Using our model, we chose three plasma parameters: $n_e = 8 \times 10^{20}$ cm^{-3}, $T_e = 1800$ eV, and $d = 12.5$ μm, which roughly explain both conversion efficiencies and their ratio in the experiment [21]. Let us estimate the emissive power, I_0, from a volume of $V = \pi r^2 L = 1.7 \times 10^{-7}$ cm^3: $I_0 = \breve{N}_u E_{tr} A_{ul}$, where $\breve{N}_u$ is the time-averaged number of ions in a given excited state in the volume V, E_{tr} is the transition energy, and A_{ul} is the radiative transition probability from the upper to the lower working level. These data are presented in the table; also given here are the Voigt transitions widths $\Delta\nu$ and the gains $\hat{g}$ averaged over an interval $\tau_{\text{las}} \sim L/c = 4.67$ ps. The last column gives the energy yield calculated with amplification: $E_{\text{las}}^{\text{out}} = I_0 \exp(gL)\tau_{\text{las}}$. For the five lines in the region 13–13.9 nm, the mean total value is $E_{\text{las}}^{\text{out}} \approx 6 \times 10^{15}$ eV, which is approximately two times lower than the experimental value from [21], where 6×10^{15} eV in 2π steradians was recorded. The total energy yield on the $\lambda = 11.3$ nm transition was 10^{16} eV (<1% of the pumping pulse energy); for the $\lambda = 4$ nm line, $E_{\text{las}}^{\text{out}} = 5 \times 10^{16}$ eV > 4%. The energy yield on the $\lambda = 11.3$ nm transition increases sharply for a slight increase in parameters: $n_e \approx 9 \times 10^{20}$, $T_e \approx 2000$ eV, and $d \approx 15$ μm, while $E_{\text{las}}^{\text{out}}$ for the transitions near 13 nm increases more slowly. At constant T_e and d, the yield is at a maximum for $n_e = 10^{21}$ cm^{-3} (the Xe^{26+} ion density $n_i = 3.6 \times 10^{19}$ cm^{-3}). We believe that the intensity peak of the emergent radiation observed in the experiment [21] while varying the pressure in the valve can be explained by a change in the cluster density in the beam until optimal values of n_e and n_i are reached; once the optimal pressure region has been passed, the intensity decreases. If the temperature is stationary, the gain increases with density due to an increase in the rates of excitation by an electron collision, but the line width leading to a decrease in the gain also increases. In addition, the lifetime of a Ni-like ion decreases with increasing density. Therefore, $\hat{g}$ is at a maximum at a certain value of n_e. Characteristically, no extreme pressure dependences are observed for nonlasing lines. The optimal value of n_e is theoretically substantiated in [24].

We obtained our estimate by assuming that the plasma was spatially uniform in T_e and n_e. As was noted in [21], a significant fraction of the pumping pulse energy is absorbed in the adjacent cluster layers. We believe that a steep density gradient is responsible for the large divergence of the laser beam observed in the experiments [21]; therefore, the intensity along the plasma axis is only a factor of about 3 higher than that at an angle to the axis.

Similar studies were performed in [20], where lasers with various wavelengths, pulse durations and energies, and focal spot sizes were used. As the pressure in the valve rose from 0.1 to 12 atm, the cluster size increased from 10^2 to 5×10^6 at. per cluster. The studies were carried out at a pressure of 10 atm. Three types of pumping lasers were used to investigate the quantum yield of the xenon plasma radiation: Ti:Sapphire (t_p = 120 fs, 120 ps, and 8 ns, E = 3.5–49 mJ, λ = 745–800 nm), KrF (t_p = 500 fs, E = 24 mJ and t_p = 10 ns, E = 670 mJ, λ = 248 nm), and Nd:YAG (t_p = 9 ns, E = 450 mJ, λ = 1064 nm). The same experimental setup as that in [21] was used here, but the only spectrometer was perpendicular to the plasma axis. The density and radial distribution of atomic xenon were measured in [20]: $n_i \approx 3 \times 10^{19}$ cm^{-3} ($n_e = 8 \times 10^{20}$ cm^{-3}) in the immediate vicinity of the nozzle and $n_i = 5 \times 10^{18}$ cm^{-3} ($n_e = 1.4 \times 10^{20}$ cm^{-3}) at a distance of 2 mm from the nozzle. The laser beam was focused on the xenon cluster beam at a distance of 1–2 mm from the chamber hole. The highest conversion efficiency into the radiation with λ = 5–18 nm was achieved with the KrF laser (500 fs, 24 mJ, d = 10 μm, L = 2 mm). The total yield was 10% in 4π steradians for λ = 5–18 nm and 0.03% per steradian for $\lambda = 13.4 \pm 2\%$ nm, which is approximately two times lower than that in [21]. According to our calculations, such a yield is possible at $n_e \approx 3 \times 10^{20}$ cm^{-3}, $T_e \approx 2500$ eV, and $d \sim$ 10–12 μm. At such low densities, the series of transitions near 4 and 10 nm dominate in the spectrum; some of the transitions in the region 13–13.9 nm are also fairly strong.

The radiation spectra for a plasma of a relatively large volume ($V \sim 10^{-5}$ cm^3) were also investigated in experiment [20]. They were obtained by using pumping lasers with pulse energies of 5–6 mJ and focal spot diameters of 30–100 μm. In this case, the mean electron energy was several dozen eV, which is enough only for low degrees of ionization, Xe^{7+}–Xe^{12+}, whose resonance transition spectra also lie in the region 5–18 nm, to be achieved. In this case, the maximum conversion efficiency was several times lower than that for a high-temperature plasma.

The studies [21] were continued in [22] using longer pumping pulses: 30, 300, and 3000 ps with intensities of 10^{15}, 10^{14}, and 10^{13} W cm^{-2}, respectively. Here, a train of 100 pulses with an energy of 0.024 J = 1.4×10^{17} eV was formed in each pulse. The pulse was focused on the cluster beam at a distance of 1 mm from the nozzle. The minimum time interval between the pulses in the train at which the state of the cluster beam was completely renewed at a plasma diameter of 10 μm and a pressure of 30–40 bar was determined in [22]. Under the given parameters of the facility, the maximum pulse repetition rate was 125000 s^{-1}. It was also established in [22] that a 100% absorption of the pulse energy for these durations occurs at a liquid xenon pressure in the valve of more than 30 bar. A high intensity of the emergent radiation was observed in the region 10–10.7 nm. The energy yield was recorded only for $\lambda = 13.4$ nm ± 2%. The highest conversion efficiency, ~0.2% in 2π steradians, was achieved by using a 30-ps pulse. The conversion efficiency in this work was measured using a 10-ns laser pulse with an energy of $0.975 \text{ J} \approx 6 \times 10^{18}$ eV and an intensity of 10^{14} W cm^{-2}. In this case, the conversion efficiency was 0.26% in 2π steradians, which was quite an unexpected result.

Note that a Coulomb (slower) cluster decay mechanism is realized when long pulses are used; the plasma is heated through the absorption of the laser pulse energy by free electrons. The ionization proceeds successively; it follows from the time-integrated spectra that very high ionization stages, including Xe XXVII, are reached in the experiment [22]. When using long pulses with a moderate intensity ($I_{\text{pump}} \sim 10^{14}$ W cm^{-2}), the time it takes to reach the Ni-like stage from the Cu-like stage is comparable to the level excitation time for a Ni-like ion. The short-lived inversion mechanism is not realized here due to collisional level mixing as the Ni-like stage is reached. In this case, quasi-stationary inversion, which is possible on the transitions in the region 13–13.8 nm and near 10 nm, is realized.

When fairly high degrees of ionization are reached, the plasma energy is spent mainly on recombination radiation and bremsstrahlung. The radiative losses through the radiation on the transitions between coupled levels are only a few percent. Detailed formulas to calculate the radiative losses in plasma are given in [46]. In the case of a xenon plasma under conditions of optimal n_e and T_e for the maximum values of gL to be reached, the energy losses including all radiative processes are approximately 0.5 keV ps^{-1}. Therefore, for a fairly long pumping pulse ($\tau_{\text{pump}} > 10$ ps), the key factor is the pulse energy that must be enough for the optimal values of T_e to be maintained over the lifetime of the inverted state of the working Xe^{26+} ion.

5. CONCLUSIONS

The spectra in the region 0.8–1.9 nm, which correspond to the resonance transitions of Ni-like xenon and ions with higher degrees of ionization, were also demonstrated in all the experiments that recorded an anomalously high conversion efficiency of the pumping laser energy into the xenon plasma radiation energy in the region 10–15 nm. The conversion efficiency for the resonance transitions to this region (~0.1%) [19, 38] is two orders of magnitude lower than that for the transitions between excited states (~10%) [20, 21]. In conventional spectroscopic studies with a point source, the spectrum-integrated intensities of the resonance lines are several orders of magnitude higher than those of the transitions between excited states.

The lines of the transitions between excited states in Xe^{26+} are in the same spectral region as the resonance transitions in Xe^{10+}–Xe^{12+}. For this reason, the anomalously high conversion efficiency was assumed in previous studies to correspond to the transitions in these low-charge ions. These assumptions are actually refuted in [20], where various pumping lasers were used to produce a plasma with T_e equal to several dozen eV; in this case, the conversion efficiency into radiation in the region 8–18 nm was found to be several orders of magnitude lower than that in the experiments with a high-temperature plasma [20, 21].

In this paper, we showed that a high conversion efficiency is possible in a xenon plasma with optimal parameters for the amplification of spontaneous radiation on Xe XXVII transitions to be observed. This is confirmed by the anisotropy in the emergent radiation along and at an angle to the plasma axis, as well as by the equality of the wavelengths and energy yields of the most intense lines described in [21] to their theoretical values obtained in this paper. Optimal plasma parameters for the lasing effect to emerge were found in principle by the fitting method in the experiments [20, 21]: $n_e = (8–9) \times 10^{20}$ cm^{-3} and $T_e = 1.8–2$ keV. However, the radial density distribution in the plasma filament had a steep gradient, which led to a large spatial divergence of the emergent radiation.

In our view, the spatial plasma homogeneity can be improved by using a slit valve and a slit hole of the chamber. In this case, the xenon pressure in the valve should probably be higher than that for a circular hole. The flow of clusters is a “ribbon” with thickness D and length L. To achieve the maximum energy absorption, the pumping pulse should be focused along the slit (the focal spot diameter $d \approx D$). The insignificant influence of edge inhomogeneities still remains; it leads to a divergence of the emergent beam into a plane angle θ. In this experimental setup, the flow of large charged particles destroying the optical instruments decreases significantly.

Clearly, different pumping lasers and, accordingly, different slit hole sizes are needed to achieve the maximum energy yield on each of the transitions. A short-lived inversion on the transitions with $\lambda = 4$, 11.3, and 13.6 nm can be excited only by using ultrashort (30–100 fs) pulses. In currently available femtosecond lasers, the maximum energy of a single pulse is ~0.5–0.8 J. On this basis and given that the amplification on these transitions decays in 3–5 ps, we determine the plasma sizes as $30^2\ \mu\text{m}^2 \times 1$ mm ($V \sim 9 \times 10^{-7}$ cm^3). For these transitions, the maximum value of $gL \sim 9–10$ at $T_e \sim 2$ keV and $n_e = (0.9–1) \times 10^{21}$ cm^{-3}, which provides a yield of $10^{16}–10^{17}$ eV in the plane angle θ.

For the transitions near 10 nm and in the region 13–13.9 nm attributable to quasi-stationary inversion, we choose the optimal parameters $n_e = 5 \times 10^{20}$ cm^{-3} and $T_e = 0.8–1$ keV from the condition of the maximum

$gL = 6$–8 at the maximum L/d ratio (see Fig. 2 in [23]). Under these conditions, the Ni-like stage persists for 20–30 ps; a pulse energy of ~100 J at pulse duration and intensity of 100–300 ps and 10^{14}–5×10^{14} W cm^{-2}, respectively, is required to maintain T_e for this period in a 100^2 μm$^2 \times 0.5$ cm plasma. The suggested plasma geometry minimizes the effect of edge inhomogeneities; the emergent beam will be narrow with an energy yield $E_{\text{out}} \geq 0.5$ J for both values of λ. Thus, at a pumping pulse repetition rate of 10^4 Hz, the output power on the transitions with a short-lived inversion ($\lambda = 4$, 11.4, and 13.6 nm) is $W \sim 100$ W; its maximum possible value on the transitions with a quasi-stationary inversion ($\lambda = 10$ and 13–13.9 nm) is $W \approx 5 \times 10^3$ W.

Interpreting the experimental results allows some of the important aspects that were not touched on in [19–22] to be pointed out. First, time-integrated radiation spectra are provided; meanwhile, the time dependences of the emission of the most intense lines can provide information for diagnosing the plasma and testing the theoretical dependences $g(\tau)$. Second, the spatial intensity distribution in a femtosecond laser beam is an important pumping characteristic. Further studies aimed at improving the spatial homogeneity of the pumping pulse intensity are probably needed. Third, fairly intense coherent radiation on the $3d^94f$ $[J = 1]$–$3d^94d$ $[J = 1]$ transition with $\lambda = 11.3$ nm can be observed in the transverse direction away from a cylindrical plasma (in this case, the plasma length and width are d and L, respectively). This is attributable to the strong dependence of the gain for this transition on the plasma diameter and to the subpicosecond time it takes for $g(\tau)$ to reach its maximum, which can be as high as 300–600 cm^{-1} at $T_e \geq 3$ keV and $d \sim 30$ μm. This transition is promising for producing subpicosecond soft X-ray pulses when using slit valves and a transverse pumping scheme (focusing into a line). However, the 4-nm region, where the strongest effect should be observed, has never been investigated.

The lack of spectroscopic data for highly charged ions, including the transitions between the states with the excitation of the inner shell of the core, impedes further progress in producing superpowerful sources of monochromatic radiation. The wavelengths of the transitions between these states, $2s2p^63s$–$2s2p^63p$ and $2s2p^63p$–$2s2p^63d$, in the highly charged Ne-like Sc XII–Ni XIX ions were experimentally studied by means of precision spectroscopy in [47], where good agreement with the results of preliminary calculations by the method of relativistic perturbation theory with the zeroth-approximation model potential [48] was demonstrated. The good agreement between the theoretical and experimental [36–38] data for the resonance transitions to the ground state of Ni-like xenon from the $3p^53d^{10}4s$, $4d$ $[J = 1]$ states (Section 2, Fig. 2) confirms the reliability of this method.

The results presented here show that the atomic–kinetic calculation is a computer experiment that can be used to interpret the radiation spectra of a nonequilibrium plasma to determine the optimal parameters and gains on the transitions of a multiply charged ion. A comparison of the results of the computer experiment with the experimental results presented in [20–22] allows us to determine the experimental plasma parameters and to propose optimal pumping schemes to achieve the maximum possible energy yields for each available plasma pumping source. To estimate the gain, we use a time-averaged value of $\hat{g}$ that faithfully reproduces the experimental situation. Our theory is valid for any short pumping pulses when the plasma expansion is insignificant and the spontaneous radiation is amplified in the ionization regime of the working ion. The spontaneous radiation in plasma is amplified until the end of the pumping pulse passage through the target in time τ_{pump}. Clearly, a nonlinear amplification of short-wavelength radiation with duration τ_{las} can be observed if $\tau_{\text{las}} > \tau_{\text{pump}} \approx L/c$. This is a fundamental constraint on the plasma length L.

The error in the calculated gains related to the uncertainties in the electron and ion energy distribution functions and to the uncertainty in the ionization balance is 10–20%. A satisfactory accuracy of the calculation was proven by comparing our theoretical and experimental gains for the transitions in various ions [23–26]. The reliability of the results for $g(\tau)$ is attributable to the high accuracy of calculating the atomic constants and rate coefficients for both the low-lying and high-lying states of the working ion by the method of the relativistic perturbation theory with the zeroth-approximation model potential [27, 28, 42–44, 48–51].

In conclusion, note that, at present, the methods for producing a dusty plasma from clusters of various elements are being intensively developed (see, e.g., [3–6]), and the cluster and plasma properties are being studied [52, 53]. In prospect, superpowerful sources of narrowly beamed radiation over a wide, soft X-ray wavelength range can be produced by using clusters of other elements in the scheme considered here.

ACKNOWLEDGMENTS

We thank N.A. Zinov’ev for help in preparing the figures.

This work was supported by the Russian Foundation for Basic Research, project no. 04-02-17336a and by the Human Capital Foundation, grant no. 20.

REFERENCES

1. T. Ditmire, T. Donelly, A. M. Rubenchik, *et al.*, Phys. Rev. A **53**, 3379 (1996).
2. A. McPherson, B. J. Thompson, A. B. Borisov, *et al.*, Nature **370**, 631 (1994).

3. T. Ditmire, J. W. G. Tisoh, E. Springate, *et al.*, Nature **386**, 54 (1997).
4. M. Lezius, S. Dobosz, D. Normand, and M. Schmidt, Phys. Rev. Lett. **80**, 261 (1998).
5. M. A. Lebeault, J. Viallon, J. Chevaleyre, *et al.*, Eur. Phys. J. D **20**, 233 (2002).
6. J. Zweiback, T. Ditmire, and M. D. Perry, Phys. Rev. A **59**, R3166 (1999).
7. V. P. Krainov and M. B. Smirnov, Phys. Rep. **370**, 237 (2002).
8. O. F. Hagena and W. Obert, J. Chem. Phys. **56**, 1793 (1972).
9. J. Farges, M. F. de Feraudy, B. Raoult, and G. Torchet, J. Chem. Phys. **84**, 3491 (1986).
10. S. Dobosz, M. Lezius, M. Schmidt, *et al.*, Phys. Rev. A **56**, R2526 (1997).
11. L. Köller, M. Schumacher, J. Köhn, *et al.*, Phys. Rev. Lett. **82**, 3783 (1999).
12. E. Springate, N. Hay, J. W. G. Tisch, *et al.*, Phys. Rev. A **61**, 063201 (2000).
13. T. Ditmire, T. Donnelly, R. W. Falcone, and M. D. Peny, Phys. Rev. Lett. **75**, 3122 (1995).
14. T. Auguste, P. D'Oliveira, S. Hulin, *et al.*, Pis'ma Zh. Éksp. Teor. Fiz. **72**, 54 (2000) [JETP Lett. **72**, 38 (2000)].
15. A. S. Boldarev, V. A. Gasilov, F. Blasko, *et al.*, Pis'ma Zh. Éksp. Teor. Fiz. **73**, 583 (2001) [JETP Lett. **73**, 514 (2001)].
16. V. P. Krainov and M. B. Smirnov, Phys. Rep. **370**, 237 (2002).
17. V. P. Kraĭnov and M. B. Smirnov, Zh. Éksp. Teor. Fiz. **121**, 867 (2002) [JETP **94**, 745 (2002)].
18. M. B. Smirnov and V. P. Krainov, Phys. Plasmas **10**, 443 (2003).
19. H. Honda, E. Miura, K. Katsura, *et al.*, Phys. Rev. A **61**, 023201 (2000).
20. M. Mori, T. Shiraishi, E. Takahashi, *et al.*, J. Appl. Phys. **90**, 3595 (2001).
21. S. Ter-Avetisyan, M. Schnürer, H. Stiel, *et al.*, Phys. Rev. E **64**, 036404 (2001).
22. S. Ter-Avetisyan, U. Vogt, H. Stiel, *et al.*, J. Appl. Phys. **94**, 5489 (2003).
23. E. P. Ivanova, N. A. Zinov'ev, and L. V. Knight, Kvantovaya Élektron. (Moscow) **31**, 683 (2001).
24. E. P. Ivanova and N. A. Zinov'ev, Kvantovaya Élektron. (Moscow) **27**, 207 (1999).
25. E. P. Ivanova and N. A. Zinoviev, Phys. Lett. A **274**, 239 (2000).
26. E. P. Ivanova and A. L. Ivanov, Quantum Electron. (Moscow) **34**, 1013 (2004).
27. A. L. Gogava and E. P. Ivanova, Opt. Spektrosk. **59**, 1310 (1985) [Opt. Spectrosc. **59**, 785 (1985)].
28. E. P. Ivanova and A. V. Gulov, At. Data Nucl. Data Tables **49**, 1 (1991).
29. J. H. Scofield and B. J. MacGowan, Phys. Scr. **46**, 361 (1992).
30. G. D. Enright, D. M. Villeneuve, J. Dunn, *et al.*, J. Opt. Soc. Am. B **8**, 2047 (1991).
31. S. B. Healy, K. A. Janulewiez, and G. J. Pert, Opt. Commun. **144**, 24 (1997).
32. V. I. Derzhiev, A. G. Zhidkov, and S. I. Yakovlenko, *Emission of Ions in a Nonequilibrium Dense Plasma* (Énergoatomizdat, Moscow, 1986) [in Russian].
33. E. Fill, J. Quant. Spectrosc. Radiat. Transf. **39**, 489 (1988).
34. A. Klisnick, A. Carrillon, G. Jamelot, *et al.*, Proc. SPIE **3776**, 282 (1999).
35. A. N. Ryabtsev and S. S. Churilov, in *Spectroscopy of Multi-Charge Ions* (Nauka, Moscow, 1991), p. 76 [in Russian].
36. C. Chenais-Popovics, V. Malka, J.-C. Gathier, *et al.*, Phys. Rev. E **65**, 046418 (2002).
37. K. Boyer, B. D. Thompson, A. McPherson, and C. K. Rhodes, J. Phys. B: At. Mol. Opt. Phys. **27**, 4373 (1994).
38. T. Ditmire, P. K. Patel, R. A. Smith, *et al.*, J. Phys. B: At. Mol. Opt. Phys. **31**, 2825 (1998); T. Ditmire, R. A. Smith, R. S. Marjoribanks, *et al.*, Appl. Phys. Lett. **71**, 166 (1997).
39. K. J. Whitney, A. Dasgupta, and P. E. Pulsifer, Phys. Rev. E **50**, 468 (1994).
40. D. Benredjem, A. Sureau, and C. Möller, Inst. Phys. Conf. Ser., No. 151, 333 (1996).
41. B. E. Lemoff, C. P. J. Barty, and S. E. Harris, Opt. Lett. **19**, 569 (1994).
42. L. N. Ivanov, E. P. Ivanova, and L. V. Knight, Phys. Lett. A **206**, 89 (1995).
43. L. N. Ivanov, E. P. Ivanova, and L. V. Knight, Phys. Rev. A **48**, 4365 (1993).
44. E. P. Ivanova and I. P. Grant, J. Phys. B: At. Mol. Opt. Phys. **31**, 2871 (1998).
45. L. N. Ivanov, E. P. Ivanova, L. V. Knight, and A. G. Molchanov, Phys. Scr. **53**, 653 (1996).
46. Y. Abou-Ali, A. Demir, G. F. Tallent, *et al.*, J. Phys. B: At. Mol. Opt. Phys. **36**, 4097 (2003).
47. C. Jupen, U. Litzen, and E. Träbert, Phys. Lett. A **214**, 273 (1996).
48. E. P. Ivanova and A. V. Glushkov, J. Quant. Spectrosc. Radiat. Transf. **36**, 127 (1986).
49. E. P. Ivanova, A. L. Ivanov, N. A. Zinoviev, and L. V. Knight, Proc. SPIE **3735**, 266 (1999).
50. E. P. Ivanova and N. A. Zinoviev, J. Phys. IV **11**, 152 (2001).
51. E. P. Ivanova, AIP Conf. Proc. **641**, 247 (2002).
52. I. A. Belov, A. S. Ivanov, D. A. Ivanov, *et al.*, Pis'ma Zh. Tekh. Fiz. **25** (15), 89 (1999) [Tech. Phys. Lett. **25**, 630 (1999)].
53. A. G. Leonov, A. F. Pal', A. N. Starostin, and A. V. Filippov, Pis'ma Zh. Éksp. Teor. Fiz. **77**, 577 (2003) [JETP Lett. **77**, 482 (2003)].

Translated by V. Astakhov

Journal of Experimental and Theoretical Physics, Vol. 100, No. 5, 2005, pp. 857–866.
From Zhurnal Éksperimental'noĭ i Teoreticheskoĭ Fiziki, Vol. 127, No. 5, 2005, pp. 973–983.
Original English Text Copyright © 2005 by Openov.

ATOMS, MOLECULES, OPTICS

Auxiliary-Level-Assisted Operations with Charge Qubits in Semiconductors[¶]

L. A. Openov
Moscow Engineering Physics Institute, Moscow, 115409 Russia
e-mail: opn@supercon.mephi.ru

Received October 22, 2004

Abstract—We present a new scheme for rotations of a charge qubit associated with a singly ionized pair of donor atoms in a semiconductor host. The logical states of such a qubit proposed recently by Hollenberg *et al.* [16] are defined by the lowest two energy states of the remaining valence electron localized around one or another donor. We show that an electron located initially at one donor site can be transferred to another donor site via an auxiliary molecular level formed upon the hybridization of the excited states of two donors. The electron transfer is driven by a single resonant microwave pulse in the case where the energies of the lowest donor states coincide or by two resonant pulses in the case where they differ from each other. Depending on the pulse parameters, various one-qubit operations—including the phase gate, the NOT gate, and the Hadamard gate—can be realized in short times. Decoherence of an electron due to the interaction with acoustic phonons is analyzed and shown to be weak enough for coherent qubit manipulation to be possible, at least in proof-of-principle experiments on one-qubit devices. *© 2005 Pleiades Publishing, Inc.*

1. INTRODUCTION

Solid-state systems are of great interest in search for a scalable quantum computer technology. Several schemes for solid-state quantum information processing have been proposed [1–3]. For example, the coherent control of superconducting qubits, [4] and their coupling [5] have been demonstrated, the qubits being encoded in the states of a Cooper-pair box. One promising area of current investigation is concerned with the semiconductor-based devices. In Kane's proposal [6], the qubits are defined by long-lived nuclear spins of phosphorous dopants in a silicon host. They are manipulated by external surface gates and radio-frequency magnetic fields. While long coherence times of nuclear spins make the Kane scheme very promising, the single-spin measurement remains a significant challenge [7]. This also concerns an alternative Si : P architecture that uses electron spin states as qubits [8].

Along with spin-based qubits, the charged-based qubits in semiconductors are currently discussed as well. The logical states of a charge semiconductor qubit may be formed by, e.g., the ground state and the excited state of the electron in a single quantum dot [1] or the spatially separated states of the electron in two different quantum dots [9–13]. Although decoherence of the charge-based qubits is rather strong [14, 15], the charge qubits are nevertheless believed to be realizable at the present technological level due to their short operation times [16]. One of the obstacles to the practical realization of scalable quantum computation in the system of quantum dots is that it is extremely difficult, if at all possible, to manufacture a set of quantum dots with identical or at least predetermined characteristics each. This complicates the issue, introducing errors into the operations with qubits [17] and resulting in a need for numerous ancillary corrective gates. In this respect, it would be more reasonable to use natural atoms (instead of "artificial" ones) as the localization centers for the electrons carrying the quantum information. Recent advances in manipulation with single atoms on the solid surface [18] and atomically precise placement of single dopants in semiconductors [19, 20] allow construction of rather complex solid-state atomic architectures.

Recently, Hollenberg *et al.* proposed a two-atom charge-qubit scheme [16] and reported the first results on its fabrication and characterization [20] in the case of phosphorous dopants in silicon. In that scheme, the buried donor charge qubit consists of two dopant atoms about 50 nm apart in a semiconductor host. One of the donors is singly ionized. The logical states are formed by the lowest two energy states of the remaining valence electron localized at the left or the right donor, $|0\rangle = |L\rangle$ and $|1\rangle = |R\rangle$, see Fig. 1. The qubit is controlled by the surface electrodes through adiabatic variations of the donor potentials. Initialization and readout of the qubit are facilitated by a single-electron transistor. The coupling of such qubits via the Coulomb interaction, in principle, allows realizing the conditional two-qubit gates [16].

It was shown in [16] that although the coherence time $\tau_{coh} \sim 1$ ns for charge-based qubits is much shorter than for their spin-based counterparts, the corresponding gate operations times are also shorter, of the order

---

[¶] This article was submitted by author in English.

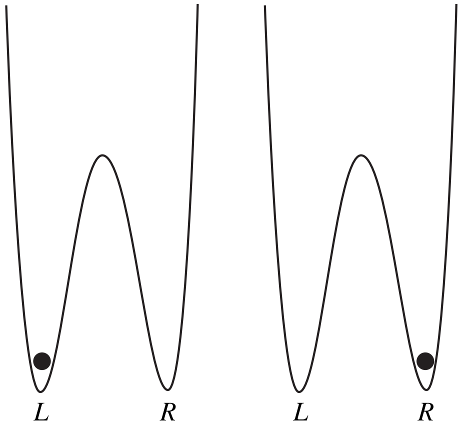

Fig. 1. Logical states $|0\rangle = |L\rangle$ and $|1\rangle = |R\rangle$ of the buried donor charge qubit.

of $\tau_{\mathrm{op}} \sim 50$ ps. We note, however, that the ratio $\tau_{\mathrm{op}}/\tau_{\mathrm{coh}} \sim 10^{-1}$ seems to be insufficiently small for the fault-tolerant scalable quantum computation being possible [21]. In this paper, we propose an alternative scheme for operations with buried donor charge qubits, instead of applying biases to the surface gates. Our scheme is based on the effect of electron transfer between the lowest states localized at different donors upon the influence of a resonant pulse [9] or two resonant pulses [22]. Such a transfer occurs via an excited molecular level of the double-donor system and allows implementation of different one-qubit rotations. The operation times can be made orders of magnitude shorter than in the original proposal [16].

The paper is organized as follows. In Section 2, we describe a three-level model for the resonant electron transfer between the donors and briefly discuss the relevant one-electron states of a P_2^+ molecular ion in Si. We next present the analytical solution for the unitary electron evolution under the influence of microwave pulses. In Section 3, we show that in the P_2^+ : Si system, it is possible to realize various one-qubit operations, including the NOT gate, the phase gate, and the Hadamard transformation. Decoherence due to the electron interaction with acoustic phonons is studied in Section 4. Discussion of the results is given in Section 5.

2. MODEL FOR THE RESONANT ELECTRON TRANSFER

We consider a singly ionized pair of phosphorous atoms embedded in silicon. The remaining valence electron is described by the Hamiltonian

$$\hat{H}_0 = \sum_n E_n |\chi_n\rangle\langle\chi_n|, \qquad (1)$$

where E_n and $|\chi_n\rangle$ are the respective one-electron eigenenergies and eigenstates of the molecular ion P_2^+ : Si. In general, to calculate the energy spectrum and the wavefunctions $\langle \mathbf{r}|\chi_n\rangle$ of the single-electron/double-donor system beneath the surface, one should account for the conduction-band anisotropy, the intervalley terms, the surface effects, the potentials induced in the substrate by the gate voltages, etc. This necessarily requires numerical calculations (see, e.g., [23]). We note that although the edge of the conduction band of bulk silicon has six degenerate minima, it has been shown both experimentally [24] and theoretically [25] that substitutional impurities break the translational symmetry of the crystal lattice, thus lifting the degeneracy. The spacing between energy levels in the ground-state and excited-state multiplets may be further increased by appropriately choosing the gate potentials. Anyway, to quantify the structure of the P_2^+ : Si energy spectrum and wavefunctions, one should make sophisticated numerical calculations for a specific donor configuration. In this paper, however, we restrict ourselves to a semiquantitative consideration based on an isotropic effective mass approximation [26] that allows an explicit analytical solution. The problem then reduces to that for a hydrogen-like molecular ion with an effective Bohr radius of $a_B^* \approx 3$ nm and an effective Hartree unit of energy $E^* = e^2/\varepsilon a_B^* \approx 40$ meV, where $\varepsilon \approx 11.7$ is the dielectric constant for silicon.[1] The energy spectrum of the H_2^+ ion for different atomic separations is known with high accuracy [28].

We approximate the Hamiltonian $\hat{H}_0$ in Eq. (1) by the reduced three-level Hamiltonian

$$\hat{H}_r = E_1|\chi_1\rangle\langle\chi_1| + E_2|\chi_2\rangle\langle\chi_2| + E_{TR}|\chi_{TR}\rangle\langle\chi_{TR}|, \qquad (2)$$

where $|\chi_1\rangle$ and $|\chi_2\rangle$ are the lowest molecular states $1s\sigma_g$ and $2p\sigma_u$, whose respective wavefunctions are, respectively, symmetric and antisymmetric about the midpoint of the line joining the two donors (Fig. 2), and $|\chi_{TR}\rangle$ is one of the excited molecular states discussed below. It is convenient to pass from the states $|\chi_1\rangle$ and $|\chi_2\rangle$ delocalized over the P_2^+ : Si ion to the states

$$|L\rangle = \frac{|\chi_1\rangle + |\chi_2\rangle}{\sqrt{2}} \quad \text{and} \quad |R\rangle = \frac{|\chi_1\rangle - |\chi_2\rangle}{\sqrt{2}}$$

localized at the left and the right donor, respectively. For donor separations $R_d \gg a_B^*$, wavefunctions $\langle \mathbf{r}|L\rangle$

---

[1] We note that the isotropic effective mass approximation gives the value $E = -E^*/2 \approx -20$ meV for the ground-state energy of a single phosphorous donor in silicon, which is about half the experimentally observed value $E = -45.5$ meV (see, e.g. [27]).

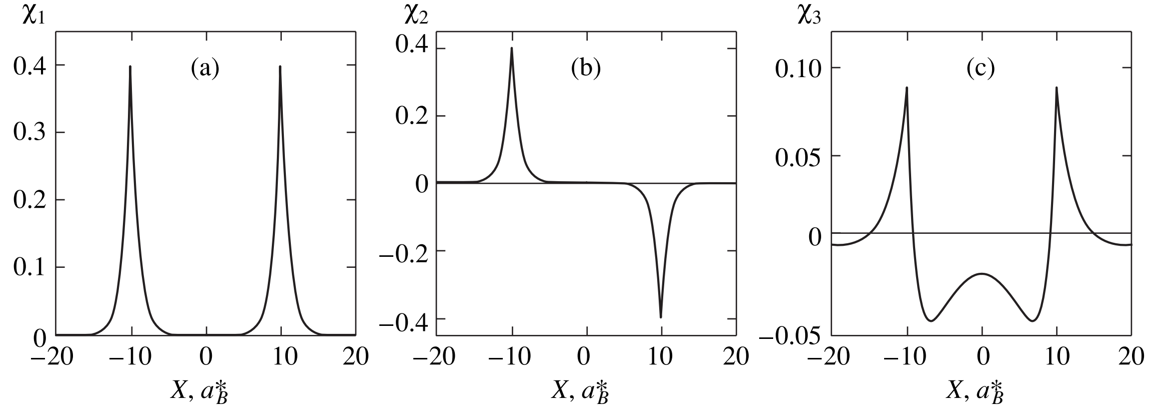

Fig. 2. One-electron wavefunctions of the lowest two states, $1s\sigma_g$ (a) and $2p\sigma_u$ (b), and the excited state $3d\sigma_g$ (c) of the molecular ion P_2^+ : Si in the isotropic effective mass approximation. The x coordinate is along the line joining the two donors. The donor separation is $R_d = 20a_B^*$. The symmetric and antisymmetric linear superpositions of the $1s\sigma_g$ and $2p\sigma_u$ states correspond to the respective $1s$ atomic states $|L\rangle$ and $|R\rangle$ localized at the left and the right donor. They form the qubit logical states $|0\rangle = |L\rangle$ and $|1\rangle = |R\rangle$. The excited state $3d\sigma_g$ is an auxiliary ("transport") state needed to transfer an electron between $|L\rangle$ and $|R\rangle$ states under the influence of external electromagnetic field.

and $\langle \mathbf{r}|R\rangle$ are almost indistinguishable from the one-electron $1s$ orbitals of the corresponding donor atoms.

The states $|L\rangle$ and $|R\rangle$ form the respective qubit logical states $|0\rangle$ and $|1\rangle$. These states are well defined if the thermal energy k_BT is much lower than the differences $\Delta E_{31} = E_3 - E_1$ and $\Delta E_{32} = E_3 - E_2$ between the energy E_3 of the excited molecular state $|\chi_3\rangle$ and the respective energies E_1 and E_2. At $R_d \gg a_B^*$, we have $E_1 \approx E_2 \approx -E^*/2$ and $E_3 \approx -E^*/8$, and therefore $\Delta E_{31} \approx \Delta E_{32} \approx 3E^*/8 \approx 15$ meV. Because the states $|L\rangle$ and $|R\rangle$ are not the exact eigenstates of the Hamiltonian $\hat{H}_r$, the initial qubit state $|\Psi(0)\rangle = \alpha|L\rangle + \beta|R\rangle$ evolves with time in the absence of external fields as

$$|\Psi(t)\rangle = \exp\left(-\frac{i\hat{H}_r t}{\hbar}\right)|\Psi(0)\rangle = \exp\left(-\frac{iE_1 t}{\hbar}\right) \times\left\{|\Psi(0)\rangle + i(\beta-\alpha)\exp\left(-\frac{i\Delta E_{21}t}{2\hbar}\right) \times \sin\left(\frac{\Delta E_{21}t}{2\hbar}\right)[|L\rangle - |R\rangle]\right\}, \tag{3}$$

where $\Delta E_{21} = E_2 - E_1$. We note that at $t \ll t_0 = \hbar/\Delta E_{21}$, the initial qubit state remains almost unchanged (not counting the common phase). Because the value of ΔE_{21} is exponentially small at $x = R_d/a_B^* \gg 1$ [29, 30],

$$\frac{\Delta E_{21}}{E^*} = 4xe^{-x-1}\left[1 + \frac{1}{2x} + O\left(\frac{1}{x^2}\right)\right], \tag{4}$$

the period $t_0 \sim \hbar/\Delta E_{21}$ that it takes for the qubit state to change is rather long, $t_0 > 1$ μs at $R_d > 60$ nm. In what follows, we consider the processes occurring in time intervals much shorter than t_0 and hence ignore the off-diagonal term $[-(\Delta E_{21}/2)|L\rangle\langle R| + \text{H.c.}]$ in $\hat{H}_r$ that gives rise to the electron tunneling $|L\rangle \longleftrightarrow \langle R|$. Then Hamiltonian (2) takes the form

$$\hat{H}_r \approx \frac{E_1 + E_2}{2}[|L\rangle\langle L| + |R\rangle\langle R|] + E_{TR}|\chi_{TR}\rangle\langle\chi_{TR}|, \tag{5}$$

where $(E_1 + E_2)/2 \approx E_1 \approx E_2$ at $R_d \gg a_B^*$. In the general case where the qubit is biased by gate voltages, the energies E_L and E_R of the respective lowest states localized at the left and the right donor differ from each other. In this case, the localized states are all better approximations to the energy eigenstates, and the Hamiltonian $\hat{H}_r$ becomes

$$\hat{H}_r \approx E_L|L\rangle\langle L| + E_R|R\rangle\langle R| + E_{TR}|\chi_{TR}\rangle\langle\chi_{TR}|. \tag{6}$$

We now let the buried donor charge qubit interact with an external electromagnetic field $\mathbf{E}(t)$. Then the Hamiltonian becomes

$$\hat{H}(t) = \hat{H}_r + \hat{V}(t), \tag{7}$$

where the interaction term $\hat{V}(t)$ is

$$\hat{V}(t) = \mathbf{E}(t)[\mathbf{d}_L|\chi_{TR}\rangle\langle L| + \mathbf{d}_R|\chi_{TR}\rangle\langle R| + \text{H.c.}], \tag{8}$$

with $\mathbf{d}_L = \langle\chi_{TR}| - e\mathbf{r}|L\rangle$ and $\mathbf{d}_R = \langle\chi_{TR}| - e\mathbf{r}|R\rangle$ being the electric dipole moments for the transitions $|L, R\rangle \longleftrightarrow |\chi_{TR}\rangle$ between the respective localized states $|L\rangle$ and $|R\rangle$ and one of the excited molecular states $|\chi_{TR}\rangle$ delocalized over the double-donor system. For definiteness, we choose this state to be the third one-electron state $|\chi_3\rangle$ of the molecular ion P_2^+ : Si. At $E_L = E_R$ and $R_d/a_B^* > 6$, this is the $3d\sigma_g$ state whose wavefunction $\langle \mathbf{r}|\chi_3\rangle$ is symmetric about the midpoint of the line joining the two donors and has its maxima at the donor locations [31], see Fig. 2. If the donors are arranged along the x axis, the state $|\chi_3\rangle$ is formed upon the hybridization of $|2S\rangle_{L,R}$ and $|2P_x\rangle_{L,R}$ atomic states of the donors, and the wave function $\langle \mathbf{r}|\chi_3\rangle$ in the vicinity of the left/right donor is equal to $[\langle \mathbf{r}|2S\rangle_{L,R} \mp \langle \mathbf{r}|2P_x\rangle_{L,R}]/2$ at $R_d \gg a_B^*$. We note that for such a choice of the state $|\chi_3\rangle$, the electric field should have a nonzero x component in order that $\mathbf{d}_{L,R} \neq 0$.

We consider two cases: (a) $E_L = E_R \approx E_1$ and (b) $E_L \neq E_R$, the desired value of the difference $E_R - E_L$ being discussed below. In case (a), we suppose $\mathbf{E}(t)$ to oscillate at a frequency $\omega = (E_{TR} - E_{L,R})/\hbar$,

$$\mathbf{E}(t) = \mathbf{E}_0(t)\cos\omega t, \tag{9}$$

where $\mathbf{E}_0(t)$ is the slowly varying envelope of the field. Using of the resonant approximation,[2] i.e., omitting the rapidly oscillating terms with the frequencies $\pm(\omega + E_{TR}/\hbar - E_{L,R}/\hbar)$ from the Hamiltonian, we have

$$\hat{V}(t) = \frac{1}{2}e^{-i\omega t}[\lambda_L(t)|\chi_{TR}\rangle\langle L| + \lambda_R(t)|\chi_{TR}\rangle\langle R|] + \text{H.c.}, \tag{10}$$

where $\lambda_{L,R}(t) = \mathbf{E}_0(t)\mathbf{d}_{L,R}$. In case (b), the field $\mathbf{E}(t)$ has two components oscillating at the frequencies $\omega_L = (E_{TR} - E_L)/\hbar$ and $\omega_R = (E_{TR} - E_R)/\hbar$,

$$\mathbf{E}(t) = \mathbf{E}_{01}(t)\cos(\omega_L t) + \mathbf{E}_{02}(t)\cos(\omega_R t + \phi), \tag{11}$$

where ϕ is the phase shift between the two components. In the resonant approximation,[2] we have

$$\begin{aligned}\hat{V}(t) &= \frac{1}{2}\exp(-i\omega_L t)\lambda_L(t)|\chi_{TR}\rangle\langle L| \\ &+ \frac{1}{2}\exp(-i\omega_R t - i\phi)\lambda_R(t)|\chi_{TR}\rangle\langle R| + \text{H.c.},\end{aligned} \tag{12}$$

where $\lambda_{L,R}(t) = \mathbf{E}_{01,2}(t)\cdot\mathbf{d}_{L,R}$. In this paper, we restrict ourselves to the rectangular pulse shape, and therefore $\mathbf{E}_0(t)$ in Eq. (9) and both $\mathbf{E}_{01}(t)$ and $\mathbf{E}_{02}(t)$ in Eq. (11) are constant at $0 < t < \tau_{\text{op}}$ and zero elsewhere.

It is straightforward to solve the nonstationary Schrödinger equation for the state vector $|\Psi(t)\rangle$,

$$i\hbar\frac{\partial|\Psi(t)\rangle}{\partial t} = \hat{H}(t)|\Psi(t)\rangle, \tag{13}$$

with the Hamiltonian $\hat{H}(t)$ in Eq. (7) given by Eqs. (5) and (10) in case (a) or Eqs. (6) and (12) in case (b), and to find the coefficients $C_L(t)$, $C_R(t)$, and $C_{TR}(t)$ in the expansion of $|\Psi(t)\rangle$ in terms of the states $|L\rangle$, $|R\rangle$, and $|\chi_{TR}\rangle$,

$$\begin{aligned}|\Psi(t)\rangle &= C_L(t)\exp\left(-\frac{iE_Lt}{\hbar}\right)|L\rangle \\ &+ C_R(t)\exp\left(-\frac{iE_Rt}{\hbar}\right)|R\rangle + C_{TR}(t)\exp\left(-\frac{iE_{TR}t}{\hbar}\right)|\chi_{TR}\rangle,\end{aligned} \tag{14}$$

provided that $|\Psi(0)\rangle = \alpha|L\rangle + \beta|R\rangle$, where $|\alpha|^2 + |\beta|^2 = 1$. In case (a), we have

$$\begin{aligned}C_L(t) &= \alpha\left[1 - \frac{2|\lambda_L|^2}{|\lambda_L|^2 + |\lambda_R|^2}\sin^2\Omega t\right] \\ &- \beta\frac{2\lambda_L^*\lambda_R}{|\lambda_L|^2 + |\lambda_R|^2}\sin^2\Omega t, \\ C_R(t) &= -\alpha\frac{2\lambda_L\lambda_R^*}{|\lambda_L|^2 + |\lambda_R|^2}\sin^2\Omega t \\ &+ \beta\left[1 - \frac{2|\lambda_R|^2}{|\lambda_L|^2 + |\lambda_R|^2}\sin^2\Omega t\right], \\ C_{TR}(t) &= -i\frac{\alpha\lambda_L + \beta\lambda_R}{\sqrt{|\lambda_L|^2 + |\lambda_R|^2}}\sin 2\Omega t,\end{aligned} \tag{15}$$

where

$$\Omega = \frac{\sqrt{|\lambda_L|^2 + |\lambda_R|^2}}{4\hbar}. \tag{16}$$

In case (b), the coefficients $C_L(t)$, $C_R(t)$, and $C_{TR}(t)$ are also given by Eqs. (15) and (16) with the only exception that λ_R must be replaced by $\lambda_R\exp(-i\phi)$. From Eqs. (15) and (16), we can see that at $t = \tau_{\text{op}} = \pi k/2\Omega$ (hereafter, k is a positive integer), the coefficient C_{TR} vanishes, and hence the state vector $|\Psi(t)\rangle$ remains in the qubit subspace $\{|L\rangle, |R\rangle\}$ and $|C_L(\tau_{\text{op}})|^2 + |C_R(\tau_{\text{op}})|^2 = 1$. In particular, if $C_L(0) = 1$ and $C_R(0) = 0$, then $C_R(\tau_{\text{op}}) = 0$ and $C_R(\tau_{\text{op}}) = \pm 1$ at $\lambda_L = \mp\lambda_R$ and odd k, i.e., there is a complete population transfer $|L\rangle \longrightarrow |R\rangle$, see [9]. Thus, the auxiliary excited state $|\chi_{TR}\rangle$ plays the role of the "transport" state, in that it assists the qubit evolution by means of the electron transfer between the states $|L\rangle$ and

---

[2] The resonant approximation is valid if the absolute value of the detuning from resonance, $\hbar\delta = \hbar\omega - (E_{TR} - E_{L,R})$, is small compared to the spacing between the energy E_{TR} of the state $|\chi_{TR}\rangle$ and the energy E' of the state $|\chi'\rangle$ nearest to $|\chi_{TR}\rangle$. In the case where there are two components in $\mathbf{E}(t)$, the absolute values of both $\hbar\delta_L = \hbar\omega_L - (E_{TR} - E_L)$ and $\hbar\delta_R = \hbar\omega_R - (E_{TR} - E_R)$ should be small compared to $|E' - E_{TR}|$.

$|R\rangle$ as the pulse is on but remains unpopulated after the pulse is off.

3. QUBIT ROTATIONS

In this section, we show that the auxiliary-state-assisted electron transfer between the two donors allows various qubit rotations. In case (a), where the two donors in the molecular ion P_2^+ : Si are equivalent, i.e., $E_L = E_R$ and $|\lambda_L| = |\lambda_R|$, the qubit state $|\Psi(t)\rangle$ at the operation time τ_{op} remains unchanged,

$$|\Psi(\tau_{\mathrm{op}})\rangle = \exp\left(-\frac{iE_L\tau_{\mathrm{op}}}{\hbar}\right)|\Psi(0)\rangle \tag{17}$$

if $\tau_{\mathrm{op}} = \pi k/\Omega$, or changes into

$$|\Psi(\tau_{\mathrm{op}})\rangle = \pm\exp\left(-\frac{iE_L\tau_{\mathrm{op}}}{\hbar}\right)[\beta|L\rangle + \alpha|R\rangle] \tag{18}$$

if $\tau_{\mathrm{op}} = \pi(2k-1)/2\Omega$ and $\lambda_L = \mp\lambda_R$, see Eqs. (14) and (15). The latter corresponds to the quantum NOT operation.

Case (b) seems to be more realistic because of the different local atomic surroundings of the donors in the pair due to both the uncontrollable damage of the host upon ion implantation and the probabilistic variations in the path taken through the substrate by each implanted ion [20]. In addition, the surface gates can be used to intentionally tune E_L and E_R to the predetermined values. Moreover, one can change the values of λ_L and λ_R separately by changing the electric field amplitudes E_{01} and E_{02}. It follows from Eqs. (14) and (15) that the relative phase shift operation is implemented at $\tau_{\mathrm{op}} = \pi k/\Omega$,

$$\begin{aligned}|\Psi(\tau_{\mathrm{op}})\rangle &= \exp\left(-\frac{iE_L\tau_{\mathrm{op}}}{\hbar}\right)\\ &\times\left[\alpha|L\rangle + \beta\exp\left[-\frac{i(E_R-E_L)\tau_{\mathrm{op}}}{\hbar}\right]|R\rangle\right],\end{aligned} \tag{19}$$

while the value of $\tau_{\mathrm{op}} = \pi(2k-1)/2\Omega$ corresponds to realization of the quantum NOT operation,

$$|\Psi(\tau_{\mathrm{op}})\rangle = \pm\exp\left(-\frac{iE_L\tau_{\mathrm{op}}}{\hbar} - i\phi\right)[\beta|L\rangle + \alpha|R\rangle], \tag{20}$$

if $\lambda_L = \mp\lambda_R$ and $\phi = \pi n + (E_R - E_L)\tau_{\mathrm{op}}/2\hbar$ (hereafter, n is an integer), or to the Hadamard transformation,

$$|\Psi(\tau_{\mathrm{op}})\rangle = \pm\exp\left(-\frac{iE_L\tau_{\mathrm{op}}}{\hbar}\right)\left[\frac{\alpha+\beta}{\sqrt{2}}|L\rangle + \frac{\alpha-\beta}{\sqrt{2}}|R\rangle\right], \tag{21}$$

if $(E_R - E_L)\tau_{\mathrm{op}}/\hbar = 2\pi m$ (where m is a positive integer). Here, the plus sign corresponds to the values of $\phi = 2\pi n$ and $\lambda_L = -\lambda_L(\sqrt{2} - 1)$ or $\phi = \pi(2n + 1)$ and $\lambda_L = \lambda_R(\sqrt{2} - 1)$, and the minus sign corresponds to the values of $\phi = 2\pi n$ and $\lambda_L = \lambda_R(\sqrt{2} + 1)$ or $\phi = \pi(2n + 1)$ and $\lambda_L = -\lambda_R(\sqrt{2} + 1)$.

Therefore, various one-qubit operations can be implemented on the buried donor charge qubit through appropriate choices of the pulse frequency, phase, amplitude, and duration. Let us estimate the value of the operation time

$$\tau_{\mathrm{op}} \sim 1/\Omega \sim \hbar/|\lambda_{L,R}| \sim \hbar/ea_B^*E_0,$$

see Section 2. For the field amplitude $E_0 \sim 1$ V/cm, we have $\tau_{\mathrm{op}} \sim 1$ ns. An increase in the pulse intensity causes the value of τ_{op} to decrease to the picosecond time scale, such that the value of τ_{op} can be made orders of magnitude shorter than the period t_0 that it takes for the qubit state to change due to the direct electron tunneling $|L\rangle \longleftrightarrow |R\rangle$, see Section 2, as well as the operation times in the case where the qubit is manipulated by adiabatically varying the potentials of the surface gates [16]. We note that in case (b), the energies E_L and E_R should be sufficiently different from each other in order that all these operations could be implemented in short times to avoid decoherence, as discussed below. For example, at $\tau_{\mathrm{op}} \sim 1$ ps, we should have $E_R - E_L \sim 3$ meV.

4. DECOHERENCE EFFECTS

An uncontrolled interaction of the quantum system with its environment leads to entanglement between the states of the system and the environmental degrees of freedom. This disturbs the unitary evolution of the system and results in the loss of coherence. There are various sources of decoherence in solids. For the charge qubit considered in this paper, the decoherence due to the phonon emission/absorption processes was studied in [16, 26] and was found to be much weaker than the decoherence due to both Nyquist–Johnson voltage fluctuations in the surface electrodes and the $1/f$ noise from the background charge fluctuations. We note, however, that there are two mechanisms of the phonon-induced decoherence, which are caused by either the energy relaxation processes or the virtual-phonon dephasing processes. Which one of those mechanisms is dominant depends on the specific parameters of the quantum system and its environment, as well as on the operation times. Here, we show that the dephasing processes play a decisive role in limiting the fault tolerance of the buried donor charge qubit. For simplicity, we consider the qubit at zero temperature and assume isotropic acoustic phonons with the linear dispersion law $\omega_{\mathbf{q}} = sq$, where s is the speed of sound.

We first recall some general concepts concerning the transition probability for an electron moving in a time-dependent potential. If the electron, being initially in a state $|i\rangle$ of the discrete energy spectrum, interacts with the harmonic field

$$\hat{V}(t) = \hat{F}e^{-i\omega t} + \hat{F}^{+}e^{i\omega t}, \qquad (22)$$

then the probability amplitude of finding it in a state $|f\rangle$ at a time t is given by the following expression that results from first-order perturbation theory [32]:[3]

$$\begin{aligned} a_{i\to f}(\omega, t) &= F_{fi}\frac{\exp[-i(\omega_{if}+\omega)t]-1}{\hbar(\omega_{if}+\omega)} \\ &+ F_{if}^{*}\frac{\exp[-i(\omega_{if}-\omega)t]-1}{\hbar(\omega_{if}-\omega)}, \end{aligned} \qquad (23)$$

where $\omega_{if} = (E_i - E_f)/\hbar$. The common approach is to ignore the first term in Eq. (23) and use the expression

$$\lim_{t\to\infty}\frac{\sin^2(\epsilon t)}{\pi t\epsilon^2} = \delta(\epsilon), \qquad (24)$$

thus arriving at the so-called Fermi golden rule for the transition probability,

$$\begin{aligned} W_{i\to f}(\omega, t) &= |a_{i\to f}(\omega, t)|^2 \\ &\approx |F_{if}|^2\frac{4\sin^2[(\omega_{if}-\omega)t/2]}{\hbar^2(\omega_{if}-\omega)^2} \\ &\approx \frac{2\pi}{\hbar}|F_{if}|^2\delta(\hbar\omega_{if}-\hbar\omega)t \equiv \Gamma_{i\to f}(\omega)t, \end{aligned} \qquad (25)$$

where $\Gamma_{i\to f}(\omega)$ is the time-independent transition rate. The δ-function reflects the energy conservation, $\hbar\omega_{if} = \hbar\omega$, for such a transition.

The electron–phonon coupling in confined systems is described by the Hamiltonian

$$\hat{H}_{\text{el-ph}} = \sum_{\mathbf{q}}\lambda(\mathbf{q})\hat{\rho}(\mathbf{q})[\hat{b}_{\mathbf{q}}^{\dagger} + \hat{b}_{-\mathbf{q}}], \qquad (26)$$

where $\hat{b}_{\mathbf{q}}^{\dagger}$ and $\hat{b}_{\mathbf{q}}$ are the respective operators of creation and annihilation of a phonon with the wave vector $\mathbf{q}$, $\hat{\rho}(\mathbf{q}) = \int d\mathbf{r}\exp(i\mathbf{q}\cdot\mathbf{r})\hat{\rho}(\mathbf{r})$ is the Fourier transform of the electron density operator $\hat{\rho}(\mathbf{r}) = \sum_{mn}\Psi_m^{*}(\mathbf{r})\Psi_n(\mathbf{r})|m\rangle\langle n|$, and $\lambda(\mathbf{q})$ is the microscopic electron–phonon interaction matrix element, which can be expressed in terms of the deformation potential D and the density of the crystal ρ as

$$\lambda(\mathbf{q}) = qD\sqrt{\frac{\hbar}{2\rho\omega_{\mathbf{q}}V}}, \qquad (27)$$

with V being the normalizing volume. If harmonic field (22) is associated with a deformation phonon having the frequency $\omega_{\mathbf{q}}$, then, taking into account that the deformation fields produced by the phonons with different wave vectors are not correlated, we have the total transition rate [33][4]

$$\Gamma_{i\to f} = \frac{2\pi}{\hbar}\sum_{\mathbf{q}}|F_{if}(\mathbf{q})|^2\delta(\hbar\omega_{if}-\hbar\omega_{\mathbf{q}}), \qquad (28)$$

where

$$F_{if}(\mathbf{q}) = \lambda(\mathbf{q})\langle i|e^{i\mathbf{q}\cdot\mathbf{r}}|f\rangle. \qquad (29)$$

4.1. Decoherence during Adiabatic Variations of the Surface Gate Potentials

In the case where the buried donor charge qubit is controlled by the surface gates [16], such that the state vector $|\Psi(t)\rangle$ remains in the qubit subspace $\{|L\rangle, |R\rangle\}$ during the operation and the overlap $\langle L|R\rangle$ is negligibly small, Hamiltonian (26) can be written in the spin-boson form [34]

$$\hat{H}_{\text{el-ph}} = \hat{\sigma}_z\sum_{\mathbf{q}}g(\mathbf{q})[\hat{b}_{\mathbf{q}}^{\dagger} + \hat{b}_{-\mathbf{q}}], \qquad (30)$$

where $\hat{\sigma}_z = |L\rangle\langle L| - |R\rangle\langle R|$ and

$$g(\mathbf{q}) = \frac{\lambda(\mathbf{q})}{2}[\langle L|e^{i\mathbf{qr}}|L\rangle - \langle R|e^{i\mathbf{qr}}|R\rangle]. \qquad (31)$$

Since $\langle\mathbf{r}|L, R\rangle = (\pi a_B^{*3})^{-1/2}\exp(-|\mathbf{r} - \mathbf{r}_{L,R}|/a_B^{*})$ for 1s-orbitals, where $\mathbf{r}_{L,R}$ are the donor coordinates, we have [14]

$$g(\mathbf{q}) = -i\lambda(\mathbf{q})\frac{\sin(q_xR_d/2)}{[1+(qa_B^{*})^2/4]^2}, \qquad (32)$$

where q_x is the component of the phonon wavevector along the line joining the two donors, and we chose the origin of the coordinates in between the donors, such that $\mathbf{r}_{L,R} = \mp(R_d/2)\mathbf{e}_x$.

Fedichkin and Fedorov [14] have shown that at $T = 0$, decoherence upon implementing the phase operation emerges as pure dephasing, the electron density matrix being given by the general expression [35, 36]

---

[3] We note that Eq. (23) is applicable as long as $|a_{i\to f}(\omega, t)| \ll 1$.

[4] We note that at $T = 0$, there are no phonons in the sample, and hence only the second term in Eq. (22) is relevant for the electron–phonon interaction because the initial and final phonon states, $|i_{\text{ph}}\rangle$ and $|f_{\text{ph}}\rangle$, are the respective states $|0_{\mathbf{q}}\rangle\exp(-iE_0t)$ and $|1_{\mathbf{q}}\rangle\exp[-i(E_0 + \omega_{\mathbf{q}})t]$, where $E_0 = \sum_{\mathbf{q}}(\hbar\omega_{\mathbf{q}}/2)$, and hence $\langle f_{\text{ph}}|\hat{b}_{\mathbf{q}}^{+}|i_{\text{ph}}\rangle = \exp(i\omega_{\mathbf{q}}t)$.

$$\begin{pmatrix} \rho_{LL}(0) & \rho_{LR}(0)\exp\left[-B^2(t)+i\frac{(E_R-E_L)t}{\hbar}\right] \\ \rho_{RL}(0)\exp\left[-B^2(t)-i\frac{(E_R-E_L)t}{\hbar}\right] & \rho_{RR}(0) \end{pmatrix} \qquad (33)$$

with the spectral function

$$B^2(t) = \frac{8}{\hbar^2}\sum_{\mathbf{q}}\frac{|g(\mathbf{q})|^2}{\omega_{\mathbf{q}}^2}\sin^2\frac{\omega_{\mathbf{q}}t}{2}. \qquad (34)$$

There is no relaxation in this case because for the phase operation to be implemented, energies E_L and E_R must be sufficiently different from each other [14], so that the basis $\{|L\rangle, |R\rangle\}$ coincides with the energy basis of the electron in the double donor system and electron term (6) commutes with interaction term (30) in the Hamiltonian. As a result, the diagonal elements of the density matrix remain unchanged. On the other hand, decoherence upon implementing the quantum NOT operation (where $E_L = E_R$ and the energy basis of the electron is formed by states $|\chi_{1,2}\rangle = [|L\rangle \pm |R\rangle]/\sqrt{2}$, see Section 2) was suggested to be caused by relaxation [14], such that both off-diagonal and diagonal elements of the density matrix decrease exponentially with time, the relaxation rate $\Gamma_{2\to 1}$ (see Eq. (28)) being [14, 26]

$$\Gamma_{2\to 1} = \frac{D^2}{4\pi\rho\hbar s^2}\frac{q_{21}^3}{[1+(q_{21}a_B^*)^2/4]^4} \times\left(1-\frac{\sin(q_{21}R_d)}{q_{21}R_d}\right), \qquad (35)$$

where $q_{21} = \Delta E_{21}/s\hbar$, see Eq. (4).

We note, however, that approximation (25) for $W_{i\to f}(\omega, t)$ and, accordingly, Eq. (28) for $\Gamma_{i\to f}$ are valid if the time t is sufficiently long, see Eq. (24). To quantify the applicability of this approximation, we analyze the more general expression for $W_{i\to f}(t)$ that follows from Eq. (25),

$$W_{i\to f}(t) = \frac{4}{\hbar^2}\sum_{\mathbf{q}}|F_{if}(\mathbf{q})|^2\frac{\sin^2[(\omega_{if}-\omega_{\mathbf{q}})t/2]}{(\omega_{if}-\omega_{\mathbf{q}})^2}. \qquad (36)$$

We can roughly distinguish two phonon contributions to $W_{i\to f}(t)$, one being from the "resonant component," i.e., from the δ-function-like peak of $\sin^2[(\omega_{if} - \omega_{\mathbf{q}})t/2]/(\omega_{if} - \omega_{\mathbf{q}})^2$ as a function of q at $q = q_{if} = \omega_{if}/s$, with a height of $t^2/4$ and a width of $\sim 1/st$, and the other from the remaining "nonresonant background" of the phonon spectrum. The former can be estimated as

$$W^{(1)}_{i\to f}(t) \sim \frac{\nu q_{if}^2}{\hbar^2 s}|F_{if}(q_{if})|^2 t, \qquad (37)$$

and the latter as

$$W^{(2)}_{i\to f}(t) \sim \frac{\nu\Delta q}{\hbar^2 s^2}|F_{if}(q_{\max})|^2 \qquad (38)$$

at $q_{if} \ll q_{\max}$, and

$$W^{(2)}_{i\to f}(t) \sim \frac{\nu\Delta q}{\hbar^2 s^2}\left(\frac{q_{\max}}{q_{if}}\right)^2|F_{if}(q_{\max})|^2 \qquad (39)$$

at $q_{if} \gg q_{\max}$, where $q_{\max}$ is the wave vector at which the function $|F_{if}(q)|^2$ has a maximum and Δq is a characteristic width of $|F_{if}(q)|^2$ in the maximum. The specific values of Δq, $q_{\max}$, and $F_{if}(q_{\max})$ depend on the specific type of wavefunctions $\langle \mathbf{r}|i\rangle$ and $\langle \mathbf{r}|f\rangle$ in the matrix element $\langle i|\exp(i\mathbf{q}\cdot\mathbf{r})|f\rangle$. Next, if, e.g., $q_{if} \ll q_{\max}$ and we are interested in the transition probability $W_{i\to f}(t)$ at a moment of time t such that $sq_{if}^2|F_{if}(q_{if})|^2 t \ll \Delta q|F_{if}(q_{\max})|^2$, then $W^{(1)}_{i\to f}(t) \ll W^{(2)}_{i\to f}(t)$, and hence the Fermi golden rule appears to be broken [37, 38]. This is due to the violation of the energy conservation at short times [32].

Inspection of the phonon-induced transitions between the states $|\chi_{1,2}\rangle = [|L\rangle \pm |R\rangle]/\sqrt{2}$ of the double-donor system with $E_L = E_R$ and the donor separation $R_d \gg a_B^*$ (these transitions are relevant for decoherence during the implementation of the NOT operation [14]) provides an illustrative example of the departure from the Fermi golden rule. In this case,

$$\langle 2|e^{i\mathbf{q}\cdot\mathbf{r}}|1\rangle = [\langle L|e^{i\mathbf{q}\cdot\mathbf{r}}|L\rangle - \langle R|e^{i\mathbf{q}\cdot\mathbf{r}}|R\rangle]/2,$$

and hence $F_{21}(\mathbf{q}) = g(\mathbf{q})$, see Eq. (32), and the resonant component of the transition probability is $W^{(1)}_{2\to 1}(t) \sim q_{21}^3 D^2 t/\rho\hbar s^2$, in accordance with the value of the relaxation rate $\Gamma_{2\to 1}$ given by Eq. (35). Since the value of $q_{21} = \Delta E_{21}/\hbar s$ decreases exponentially with R_d, see

Eq. (4), the value of $\Gamma_{2\to 1}$ decreases exponentially as well, going below 10^3 s^{-1} at $R_d/a_B^* > 10$ (see Fig. 5 in [26]). On the other hand, because $q_{21} \ll q_{\max} \sim 1/a_B^*$, we have $W_{2\to 1}^{(2)}(t) \sim D^2/\rho\hbar s^3 a_B^{*2}$ from Eq. (38). More accurate calculations result in $W_{2\to 1}^{(2)}(t) = B^2(t)/2$ see Eq. (34). If the operation time τ_{op} is long compared to the phonon transit time, a_B^*/s (≈0.3 ps for P_2^+ : Si), it follows from Eq. (34) (see [14]) that

$$B^2(\tau_{\text{op}}) = \frac{D^2}{3\pi^2\rho\hbar s^3 a_B^{*2}}, \tag{40}$$

and therefore spectral function (34) appears to be a material constant, being about 6×10^{-3} for the phosphorous donors in silicon [14], where $D = 3.3$ eV, $s = 9 \times 10^5$ cm/s, and $\rho = 2.33$ g/cm^3. Hence, $W_{2\to 1}^{(2)}(t) \gg W_{2\to 1}^{(1)}(t)$ at $R_d/a_B^* = 10$ and $t \ll \tilde{t} \approx 3 \times 10^{-6}$ s, the time $\tilde{t}$ being exponentially longer for larger values of R_d/a_B^*, and in any case longer than the operation time τ_{op}, see Section 3.

Therefore, contrary to suggestions [14, 26] that the phonon-induced decoherence in the case of the NOT operation is determined by the value of the relaxation rate $\Gamma_{2\to 1}$ given by Eq. (35), we see that at sufficiently short operation times, decoherence in the cases of both phase and NOT operations is determined by the same spectral function $B^2(t)$, see Eq. (34). The distinction between the two cases is that the diagonal elements of the density matrix remain unchanged in the case of the phase operation because there is no relaxation, while they decay exponentially (along with the off-diagonal matrix elements) in the case of the NOT operation [14].

4.2. Decoherence during the Auxiliary-State-Assisted Operations

Because the excited "transport" level $|TR\rangle$ becomes temporarily populated during the resonant-pulse operations on the P_2^+ : Si qubit, the phonon-induced electron transitions $|TR\rangle \longleftrightarrow |L, R\rangle$ and $|TR\rangle \longleftrightarrow |\chi_{1,2}\rangle$ can have a detrimental effect on the qubit evolution, along with the transitions $|L\rangle \longleftrightarrow |R\rangle$ and $|\chi_1\rangle \longleftrightarrow |\chi_2\rangle$ studied above. We now clarify which type of the phonon-induced electron transitions ("resonant" or "nonresonant") is dominant in this case and estimate the transition probability. We follow the line of reasoning outlined above and start with calculations of the matrix elements $\langle TR|\exp(i\mathbf{q}\cdot\mathbf{r})|L, R\rangle$. For our choices of the "transport" state $|TR\rangle = |\chi_3\rangle$ and the double donor orientation (see Section 2) at $R_d \gg a_B^*$, we have $|TR\rangle \approx [|2S\rangle_L - |2P_x\rangle_L + |2S\rangle_R + |2P_x\rangle_R]/2$, where

$$\langle\mathbf{r}|2S\rangle_{L,R} = \frac{1}{\sqrt{8\pi a_B^{*3}}}\left(1 - \frac{|\mathbf{r} - \mathbf{r}_{L,R}|}{2a_B^*}\right)\exp\left(-\frac{|\mathbf{r} - \mathbf{r}_{L,R}|}{2a_B^*}\right),$$

$$\langle\mathbf{r}|2P_x\rangle_{L,R} = \frac{1}{\sqrt{32\pi a_B^{*5}}}(x - x_{L,R})\exp\left(-\frac{|\mathbf{r} - \mathbf{r}_{L,R}|}{2a_B^*}\right).$$

Neglecting the exponentially small overlap between the localized atomic-like orbitals centered at different donors, we have

$$\langle TR|e^{i\mathbf{q}\cdot\mathbf{r}}|L, R\rangle = 2\sqrt{2}\frac{(qa_B^*)^2 \mp 3i(q_x a_B^*)/2}{[9/4 + (qa_B^*)^2]^3}\exp\left(\mp\frac{iq_x R}{2}\right). \tag{41}$$

Depending on the relative values of E_L and E_R, the lowest energy eigenstates of P_2^+ : Si are either $|L\rangle$ and $|R\rangle$ (if $E_L \neq E_R$) or χ_1 and χ_2 (if $E_L = E_R$), and therefore, in order to find the probability $W_{TR}(t)$ of the electron escape from the "transport" state at $T = 0$, we must add the respective probabilities of the $|TR\rangle \longrightarrow |L\rangle$ and $|TR\rangle \longrightarrow |R\rangle$ or $|TR\rangle \longrightarrow |\chi_1\rangle$ and $|TR\rangle \longrightarrow |\chi_2\rangle$ electron transitions. If the value of $E_R - E_L$ is much less than the difference between E_{TR} and $E_{L,R}$, then we have the same result in both cases, and hence $W_{TR}(t)$ is given by Eq. (36), where now $\omega_{if} \approx \Delta E_{31}/\hbar \approx 3E^*/8\hbar$ is independent of R_d at $R_d \gg a_B^*$, and

$$|F_{if}(\mathbf{q})|^2 = 16\frac{(qa_B^*)^4 + 9(q_x a_B^*)^2/4}{[9/4 + (qa_B^*)^2]^6}|\lambda(\mathbf{q})|^2. \tag{42}$$

Taking into account that

$$q_{if} a_B^* = \frac{\omega_{if} a_B^*}{s} \approx \frac{3e^2}{8\varepsilon\hbar s} \approx 8 \gg q_{\max} a_B^* \sim 1$$

and using Eq. (36), it is straightforward to derive the following expressions for the respective probabilities of the "resonant" and "nonresonant" transitions:

$$W_{TR}^{(1)}(t) \approx \frac{8D^2}{\pi\rho\hbar s^2 a_B^{*3}}(q_{if} a_B^*)^5 \frac{3/4 + (q_{if} a_B^*)^2}{[9/4 + (q_{if} a_B^*)^2]^6} t \tag{43}$$

and

$$W_{TR}^{(2)}(t) \approx \frac{176D^2}{3645\pi^2\rho\hbar s^3 (a_B^*)^2 (q_{if} a_B^*)^2}. \tag{44}$$

It follows from Eqs. (43) and (44) that $W_{TR}^{(1)}(t) = \Gamma_{TR}t$, where $\Gamma_{TR} \approx 3 \times 10^7\ \mathrm{s}^{-1}$, and $W_{TR}^{(2)}(t) \approx 10^{-5}$, and hence the "resonant" transitions are dominant at $t > 0.3$ ps.

We now check what states among those involved in the auxiliary-state-assisted qubit evolution are most sensitive to phonon-induced decoherence. As we have seen above, decoherence of the low-energy states $|L\rangle$ and $|R\rangle$ (or $|\chi_1\rangle$ and $|\chi_2\rangle$) is quantified by the error rate [14], i.e., the error generated during the operation time, $D(t) = B^2(t)/2 \approx 3 \times 10^{-3}$. This value is greater than $W_{TR}^{(2)}(t)$ but less than $W_{TR}^{(1)}(t)$ at $t > 10^{-10}$ s, where the processes of the spontaneous phonon emission by an electron temporarily occupying the "transport" level begin to prevail. Hence at $\tau_{\mathrm{op}} < 100$ ps, the error rate does not exceed a value of $D(\tau_{\mathrm{op}}) \approx 3 \times 10^{-3}$.

5. DISCUSSION

Fast auxiliary-state-assisted evolution of the double-donor charge qubit driven by the resonant electromagnetic field allows implementation of various one-qubit rotations in very short operation times $\tau_{\mathrm{op}} < 100$ ps, thus minimizing the unwanted decoherence effects. At such times, the error rate due to acoustic phonons is $D(\tau_{\mathrm{op}}) \approx 3 \times 10^{-3}$ at $T = 0$. At finite temperatures, such that $k_BT > \hbar\omega_0$, where $\hbar\omega_0 = \hbar s/a_B^* \approx 2$ meV for dephasing processes and "nonresonant" emission/absorption transitions, and $\hbar\omega_0 = |E_i - E_f|$ for the "resonant" $|i\rangle \longleftrightarrow |f\rangle$ transitions, the error rate increases by a factor of $\sim k_BT/\hbar\omega_0$.

The strongest increase in the error rate at $T \neq 0$ occurs if the two donors in the molecular ion P_2^+ : Si are equivalent, because the energies E_L and E_R of the lowest localized states $|L\rangle$ and $|R\rangle$ are then equal to each other, and the difference $E_2 - E_1$ between the eigenenergies of the two lowest delocalized molecular states $|\chi_1\rangle$ and $|\chi_2\rangle$ is exponentially small at large donor separations, e.g., $E_2 - E_1 \approx 10^{-6}$ meV at $R_d = 60$ nm, see Eq. (4). To weaken the decoherence, it would be reasonable to use the surface gates in order to increase the difference $E_R - E_L$ up to $E_R - E_L \sim 1$ meV such that the energy basis of the electron be formed by the states $|L\rangle$ and $|R\rangle$ instead of the states $|\chi_1\rangle$ and $|\chi_2\rangle$. In this case, the electromagnetic field should have two components driving the electron transitions $|L\rangle \longleftrightarrow |TR\rangle$ and $|R\rangle \longleftrightarrow |TR\rangle$ between the states $|L, R\rangle$ and the auxiliary "transport" state $|TR\rangle$.

At $T \neq 0$, the processes of the phonon absorption by an electron temporarily occupying the "transport" state also contribute to decoherence. For our choice of the transport state, $|TR\rangle = |\chi_3\rangle$, the state nearest to it in energy is the state $|\chi_4\rangle$. In the case where the two donors are equivalent and $R/a_B^* > 15$, this is the $4f\sigma_u$ state $|\chi_4\rangle \approx [|2S\rangle_L - |2P_x\rangle_L - |2S\rangle_R - |2P_x\rangle_R]/2$, whose wavefunction $\langle \mathbf{r}|\chi_4\rangle$ is antisymmetric about the midpoint of the line joining the two donors [31]. At $x = R_d/a_B^* \gg 1$, the energy separation [30]

$$E_4 - E_3 = E^*\frac{x^3}{4}\exp\left(-\frac{x}{2} - 2\right)\left[1 + O\left(\frac{1}{x}\right)\right]$$

is small but greatly exceeds the value of $E_2 - E_1$, e.g., $E_4 - E_3 \approx 0.3$ meV at $R_d = 60$ nm. The donor asymmetry in the presence of gate potentials results in a further increase in $E_4 - E_3$, and therefore the phonon absorption processes does not contribute much to decoherence at sufficiently low temperatures $T < 10$ K.

Thus, the error rate due to phonon-induced decoherence is $D(\tau_{\mathrm{op}}) \approx 3 \times 10^{-3}$ at $\tau_{\mathrm{op}} < 100$ ps and $T < 10$ K. This value is to be compared to the error rates due to other sources of decoherence. The lowest bounds for the decoherence times associated with the Johnson noise from the gates and the environmental charge fluctuations are [16, 20, 26], respectively, $\tau \sim 1$ μs and $\tau \sim 1$ ns, and hence the corresponding error rates [14] $D(\tau_{\mathrm{op}}) = 1 - \exp(-\tau_{\mathrm{op}}/\tau)$ do not exceed that due to phonons at $\tau_{\mathrm{op}} < (1–10)$ ps. Hence, the performance of the buried donor charge qubit appears to be limited primarily by the electron–phonon interaction. In this paper, we concentrated on the phosphorous donors in silicon. Since spectral function (34) that ultimately determines the error rate for one-qubit operations is a material constant, it would be worthwhile to search for other materials and/or doping elements for the buried donor charge qubit, in order to weaken the decoherence effects.

Although we restricted ourselves to rectangular shapes of the resonant pulses, our consideration can be generalized to other pulse shapes [39]. The results obtained can also be applied to quantum-dot structures and Josephson three-level gates [39–42]. Finally, once a fundamental possibility of the auxiliary-state-assisted operations has been demonstrated, it is straightforward task to organize the coupling of P_2^+ : Si qubits for conditional quantum operations [16, 20].

In summary, we have proposed a scheme for fast rotations of the buried donor charge qubit through an auxiliary-state-assisted electron evolution under the influence of resonant microwave pulses. This scheme allows implementing one-qubit operations in times as short as $\tau_{\mathrm{op}} \sim 1$ ps. With the example of the P_2^+ : Si qubit, we have shown that dephasing and "nonresonant" relaxation due to acoustic phonons are the main sources of decoherence. The error rate at $T < 10$ K and operation times $\tau_{\mathrm{op}} = (1–10)$ ps is about 3×10^{-3}, i.e., greater than the fault-tolerance threshold for quantum computation but sufficiently low to investigate the small-scale devices and thus to demonstrate the experimental feasibility of the scheme.

ACKNOWLEDGMENTS

Discussions with A. V. Tsukanov, L. Fedichkin, and M. S. Litsarev are gratefully acknowledged.

REFERENCES

1. A. Barenco, D. Deutsch, A. Ekert, and R. Jozsa, Phys. Rev. Lett. **74**, 4083 (1995).
2. A. Shnirman, G. Schon, and Z. Hermon, Phys. Rev. Lett. **79**, 2371 (1997).
3. D. Loss and D. P. DiVincenzo, Phys. Rev. A **57**, 120 (1998).
4. Y. Nakamura, Yu. A. Pashkin, and J. S. Tsai, Nature **398**, 786 (1999).
5. Yu. A. Pashkin, T. Yamamoto, O. Astafiev, *et al.*, Nature **421**, 823 (2003).
6. B. E. Kane, Nature **393**, 133 (1998).
7. B. E. Kane, N. S. McAlpine, A. S. Dzurak, *et al.*, Phys. Rev. B **61**, 2961 (2000).
8. R. Vrijen, E. Yablonovitch, K. Wang, *et al.*, Phys. Rev. A **62**, 012306 (2000).
9. L. A. Openov, Phys. Rev. B **60**, 8798 (1999).
10. L. Fedichkin, M. Yanchenko, and K. A. Valiev, Nanotechnology **11**, 387 (2000).
11. T. Tanamoto, Phys. Rev. A **61**, 022305 (2000).
12. J. H. Oh, D. Ahn, and S. W. Hwang, Phys. Rev. A **62**, 052306 (2000).
13. T. Hayashi, T. Fujisawa, H. D. Cheong, *et al.*, Phys. Rev. Lett. **91**, 226804 (2003).
14. L. Fedichkin and A. Fedorov, Phys. Rev. A **69**, 032311 (2004).
15. J. R. Petta, A. C. Johnson, C. M. Marcus, *et al.*, cond-mat/0408139.
16. L. C. L. Hollenberg, A. S. Dzurak, C. Wellard, *et al.*, Phys. Rev. B **69**, 113301 (2004).
17. A. V. Tsukanov and L. A. Openov, Fiz. Tekh. Poluprovodn. (St. Petersburg) **38**, 94 (2004) [Semiconductors **38**, 91 (2004)].
18. D. M. Eigler and E. K. Schweizer, Nature **344**, 524 (1990).
19. S. R. Schofield, N. J. Curson, M. Y. Simmons, *et al.*, Phys. Rev. Lett. **91**, 136104 (2003).
20. A. S. Dzurak, L. C. L. Hollenberg, D. N. Jamieson, *et al.*, cond-mat/0306265.
21. D. P. DiVincenzo, Fortschr. Phys. **48**, 771 (2000).
22. L. A. Openov and A. V. Tsukanov, Pis'ma Zh. Éksp. Teor. Fiz. **80**, 572 (2004) [JETP Lett. **80**, 503 (2004)]; L. A. Openov, Phys. Rev. B **70**, 233313 (2004).
23. L. M. Kettle, H.-S. Goan, S. C. Smith, *et al.*, Phys. Rev. B **68**, 075317 (2003).
24. R. L. Aggarwal, Solid State Commun. **2**, 163 (1964).
25. A. Baldereschi, Phys. Rev. B **1**, 4673 (1970).
26. S. D. Barrett and G. J. Milburn, Phys. Rev. B **68**, 155307 (2003).
27. S. T. Pantelides and C. T. Sah, Phys. Rev. B **10**, 621 (1974).
28. D. R. Bates and R. H. G. Reid, Adv. At. Mol. Phys. **4**, 13 (1968).
29. N. Bardsley, T. Holstein, B. R. Junker, and S. Sinha, Phys. Rev. A **11**, 1911 (1975).
30. T. C. Scott, A. Dalgarno, and J. D. Morgan III, Phys. Rev. Lett. **67**, 1419 (1991).
31. S. Fujinaga, *Method of Molecular Orbitals* (Iwanami Shoten, Tokyo, 1980; Mir, Moscow, 1983) [translated from Japanese to Russian].
32. L. D. Landau and E. M. Lifshitz, *Course of Theoretical Physics*, Vol. 3: *Quantum Mechanics: Non-Relativistic Theory*, 3rd ed. (Nauka, Moscow, 1974; Pergamon, New York, 1977), Chap. 6.
33. U. Bockelmann and G. Bastard, Phys. Rev. B **42**, 8947 (1990).
34. T. Brandes and T. Vorrath, Phys. Rev. B **66**, 075341 (2002).
35. N. G. van Kampen, J. Stat. Phys. **78**, 299 (1995).
36. D. Mozyrsky and V. Privman, J. Stat. Phys. **91**, 787 (1998).
37. F.-S. Liu, K.-D. Peng, and W.-F. Chen, Int. J. Theor. Phys. **40**, 2037 (2001).
38. L. A. Openov, Phys. Rev. Lett. **93**, 158901 (2004).
39. E. Paspalakis, Z. Kis, E. Voutsinas, and A. F. Terzis, Phys. Rev. B **69**, 155316 (2004).
40. Z. Kis and E. Paspalakis, Phys. Rev. B **69**, 024510 (2004).
41. C.-P. Yang, S.-I. Chu, and S. Han, Phys. Rev. A **67**, 042311 (2003).
42. M. H. S. Amin, A. Yu. Smirnov, and A. M. van den Brink, Phys. Rev. B **67**, 100508 (2003).

Journal of Experimental and Theoretical Physics, Vol. 100, No. 5, 2005, pp. 867–883.
Translated from Zhurnal Éksperimental'noĭ i Teoreticheskoĭ Fiziki, Vol. 127, No. 5, 2005, pp. 984–1004.
Original Russian Text Copyright © 2005 by Karpov, Korobkin.

Stimulated Thermal Scattering Induced by Two-Photon Absorption and Experimental Observation of Stimulated Brillouin Scattering in the UV Region

V. B. Karpov and V. V. Korobkin

Coherent and Nonlinear Optics Department, Prokhorov General Physics Institute, Russian Academy of Sciences, Moscow, 119991 Russia
e-mail: karpov@kapella.gpi.ru; korobkin@kapella.gpi.ru

Received April 8, 2004

Abstract—An analysis of the results of previous studies of stimulated scattering of UV pulses in liquids has shown that they disagree with the theory of stimulated scattering. To resolve the inconsistency, stimulated scattering of XeCl excimer laser radiation ($\lambda = 308$ nm) with pulse duration $\tau \approx 8$ ns in liquid hexane is investigated experimentally. A theoretical analysis of the results obtained revealed a new nonlinear optical phenomenon: stimulated thermal scattering induced by the heating due to two-photon absorption, called two-photon stimulated thermal scattering (two-photon STS-2). The stimulated backscatter spectrum contains a previously unknown line corresponding to two-photon STS-2 and a newly discovered SBS line in the UV region. The line is observed in experiment on liquid hexane and is characterized by the frequency shift $\Omega_B = 0.33$ cm^{-1} relative to the pump wavelength $\lambda = 308$ nm, in complete agreement with the theory of stimulated Brillouin scattering (SBS). The spectral line called the *SBS line* in previous studies has a frequency shift much smaller than that predicted by the SBS theory and must be interpreted as an unshifted two-photon STS-2 line. When two-photon STS-2 is used to obtain a phase-conjugate wave, the phase-conjugation fidelity is lower than that achieved by using SBS because of thermal self-action and slow decay of the thermal grating. © *2005 Pleiades Publishing, Inc.*

1. INTRODUCTION

Stimulated scattering (SS) is widely used in scientific research and practical applications. This motivates studies of the physical mechanisms responsible for stimulated scattering in various spectral regions. The most important applications of stimulated scattering lie in phase conjugate optics. Phase conjugation via stimulated backscattering was discovered in the Laboratory of Quantum Radiophysics, of the Lebedev Physical Institute by Zel'dovich, Popovichev, Ragulskii, and Faizullov in 1971 (see [1]). However, stimulated Brillouin scattering (SBS), stimulated Raman scattering (SRS), and other SS mechanisms have specific physical characteristics (frequency shift, decay time, etc.) that must manifest themselves in the properties of the respective phase conjugate waves.

Detailed experimental studies of stimulated scattering in various media have been conducted only in the near IR region for historical reasons: the pump beam produced by the radiation source must have both high power and narrow linewidth. The first sources of this kind were Q-switched single-mode ruby and Nd:glass lasers, which generated giant pulses with $\lambda = 0.69$ and 1.06 μm, respectively [2–4], and usually generated single SBS lines in spectra of liquids (such as water or methanol) characterized by relatively weak linear light absorption. When linear light absorption was stronger, a line corresponding to stimulated thermal scattering due to linear absorption (linear STS-2) was observed. Multiphoton IR absorption could not be observed, because the liquids used in the studies were transparent in the IR and visible spectral regions, while five to ten IR photons with energies between 1 and 2 eV were required to obtain the nearest electron resonance at an energy of about 10 eV.

Theoretical studies of stimulated scattering have mostly relied on experimental results obtained for the near IR region. Thus, the modern theory of stimulated scattering applies only to linearly absorbing media, while no complete and consistent theory has been developed to this day. In particular, the theory of stimulated thermal scattering proposed in [5] allows only for linear light absorption (see [1]).

Experimental investigations of stimulated scattering in the near UV region have never been conducted for two reasons. First, reliable UV radiation sources (discharge excimer lasers [6]) became available ten years later than solid-state lasers. Second, the methods used to narrow the bandwidths of solid-state lasers (characterized by lasing times on the order of 1 μ) could not be

Table 1. Results of experimental studies of stimulated backscattering in hexane at different pump wavelengths in the near UV region corresponding to ArF (λ = 193 nm), KrF (λ = 248 nm), XeCl (λ = 308 nm), and XeF (λ = 351 nm) excimer lasers

Reference	Pump wavelength, nm	Pump intensity, W/cm^2	Measured frequency shift for stimulated backscattering in hexane, cm^{-1}	Physical mechanism of stimulated scattering in hexane suggested by authors
[9]	193	$\approx 10^{10}$	≈ 0.2	SBS
[8]	248	$> 2 \times 10^{10}$	≈ 0.1	SBS
[11]	248	$> 10^{10}$	≈ 0.1	SBS
[10]	308	$> 10^{11}$	< 0.15	SBS
[13]	308	$> 10^{12}$	0.24	SBS
[7]	351	$> 5 \times 10^{9}$	0.2	SBS
[14]	248	$> 10^{11}$	< 0.02	linear STS-2

extended to excimer lasers, which had much shorter lasing times (<100 ns). Thus, when experimentalists had to deal with stimulated scattering in studies of phase conjugation driven by excimer laser beams, the theory developed for linear IR absorption was applied to the UV spectral region.

2. PROBLEMS IN EXPERIMENTAL STUDIES OF STIMULATED LIGHT SCATTERING AND PHASE CONJUGATION IN THE NEAR ULTRAVIOLET REGION

Studies of phase conjugation via stimulated scattering in the UV region were motivated by the use of excimer lasers as promising radiation sources in fusion research, materials treatment, and photolithography [6–9]. The first results concerning phase conjugation via stimulated backscattering were reported in [7] (for XeF laser, λ = 351 nm), [10] (XeCl laser, λ = 308 nm), [8, 11] (KrF laser, λ = 248 nm), and [9] (ArF laser, λ = 193 nm). In those and subsequent studies [12, 13], experimental SS spectra contained single lines, which were attributed to stimulated Brillouin scattering. Note that the "SBS" frequency shift relative to the corresponding pump frequency could not be measured in [9–11], because they were comparable to the spectral resolution of the laser system. The reflection coefficient of the "SBS" mirror measured in [11] gradually decreased with increasing pump intensity I_L from approximately 25% at the threshold ($I_L \approx 10^{10}$ W/cm^2) to approximately 10% at $I_L \approx 10^{11}$ W/cm^2. It should be noted that the decrease in reflection coefficient observed in that experiment was caused by a decrease in phase-conjugation fidelity. In [7, 8, 10, 12], the phase-conjugation fidelity achieved by reflection from a "Brillouin" mirror was found to degrade with increasing linear absorption coefficient of a nonlinear medium. In [14], the stimulated backscatter spectrum of hexane obtained by using a KrF laser (λ = 248 nm) also contained a single line, and phase conjugation was attributed to "linear STS-2."

The linear absorption coefficients α of nonlinear liquids measured in the studies of the "SBS" mechanism [7–13] varied from 0.02 to 0.1 cm^{-1} and amounted to 0.22 cm^{-1} in the investigation of "linear STS-2" reported in [14].

Studies of effects of resonance absorption on nanosecond nonlinear optical phenomena must take into consideration both wave attenuation and the phase variation due to heating. In [7–14], the pump beams were focused into nonlinear liquids by lenses with focal lengths between 5 and 10 cm. The corresponding length of the region of nonlinear interaction is $L \leq 0.1$ cm. Considerable attenuation over such distances can occur when $\alpha > 2$ cm^{-1}, which substantially exceeds the values mentioned above.

Table 1 summarizes the experimental results obtained in previous studies of stimulated backscattering in hexane [7–11, 13, 14]. The second and third columns of the table present the pump wavelength λ and intensity I_L; the fourth one, the measured shift Ω of the scattered wave relative to the pump frequency. The physical mechanisms responsible for the observed SS processes suggested by the respective authors are listed in the last column.

The theoretically predicted SBS frequency shift Ω_B depends on the pump frequency ω_L corresponding to λ (see Eq. (8) below). Table 2 shows the values of Ω_B given by (8) for the pump wavelengths listed in Table 1. It is clear that the predicted values of Ω_B shown in Table 2 are substantially larger than the corresponding measured values of Ω listed in Table 1 and attributed to "SBS" in [7–11, 13].

In summary, analysis of previous experimental results concerning stimulated scattering and phase conjugation in the near UV region leads to the following general conclusions.

I. The Brillouin frequency shifts measured in [7–11, 13] disagree with predictions of the SBS theory. The disagreement is too large to be entirely caused by experimental errors.

II. Since the measured SBS frequency shifts are substantially smaller than those predicted by the theory for the pump wavelengths ranging from $\lambda = 193$ to 351 nm in [7–11, 13], these discrepancies must have a common origin.

III. The decrease in phase-conjugation fidelity observed in [11] when the pump intensity was slightly above the threshold is not characteristic of SBS in transparent media.

Thus, the complex problems yet to be solved in this field of research concern both temporal and spatial behavior of laser beams propagating through nonlinear media as manifested by SBS frequency shift and phase-conjugation fidelity, respectively. However, the “abnormal” SBS was observed in a variety of studies conducted in different countries for nearly a decade [7–11, 13], which rules out the possibility of accidental experimental errors. These problems should be resolved by analyzing not only experimental errors, but also basic physical mechanisms responsible for stimulated light scattering.

3. PRELIMINARY ANALYSIS OF FEASIBLE MECHANISMS OF STIMULATED SCATTERING

Before proceeding to new experiments, one should review the results of previous studies in order to understand which physical mechanisms of stimulated scattering may work under the experimental conditions of [7–14].

The near-UV beams used as pumps in previous experiments had the wavelengths and intensities listed in Table 1, while the corresponding pulse durations varied between 5 and 10 ns. The nonlinear liquids used in those studies (hexane, heptane, and others) were transparent in the UV region: their linear absorption coefficients varied between 0.02 and 0.22 cm^{-1}.

3.1. Mechanisms of Stimulated Light Scattering

Light scattering is a process in which an atom or a medium absorbs an incident photon and emits a secondary photon. Depending on the mechanism responsible for the photon emission, scattering can be either spontaneous or stimulated [15].

In classical theories, scattering by transparent, macroscopically homogeneous, nonionized media is explained by permittivity fluctuations due to fluctuations of thermodynamic state variables (density or temperature) and physicochemical properties of the medium (such as concentration, anisotropy, or polarizability).

When the optical inhomogeneity of a medium is entirely due to thermal fluctuations of its properties, the scattering is called spontaneous or thermal [2, 16]. If the pump electric field is sufficiently strong, then stimulated light scattering is observed. At the initial stage, a weak scattered wave is generated by spontaneous scattering of the pump beam. Under certain conditions, the modes responsible for the initial spontaneous scattering are amplified as both pump and scattered waves resonantly interact with internal motion in the medium. This leads to an increase in scattering efficiency. In the ensuing steady state, the scattered light intensity I_S in the absence of pump attenuation is expressed as the nonlinear function [3]

$$I_S(L) = I_S^0 \exp(G I_L L), \qquad (1)$$

where I_S^0 is the intensity of the thermally scattered wave, G is the gain factor for a particular SS process, I_L is the pump intensity, and L is the length of the region of nonlinear interaction.

Stimulated scattering is a special case of three-wave mixing between two light waves and a polarization wave. They are effectively coupled if

$$\omega_L - \omega_S = \Omega, \qquad (2)$$

$$\mathbf{k}_L - \mathbf{k}_S = \mathbf{q}, \qquad (3)$$

where ω_L, $\mathbf{k}_L$ and ω_S, $\mathbf{k}_S$ denote, respectively, the frequencies and wavevectors of the pump wave

$$E_L \exp[i(\mathbf{k}_L \cdot \mathbf{r} - \omega_L t)] + \text{c.c.}$$

and the scattered wave

$$E_S \exp[i(\mathbf{k}_S \cdot \mathbf{r} - \omega_S t)] + \text{c.c.},$$

Ω and $\mathbf{q}$ are the polarization-wave frequency and wavevector, respectively.

In an SS process, the polarization wave propagates in such a medium with cubic nonlinearity that phase matching conditions (2) and (3) are satisfied automatically [2, 17]. Since the pump beam is the only source of energy, the time profile of the complex amplitude of the pump determines the dynamics of nonlinear light–matter interaction. Therefore, the pump wave must be highly coherent.

The physical mechanism of an SS process must ensure that two conditions are satisfied:

(i) the cross term in the squared electric field strength must resonantly amplify a mode of internal motion;

(ii) the resonant mode must modulate the permittivity of the medium.

A mechanism of this kind underlies each known SS process [17, 18]: SBS, SRS, stimulated Raleigh wing scattering (SRWS), and stimulated thermal scattering (STS-1 and linear STS-2).

Mathematical models of stimulated scattering are based on systems of material and wave equations. Their solutions are used to find the gain factor G in (1) and the decay time for the resonant mode in each SS mechanism.

In experiments with pump beams with $\tau \geq 10$ ns (excimer and solid-state lasers), SBS and linear STS-2 are observed most frequently, because the corresponding values of G for condensed matter and compressed gas (most widespread nonlinear media) are higher than those characteristic of other SS processes. Accordingly, the threshold pump intensities for these processes are lower. However, since the pump is depleted because of saturation, only the SS process characterized by the highest gain is normally observed.

Since SBS and linear STS-2 play a particularly important role in stimulated scattering of nanosecond pulses in liquids, we discuss their basic characteristics to be used below in analyzing SS processes observed under various conditions.

3.1.1. Basic SBS characteristics. Adiabatic pressure fluctuations are waves propagating at the speed of sound [19]. The hydrodynamic equations used in SBS models include an electrostrictive force that drives the fluid into regions of higher electric field strength. The cross term in the expression for electrostrictive pressure is responsible for resonant generation of a hypersonic wave with wavevector **q** and frequency

$$\Omega_B(\mathbf{q}) = |\mathbf{q}|v, \tag{4}$$

where v is the speed of sound. The SBS Stokes shift Ω_B satisfies condition (2). The acoustic wave amplitude is determined by viscous dissipation, and the decay rate Γ_B is related to the SBS decay time:

$$\Gamma_B(\mathbf{q}) = A|\mathbf{q}|^2, \quad \tau_B \approx \Gamma_B^{-1}. \tag{5}$$

For liquids, $A = 2\eta/(3\rho)$, where ρ is density and η is shear viscosity [17, 20].

The density modulation in the acoustic wave gives rise to a dynamic grating (phase hologram). The scattered wave is amplified via interaction between the pump and the grating. According to [3, 17], the steady-state gain factor under conditions near the Stokes resonance peak is

$$G_B = \frac{\rho^2(\partial\varepsilon/\partial\rho)^2}{1+(\omega_L-\omega_S-\Omega_B)^2/\Gamma_B^2}\frac{\omega_S q^2}{4\Omega_B\Gamma_B\varepsilon\rho c^2}. \tag{6}$$

The highest gain is achieved when $\omega_L - \omega_S = \Omega_B$.

When the scattered wave propagates at an angle θ relative to the pump beam, condition (3) yields

$$\begin{aligned} q = |\mathbf{q}| &= |\mathbf{k}_L - \mathbf{k}_S| \approx 2|\mathbf{k}_L|\sin(\theta/2) \\ &= 2(\omega_L\sqrt{\varepsilon}/c)\sin(\theta/2). \end{aligned} \tag{7}$$

Accordingly, the SBS frequency shift given by (4) is expressed as

$$\Omega_B = qv = 2\omega_L\sqrt{\varepsilon}(v/c)\sin(\theta/2). \tag{8}$$

3.1.2. Basic characteristics of linear STS-2. Entropy fluctuations at constant pressure do not propagate through the medium and only dissipate into heat [19, 21]. In the thermodynamic model of linear STS-2, the dissipation is modulated by the cross term in the expression for squared electric field strength. Since permittivity depends on temperature, a dynamic grating (phase hologram) is created in the medium. The scattered wave is amplified via interaction between the pump and the grating. According to [3, 17], the steady-state gain factor under conditions near the Stokes resonance peak is

$$\begin{aligned} G_T &\approx \frac{\omega_S\alpha}{cn\rho c_p}\frac{\partial\varepsilon}{\partial T}\frac{\Omega}{\Gamma_T^2+\Omega^2} \\ &\approx \frac{\omega_S\alpha}{cn\rho c_p\Gamma_T}\frac{\partial\varepsilon}{\partial T}\frac{\Omega/\Gamma_T}{1+\Omega^2/\Gamma_T^2}, \end{aligned} \tag{9}$$

where c_p is specific heat, χ is thermal diffusivity, and n is the unperturbed refractive index. The decay rate Γ_T is related to the decay time for linear STS-2:

$$\Gamma_T = \chi|\mathbf{q}|^2, \quad \tau_T \approx \Gamma_T^{-1}. \tag{10}$$

Since $\partial\varepsilon/\partial T$ is negative for most substances, optical gain corresponds to an anti-Stokes shift $\Omega < 0$. The highest gain is achieved when

$$\omega_L - \omega_S = \Omega_T = -\Gamma_T.$$

3.1.3. Phase mismatch for SBS in linearly absorbing media. An SS process can be substantially changed even by a weak absorption that affects only the phases of waves. Indeed, since stimulated scattering can be implemented only if conditions (2) and (3) are satisfied, the phase matching (between the reference and acoustic waves in SBS) must hold over a time period corresponding to the pump pulse duration. Then, steady-state amplitudes of the acoustic wave and phase hologram are reached within the decay time τ_B, and the highest conversion efficiency is achieved.

When the permittivity of the medium varies with time, the pump and scattered wavelengths vary, and both acoustic wave and phase hologram vary accordingly. Since electromagnetic field is massless, while acoustic waves have a finite response time, the phase matching conditions are violated. As a result, a time-dependent SS process characterized by a lower conversion efficiency is observed. A substantial change in permittivity over the pulse duration may lead to SBS breakdown.

Now, consider the change in SBS due to the heating caused by linear light absorption with absorption coefficient α [3, 4]. Using a plane-wave approximation, we assume that the pump beam enters the nonlinear medium at $z = L$ and propagates leftwards along the z axis, while the Stokes wave propagates rightwards.

If the respective wave intensities at $z = L$ by $I_L(L)$ and $I_S(L)$, then

$$\eta = \frac{I_S(L)}{I_L(L)}$$

is the efficiency of conversion of pump energy into SBS signal over the length L of the region of nonlinear interaction. Sometimes, η is called *SBS mirror reflectivity* [17]. The dependence of η on $I_L(L)$ is given by the relation [3, 4]

$$\begin{aligned} &h(D + \ln\eta) \\ &= \Gamma_B G_B \arctan\{I_L(L)(1-\eta)Lh/\Gamma_B\}, \end{aligned} \tag{11}$$

where

$$D = 25\text{–}30,$$

$$G_B = \frac{\rho(\partial\varepsilon/\partial\rho)^2\omega^2}{2c^3 v n \Gamma_B}$$

is the peak value of the backward SBS gain factor given by (6),

$$h = \frac{\alpha\omega(\partial\varepsilon/\partial T)}{2cn\rho c_p},$$

v is the speed of sound, and $\omega = \omega_L$.

Numerical calculations of $\eta[I_L(L)]$ given by (11) as a function of α yield a threshold value α_{CR} corresponding to SBS breakdown [3, 4].

4. EXPERIMENTAL SETUP AND TECHNIQUE

4.1. General Requirements for Experimental Setup

To investigate the physical mechanisms responsible for stimulated scattering of nanosecond pulses in the near UV region, we constructed an experimental setup based on an industrial ELI-91 XeCl excimer laser (λ = 308 nm) [22–24]. Hexane was used as a nonlinear liquid. Our experimental setup was designed by relying on the following considerations.

Table 2. Frequency shifts Ω_B predicted for backward SBS ($\theta = \pi$) in hexane by expression (8) for pump wavelengths in the near UV region corresponding to ArF (λ = 193 nm), KrF (λ = 248 nm), XeCl (λ = 308 nm), and XeF (λ = 351 nm) excimer lasers

Pump wavelength, nm	Frequency shift predicted for backward SBS in hexane, cm^{-1}
193	0.49
248	0.41
308	0.33
351	0.30

I. Since each SS mechanism is characterized by a specific shift of the scattered wave relative to the pump frequency, analysis of spectral characteristics is of special interest.

The SBS frequency shift predicted by (8) for λ = 308 nm and $\theta = \pi$ is $\Omega_B = 0.33\ \text{cm}^{-1}$ (see Table 2). The linear-STS-2 shift predicted by (7) for λ = 308 nm and $\theta = \pi$ is $\Omega_T \approx -\Gamma_T \approx -0.01\ \text{cm}^{-1}$. Reliable discrimination between SBS and linear STS-2 requires a spectral resolution $\leq 10^{-1}\ \text{cm}^{-1}$.

II. Analysis of nonlinear light–matter interaction requires the use of a narrow-divergence, narrow-bandwidth laser beam. This requirement is met when the laser operates in the single-mode regime, producing a single longitudinal mode and the fundamental transverse mode TEM_{00q}.

III. Nonlinear optical phenomena occur when the beam intensity is sufficiently high. Since the focused beam has a finite diameter, this implies that a high-power pump is required.

The required conditions can be implemented in a setup designed as a master-oscillator–power-amplifier (MOPA) system. The master oscillator (MO) generates a weak narrow-divergence, narrow-bandwidth beam. The beam is then amplified, and its spatial and temporal coherence is maintained.

Figure 1 schematizes the experimental setup MOPA system based on an XeCl excimer laser (λ = 308 nm).

4.2. Master Oscillator

A detailed description of the master oscillator can be found in [23–26].

The diffraction-limited divergence of the beam produced by the master oscillator was controlled by two aperture stops of radius $r_0 = 0.8$ mm mounted on both sides of the active cell.

The spectrum of the pulse generated by the master oscillator was narrowed by means of a frequency-selec-

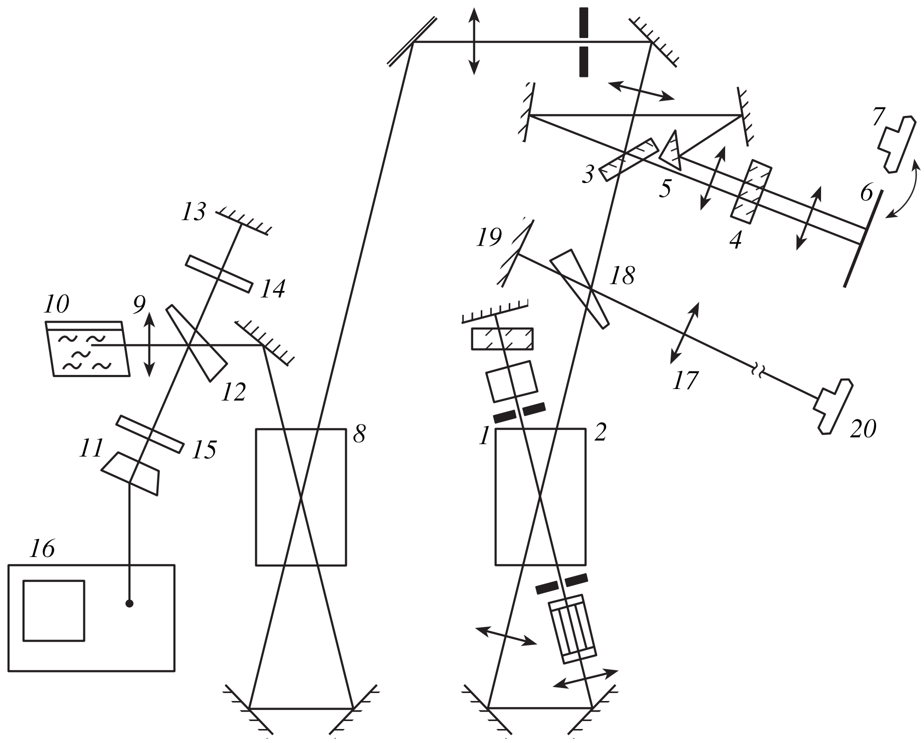

Fig. 1. Experimental setup for studying mechanisms of stimulated scattering of XeCl excimer laser beams (λ = 308 nm) in hexane: (*1*, *2*) MOPA system based on an ELI-91 XeCl laser; (*3*, *12*, *18*) beamsplitters; (*4*, *5*) spectrum analyzer (Fabry–Perot etalon combined with prism); (*6*) luminescent screen; (*7*, *20*) cameras; (*8*) round-trip amplifier based on an ELI-91 XeCl laser; (9) lens; (*10*) cell filled with hexane; (*11*) FEK-29KPU photodiode (time resolution about 200 ps); (*13*, *19*) mirrors; (*14*, *15*) neutral filters; (*16*) S7-19 oscilloscope (bandwidth about 5 GHz); (*17*) long-focal-length lens of divergence analyzer (f_1 = 3 m).

tive cavity with a nontransparent mirror at one end and a mode selector at the other. The selector operates as an interference filter with a frequency-dependent reflection coefficient. Originally, a selector of this kind was used in [27] to narrow the bandwidth of an Nd laser characterized by a long cavity photon lifetime (about 1 μs). For the XeCl laser, the photon lifetime is approximately 20 ns. For a 1 m long cavity, the corresponding number of round trips is approximately 6, which is not sufficient to select a single longitudinal mode. Therefore, the optical system proposed in [27] is useless as applied to the ELI-91 XeCl excimer laser. However, a single longitudinal mode was selected by using a Fabry–Perot etalon placed inside the MO cavity.

The MO output characteristics are specified in the third column of Table 3; the characteristics of the industrial ELI-91 laser, in the second column.

Table 3. Laser parameters

Parameter	ElI-91 (industrial) laser	Master oscillator	Amplified beam
Bandwidth	15 cm^{-1}	5×10^{-3} cm^{-1}	5×10^{-3} cm^{-1}
Aperture	10 mm × 20 mm	∅1.6 mm	8 mm × 10 mm
Divergence	10^{-2} rad	6×10^{-4} rad	3×10^{-4} rad
FWHM	20 ns	8 ns	8 ns
Pulse energy	50 mJ	50 μJ	3 mJ
Wavelength	308 nm	308 nm	308 nm

4.3. Experimental Setup

The MOPA system based on an ELI-91 XeCl laser combined master oscillator *1* and preamplifier *2*. The beam generated by the master oscillator was expanded by a telescope amplified in the same active cell to approximately 1 mJ. After passing through the round-trip amplifier *8* based on another ELI-91 XeCl laser, the pulse had a Gaussian shape, an energy of about 3 mJ, a duration of about 8 ns, and a bandwidth of about 5×10^{-3} cm^{-1}. The characteristics of the amplified beam are specified in the last column of Table 3.

The amplified beam was focused by lens *9* with focal length *F* into cell *10* filled with hexane. The nonlinear interaction between the pump and the liquid took place in the waist of the beam focused by lens *9*. The SBS-backscattered wave was guided back through the optical system and amplified by round-trip amplifier *8*.

Beamsplitter *12* was used to guide both forward- and backward-propagating beams into a time-domain analyzer. The time profiles of both beams were measured by means of FEK-29KPU photodiode *11* (with a time resolution of about 200 ps) and S7-19 oscilloscope *16* (with a bandwidth of about 5 GHz).

Beamsplitter *3* was used to guide both forward- and backward-propagating beams into a spectrum analyzer (Fabry–Perot etalon *4* combined with prism *5*), which simultaneously produced images of pump and signal spectra on luminescent screen *6* or camera *7*.

Beamsplitter *18* was used to guide both forward- and backward-propagating beams into a divergence analyzer. Beam divergence was evaluated by using the focal spot diameter obtained by means of lens *17* with a focal length of $f_1 = 3$ m.

4.4. Nonlinear Liquids and Cells

The liquids used as nonlinear media in previous studies of stimulated scattering and phase conjugation in the near UV region [7–14] were organic solvents utilized in UV chromatography, such as hexane, heptane, *iso*-octane, ethanol. Similar results were obtained for different liquids. Since hexane was used in almost all of these studies (see Table 1), we also used it in our experiments.

We used HPLC (chromatography) grade hexane produced by Oldrich Chemical Co., Milwaukee, WI, and domestically produced “chemically pure” hexane. Their linear absorption coefficients measured at λ = 308 nm were $\alpha = 0.01 \pm 0.003$ cm^{-1} and $\alpha = 0.046 \pm 0.003$ cm^{-1}, respectively.

We added small amounts of acetone to hexane to increase the linear absorption coefficient, so that the cells used in our experiments were filled with liquids characterized by α = 0.01, 0.046, 0.08, and 0.17 cm^{-1} at λ = 308 nm.

The nonlinear liquid filled a cylindrical glass cell with fused-silica windows sloped at an angle of 5° to avoid spurious reflections. We used a 5 cm (“short”) cell in combination with lens *9* having F = 11 cm and a 30 cm (“long”) cell in combination with lens *9* having F = 50 or 100 cm. All cells had an internal diameter of 40 mm.

The refractive index of hexane at λ = 308 nm is $n \approx 1.4$, and its temperature derivative is [18]

$$\left(\frac{\partial n}{\partial T}\right)_p = -53 \times 10^{-5}\ \mathrm{K}^{-1}.$$

The corresponding permittivity and its derivative are

$$\varepsilon = n^2 \approx 2,$$

$$\left(\frac{\partial \varepsilon}{\partial T}\right)_p = \frac{\partial \varepsilon}{\partial n}\left(\frac{\partial n}{\partial T}\right)_p = 2n\left(\frac{\partial n}{\partial T}\right)_p \approx -1.5 \times 10^{-3}\ \mathrm{K}^{-1}.$$

5. EXPERIMENTAL RESULTS

5.1. Experiment 1: Dependence of Temporal Stimulated Backscatter Spectrum on Pump Intensity

When the pulse power is held constant, the intensity of radiation in cell *10* (see Fig. 1) can be varied by means of neutral filters or by changing the focal length of lens *9*.

The amplified-pulse energy was approximately 3 mJ (see Table 3). In our experiments, the stimulated scattering pumped by such a pulse was close to threshold conditions for lens *9* of any type employed. Therefore, we could not use neutral filters to reduce the beam power. The pump intensity I_L was varied only by changing the focal length F of lens *9*.

The spectrum analyzer scheme described above was used to obtain a single photographic image of both pump and signal spectra simultaneously with each lens *9* (with F = 11, 50, and 100 cm), which facilitated measurement of frequency shift. Only the chromatography grade hexane (with α = 0.01 cm^{-1}) was used in this experiment.

The three photographic images of temporal spectra shown in Figs. 2a–2c were obtained for the three different F and α = 0.01 cm^{-1} = const. The stimulated backscatter spectrum has a single unshifted component when F = 11 cm (Fig. 2a), an unshifted component and a Stokes one when F = 50 cm (Fig. 2b), and a single Stokes component shifted by 0.33 cm^{-1} when F = 100 cm (Fig. 2c).

5.2. Experiment 2: Dependence of SS Temporal Spectrum on Pump Intensity and Linear Absorption Coefficient

We used all cells with hexane mixtures having α = 0.01, 0.046, 0.08, and 0.17 cm^{-1} to examine the dependence of the stimulated backscatter spectrum on pump intensity, which was varied by changing the focal length of lens *9*. The dependence of the stimulated backscatter spectrum on F for α = 0.046 and 0.08 cm^{-1} was similar to that illustrated by Figs. 2a–2c for α = 0.01 cm^{-1}. Each spectrum obtained for α = 0.17 cm^{-1} with F = 11, 50, 100 cm contained a single unshifted component (as in Fig. 2a).

5.3. Experiment 3: Dependence of Phase-Conjugation Fidelity on Pump Intensity

We measured both pump and backscattered beam divergences at the location of beamsplitter *18* (see Fig. 1) to determine the dependence of the latter on the former. The pump intensity was varied by changing the focal length of lens *9*. After a beam passes through amplifier *8*, its divergence increases by three times. The experiment provided information about the phase-conjugation fidelity: when the phase conjugation is “good,”

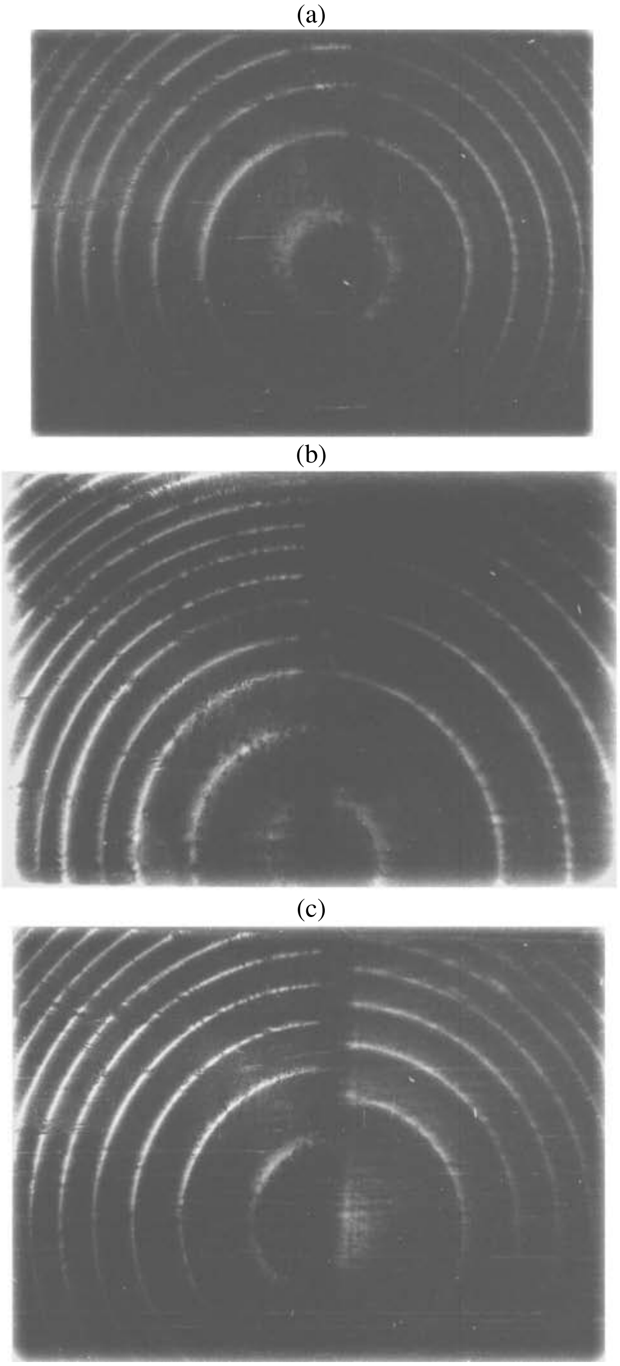

Fig. 2. Results of Experiments 1 and 2: Photographic images of temporal spectra obtained with F = (a) 11, (b) 50, and (c) 100 cm for hexane at constant linear absorption coefficient. Each photograph contains two images: pump spectrum (right) and stimulated backscatter spectrum (left). The dispersion-free region of the Fabry–Perot etalon is 0.66 cm^{-1}. The dependence of stimulated backscatter spectrum on F is similar for α = 0.01, 0.046, and 0.08 cm^{-1}.

the spatial spectrum of the backscattered wave must be unaffected by amplifier *8*. We used only the chromatography grade hexane (with $\alpha = 0.01\ \text{cm}^{-1}$) to avoid the thermal self-action caused by linear absorption.

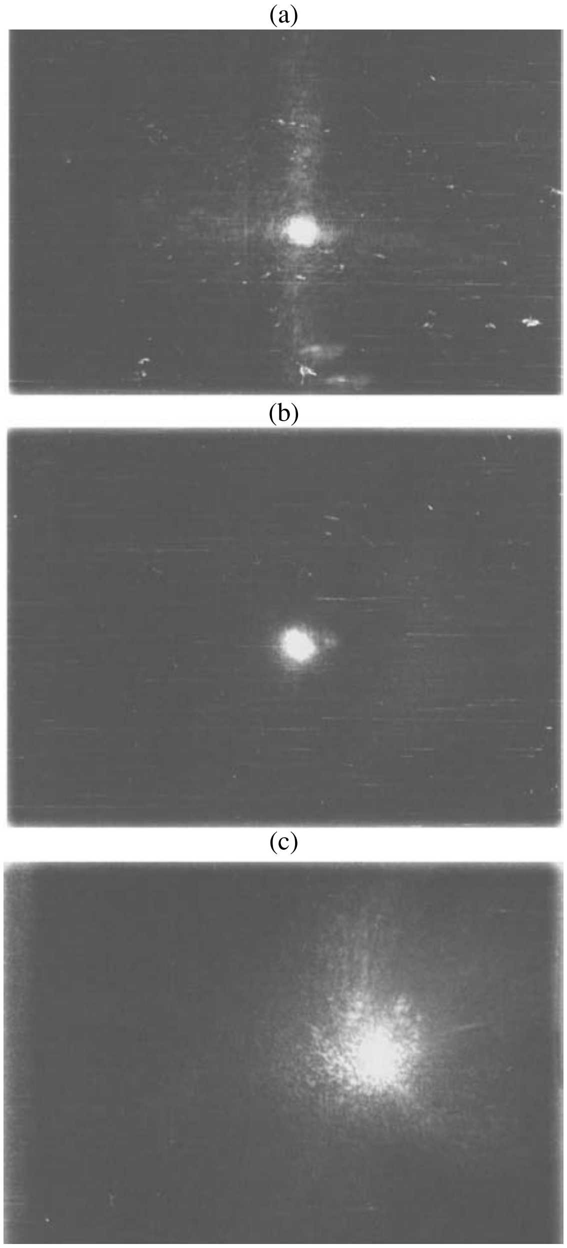

Fig. 3. Results of Experiment 3: Photographic images of the focal spots obtained with lens *17* (f_1 = 3 m): (a) forward-propagating beam; (b) backward-propagating beam (F = 100 cm, “good” phase-conjugation fidelity); (c) backward-propagating beam (F = 11 cm, “poor” phase-conjugation fidelity); hexane with $\alpha = 0.01\ \text{cm}^{-1}$.

Figures 3a–3c show photographic images of the focal spots obtained for the pump beam with lens *17*, for the backscattered beam with F = 100 cm, and for the backscattered beam with F = 11 cm, respectively. Since phase aberration transforms into amplitude aberration in the far-field region, the beam divergences can be obtained by using these images and the relation

$$\theta \approx d/f_1, \tag{12}$$

where θ is the required divergence, d is the focal spot diameter, and $f_1 = 3$ m is the focal length of lens *17*. The resulting divergences are $\theta \approx 3 \times 10^{-4}$ rad for the forward-propagating beam (Fig. 3a), $\theta \approx 3 \times 10^{-4}$ rad for the "good" backscattered beam obtained with $F = 100$ cm (Fig. 3b), and $\theta \approx 2 \times 10^{-3}$ rad for the "poor" backscattered beam obtained with $F = 11$ cm (Fig. 3c).

5.4. Experiment 4: Time Profiles of Pulse Intensity

Analysis of the time evolution of pulses is important for studies of stimulated scattering, because nonlinear effects may change their amplitudes, durations, and shapes. We used the time-domain analyzer mentioned above. The phase-conjugation mirror reflectivity was determined as the ratio of the peak backscattered intensity to the peak intensity of the amplified beam. We used all cells with hexane mixtures having $\alpha = 0.01$, 0.046, 0.08, and 0.17 cm^{-1}.

The backscattered intensity profile was found to have a nearly Gaussian shape and an FWHM of approximately 7 ns. The slightly shorter duration of the backscattered pulse as compared to the pump can be attributed to the near-threshold scattering conditions.

The phase-conjugation mirror reflectivity was almost 20% with both $F = 11$ cm and 100 cm for $\alpha = 0.01$ cm^{-1} and decreased with increasing α. Note that the reflectivity increased as the beam waist was moved toward the entrance window.

5.5. Experimental Results Requiring Theoretical Analysis

The trends revealed in Experiments 1–4 on hexane with $\lambda = 308$ nm that require further theoretical analysis are summarized as follows.

1. The presence of two components in the backscattered wave spectra obtained with $F = 50$ cm for $\alpha = 0.01$–0.08 cm^{-1}: an unshifted one (up to 0.02 cm^{-1}) and a Stokes one shifted by 0.33 cm^{-1} (Fig. 2b).

2. The dependence of the backscattered wave spectra obtained for $\alpha = 0.01$–0.08 cm^{-1} on the focal length F of lens *9*:

(2.1) the disappearance of the unshifted component observed when F is increased from 50 to 100 cm (Figs. 2b and 2c);

(2.2) the disappearance of the shifted component observed when F is reduced from 50 to 11 cm (Figs. 2a and 2b);

3. The dependence of the backscattered wave spectrum on the linear absorption coefficient α of hexane:

(3.1) the disappearance of the shifted component observed when $F = 50$ or 100 cm and α is increased from 0.08 to 0.17 cm^{-1};

(3.2) the appearance of the unshifted component observed when $F = 100$ cm and α is increased from 0.08 to 0.17 cm^{-1}.

4. The substantial increase in the backscattered beam divergence observed when F is reduced from 100 to 11 cm and $\alpha = 0.01$ cm^{-1} is held constant (Figs. 3b and 3c).

6. ANALYSIS AND INTERPRETATION OF EXPERIMENTAL RESULTS

6.1. Characteristics of Stimulated Scattering

According to (1) (see [3, 17]), the threshold condition for stimulated scattering is

$$(I_L G L)^{\text{thr}} \approx 25\text{–}30. \tag{13}$$

If the total gain $I_L GL$ is below the threshold given by (13) for some SS process, then the process does not contribute to the overall SS wave pattern observed in experiment.

The length of a light pulse of duration $\tau \approx 8$ ns is $L_\text{p} \approx 2.4$ m. The amplified laser pulse of duration about 8 ns has an energy of approximately 3 mJ, a diameter of approximately 1 cm, and a divergence of $\theta \approx 3 \times 10^{-4}$ rad (Table 3). The pulse is focused by lens *9* with focal length varying from 11 to 100 cm into a cell containing a nonlinear liquid. The beam waist length varies from $L \approx 0.6$ mm for $F = 11$ cm to $L \approx 6$ cm for $F = 100$ cm. For each F, the following "long-pulse" condition is satisfied: $L_\text{p} \gg L$. At any instant, the field strength can be treated as constant over the entire waist length L, which is approximately equal to the length of the region of nonlinear interaction.

To simplify analysis, we assume that pump intensity I_L is uniformly distributed over a beam waist of diameter d_f and length L. It can be shown that the product $I_L L$ is independent of the focal length F of the lens that focuses a pump beam with power W_L, radius R_L, and divergence θ_L. Indeed,

$$I_L \approx \frac{W_L}{S_\text{f}}, \tag{14}$$

$$S_\text{f} = \frac{\pi (d_\text{f})^2}{4} \approx \frac{\pi (F\theta_L)^2}{4}, \tag{15}$$

$$L \approx \frac{d_\text{f}}{\theta_0/2} \approx \frac{2F\theta_L}{2R_L/F} = \frac{F^2\theta_L}{R_L}, \tag{16}$$

where W_L, R_L, and θ_L are independent of F; $df \approx F\theta_L$ is the diameter of the beam waist; $S_\text{f} = \pi(d_\text{f})^2/4$ is its cross-sectional area; and $\theta_0 \approx 2R_L/F$ is the convergence angle of the beam focused by the lens. We obtain

$$I_L \propto (F)^{-2}, \quad L \propto (F)^2 \longrightarrow I_L L \approx \text{const}. \tag{17}$$

Table 4. Gain factors G_T, G_B and total gain $I_LG_\text{T}L$, $I_LG_\text{B}L$ for linear STS-2 and SBS in hexane calculated for different α, but constant $I_LL \approx 1.4 \times 10^3$ MW/cm, $\lambda = 308$ nm, and $\theta = \pi$ (our experiments)

α, cm^{-1}	G_T, cm/MW	Total gain for linear STS-2 $I_LG_\text{T}L$	G_B, cm/MW	Total gain for SBS $I_\text{L}G_\text{B}L$
0.01	0.0024	3.3	0.022	31
0.046	0.011	15	0.022	31
0.1	0.024	33	0.022	31

It is essential that the values of I_LL corresponding to all values of the focal length F of lens *9* are equal:

$$I_LL \approx 1.4 \times 10^3 \text{ MW/cm}. \tag{18}$$

Since we varied F and α in our experiments, the only parameter that affects the scattering conditions as determined by value of I_LGL is α (when only linear light absorption is taken into account). If the mechanism of a stimulated scattering process does not involve α, then G is independent of α and the SS conditions do not change in our experiments.

The diameter of the amplified beam incident on lens *9* is $D_L \le 1$ cm (Table 3). The focal length of lens *9* was $F > 10$ cm. Therefore, $D_L/F < 0.1$, and the beam waist was not distorted by the spherical aberration of lens *9* or the jump in refractive index across the air–cell boundary.

6.2. Dynamics of SS Spectral Components for a Linearly Absorbing Medium

6.2.1. Total gain I_LGL for linear STS-2 and SBS. First, we estimate the decay times for linear STS-2 and SBS.

The decay time of a thermal grating is determined by expressions (7) and (10). For hexane (see [28]),

$$\tau_\text{T} = \Gamma_\text{T}^{-1} \approx \frac{1.4 \times 10^{-7}\lambda^2}{[2\sin(\theta/2)]^2} \text{ s}, \tag{19}$$

where λ is the wavelength measured in micrometers and θ is the scattering angle. For $\lambda = 0.308$ μm and $\theta = \pi$, formula (19) yields $\tau_\text{T} \approx 3$ ns. Even though this time is shorter than the pump duration ($\tau \approx 8$ ns) by almost a factor of 3, we cannot reliably use a time-independent model. Since we explore the possibility of experimental implementation of linear STS-2 rather than maximization of its efficiency, we use the steady-state gain factor G_T given by (9) to simplify further analysis.

For $q_\text{T} \approx 2k_L$ and $n \approx 1.4$, the thermal-grating step Λ_T associated with SS backscattering is estimated as

$$\Lambda_\text{T} = \frac{2\pi}{q_\text{T}} \approx \frac{2\pi}{2k_L} = \frac{n\lambda}{2} \approx 2 \times 10^{-7} \text{ m}. \tag{20}$$

Estimating the speed of sound as $v \approx 10^3$ m/s, we find the time of pressure relaxation over Λ_T:

$$\tau_\text{pr} = \frac{\Lambda_\text{T}}{v} \approx 2 \times 10^{-10} \text{ s}. \tag{21}$$

Since $\tau_\text{pr} \ll \tau$, the value of G_T can be obtained by using

$$\left(\frac{\partial\varepsilon}{\partial T}\right)_p \approx -1.5 \times 10^{-3} \text{ K}^{-1}.$$

For a hypersonic grating, the decay time $\tau_\text{B} \approx (\Gamma_\text{B})^{-1}$ given by formula (5) (see also (7) and [16]) for hexane in the case of $\lambda = 0.308$ μm and $\theta = \pi$ is $\tau_\text{B} \approx 0.3$ ns. Since $\tau_\text{B} \ll \tau$, we can apply a time-independent SBS model. Then, G_B is given by expression (6).

Both the STS-2 and SBS gain factors G_T and G_B (optimized with respect to frequency) and the total gains $I_LG_\text{T}L$ and $I_LG_\text{B}L$ calculated in hexane for $\lambda = 308$ nm, $\theta = \pi$, and several values of α such that

$$I_LL \approx 1.4 \times 10^3 \text{ MW/cm}$$

as in our experiments, are listed in Table 4.

The theoretical estimates presented in Table 4 lead to the following conclusions.

First, the total gain for linear STS-2 (which depends on α through G_T) is much lower than the threshold value given by (13) both for the "chemically pure" hexane ($\alpha = 0.046$ cm^{-1}) and a fortiori for the chromatography grade hexane ($\alpha = 0.01$ cm^{-1}). The threshold value of the linear-STS-2 total gain is reached when $\alpha \approx 0.1$ cm^{-1}.

Second, the total SBS gain $I_LG_\text{B}L$ (independent of α) is higher than threshold value (13) for any value of α.

According to the standard SS theory (which allows only for linear light absorption), this implies that SBS must be observed in all of our experiments, whereas linear STS-2 can never be observed in experiments on chemical or chromatography grade hexane.

6.2.2. Analysis of the shifted component of SS spectra. Since $I_LG_\text{B}L$ exceeds the threshold (Table 4) and the measured frequency shift 0.33 cm^{-1} (Figs. 2b and 2c) agrees with theoretical formula (8) for SBS in hexane at $\lambda = 308$ nm and $\theta = \pi$ (Table 2), it is obvious that the shifted component in the stimulated backscatter spectrum should be attributed to SBS.

To explain the absence of a shifted component in the spectra obtained for both chromatography grade (α =

0.01 cm^{-1}) and “chemically pure” ($\alpha = 0.046\ \mathrm{cm}^{-1}$) hexane (Fig. 2a), we explore the possibility of SBS breakdown.

The only mechanism that can suppress SBS under these conditions is the phase mismatch for SBS in absorbing media [3, 4]. Figure 4 shows the SBS conversion efficiency

$$\eta = \frac{I_S(L)}{I_L(L)}$$

evaluated numerically by using relation (11) as a function of the gain normalized to its threshold value,

$$x = \frac{I_L G_B L}{D}$$

for several values of α at $\lambda = 0.308\ \mu\mathrm{m}$. It is clear that the critical value corresponding to curve d is $\alpha_{CR} \approx 0.1\ \mathrm{cm}^{-1}$.

Since the values of α for both chemical and chromatography grade hexane are lower than $\alpha_{CR} \approx 0.1\ \mathrm{cm}^{-1}$, no SBS suppression due to breakdown of phase mismatch should be observed in these cases (when only linear light absorption is taken into account).

6.2.3. Analysis of the unshifted component of SS spectra. It is well known that phase conjugation can be caused by SS processes other than SBS [17, 29]. Since the measured shift relative to the pump frequency does not exceed 0.02 cm^{-1} (experimental error), we should consider both stimulated thermal scattering (STS-1 and linear STS-2) and stimulated Raleigh wing scattering (SRWS).

Since the molecular anisotropy of liquid hexane is weak [30], SRWS signal cannot be generated. Normally (see [29]), the SRWS gain factor does not exceed

$$(G_{RW})_{\max} \approx 10^{-3}\ \mathrm{cm/MW}.$$

Therefore, the total SRWS gain evaluated for our experimental conditions ($I_L L \approx 1.4 \times 10^3$ MW/cm) is $I_L G_{RW} L \approx 1.4$, which is much lower than the threshold value given by (13).

First, we consider STS-1. According to [29], the STS-1 to SBS gain factor ratio is

$$\frac{G_{RL}}{G_B} = \frac{\gamma^R \Gamma_B}{\gamma^e \Gamma_{RL}} = \frac{(\delta - 1)c\Gamma_B}{4\pi v \omega_2}, \qquad (22)$$

where ω_2 is the backscattered-wave frequency,

$$\gamma^e = \rho\left(\frac{\partial \varepsilon}{\partial \rho}\right)_T,$$

$$\gamma^R = \frac{(\delta - 1)c\gamma^e \Gamma_{RL}}{4\pi v \omega_2},$$

$$\delta = \frac{C_p}{C_v},$$

and v is the speed of sound.

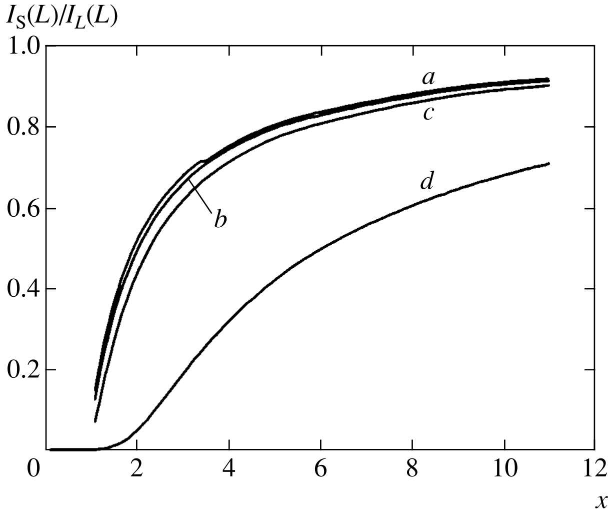

Fig. 4. Predicted SBS conversion efficiency $\eta = I_S(L)/I_L(L)$ vs. threshold value of $x = I_L G_B L/D$ for hexane at $\lambda = 0.308\ \mu\mathrm{m}$ and α = (a) 0.0001, (b) 0.03, (c) 0.05, and (d) 0.1 cm^{-1}.

For hexane at $\lambda = 308$ nm, we obtain $\delta = 1.4$, $v \approx 10^3$ m/s, $\Gamma_B \approx 3 \times 10^9$ Hz, and $\omega_2 \approx 10^{15}$ Hz. Then,

$$G_{RL}/G_B \approx 2 \times 10^{-2}.$$

A comparison with the values of G_B listed in Table 4 shows that threshold condition (13) cannot be satisfied for SRWS in our experiments ($I_L L \approx 1.4 \times 10^3$ MW/cm), since $I_L G_{RL} L \approx 0.6$.

Since the physical mechanisms of SRWS and STS-1 do not involve absorption of radiation, the corresponding threshold conditions must be independent of α (Table 4). Therefore, the SBS, SRWS, and STS-1 threshold conditions did not change in our experiments ($I_L L \approx$ const).

However, absorption is involved in linear STS-2 processes, and the corresponding threshold conditions vary with α while $I_L L$ was constant. In particular, linear STS-2 is possible under our experimental conditions (Table 4) only when $\alpha > 0.1\ \mathrm{cm}^{-1}$.

6.3. Analysis of Decrease in Phase-Conjugation Fidelity for a Linearly Absorbing Medium

Consider the following cylindrically symmetric problem, denoting the radial coordinate by R. A pump with a plane wavefront, a spatially nonuniform intensity $I_L(R, t)$, and a duration of τ enters a nonlinear medium at $t = 0$ across the boundary $z = L$ and propagates toward the boundary $z = 0$. The phase conjugate wave with intensity $I_S \ll I_L$ generated in the medium propagates from $z = 0$ to $z = L$. The linearly absorbing medium is characterized by the coefficient α. Suppose that heat conduction does not contribute to the temperature redistribution over the beam cross section. Then, the temperature increment over a time t is

$$\begin{aligned}\Delta T(R, t) &= \frac{1}{\rho C_p}\int_0^t \alpha I_L(R, \tau)d\tau \\ &= \frac{\alpha}{\rho C_p}\int_0^t I_L(R, \tau)d\tau.\end{aligned} \tag{23}$$

Since refractive index depends on temperature, its initially uniform distribution will be perturbed:

$$n = n_0 + \delta n(T),$$

where the nonlinear term is a function of R and t:

$$\begin{aligned}\delta n(R, t) &= \frac{\partial n}{\partial T}\Delta T(R, t) \\ &= \frac{\partial n}{\partial T}\frac{\alpha}{\rho C_p}\int_0^t I_L(R, \tau)d\tau.\end{aligned} \tag{24}$$

The perturbed wavenumber is

$$k = k_0 + \delta k = \frac{\omega}{c}(n_0 + \delta n),$$

and the nonlinear phase incursion over the distance L is

$$\begin{aligned}\Delta\Phi(R, t) &= \delta kL = \frac{\omega L}{c}\delta n(R, t) \\ &= \frac{\omega L}{c}\left(\frac{\partial n}{\partial T}\right)\frac{\alpha}{\rho C_p}\int_0^t I_L(R, \tau)d\tau.\end{aligned} \tag{25}$$

According to (25), a radially nonuniform nonlinear phase incursion will develop in a wave that has a plane front at $z = 0$; i.e., the wave will have a distorted front at $z = L$. The phase incursion is zero at $t = 0$ and highest at the trailing edge of the pulse.

Thus, the phase conjugate backscattered wave will be coupled to a dynamically distorted beam, rather than a beam with diffraction-limited divergence; i.e., it will also have a distorted front.

As shown above, the product $I_L L$ contained in expression (25) for the nonlinear phase incursion remains invariant when the focal length F is changed. Therefore, linear absorption with $\alpha = 0.01$ cm^{-1} cannot explain not only the decrease in phase-conjugation fidelity, but not even the substantial increase in the nonlinear phase self-modulation of the pump in hexane observed when the focal length is reduced from $F = 100$ cm to $F = 11$ cm (Figs. 3b and 3c).

6.4. Stimulated Scattering Induced by Two-Photon Absorption

In summary, the standard SBS theory developed for linearly absorbing media cannot explain the totality of our experimental results concerning the mechanisms of stimulated scattering of XeCl excimer laser radiation ($\lambda = 308$ nm) in hexane. First, since linear absorption with $\alpha < 0.1$ cm^{-1} is not sufficiently strong to give rise to linear STS-2, the origin of the unshifted component observed when $\alpha < 0.1$ cm^{-1} (Figs. 2a and 2b) remains unclear. Second, since linear absorption with $\alpha < 0.1$ cm^{-1} is not strong enough to suppress the SBS signal via phase mismatch, the disappearance of the SBS component observed when the focal length of lens *9* is reduced from $F = 50$ cm to $F = 11$ cm for $\alpha < 0.1$ cm^{-1} (Figs. 2a and 2b) is yet to be explained. Third, linear absorption with $\alpha = 0.01$ cm^{-1} = const cannot explain the substantial decrease in phase-conjugation fidelity caused by the mere decrease in the focal length of lens *9* from $F = 100$ cm to $F = 11$ cm (Figs. 3b and 3c).

It is well known that two-photon absorption should be expected to occur in hexane at $\lambda < 400$ nm [31]. Suppose that our experimental results concerning the mechanisms of stimulated scattering of XeCl excimer laser radiation ($\lambda = 308$ nm) in hexane reflect a strong effect of two-photon absorption. More specifically, assume that the unshifted line in the measured backscattered wave spectrum (Figs. 2a and 2b) corresponds to an STS-2 mechanism associated with the heating caused by two-photon absorption. In what follows, we call this new SS mechanism *two-photon STS-2*, as distinct from the previously known STS-2 induced by linear (single-photon) absorption, i.e., linear STS-2.

The variation of light intensity controlled by two-photon absorption is described by the equation [29, 32]

$$\frac{dI}{dz} = -\gamma I^2, \tag{26}$$

where I is the intensity of radiation propagating along the z axis and γ is the two-photon absorption coefficient. Its solution is

$$I(z) = \frac{I_0}{1 + I_0\gamma z}, \tag{27}$$

where $I_0 = I(0)$. In the case of weak absorption ($I_0\gamma z \ll 1$), this solution reduces to

$$I(z) = I_0(1 - I_0\gamma z). \tag{28}$$

In our experiments, $I_L L \approx 1.4 \times 10^3$ MW/cm and $\gamma \approx 10^{-4}$ cm/MW (see below), and we have $I_L\gamma L < 0.2$. Thus, we can use expression (28).

The variation of light intensity controlled by weak linear absorption with coefficient α is described by the equation

$$I(z) = I_0(1-\alpha z). \tag{29}$$

It follows from (28) and (29) that $I_L\gamma$ plays the role of α in our experiments, and we can define the total absorption coefficient α_Σ as

$$\alpha_\Sigma = \alpha + I_L\gamma. \tag{30}$$

The quantity $I_L L$ can be treated as the two-photon contribution to the total absorption coefficient α_Σ.

Note that the equivalence should be understood only in a quantitative sense. Linear (single-photon) and two-photon absorption can be treated as similar processes only with respect to the final result of resonant light–matter interaction, i.e., irreversible dissipation of electromagnetic energy into heat. However, the resonant interactions responsible for linear and two-photon absorption are different in terms of both quantum mechanical processes involved and dipole matrix elements contained in the expressions for the respective scattering cross sections. In other words, linear STS-2 and two-photon STS-2 are essentially different, being roughly similar only with respect to the final stage of electromagnetic energy dissipation, i.e., transformation of temperature fluctuations into permittivity fluctuations.

6.5. Calculation of the Cross Section of Two-Photon Absorption from the Threshold Pump Intensity for Two-Photon STS-2

As indicated above, when $I_L L$ = const, linear STS-2 is characterized by a threshold value of α: it can occur only if $\alpha \geq \alpha_{\text{sts}}^{\text{thr}}$. By analogy with linear STS-2, two-photon STS-2 must also exhibit threshold behavior, but with respect to $I_L\gamma$ rather than α. Therefore, when $I_L L$ = const and the material properties (α and γ) are held constant, an increase in I_L caused by a decrease in F must lead to totally different changes in the linear and two-photon STS-2 mechanisms. In particular, the total gain $(I_L G_T L)$ must remain invariant for linear STS-2 and increase for two-photon STS-2 since $G_T \propto \alpha$ = const and $G_T \propto (I_L\gamma) \propto I_L$ in the former and latter processes, respectively.

Linear and two-photon STS-2 can be distinguished experimentally: if a medium with a constant $\alpha \ll \alpha_{\text{sts}}^{\text{thr}}$ is used and I_L is gradually increased while $I_L L$ is held constant, then a component corresponding to "pure" two-photon STS-2 must appear in the stimulated backscatter spectrum when $I_L\gamma \approx \alpha_{\text{sts}}^{\text{thr}}$.

Table 5. Two-photon contribution $I_L\gamma$ to the total coefficient of absorption at λ = 308 nm in hexane for three values of the focal length of lens *9* and the corresponding pump intensities

F, cm	I_L, W/cm^2	$I_L\gamma$, cm^{-1}
11	$\geq 10^{10}$	≥ 1.0
50	10^9	≈ 0.1 (experiment)
100	2.5×10^8	≈ 0.025

Let us find $I_L\gamma$ using the threshold condition for two-photon STS-2. According to Table 4, the gain for STS-2 reaches a threshold value when

$$\alpha_\Sigma^{\text{thr}} \approx \alpha_{\text{sts}}^{\text{thr}} \approx 0.1 \text{ cm}^{-1}.$$

It follows from our experimental results that an unshifted STS-2 component appears in the stimulated backscatter spectrum for α = 0.01 cm^{-1} (Fig. 2b) when $I_L^{\text{thr}} \approx 10^9$ W/cm^2 (F = 50 cm). Indeed, when $I_L \approx 2.5 \times 10^8$ W/cm^2 (F = 100 cm), no unshifted component is observed (Fig. 2c); i.e., the STS-2 threshold is not reached. Since α is small,

$$\alpha = 0.01 \text{ cm}^{-1} \ll \alpha_{\text{sts}}^{\text{thr}} \approx 0.1 \text{ cm}^{-1},$$

it is obvious that the observed neutral STS-2 component (Fig. 2b) can be attributed only to two-photon STS-2. Therefore, the threshold pump intensity $I_L^{\text{thr}} \approx 10^9$ W/cm^2 can be used to obtain the estimate

$$\alpha_\Sigma^{\text{thr}} = \alpha + (I_L^{\text{thr}}\gamma) \approx (I_L^{\text{thr}}\gamma) \approx \alpha_{\text{thr}}^{\text{sts}} \approx 0.1 \text{ cm}^{-1}.$$

The coefficient γ of two-photon absorption at a particular wavelength is a property of the medium (in our case, chromatography grade hexane). If $I_L\gamma$ corresponding to a particular value of I_L is known, then it can readily be calculated for other values of I_L. The values of $I_L\gamma$ calculated for the pump intensities I_L corresponding to the three focal lengths of lens *9* used in our experiments are listed in Table 5.

Using a known value of $I_L\gamma$, we can find γ for λ = 308 nm:

$$\gamma = \frac{I_L\gamma}{I_L} = \frac{0.1 \text{ cm}^{-1}}{10^9 \text{ W/cm}^2} \tag{31}$$
$$= 10^{-10} \text{ cm/W} = 10^{-4} \text{ cm/MW}.$$

We can also calculate the cross section σ_2 for two-photon absorption in a nonlinear medium. Indeed,

$$I_L\gamma = \sigma_2 I_L N, \tag{32}$$

Table 6. Physical mechanisms of stimulated backscattering of beams with $\lambda = 308$ nm and $\tau \approx 8$ ns in liquid hexane for different values of linear absorption coefficient and pump intensity, but constant $I_L L \approx 1.4 \times 10^3$ MW/cm (L is the length of the region of nonlinear interaction)

F, cm	I_L, W/cm^2	Physical mechanisms of stimulated backscattering	
		$\alpha = 0.01$–0.08 cm^{-1}	$\alpha = 0.17$ cm^{-1}
100	2.5×10^8	SBS	linear STS-2
50	10^9	SBS + two-photon STS-2	linear STS-2 + two-photon STS-2
11	$\geq 10^{10}$	two-photon STS-2	

where I_L is the pump intensity (photon cm^{-2} s^{-1}), $N = \rho/M$ is the molecular density (ρ is density, M *is* molecular mass). For hexane (C_6H_{14}), we have $N \approx 4 \times 10^{21}$ cm^{-3}. The photon energy corresponding to $\lambda = 308$ nm ($\omega = 10^{15}$ Hz) is $\hbar\omega \approx 4$ eV $\approx 6.4 \times 10^{-19}$ J. Since $I_L\gamma = 0.1$ cm^{-1} and $I_L = 10^9$ W/cm^2 (Table 5), we obtain

$$\sigma_2 = \frac{\hbar\omega I_L\gamma}{I_L N} \approx (2 \pm 1) \times 10^{-50} \text{ cm}^4 \text{ s}. \tag{33}$$

The accuracy of the calculation of σ_2 is estimated as follows:

$$\frac{\delta\sigma_2}{\sigma_2} = \frac{\delta\alpha^{\text{thr}}}{\alpha^{\text{thr}}} + \frac{\delta I_L}{I_L} = 0.2 + 0.3 = 0.5, \tag{34}$$

where α^{thr} is the STS-2 threshold value of linear absorption coefficient.

For comparison, consider two-photon nonresonant ionization of many-electron atoms at a moderate field strength. The cross section for this process does not involve any substantial contributions due to near-threshold absorption, multiple ionization, and perturbation of atomic spectrum [33, 34], and its typical value is

$$\sigma_2^i \approx 10^{-49}\text{–}10^{-48} \text{ cm}^4 \text{ s}.$$

Normally, σ_2^i is much smaller than the cross sections for bound–bound transitions in atoms or molecules at the absorption-line center. The value of σ_2 extracted from experimental data is smaller than the two-photon ionization cross section. This substantiates our assumption about a dominant contribution of two-photon absorption to the STS-2 gain. The relatively small value of σ_2 may be explained by the fact that the final excited level in the two-photon absorption scheme ($\lambda/2 = 154$ nm for hexane) corresponds to the wing of an absorption line.

6.6. Phase Mismatch for SBS Enhanced by Two-Photon Absorption

The relationship between the two-photon contribution $I_L\gamma$ to total absorption coefficient (30) and the focal length F of lens *9* (see Table 5) explains the SBS component is not observed in the stimulated backscatter spectrum for chromatography grade hexane ($\alpha = 0.01$ cm^{-1}) when lens *9* with $F = 11$ cm is used (Fig. 2a). Indeed, $I_L \geq 10^{10}$ W/cm^2 in this case, and the total absorption coefficient (Table 5)

$$\alpha_\Sigma = \alpha + I_L\gamma \approx I_L\gamma \geq 1.0 \text{ cm}^{-1}$$

is much larger than its critical value $\alpha_{\text{CR}} \approx 0.1$ cm^{-1} corresponding to SBS breakdown due to phase mismatch (Fig. 4). The heating due to two-photon absorption is then sufficiently large to cause SBS breakdown.

6.7. Analysis of Decrease in the Fidelity of Phase Conjugation Induced by Two-Photon Absorption

Assuming that two-photon absorption plays a dominant role, we replace α with $I_L\gamma$ in (23), and expression (25) for the nonlinear phase incursion over the distance L becomes

$$\begin{aligned}\Delta\Phi(R, t) &= \delta k L = \frac{\omega L}{c}\delta n(R, t) \\ &= \frac{\omega L}{c}\frac{\partial n}{\partial T}\frac{\gamma}{\rho C_p}\int_0^t I_L^2(R, \tau)d\tau.\end{aligned} \tag{35}$$

The quantity LI_L^2 in (35) increases with the pump intensity in the beam waist as F decreases. Thus, two-photon absorption explains the increase in the nonlinear phase self-modulation of the pump in hexane observed when the focal length is reduced from $F = 100$ cm to $F = 11$ cm.

In our experiments, the hypersonic-grating decay time for hexane is $\tau_B \approx 0.3$ ns (see above), which is smaller than the pump pulse duration, $\tau \approx 8$ ns, by a factor of almost 30. This means that SBS can be considered as a zero-inertia process: the written phase hologram instantly adjusts to the varying pump field. Therefore, even if we take into account the dynamic variation of the spatial pump profile associated with the self-action due to the heating caused by two-photon absorption, then the complex conjugate SBS wave must ensure a high fidelity of phase conjugation.

The thermal-grating decay time for hexane in our experiments is $\tau_T \approx 3$ ns (see above), which is smaller than the pump pulse duration, $\tau \approx 8$ ns, by only about three times. Therefore, two-photon absorption cannot be considered as an zero-inertia process. Dynamic variations of the induced grating cannot keep pace with the variations of the pump field. Since an advanced field is scattered by a retarded hologram, the fidelity of phase conjugation is degraded.

6.8. Stimulated-Scattering Mechanisms Consistent with Our Experiments

Table 6 summarizes the results of experimental and theoretical studies of stimulated backscattering of pulses with $\lambda = 308$ nm and $\tau \approx 8$ ns in liquid hexane. The first column shows the values of the focal length of lens *9* in our experiments. The second column shows the values of pump intensity I_L in the region of nonlinear interaction of length L. Since this region corresponds to the waist of the beam focused by lens *9*, the quantity $I_L L \approx 1.4 \times 10^3$ MW/cm is the same for all values of F. The last two columns list the stimulated backscattering mechanisms revealed for two characteristic values of the linear absorption coefficient of hexane: $\alpha = 0.01$–0.08 cm^{-1} and $\alpha = 0.17$ cm^{-1}.

Note that some cells in Table 6 contain unique mechanisms (SBS, linear STS-2, or two-photon STS-2); others, two mechanisms (SBS + two-photon STS-2 or linear STS-2 + two-photon STS-2). An analysis of the case of $I_L \approx 2.5 \times 10^8$ W/cm^2 ($F = 100$ cm), when the contribution of two-photon absorption to the overall pattern of stimulated scattering is insignificant (see Table 5), leads to the following conclusions.

1. "Linear STS-2" is present when α is greater than 0.08 cm^{-1}, but smaller than 0.17 cm^{-1}. This agrees with the threshold value estimated for linear STS-2, $\alpha_{\text{sts}}^{\text{thr}} \approx$ 0.1 cm^{-1} (see Table 4).

2. The absence of "SBS" for $\alpha = 0.17$ cm^{-1} and its presence for $\alpha \le 0.08$ cm^{-1} is consistent with our theoretical conclusion that phase mismatch is effective for SBS when $\alpha \ge \alpha_{\text{CR}} \approx 0.1$ cm^{-1} (see Fig. 4).

3. The absence of the "SBS + linear STS-2" combination is explained by the fact that $\alpha_{\text{sts}}^{\text{thr}} \approx 0.1$ cm^{-1} is close to $\alpha_{\text{CR}} \approx 0.1$ cm^{-1} for SBS phase mismatch, while the steps of α variation from 0.08 cm^{-1} to 0.17 cm^{-1} in our experiments is not sufficiently small to observe both processes simultaneously.

The presence of the "SBS + two-photon STS-2" combination in Table 6 indicates that the steps of variation of $\alpha_\Sigma = \alpha + I_L\gamma$ in our experiments is sufficient for simultaneous observation of both processes. The presence of the "linear STS-2 + two-photon STS-2" combination in Table 6 is yet to be substantiated. In contrast to the "SBS + STS-2" combination, these two processes are virtually impossible to distinguish in experimental stimulated backscatter spectra. Our theoretical analysis shows that neither linear not two-photon STS-2 can be singled out as the dominant one when $\alpha > 0.1$ cm^{-1} and $I_L > 10^9$ W/cm^2.

6.9. Experimental Observation of SBS in the UV Region

According to the standard SBS theory, taking into account only linear absorption (see Table 4 and Fig. 4), the condition $I_L L \approx$ const implies that the only mechanism that can work in our experiments with $\alpha <$ 0.1 cm^{-1} is SBS, while only linear STS-2 can work when with $\alpha > 0.1$ cm^{-1} (in view of phase mismatch for SBS). It is no surprise that these very mechanisms are listed in the last column of Table 1 as those suggested in previous experimental studies.

It can be shown that both "SBS" and "linear STS-2" listed Table 1 are incorrect. Indeed, it follows from the data in the third column of Table 1 that $I_L \ge 10^{10}$ W/cm^2 in all previous experimental studies. However, according to Table 6, either "two-photon STS-2" or "linear STS-2 + two-photon STS-2" should be observed in hexane when $\alpha < 0.1$ cm^{-1} and $\alpha > 0.1$ cm^{-1}, respectively. Therefore, "SBS" should be replaced with "two-photon STS-2" in all rows of Table 1 except for the last one, while "linear STS-2" should be replaced with "linear STS-2 + two-photon STS-2" in the last row. These considerations are corroborated by the fact that the measured frequency Ω in the fourth column of Table 1 is much less than the Brillouin shift Ω_{B} predicted theoretically for the same value of λ (Table 2). It can be concluded that genuine SBS has never been observed in all previous studies of stimulated scattering in the near UV region.

In our experiments on stimulated scattering in hexane at the pump frequency $\lambda = 308$ nm, we observed an SBS line with a Brillouin shift $\Omega_{\text{B}} = 0.33$ cm^{-1} (see Figs. 2b and 2c) that fully agreed with that predicted by the SBS theory (see Table 2). Thus, we were the first to observe a genuine SBS line in the near UV region.

To "grasp" the genuine SBS line in our experiments, we had to reduce the pump intensity from $I_L \ge$ 10^{10} W/cm^2 (Fig. 2a) used in previous studies (Table 1) to $I_L \le 10^9$ W/cm^2 (Figs. 2b and 2c) while keeping the conditions for SBS invariant ($I_L L \approx$ const). This made it possible to reduce the two-photon contribution to the total absorption coefficient of hexane and thus weaken the effect of SBS phase mismatch due to the heating caused by two-photon absorption.

7. CONCLUSIONS

The present study focuses on the physical mechanisms of stimulated light scattering in the near UV region. The complex problems yet to be solved in this field of research concern both temporal and spatial behavior of laser beams in SS processes. With regard to temporal behavior, the problem of frequency shift is of primary importance. With regard to spatial behavior, the principal problem is the decrease in phase-conjugation fidelity with increasing pump intensity.

To deal with these problems, we constructed an experimental setup based on a XeCl excimer laser (λ = 308 nm), which generated a single-mode pulse with a duration of $\tau \approx 8$ ns, an energy of about 3 mJ, and a bandwidth of approximately 5×10^{-3} cm^{-1}. We chose liquid hexane (C_6H_{14}) as a nonlinear medium. The setup was used to conduct experimental studies of both temporal stimulated backscatter spectra and phase-conjugation fidelity. An analysis of the experimental results shows that the standard theory of stimulated scattering, which takes into account only linear absorption, cannot explain these results. The problems are resolved only by introducing a new physical mechanism: stimulated thermal scattering induced by the heating caused by two-photon absorption (two-photon STS-2).

First, the “abnormal” SBS lines observed in previous experiments, with frequency shifts much smaller than expected, actually were unshifted two-photon STS-2 lines.

Second, the decrease in SBS phase-conjugation fidelity should be interpreted as decrease in two-photon STS-2 phase-conjugation fidelity, because two-photon STS-2, in contrast to SBS, involves thermal self-action and is characterized by a relatively long decay time.

Third, we used measured threshold pump intensities for two-photon STS-2 to evaluate the cross section for two-photon absorption at λ = 308 nm in a nonlinear medium (hexane). On the one hand, the obtained value of the cross section substantiates the very existence of two-photon STS-2. Oh the other hand, the two-photon absorption characterized by this cross section explains certain experimentally observed phenomena, such as SBS breakdown due to phase mismatch caused by two-photon absorption.

A comparison of characteristics of linear and two-photon STS-2 shows that these are essentially different mechanisms of stimulated scattering and the corresponding lines can readily be distinguished in stimulated backscatter spectra. The total inconsistency of the experimentally observed behavior of the two-photon STS-2 line with the well-known behavior of the linear STS-2 line explains the fact that the two-photon STS-2 lines observed in the studies of stimulated scattering in the near UV region were attributed to SBS for almost a decade. The genuine SBS line was found in the UV region in our experiments only by using a pump beam of much lower intensity. The mechanism of two-photon STS-2 is not specific to the near UV spectral region.

REFERENCES

1. V. G. Dmitriev, *Nonlinear Optics and Wave Front Reversal* (Fizmatlit, Moscow, 2003) [in Russian].
2. I. L. Fabelinskiĭ, *Molecular Scattering of Light* (Nauka, Moscow, 1965; Plenum, New York, 1968).
3. V. V. Kuz’min, Tr. Fiz. Inst. im. P. N. Lebedeva, Akad. Nauk SSSR **207**, 3 (1991).
4. S. F. Grigor’ev, O. P. Zaskal’ko, and V. V. Kuz’min, Zh. Éksp. Teor. Fiz. **92**, 1246 (1987) [Sov. Phys. JETP **65**, 697 (1987)].
5. V. S. Starunov, Zh. Éksp. Teor. Fiz. **57**, 1012 (1969) [Sov. Phys. JETP **30**, 553 (1970)].
6. V. Yu. Baranov, V. M. Borisov, and Yu. Yu. Stepanov, *Electric-Discharge Excimer Lasers on Inert Gas Halogenides* (Énergoatomizdat, Moscow, 1988) [in Russian].
7. M. Statkine, I. J. Bigio, B. J. Feldman, and R. A. Fisher, Opt. Lett. **7**, 108 (1982).
8. M. C. Gower, Opt. Lett. **7**, 423 (1982).
9. M. C. Gower, Opt. Lett. **8**, 70 (1983).
10. E. Armandillo and D. Proch, Opt. Lett. **8**, 523 (1983).
11. M. C. Gower and R. G. Caro, Opt. Lett. **7**, 162 (1982).
12. G. M. Davis and M. C. Gower, IEEE J. Quantum Electron. **27**, 496 (1991).
13. S. S. Alimpiev, V. S. Bukreev, S. K. Vartapetov, *et al.*, Kratk. Soobshch. Fiz., No. 12, 11 (1989).
14. A. I. Alimpiev, V. S. Bukreev, S. K. Vartapetov, *et al.*, Kvantovaya Élektron. (Moscow) **18**, 89 (1991).
15. N. B. Delone, *Interaction of Laser Radiation with Matter* (Nauka, Moscow, 1989) [in Russian].
16. V. S. Starunov and I. L. Fabelinskiĭ, Usp. Fiz. Nauk **98**, 441 (1969) [Sov. Phys. Usp. **12**, 463 (1970)].
17. B. Ya. Zel’dovich, N. F. Pilipetskiĭ, and V. V. Shkunov, *Wave Front Reversal* (Nauka, Moscow, 1985) [in Russian].
18. S. Kielich, *Molecular Nonlinear Optics* (Wydawn. Naukowe Uniw., Poznan’, 1972; Nauka, Moscow, 1981).
19. L. D. Landau and E. M. Lifshitz, *Course of Theoretical Physics*, Vol. 8: *Electrodynamics of Continuous Media*, 2nd ed. (Nauka, Moscow, 1982; Pergamon, Oxford, 1984).
20. M. B. Vinogradova, O. V. Rudenko, and A. P. Sukhorukov, *The Theory of Waves* (Nauka, Moscow, 1979) [in Russian].
21. L. D. Landau and E. M. Lifshitz, *Course of Theoretical Physics*, Vol. 5: *Statistical Physics* (Nauka, Moscow, 1976; Pergamon, Oxford, 1980), Part 1.
22. V. B. Karpov, I. N. Knyazev, V. V. Korobkin, and A. K. Naboĭchenko, in *Proceedings of 2nd All-Union Conference OVF-89* (Inst. Fiz. Akad. Nauk BSSR, Minsk, 1990), p. 245.
23. V. B. Karpov and A. K. Naboĭchenko, Tr. Inst. Obshch. Fiz., Ross. Akad. Nauk **41**, 173 (1993).

24. V. B. Karpov, I. N. Knyazev, V. V. Korobkin, and A. K. Naboichenko, in *Short Wavelength Lasers and Their Applications* (Nova Sci., New York, 1991), p. 391.
25. V. B. Karpov, I. N. Knyasev, V. V. Korobkin, and A. M. Prokhorov, in *Proceedings of International Conference LASERS-89* (STS Press, VA, USA, 1990), p. 325.
26. V. B. Karpov, V. V. Korobkin, and D. A. Dolgolenko, in *Proceedings of International Conference ECO-4* (The Hague, Netherlands, 1991).
27. A. L. Egorov, V. V. Korobkin, and R. V. Serov, Kvantovaya Élektron. (Moscow) **2**, 513 (1975).
28. N. N. Zhukov, O. P. Zaskal'ko, and I. G. Kuznetsov, Kvantovaya Élektron. (Moscow) **18**, 234 (1991).
29. Y. R. Shen, *The Principles of Nonlinear Optics* (Wiley, New York, 1984; Nauka, Moscow, 1989).
30. P. P. Ho and R. R. Alfano, Phys. Rev. A **20**, 2170 (1979).
31. A. J. Gordon and R. A. Ford, *The Chemist's Companion* (Wiley, 1972).
32. Yu. N. Karamzin, A. P. Sukhorukov, and V. A. Trofimov, *Mathematical Modeling in Nonlinear Optics* (Mosk. Gos. Univ., Moscow, 1989) [in Russian].
33. M. Ammosov, N. Delone, M. Ivanov, *et al.*, Adv. At. Mol. Opt. Phys. **29**, 34 (1992).
34. N. B. Delone and V. P. Kraĭnov, *Nonlinear Ionization of Atoms by Laser Radiation* (Fizmatlit, Moscow, 2001) [in Russian].

Translated by A. Betev

Journal of Experimental and Theoretical Physics, Vol. 100, No. 5, 2005, pp. 884–894.
Translated from Zhurnal Éksperimental'noĭ i Teoreticheskoĭ Fiziki, Vol. 127, No. 5, 2005, pp. 1005–1016.

Amplification of Light during the Scattering of a Relativistic Electron by a Nucleus in a Moderately Strong Field of a Circularly Polarized Light Wave

S. P. Roshchupkin* and V. A. Tsybul'nik

Institute of Applied Physics, National Academy of Sciences of Ukraine, Sumy, 40030 Ukraine
**e-mail: rsp@roshchupkin.sumy.ua*

Received September 27, 2004

Abstract—The amplification (attenuation) factor of an electromagnetic wave during the scattering of a relativistic electron by a nucleus in a moderately strong field of a circularly polarized electromagnetic wave is studied theoretically. The effect of amplification of an electromagnetic field is discovered in a certain interval of polar angles of the incident electron; this interval of angles essentially depends on the electron energy and the field intensity. It is shown that the amplification of a field attains its maximum for nonrelativistic electrons in the range of medium fields. As the electron energy increases, the amplification decreases and vanishes for ultrarelativistic electrons. An increase in the field intensity for a given electron energy also leads to a slow decrease in the amplification of a field. At high intensities of the wave, the effect of amplification vanishes. It is shown that, in the range of optical frequencies for medium fields ($F \sim 10^6$ V/cm), the amplification factor of laser light may amount to about $\mu \sim 10^{-1}$ cm^{-1} for sufficiently high-power electron beams. © *2005 Pleiades Publishing, Inc.*

1. INTRODUCTION

A quantum-mechanical calculation of the attenuation (amplification) factor of an electromagnetic wave during the scattering of an electron by a nucleus in the field of a linearly polarized electromagnetic wave has been known for a rather long time (see the fundamental paper by Marcuse [1], as well as papers [2–5] and monographs [6–9]). It is characteristic that the amplification of an electromagnetic field (the Marcuse effect) was discovered in a weak field (in the first order of perturbation theory), whereas, in the limit of a strong field (when the velocity of the quivery motion of an electron is much greater than the velocity of its translational motion), the effect of amplification of a light wave vanished and the wave was absorbed. However, the region of intermediate intensities of the electromagnetic field (between weak and strong fields) was not studied. In [10], we investigated this effect in the nonrelativistic limit of electron velocities (in the dipole approximation) for a circularly polarized wave in the intermediate range of field intensities when the velocity of the quivery motion of an electron is on the same order as or less than the velocity of its translational motion. We demonstrated that the amplification of a wave occurs when the momenta of the initial electron lie within a cone whose axis lies in the polarization plane of the wave.

In the present study, we calculate the amplification (attenuation) factor of an electromagnetic wave during the scattering of an electron by a nucleus in the field of a circularly polarized electromagnetic wave for weak, medium, and moderately strong fields. We find out the effect of amplification of an electromagnetic wave that essentially depends on the scattering kinematics of electrons, their energy, and the field intensity. Throughout this paper, we use the relativistic system of units: $\hbar = c = 1$.

2. TOTAL CROSS SECTION OF STIMULATED EMISSION AND ABSORPTION OF BREMSSTRAHLUNG

Let us choose a 4-potential of an external field in the form of a circularly polarized electromagnetic wave that propagates along the z axis:

$$A(\varphi) = \frac{F}{\omega}(e_x\cos\varphi + \delta e_y \sin\varphi),\qquad \varphi = \omega(t - z). \tag{1}$$

Here, $e_x = (0, \mathbf{e}_x)$ and $e_y = (0, \mathbf{e}_y)$ are 4-vectors of the wave polarization, and F, ω, and $\delta = \pm 1$ are the intensity, frequency, and polarization of the wave, respectively. There are two characteristic parameters in this problem: the classical relativistically invariant parameter

$$\eta = \frac{e\sqrt{-A^2}}{m} = \frac{eF}{m\omega} \tag{2}$$

and the quantum multiphoton parameter [2, 4] (the

Bunkin–Fedorov parameter)

$$\gamma_0 = \eta \frac{m v_i}{\omega}. \tag{3}$$

Here, e, m, and v_i (see (12) below) are the charge, mass, and initial velocity of the electron, respectively. Note that, for relativistic electrons in the range of optical frequencies ($\omega \sim 10^{15}\ \mathrm{s}^{-1}$), the parameters η and γ_0 are on the order of unity in fields of $F \sim 10^{10}$–10^{11} and $F \sim 10^5$–10^6 V/cm, respectively.

We will study this problem in the Born approximation with respect to the interaction between electrons and the field of a nucleus ($Ze^2/v_{i,f} \ll 1$) for the intensity of the external electromagnetic field (1) satisfying the condition

$$\eta^2 \ll 1, \tag{4}$$

we will assume that the photon energy of the wave is small compared with the electron energy,

$$\begin{gathered} \frac{2\omega}{m v_i^2} \ll 1, \text{ if } v_i \ll 1, \\ \frac{\omega}{E_i} \ll 1, \text{ if } E_i \gtrsim m. \end{gathered} \tag{5}$$

In the general relativistic case, the cross section of stimulated emission and absorption of bremsstrahlung (SEAB) in the field of a plane wave was obtained in [11] (see also [12–14]); for a circularly polarized external field (1) in the range of intensities (4), this cross section is

$$d\sigma = \sum_{l=-\infty}^{\infty} d\sigma_l, \tag{6}$$

where the partial differential cross section of the scattering of a relativistic electron by a nucleus Ze accompanied by the emission ($l > 0$) and absorption ($l < 0$) of $|l|$ photons is given by

$$\begin{aligned} d\sigma_l &= \frac{2(Ze^2)^2}{|\mathbf{p}_i| E_f}(m^2 + E_i E_f + \mathbf{p}_i \cdot \mathbf{p}_f) \\ &\quad \times \frac{\delta(q_0)}{\mathbf{q}^4} J_l^2(\gamma) d\mathbf{p}_f. \end{aligned} \tag{7}$$

Here, $p_{i,f} = (E_{i,f}, \mathbf{p}_{i,f})$ is the 4-momentum of the electron in the initial and final states and $q = (q_0, \mathbf{q})$ is the transferred 4-momentum, which is determined by the 4-quasimomentum of the electron $\tilde{p}_{i,f} = (\tilde{E}_{i,f}, \tilde{\mathbf{p}}_{i,f})$ and the 4-momentum of the photon of the external field $k = (\omega, \mathbf{k})$:

$$\begin{aligned} q &= \tilde{p}_f - \tilde{p}_i + lk, \\ \tilde{p}_{i,f} &= p_{i,f} + \eta^2 \frac{m^2}{2kp_{i,f}} k. \end{aligned} \tag{8}$$

The argument of the Bessel function $J_l(\gamma)$ in the partial cross section (7) is given by

$$\begin{gathered} \gamma = \eta m \sqrt{(e_x Q_{fi})^2 + (e_y Q_{fi})^2} = \eta m \sqrt{-Q_{fi}^2}, \\ Q_{fi} = \frac{p_f}{kp_f} - \frac{p_i}{kp_i}. \end{gathered} \tag{9}$$

We emphasize that expression (9) for the quantum parameter γ can be represented as

$$\gamma = \gamma_0 \frac{\omega}{v_i} |\mathbf{Q}_{fi}| \sin\theta, \quad \theta = \angle(\mathbf{k}, \mathbf{Q}_{fi}). \tag{10}$$

Formula (10) shows that the argument of the Bessel function in the Bunkin–Fedorov kinematic domain (when $\sin\theta \approx 1$) satisfies the relation $\gamma \sim \gamma_0$ (see also [12, 13]). Outside the Bunkin–Fedorov domain, the polar angles θ are close either to zero or π. Therefore, $\sin\theta \approx \Delta\theta \ll 1$ (vector $\mathbf{Q}_{fi}$ lies in a narrow cone and is directed either along the propagation vector of the wave or oppositely, and $\Delta\theta$ is a small opening angle of the cone), and the quantum parameter γ becomes small.

For the wave intensities satisfying (4), the energy conservation law (see the argument of Dirac's δ function in (7)) can be represented as follows:

$$E_f \approx E_i - \eta^2 \frac{m^2}{2E_i}\left(\frac{1}{\kappa_f} - \frac{1}{\kappa_i}\right) - l\omega, \tag{11}$$

$$\begin{gathered} \kappa_{i,f} = 1 - v_i \cos\theta_{i,f}, \quad \theta_{i,f} = \angle(\mathbf{k}, \mathbf{p}_{i,f}), \\ v_{i,f} = |\mathbf{p}_{i,f}|/E_{i,f}. \end{gathered} \tag{12}$$

Note that the small corrections to the electron energy E_i on the right-hand side of (11) are important for calculating the total cross section of SEAB (see (22) and (23)). Integrating (7) with respect to the energy of the final electron E_f (11), after straightforward calculations we obtain the following expression for the partial differential cross section of SEAB during the scattering of an electron by a nucleus into a solid-angle element $d\Omega$:

$$\frac{d\sigma_l}{d\Omega} = 2Z^2 r_e^2 \left(\frac{mE_i}{\mathbf{p}_i^2}\right)^2 \rho_l \frac{\Psi_l}{g_l^2} J_l^2(\gamma). \tag{13}$$

Here, $r_e = e^2/m$ is the classical radius of the electron,

$$\begin{aligned} \Psi_l &= 1 + \delta_l + \frac{\mathbf{p}_i^2}{E_i^2} \\ &\quad \times [\rho_l(\cos\theta_f \cos\theta_i + \sin\theta_f \sin\theta_i \cos\phi) - 1], \end{aligned} \tag{14}$$

$$g_l = 1 + \rho_l^2 - 2\rho_l(\cos\theta_\mathrm{f}\cos\theta_\mathrm{i} + \sin\theta_\mathrm{f}\sin\theta_\mathrm{i}\cos\phi) + \varepsilon_l\frac{|\mathbf{p}_\mathrm{i}|}{E_\mathrm{i}}(\rho_l\cos\theta_\mathrm{f} - \cos\theta_\mathrm{i}) + \left(\frac{|\mathbf{p}_\mathrm{i}|}{2E_\mathrm{i}}\varepsilon_l\right)^2, \tag{15}$$

$$\rho_l = \frac{|\mathbf{p}_\mathrm{f}|}{|\mathbf{p}_\mathrm{i}|} = \sqrt{1 - \varepsilon_l + \left(\frac{|\mathbf{p}_\mathrm{i}|}{2E_\mathrm{i}}\varepsilon_l\right)^2}, \quad \delta_l = \frac{E_\mathrm{f}}{E_\mathrm{i}} = 1 - \varepsilon_l\frac{\mathbf{p}_\mathrm{i}^2}{2E_\mathrm{i}^2}, \tag{16}$$

$$\varepsilon_l = l\varepsilon_1 + \varepsilon_0, \quad \varepsilon_1 = \frac{2\omega E_\mathrm{i}}{\mathbf{p}_\mathrm{i}^2}, \quad \varepsilon_0 = \eta^2\frac{mE_\mathrm{i}}{\mathbf{p}_\mathrm{i}^2}\left(\frac{1}{\kappa_\mathrm{f}} - \frac{1}{\kappa_\mathrm{i}}\right), \tag{17}$$

$$\phi = \varphi_\mathrm{f} - \varphi_\mathrm{i}, \quad \varphi_\mathrm{i,\,f} = \angle(\mathbf{e}_x, \mathbf{p}_\mathrm{i,\,f}^{\parallel}). \tag{18}$$

Here, $\mathbf{p}_\mathrm{i,\,f}^{\parallel}$ is the projection of the momentum $\mathbf{p}_\mathrm{i,\,f}$ onto the plane xy. The argument γ (9) of the Bessel function in (13) can be represented as

$$\gamma = \gamma_0 f_l, \quad f_l = \left[\left(\frac{\Delta_l\sin\theta_\mathrm{f}}{1 - \Delta_l v_\mathrm{i}\cos\theta_\mathrm{f}}\right)^2 + \left(\frac{\sin\theta_\mathrm{i}}{\kappa_\mathrm{i}}\right)^2 - \frac{2\Delta_l\sin\theta_\mathrm{f}\sin\theta_\mathrm{i}\cos\phi}{\kappa_\mathrm{i}(1 - \Delta_l v_\mathrm{i}\cos\theta_\mathrm{f})}\right]^{1/2}, \tag{19}$$

$$\Delta_l = v_\mathrm{f}/v_\mathrm{i} = \rho_l/\delta_l. \tag{20}$$

Note that, under conditions (4) and (5), the Bunkin–Fedorov quantum parameter γ_0 is bounded from above by

$$\gamma_0 \ll \frac{mv_\mathrm{i}}{\omega\eta}, \quad \frac{mv_\mathrm{i}}{\omega\eta} \gg 1. \tag{21}$$

The amplification factor of the electromagnetic wave is defined by the expression [8, 9]

$$\mu = 8\pi n_\mathrm{a} n_\mathrm{e}\frac{\omega|\mathbf{p}_\mathrm{i}|}{E_\mathrm{i}F^2}\sigma_\mathrm{t} = 8\pi n_\mathrm{a} n_\mathrm{e}\frac{\lambdabar\lambdabar_c r_\mathrm{e}|\mathbf{p}_\mathrm{i}|}{E_\mathrm{i}\eta^2}\sigma_\mathrm{t}, \tag{22}$$

where n_e and n_a are the electron and ion densities, respectively; $\lambdabar_c = 1/m$ is the Compton wavelength of the electron; $\lambdabar = 1/\omega$; and

$$\sigma_\mathrm{t} = \sum_{l=-\infty}^{\infty} l\sigma_l \tag{23}$$

is the so-called total cross section of stimulated bremsstrahlung. Here, the sum is taken over all possible values of the integer-valued index l, and the partial cross section of the multiphoton SEAB of an electron by a nucleus is given by

$$\sigma_l = 2Z^2 r_\mathrm{e}^2\left(\frac{mE_\mathrm{i}}{\mathbf{p}_\mathrm{i}^2}\right)^2\int_0^{\pi}\rho_l\sin\theta_\mathrm{f}\,d\theta_\mathrm{f} \times \int_0^{2\pi}\frac{\Psi_1}{g_l^2}J_l^2(\gamma)\,d\varphi_\mathrm{f}. \tag{24}$$

It is obvious that the partial (24) and total (23) cross sections are independent of the azimuth φ_i of the initial electron. Indeed, passing to the partial cross section (24) when integrating with respect to the azimuth from φ_f to ϕ (18), after straightforward calculations we obtain

$$\sigma_l = 4Z^2 r_\mathrm{e}^2\left(\frac{mE_\mathrm{i}}{\mathbf{p}_\mathrm{i}^2}\right)^2\int_0^{\pi}\rho_l\sin\theta_\mathrm{f}\,d\theta_\mathrm{f} \times \int_0^{\pi}\frac{\Psi_l}{g_l^2}J_l^2(\gamma)\,d\phi. \tag{25}$$

Formulas (22), (23), and (25) show that the amplification (attenuation) of an electromagnetic wave will occur if the total cross section σ_t is positive (negative). Taking into account (22)–(25), we can represent the total cross section of SEAB (23) and the amplification factor (22) of the wave as

$$\sigma_\mathrm{t} = 4Z^2 r_\mathrm{e}^2\left(\frac{mE_\mathrm{i}}{\mathbf{p}_\mathrm{i}^2}\right)^2 D_\mathrm{i}, \tag{26}$$

$$\mu = \mu_0\frac{4m\omega E_\mathrm{i}}{|\mathbf{p}_\mathrm{i}|^3\eta^2}D_\mathrm{i}, \quad \mu_0 = 8\pi Z^2 n_\mathrm{i} n_\mathrm{e}\lambdabar^2 r_\mathrm{e}^3, \tag{27}$$

where

$$D_\mathrm{i} = \sum_{l=1}^{\infty} l\int_0^{\pi}\sin\theta_\mathrm{f}\,d\theta_\mathrm{f}\int_0^{\pi}M_l\,d\phi, \quad M_l = \rho_l\frac{\Psi_l}{g_l^2}J_l^2(\gamma_0 f_l) - \rho_{-l}\frac{\Psi_{-l}}{g_{-l}^2}J_{-l}^2(\gamma_0 f_{-l}). \tag{28}$$

Below, we consider the amplification factor of a wave (27), (28) for medium and moderately strong intensities of the electromagnetic field.

3. AMPLIFICATION FACTOR OF A WAVE FOR MEDIUM FIELDS

First, we will study the case of medium and weak fields ($\gamma_0 \lesssim 1$), where the intensity η satisfies the following condition:

$$\eta \lesssim \frac{\omega}{m v_\mathrm{i}} \ll 1. \qquad (29)$$

Under condition (29), we can neglect the second term (ε_0) in (17) compared with the first term; then, the expression for ε_l takes the form

$$\varepsilon_l = l\varepsilon_l. \qquad (30)$$

Note that $|\varepsilon_l| \lesssim \gamma_0 e_1 \ll 1$ for any number of emitted and absorbed photons of the wave that make a significant contribution to the sum of the function D_i (28). Taking this fact into account, we expand the functions ρ_l, Ψ_l, g_l^{-2}, $J_l^2(\gamma_0 f_l)$ in (28) in the Taylor series up to the third-order terms in ε_l (the terms proportional to ε_l^2 and ε_l^3 are essential when integrating with respect to the angle of the outgoing electron over a small neighborhood of a singular point when scattering by zero angle). After straightforward calculations, we obtain

$$\rho_l \approx 1 - \frac{1}{2}\varepsilon_l - \frac{m^2}{8E_\mathrm{i}^2}\varepsilon_l^2 - \frac{1}{16}\varepsilon_l^3, \qquad (31)$$

$$\begin{aligned}\Psi_l \approx {} & \left(2 - a_+\frac{\mathbf{p}_\mathrm{i}^2}{E_\mathrm{i}^2}\right) - (2 - a_+)\frac{\mathbf{p}_\mathrm{i}^2}{2E_\mathrm{i}^2}\varepsilon_l \\ & - \frac{1}{8}\left(\frac{m\mathbf{p}_\mathrm{i}}{E_\mathrm{i}^2}\right)^2\varepsilon_l^2 - \frac{\mathbf{p}_\mathrm{i}^2}{16E_\mathrm{i}^2}\varepsilon_l^3,\end{aligned} \qquad (32)$$

$$\begin{aligned}g_l^{-2} \approx \frac{1}{4b_l^2}\Bigg\{ & 1 + \frac{\varepsilon_l}{b_l}\left[a_+ - (\cos\theta_\mathrm{f} - \cos\theta_\mathrm{i})\frac{|\mathbf{p}_\mathrm{i}|}{E_\mathrm{i}}\right] \\ & - \frac{\varepsilon_l^3}{8b_l}\left[1 - \frac{4m^2|\mathbf{p}_\mathrm{i}|}{E_\mathrm{i}^3}\cos\theta_\mathrm{f}\right]\Bigg\},\end{aligned} \qquad (33)$$

$$f_l \approx a_l - \frac{b_\mathrm{fi}}{2a_l}\varepsilon_l + \frac{c_\mathrm{fi}}{2a_l}\varepsilon_l^3, \qquad (34)$$

$$\begin{aligned}J_l^2(\gamma_0 f_l) \approx {} & J_l^2(\gamma_0 a_l) - \left[\frac{\gamma_0 b_\mathrm{fi}}{2a_l}\varepsilon_l - \frac{\gamma_0 c_\mathrm{fi}}{2a_l}\varepsilon_l^3\right] \\ & \times J_l(\gamma_0 a_l)[J_{l-1}(\gamma_0 a_l) - J_{l+1}(\gamma_0 a_l)].\end{aligned} \qquad (35)$$

Here, the following notation is introduced:

$$a_\pm = 1 - (\sin\theta_\mathrm{f}\sin\theta_\mathrm{i}\cos\phi \pm \cos\theta_\mathrm{f}\cos\theta_\mathrm{i}), \qquad (36)$$

$$b_l = a_+ + \frac{1}{8}\varepsilon_l^2\left[\frac{m^2}{E_\mathrm{i}^2} + 2\frac{|\mathbf{p}_\mathrm{i}|}{E_\mathrm{i}}\left(\frac{|\mathbf{p}_\mathrm{i}|}{E_\mathrm{i}} - \cos\theta_\mathrm{f}\right)\right], \qquad (37)$$

$$a_l = \sqrt{f_0^2 + \frac{\varepsilon_l^2}{4}\left(\frac{m}{\kappa_\mathrm{f}E_\mathrm{i}}\right)^4\sin^2\theta_\mathrm{f}}, \qquad (38)$$

$$b_\mathrm{fi} = \left(\frac{m}{\kappa_\mathrm{f}E_\mathrm{i}}\right)^2\left(\frac{\sin\theta_\mathrm{f}}{\kappa_\mathrm{f}} - \frac{\sin\theta_\mathrm{i}\cos\phi}{\kappa_\mathrm{i}}\right)\sin\theta_\mathrm{f}, \qquad (39)$$

$$c_\mathrm{fi} = \frac{1}{8}\left(\frac{m}{\kappa_\mathrm{f}E_\mathrm{i}}\right)^4\left(3 - \frac{2m^2}{\kappa_\mathrm{f}E_\mathrm{i}^2}\right)\sin^2\theta_\mathrm{f}. \qquad (40)$$

The function f_0 in (38) is determined by the expressions for f_l (19) with $l = 0$ ($\Delta_{l=0} = 1$). Note that, in the terms proportional to ε_l^2 and ε_l^3 in (32)–(40), we dropped the terms that are small in the neighborhood of the singular point (for scattering of the final electron by zero angle, when $f_0 \longrightarrow 0$, $a_+ \longrightarrow 0$, and $b_\mathrm{fi} \longrightarrow 0$). Taking into account formulas (31)–(35), one can easily calculate M_l in (28) up to the third-order terms in the small parameter ε_l (in this case, only the terms proportional to odd powers of ε_l are nonzero). As a result, the expression for the function D_i (28) is rewritten as

$$D_\mathrm{i} = \frac{\omega}{E_\mathrm{i}v_\mathrm{i}^2}\int_0^\pi \sin\theta_\mathrm{f}\,d\theta_\mathrm{f}\int_0^\pi Y_\mathrm{fi}\,d\phi, \qquad (41)$$

$$\begin{aligned}Y_\mathrm{fi} = {} & \left(2 - a_+\frac{\mathbf{p}_\mathrm{i}^2}{E_\mathrm{i}^2}\right)\left[a_+ - \frac{|\mathbf{p}_\mathrm{i}|}{E_\mathrm{i}}(\cos\theta_\mathrm{f} - \cos\theta_\mathrm{i})\right]S_1 \\ & - \left[1 + \frac{\mathbf{p}_\mathrm{i}^2}{E_\mathrm{i}^2}(1 - a_+)\right]S_2 - \frac{\gamma_0 b_\mathrm{fi}}{2}\left(2 - a_+\frac{\mathbf{p}_\mathrm{i}^2}{E_\mathrm{i}^2}\right)S_3 \\ & - \varepsilon_1^2\Bigg\{\frac{1}{4}\left[1 - 4\frac{m^2|\mathbf{p}_\mathrm{i}|}{E_\mathrm{i}^3}\cos\theta_\mathrm{f}\right]S'_1 \\ & + \frac{1}{16}\left[2 - \frac{\mathbf{p}_\mathrm{i}^2}{E_\mathrm{i}^2}\left(2 - 3\frac{\mathbf{p}_\mathrm{i}^2}{E_\mathrm{i}^2}\right)\right]S'_2 - \gamma_0 c_\mathrm{fi}S'_3\Bigg\},\end{aligned} \qquad (42)$$

$$\begin{aligned}& S_1 = \sum_{l=1}^{\infty}\frac{l^2}{b_l^3}J_l^2(\gamma_0 a_l), \quad S_2 = \sum_{l=1}^{\infty}\frac{l^2}{b_l^2}J_l^2(\gamma_0 a_l), \\ & S_3 = \sum_{l=1}^{\infty}\frac{2l^2}{a_l b_l^2}J_l(\gamma_0 a_l)J'_l(\gamma_0 a_l),\end{aligned} \qquad (43)$$

$$S'_1 = \sum_{l=1}^{\infty} \frac{l^4}{b_l^3} J_l^2(\gamma_0 a_l), \quad S'_2 = \sum_{l=1}^{\infty} \frac{l^4}{b_l^2} J_l^2(\gamma_0 a_l),$$
$$S'_3 = \sum_{l=1}^{\infty} \frac{2l^4}{a_l b_l^2} J_l(\gamma_0 a_l) J'_l(\gamma_0 a_l). \tag{44}$$

In (43) and (44), $J'_l(x)$ is the derivative of the Bessel function $J_l(x)$ with respect to the argument. When calculating the sums (43) and (44), we will take into account that, for medium fields (29), the arguments of the Bessel functions are on the order of unity and that the effective values of the integer parameter l are small; moreover, in (37) and (38), the terms proportional to ε_l^2, which are important in a small neighborhood of the singular point, are small. Therefore, we will carry out calculations in two steps: away from the singular point, where we can set

$$b_l \approx a_+, \quad a_l \approx f_0, \quad (|a_+| \sim 1, |f_0| \sim 1), \tag{45}$$

and in a small neighborhood of the singular point, where

$$|b_l| \ll 1, \quad |a_l| \ll 1, \tag{46}$$

we then match these two solutions. For example, in the domains (45) and (46), we obtain the following solutions for the sums S_1 and S'_1, respectively [15]:

$$S_1 \approx \frac{1}{a_+^3} \sum_{l=1}^{\infty} l^2 J_l^2(\gamma_0 f_0) = \frac{(\gamma_0 f_0)^2}{4a_+^3},$$
$$S'_1 \approx \frac{1}{a_+^3} \sum_{l=1}^{\infty} l^4 J_l^2(\gamma_0 f_0) = \frac{(\gamma_0 f_0)^2}{4a_+^3}\left[1 + \frac{3}{4}(\gamma_0 f_0)^2\right] \tag{47}$$

and

$$S_1 \approx \frac{1}{b_1^3} J_1^2(\gamma_0 a_1) \approx \frac{(\gamma_0 a_1)^2}{4b_1^3},$$
$$S'_1 \approx \frac{1}{b_1^3} J_1^2(\gamma_0 a_1) \approx \frac{(\gamma_0 a_1)^2}{4b_1^3}. \tag{48}$$

Here, b_1 and a_1 are the values of the functions b_l (37) and a_l (38) for $l = 1$. Note that, in formulas (47), the summation is extended to infinity owing to the rapid convergence of the sums, whereas, in (48) one can restrict the summation to a single term with $l = 1$ because of the small value of the argument of the Bessel functions. Solutions (47) and (48) can easily be sewn together for the entire range of angles of the outgoing electron. As a result, we obtain

$$S_1 \approx \frac{(\gamma_0 a_1)^2}{4b_1^3}, \quad S'_1 \approx \frac{(\gamma_0 a_1)^2}{4b_1^3}\left[1 + \frac{3}{4}(\gamma_0 a_1)^2\right]. \tag{49}$$

By analogy, we calculate the following values for other sums:

$$S_2 \approx \frac{(\gamma_0 a_1)^2}{4b_1^2}, \quad S'_2 \approx \frac{(\gamma_0 a_1)^2}{4b_1^2}\left[1 + \frac{3}{4}(\gamma_0 a_1)^2\right], \tag{50}$$

$$S_3 \approx \frac{\gamma_0}{2b_1^2}, \quad S'_3 \approx \frac{\gamma_0}{2b_1^2}\left[1 + \frac{3}{2}(\gamma_0 a_1)^2\right]. \tag{51}$$

Substituting (49)–(51) into (42), we obtain the following expression for the function D_i (41):

$$D_\mathrm{i} = \frac{\omega E_\mathrm{i}}{4\mathbf{p}_\mathrm{i}^2} \gamma_0^2 B_\mathrm{i}, \tag{52}$$

where

$$B_\mathrm{i} = \int_0^{\pi} \sin\theta_\mathrm{f} d\theta_\mathrm{f} \int_0^{\pi} H_\mathrm{middle} d\phi, \tag{53}$$

$$H_\mathrm{middle} = \frac{1}{b_1^2}\left(2 - a_+ \frac{\mathbf{p}_\mathrm{i}^2}{E_\mathrm{i}^2}\right)$$
$$\times \left\{\frac{a_1^2}{b_1}\left[a_+ - \frac{|\mathbf{p}_\mathrm{i}|}{E_\mathrm{i}}(\cos\theta_\mathrm{f} - \cos\theta_\mathrm{i})\right] - b_\mathrm{fi}\right\} \tag{54}$$
$$- \frac{a_1^2}{b_1^2}\left[1 + \frac{\mathbf{p}_\mathrm{i}^2}{E_\mathrm{i}^2}(1 - a_+)\right] - \varepsilon_1^2 G_\mathrm{fi},$$

$$G_\mathrm{fi} = \frac{a_1^2}{4b_1^3}\left(1 + \frac{3}{4}\gamma_0^2 a_1^2\right)\left(1 - 4\frac{m^2|\mathbf{p}_\mathrm{i}|}{E_\mathrm{i}^3}\cos\theta_\mathrm{f}\right)$$
$$- \frac{1}{4b_1^2}\left(1 + \frac{3}{2}\gamma_0^2 a_1^2\right)\left(\frac{m}{\kappa_\mathrm{f} E_\mathrm{i}}\right)^4 \tag{55}$$
$$\times \left(3 - \frac{2m^2}{\kappa_\mathrm{f} E_\mathrm{i}^2}\right)\sin^2\theta_\mathrm{f}.$$

We emphasize that, in the expression for H_middle (54), the function G_fi (55), which is proportional to the small quantity $\varepsilon_1^2 \ll 1$, makes a substantial contribution to the integral (53) only when integrating over the neighborhood of the singular point (when an electron is scattered by zero angle), where $|G_\mathrm{fi}| \sim \varepsilon_1^{-4}$ and $\varepsilon_1^2 |G_\mathrm{fi}| \sim \varepsilon_1^{-2} \gg 1$. Substituting expressions (52)–(55) into (26) and (27), we obtain the required expressions for the total cross section of SEAB and for the amplification factor of a wave for medium and weak fields (29) in the general relativistic case:

$$\sigma_{\mathrm{t}} = Z^2 r_{\mathrm{e}}^2 \left(\frac{m}{\mathbf{p}_{\mathrm{i}}}\right)^4 \frac{E_{\mathrm{i}}}{\omega} \eta^2 B_{\mathrm{i}}, \tag{56}$$

$$\mu = \mu_0 \left(\frac{m}{|\mathbf{p}_{\mathrm{i}}|}\right)^3 B_{\mathrm{i}}. \tag{57}$$

Note that, in the case of weak fields ($\gamma_0 \ll 1$),

$$\eta \ll \frac{\omega}{m v_{\mathrm{i}}} \ll 1, \tag{58}$$

one can neglect the term proportional to $(\gamma_0 a_1)^2 \ll 1$ in (55), and the function G_{fi} takes the form

$$\begin{aligned} G_{\mathrm{fi}} &= \frac{a_1^2}{4b_1^3}\left(1 - 4\frac{m^2|\mathbf{p}_{\mathrm{i}}|}{E_{\mathrm{i}}^3}\cos\theta_{\mathrm{f}}\right) \\ &- \frac{1}{4b_1^2}\left(\frac{m}{\kappa_{\mathrm{f}} E_{\mathrm{i}}}\right)^4 \left(3 - \frac{2m^2}{\kappa_{\mathrm{f}} E_{\mathrm{i}}^2}\right)\sin^2\theta_{\mathrm{f}}. \end{aligned} \tag{59}$$

Therefore, the function B_{i} defined by expressions (53), (54), and (59) does not depend on the field intensity but is determined only by the initial parameters of the electron (its energy and the polar angle of the incident electron) and the wave frequency.

For medium fields ($\gamma_0 \approx 1$), the function B_{i} (53)–(55) weakly depends on the Bunkin–Fedorov quantum parameter γ_0, which enters only into the function G_{fi}. The function G_{fi} makes a significant contribution to the integral (53) only in a small neighborhood of angles when the electron is scattered by zero angle; therefore, $|a_1| \ll 1$. Hence, the product $\gamma_0^2 a_1^2$ takes significant values in a certain range of angles in a small neighborhood of the singular point and may influence the function B_{i} only on the upper boundary of the applicability domain of the expressions obtained, where $\gamma_0^2 \gg 1$ (but $\gamma_0 \approx 1$). Therefore, in the general relativistic case, the total cross section of SEAB (56) in the range of medium fields is proportional to the square of the electric field strength of the wave ($\sigma_t \propto F^2$), and the amplification (attenuation) factor (57) of the wave is virtually independent of the field strength (see Fig. 6 below). Formulas (53)–(55) show that the function B_{i} weakly depends on the energy of electrons (this result is confirmed by the numerical calculations of B_{i} for various electron velocities; see Figs. 1–3 and 6 below). Therefore, the dependence of the amplification factor of the wave on the electron energy is primarily determined by the coefficient of the function B_{i} (see (57)); i.e.,

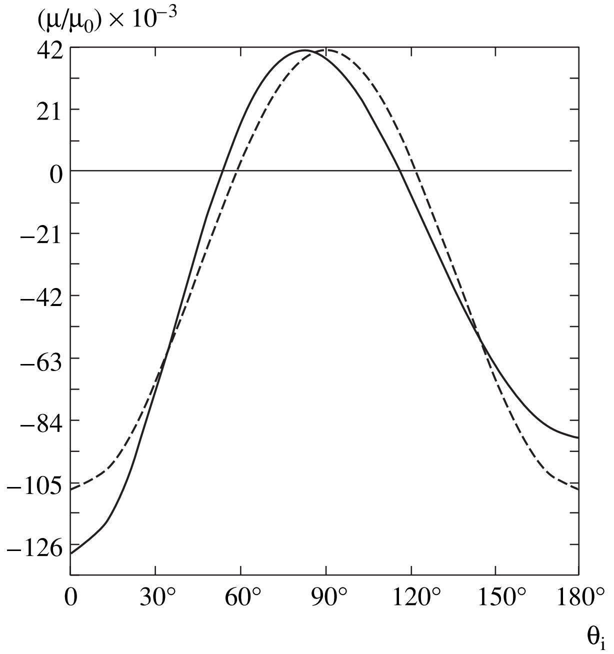

Fig. 1. Amplification (attenuation) factor μ (62) as a function of the polar angle of an incident nonrelativistic electron with energy $E_{\mathrm{i}} \approx 2.5$ keV in the range of medium fields of a laser: $\omega = 2$ eV and $F = 1.04 \times 10^6$ V/cm. The dashed curve corresponds to the dipole approximation (see (63)–(66)), and the solid curve is obtained outside the applicability domain of the dipole approximation (see (53)–(55)). The range of polar angles in which $\mu > 0$ ($\mu < 0$) corresponds to the amplification (attenuation) of light.

$$\mu \propto \left(\frac{m}{|\mathbf{p}_{\mathrm{i}}|}\right)^3 \propto \begin{cases} v_1^{-3} \gg 1, \text{ if } v_{\mathrm{i}} \ll 1, \\ 1, \text{ if } E_{\mathrm{i}} \approx m, \\ (m/E_{\mathrm{i}})^3 \ll 1, \text{ if } E_{\mathrm{i}} \gg m. \end{cases} \tag{60}$$

Hence, the amplification factor of the wave attains its maximum value for nonrelativistic electrons. It rapidly decays as the electron energy increases.

For nonrelativistic electrons, the expressions for the total cross section (56) and the amplification factor of the wave (57) reduce to

$$\sigma_{\mathrm{t}} = \left(\frac{Ze^2}{m v_{\mathrm{i}}^2}\right)^2 \frac{m}{\omega} \eta^2 B_{\mathrm{i}}, \tag{61}$$

$$\mu = \mu_0 v_{\mathrm{i}}^{-3} B_{\mathrm{i}}. \tag{62}$$

One can easily show that, in the dipole approximation, the function B_{i} (53) becomes symmetric with respect to

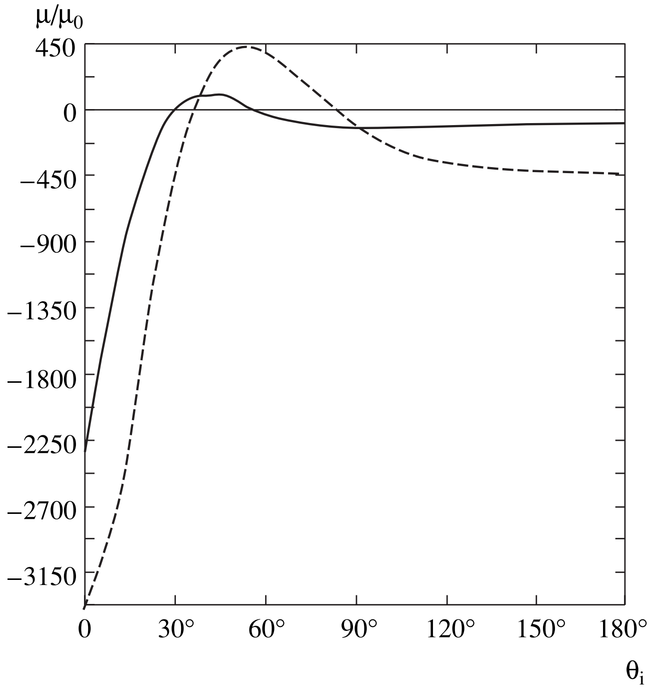

Fig. 2. Amplification (attenuation) factor μ ((57) and (53)–(55)) as a function of the polar angle of an incident relativistic electron in the range of medium fields of a laser: ω = 2 eV and $F = 1.04 \times 10^6$ V/cm. The dashed curve corresponds to electron energy of $E_i \approx 0.58$ MeV, and the solid curve, to $E_i \approx 0.70$ MeV. The range of polar angles in which $\mu > 0$ ($\mu < 0$) corresponds to the amplification (attenuation) of light.

the value $\theta_i = \pi/2$ of the polar angle of the incident electron and takes the form

$$B_i = \int_0^{\pi/2} d\theta_f \sin\theta_f \int_0^{\pi} H_0 d\phi, \tag{63}$$

where

$$\begin{aligned} H_0 = {} & a_1^2\left[\frac{1}{b_+^2}\left(\frac{2a_+}{b_+} - 1\right) + \frac{1}{b_-^2}\left(\frac{2a_-}{b_-} - 1\right)\right] \\ & - 2b_{fi}\left(\frac{1}{b_+^2} + \frac{1}{b_-^2}\right) \\ & - \frac{\varepsilon_1^2}{4}\left\{a_1^2\left(1 + \frac{3}{4}\gamma_0^2 a_1^2\right)\left(\frac{1}{b_+^3} + \frac{1}{b_-^3}\right)\right. \\ & \left. - \sin^2\theta_f\left(1 + \frac{3}{2}\gamma_0^2 a_1^2\right)\left(\frac{1}{b_+^2} + \frac{1}{b_-^2}\right)\right\}, \end{aligned} \tag{64}$$

$$\begin{gathered} b_\pm = a_\pm + \frac{1}{8}\varepsilon_1^2, \quad a_1 = \sqrt{f_0^2 + \frac{\varepsilon_1^2}{4}\sin^2\theta_f}, \\ \varepsilon_1 = \frac{2\omega}{m v_i^2}, \end{gathered} \tag{65}$$

$$\begin{gathered} f_0^2 = (\sin\theta_f - \sin\theta_i\cos\phi)^2 + \sin^2\theta_i\sin^2\phi, \\ b_{fi} = \sin\theta_f(\sin\theta_f - \sin\theta_i\cos\phi). \end{gathered} \tag{66}$$

The quantities $a_\pm$ in (65) are determined by equation (36). Note that Eqs. (61)–(66) coincide with similar expressions obtained in [10] in the dipole approximation in the case of a weak field, when $\gamma_0 \ll 1$.

Figure 1 represents the amplification (attenuation) factor of a wave as a function of the polar angle of incident nonrelativistic electrons ($v_i = 0.1$) in the range of medium fields (29) ($\eta = 2 \times 10^{-5}$ and $\gamma_0 = 0.5$) outside the applicability domain of the dipole approximation (see (62) and (53)–(55)) and in the dipole approximation (see (62) and (63)–(66)). One can see that, due to the nondipole character of the interaction between the electron and the field of the wave, the amplification factor versus the polar angle of the incident electron becomes nonsymmetric with respect to its maximum value, and the maximum moves toward smaller angles ($90° \longrightarrow 84°$). It is noteworthy that the maximum of the amplification factor of the wave is determined by the angle of the incident electron, which satisfies the relation

$$\theta_i = \theta_{max}, \quad \theta_{max} \approx \arccos v_i. \tag{67}$$

The range of angles of the incident electron in which the amplification of electromagnetic radiation occurs is given by $53° \le \theta_i \le 115°$. Outside this interval, the wave is absorbed in medium fields.

Figure 2 represents the amplification factor of the wave ((57) and (53)–(55)) as a function of the polar angle of incident relativistic electrons ($v_i = 0.5, 0.7$) for a wave intensity of $\eta = 2 \times 10^{-5}$ ($\gamma_0 = 2.5, 3.5$). One can see that the maximum of the amplification factor rapidly decreases (see (60)) as the electron energy increases. A comparison of μ_{max} for electron velocities of $v_i = 0.1$ (see Fig. 1) and $v_i = 0.5$ (Fig. 2) shows that the amplification factor decreases nearly by two orders of magnitude. In this case, the position of μ_{max} shifts toward smaller angles (see (67)), and the interval of angles in which amplification of the wave occurs becomes narrower. For example, for $v_i = 0.5$, we have $\theta_{max} \approx 55°$ and $38° \le \theta_i \le 84°$, whereas, for $v_i = 0.7$, we have $\theta_{max} \approx 46°$ and $30° \le \theta_i \le 54°$. As the electron energy increase further, the position of μ_{max} shifts to the origin (see (67), the interval of angles in which amplification occurs becomes still narrower, and the absolute value of μ_{max} sharply decreases. Hence, the effect of wave amplification manifests itself largely for nonrelativistic and relativistic electron energies (for ultrarelativistic energies, it becomes small).

4. AMPLIFICATION FACTOR OF A WAVE FOR MODERATELY STRONG FIELDS

Now, consider the case of a moderately strong field ($1 \ll \gamma_0 \ll \varepsilon_1^{-1}$), when the wave intensity satisfies the condition

$$\frac{\omega}{m v_{\mathrm{i}}} \ll \eta \ll \begin{cases} v_{\mathrm{i}}, & \text{if } v_{\mathrm{i}} \ll 1, \\ 1, & \text{if } E_{\mathrm{i}} \gtrsim m. \end{cases} \qquad (68)$$

Under condition (68), $|\varepsilon_l| \ll 1$ for all possible values of the number of emitted and absorbed photons that make the main contribution to sum (28). Therefore, we can restrict ourselves to the first-order terms in the Taylor series expansion of the functions ρ_l, Ψ_l, g_l^{-2}, and f_l in (28) (see (31)–(34)) in the small parameter $|\varepsilon_l|$. In this case, the expansion of the Bessel function (35) is not valid. For moderately strong fields (68), the argument of the Bessel function is large compared with $|l|$ everywhere except for a small neighborhood of angles of the outgoing electron, where

$$f_0 \lesssim \frac{|l|}{\gamma_0}. \qquad (69)$$

In the range of angles of the outgoing electron where

$$f_0 \gg \frac{|l|}{\gamma_0}, \qquad (70)$$

we can use the following asymptotic expression for large values of the argument for the Bessel function (28):

$$\begin{aligned} J_l^2(\gamma_0 f_l) &\approx \frac{2}{\pi\gamma_0 f_l}\cos^2\left(\gamma_0 f_l - \frac{\pi}{2}l - \frac{\pi}{4}\right) \\ &\approx \frac{1}{\pi\gamma_0 f_0}\left(1 + \varepsilon_l \frac{b_{\mathrm{fi}}}{2 f_0^2}\right). \end{aligned} \qquad (71)$$

Here, we averaged the squared cosine over fast oscillations in the integral in (28) and took into account expansion (34) of the function f_l.

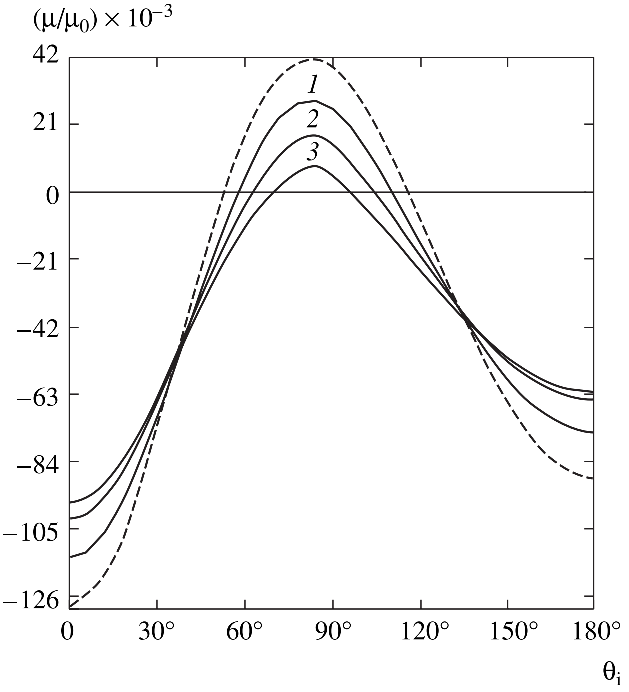

Fig. 3. Amplification factor of a wave ((62) and (79)) as a function of the polar angle of an incident nonrelativistic electron with energy $E_{\mathrm{i}} \approx 2.5$ keV in a moderately strong field of a laser ($\omega = 2$ eV). The field strength is (*1*) $F = 1.04 \times 10^8$, (*2*) 5.20×10^8, and (*3*) 2.60×10^9 V/cm; the dashed curve corresponds to a medium field of $F = 1.04 \times 10^6$ V/cm (see (53)–(55)). The range of polar angles in which $\mu > 0$ ($\mu < 0$) corresponds to the amplification (attenuation) of light.

For the range of small scattering angles of the final electron, where $f_0 \ll 1$ ($f_0\gamma_0 \lesssim 1$), the asymptotic expression for the squared Bessel function (71) is not valid. This situation occurs in a small neighborhood of the scattering angle when an electron is scattered by zero angle and outside the Bunkin–Fedorov kinematic domain (see the text after formula (10)). This kinematic domain was studied in detail in [12] (see also [13]) and is determined by the scattering of an electron that occurs practically in a single plane formed by the initial momentum of the electron and the propagation vector of the wave. The appropriate azimuths are equal to (with regard to small smearing of $\Delta\varphi_{\mathrm{f}}$)

$$\varphi_{\mathrm{f}} = \varphi_{\mathrm{i}} \pm \Delta\varphi_{\mathrm{f}}, \quad \Delta\varphi_{\mathrm{f}} \lesssim 1/\gamma_0 \ll 1, \qquad (72)$$

and the polar angles are related by the following formula:

$$\begin{aligned} \theta_{\mathrm{f}} &= \theta_{\mathrm{i}}^* \pm \Delta\theta_{\mathrm{f}}, \\ \theta_{\mathrm{i}}^* &= 2\arctan\left[\frac{(E_{\mathrm{i}} - |\mathbf{p}_{\mathrm{i}}|)}{(E_{\mathrm{i}} + |\mathbf{p}_{\mathrm{i}}|)}\tan^{-1}\frac{\theta_{\mathrm{i}}}{2}\right], \\ \Delta\theta_{\mathrm{f}} &\lesssim \frac{1}{\gamma_0} \ll 1. \end{aligned} \qquad (73)$$

Therefore, when integrating over the angles of the outgoing electron, where $f_0 \lesssim \gamma_0^{-1} \ll 1$, one should calculate the amplification factor of the wave by the formula for medium fields (57) and (53)–(55). Formula (73) implies that each angle of the incident electron corresponds to a certain angle of the outgoing electron, and the equation $\theta_{\mathrm{f}} = \theta_{\mathrm{i}} \pm \Delta\theta_{\mathrm{f}}$ (i.e., the angle of the outgoing electron belongs to a certain neighborhood of the scattering by zero angle) holds only under condition (67).

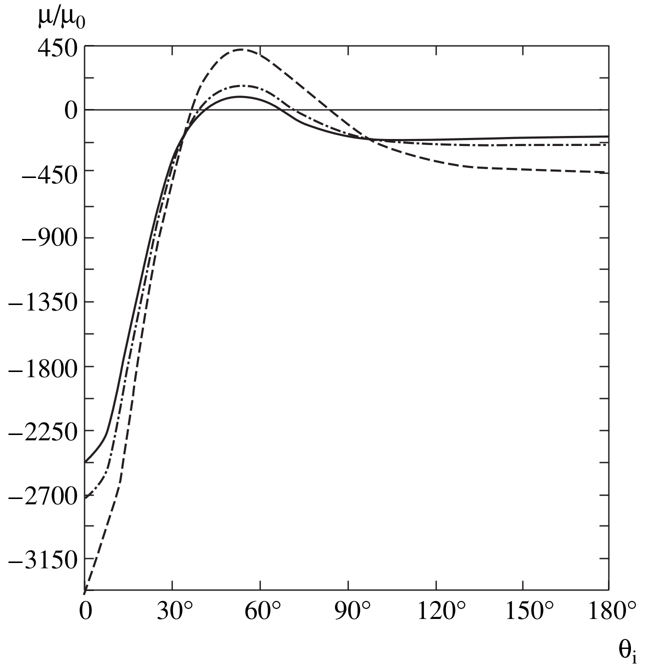

Fig. 4. Amplification factor μ of a wave ((57) and (79)) as a function of the polar angle of an incident relativistic electron with energy $E_i = 0.58$ MeV in a moderately strong field of a laser ($\omega = 2$ eV). The dot-and-dash curve corresponds to a field intensity of $F = 5.20 \times 10^8$ V/cm, the solid curve, to $F = 2.60 \times 10^9$ V/cm, and the dashed curve, to a medium field of $F = 1.04 \times 10^6$ V/cm (see (53)–(55)). The range of polar angles in which $\mu > 0$ ($\mu < 0$) corresponds to the amplification (attenuation) of light.

Taking into account expressions (31)–(33) for the functions ρ_l, Ψ_l, and g_l^{-2} and (71) for the squared Bessel function, after straightforward calculations we can rewrite expression (28) for D_i (up to the first order terms in ε_l) as

$$D_i = -\frac{3\varepsilon_1}{4\gamma_0}\int_0^{\pi}\sin\theta_f d\theta_f \int_0^{\pi} S\frac{H_{\mathrm{strong}}}{f_0^3}d\phi. \qquad (74)$$

Here,

$$S = \sum_{l=1}^{f_0\gamma_0} l^2\xi\left(f_0 - \frac{l}{\gamma_0}\right) \approx \int_1^{f_0\gamma_0} l^2\xi\left(f_0 - \frac{l}{\gamma_0}\right)dl, \qquad (75)$$

$$H_{\mathrm{strong}} = \frac{2}{3\pi a_+^2}\left\{\left(2 - a_+\frac{\mathbf{p}_i^2}{E_i^2}\right)\right.$$
$$\left.\times\left[f_0^2\frac{|\mathbf{p}_i|}{E_i a_+}(\cos\theta_f - \cos\theta_i) - \frac{b_{fi}}{2}\right] - f_0^2\frac{m^2}{E_i^2}\right\}. \qquad (76)$$

Formula (75) contains the Heaviside function $\xi(x)$ under the summation sign; it allows us to take into account conditions (69) and (70) when summing over l. Let us choose the Heaviside function as

$$\xi\left(f_0 - \frac{l}{\gamma_0}\right) = \lim_{\alpha\to\infty}\left[\frac{1}{2} + \frac{1}{\pi}\arctan\alpha\left(f_0 - \frac{l}{\gamma_0}\right)\right]$$
$$= \begin{cases} 1, & f_0 > l/\gamma_0, \\ 0, & f_0 < l/\gamma_0; \end{cases} \qquad (77)$$

then, we can easily calculate the integral in (75):

$$S \approx -\frac{1}{6}(f_0\gamma_0)^3. \qquad (78)$$

Taking into account (74) and (78), we can reduce the expressions for the total cross section and for the amplification (attenuation) factor to forms (56) and (57), respectively, in which

$$B_i = \int_0^{\pi}\sin\theta_f d\theta_f \int_0^{\pi} H d\phi,$$
$$H = \begin{cases} H_{\mathrm{strong}}, & f_0\gamma_0 \gg 1, \\ H_{\mathrm{middle}}, & f_0\gamma_0 \lesssim 1. \end{cases} \qquad (79)$$

Here, the expressions for the functions H_{strong} and H_{middle} are given by (76) and (54). Note that, for $\gamma_0 \lesssim 1$, the expression for the amplification factor obtained in the range of moderately strong fields (see formulas (57) and (79)) reduces to the formulas for medium fields (57) and (53); i.e., it describes the amplification factor of the wave in the entire range of field intensities $\eta \ll v_i$.

Taking into account (67), we can write out an approximate expression for the maximal amplification factor of the wave as a function of the electron velocity:

$$\mu_{\max} = \mu_0\left(\frac{m}{|\mathbf{p}_i|}\right)^3 B_{i\max},$$
$$B_{i\max} \approx B_i|_{\theta_i = \arccos v_i}. \qquad (80)$$

Here, the formula for $B_{i\max}$ is determined by the function B_i (79) in which the angle of the incident electron satisfies condition (67).

Figures 3 and 4 represent the amplification factor of the wave (57), (79) as a function of the polar angles of incident nonrelativistic ($v_i = 0.1$) and relativistic ($v_i = 0.5$) electrons, respectively, in the range of moderately strong fields for various intensities of the wave (in Fig. 3, curve *1* corresponds to $\eta = 2 \times 10^{-3}$ and $\gamma_0 = 50$; curve *2* corresponds to $\eta = 10^{-2}$ and $\gamma_0 = 250$, and curve *3* corresponds to $\eta = 5 \times 10^{-2}$ and $\gamma_0 = 1250$; in Fig. 4, the dot-and-dash curve corresponds to $\eta = 10^{-2}$ and $\gamma_0 = 1250$, and the solid curve corresponds to $\eta = 5 \times 10^{-2}$ and $\gamma_0 = 6250$). One can see that the position of the maximum of the amplification factor does not

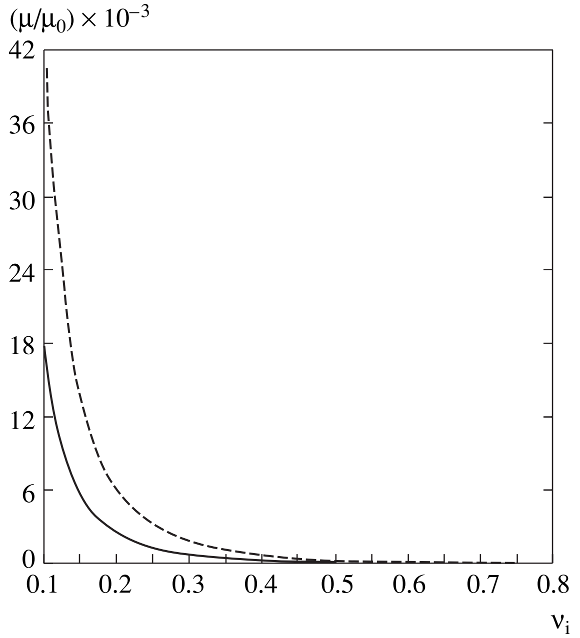

Fig. 5. The maximal amplification factor μ_{max} (80) as a function of the velocity of the initial electron for a medium and a moderately strong laser field (ω = 2 eV); the dashed curve corresponds to the field intensity of $F = 1.04 \times 10^6$, and the solid curve, to $F = 5.20 \times 10^8$ V/cm.

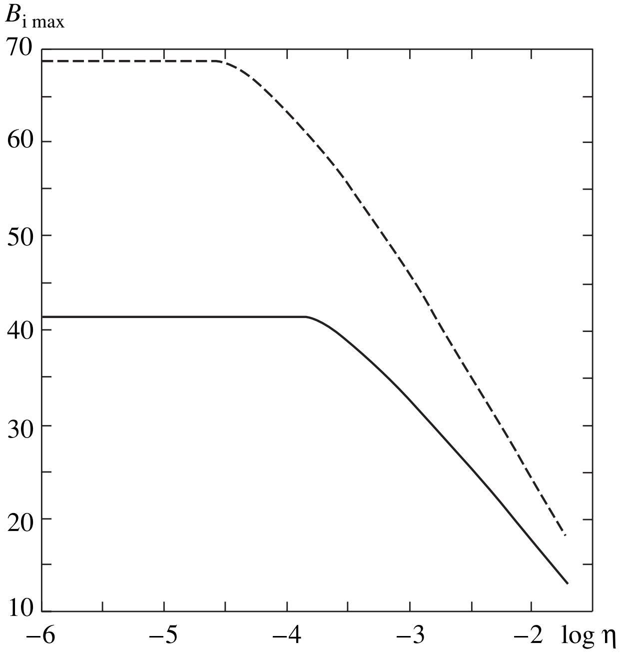

Fig. 6. The function $B_{i\,max}$ (80) versus the intensity of a laser field η (ω = 2 eV). The dashed curve corresponds to electron energy of $E_i \approx 0.58$ MeV, and the solid curve, to $E_i \approx$ 2.5 keV.

depend on the wave intensity and is determined by formula (67). The interval of angles in which the amplification of the wave occurs narrows, and the absolute value of μ decreases rather slowly. For example, Fig. 3 shows that, as the field intensity increases from $\eta = 2 \times 10^{-5}$ to $\eta = 10^{-2}$, the interval of angles in which $\mu > 0$ varies from $53° \le \theta_i \le 115°$ to $63° \le \theta_i \le 105°$, and the maximum of the amplification factor varies from $\mu_{max}/\mu_0 \approx 41 \times 10^3$ to $\mu_{max}/\mu_0 \approx 17 \times 10^3$. Thus, as the field intensity increases nearly by three orders of magnitude, μ_{max} decreases only by a factor of 2.4. In this case, the total cross section grows quite rapidly, as η^2 (see (61)). A further increase in the field intensity leads to a further decrease in the range of fields in which $\mu > 0$, so that, for intensities of $\eta \gg v_i$, the amplification factor becomes negative for all possible polar angles of the incident electron; i.e., as expected, the effect of wave amplification vanishes (the wave is only absorbed). Figure 5 shows the maximum of the amplification factor of the wave, μ_{max} (80), as a function of the velocity of the initial electron for medium and moderately strong fields. One can see that μ_{max} attains its maximal values for medium fields and nonrelativistic electron energies and rapidly decreases as the electron velocity increases (60). Figure 6 represents the function $B_{i\max}$ (80) versus the wave intensity η for relativistic and nonrelativistic energies of electrons. One can see that, for a given energy of electrons, the amplification factor of the wave attains its maximum in the range of medium fields and remains virtually constant ($\mu_{max} \approx$ const), whereas, in the range of moderately strong fields, μ_{max} monotonically decreases.

Let us estimate the amplification factor of the wave. Unfortunately, in the range of optical frequencies and for ordinary concentrations of electron beams, the amplification factor is small. For example, for $Z = 1$, $\omega = 2$ eV, $n_e = 3 \times 10^{11}$ cm^{-3}, and $n_i = 10^{19}$ cm^{-3}, formula (27) yields $\mu_0 \approx 1.65 \times 10^{-16}$ cm^{-1}. Then, for polar angles of incident nonrelativistic electrons near $\theta_i \approx 84°$, $\mu \approx 0.7 \times 10^{-11}$ cm^{-1} in the range of medium fields (see Fig. 3). Considerable values of the amplification factor for laser light can be obtained with electron beams with sufficiently high concentration of electrons. For example, for an electron beam of $I \approx 10$ kA [16] with a kinetic energy of $E = 2.5$ keV and a beam diameter $\lambda \approx 0.6$ μm, the concentration of electrons is $n_e \approx 7.4 \times 10^{21}$ cm^{-3}. For this concentration of nonrelativistic electrons, we obtain $\mu_0 \approx 4 \times 10^{-6}$ cm^{-1}, and the amplification factor of laser light near $\theta_i \approx 84°$ is equal to $\mu \approx 0.16$ cm^{-1}.

Note that such high concentrations of electrons can be achieved in a plasma in a very strong static electric field. In such a plasma, strong collisionless instabilities may occur that may mask the amplification of a wave due to collisions. Therefore, in order to observe the effect of amplification of laser light in such a plasma, one has to create conditions under which collisionless instabilities are suppressed.

We emphasize that, in the case of a linearly polarized electromagnetic wave, in addition to the quantum multiphoton parameter γ_0 (3), we have a quantum parameter $\beta_0 = \eta^2 m v_i/\omega$ in this problem (for nonrelativistic electron energies in the dipole approximation, $\beta_0 = 0$). Therefore, instead of the Bessel functions that determine the probability of multiphoton processes, we have so-called generalized Bessel functions ($J_l(\gamma_0) \longrightarrow J_l(\gamma_0, \beta_0)$), which were studied in detail by Reiss [17]. As a result, the calculation of the amplification (attenuation) factor of a wave is significantly complicated compared with then case of a circularly polarized wave. Here, the qualitative behavior of the amplification factor of the wave as a function of the field strength for circular and linear polarizations remains the same.

5. CONCLUSIONS

Thus, we have studied the amplification of a wave during the scattering of a relativistic electron by a nucleus in the field of a circularly polarized light wave of weak, medium, and moderately strong intensities. The results obtained complement the available results that were obtained by calculating the amplification (attenuation) factor of a linearly polarized electromagnetic wave in two limit cases: for weak and strong fields.

The results of the study can be summarized as follows.

1. The amplification of a circularly polarized electromagnetic wave occurs in a definite range of angles of the incident electron with respect to the propagation direction of the wave and essentially depends on the electron energy and the field intensity.

2. The maximal amplification of laser light occurs in the case of nonrelativistic electrons in the range of medium fields (29). In this case, the diagram of the amplification factor of the wave versus the polar angle of the incident electron has a pronounced peak (whose position is approximately defined by (67)) and is characterized by the maximal interval of angles in which $\mu > 0$.

3. As the electron energy increases for a given field intensity, the position of the peak $\mu_{\max}$ shifts toward smaller angles ($\theta_{\max} \approx 84°$ for nonrelativistic electrons and $\theta_{\max} \longrightarrow 0°$ for ultrarelativistic electrons; see Figs. 1 and 2), while its magnitude decreases as $(m/|\mathbf{p}_i|)^3$.

4. As the field intensity increases for a given electron energy, the position of the peak $\mu_{\max}$ remains virtually unchanged with respect to the polar angles of the incident electron; however, its absolute value decreases, and the interval of angles in which $\mu > 0$ becomes narrower. The latter processes are rather slow (when the field intensity increases by several orders of magnitude, $\mu_{\max}$ decreases only by several times; see Figs. 3 and 4).

5. In the range of medium fields, the maximal amplification factor is virtually constant ($\mu_{\max} \approx \text{const}$), and it monotonically decreases only in moderately strong fields (see Fig. 6).

6. For high intensities of the field, when $\eta \gg v_i$, the effect of wave amplification vanishes, as should be expected (the wave is only absorbed).

7. The amplification of laser light can be used in practice only for sufficiently high power electron beams.

ACKNOWLEDGMENTS

We are grateful to professor M.V. Fedorov for discussions and valuable remarks.

REFERENCES

1. D. Marcuse, Bell Syst. Tech. J. **41**, 1557 (1962).
2. F. V. Bunkin and M. V. Fedorov, Zh. Éksp. Teor. Fiz. **49**, 1215 (1965) [Sov. Phys. JETP **22**, 844 (1966)].
3. M. Gavrila and M. van der Wiel, Comments At. Mol. Phys. **8**, 1 (1978).
4. F. V. Bunkin, A. E. Kazakov, and M. V. Fedorov, Usp. Fiz. Nauk **107**, 559 (1972) [Sov. Phys. Usp. **15**, 416 (1972)].
5. R. V. Karapetyan and M. V. Fedorov, Kvantovaya Élektron. (Moscow) **4**, 2214 (1977).
6. V. Mitlleman, *Theory of Laser–Atom Interaction* (Plenum, New York, 1982).
7. A. Weingartshofer and C. Jung, in *Multiphoton Ionization of Atoms*, Ed. by S. L. Chin and P. Lambropoulos (Academic, Toronto, 1984).
8. M. V. Fedorov, *Electron in a Strong Light Field* (Nauka, Moscow, 1991) [in Russian].
9. M. V. Fedorov, *Atomic and Free Electrons in a Strong Light Field* (World Sci., New York, 1997).
10. V. A. Tsibul'nik and S. P. Roshchupkin, Laser Phys. Lett. **1**, 357 (2004).
11. M. M. Denisov and M. V. Fedorov, Zh. Éksp. Teor. Fiz. **53**, 1340 (1967) [Sov. Phys. JETP **26**, 779 (1968)].
12. S. P. Roshchupkin, Zh. Éksp. Teor. Fiz. **106**, 102 (1994) [JETP **79**, 54 (1994)].
13. S. P. Roshchupkin, Zh. Éksp. Teor. Fiz. **109**, 337 (1996) [JETP **82**, 177 (1996)].
14. S. P. Roshchupkin, V. A. Tsubyl'nik, and A. N. Chmirev, Laser Phys. **10**, 1231 (2000).
15. A. P. Prudnikov, Yu. A. Brychkov, and O. I. Marichev, *Integrals and Series. Special Functions* (Nauka, Moscow, 1983; Gordon and Breach, New York, 1986).
16. A. A. Rukhadze, L. S. Bogdankevich, and S. E. Rosinskiĭ, *Physics of Heavy-Current Relativistic Electron Beams* (Atomizdat, Moscow, 1980) [in Russian].
17. H. R. Reiss, Phys. Rev. A **22**, 1786 (1980).

Translated by I. Nikitin

Journal of Experimental and Theoretical Physics, Vol. 100, No. 5, 2005, pp. 895–902.
Translated from Zhurnal Éksperimental'noĭ i Teoreticheskoĭ Fiziki, Vol. 127, No. 5, 2005, pp. 1017–1025.
Original Russian Text Copyright © 2005 by Zhmoginov, Fraiman.

ATOMS, MOLECULES, OPTICS

Generation of Harmonics of Intense Laser Radiation in a Transparent Collisionless Plasma

A. I. Zhmoginov and G. M. Fraiman
Institute of Applied Physics, Russian Academy of Sciences, ul. Ul'yanova 46, Nizhni Novgorod, 603600 Russia
e-mail: azhmogin@princeton.edu

Received November 22, 2004

Abstract—The spectral composition of a relativistically strong uniform nonlinear electromagnetic wave in a transparent collisionless plasma is analyzed. The vortex and potential components of the wave field are shown to contain only odd and even harmonics, respectively; in a transparent plasma, the wave remains quasi-monochromatic, since the intensities of the harmonics decrease exponentially with increasing harmonic number. An equation that includes diffraction effects is derived to describe the propagation of wavepackets. The results obtained are compared with experimental data. © *2005 Pleiades Publishing, Inc.*

1. INTRODUCTION

At present, with the development of femtosecond lasers, it has become possible to produce laser pulses with intensities reaching 10^{19}–10^{21} W cm^{-2} and durations shorter than a picosecond. In the fields of such pulses in a transparent plasma, the electron oscillation velocity approaches the speed of light, and both the motion of a single particle and the collective motions become essentially nonlinear. The latter, in turn, makes the propagation of a laser pulse in plasma a nonlinear process.

The nonlinear interaction of intense laser radiation with plasma has been the subject of many experimental and theoretical studies in the past decade. These include review [1] and papers [2–7]. One of the subjects considered in these papers is the excitation of plasma oscillations after the passage of an intense laser pulse through plasma. For example, it was shown in [7] that only short pulses (the pulse scale length must be much smaller than the plasma wavelength) could effectively excite plasma oscillations if the phasing is proper.

However, an analysis of the radiation at various harmonics in the field of such an intense laser pulse is of greatest interest and richest in possible applications. The unexpectedly high harmonic radiation efficiency detected experimentally [1] suggests that ultraviolet and X-ray sources can be produced on the basis of this phenomenon. Thus, for example, the incoherent radiation of harmonics in the direction opposite to the pulse propagation was theoretically analyzed in [2]. In particular, the results obtained are indicative of a high harmonic generation efficiency. On this basis, the authors proposed a design for a laser synchrotron source of X-ray radiation that differs from known analogs by a number of significant advantages.

In particular, the radiation of harmonics in the direction of laser-pulse propagation was considered in several papers [3–7]. Here, both the harmonic generation efficiency as a function of the pulse duration and the spectral composition of the plasma response and its dependence on the longitudinal component were analyzed. However, for example, in [5], to determine the plasma radiation spectrum, the motion of electrons is considered only in the field of a strictly monochromatic incident wave without including the radiation field of the plasma itself. This approach yields the correct result only for the harmonics no higher than the third harmonic.

In this paper, we also analyze the spectral composition of an intense electromagnetic disturbance propagating in plasma. We consider the problem of a uniform traveling nonlinear wave in a transparent plasma (the electron density n_e is much lower than the critical density n_{cr}). In studying the uniform wave, we derive a dispersion relation for it and calculate the approximate amplitudes of its harmonics. Knowing the dispersion relation, in turn, allows us to analyze the dynamics of smoothly nonuniform wavepackets by deriving abridged equations for the pulse envelope from it.

The idea of considering this problem is related to the recently published experimental review [1], which is devoted to studying the forward radiation of high harmonics in a transparent plasma as a relativistically strong laser pulse propagates in it. It was found, in particular, that high harmonics with frequencies that are a significant number of times higher than the frequency of the incident wave, feature prominently in the induced forward radiation. In addition, even harmonics, which are of the same order of magnitude as the odd harmonics when the original wave is circularly polarized, are also present there. The first simple explanation of the results by the authors of this work involves com-

1063-7761/05/10005-0895$26.00 © 2005 Pleiades Publishing, Inc.

plex electron paths in the field of a relativistic wave. An electron in the field of an intense monochromatic wave is known to describe a complex path in the shape of a figure eight with a rich spectrum, which must seemingly produce a spectrally rich electromagnetic radiation. However, when an ensemble of electrons is considered, their collective radiation in the field of a relativistic wave exhibits no such rich spectrum. The sought-for nonlinear wave represents an intense monochromatic wave along with many weak accompanying transversally polarized harmonics and longitudinal electromagnetic oscillations. The spectrum of such a wave is extremely poor, since each harmonic is several times weaker than a harmonic whose number is smaller by two, which is equal in order of magnitude to n_e/n_{cr}.

One can easily explain why the plasma wave is quasi-monochromatic. The complex figure-eight path of an electron in the field of an intense quasi-monochromatic wave is characterized by the longitudinal motion of charged particles. Given that this motion is relativistic, it also leads to a significant electron density nonuniformity. As a result, although the transverse velocity of electrons in relativistically strong fields has many harmonics, the transverse component of the macroscopic current, which is proportional to the product of the density by the transverse velocity of the electron, actually contains only one harmonic [9]. It is for this reason that a uniform nonlinear wave in a plasma is a monochromatic wave accompanied by harmonics, with each succeeding harmonic being much weaker than the preceding one. Note that the polarization of the harmonics is identical to that of the first harmonic.

To solve the formulated problem, we use the hydrodynamic description of a cold plasma by writing the Maxwell vacuum equations for the field in it. The relationship of the macroscopic current and the space charge density to the potentials of the electromagnetic field can be found by considering the problem of the motion of a single electron in the wave field. As a result, we obtain a self-consistent system of equations containing the vector and scalar potentials of the field. This system is described by a Lagrangian that depends only on one small parameter in new variables. The description of this problem by a Lagrangian was discussed in [10]. However, in contrast to this paper, the Lagrangian was obtained in [10] not for the potentials of the electromagnetic field of a nonlinear wave, but for the electron momentum components. In addition, the authors of [10] restricted their analysis of the problem to deriving the Lagrangian, without touching on the determination of the radiation at various harmonics, as in this paper. After analyzing the spectral composition of the nonlinear wave, we consider the coherence of the plasma radiation. Subsequently, we derive a dispersion relation for the nonlinear wave from the system obtained and then an abridged equation describing the propagation of the envelope of a smoothly nonuniform wavepacket.

2. CONSTITUTIVE RELATIONS

Let us ascertain how the potentials of an electromagnetic field in plasma are related to the current of the resultant motion of charged particles. To this end, consider the problem of the motion of a relativistic electron in the field of a superposition of plane uniform monochromatic transverse waves with frequencies $m\omega$ ($m = 1, 2, \ldots$) and wave vectors

$$m\mathbf{k} = \mathbf{z}_0\omega n m/c$$

($n = \omega/ck$ is the unknown refractive index of the medium close to 1; thus, $\chi = 1 - n$ is a small parameter of the problem) and longitudinal electromagnetic disturbances at the same frequencies and with the same wave vectors. Passing to a new “time” $\theta = \omega t - kz$ (the phase of the first harmonic is chosen as the latter) in the Lagrangian of this problem, we can easily obtain the Hamiltonian of the problem (the Hamiltonian without the scalar potential was calculated in [9])

$$H(\theta, \mathbf{w}, u) = -\frac{\sqrt{(u-nf)^2 + (1-n^2)(1+(\mathbf{a}+\mathbf{w})^2)}}{1-n^2} - \frac{cf}{\omega} + \frac{cn(u-nf)}{\omega(1-n^2)} = -\frac{c}{\omega}(\gamma + f). \tag{1}$$

Here,

$$u = -p_z/mc + n\gamma(\theta) + nf(\theta),$$

$$\mathbf{w} = -\mathbf{p}_\perp/mc - \mathbf{a}(\theta)$$

are the new momenta of the problem,

$$\mathbf{a}(\theta) = e\mathbf{A}/mc^2 = \sum_{l=-\infty}^{\infty} \mathbf{a}_l e^{il\theta},$$

$$f(\theta) = e\varphi/mc^2 = \sum_{l=-\infty}^{\infty} f_l e^{il\theta}$$

are the normalized vector and scalar potentials of the field, and γ is the gamma-factor of the electron. Knowing the Hamiltonian, we can now derive expressions for the electron velocity (in the new time), i.e., determine its path.

Since the Hamiltonian does not depend explicitly on the coordinates, the momenta u and $\mathbf{w}$ do not change during the electron motion. Based on the properties of the solution for the wave potentials described above, we can easily obtain the relationship between these integrals of motion and the electron drift momenta $\mathbf{p}^{\mathrm{dr}}$

$$\mathbf{w} = -\langle \mathbf{p}_\perp \rangle_\theta / mc = -\mathbf{p}_\perp^{\mathrm{dr}}/mc, \tag{2}$$

$$u - nf_0 \approx -\frac{p_z^{\mathrm{dr}}}{mc} + \sqrt{1 + \frac{(\mathbf{p}^{\mathrm{dr}})^2}{m^2c^2} + \langle a^2 \rangle_\theta} + O(\chi). \tag{3}$$

In a frame of reference where the electron is, on average, at rest, these expressions are simplified to (in what follows, we set $f_0 = 0$)

$$\mathbf{w} = 0, \tag{4}$$

$$u = \mathscr{E} \approx \sqrt{1 + \langle a^2 \rangle}. \tag{5}$$

In principle, relations (1)–(3) allow the path of an individual electron in the wave field to be determined. Let us now calculate the current in plasma. To find the spatial distribution of the current, we integrate the expression for the current of a single electron with a drift momentum $\mathbf{p}$ ($|\mathbf{p}| \ll mc$) over the coordinate of the drift center of its path $\mathbf{r}_0$ at the initial time (using this approach requires making a transition from the sum over the particles to an integral over the drift centers, which is possible if the induced radiation is coherent). We assume that the electron motion is described by the expression

$$\mathbf{r}(t) = \mathbf{r}_0 + \delta\mathbf{r}(\mathbf{r}_0, t),$$

where $\delta\mathbf{r}(\mathbf{r}_0, t)$ is chosen in such a way that $\delta\mathbf{r}(\mathbf{r}_0, 0) = 0$; i.e., $\mathbf{r}_0$ is the position of the electron at the initial time, and this position characterizes the particle path at later times. For the total current in plasma, we then have the general expression

$$\mathbf{j}_\mathbf{p}(\mathbf{r}, t) = en_e\delta\mathbf{v}'(\mathbf{r}'_0, t) \times \left|\frac{D(x'_0 + \delta x(\mathbf{r}'_0, t), y'_0 + \delta y, z'_0 + \delta z)}{D(x'_0, y'_0, z'_0)}\right|^{-1}, \tag{6}$$

where $D(\ldots)/D(\ldots)$ is the transition Jacobian, and $\mathbf{r}'_0$ is the initial position of the electron located at point $\mathbf{r}$ at a given time; this position can be determined from the equality

$$\mathbf{r}'_0 + \delta\mathbf{r}(\mathbf{r}'_0, t) = \mathbf{r}.$$

In the derived expression, $e\delta\mathbf{v}(\mathbf{r}'_0, t)$ acts as the current produced by a single electron, while the remaining part $n_e|\ldots|^{-1}$ has the meaning of the electron density at a given point in space.

Using the fact that only the z_0 dependence is present in all expressions in the problem under consideration and expressing the electron velocity and the partial derivative of the particle deflection with respect to the initial position in terms of $d\mathbf{r}/d\theta$, we obtain

$$\mathbf{j}_\mathbf{p}(\mathbf{r}, t) = en_e\omega\frac{d\mathbf{r}}{d\theta}, \tag{7}$$

whence we have for the individual components

$$\mathbf{j}_{\mathbf{p}\perp}(\mathbf{r}, t) = -\frac{en_ec(\mathbf{w} + \mathbf{a})}{\sqrt{(u - nf)^2 + (1 - n^2)(1 + (\mathbf{w} + \mathbf{a})^2)}}, \tag{8}$$

$$j_{\mathbf{p}z}(\mathbf{r}, t) = \frac{en_ec}{1 - n^2} \times \left(n - \frac{u - nf}{\sqrt{(u - nf)^2 + (1 - n^2)(1 + (\mathbf{w} + \mathbf{a})^2)}}\right). \tag{9}$$

Let us now consider how these expressions will change if we take into account the thermal motion by assuming that it is essentially nonrelativistic, i.e., the thermal energy of the electron is negligible compared to its oscillatory energy in the wave field. Let the isotropic electron drift velocity distribution function be known at a given temperature, $g_0(\mathbf{p}) = g(p)$. The complete expression for the spatial distribution of currents, to terms of the order of $((p_T/mca)^2 \ll 1$ (p_T is the characteristic thermal spread in electron momenta), is then

$$\mathbf{j}_\perp(\mathbf{r}, t) = \int \mathbf{j}_{\mathbf{p}\perp}(\mathbf{r}, t)g(p)d^3p \approx \mathbf{j}_{0\perp} - \frac{en_ec\eta\mathbf{a}}{3((\mathscr{E} - nf)^2 + (1 - n^2)(1 + a^2))^{3/2}}, \tag{10}$$

$$j_z(\mathbf{r}, t) = \int j_{\mathbf{p}z}(\mathbf{r}, t)g(p)d^3p \approx j_{0z}, \tag{11}$$

where

$$\eta = \int 4\pi p^4 g(p)dp/(mc)^2 \sim kT_e/mc^2,$$

and $\mathbf{j}_0$ is the current at zero temperature (it can be determined from Eqs. (8) and (9) by substituting in $\mathbf{p} = 0$). We see from the formulas for the components of the vector $\mathbf{j}$ that the expressions for $\mathbf{j}_\perp$ and $\mathbf{j}_z$ contain only odd and even harmonics, respectively (if the particle drift velocity distribution function were anisotropic, then all harmonics would generally be present in the expressions for the currents).

It should be noted, in particular, that the assumption about the smallness of the succeeding harmonics $\mathbf{a}_{m+2}$ and φ_{m+2} compared to the preceding harmonics $\mathbf{a}_m$ and φ_m suggests that the same characteristic feature of the spectrum, i.e., the succeeding harmonics are weaker than the preceding ones, will be observed in the formulas for the currents.

3. THE SELF-CONSISTENT PROBLEM

In the previous section, we derived an expression for the density of the macroscopic current produced by a laser beam. Let us now consider the problem of the radiation of such a system of currents, and let us determine the form of the self-consistent electromagnetic disturbance and the relationship of the propagation velocity of such disturbances in plasma to their amplitude and the plasma density.

We consider a rarefied plasma in which the electron density is much lower than its critical value, but $n_e^{1/3}\lambda \gg 1$; i.e., the hydrodynamic approximation can be used. Let us write the Maxwell equations in the medium under consideration:

$$\begin{aligned} \mathrm{div}\mathbf{H} &= 0, \\ \mathrm{div}\mathbf{E} &= 4\pi(\rho_e - \rho_0), \\ c\,\mathrm{curl}\mathbf{H} &= 4\pi\mathbf{j} + \partial\mathbf{E}/\partial t, \\ c\,\mathrm{curl}\mathbf{E} &= -\partial\mathbf{H}/\partial t. \end{aligned} \tag{12}$$

Passing to the new time of the problem $\theta = wt - kz$ and substituting the derivatives of the potentials for the fields yields

$$\begin{aligned} \omega k\frac{d^2\varphi}{d\theta^2} &= -4\pi j_{\parallel}, \\ c\left(\frac{\omega^2}{c^2} - k^2\right)\frac{d^2\mathbf{A}}{d\theta^2} &= 4\pi\mathbf{j}_{\perp}. \end{aligned} \tag{13}$$

Reducing the field potentials **A** and φ to dimensionless form, substituting the expressions for the current and the charge density (8), and (9) using (4) and (5), we obtain

$$\begin{aligned} \frac{\mu}{n}\frac{d^2 f}{d\theta^2} &= -1 + \frac{n(\mathcal{E} - nf)}{\sqrt{(\mathcal{E} - nf)^2 + (1 - n^2)(1 + a^2)}}, \\ \frac{\mu}{n^2}\frac{d^2\mathbf{a}}{d\theta^2} &= -\frac{\mathbf{a}}{\sqrt{(\mathcal{E} - nf)^2 + (1 - n^2)(1 + a^2)}}, \end{aligned} \tag{14}$$

where

$$\mu = \frac{mc^2k^2(1 - n^2)}{4\pi e^2 n_e}. \tag{15}$$

We are interested only in the highest terms in the expansion of the harmonic amplitudes in terms of the small parameter χ. It is easy to verify that the factors μ/n and μ/n^2 on the left-hand sides of these equations can be approximately substituted by μ, since n is close to unity, and, hence, including it as a factor changes the spectra of the sought-for functions by values of a higher order of smallness in χ. In addition, note that several approximations can be made in the expression $\mathcal{E} - nf$. Thus, we may disregard the constant n, whereas we take into account the dependence of $\mathcal{E}$ on only the first harmonic, rather than not on all the sought-for harmonic amplitudes of the potentials and (assuming the electromagnetic fields to be quasi-monochromatic) by assuming that

$$\mathcal{E} \approx \sqrt{1 + 2a_1^2}.$$

Let us introduce the small parameter

$$\nu = 2\chi/\mathcal{E}^2.$$

Given the aforesaid, the derived system (14) can then be described in terms of the new variables

$$f_* = f/\mathcal{E} \ll 1, \quad \mathbf{a}_* = \sqrt{\nu}\mathbf{a} \ll 1, \quad \eta = \theta/\sqrt{\mathcal{E}\mu}$$

using the Lagrangian

$$L = \frac{f_*'^2}{2} + \frac{\mathbf{a}_*'^2}{2} - \sqrt{(1 - f_*)^2 + \nu + \mathbf{a}_*^2} - f_*. \tag{16}$$

The problem is now characterized by only one small parameter ν, whose value completely determines the form of the nonlinear solution.

The energy and angular momentum conservation laws, i.e., the two integrals of the problem, can be easily obtained from the Lagrangian:

$$\begin{aligned} E &= \frac{f_*'^2}{2} + \frac{\mathbf{a}_*'^2}{2} \\ &+ \sqrt{(1 - f_*)^2 + \nu + \mathbf{a}_*^2} + f_* = \text{const}, \end{aligned} \tag{17}$$

$$M_u = a_{*x}a'_{*y} - a_{*y}a'_{*x} = \text{const}. \tag{18}$$

The possibility of describing the self-consistent problem of uniform plasma waves by using the Lagrangian and the easy separation of the two integrals of motion were pointed out by Akhiezer *et al.* [10]. However, they obtained this result for the normalized electron momentum. In addition, the authors of [10] were not interested in the high-harmonic amplitudes of the plasma response, since this question was of no particular interest when the paper was written.

The subsequent analysis shows that, even if we are interested in the harmonic amplitudes up to the highest term in small parameter ν, we cannot discard the terms of the higher order of smallness in the expansion in the derived Lagrangian. Thus, expanding the square root in Lagrangian (16) into a Taylor series yields an equivalent system for the self-consistent field:

$$\begin{aligned} \frac{d^2 f_*}{d\eta^2} &= -\sum_{k=1}^{\infty} c_{k+1}\frac{(\nu + a_*^2)^k}{(1 - f_*)^{2k}}, \\ \frac{d^2 a_*}{d\eta^2} &= \sum_{k=1}^{\infty} c_k\frac{(\nu + a_*^2)^{(k-1)}a_*}{(1 - f_*)^{2k-1}}, \end{aligned} \tag{19}$$

where

$$c_k = \frac{(-1)^k(2k - 3)!!}{(2k - 2)!!}.$$

One important property of the sought-for solution follows from the derived system: assuming that $\mathbf{a}_*$ is an odd function, i.e., it contains only odd harmonics, we can easily find that f_* is an even function; i.e., it contains only even harmonics. In addition, when a circularly, rather linearly, polarized stationary wave is considered, the harmonics of neither the vector potential nor the scalar potential will be excited, because the motion of electrons in the field of a circularly polarized wave is strictly transverse, and it cannot be accompanied by the formation of a nonuniform electron density.

Since the derived system is still too complex to analyze, we use yet another simplification. After writing the equations for the harmonics of the potentials, it turns out that disregarding the term ν in the sum $\nu + a^2$ distorts the results for the harmonic amplitudes only by values of higher orders of smallness in ν. This can be elucidated by removing the parentheses in the expression $(\nu + a_*^2)^k$. Indeed,

$$(\nu + a_*^2)^k = \nu^k(1 + a^2)^k$$
$$= \nu^k(a^{2k} + C_k^1 a^{2k-2} + \ldots + 1).$$

Assuming the potentials to be quasi-monochromatic ($a_{2k+1} \sim \nu^k a_1$, $f_{2k} \sim \nu^k a_1$), we note that the harmonic with the number $2m$ is of the order of ν^m in the first term of the sum, ν^{m+1} in the second term, etc. This suggests that, apart from a^{2k}, no terms need to be included in the above sum. Thus, the system under consideration finally takes the form

$$\begin{aligned} \frac{d^2 f_*}{d\eta^2} &= -\sum_{k=1}^{\infty} c_{k+1} \frac{a_*^{2k}}{(1-f_*)^{2k}}, \\ \frac{d^2 \mathbf{a}_*}{d\eta^2} &= \sum_{k=1}^{\infty} c_k \frac{a_*^{2k-2}\mathbf{a}_*}{(1-f_*)^{2k-1}}. \end{aligned} \tag{20}$$

This system of equations corresponds to the Lagrangian

$$L = \frac{f_*'^2}{2} + \frac{\mathbf{a}_*'^2}{2} - \sqrt{(1-f_*)^2 + \mathbf{a}_*^2} - f_*. \tag{21}$$

Considering the equations for the individual harmonics of the potentials, we can now easily understand that the simplified system (20) actually has a quasi-monochromatic solution of the sought-for form, in agreement with our assumption made above,

$$a_{2m+1} \sim \nu^m, \quad f_{2m} \sim \nu^m. \tag{22}$$

This important conclusion shows that the amplitude of the harmonics in a rarefied plasma decreases exponentially with increasing harmonic number. Therefore, the observability of high harmonics of the coherent radiation seems questionable.

Formally, to find the self-consistent field, we must solve system of equations (20) with periodic boundary conditions on some unknown (in advance) period of the variable η, which can be determined from the condition for the existence of a nondegenerate solution. Since the period of the sought-for disturbances in variable θ is 2π, we can easily derive an expression for ν and, hence, determine the wave velocity. Given that the wave is quasi-monochromatic, let us do this by considering the second equation in system (20) for the first harmonic:

$$\nu = \frac{\omega_p^2}{\omega^2 \mathcal{E}^3}, \tag{23}$$

$$v = c(1+\chi) \approx c\left(1 + \frac{\omega_p^2}{2\omega^2 \mathcal{E}}\right), \tag{24}$$

where $\mathcal{E} = \sqrt{1 + 2a_1^2}$. Writing out the equations for the various harmonics of the scalar and vector potentials in turn, we now find their amplitudes:

$$f_2 \approx \mathcal{E}\frac{\nu a_1^2}{8}, \quad a_3 \approx -\frac{3\nu a_1^3}{64}, \tag{25}$$

$$f_4 \approx -\mathcal{E}\frac{19\nu^2 a_1^4}{2^{10}}, \quad a_5 \approx \frac{61\nu^2 a_1^5}{2^{13}}, \tag{26}$$

$$f_{2m} \sim \mathcal{E}\nu^m a_1^{2m} O(1), \tag{27}$$

$$a_{2m+1} \sim \nu^m a_1^{2m+1} O(1). \tag{28}$$

The expression for the third harmonic is identical to that derived in [3], but it differs from the incorrect (in our view) expression in [5]. Thus, we determined not only the phase velocity of a nonlinear plane wave in plasma, but also its spectral composition.

Since we used a number of approximations in our analysis, we tested our results by means of a numerical experiment. The original system of nonlinear differential equations was solved numerically, and the self-consistent solution obtained was compared with the above solution. The results proved to be identical with the assumed degree of accuracy.

It should be noted, in particular, that the wave properties in a rarefied plasma are determined only by the frequency, the plasma density, and the amplitude of the first harmonic. Note also that expression (24) is nothing but an approximate dispersion relation for the nonlinear waves found:

$$k = \frac{\omega}{c}\left(1 - \frac{\omega_p^2}{2\omega^2\sqrt{1 + \langle a^2 \rangle}}\right). \tag{29}$$

It is important to note that the derived dispersion relation can be used both for uniform waves in plasma and for obtaining an abridged equation for smoothly nonuniform nonlinear waves in a medium. For such a wave, we are interested in the change of its first harmonic; all of the higher harmonics are locally coupled with it in a known way. The abridged equation for the envelope of a wavepacket derived from (29) is

$$c\frac{\partial \mathbf{a}}{\partial z}-\frac{\partial \mathbf{a}}{\partial t}+\frac{c^2\Delta_\perp \mathbf{a}}{2\omega}+\frac{\omega_p^2\mathbf{a}}{2\omega\sqrt{1+aa^*/2}} = 0. \qquad (30)$$

4. CONCLUSIONS

Thus, when considering the problem of a uniform traveling, relativistically strong nonlinear electromagnetic wave in a transparent plasma, we derived a system of equations for the scalar and vector potentials of its self-consistent electromagnetic field. This system was found to be described by a Lagrangian by simplifying which sole parameter of the problem could be left. As a result, we showed that the sought-for nonlinear wave is quasi-monochromatic; i.e., the first harmonic predominates in it. For such a wave, we found a dispersion relation and established its spectral composition. The main property of the spectrum obtained is that the intensity of the harmonics decreases rapidly with increasing harmonic number:

$$a_{2m+1}\sim (n_e/n_{\text{crit}})^m, \quad f_{2m}\sim (n_e/n_{\text{crit}})^m.$$

In conclusion, we will say a few words about the validity conditions for the approach used. Let us analyze the conditions for making a transition from the exact summation of the delta functions over the particles to integration of the particle density over a physically infinitesimal volume when calculating the macroscopic current. This transition is possible if the radiation field of the current of individual electrons in the wave zone fluctuates only slightly about its mean for a small change in the particle position, i.e., if the radiation is coherent.

We use the expression for the Fourier components of the vector potential of the radiation field of a moving charge in the wave zone [8] (since, in our case, the path of the particle is periodic, A_Ω is the sum of the delta functions of the frequency difference $\mathbf{\Omega} - n\omega$, where ω is the frequency of the incident wave):

$$\mathbf{A}_\Omega = e\frac{\exp(ikR_0)}{cR_0}\int \exp(i(\Omega t-\mathbf{k}\cdot\mathbf{r}))d\mathbf{r}, \qquad (31)$$

where $\mathbf{r}(t)$ is the path of the particle (the coordinate origin is chosen inside the radiating volume), $\mathbf{R}_0 = R_0\mathbf{n}$ is the position of the point of observation, and $\mathbf{k} = \mathbf{n}\Omega/c$.

Let the electrons be, on average, at rest. The path of a single electron is then characterized solely by its initial position, and we can write for it

$$\mathbf{r} = \mathbf{r}_0+\mathbf{r}_{\sim}(\theta), \qquad (32)$$

where $\mathbf{r}_0$ is the position of the drift center of the electron path. Substituting the expression following from this for the dependence

$$t(\theta) = \omega^{-1}(\theta + hz_0 + hz_{\sim}(\theta))$$

($h = \omega/c$ is the wavevector of the incident wave) in (31) yields

$$\mathbf{A}_\Omega = e\frac{\exp(ikR_0)}{cR_0}$$
$$\times\int \exp\left(i\left(\frac{\Omega}{\omega}(\theta+hz_0+hz_{\sim}(\theta))-\mathbf{k}\cdot\mathbf{r}_0-\mathbf{k}\cdot\mathbf{r}_{\sim}(\theta)\right)\right) \qquad (33)$$
$$\times\frac{d\mathbf{r}_{\sim}(\theta)}{d\theta}d\theta,$$

whence we obtain for the system of charges with the positions of the drift centers $\mathbf{r}_m$

$$\mathbf{A}_\Omega^\Sigma = e\frac{\exp(ikR_0)}{cR_0}$$
$$\times\int \exp\left(i\left(\frac{\Omega\theta}{\omega}+kz_{\sim}(\theta)-\mathbf{k}\cdot\mathbf{r}_{\sim}(\theta)\right)\right) \qquad (34)$$
$$\times\frac{d\mathbf{r}_{\sim}(\theta)}{d\theta}d\theta\sum_{m=1}^{N}\exp(i(kz_m-\mathbf{k}\cdot\mathbf{r}_m)),$$

where N is the total number of particles. In this expression, the integral represents the radiation field of a single electron and the sum describes the collective effects. Thus, the problem was reduced to analyzing the possible deviations of this sum from its mean value for various electron-density fluctuations.

Before we rigorously consider the formulated problem, let us qualitatively analyze the sum in Eq. (34). This sum is nothing but the Fourier spectrum of the density of the electron drift centers over the entire radiation volume. Let us first consider the simplest situation where the electrons are arranged regularly in the volume. In this case, the Fourier spectrum of the density of the drift centers is clearly a series of peaks $2\pi/L$ in thickness at the grid points with a period of $2\pi/l$, where l is the interparticle separation and L is the scale length of the radiation volume. This implies that, since the wavenumber of the incident radiation is small compared to $2\pi/l$, we can discard all the high harmonics of the spectrum in (34), i.e., retaining only the zeroth harmonic that corresponds to the average electron density. However, it is clear that, if the angle of observation is large, the sum in Eq. (34) is close to zero, because the wavevectors of the harmonics of interest are much smaller than $2\pi/l$, but larger than $2\pi/L$. In this case, small fluctuations in the positions of the electron drift centers can lead to pronounced fluctuations in the harmonic amplitude against the background of its nearly zero mean value, which corresponds to incoherent radiation. The situation where the wavevector $k\mathbf{z}_0 - \mathbf{k}$ is close enough to zero for the mean amplitude of the sought-for harmonic to appreciably exceed its fluctuations, i.e., for the radiation to be coherent, is possible only at small angles of observation and at moderately large sizes of the radiating volume (which increases the line width in the spectrum of the density of the drift centers).

An accurate statistical analysis of the Fourier spectrum of the density of the electron drift centers requires specifying a model of the medium and a configuration of the electromagnetic pulse. For our estimates, we consider the simplest model of a homogeneous cold plasma with noninteracting electrons and assume the pulse to be sharp, with a characteristic scale r. In this case, the coherence condition takes the form [14]

$$\lambda_0^3 n_e \gg 100\frac{r}{\lambda_0} l^4 \alpha^4, \tag{35}$$

where λ_0 is the wavelength of the incident radiation, α is the angle between the directions of propagation and observation, and l is the number of the observed harmonic.

The estimates obtained for the experimental work [1] show that the characteristic angle at which the coherent radiation of the harmonics up to ten can be observed is several degrees.

Let us now discuss the relationship between the results obtained and the experimental data from the experimental review [1]. As was shown in this review, high harmonics with frequencies that are a significant number of times higher than the frequency of the incident wave feature prominently in the induced forward radiation (the efficiency is ~10^{-7}–10^{-6}). In addition, even harmonics, which are of the same order of magnitude as the odd harmonics for a circularly polarized original wave, are also present in this radiation. It was also shown that the intensity of all the observed odd harmonics is proportional to the plasma density squared, while the power for the even harmonics lies within the range 1.2–1.4. In addition, it was found that, for example, the eighth harmonic vanishes altogether when the intensity of the beam incident on plasma falls below 10^{17} W cm^{-2}, with the position of this threshold being independent of the plasma density. The authors believed that these and other observed effects, which significantly distinguish this situation from the classical weak-field approximation, could be explained by the complex (figure-eight) path of an electron moving in the field of a relativistic monochromatic wave.

In this paper, however, we reached several conclusions that are applicable to the conditions of the experiment under discussion (the forward radiation in a transparent plasma), but entirely inconsistent with the observed effects: the absence of radiation at high harmonics for a circularly polarized laser pulse, the extremely low generation efficiency of even harmonics compared to odd (even harmonics are radiated only near the pulse boundaries; no even harmonics are represented in the plasma radiation for a uniform wave), and the rapid decrease in the harmonic amplitudes with increasing harmonic number,

$$a_{2m+1} \sim (n_e/n_{\text{crit}})^m, \quad f_{2m} \sim (n_e/n_{\text{crit}})^m.$$

Thus, for the conditions discussed in [1], the generation efficiency of the third harmonic must be ~10^{-12}, which is much lower than the experimentally observed values. For higher harmonics, this difference must be even larger in view of the exponential dependence (27), (28) of the radiation harmonics on the plasma density. Even if we assume that there is a mechanism destroying the “phasing-in” of the electron radiation, as a result of which the plasma forward radiation ceases to be coherent and our approach based on calculating the radiation of the currents becomes unjustified, the incoherent plasma radiation at a small angle to the direction of laser-pulse propagation can be easily estimated. For the experimental conditions in [1], the generation efficiency of the third and fifth harmonics does not exceed 10^{-12}–10^{-11}, which is much lower than the efficiencies obtained during the experiment.

Thus, for the experimentally observed results to be successfully described, we must find a different high harmonic generation mechanism. A detailed discussion of this question is beyond the scope of our paper. Note, however, that the coherent bremsstrahlung of the electrons photoionized in the field of a laser pulse, which was considered in detail in [15] (the review [16] should also be mentioned here), could be one of these mechanisms. The authors of [15] discussed emission by the electrons released from wave-ionized atoms when the ionization potential is suppressed. The characteristic intensities at which photoionization takes place and the model [15] reaches an optimum are known to be no higher than 10^{15}–10^{16} W cm^{-2} in order of magnitude. However, the intensities discussed both in our paper and in the review [1] are within the range of relativistic intensities, ~10^{18}–10^{21} W cm^{-2}.

Collisional plasma radiation, which was considered in detail in [11, 12], could be another possible mechanism behind the observed effects. In these papers, the plasma is assumed to be completely ionized; i.e., the intensity restriction is removed. For example, the fact that a complex dependence of the intensity of the coherent radiation of a collisional current on the plasma density was found in [12], as in the experimental review [1], argues that this explanation is plausible. This radiation must be strongest at the boundary of a certain small-angle cone whose axis coincides with the direction of laser-pulse propagation. The dependence of the harmonic intensity on the angle of observation given in [1] has no local maximum in the direction of pulse propagation, which, however, can be explained by the low resolution of the recording instrument. The similarity between the generation efficiency of the third harmonic obtained in this model and its experimentally observed value is the main reason to believe that the theory of collisional radiation can explain the observed dependences. Further studies are required for a more detailed elucidation of the detected relationships of this theory.

ACKNOWLEDGMENTS

This work was supported by the Russian Foundation for Basic Research, project no. 02-02-17275.

REFERENCES

1. S. Banerjee, A. R. Valenzuela, R. C. Shah, *et al.*, Phys. Plasmas **9**, 2393 (2002).
2. E. Esarey, S. K. Ride, and P. Sprangle, Phys. Rev. E **48**, 3003 (1993).
3. W. B. Mori, C. D. Decker, and W. P. Leemans, IEEE Trans. Plasma Sci. **21**, 110 (1993).
4. G. Zeng, B. Shen, W. Yu, and Z. Xu, Phys. Plasmas **3**, 4220 (1996).
5. E. Esarey, A. Ting, P. Sprangle, *et al.*, IEEE Trans. Plasma Sci. **21**, 95 (1993).
6. P. Sprangle, E. Esarey, and A. Ting, Phys. Rev. A **41**, 4463 (1990).
7. J. M. Rax and N. J. Fisch, Phys. Fluids B **5**, 2578 (1993).
8. L. D. Landau and E. M. Lifshitz, *Course of Theoretical Physics*, Vol. 2: *The Classical Theory of Fields*, 7th ed. (Nauka, Moscow, 1988; Pergamon, Oxford, 1975).
9. M. D. Tokman, Fiz. Plazmy (Moscow) **25**, 160 (1999) [Plasma Phys. Rep. **25**, 140 (1999)].
10. A. I. Akhiezer, I. A. Akhiezer, R. V. Polovin, *et al.*, *Plasma Electrodynamics: Linear Theory* (Nauka, Moscow, 1974; Pergamon, New York, 1975).
11. G. M. Fraiman, V. A. Mironov, and A. A. Balakin, Phys. Rev. Lett. **82**, 319 (1999).
12. A. A. Balakin and G. M. Fraĭman, Zh. Éksp. Teor. Fiz. **120**, 797 (2001) [JETP **93**, 695 (2001)].
13. A. I. Zhmoginov and G. M. Fraiman, in *Proceedings of 30th EPS Conference on Control Fusion and Plasma Physics* (St. Petersburg, 2003), Vol. 27A, p. 58.
14. S. M. Rytov, Yu. A. Kravtsov, and V. I. Tatarskij, *Principles of Statistical Radiophysics* (Springer, Berlin, 1988), Vol. 2, p. 231.
15. V. P. Silin, Zh. Éksp. Teor. Fiz. **121**, 291 (2002) [JETP **94**, 244 (2002)].
16. G. L. Yudin and M. Yu. Ivanov, Phys. Rev. A **63**, 033404 (2001).

Translated by V. Astakhov

Journal of Experimental and Theoretical Physics, Vol. 100, No. 5, 2005, pp. 903–910.
Translated from Zhurnal Éksperimental'noĭ i Teoreticheskoĭ Fiziki, Vol. 127, No. 5, 2005, pp. 1026–1034.
Original Russian Text Copyright © 2005 by Kostyukov.

ATOMS, MOLECULES, OPTICS

Stochastic Heating and Stochastic Outer Ionization of an Atomic Cluster in a Laser Field

I. Yu. Kostyukov
Institute of Applied Physics, Russian Academy of Sciences, Nizhni Novgorod, 603950 Russia
e-mail: kost@appl.sci-nnov.ru

Received December 20, 2004

Abstract—The dynamics of cluster electrons in a laser field is considered in the framework of the nonlinear oscillator model. The point map describing the motion of a cluster electron in the laser field is constructed. The critical value of the laser field, at which a transition to stochastic motion takes place, is determined. As a result of random walk in the energy space, an electron may accumulate an energy sufficient for overcoming the cluster potential barrier and for passing to the continuum. In this case, outer ionization of the cluster takes place. Estimates are obtained for the heating rate and the time of stochastic outer ionization of the cluster. *© 2005 Pleiades Publishing, Inc.*

1. INTRODUCTION

Laser targets of atomic clusters have become important objects of investigation in recent years. Although the average density of such a target is close to the gas density, the density of an individual cluster may attain values characteristic of solids. As a result, atomic clusters combine a number of advantages of solid targets (absorb almost the entire laser energy [1]) and gaseous targets (large radiation penetration depth and the absence of surface effects). Among interesting phenomena discovered as a result of interaction of laser radiation with cluster targets, generation of ions with energies up to several megaelectronvolts [2], high-energy electrons [3], higher harmonics [4], and X-rays [5] are worth noting. Deuterium-based cluster targets can be used as sources of neutrons [6].

The jelly model [7] or the cluster nanoplasma model [8] is one of the models for describing the interaction of laser radiation with atomic clusters. In the framework of this model, a cluster in a laser field is treated as oscillations of an electron cloud about an expanding ion core. Using such a model, we studied phenomena like plasma resonance in an ionized cluster [9], over-the-barrier ionization of a cluster [10], backward bremsstrahlung absorption [11], absorption associated with Landau damping [12], resonant and autoresonance absorption of laser radiation in a cluster plasma [13], etc.

If the laser field is not strong enough and the amplitude of electron cloud oscillations is much smaller than the cluster radius, the electron field induced as a result of displacement of a homogeneous electron sphere relative to the ionic sphere is proportional to this displacement. In this case, the electron cloud performs harmonic oscillations under the action of the laser field relative to the ion core [13]. In the case of a strong laser field, the amplitude of oscillations becomes comparable to or greater than the cluster radius. The oscillations are nonlinear since the distribution of the electric field of ions outside the core in the nanoplasma model is described by the Coulomb law. If the laser field is strong, oscillations can be chaotic. Chaos is responsible for diffusion in the electron energy space, which may result in electron heating [14]. Moreover, as a result of random walk in the energy space, an electron may accumulate energy sufficient for overcoming the cluster potential barrier and to pass to the continuum. Such a process corresponds to outer ionization of the cluster.

In the case of an excited hydrogen-like atom, in which the electron is at high energy levels, stochastic ionization was studied in detail in the framework of classical mechanics (see, for example, 15, 16]). In these publications, the critical value of the high-frequency energy field causing ionization and the ionization rate were determined. In the present study, we generalize the results obtained for hydrogen-like atoms to the case of cluster potential. Moreover, since the cluster size is much larger than the size of an individual atom, a cluster is an even more classical object than an atom. It should be noted that the mechanism of vacuum heating was used for describing stochastic heating of an ionized cluster [17]. In this case, heating occurs when an electron oscillating in a laser field intersects the boundary between the plasma and vacuum. In our model, we take into account the cluster potential and energy transfer between the electron, and the laser field occurs on all segments of the trajectory. Using numerical simulation, if has been proved recently that high-energy cluster electrons intersecting the cluster play an important role in its heating [18].

We assume that most electrons have left the cluster and that the charge of the remaining electrons is much smaller than the charge of the ion core. In the present case, when the amplitude of electron oscillations is much larger than the cluster size, the electron charge is distributed over a much larger volume than the volume of the ion core. In this case, the electric field of electrons is weaker than the field of the ion core. Thus, we study the motion of an electron in the laser field and in the field of the ion core. This description can also be used at the initial stage of heating, when the electron cloud has not disintegrated. Ignoring the internal dynamics of the cloud, the latter can be treated as a point charge with a mass and charge equal to the mass and charge of all electrons in the cloud, respectively. In this case, the problem is reduced to analysis of the motion of a point charge in a laser field and in the field of cluster ions.

In Section 2, we present the Hamiltonian formulation of the problem and determine the action–angle variables. To describe the motion of an electron outside the cluster, where the field of the ion core of the cluster approaches the Coulomb field, we will use a new time variable. The energy transfer between a laser field and an electron in the field of the core will be calculated in Section 3. We will construct a point map connecting the electron energy and phase with their values after half the period of electron oscillations in the field of the core. To preserve the area of the map, it will be constructed using a generating function. The large-amplitude limit of electron oscillations will be considered in Section 4. We will determine the critical energy of the laser field, for which a transition is made to the stochastic dynamics of the electron. In Section 5, the estimates for the heating rate and the outer ionization time of the cluster will be obtained.

2. HAMILTONIAN FORMULATION AND ACTION–ANGLE VARIABLES

We assume that the core of the cluster is a uniformly charged sphere of radius a with an ion number density n_i; then the cluster potential can be written in the form [7]

$$U(r) = \begin{cases} -(3-r^2)/2, & r \le 1, \\ -1/r, & r > 1. \end{cases} \tag{1}$$

In this expression and below, dimensionless units are used; the time is normalized to $\sqrt{3}/\omega_p$; the length is normalized to a, the momentum, to $ma\omega_p/\sqrt{3}$; the energy, to $ma^2\omega_p^2/3$, where $\omega_p^2 = 4\pi Ze^2n_i/m$ is the square of the electron frequency of the plasma; Z is the charge number of the ion; e is the electron charge; and m is the electron mass. The motion of an electron in the field of an ion core and in the laser field in the nonrelativistic and dipole approximations is described by the Hamiltonian

$$H(p, x, t) = \frac{p^2}{2} + U(x) + Fx\cos(\alpha t), \tag{2}$$

where $F = 3eE/ma\omega_p^2$, $\alpha = \sqrt{3}\,\omega/\omega_p$, and ω and E are the frequency and amplitude of the laser field, respectively. For simplicity, we consider only radial oscillations.

Let us first study unperturbed oscillations of electrons in the cluster potential in zero laser field ($F = 0$). For electrons with energy $w = p^2/2 + U(x)$, the amplitude of unperturbed electron oscillations is $x_0 = 1/|w|$. Here, we consider the regime when the amplitude of oscillations is larger than the cluster size ($x_0 > 1$, $-1 < w < 0$). In this regime, oscillations are nonlinear. Using the canonical transformation, we pass from the momentum and coordinate to the action–angle variables,

$$I = \frac{2\sqrt{2}}{\pi}\left(\frac{\pi}{2\sqrt{|w|}} - \frac{\sqrt{1-|w|}}{2} + \frac{3-2|w|}{2\sqrt{2}} \times \arcsin\frac{1}{\sqrt{3-2|w|}} - \frac{1}{\sqrt{|w|}}\arcsin\sqrt{|w|}\right), \tag{3}$$

$$\theta = \Omega\arcsin\frac{x}{\sqrt{3-2|w|}}, \quad 0 < x < 1,$$

$$\theta = \theta_0 + \frac{\Omega}{\Omega_C}\left[\arcsin\sqrt{x|w|} - \sqrt{x|w|(1-x|w|)}\right], \quad 1 < x < \frac{1}{|w|}, \tag{4}$$

where

$$\theta_0 = \Omega\arcsin\frac{1}{\sqrt{3-2|w|}} - \frac{\Omega}{\Omega_C}\left(\arcsin\sqrt{|w|} - \sqrt{|w|(1-|w|)}\right), \tag{5}$$

$$\Omega = \Omega_C\frac{\pi}{2}\left(\frac{\pi}{2} + \sqrt{|w|(1-|w|)} + \sqrt{2}|w|^{3/2}\arcsin\frac{1}{\sqrt{3-2|w|}} - \arcsin\sqrt{|w|}\right)^{-1}, \tag{6}$$

$\Omega_C = \sqrt{2}\,|w|^{3/2}$ is the oscillation frequency of an electron in the Coulomb potential, which appears in the problem on stochastic ionization of the atom [19]. Action $I = (1/2\pi)\int p\,dx$ is defined as the area bounded by the electron trajectory in the phase space. Angular variable θ is canonically conjugate to the action.

The unperturbed part of the Hamiltonian in the action–angle variables has a simple form

$$H_0(I) = w(I), \qquad (7)$$

where the relation for $w(I)$ can be derived from expression (3) for the action. The period of electron oscillations in the cluster potential can be written in the form

$$T = 2\pi\left(\frac{dH_0}{dI}\right)^{-1} = 2\pi\frac{dI(w)}{dw} = \frac{2\pi}{\Omega(w)}. \qquad (8)$$

We introduce a new time variable ξ for describing the motion of electrons in the Coulomb field outside the cluster core [20]. Let an electron be at the maximal distance from the core ($\xi = -\pi/2$) at the initial instant $t = t_0$. Then the relation connecting the new time variable and the old variable has the form

$$t = t_0 + \psi_n(\xi), \qquad (9)$$

$$\psi_n(\xi) = \frac{nT}{2} + \frac{1}{2\Omega_C}[2\xi - \sin 2\xi - \pi(2n-1)]. \qquad (10)$$

Outside the cluster, the electron is at instants

$$-t_2 + \frac{nT}{2} < t - t_0 \le t_2 + \frac{nT}{2}, \quad n = 0, 1, \ldots,$$

where

$$t_2 = \frac{\pi + \sin 2\xi_0 - 2\xi_0}{2\Omega_C}$$

and $\xi_0 = \arcsin\sqrt{|w|}$; here, variable ξ changes in the limits

$$\pi(n-1) + \xi_0 < \xi \le \pi n - \xi_0, \quad n = 0, 1, \ldots.$$

Within the cluster, the electron is at instants

$$t_2 + \frac{nT}{2} < t - t_0 \le t_2 + 2t_1 + \frac{nT}{2}, \quad n = 0, 1, \ldots,$$

where

$$t_1 = \arcsin\frac{1}{\sqrt{3 - 2|w|}}.$$

It can easily be verified that $T = 4(t_1 + t_2)$.

Using Eqs. (4)–(6), we can find the dependence between variables ξ, t, and x:

$$x = \sqrt{3 - 2|w|}\sin\left[t - t_0 - \frac{T}{4}(1 + 2n) + \pi n\right],$$

$$t_2 + nT/2 < t - t_0 \le t_2 + 2t_1 + nT/2,$$

$$x = -\frac{1 - \cos 2\xi}{2|w|}, \quad -t_2 + nT < t - t_0 \le t_2 + nT, \qquad (11)$$

$$x = \frac{1 - \cos 2\xi}{2|w|},$$

$$-t_2 + T\left(n + \frac{1}{2}\right) < t - t_0 \le t_2 + T\left(n + \frac{1}{2}\right),$$

where $n = 0, 1, \ldots$. The expressions derived above imply that the electron intersects the cluster boundary ($|x| = 1$) at instants $t = t_0 \pm t_2 + nT/2$ ($\xi = \pm\xi_0 + \pi n$, $n = 0, 1, \ldots$). Using the Hamilton equations and Eqs. (9)–(11), we obtain the equations of motion in the form

$$\frac{dw}{dt} = F\sqrt{3 - 2|w|}\cos\left[t - t_0 - \frac{T}{4}(1 + 2n) + \pi n\right]\cos\alpha t,$$

$$-t_2 + \frac{nT}{2} < t - t_0 \le t_2 + 2t_1 + \frac{nT}{2},$$

$$\frac{dw}{d\xi} = \frac{F\sin 2\xi\cos\alpha t}{2|w|},$$

$$\xi_0 + \pi(2n-1) < \xi \le 2n\pi - \xi_0, \qquad (12)$$

$$\frac{dw}{d\xi} = -\frac{F\sin 2\xi\cos\alpha t}{2|w|},$$

$$\xi_0 + 2\pi n < \xi \le \pi(2n+1) - \xi_0,$$

$$\frac{dt}{d\xi} = \frac{1 - \cos\xi}{\Omega_C(w)}, \quad \pi(n-1) + \xi_0 < \xi \le \pi n - \xi_0, \qquad (13)$$

where $n = 0, 1, \ldots$. In deriving these equations, we considered the action of the laser field as perturbation and retained only the first-order terms in F.

3. POINT MAP FOR A CLUSTER

It is more convenient to analyze the dynamics of cluster electrons using the point map instead of solving equations of motion (12) and (13) directly. We construct a point map, which provides the expression for a change in the action–angle variables in terms of the half-period between the instants at which an electron is at the maximal distance from the core. Integrating the equations of motion from $t = t_0$ to $t = t_0 + T/2$, we can find the increment of action w beginning from the instant when the distance between the electron and the core is maximal ($\xi = -\pi/2$). This gives

$$\begin{aligned}\Delta w &= F[A_1(w)\cos\phi - A_2(w)\sin\phi]\\ &+ F[B_1(w)\cos\phi - B_2(w)\sin\phi],\end{aligned} \tag{14}$$

$$\begin{aligned}A_1(w) &= \frac{1}{2|w|}\int\limits_{\xi_0}^{\pi/2}\sin(2\xi)\cos(\phi_0 + \alpha\psi_1(\xi))d\xi\\ &+ \frac{1}{2|w|}\int\limits_{-\pi/2}^{-\xi_0}\sin(2\xi)\cos(\phi_0 + \alpha\psi_0(\xi))d\xi,\end{aligned} \tag{15}$$

$$\begin{aligned}A_2(w) &= \frac{1}{2|w|}\int\limits_{\xi_0}^{\pi/2}\sin(2\xi)\sin(\phi_0 + \alpha\psi_1(\xi))d\xi\\ &+ \frac{1}{2|w|}\int\limits_{-\pi/2}^{-\xi_0}\sin(2\xi)\sin(\phi_0 + \alpha\psi_0(\xi))d\xi,\end{aligned} \tag{16}$$

$$\begin{aligned}B_1(w) &= \frac{\cos(\alpha T/4)}{1-\alpha^2}\\ &\times[\cos(\alpha t_1) - \alpha\sqrt{2-2|w|}\sin(\alpha t_1)],\end{aligned} \tag{17}$$

$$\begin{aligned}B_2(w) &= \frac{\sin(\alpha T/4)}{1-\alpha^2}\\ &\times[\cos(\alpha t_1) - \alpha\sqrt{2-2|w|}\sin(\alpha t_1)],\end{aligned} \tag{18}$$

where $\phi_0 = \alpha t_0$ is the laser field phase at the instant when the electron is at the maximal distance from the cluster core and the dependence $\psi_n(\xi)$ follows from expression (10). The first term in expression (14) defines the increment of the electron energy outside the cluster core, while the second term defines the energy increment inside the core. Analogously, we can find the change in angular variable αt over the time interval $t_0 < t < t_0 + T/2$:

$$\begin{aligned}\Delta(\alpha t) &= g(w) = \alpha T/2\\ &= 2\chi(\pi + 2\Omega_C t_1 - 2\xi_0 + \sin(2\xi_0)),\end{aligned} \tag{19}$$

where $\chi = \alpha/2\Omega_C$.

In the case of a pointlike cluster ($a \longrightarrow 0$), the energy acquires an increment outside the cluster, where the form of the potential is determined by the Coulomb law. This limit describes the electron heating by a laser field in an excited hydrogen atom. Proceeding to the limit $a \longrightarrow 0$ for a constant charge $Q = 4\pi e n_i a^3/3 =$ const of the core, we obtain

$$\begin{aligned}\Delta w &= \frac{F}{4|w|}\int\limits_{-\pi}^{\pi}\sin x\sin(\chi x - \chi\sin x)dx\\ &= \frac{F\pi}{2|w|}\mathrm{J}'_\chi(\chi),\end{aligned} \tag{20}$$

where $\mathrm{J}'_\chi(\chi)$ is the derivative of the Anger function [21]. This expression coincides with the relation derived in [19] for the hydrogen atom.

Considering w and ϕ as a pair of canonically conjugate variables, we can obtain a canonical point map connecting the values of w and ϕ at two consecutive instants at which the electron was at the maximal distance from the core. For the sought map to preserve its area, we will use the generating function

$$\begin{aligned}G(\bar{w}, \phi) &= \bar{w}\phi + F[A_1(\bar{w}) + B_1(\bar{w})]\sin\phi\\ &+ F[A_2(\bar{w}) + B_2(\bar{w})]\cos\phi + \int g(\bar{w})d\bar{w}.\end{aligned} \tag{21}$$

In this case, the "cluster" map is defined by the equations

$$\begin{aligned}w &= \frac{\partial G}{\partial\phi} = \bar{w} + F[A_1(\bar{w}) + B_1(\bar{w})]\cos\phi\\ &- F[A_2(\bar{w}) + B_2(\bar{w})]\sin\phi,\\ \bar{\phi} &= \frac{\partial G}{\partial\bar{w}} = \phi + g(\bar{w}) + F\sin\phi[A'_1(\bar{w}) + B'_1(\bar{w})]\\ &+ F\cos\phi[A'_2(\bar{w}) + B'_2(\bar{w})].\end{aligned} \tag{22}$$

To calculate the critical value of the electric field, at which a transition to the stochastic motion takes place, we linearize the generating function in the vicinity of the initial energy w_0:

$$\begin{aligned}G(\bar{w}, \phi) &= \bar{w}\phi + F[A_1(\bar{w}_0) + B_1(\bar{w}_0)]\sin\phi\\ &+ F[A_2(\bar{w}_0) + B_2(\bar{w}_0)]\cos\phi + (\bar{w} - \bar{w}_0)g(\bar{w}_0)\\ &+ \frac{(\bar{w} - \bar{w}_0)^2 g'(\bar{w}_0)}{2}.\end{aligned} \tag{23}$$

It is convenient to write this function in the form

$$G(\bar{w}, \varphi) = \bar{w}\varphi + FR(\bar{w}_0)\sin\varphi + (\bar{w} - \bar{w}_0)g(\bar{w}_0) + \frac{(\bar{w} - \bar{w}_0)^2 g'(\bar{w}_0)}{2}, \tag{24}$$

where

$$R^2(\bar{w}_0) = [A_1(\bar{w}_0) + B_1(\bar{w}_0)]^2 + [A_2(\bar{w}_0) + B_2(\bar{w}_0)]^2, \tag{25}$$

$$\varphi = \phi + \delta\phi, \tag{26}$$

$$\arctan(\delta\phi) = \frac{A_2(\bar{w}_0) + B_2(\bar{w}_0)}{A_1(\bar{w}_0) + B_1(\bar{w}_0)}. \tag{27}$$

As a result, we obtain the “standard” map [22]

$$\bar{w} = w + f\sin\varphi, \quad \bar{\varphi} = \varphi + T\bar{w}, \tag{28}$$

where $f = FR(w_0)$, $T = g'(w_0)$, and an insignificant constant in the second equation is omitted. The chaotic regime of oscillations emerges when the stochasticity parameter $K = fT$ becomes greater than unity [22]. Using this condition, we can estimate the critical value of the laser field as follows:

$$F_c \approx \frac{1}{R(w_0)|g'(w_0)|}. \tag{29}$$

This expression implies that the critical value of the laser field is inversely proportional to the energy exchange between the electron and the field during the half-period of oscillations. The stronger the energy exchange, the smaller the laser field amplitudes at which a transition to the stochastic regime of oscillations takes place. A typical form of the phase space in the presence of regular and stochastic trajectories obtained by solving the equations of motion, which are defined by Hamiltonian (2), is shown in the figure.

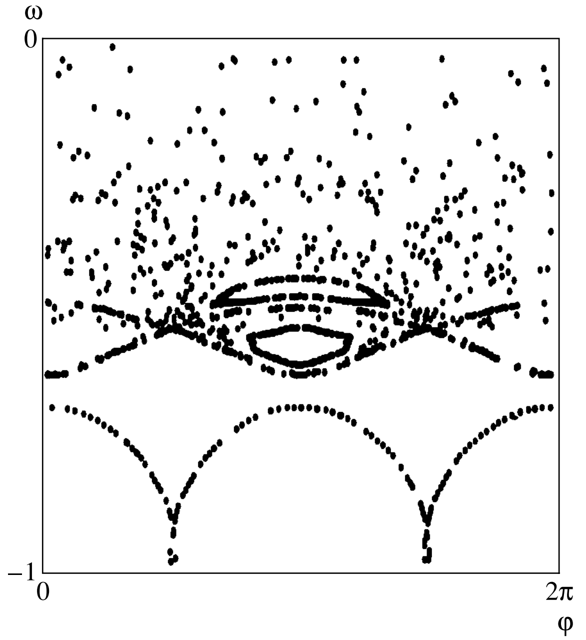

Phase plane w, ϕ obtained by solving the equations of motion for parameters $\alpha = 1$ and $F = 0.05$. Five chaotic and regular trajectories are shown.

4. CLUSTER MAP IN THE LIMIT OF LARGE AMPLITUDES OF ELECTRON OSCILLATIONS

In the general case, the expression for coefficient $R(w)$ is difficult to analyze. We will study this expression in the limit of a large amplitude of unperturbed oscillations ($|w| \ll 1$), assuming that $\chi = \alpha|w|^{-3/2}/\sqrt{2} \gg 1$ in this case. In this limit, $t_1 \approx \arcsin(1/\sqrt{3})$, $\xi_0 \approx \sqrt{|w|} \ll 1$, and the main contribution to integrals (15) and (16) comes from the neighborhood of ξ in the vicinity of $\pm\xi_0$. This gives

$$A_1(w) \approx \frac{1}{2|w|}\int_{2\xi_0}^{\infty} x\cos\left(\beta_+ + \frac{\chi x^3}{6}\right)dx + \frac{1}{2|w|}\int_{-\infty}^{-2\xi_0} x\cos\left(\beta_- + \frac{\chi x^3}{6}\right)dx, \tag{30}$$

$$A_2(w) \approx \frac{1}{2|w|}\int_{2\xi_0}^{\infty} x\sin\left(\beta_+ + \frac{\chi x^3}{6}\right)dx + \frac{1}{2|w|}\int_{-\infty}^{-2\xi_0} x\sin\left(\beta_- + \frac{\chi x^3}{6}\right)dx, \tag{31}$$

where $\beta_- = \pi\chi$ and $\beta_+ = \alpha T/2 - \pi\chi$. Integrals (30) and (31) can be expressed in terms of the integral exponential

$$A_1(w) \approx \frac{\xi_0^2}{3|w|}\mathrm{E}_{1/3}(-i\rho)[\exp(i\beta_+) - \exp(-i\beta_-)] + \frac{\xi_0^2}{3|w|}\mathrm{E}_{1/3}(i\rho)[\exp(-i\beta_+) - \exp(i\beta_-)], \tag{32}$$

$$A_2(w) \approx \frac{i\xi_0^2}{3|w|}\mathrm{E}_{1/3}(i\rho)[\exp(-i\beta_+) + \exp(i\beta_-)] - \frac{i\xi_0^2}{3|w|}\mathrm{E}_{1/3}(-i\rho)[\exp(i\beta_+) + \exp(-i\beta_-)], \tag{33}$$

where $\rho = 4\chi\xi_0^3/3$, and

$$\mathrm{E}_n(x) = \int_1^{\infty} dt \frac{\exp(-xt)}{t^n}$$

is the integral exponential [21]. The argument of the integral exponential can be reduced to the form $\rho \approx \sqrt{2}\,\alpha/3$ and depends only on parameter α. For this reason, we will consider a dense cluster with a supercritical value of density $\alpha \ll 1$ and the opposite case of a low-density cluster with a subcritical value of density $\alpha \gg 1$. The latter case can emerge due to expansion of the cluster, as a result of which the cluster density may become much lower than the critical value $n_c = \omega^2 m/4\pi Z e^2$ [9]. Let us first consider a low-density cluster ($\alpha \gg 1$). In this limit, expressions (32) and (33) assume the form

$$\begin{aligned} A_1(w) &\approx \frac{\sqrt{2}}{\alpha}\cos(\alpha t_1)\sin\left(\frac{\sqrt{2}\alpha}{3} - \pi\chi\right), \\ A_2(w) &\approx \frac{\sqrt{2}}{\alpha}\cos(\alpha t_1)\cos\left(\frac{\sqrt{2}\alpha}{3} - \pi\chi\right), \end{aligned} \tag{34}$$

$$\begin{aligned} B_1(w) &\approx \frac{\sqrt{2}}{\alpha}\cos(\pi\chi)\sin(\alpha t_1), \\ B_2(w) &\approx \frac{\sqrt{2}}{\alpha}\sin(\pi\chi)\sin(\alpha t_1). \end{aligned} \tag{35}$$

The coefficients of the standard map can be written in the form

$$\begin{aligned} R &\approx \frac{\sqrt{2}}{\alpha}\sqrt{1 + \sin(2\alpha t_1)\sin\frac{\sqrt{2}\alpha}{3}}, \\ g(w_0) &\approx \frac{\pi\alpha}{\sqrt{2}|w_0|^{3/2}}. \end{aligned} \tag{36}$$

As a result, we find that the critical value of the laser field is given by

$$\begin{aligned} F_c &\approx \frac{2|w_0|^{5/2}}{3\pi} \\ &\times \{\sqrt{(1 + \sin[2\alpha\arcsin(1/\sqrt{3})])\sin(\sqrt{2}\alpha/3)}\}^{-1/2}. \end{aligned} \tag{37}$$

For most values of energy α, the critical value is close to $F_c \approx 2|w_0|^{5/2}/3\pi$. However, values of α also exist, which are close to resonant values defined by the equation

$$\sin\left(2\alpha\arcsin\frac{1}{\sqrt{3}}\right)\sin\frac{\sqrt{2}\alpha}{3} = -1, \tag{38}$$

for which the energy transfer between an electron and the field is insignificant (energy accumulation/loss outside the cluster are compensated by the loss/accumulation of energy inside the cluster), and a strong laser field is required for a transition to the stochastic mode.

Let us now consider a high-density cluster ($\alpha \ll 1$). In this limit, expressions (32) and (33) assume the form

$$\begin{aligned} A_1(w) &\approx -\frac{\Gamma(2/3)3^{1/6}2^{2/3}}{\alpha^{2/3}}\sin\frac{\alpha T}{4}, \\ A_2(w) &\approx \frac{\Gamma(2/3)3^{1/6}2^{2/3}}{\alpha^{2/3}}\cos\frac{\alpha T}{4}, \end{aligned} \tag{39}$$

$$B_1(w) \approx \cos\frac{\alpha T}{4}, \quad B_2(w) = \sin\frac{\alpha T}{4}, \tag{40}$$

and the standard map coefficients are given by

$$R \approx \frac{\Gamma(2/3)3^{1/6}2^{2/3}}{\alpha^{2/3}}, \quad g(w_0) \approx \frac{\pi\alpha}{\sqrt{2}|w_0|^{3/2}}, \tag{41}$$

where $\Gamma(x)$ is a gamma function [21]. Thus, the critical value of the laser field in this limit is

$$F_c \approx \frac{2^{5/6}}{\pi\Gamma(2/3)3^{7/6}}\frac{|w_0|^{5/2}}{\alpha^{1/.3}}. \tag{42}$$

The same expression can be obtained in the limit of a pointlike cluster ($a = 0$) with a constant nuclear charge $Q = 4\pi e n_i a^3/3 = \text{const}$. In atomic units, $n_0 = (-2w_0)^{-1/2}$ corresponds to the number of the atomic level, $\epsilon_c = F_c n_0^4$ and $\omega_0 = \omega n_0^3$; consequently, the above expression can be written as follows: $\epsilon_c \approx 1/49\,\omega_0^{1/3}$. In this form, it coincides with expression (18) derived in [19] for the critical value of the high-frequency electric field, for which the motion of an electron in an excited hydrogen-like atom becomes chaotic.

5. STOCHASTIC HEATING AND OUTER IONIZATION

In the stochastic regime, the electron dynamics can be described as diffusion in the energy space [14], where the diffusion coefficient is defined as [19]

$$D(w_0) = \frac{\langle(\Delta w)^2\rangle}{\Delta t} \approx \frac{F^2 R^2(w_0)}{2}. \tag{43}$$

The heating rate can be determined using the relation connecting the mobility and the diffusion coefficient in the diffusion equation:

$$\gamma = \frac{d\langle\Delta w\rangle}{dt} = \frac{1}{2}\frac{\partial D(w_0)}{\partial w_0}. \tag{44}$$

This relation can be written if the system under investigation is a Hamiltonian system as in our case [14]. Expressions (36) and (41) for coefficient R imply that the diffusion coefficient is independent of energy in the approximation considered here. Thus, to estimate the heating rate, we must find the next terms in the expansion in w. Let us confine our analysis to the case $\alpha \ll 1$. In this limit, we can calculate coefficient R taking into account the terms proportional to w_0:

$$R \approx \frac{\Gamma(2/3)}{\sqrt{3}}\left(\frac{6}{\alpha}\right)^{2/3} + \frac{\Gamma(4/3)}{5\sqrt{3}}\left(\frac{6}{\alpha}\right)^{4/3} w_0 + O(w_0^2). \quad (45)$$

Using formula (44), we obtain

$$\gamma \approx \frac{12}{5}F^2\Gamma\left(\frac{2}{3}\right)\Gamma\left(\frac{4}{3}\right)\frac{1}{\alpha^2}. \quad (46)$$

Thus, the heating rate increases with the density of the cluster.

Ionization occurs at the instant when the electron crosses the boundary $w = 0$ and falls in the region of positive energy values. The maximal increment of the electron energy as a result of interaction with the laser field during time period $T/2$ is FR. Consequently, if the electron energy $|w_0| < FR$, the electron can leave the cluster during one period of oscillations about the cluster. The map constructed in this case is not valid for positive energy values; consequently, to determine the instant of ionization, we can use the procedure proposed in [19]. The ionization time can be estimated as the time required to attain, as a result of diffusion, the region $-FR < w < 0$ from which the electron may pass to the continuum over a period of oscillations. Thus, we find that

$$T_1 \approx \frac{w_0^2}{D(w_0)}. \quad (47)$$

Using expressions (36) and (41), we can estimate the stochastic ionization time of the cluster as

$$T_I \approx \frac{w_0^2\alpha^{4/3}}{F^2\Gamma^2(2/3)6^{1/3}}, \quad \alpha \ll 1, \quad (48)$$

$$T_I \approx \frac{w_0^2\alpha^2}{F^2[1 + \sin(2\alpha t_1)\sin(\sqrt{2}\alpha/3)]}, \quad \alpha \gg 1. \quad (49)$$

It follows from these expressions that the outer ionization time for a dense cluster is much shorter than the outer ionization time for a rarefied cluster.

6. CONCLUSIONS

In this study, we analyzed the nonlinear dynamics of electrons of a cluster in a laser field. It is convenient to do this by using the point map connecting the electron energy and phase in half the period of oscillations. Using the Chirikov criterion [22], the critical value of the laser field leading to a chaotic regime of oscillations was calculated. In the framework of diffusion description, an estimate for the outer ionization time was obtained.

In the model considered here, the influence of the remaining electrons was ignored. Obviously, such a model is valid if the majority of electrons have left the cluster as a result of outer ionization. Moreover, in the case of a large amplitude of electron oscillations (the amplitude of electron oscillations is much larger than the ion core of a cluster), the electron charge is spatially distributed over much larger volume than the ion charge. In this case, the mean electric field of electrons is much weaker than the electric field produced by the ions and the action of the electron charge can be ignored. This description is apparently also applicable at the initial stage of interaction, when the electron cloud can be treated as a point charge disregarding its intrinsic dynamics. However, the effect of electrons should be taken into account for analyzing electron dynamics in more general situations.

It is well known that an ionized cluster expands and its density strongly decreases in this process. In our model, this leads to an increase in parameter α with time. Since the cluster expansion time is much longer than the period of oscillations as a rule, the effect of the process of expansion on the dynamics of cluster electrons in our model can be taken into account by using the smooth time dependence of the “cluster” map parameters.

Since the external stochastic ionization time is quite long (tens of laser periods), this ionization mechanism may be important for interaction with long laser pulses (of hundreds of femtoseconds). In particular, numerical simulation of the interaction of the atomic cluster with laser radiation revealed that electrons performing large-amplitude oscillations pay an important role in heating of the cluster [18]. These electrons gain energy as a result of interaction with the laser field and the electrostatic field of the cluster. On the other hand, outer ionization of the cluster as a result of interaction with short laser pulses is apparently determined by other mechanisms (barrier “suppression” [23], thermal emission [7], and so on).

It should be noted that stochastic heating of electrons leaving the cluster is also possible when an electron moves in the field of laser waves incident on and reflected from the cluster. Obviously, such a process is realized for a dense (the cluster density must be higher than the critical value) and large cluster (the laser field penetration depth in the cluster must be much smaller than the cluster size). Such a mechanism of electron heating as applied to solid laser targets was considered recently in [24–26]. The stronger the laser field (namely, the larger the parameter $\mu = eE/mc\omega$ determining the ratio of the laser field E to the relativistic field strength $mc\omega/e$), the more effective the given process. Especially strong heating occurs for relativistic laser radiation intensities. In the limit of a weakly relativistic laser field ($\mu \ll 1$), the characteristic electron diffusion time in the energy space is $\omega t_D \approx (\pi/\sqrt{2})\mu^3$ [26]. Using expression (48), we can easily estimate that the electron heating mechanism, taking into account the reflected laser wave, dominates over the mechanism considered here only in the case of a strong laser field $\mu > 0.3$ for $n/n_c = 10$, $\lambda = 820$ nm (λ is the laser radiation wavelength), and $a = 50$ nm. Moreover, this threshold in the field only increases with time due to a decrease in the cluster density as a result of expansion. Nevertheless, the mechanism of electron heating of a cluster, which is associated with the dynamics of an electron in the incident and reflected laser waves can be substantial for relativistically strong laser fields.

ACKNOWLEDGMENTS

This study was supported by the Russian Foundation for Basic Research (project no. 04-02-16684) and the Ministry of Industry, Science, and Technologies of the Russian Federation (grant no. MK-3249.2004.2).

REFERENCES

1. T. Ditmire, R. A. Smith, J. W. G. Tisch, and M. H. R. Hutchinson, Phys. Rev. Lett. **78**, 3121 (1997).
2. T. Ditmire, J. W. G. Tisch, E. Springate, *et al.*, Nature **386**, 54 (1997).
3. Y. L. Shao, T. Ditmire, J. W. G. Tisch, *et al.*, Phys. Rev. Lett. **77**, 3343 (1996).
4. T. D. Donnelly, T. Ditmire, K. Neuman, *et al.*, Phys. Rev. Lett. **76**, 2472 (1996).
5. T. Ditmire, J. Zweiback, V. P. Yanovsky, *et al.*, Nature **398**, 489 (1999).
6. J. Zweiback, R. A. Smith, T. E. Cowan, *et al.*, Phys. Rev. Lett. **84**, 2634 (2000).
7. V. P. Kraĭnov and M. B. Smirnov, Usp. Fiz. Nauk **170**, 969 (2000) [Phys. Usp. **43**, 901 (2000)].
8. T. Ditmire, T. Donnelly, A. M. Rubenchik, *et al.*, Phys. Rev. A **53**, 3379 (1996).
9. E. Springate, N. Hay, J. W. G. Tisch, *et al.*, Phys. Rev. A **61**, 044101 (2000).
10. M. B. Smirnov and V. P. Kraĭnov, Zh. Éksp. Teor. Fiz. **115**, 2014 (1999) [JETP **88**, 1102 (1999)].
11. I. Yu. Kostyukov, Pis'ma Zh. Éksp. Teor. Fiz. **73**, 438 (2001) [JETP Lett. **73**, 393 (2001)].
12. D. F. Zaretsky, Ph. A. Korneev, S. V. Popruzhenko, and W. Becker, J. Phys. B: At. Mol. Opt. Phys. **37**, 4817 (2004).
13. I. Kostyukov and J.-M. Rax, Phys. Rev. E **67**, 066405 (2003).
14. A. J. Lichtenberg and M. A. Lieberman, *Regular and Stochastic Motion* (Springer, New York, 1982; Mir, Moscow, 1984).
15. R. V. Jensen, Phys. Rev. Lett. **49**, 1365 (1982).
16. G. Casati, B. V. Chirikov, I. Guarneri, and D. Shepelyansky, Phys. Rep. **154**, 77 (1987).
17. V. P. Kraĭnov and M. B. Smirnov, Zh. Éksp. Teor. Fiz. **119**, 719 (2001) [JETP **92**, 626 (2001)].
18. T. Taguchi, T. M. Antonsen, Jr., and H. M. Milchberg, Phys. Rev. Lett. **92**, 205003 (2004).
19. G. Casti, I. Guarneri, and D. Shepelyansky, IEEE J. Quantum Electron. **24**, 1420 (1988).
20. L. D. Landau and E. M. Lifshitz, *Course of Theoretical Physics*, Vol. 2: *The Classical Theory of Fields*, 7th ed. (Nauka, Moscow, 1988; Pergamon, Oxford, 1975).
21. *Handbook of Mathematical Functions*, Ed. by M. Abramowitz and I. A. Stegun, 2nd ed. (Dover, New York, 1972; Nauka, Moscow, 1979).
22. B. V. Chirikov, Phys. Rep. **52**, 263 (1979).
23. M. B. Smirnov and V. P. Krainov, Phys. Rev. A **69**, 043201 (2004).
24. Y. Sentoku, V. Y. Bychenkov, K. Flippo, *et al.*, Appl. Phys. B **74**, 207 (2002).
25. D. Umstadter, J. Phys. B: Appl. Phys. **36**, R151 (2003).
26. V. S. Rastunkov and V. P. Krainov, Laser Phys. **15** (2005) (in press).

Translated by N. Wadhwa

Journal of Experimental and Theoretical Physics, Vol. 100, No. 5, 2005, pp. 911–919.
Translated from Zhurnal Éksperimental'noĭ i Teoreticheskoĭ Fiziki, Vol. 127, No. 5, 2005, pp. 1035–1045.
Original Russian Text Copyright © 2005 by Chapovsky.

ATOMS, MOLECULES, OPTICS

Compact Magneto-optical Trap for Rubidium Atoms

P. L. Chapovsky
Institute of Automation and Electrometry, Siberian Division, Russian Academy of Sciences,
Novosibirsk, 630090 Russia
e-mail: chapovsky@iae.nsk.su

Received December 24, 2004

Abstract—The characteristics of a magneto-optical trap (MOT) using small-diameter cooling laser beams are considered. Trapping and cooling of Rb atoms from the surrounding gas of warm atoms takes place in the trap. A compact (140 μm) and stable atomic cloud is obtained with a density of 7×10^{10} cm^{-3}, which is three orders of magnitude higher than the density of the surrounding gas. *© 2005 Pleiades Publishing, Inc.*

1. INTRODUCTION

It is well known that, during absorption and emission of light, energy exchange between radiation and a particle is accompanied by momentum transfer leading to the emergence of the effect of light pressure. Considerable advances have been made in recent years in a wide range of problems associated with this effect. Many years of studies of light pressure in atomic beams (see review [1]) culminated in the development of magneto-optical traps (MOTs), in which the capture and cooling of atoms to very low temperatures (10^{-4}–10^{-6} K) occurs under the action of light pressure [2–4]. The design of a number of traps is described in the literature; however, MOTs remain complex and expensive physical devices. On the other hand, many contemporary studies of the light pressure effect and its application are based on the use of MOTs. For this reason, further investigation and modification of MOTs remain a vital problem.

It is important and interesting to obtain a high density of trapped atoms. It was found that an increase in the density is limited by mutual repulsion of atoms, which is caused by the exchange of spontaneous radiation emitted by these atoms [1, 5]. The magnitude of this effect is determined by the optical density of atoms in the trap, $\eta = n\sigma d$, where n is the density of atoms, σ is the photoabsorption cross section, and d is the diameter of the cloud of trapped atoms. The effective exchange of radiation between atoms and their mutual repulsion take place when the optical density becomes high ($\eta \sim 1$). Consequently, it can be intuitively concluded that a high density of atoms can be attained for small diameters of the cloud (i.e., in compact traps). Another possible application of compact traps is the creating of a cloud of cold atoms with well-defined and stable coordinates. It should be noted that stable localization of the atoms in a MOT was demonstrated earlier using magnetic fields with high gradients (on the order of 10^3 G/cm) [6].

Here, we study a compact magneto-optical trap for rubidium atoms. The MOT volume was reduced by using small-diameter laser beams. It might be interesting for some readers that the technical realization of a compact MOT turned out to be simpler than an ordinary MOT and that all main parts of the experimental setup (lasers, systems for measuring and stabilizing the radiation frequency, the vacuum system, and the system for detecting trapped atoms) were designed specially for the present project. These systems have good parameters and at the same time are quite simple and can be reproduced in many optical laboratories.

2. PHYSICAL FOUNDATIONS OF MAGNETO-OPTICAL TRAPS

The operation of MOTs is based on the two main processes: laser-induced capture and laser cooling of atoms. Physical effects participating in these processes are quite diverse. Some of these effects are well known and used for developing MOTs, while others are being discussed theoretically and have not been observed experimentally (see, for example, [7]). Let us consider two main effects of light pressure underlying the first MOTs.

The first effect is laser cooling of atoms. We consider the effect of light pressure in a system of two counterpropagating light waves with a frequency ω_L smaller than the absorption frequency ω_0 of a two-level particle (Fig. 1). On account of the Doppler effect, a moving particle predominantly absorbs radiation emitted by the counterpropagating wave, which leads to deceleration of the particle and, hence, its cooling [8, 9]. In such a system, atoms may be cooled to a temperature equal to the Doppler limit $T_D = \hbar\gamma/2k_B$, where γ is the rate of spontaneous decay of the upper level [1]. The minimal temperature of cooling is attained for an optimal radiation frequency detuning of $\omega_L - \omega_0 = -\gamma/2$. The Doppler limit for rubidium is $T_D \approx 140$ μK. The three-dimensional version of cooling of an atom by counter-

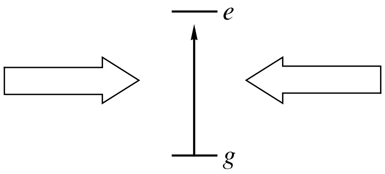

Fig. 1. Cooling of two-level atoms in the field of a standing light wave. The radiation frequency is chosen smaller than the $g \longrightarrow e$ transition frequency.

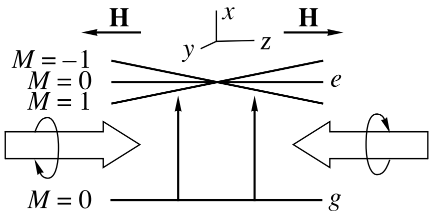

Fig. 2. Formation of a potential well with the help of the light pressure effect in a nonuniform magnetic field. The atom has the angular momentum $J_g = 0$ in the ground state and $J_e = 1$ in the excited state.

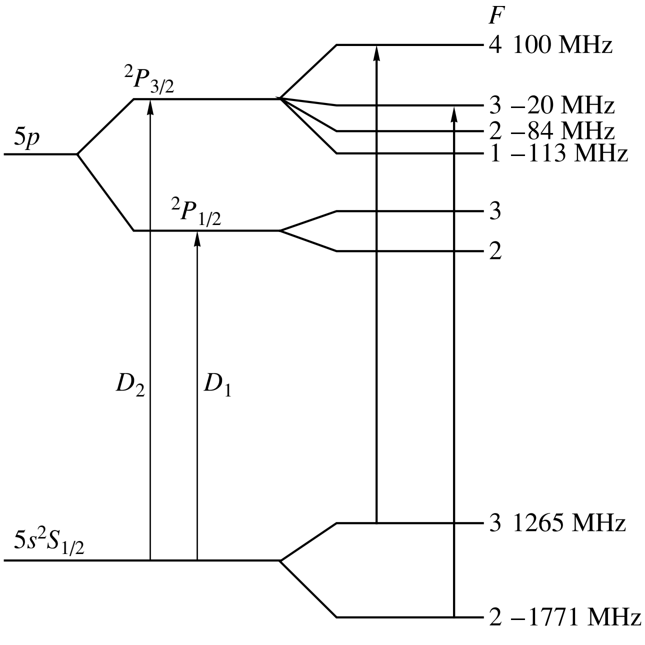

Fig. 3. Energy level diagram of ^{85}Rb. The nuclear spin is $I = 5/2$. The fine interaction splits the upper state and leads to the emergence of two absorption lines, D_1 and D_2. The right-hand side of the diagram illustrates the hyperfine splitting of the ground state and excited states of ^{85}Rb.

propagating light beams is known as optical molasses, in which atoms are effectively cooled due to viscous friction in the medium of surrounding photons [10].

However, plane waves forming optical molasses do not lead to a coordinate dependence of the light pressure force and, hence, do not produce a potential well. Such a coordinate dependence can be created for particles with degenerate levels by placing them in a nonuniform magnetic field. The method is illustrated in Fig. 2 for a particle having the ground state with an angular momentum of $J_g = 0$ and an excited state with an angular momentum of $J_e = 1$. The magnetic field, which increases linearly from the center of the trap, splits the upper state into three Zeeman sublevels. The energies of two of these levels depend on coordinate z chosen along the direction of the magnetic field. Two counterpropagating waves have opposite circular polarizations. Since the absorption of the left and right waves is possible only during the transitions $M_g = 0 \longrightarrow M_e = 1$ and $M_g = 0 \longrightarrow M_e = -1$, respectively, a coordinate dependence of the absorption probability and, hence, of the light pressure force, appears. The 3D version of such a system is known as the magneto-optical trap (MOT) [11]. The depth of the potential well in the trap is large and may attain ~1 K, which makes it possible to carry out effective trapping of atoms directly from the gas of “warm” atoms surrounding the center of the trap [12].

3. MODEL OF TRAP OPERATION

Our experiments were made with ^{85}Rb atoms excited on the D_2 line ($\lambda = 780.2$ nm). Figure 3 shows the level diagram of ^{85}Rb [13]. The absorption of a photon leads to a change in the velocity of a Rb atom only by 0.6 cm/s; consequently, absorption of many photons is required for trapping and cooling of atoms from the warm gas surrounding the trap. For this purpose, use is made of a “cycling transition” $F_g = 3 \longrightarrow F_e = 4$; the atom cannot spontaneously decay from the upper level of this transition to another hyperfine sublevel of the ground state (transitions with $|\Delta F| > 1$ are forbidden in the dipole approximation), and hence, it participates in absorption repeatedly. Nevertheless, absorption of radiation in the far wing of the line $F_g = 3 \longrightarrow F_e = 3$ leads to the atomic transition to a level of $F_e = 3$ followed by spontaneous decay to the hyperfine sublevel of the ground state $F_g = 2$ and, hence to the withdrawal of the atom from the cooling process. To resume cooling, the atom is returned to level $F_g = 3$ of the ground state by radiation from a repumping laser, which is in resonance with the transitions $F_g = 2 \longrightarrow F_e = 2, 3$.

A simple model of MOT operation is based on the concept of critical velocity v_c [12]. Atoms possessing a velocity $v < v_c$ are decelerated during their passage through the region of intersection of the beams to such an extent that they are captured in the trap. The flux of atoms with velocity $v < v_c \ll v_0$ into a unit spherical surface is

$$j = \frac{n v_0}{4\pi^{1/2}}\left(\frac{v_c}{v_0}\right)^4,$$

where v_0 is the most probable velocity of the Maxwell velocity distribution of atoms. The total rate of capture of the atoms is $R = jS$, where S is the surface area of the trap. The balance of the number N of particles in the trap is described by the simple equation

$$\frac{dN}{dt} = R - \frac{N}{\tau}, \quad (1)$$

where τ is the lifetime of an atom in the trap. Among many processes determining the time τ, the most important are collisions of cold atoms with surrounding warm Rb atoms (in our case) and particles of residual gases. In estimating the role of such collisions, it should be borne in mind that the cross sections of collisions knocking atoms from the trap turn out to be much larger than the gas-kinetic cross sections since the velocity sufficient to knock an atom from the trap must only be higher than v_c.

The mutual repulsion of atoms during exchange of radiation prevents the attaining of high densities of atoms in the traps (see, for example, [5]). This process is very complicated in the quantum limit, when the recoil energy of the atom, $\hbar\omega_r = \hbar^2k^2/2m$, becomes comparable to the energy $\hbar\omega$ of the vibrational quantum of the atom in the trap. If $\omega_r \gg \omega$, exchange of photons can be estimated disregarding the quantization of the spatial motion of the atom. In this case, the cross section of resonant absorption of photons amounts to $\sim\lambda^2$ [5].

4. LASERS

Lasers satisfying stringent requirements on the power and stability of radiation frequency are important elements of the setup. We used semiconductor laser diodes (type ML6XX24 manufactured by Mitsubishi) with an external resonator and a diffraction grating for radiation wavelength selection. The schematic diagram of the resonator is shown in Fig. 4 (the laser is described in greater detail in [14]). A semitransparent output mirror of the resonator ensures the optical coupling of the laser diode with the diffraction grating. In contrast to traditional Littrow and Littman semiconductor laser resonators [15], this simple modification makes it possible to easily select the optimal Q factor of the resonator by varying the transmission of the output mirror. (It should be noted that a similar resonator scheme was used earlier for frequency selection in a fiber laser [16].) We used diffraction grating with 600 lines/mm and a reflection coefficient of $R > 60\%$ in the fourth order (the diffraction angle $\theta = 69°$).

The design of the laser ensures two beams (Fig. 4). The low-intensity beam (4 mW) was used for measuring and stabilization of laser radiation frequency, while a high-intensity beam (14 mW) was directed to the MOT. Laser power supply was a stable dc source. Temperature stabilization of the laser diode was carried out by the active control system controlling the power supplied to the Peltier element. Temperature fluctuations of the diode casing did not exceed 0.1 mK. The temperature of the external resonator was stabilized due to good thermal contact with the surface of a massive metallic optical table.

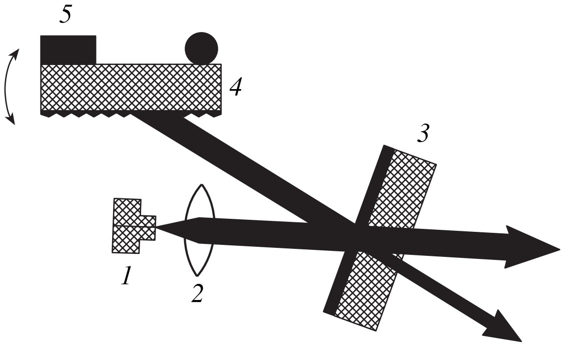

Fig. 4. Schematic of the external resonator of a semiconductor laser: *1*—laser diode, *2*—collimator, *3*—semitransparent output mirror, *4*—diffraction grating, *5*—piezoceramic.

The output laser beam has a linear polarization and an elliptical transverse intensity distribution. The laser was placed at a large distance (approximately 2 m) from the trap, at which the beam acquired a more symmetric shape. The intensity distribution in the beam was recorded with the help of a video camera. We used the beam with transverse diameters at the MOT inlet of approximately 2 mm (FWHM) and an intensity of about 1 mW.

Rough measurement of the laser radiation frequency required for tuning at the D_2 Rb absorption line frequency was performed by a home-made spectrograph consisting of a 300 lines/mm diffraction grating, a focusing spherical mirror with $f = 500$ cm, and a video camera recording the laser radiation spectrum in the focal plane of the mirror. To increase the dispersion of the grating, we operated with large diffraction angles. The precision measurement of the laser radiation frequency, which is required for tuning to a certain hyperfine transition in ^{85}Rb, was carried out using saturated absorption resonances in counterpropagating waves.

Frequency stabilization of laser radiation required for trapping and cooling of atoms in the MOT is complicated by the fact that the standard locking of frequency to the extrema of the saturation absorption spectrum is not suitable for MOT functioning. Many researchers (see, for example, [17]) solved this problem by stabilizing the laser radiation frequency to one of the extrema of the saturated absorption spectrum and shifting the radiation frequency by using an acousto-optic modulator. Apart from the obvious advantages of this method, which gives the exact value of radiation frequency, it has some drawbacks, such as the use of an additional device (acousto-optic modulator) and radiation power losses associated with it.

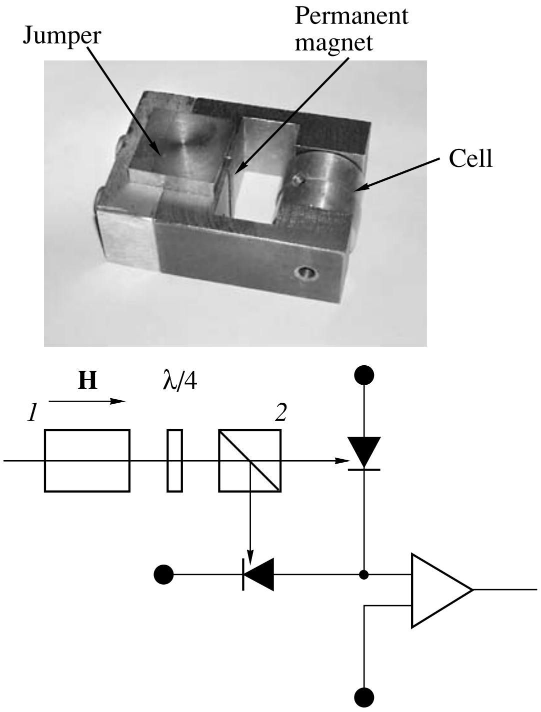

Fig. 5. DAVLL system of laser frequency stabilization: *1*—cell. *2*—Glan polarizer, λ/4 is a quarter-wave plate. The photograph shows the design of the magnet.

In our setup, the laser radiation frequency was stabilized with the help of circular dichroism and Faraday effects (dichroic atomic vapor laser lock (DAVLL) method of frequency stabilization [18, 19]). This method makes it possible to avoid laser radiation frequency modulation and to stabilize the radiation frequency at any point of the linear absorption profile. Figure 5 illustrates the operation of the stabilization system. Linear polarized radiation is directed into a cell containing Rb vapor in a longitudinal magnetic field. Two circular polarizations of this radiation acquire a relative phase difference in the cell due to the Faraday effect and are absorbed in different ways due to circular dichroism effect. The output, elliptically polarized radiation is decomposed by a quarter-wave plate into two mutually orthogonal linearly polarized components, which are subsequently separated by a Glan polarizer and directed to two photodiodes. The differential signals from these photodiodes are used for stabilizing the laser radiation frequency. Depending on the orientation of the optical axis of the quarter-wave plate and the Glan polarizer, the magnitude of the differential signal can be determined by the Faraday effect alone, the circular dichroism alone, or the combination of these two effects [19]. In the experiment, the orientation of these optical elements, the magnetic field strength, and the temperature of the cell were adjusted experimentally so that the frequency dependence of the differential signal was maximal (attaining values of ~0.4 mV/MHz in our experiments).

The magnetic field, which is optimal for the operation of the stabilization system, is a complex function of many parameters and should be adjusted experimentally. In our setup, the controllable magnetic field was produced by a permanent samarium–cobalt magnet, magnetic core, and a movable jumper to remove part of the magnetic flux. The photograph in Fig. 5 illustrates the design of the device. This system makes it possible to control the magnetic field strength in the region of the cell containing Rb vapor in an interval of 130–360 G. The field optimal for operation was found to be 200 G. The cell with Rb vapor had a diameter of 2 cm and its temperature was maintained at 37°C.

The stabilization method we used proved to be quite effective. It ensured reliable stabilization of the laser radiation frequency in a frequency range of ±300 MHz in the vicinity of the $F_g = 3 \longrightarrow F_e = 4$ transition of the ^{85}Rb isotope with a frequency locking region of about 800 MHz. Figure 6 shows the signals important for the operation of the DAVLL system: the linear absorption spectrum in Rb vapor of natural isotopic composition (72% ^{85}Rb and 28% ^{87}Rb), the saturated absorption spectrum in counterpropagating waves, and the differential signal used for laser radiation frequency stabilization.

Meticulous suppression of feedback is a necessary condition for the normal operation of a semiconductor laser with an external resonator. For this purpose, Faraday isolators are often used, which are, however, expensive devices. Owing to several fortunate design features of our MOT, we managed to do without Faraday isolators. First, the optical scheme of the laser (Fig. 4) was such that the feedback due to scattering of the “weak” beam used for radiation frequency stabilization is suppressed since this radiation does not enter directly the laser diode. Second, the optical scheme of the MOT (see below) is based on six independently tuned beams (without “retroreflection” of the beams, which is often used), which were directed to the center of the trap so that these beams did not return to the laser. Third, using a small-diameter beam, we could manage without telescopes, beam-profile correction systems and, hence, avoid additional scattering of radiation.

5. VACUUM CHAMBER AND MAGNETIC FIELD

Various designs of vacuum chambers of MOTs, ranging from complex and expensive stainless steel chambers to relatively simple chambers made entirely of quartz or glass, are described in the literature. Our vacuum chamber of the MOT, which has the form of a thin-walled glass sphere 6 cm in diameter, is apparently the simplest. It was verified that such a chamber hardly at all distorts the polarization of the beams and introduces only small distortions into their spatial distribution.

The requirements imposed on the vacuum system of the MOT are quite stringent. This is due to the fact that, as mentioned above, the atoms captured in the trap are readily knocked out during collisions with warm atoms of residual gas in the vacuum system. The vacuum in the system required for MOT operation is characterized by the fact that accumulation of atoms in the trap was terminated when the pressure in the chamber increased to 10^{-6} Torr. The vacuum chamber was permanently connected to a small ion pump with a capacity of about 10 l/s. After prolonged outgassing and heating of the entire system, a vacuum at a level of 10^{-8}–10^{-9} Torr was attained in the chamber and then maintained constantly. The absence of detachable windows, valves, and flanges in our vacuum system substantially simplified and accelerated the obtaining of high vacuum.

The chamber was filled with Rb vapor from an appendix containing metallic rubidium, which was permanently attached to the vacuum tract connecting the MOT chamber and the ion pump. This appendix was cooled by a Peltier element to 5°C to reduce the pressure of Rb vapor in the chamber, which was required to reduce the brightness of laser beam tracks in the MOT chamber.

A spherical quadrupole magnetic field was produced in the chamber by two Helmholtz coils of 5 cm in diameter, which were spaced at a distance of 5 cm from each other. The coils have 100 turns each and were cooled by air. When a current of 1.8 A was passed, the coils produced a magnetic field at the center of the system with a gradient of 20 G/cm along the symmetry axis of the coils. The electric power supply system of the coils made it possible to switch off the current in the coils in 30 μs. Because of the presence of metallic parts in the vicinity of the coils, the magnetic field decayed over a significantly larger time (about 0.5 ms).

6. OPTICAL SCHEME

The general optical scheme of the MOT is shown in Fig. 7. The splitting of the high-intensity beam produced by the trapping laser into six beams of approximately the same intensity was carried out with the help of semitransparent mirrors. These beams were directed to the center of the trap so that they did not return to the laser. The beam of the repumping laser was added to the main beam already at the first beam-splitting mirror and, hence, was present in all six beams forming the MOT.

The main laser was actively stabilized with the help of the DAVLL system described above. The preliminary adjusting of radiation frequency was carried out using the saturated absorption spectra. The final frequency adjusting of this laser was carried out using the fluorescence intensity of the cloud of trapped atoms. The radiation frequency of the repumping laser was also controlled using the saturated absorption spectra. This laser had a passively stabilized frequency sufficient for stable operation of the MOT.

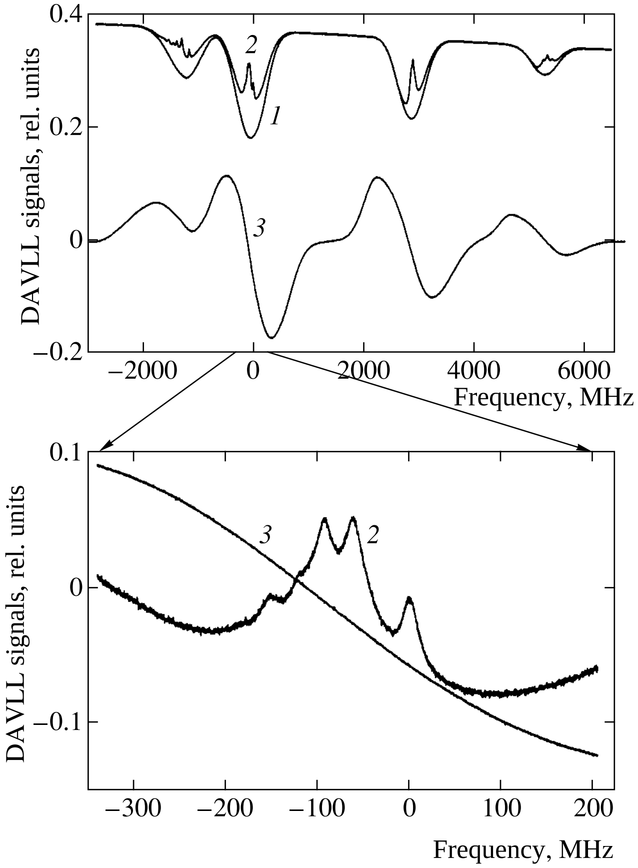

Fig. 6. Signals of the DAVLL frequency stabilization system: *1*—linear absorption spectrum, *2*—saturated absorption spectrum in counterpropagating waves, *3*—DAVLL differential signal. The lower figure shows a small fragment of signals *2* and *3*. For better visualization, the signals are made closer on the vertical axis.

The alignment of all beams at the center of the trap (at zero magnetic fields) must be performed in a MOT to a high degree of accuracy. In our case, alignment is substantially complicated because of the small diameter of the beams. To simplify the alignment, the vacuum system was designed so that the MOT vacuum chamber together with the ion pump could be withdrawn from the system without a deterioration of vacuum in the system. After the withdrawal of the chamber, a small sphere was installed at the point of desirable intersection of the beams (at zero magnetic field) and all the beams were aligned to its center. After the return of the chamber to its place and trapping of atoms, slight additional alignment of the directions of the beams was required (it was controlled by the fluorescence intensity of atoms in the trap). The circular polarizations of these beams were chosen so that the direction of rotation was matched with the direction of the local magnetic field. For the $F_g = 3 \longrightarrow F_e = 4$ transition in the ^{85}Rb isotope, the spin of photons must be antiparallel to the local magnetic field vector so that a configuration of levels and fields analogous to that shown in Fig. 2 was reproduced.

The images of atomic clouds were registered by a black-and-white CCD camera with a recording rate of 25 frames/s. An analog video signal from this camera was digitized and could be subsequently processed analytically. It should be noted that such cameras have a high sensitivity in the near IR spectral region. The cost of high sensitivity is a low time resolution of such cameras (40 ms/frame). For fast quantitative recording of fluorescence of the cloud, we used a calibrated photodiode supplied with an optical system collecting radiation from the trapped atoms. The sensitivity of the system was 2.8×10^4 atoms/mV and its time resolution was about 0.1 ms.

7. RESULTS

After the alignment of the direction of the beam, selection of their appropriate polarization, frequency, and required direction of current in the Helmholtz coils, a bright cloud of fluorescent Rb atoms was formed at the center of the MOT. The CCD camera recording the image of the cloud passed to the strong saturation mode. Figure 8 shows the image of the cloud and its evolution after the switching off the quadrupole magnetic field. In the steady-state mode, the fluorescence of the cloud was quite stable and the entire system operated independently up to 1 h without laser radiation frequency correction. After the removal of the field, the cloud left the region illuminated by laser beams in approximately 50 ms. This displacement of the cloud was, in all probability, due to small magnetic fields

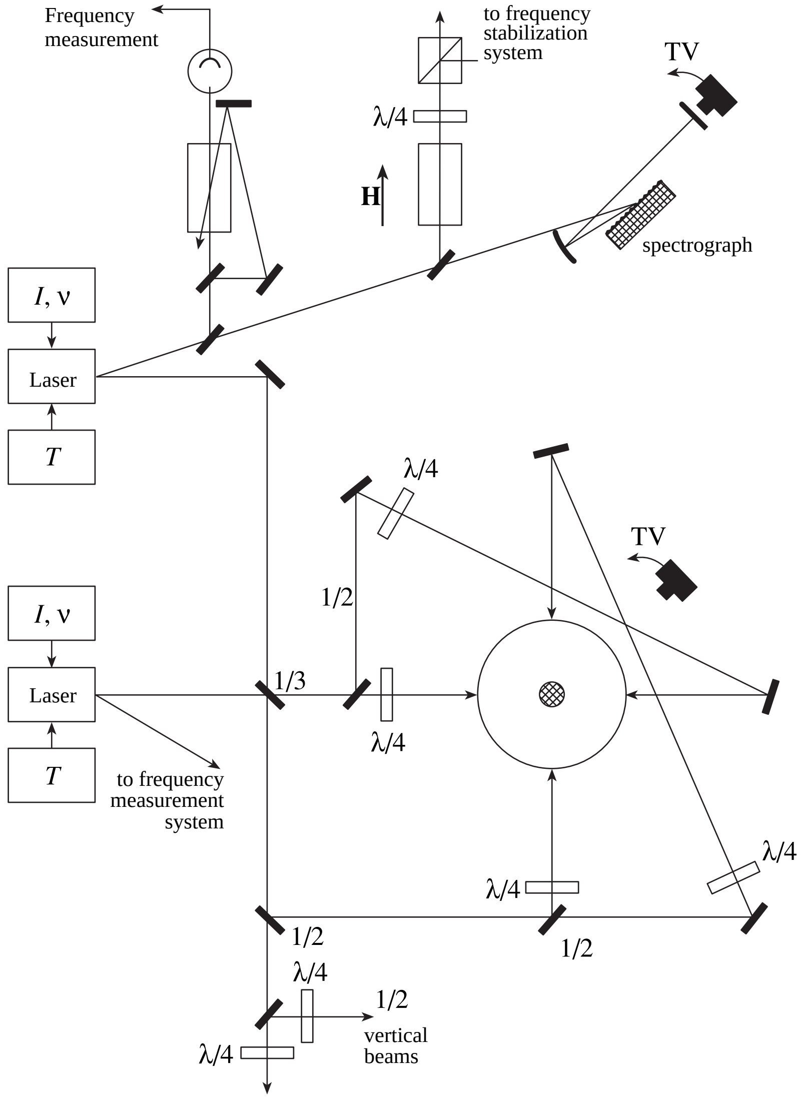

Fig. 7. Optical scheme of the setup. Numbers indicate the coefficients of beam intensity splitting by semitransparent mirrors; *I*, ν indicate the block controlling the current and laser radiation frequency; *T* is the block stabilizing the laser diode temperature; λ/4 are quarter-wave plates; the spectrograph is the grating spectrograph for "rough" measurement of the laser radiation frequency.

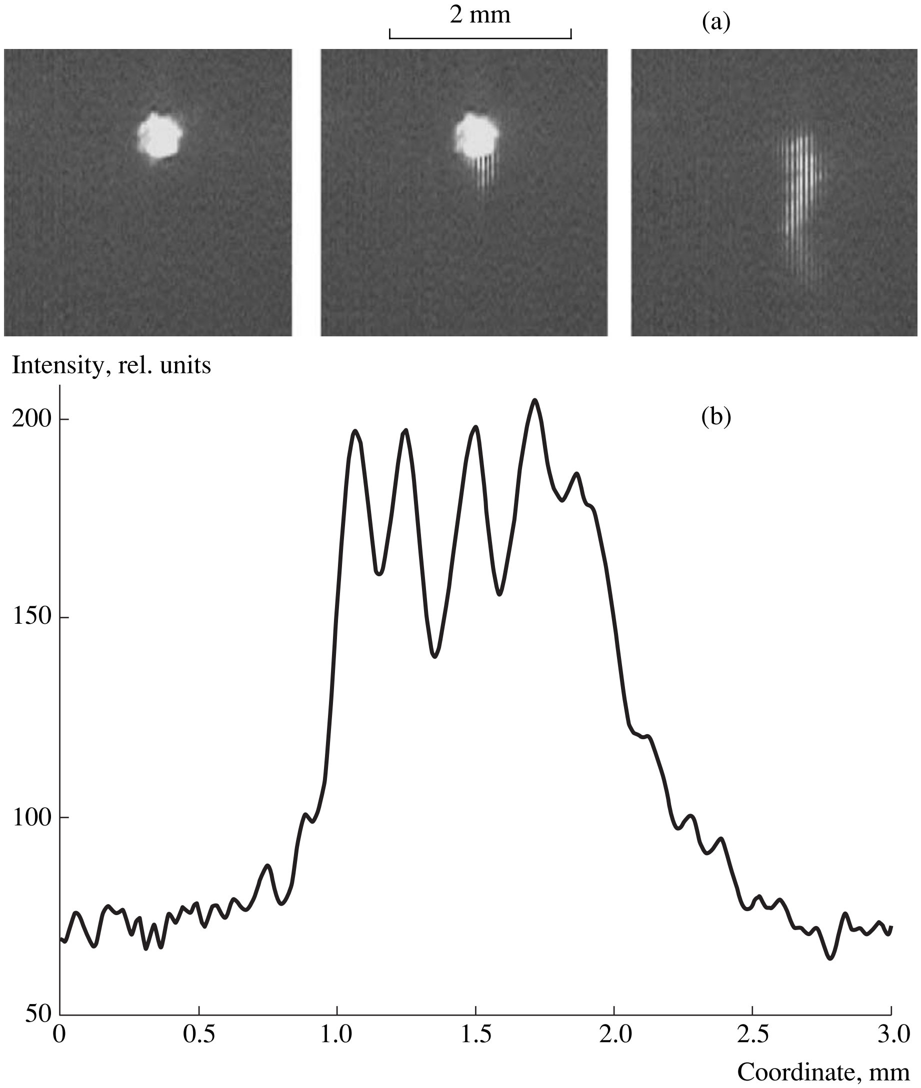

Fig. 8. (a) Fluorescence of the cloud of trapped atoms and its evolution after switching off the magnetic field. (b) Spatial modulation of fluorescence of the cloud along the direction of its motion.

remaining in the MOT chamber after switching off the current in the Helmholtz coils since residual magnetic fields produce an uncompensated light pressure force from each pair of counterpropagating laser beams. During the displacement of the cloud, two features could be observed. First, the displacement of the cloud was not accompanied by a noticeable increase in its size. Thus, the size of the cloud increases at a much lower rate than could be as a result of flying apart of atoms trapped in the MOT with a characteristic velocity of about 10 cm/s. In all probability, this can be explained by the fact that, after switching off a magnetic field, the MOT is transformed into optical molasses [10], in which the motion of atoms is not a gas-kinetic, but a diffusion process in view of the small mean free path of atoms in the medium of surrounding photons. Second, the fluorescence of the track of atoms during the motion of the cloud after the removal of the magnetic field was not continuous, but spatially modulated. The period of this structure was about 0.2 mm (see Fig. 8). The explanation of this effect requires additional investigations. We can only note that such a spatial structure could not be observed if atoms were trapped in out MOT by wide (1.5 cm) light beams. This is apparently due to the fact that such wide light beams produced a much larger cloud of trapped atoms than the period of spatial modulation observed by us.

Accumulation of atoms in the trap after the application of a magnetic field prior to saturation of the CCD camera was recorded with attenuation of fluorescence by a light filter by approximately two orders of magnitude. Figure 9a shows an example of such images. The results of measurements of the steady-state distribution of atomic fluorescence are shown in Fig. 9b (circles). This distribution is successfully approximated by a Gaussian curve of the type $a\exp(-(x-b)^2/c^2)$ with

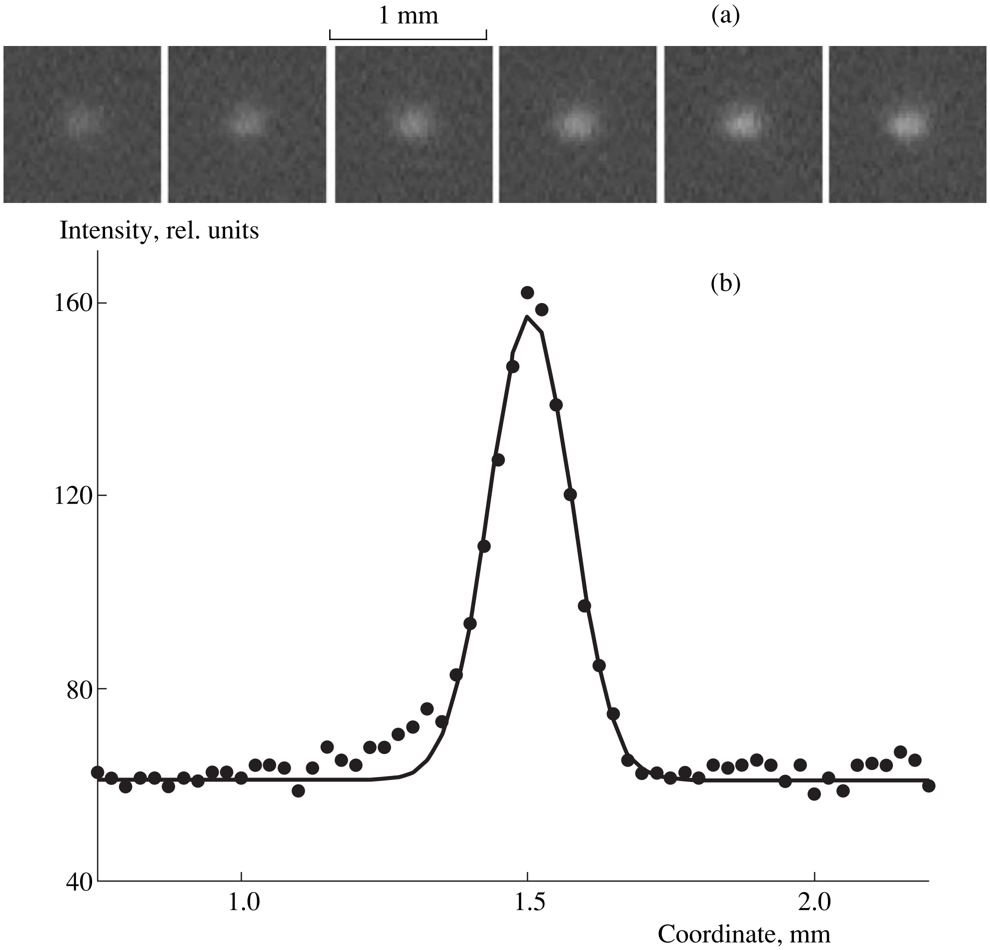

Fig. 9. Accumulation of atoms in a trap after the application of a magnetic field. (a) Image of the cloud of trapped atoms. The frames were shot with an interval of 80 ms. The fluorescence intensity is attenuated by two orders of magnitude. (b) Stationary spatial distribution of fluorescence of trapped rubidium atoms. The solid curve is the approximation of the distribution by the Gaussian curve.

parameters *a*, *b*, and *c* determined by comparison with experimental data (solid curve in Fig. 9b). According to these measurements, the cloud diameter was found to be approximately 140 μm (FWHM) (taking into account the spatial resolution of the optical system of ≤30 μm). The stability of the position of the center of the cloud was better than 20 μm over a time interval exceeding 1 s.

The dynamics and the number of trapped atoms were measured by a sensitivity-calibrated photodiode, whose signal is shown in Fig. 10. The accumulation of atoms after the application of a quadrupole magnetic field is correctly described by a function $R\tau(1 - \exp(-t/\tau))$, which is a solution to Eq. (1) (bold curve in Fig. 10). The results of approximation of experimental data by a least square fit gives a steady-state number of trapped atoms on the order of 10^5 and their lifetime in the trap $\tau \approx 0.4$ s. Taking into account the cloud diameter measured above, we obtain the following estimate for the steady-state density of trapped atoms: 7×10^{10} cm^{-3}. The concentration of warm Rb atoms in the chamber during the operation of the trap (the appendix containing metallic rubidium has a temperature of 5°C) was measured using the linear absorption of weak test radiation and amounted to 2.3×10^7 cm^{-3}. To avoid mis-

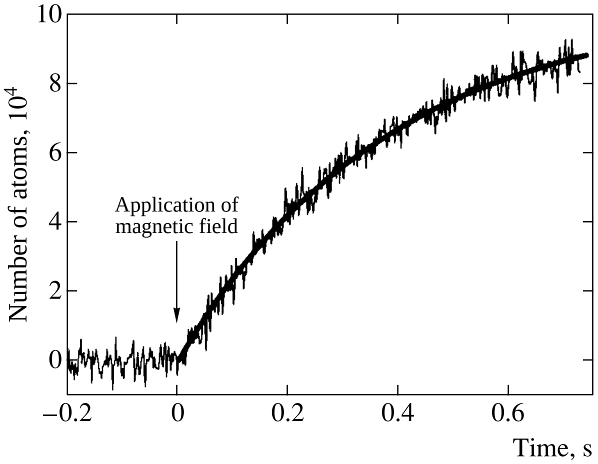

Fig. 10. Dynamics of accumulation of atoms in a trap (signal from the photodiode). The bold curve describes the dynamics of accumulation of atoms in accordance with Eq. (1).

understanding, we note that this concentration of Rb vapor is much lower than the concentration of saturated vapor at 5°C [20] due to permanent evacuation of the system by a ion pump. Thus, the concentration of atoms in the cloud exceeded the concentration of atoms in the surrounding gas by more than three orders of magnitude.

It would be interesting to estimate the critical velocity v_c. This can be done knowing the capture rate R of atoms in the trap, which can be determined most easily by measuring the rate of accumulation of atoms at the initial stage of trap filling. The accumulation rate was found to be 2.5×10^5 atoms/s. Taking into account the area of the trap surface, which was approximately 0.32 cm^2, we find that the critical velocity can be estimated as $v_c \approx 14$ m/s.

8. CONCLUSIONS

We have described the design and characteristics of a compact magneto-optical trap, in which a small cloud of trapped atoms (about 140 μm) with stable spatial parameters was obtained. In particular, the position of the center of the atomic cluster was stationary to within less than 20 μm. The density of trapped atoms was high (7×10^{10} cm^{-3}). This value was attained without a loss in the stability of spatial parameters, which is usually unavoidable for large clouds (see, for example, [21]). The atomic cluster formed in this way can be used in other experiments as a point source of cold atoms.

All main elements of the MOT (semiconductor lasers, the systems of frequency measurement and stabilization, the vacuum chamber, systems forming the magnetic field in the MOT, and the systems for visualization of atoms in the trap) were specially designed and constructed for this project. These systems are quite simple and can be reproduced in many optical laboratories. In this connection, we can mention two other realizations of MOT in Russia [7, 22].

ACKNOWLEDGMENTS

The author is grateful to O.I. Permyakova for her help and to L.V. Il'ichev, K.A. Nasyrov, I.I. Ryabtsev, and V.M. Éntin for numerous fruitful discussions and remarks.

This study was supported by the Russian Foundation for Basic Research (project no. 03-02-17553) and Presidium of the Siberian Division of the Russian Academy of Sciences (grant “Laser Cooling of Gases in Magneto-optical Traps”).

REFERENCES

1. V. I. Balykin, V. G. Minogin, and V. S. Letokhov, Rep. Prog. Phys. **63**, 1429 (2000).
2. S. Chu, Rev. Mod. Phys. **70**, 685 (1998).
3. C. Cohen-Tannoudji, Rev. Mod. Phys. **70**, 707 (1998).
4. W. D. Phillips, Rev. Mod. Phys. **70**, 721 (1998).
5. Y. Castin, J. I. Cirac, and M. Lewenstein, Phys. Rev. Lett. **80**, 5305 (1998).
6. P. A. Willems, R. A. Boyd, J. L. Bliss, and K. G. Libbrecht, Phys. Rev. Lett. **78**, 1660 (1997).
7. A. V. Yarovitskiĭ, O. N. Prudnikov, V. V. Vasil'ev, *et al.*, Kvantovaya Élektron. (Moscow) **34**, 341 (2004).
8. T. W. Hansch and A. L. Schawlow, Opt. Commun. **13**, 68 (1975).
9. D. Wineland and H. Dehmelt, Bull. Am. Phys. Soc. **20**, 637 (1975).
10. S. Chu, L. Hollberg, J. E. Bjorkholm, and A. Ashkin, Phys. Rev. Lett. **55**, 48 (1985).
11. E. L. Raab, M. Prentiss, A. Cable, *et al.*, Phys. Rev. Lett. **59**, 2631 (1987).
12. C. Monroe, W. Swann, H. Robinson, and C. Wieman, Phys. Rev. Lett. **65**, 1571 (1990).
13. G. P. Barwood, P. Gill, and W. R. C. Rowley, Appl. Phys. B **53**, 142 (1991).
14. O. I. Permyakova, A. V. Yakovlev, and P. L. Chapovsky, physics/0312047.
15. C. E. Wieman and L. Hollberg, Rev. Sci. Instrum. **62**, 1 (1991).
16. S. L. Gilbert, Opt. Lett. **16**, 150 (1991).
17. J. Zachorowski, T. Palasz, and W. Gawlik, Opt. Appl. **28**, 239 (1998).
18. K. L. Corwin, Z. Lu, C. F. Hand, *et al.*, Appl. Opt. **37**, 3295 (1998).
19. V. V. Yashchuk, D. Budker, and J. R. Davis, Rev. Sci. Instrum. **71**, 341 (2000).
20. A. N. Nesmeyanov, *Vapor Pressure of the Chemical Elements* (Akad. Nauk SSSR, Moscow, 1961; Elsevier, New York, 1963).
21. T. Walker, D. Sesko, and C. Wieman, Phys. Rev. Lett. **64**, 408 (1990).
22. V. M. Éntin and I. I. Ryabtsev, Pis'ma Zh. Éksp. Teor. Fiz. **80**, 184 (2004) [JETP Lett. **80**, 161 (2004)].

Translated by N. Wadhwa

Journal of Experimental and Theoretical Physics, Vol. 100, No. 5, 2005, pp. 920–928.
Translated from Zhurnal Éksperimental'noĭ i Teoreticheskoĭ Fiziki, Vol. 127, No. 5, 2005, pp. 1046–1054.

Theory of One-Dimensional Quantum Pump Based on a Two-Barrier Structure

L. S. Braginskiĭ, M. M. Makhmudian, and M. V. Entin*
Institute of Semiconductor Physics, Siberian Division, Russian Academy of Sciences,
Novosibirsk, 630090 Russia
**e-mail: entin@isp.nsc.ru*

Received January 10, 2005

Abstract—A 1D quantum pump based on a structure of two δ-functional harmonically oscillating potentials is considered. Such a structure can pump electrons from one bank to the other. An ac perturbation induces a steady-state current. The effect takes place in spatially asymmetric systems. Such an asymmetry is formed due to a difference in the initial heights of the barriers or in the amplitudes or phases of ac signals. The pump can operate in various modes depending on its parameters. It is shown that the current displays oscillations with a period such that the wavelength of incident or excited electrons is multiple to the separation of the δ-functions. Resonances at quasi-stationary states between the barriers, at zero energy, and with stationary states (in the case of wells) are investigated. © *2005 Pleiades Publishing, Inc.*

1. INTRODUCTION

A quantum pump is a device generating direct current under zero bias. The current in induced by an ac external field, which allows a local variation of the parameters of the system.

The quantum pump is essentially analogous to various versions of the photovoltaic effect, studied in detail mainly in Russia from the beginning of the 1980s [1–4]. The difference is that the photovoltaic effect is related to the emergence of a direct current in a homogeneous macroscopic medium (the only exception is the mesoscopic photovoltaic effect), while a pump is a microscopic object. From the phenomenological point of view, the emergence of a direct current in the pump is not surprising since any asymmetric microcontact can rectify ac voltage. However, analysis of adiabatic transport in a quantum-mechanical object leads to a new phenomenon, viz., quantization of charge transport [5].

In recent years, an enormous increase has been observed in the number of publications devoted to both theoretical [6–16] and experimental [17–20] studies of the physics of quantum pumps. Quantum pumps play an important role in biology; for example, the Thouless mechanism was employed for explaining the active transport of ions through a cellular membrane [21].

Here, we will simulate pump operation by a 1D system with the potential (Fig. 1)

$$U(x) = [u_1 + v_1(t)]\delta(x+d) + [u_2 + v_2(t)]\delta(x-d), \tag{1}$$

where $2d$ is the distance between δ-shaped barriers (wells); quantities u and v are measured in units of $\hbar^2/md$ (m is the electron mass); momentum p is measured in units of $\hbar/d$; energy E is measured in units of $\hbar^2/2md^2$; and frequency is measured in units of $\hbar/2md^2$. In the absence of an ac signal, the system has two barriers for positive values of u_1 and u_2 and two wells for negative values of these parameters. We assume that the electron gas is in equilibrium and the distribution functions are identical in the regions $x < -d$ and $x > d$. We also assume that an ac signal is harmonic,

$$v_1(t) = v_1 \sin\omega t, \quad v_2(t) = v_2\sin(\omega t + \varphi).$$

The problem is to determine the direct current induced by the ac field. This model was used, in particular, in [22], but was not analyzed in detail. At the same time, in spite of its simplicity, the potential in question leads (in view of the presence of four independent parameters in it) to a variety of possible behaviors of the solution.

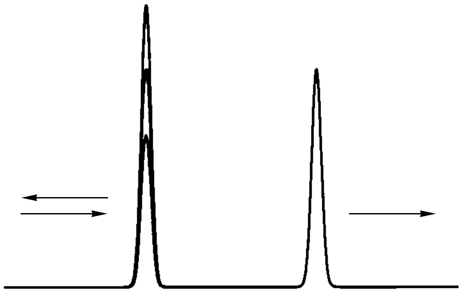

Fig. 1. Quantum pump based on the symmetric structure formed from two δ barriers, the first of which oscillates. Parameters $u_1 = u_2$, $v_2 = 0$.

This study is aimed at detailed analysis of various operation modes of the electronic pump.

A direct current can be induced only in an asymmetric system. In this case, at least one of the following conditions must be satisfied: $u_1 \neq u_2$, $v_1 \neq v_2$, and $\varphi \neq 0$. The macroscopic analogs of these cases are the linear photovoltaic effect in a polar medium (emerging due to the existence of a polar vector in the medium and analogous to a preferred direction from the first barrier to the second one); the surface photovoltaic effect (emerging due to nonuniformity of the electromagnetic field and analogous to the difference of v_1 from v_2); and the circular photovoltaic effect (emerging due to the phase shift between different Cartesian components of polarization; in the present case, the phase shift between $v_1(t)$ and $v_2(t)$).

2. BASIC EQUATIONS

We will seek the solution to the Schrödinger equation with potential (1) in the form

$$\varphi = \sum_n \exp[-i(E+n\omega)t]\begin{cases} \delta_{n,0}\exp\left(\dfrac{ip_nx}{d}\right) + r_n\exp\left(-\dfrac{ip_nx}{d}\right), & x < -d, \\ a_n\exp\left(\dfrac{ip_nx}{d}\right) + b_n\exp\left(-\dfrac{ip_nx}{d}\right), & -d < x < d, \\ t_n\exp\left(\dfrac{ip_nx}{d}\right), & x > d. \end{cases} \tag{2}$$

Here, $p_n = \sqrt{p^2 + n\omega}$ and $p = \sqrt{E}$. Wavefunction (2) corresponds to a wave incident on the barrier from the left. (In final formulas, we will mark solutions to problems with a wave incident from the left and from the right by indices “⟶” and “⟵,” respectively) Quantities t_n and r_n give the amplitudes of transmission (reflection) with absorption (for $n > 0$) or emission (for $n < 0$) of n ac field quanta, while quantity t_0 determines the amplitude of the elastic process. If the value of p_n becomes imaginary, the waves moving away from the barriers should be treated as damped waves. This means that $\operatorname{Im} p_n > 0$.

The Schrödinger equation with potential (1) leads to the boundary conditions for the wavefunction at $x = \pm d$:

$$\psi|_{\pm d} = 0, \quad \psi'|_{\mp d} = 2m[u_{1,2} + v_{1,2}(t)]\psi. \tag{3}$$

Substituting the wavefunction into the boundary condition leads to the following system of equations (incidence from the left):

$$\begin{gathered} \delta_{n,0}\exp(-ip_n) + r_n\exp(ip_n) - a_n\exp(-ip_n) \\ - b_n\exp(ip_n) = 0, \\ \delta_{n,0}\exp(-ip_n) - r_n\exp(ip_n) - a_n\exp(-ip_n) \\ + b_n\exp(ip_n) = \frac{2iu_1}{p_n} \\ \times[\delta_{n,0}\exp(-ip_n) + r_n\exp(ip_n)] \\ + \frac{v_1}{p_n}[\delta_{n+1,0}\exp(-ip_{n+1}) + r_{n+1}\exp(ip_{n+1}) \\ - \delta_{n-1,0}\exp(-ip_{n-1}) - r_{n-1}\exp(ip_{n-1})], \\ a_n\exp(ip_n) + b_n\exp(-ip_n) - t_n\exp(ip_n) = 0, \\ a_n\exp(ip_n) - b_n\exp(-ip_n) - t_n\exp(ip_n) \\ = \frac{2iu_2}{p_n}t_n\exp(ip_n) \\ + \frac{v_2}{p_n}[t_{n+1}\exp(ip_{n+1} + i\varphi) - t_{n-1}\exp(ip_{n-1} - i\varphi)]. \end{gathered} \tag{4}$$

Solving this system for $t_n = \exp(-i(p + p_n))T_n$, we obtain

$$\begin{gathered} v_1v_2g_{n-1}e^{-i\varphi}T^{\rightarrow}_{n-2} - i(v_1S_{n-1} + v_2V_ne^{-i\varphi})T^{\rightarrow}_{n-1} \\ - [2W_n + v_1v_2(g_{n-1}e^{i\varphi} + g_{n+1}e^{-i\varphi})]T^{\rightarrow}_n \\ + i(v_1S_{n+1} + v_2V_ne^{i\varphi})T^{\rightarrow}_{n+1} + v_1v_2g_{n+1}e^{i\varphi}T^{\rightarrow}_{n+2} \\ = 2ip\delta_{n,0}. \end{gathered} \tag{5}$$

Here, $g_n = \sin 2p_n/p_n$,

$$\begin{aligned} S_n &= 2u_2 g_n + \exp(-2ip_n), \\ V_n &= 2u_1 g_n + \exp(-2ip_n), \end{aligned} \tag{6}$$

$$W_n = 2u_1 u_2 g_n + (u_1 + u_2 - ip_n)\exp(-2ip_n). \tag{7}$$

The equation for the transmission coefficient $T_n^{\leftarrow}$ for a wave incident from the right has the form

$$\begin{aligned} &v_1 v_2 g_{n-1} e^{-i\varphi} T_{n-2}^{\leftarrow} - i(v_1 S_n + v_2 V_{n-1} e^{-i\varphi}) T_{n-1}^{\leftarrow} \\ &- [2W_n + v_1 v_2 (g_{n-1} e^{-i\varphi} + g_{n+1} e^{i\varphi})] T_n^{\leftarrow} \\ &+ i(v_1 S_n + v_2 V_{n+1} e^{i\varphi}) T_{n+1}^{\leftarrow} + v_1 v_2 g_{n+1} e^{i\varphi} T_{n+2}^{\leftarrow} \\ &= 2ip\delta_{n,0}. \end{aligned} \tag{8}$$

Provided that electrons from the right and left of the contact are in equilibrium and have identical chemical potentials, we can express the direct current in terms of the transmission coefficients,

$$J = \frac{e}{\pi\hbar}\int dE \sum_n \left(\left|T_n^{\rightarrow}\right|^2 - \left|T_n^{\leftarrow}\right|^2\right) f(E)\theta(E + n\omega), \tag{9}$$

where $f(E)$ is the Fermi distribution function and $\theta(x)$ is the Heaviside function.

At a low temperature, it is convenient to differentiate the current with respect to chemical potential μ:

$$\begin{aligned} \mathcal{G} &= e\frac{\partial J}{\partial \mu} \\ &= G_0 \sum_n \theta(\mu + n\omega)\left(\left|T_n^{\rightarrow}\right|^2 - \left|T_n^{\leftarrow}\right|^2\right)_{p = p_F}. \end{aligned} \tag{10}$$

Here, $G_0 = 2e^2/h$ is the conductance quantum, h being the Planck constant, and p_F is the Fermi momentum. The resultant quantity $\mathcal{G}$ has the dimension of conductance. It can be treated as a two-terminal photoconductance (the conductance for simultaneous change in the voltage across both junctions).

3. SYMMETRY IDENTITIES

Initial potential (1) exhibits symmetry to the coordinate sign reversal with simultaneous substitution u_1, $v_1 \longleftrightarrow u_2$, v_2 and $\varphi \longleftrightarrow -\varphi$ and with a time shift by $-\varphi/\omega$. Since the ac field amplitude does not change with time, the transmission coefficients and the steady-state response must possess the same symmetry; in other words, the transmission coefficient $|T_n^{\leftarrow}|^2$ from the right and $|T_n^{\rightarrow}|^2$ from the left must be transformed into each other upon the simultaneous substitution u_1, $v_1 \longleftrightarrow u_2$, v_2 and $\varphi \longleftrightarrow -\varphi$. Indeed, it follows from Eqs. (5) and (8) that $T_n^{\rightarrow} \longrightarrow T_n^{\leftarrow}\exp(in\varphi)$.

Time reversibility dictates the symmetry of wavefunction $\psi_p(x, t)$, which corresponds to the incident (departing) wave with momentum p:

$$\psi_p(x, t)\big|_{v_1(t),\, v_2(t)} = \psi^*_{-p}(x, -t)\big|_{v_1(-t),\, v_2(-t)}.$$

This leads to the following relation between the matrices of transmission from the right and left for a direct and time-inverted ac signals:

$$p \longrightarrow -p, \quad T \longrightarrow T^*,$$

$$v_1(t) \longrightarrow v_1(-t), \quad v_2(t) \longrightarrow v_2(-t).$$

In the absence of an ac signal, the quantity p is conserved for a transmitted wave, and the probabilities of transmission from the left and right coincide. Excitation by a single δ-function ($v_2 = 0$) with a harmonic signal is even in time and, hence, preserves this symmetry property for the transition channel without a change in energy, $n = 0$. The same is true for synchronous signals. However, in the presence of a phase shift, the transition channel without a change in energy is found to be asymmetric. In the framework of perturbation theory in the external signal, this means that the (asymmetric) correction to the transmission probability with energy conservation begins with the term proportional to $v_1 v_2$.

4. PERTURBATION THEORY: WEAK AC SIGNAL MODE

Let us consider the limit $v_1, v_2 \ll u_1, u_2$. The steady-state problem gives the transmission amplitude

$$\begin{aligned} T_0 &= -\frac{ip}{W_0} \\ &= -\frac{ip^2}{2u_1 u_2 \sin 2p + (u_1 + u_2 - ip)pe^{-2ip}}, \\ T_n\big|_{n \neq 0} &= 0. \end{aligned} \tag{11}$$

The scattering amplitude vanishes for $p \longrightarrow 0$ and experiences oscillations with a period $\delta p = \pi/2$. For large values of $u_{1,2}$, quantity T_0 has poles in the vicinity of points $p = \pi n/2$.

In the zeroth order of perturbation theory, the direct and reverse transmission coefficients coincide; consequently, the current vanishes. The current appears only in the second order of perturbation theory. Second-order corrections to the current come only from quantities T_0, T_1, and T_{-1}. Expanding in the ac signal, we obtain

$$\begin{aligned}\mathcal{G} = G_0\frac{p^2}{4|W_0|^2}\Bigg[&v_1^2\left(\frac{|S_0|^2-|S_{-1}|^2}{|W_{-1}|^2}\theta(\mu-\omega)+\frac{|S_0|^2-|S_1|^2}{|W_1|^2}\right)\\ &-v_2^2\left(\frac{|V_0|^2-|V_{-1}|^2}{|W_{-1}|^2}\theta(\mu-\omega)+\frac{|V_0|^2-|V_1|^2}{|W_1|^2}\right)\\ &+2v_1v_2\mathrm{Re}\left(\frac{S_0V_{-1}^*-S_{-1}V_0^*}{|W_{-1}|^2}e^{-i\varphi}\theta(\mu-\omega)+\frac{S_0V_1^*-S_1V_0^*}{|W_1|^2}e^{i\varphi}\right)\\ &+4v_1v_2\sin\varphi\,\mathrm{Im}\left(\frac{S_0V_0-S_{-1}V_{-1}}{W_0W_{-1}}-\frac{S_0V_0-S_1V_1}{W_0W_1}+2\frac{g_{-1}-g_1}{W_0}\right)\Bigg]_{p=p_F}.\end{aligned}\tag{12}$$

In the particular case when $u_1 = u_2$, functions S_n and V_n coincide, and expression (12) assumes the form

$$\begin{aligned}\mathcal{G} = G_0\frac{p^2}{4|W_0|^2}\Bigg\{&(v_1^2-v_2^2)\\ &\times\left(\frac{|S_0|^2-|S_{-1}|^2}{|W_{-1}|^2}\theta(\mu-\omega)+\frac{|S_0|^2-|S_1|^2}{|W_1|^2}\right)\\ &-4v_1v_2\sin\varphi\,\mathrm{Im}\Bigg[\frac{S_0S_{-1}^*}{|W_{-1}|^2}\theta(\mu-\omega)-\frac{S_0S_1^*}{|W_1|^2}\\ &+\frac{S_0^2-1}{W_0}\left(\frac{1}{W_{-1}}-\frac{1}{W_1}\right)\Bigg]\Bigg\}_{p=p_F}.\end{aligned}\tag{13}$$

The current is determined by corrections $T_{\pm1}$ associated with real emission (absorption) of a single photon. In addition, a correction to T_0 associated with the effect of a virtual single-photon process on the nonradiative channel also exists. Apart from the squares of ac signals v_1 and v_2, the result for the regime $u_1 = u_2$ contains a bilinear combination; consequently, it is insufficient to consider the response only at one of the signals. The latter contribution is sensitive to the relative phase of the signals.

If $u_1 = u_2 = 0$, Eq. (13) yields

$$\begin{aligned}\mathcal{G} = &-G_0v_1v_2\sin\varphi\\ &\times\left[\frac{\sin2(p-p_{-1})}{p_{-1}^2}\theta(\mu-\omega)+\frac{\sin2(p_1-p)}{p_1^2}\right.\\ &\left.+\frac{2\sin2p}{p}\left(\frac{\cos2p_{-1}}{p_{-1}}\theta(\mu-\omega)-\frac{\cos2p_1}{p_1}\right)\right]_{p=p_F}.\end{aligned}\tag{14}$$

This expression turns to infinity for $p_{-1} = 0$ (at the single photon emission threshold). This singularity can be explained by the resonance with the state of an electron with zero energy: such a "stationary" state can be interpreted as a bound state.

In addition to the above oscillations with period $\delta p = \pi/2$, the transmission amplitude experiences oscillations with periods $\delta p_{\pm1} = \pi/2$. It can be seen from expression (12) that the extrema in the dependence of the current on p are located in the vicinity of the points corresponding to the minima of functions W_0 and $W_{\pm1}$ and are connected with the elastic process as well as with the process involving the absorption or emission of a field quantum. For $v_2 = 0$ ($v_1 = 0$), the expression for the current contains only one term proportional to v_1^2 (v_2^2).

For $u_1, u_2 \gg p$, the oscillations are transformed into sharp peaks corresponding to transmission resonances. For $p \sim 1$, the transmission amplitude has a characteristic scale of $p \sim u_1, u_2$. The corresponding structure for small values of u_1 and u_2 can be treated as a resonance at zero energy. For negative values of u_1 and u_2, resonance at bound states exist (at one or two such states depending on the distance between the wells).

5. ANALYSIS OF THE BEHAVIOR OF QUANTITY $\mathcal{G}$ IN THE VICINITY OF SINGULARITIES

The singularities of quantity $\mathcal{G}$ can be classified according to their origin from the electronic spectrum as: (1) resonance associated with discrete states of the system in the absence of ac field; (2) resonances associated with quasi-stationary states; and (3) threshold singularities associated with zero energy. The presence of an rf field leads to photon recurrences with energies separated from the initial energies by intervals multiple to the ac field frequency. In a weak ac field, photon recurrences are the weaker, the higher their multiplicity. Stationary states lie in the range of negative energies and, hence, are manifested in the $\mathcal{G}(p_F)$ dependence only due to their photon recurrences. Quasi-stationary states are manifested for $|u_i| \gg 1$ or $v_i \gg 1$, when the δ-functions can "lock" electrons. Electrons are locked by barriers and wells as well as by the ac potential.

In the framework of perturbation theory, singularities appear due to zeros of functions W_0, W_1, and W_{-1}. Exact vanishing is observed only for function W_{-1} for an energy separated from the energy of the bound state by ω. The functions can vanish approximately at quasi-stationary states and their first photon recurrences. At the threshold $p \longrightarrow 0$, the numerator of expression (12) vanishes, which leads to a weak singularity in $\mathcal{G}$.

A special case is the limit $u_1 = u_2 = 0$, in which the zero of function W_0 for $p \longrightarrow 0$ is compensated by the numerator of formula (12); as a result, $\mathcal{G} \longrightarrow$ const. However, vanishing of $\mathcal{G}$ is reconstructed by taking into account the finiteness of a varying perturbation that is beyond the scope of perturbation theory. In the vicinity of momentum $\sqrt{\omega}$, quantity W_{-1} vanishes; unlike the zero of function W_0, this leads to a pole of $\mathcal{G}$. Quantity $\mathcal{G}$ cannot become infinite in view of the finiteness of the amplitude of the varying perturbation.

For finite values of u_1 and u_2, singularity of quantity $\mathcal{G}$ at point $p_{-1} = 0$, which is associated with the quantum emission threshold is a discontinuity. If $u_1 = u_2 = 0$ and v_1, $v_2 \longrightarrow 0$, the discontinuity is transformed into a pole singularity. The value at the threshold is limited to $1/v_1v_2$.

Let us consider the mechanism of the emergence and limitation of single-photon recurrence of a resonance. Let E_0 be a certain energy level of a steady-state system (probably, a complex quasi-stationary level). Such an approach is applicable to a zero-energy resonance ($E_0 = 0$) or stationary-state resonance ($E_0 < 0$). Then, in the nth equation of system (12), the coefficient of T_n vanishes at point $p_n^2 = E_0$. A finite but small ac field shifts this zero in the complex plane by a value proportional to the second power of perturbation. For a small perturbation, under nonresonant conditions, the value of T_0 is the largest, while the remaining quantities T_n decrease in powers of the perturbation. Let us suppose that $p_{-1}^2 \longrightarrow E_0$. Since the coefficient of T_{-1} in Eq. (5) with $n = -1$ is small, the quantity T_{-1} must be large and the term with T_{-1} should be taken into account in the equation with $n = 0$. At the same time, all remaining quantities T_n can be regarded as small in the general case. Using this circumstance, we can retain two equations from the entire system:

$$\begin{aligned} T_0 + \beta T_{-1} &= \alpha, \\ (p_{-1} - \sqrt{E_0} + \eta)T_{-1} + \gamma T_0 &= 0, \end{aligned} \tag{15}$$

where coefficient α is independent of the varying perturbation, coefficient η is quadratic in this perturbation, and coefficients γ and β are linear. Equations (15) lead to the solution

$$\begin{aligned} T_0 &= \alpha \frac{p_{-1} - \sqrt{E_0} + \eta}{p_{-1} - \sqrt{E_0} + \eta - \gamma\beta}, \\ T_{-1} &= -\frac{\alpha\gamma}{p_{-1} - \sqrt{E_0} + \eta - \gamma\beta}. \end{aligned} \tag{16}$$

These expressions contain a strong dependence in the vicinity of the singularity. The ac field leads to additional broadening of the resonance quadratic in the perturbation. If no initial broadening took place, the ac field leads to the emergence of this broadening. The single-photon resonance with $n = 1$ emerges and broadens according to the same mechanism.

If $|n| > 1$, a multiphoton resonance emerges on account of linked equations with numbers between zero and n. The resultant resonance contribution has a smallness of perturbation to the nth power.

The constants appearing in expression (16) are determined by the amplitudes and phases of ac fields, which affects the position and width of the resonance. In the special case of a zero-energy resonance for $u_1 = u_2 = 0$, we obtain the following equation from relations (16), which is valid in the vicinity of point $p_{-1} = 0$ above the threshold:

$$\begin{aligned} \mathcal{G} = G_0\theta(\mu - \omega)\Bigg\{ &\frac{\eta(\varphi)}{[p_{-1} + \xi(\varphi)]^2 + \zeta^2(\varphi)} \\ &- \frac{\eta(-\varphi)}{[p_{-1} + \xi(-\varphi)]^2 + \zeta^2(-\varphi)}\Bigg\}_{p = p_F}, \end{aligned} \tag{17}$$

where

$$\begin{aligned} \eta(\varphi) &= \frac{1}{4}[v_1^2 + v_2^2 + 2v_1v_2\cos(2\sqrt{\omega} + \varphi)], \\ \zeta(\varphi) &= \frac{v_1v_2}{2\sqrt{\omega}}\cos\varphi(\sin 2\sqrt{\omega} + \sinh 2\sqrt{\omega}), \\ \xi(\varphi) &= \frac{1}{4\sqrt{\omega}}[v_1^2 + v_2^2 + 2v_1v_2 \\ &\quad \times (\cos\varphi\cos 2\sqrt{\omega} - \sin\varphi\sinh 2\sqrt{\omega})]. \end{aligned} \tag{18}$$

For $p_{-1} \longrightarrow \infty$, expression (17) is inversely proportional to p_{-1}^2. Below the threshold, a singularity does not exist. It should be noted that this behavior leads to a logarithmic singularity in the current $J \propto G_0 \ln(\mu - \omega)/\Delta$, which is removed if we take into account the finiteness of the ac field. The truncation Δ of the logarithm observed in this case substantially depends on the

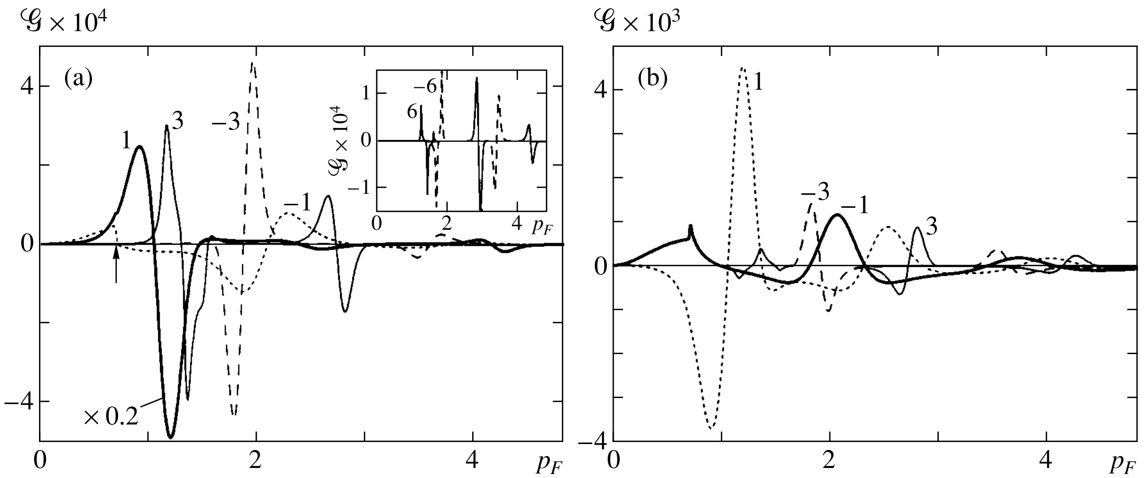

Fig. 2. Dependence of $\mathcal{G}$ on the Fermi momentum in a symmetric structure $u_1 = u_2$ in the limit of a weak ac signal: (a) $v_2 = 0$, $v_1 = 0.1$; frequency $\omega = 0.5$; (b) $v_1 = v_2 = 0.1$; phase $\varphi = \pi/2$. Figures on the curves are values of $u_1 = u_2$. The arrow marks the resonance $p_{-1} = 0$, $p_F = \sqrt{0.5}$.

amplitude and phase of ac fields. In accordance with formulas (17) and (18), broadening of the resonance is proportional to the square of the ac field. However, for $\varphi = \pi/2, 3\pi/2$, the resonance width $\zeta(\varphi)$ vanishes. In fact, this is an indication that the width has a higher order in v_1 and v_2, which exceeds the limits of the approximation used here.

6. NUMERICAL RESULTS: WEAK AC FIELD

Figure 2 shows the dependences of quantity $\mathcal{G}$ on the Fermi momentum for $u_1 = u_2$ in the presence of one, $v_2 = 0$ (Fig. 2a), or two, $v_1 = v_2$, $\varphi = \pi/2$ (Fig. 2b), ac signals. In the absence of an ac signal, such a system is symmetric. Different curves correspond to different values of coefficients of δ-functions. In the limit u_1, $u_2 \longrightarrow \infty$, the curves are transformed into a system of antisymmetric Fano resonances at the momenta corresponding to quasi-stationary levels (see the inset to Fig. 2a). Asymmetry appears due to the fact that quasi-stationary states play the role of intermediate states for the compound transition amplitude.

The dependence of quantity $\mathcal{G}$ on the Fermi momentum in the case when the current is excited by two phased-in signals (Fig. 2b) differs from the dependence corresponding to a single signal (Fig. 2a), indicating the phase-sensitive interference nature of the effect. In particular, for large values of u_1 and u_2, the resonances at quasi-stationary levels become symmetric.

The case of the absence of static barriers ($u_1 = u_2 = 0$) should be considered separately. In this case, the current appears only when signals v_1 and v_2 are present simultaneously (Fig. 3). For small values of v_1 and v_2, the behavior almost coincides with the result obtained in perturbation theory. The zero-energy resonance becomes narrow and deep. The nonlinear corrections are manifested in the range of small momenta, where these corrections lead to vanishing of $\mathcal{G}$ as well as to a limitation imposed on the resonance minimum and to the emergence of a two-photon resonance at point $p_{-2} = 0$. It can be seen from Fig. 3 that the amplitude of the one-photon resonance is large (proportional to $1/v_1v_2$), while the amplitude of the two-photon resonance is finite in accordance with the subsequent analysis.

Figure 4 shows the results of calculation of the value of $\mathcal{G}$ for a single quantum well ($u_1 = -1$), near which an

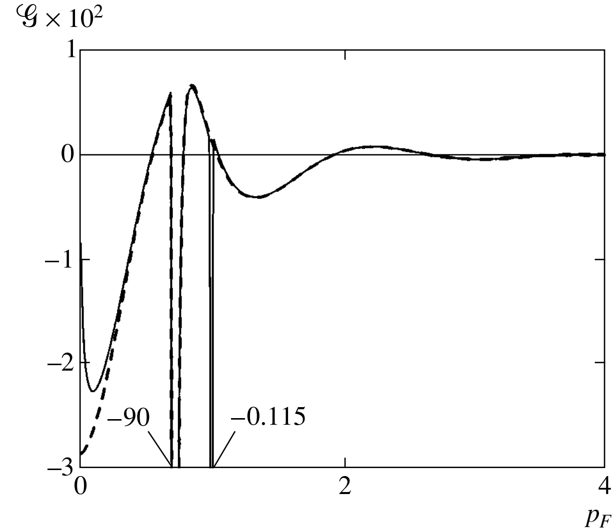

Fig. 3. The same as in Fig. 2b for $u_1 = u_2 = 0$. The solid curve describes the numerical result and the dashed curve is the result obtained in perturbation theory. Values of $\mathcal{G}$ at the minima that could not be shown in the figure are shown on the curves.

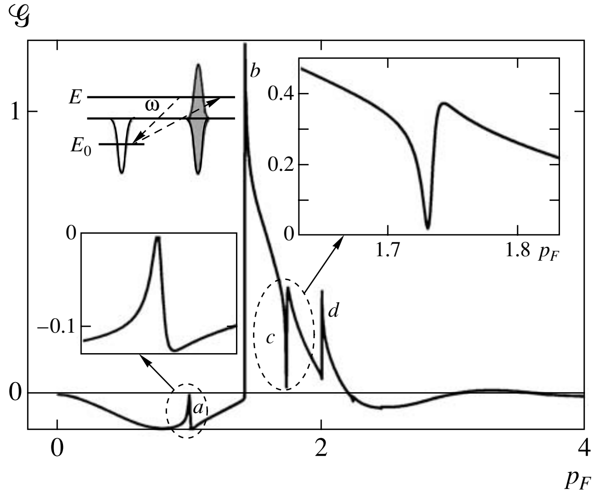

Fig. 4. Quantity 𝒢 in the structure with a single quantum well and with an oscillating barrier (well) shown in the inset. The figure illustrates the formation of one-photon (*a*) and two-photon (*c*) resonances at localized level E_0. Parameters $u_1 = -1$, $v_1 = 0$, $u_2 = 0$, $v_2 = 1$, and $\omega = 2$ are used. The insets in the frames give details of neighborhoods of resonances *a* and *c*. Letters *b* and *d* denote zero-energy one- and two-photon resonances ($E = \omega$, $E = 2\omega$).

exciting electrode is placed ($v_1 = 0$, $v_2 = 1$). In the absence of an ac signal, such a system is symmetric; only the second electrode breaks the symmetry. In contrast to the structure with barriers, one- and two-photon resonances, $E = \omega + E_0$ and $E = 2\omega + E_0$, which are associated with the localized state $E_0 = -1$, emerge in this problem. In accordance with Eq. (16), the value of 𝒢 at resonances approaches zero (is equal to zero in the one-photon case). The value at the two-photon minimum is found to be proportional to v_2^2. The small value at the minimum in the case depicted in Fig. 4 is due to slight overlapping of the potential and the wavefunction of the bound state.

Let us analyze in greater detail the mechanism of the emergence of zero-energy resonance (Fig. 4). An electron flying from the right passes through the static δ-function and then interacts with the ac potential. If its energy is ω, it will be at the bottom of the band after emitting a photon. This process has a high probability since the density of states at the bottom of the band becomes infinite. After this, the electron cannot return as a rule. However, the electron impinging from the right will return to the right for the same reason. Thus, the current flows from right to left, which is depicted in Fig. 4.

Figure 5a demonstrates the variation of current for $u_1 = u_2$, $v_2 = 0$ with the frequency $0.1 \le \omega \le 10$ of the ac signal. The figure corresponds to a system with high barriers. Sharp resonances correspond to points $p_F = \pi n/2$ (their position does not change with frequency) and their photon recurrences for $p_F = \sqrt{\pi^2 n^2/4 \pm \omega}$ (which are displaced to the right and to the left with the frequency).

Figure 5b shows the variation of quantity 𝒢 in an asymmetric system ($u_1 = 3$, $v_1 = 0.1$, $u_2 = 1$, $v_2 = 0$). It

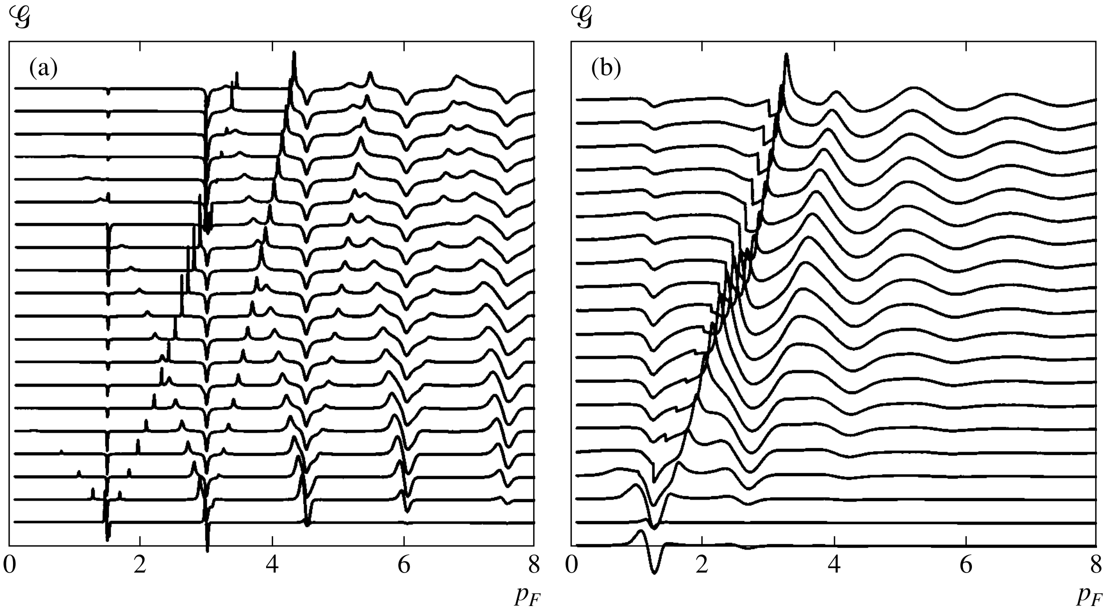

Fig. 5. Variation of quantity 𝒢 with the frequency of an ac signal $0.1 \le \omega \le 10$ for (a) $u_1 = u_2 = 10$, $v_1 = 0.1$, $v_2 = 0$ and (b) $u_1 = 3$, $u_2 = 1$, $v_1 = 0.1$, $v_2 = 0$. The curves are displaced relative to one another by a constant distance along the vertical axis. The frequency increases in the upward direction.

can be seen that resonances acquire a symmetric or asymmetric shape depending on the frequency.

7. NONLINEAR MODE OF QUANTUM PUMP OPERATION

Figure 6 shows the results of calculation of the value of $\mathcal{G}$ in the absence of a static potential for large (identical) amplitudes of ac signals. With increasing amplitude of the signal, the dependence of quantity $\mathcal{G}$ on the Fermi momentum becomes more complicated. Higher-order resonances corresponding to $E = j\omega$ or $E = \pi^2 n^2/4 \pm j\omega$ ($j = 1, 2, \ldots$) appear.

In the limit of very strong signals, the dependence becomes universal. This can be verified on the basis of Eqs. (5): for large values, quantities v_1 and v_2 appear in the transition amplitudes in the form of a product, $T_n \propto (v_1 v_2)^{-1}$ in the region $p^2 \ll v_1 v_2$; outside this region, perturbation theory operates and $T_n \propto (v_1 v_2)^{-n}$.

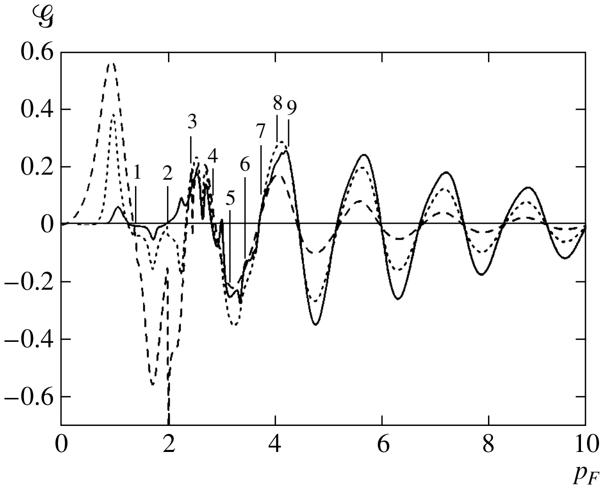

Fig. 6. Nonlinear operation of the pump. Symmetric case: $u_1 = u_2 = 1$, $v_1 = v_2 = 2$ (dashed curve), 4 (dotted curve), and 6 (solid curve); $\varphi = \pi/2$, $\omega = 2$. Positions of resonances $p = \sqrt{n\omega}$, $n = 1, \ldots, 9$, are indicated.

8. DISCUSSION

Let us consider the difference between the quantum pump and the photovoltaic effect. The latter is usually analyzed in the limit of a weak electromagnetic field (except in publication [2] which is devoted to the purely classical limit). For quantum-mechanical frequencies, the mechanism of the photovoltaic effect involves the absorption of light quanta with anisotropic excitation of electrons. During relaxation, induced optical transitions play a secondary role as compared to nonradiative processes as well as with incoherent optical processes. When the pump is in operation, the electromagnetic field is treated as classical even in the limit of a weak signal; consequently, the corrections to the transition probability include not only absorption, but also induced emission as well as the field correction to the elastic component of the transition probability. Moreover, if the field is not weak, the transition probability contains the contributions associated with the emission (absorption) of any number of photons.

Another difference between the pump and the photovoltaic effect is the local nature of the applied ac signal. An important distinguishing feature of the photovoltaic effect is the uniformity of the ac field and the homogeneity of the system. The current induced by a nonuniform electromagnetic field is associated with the transfer of the momentum of the wave to electrons, i.e., with the photon drag effect. In the initial inhomogeneous system, the current is generated by diffusion between the regions with different electron concentrations. In the pump, the action of an ac signal is manifested at distances commensurate with the electron wavelengths that are small in comparison to their mean free paths and, the more so, with the diffusion length. This makes it possible to manipulate them independently with ac signals applied in different regions.

In the problem of rectification in a microcontact, an ac voltage is applied between the "seas." At the same time, in the problem formulated here, ac signals are applied directly to the barriers. In such a problem, in the zero-frequency limit, direct current $J|_{\omega \to 0}$ cannot emerge at all in view of the above-mentioned reversibility of the static transmission probability. This distinguishes the pump from rectification in a microcontact.

ACKNOWLEDGMENTS

This study was financed by the Russian Foundation for Basic Research (project nos. 02-02-16388 and 04-02-16398) and the Program for Support of Scientific Schools in the Russian Federation (grant no. NSh-593.2003.2).

REFERENCES

1. V. I. Belinicher and B. I. Sturman, Usp. Fiz. Nauk **130**, 415 (1980) [Sov. Phys. Usp. **23**, 199 (1980)].
2. M. D. Blokh, L. I. Magarill, and M. V. Éntin, Fiz. Tekh. Poluprovodn. (Leningrad) **12**, 249 (1978) [Sov. Phys. Semicond. **12**, 143 (1978)].
3. É. M. Baskin, L. I. Magarill, and M. V. Éntin, Fiz. Tverd. Tela (Leningrad) **20**, 2432 (1978) [Sov. Phys. Solid State **20**, 1403 (1978)].
4. E. L. Ivchenko and G. E. Pikus, Pis'ma Zh. Éksp. Teor. Fiz. **27**, 640 (1978) [JETP Lett. **27**, 604 (1978)].
5. D. J. Thouless, Phys. Rev. B **27**, 6083 (1983).
6. M. Moskalets and M. Büttiker, Phys. Rev. B **68**, 161311 (2003).
7. J. E. Avron, A. Elgart, G. M. Graf, and L. Sadun, Phys. Rev. B **62**, R10618 (2000).

8. J. E. Avron, A. Elgart, G. M. Graf, and L. Sadun, Phys. Rev. Lett. **87**, 236601 (2001).
9. O. Entin-Wohlman and A. Aharony, Phys. Rev. B **65**, 195411 (2002).
10. D. Cohen, Phys. Rev. B **68**, 155303 (2003).
11. Huan-Qiang Zhou, Sam Young Cho, and R. H. McKenzie, Phys. Rev. Lett. **91**, 186803 (2003).
12. M. Moskalets and M. Büttiker, Phys. Rev. B **66**, 205320 (2002).
13. F. Renzoni and T. Brandes, Phys. Rev. B **64**, 245301 (2001).
14. Shi-Liang Zhu and Z. D. Wang, Phys. Rev. B **65**, 155313 (2002).
15. C. S. Tang and C. S. Chu, Solid State Commun. **120**, 353 (2001).
16. Baigeng Wang, Jian Wang, and Hong Guo, Phys. Rev. B **68**, 155326 (2003).
17. M. Switkes, C. M. Marcus, K. Campman, and A. C. Gossard, Science **283**, 1905 (1999).
18. T. Altebaeumer and H. Ahmed, Jpn. J. Appl. Phys., Part 1 **41** (4B), 2694 (2002).
19. Y. Ono and Y. Takahashi, Appl. Phys. Lett. **82**, 1221 (2003).
20. S. V. Lotkhov, S. A. Bogoslovsky, A. B. Zorin, and J. Niemeyer, Appl. Phys. Lett. **78**, 946 (2001).
21. R. D. Astumian, Phys. Rev. Lett. **91**, 118102 (2003).
22. S. W. Kim, Phys. Rev. B **66**, 235304 (2002).

Translated by N. Wadhwa

Journal of Experimental and Theoretical Physics, Vol. 100, No. 5, 2005, pp. 929–948.
From Zhurnal Éksperimental'noĭ i Teoreticheskoĭ Fiziki, Vol. 127, No. 5, 2005, pp. 1055–1074.
Original English Text Copyright © 2005 by Kopeliovich, Shunderuk.

NUCLEI, PARTICLES, FIELDS, GRAVITATION, AND ASTROPHYSICS

Flavored Exotic Multibaryons and Hypernuclei in Topological Soliton Models[¶]

V. B. Kopeliovich and A. M. Shunderuk

Institute for Nuclear Research, Russian Academy of Sciences, Moscow, 117312 Russia
e-mail: kopelio@al20.inr.troitsk.ru, kopelio@cpc.inr.ac.ru

Received December 27, 2004

Abstract—The energies of baryon states with positive strangeness, or anticharm (antibeauty), are estimated in the chiral soliton approach, in the "rigid oscillator" version of the bound-state soliton model proposed by Klebanov and Westerberg. Positive strangeness states can appear as relatively narrow nuclear levels (Θ-hypernuclei), and the states with heavy antiflavors can be bound with respect to strong interactions in the original Skyrme variant of the model (SK4 variant). The binding energies of antiflavored states are also estimated in the variant of the model with a sixth-order term in chiral derivatives added to the Lagrangian to stabilize solitons (SK6 variant). This variant is less attractive, and nuclear states with anticharm and antibeauty can be unstable relative to strong interactions. The chances of obtaining bound hypernuclei with heavy antiflavors increase within the "nuclear variant" of the model with a rescaled model parameter (the Skyrme constant e or e' decreased by about 30%), which is expected to be valid for baryon numbers greater than $B \sim 10$. The rational map approximation is used to describe multiskyrmions with a baryon number of up to about 30 and to calculate the quantities necessary for their quantization (moments of inertia, sigma term, etc.). *© 2005 Pleiades Publishing, Inc.*

1. INTRODUCTION

The remarkable recent discovery of the positive-strangeness pentaquark state [1] and its confirmation by several experiments [2] has provided strong motivation for searches of other exotic states and revision of the existing ideas on the structure of hadrons and the role of the valence-quark picture in their description [3–8]. Subsequently, the discovery of the strangeness $S = -2$ state with charge –2, also manifestly exotic [9] (see [10] for a review of the previously existing data), and evidence for a narrow anticharmed baryon state [11] have been reported. Some experiments, however, did not confirm these results (see, e.g., [12, 13]), where some negative results were summarized and a pessimistic point of view was formulated. The high-energy physics community is now awaiting the results of high-statistics experiments; some plans for future pentaquark searches are presented, e.g., in [14].

The possible existence of such states had been foreseen theoretically within the quark models [15–17],[1] as well as in chiral soliton models. The prediction of exotic states in chiral soliton models has a complex and instructive history—from the papers where the exotic antidecuplet and 27-plet of baryons were mentioned [18], a resonant behavior of the kaon–nucleon phase shift in the Θ channel was obtained in some version of the Skyrme model [19], first estimates of the antidecuplet mass were made [20, 21], and the masses of exotic baryon states were roughly estimated for arbitrary baryon numbers B [22], to papers where more detailed calculations of the antidecuplet spectrum were performed [23–25] (see also [26] for a recent discussion). The mass of the dibaryon with $S = +1$, $I = 1/2$ was determined to be only 590 MeV above the nucleon–nucleon threshold within the soft rotator quantization scheme [27]. We note that paper [24], which predicted narrow width and low mass of the positive-strangeness state called[2] Θ^+, stimulated experimental searches for such states, in particular, experiments [1] have been specially arranged to check the prediction of [24].

Theoretical ideas and methods that led to the prediction of such states within the chiral soliton models [23–25] have been criticized with quite sound reasoning in [4] and, in the large-N_c limit, in [29, 30]. In the absence of a complete theory of strong interactions, it was impossible in principle to provide firm predictions for the masses of states with the accuracy better than about several tens of MeV, and similarly for the widths of such states. One can agree with [29]: in some cases, predictions that coincided with the observed mass of the Θ^+ hyperon can be considered "accidental" (see also [28]).

[¶] This article was submitted by authors in English.

[1] The parity of lowest exotic states considered here is negative (see [7], however), in contrast to the chiral soliton model predictions, where it is positive. Spin and parity of exotic baryons have not yet been measured.

[2] As was admitted recently in [28], the prediction of the low value of the mass $M_\Theta \approx 1530$ MeV "was to some extent luck."

On the other hand, from the practical standpoint, the chiral soliton approach is useful and has a remarkable predictive power when at least one of the exotic baryon masses is fitted. The masses of exotic baryons with a strangeness of $S = -2$ and isospin of $I = 3/2$ predicted in this way [31], 1.79 GeV for the antidecuplet component and 1.85 GeV for the 27-plet component, are close to the value 1.86 GeV measured later [9]. Calculations of the baryon spectra within the chiral soliton approach were performed more recently in [32–36], not in contradiction with [31]; recent paper [37], where the interplay of rotational and vibrational modes has been investigated, should be especially mentioned. Some reviews and a comparison of the chiral soliton approach with other models can be found, e.g., in [38].

The particular case of strangeness is in a certain respect more complicated in comparison with the case of other flavors: the rigid rotator quantization scheme is not quite valid in this case [29], whereas the bound-state approach is not really good either [30]. In the case of heavy flavors, the rotator quantization is not valid at all, but the bound-state approach becomes more adequate compared to strangeness [30].

Baryons with heavy antiflavors are certainly not a new issue: they have long been discussed in the literature, with various results obtained for the energies of such states. The strange anticharmed pentaquark was obtained bound [39] in a quark model with the (u, d, s) $SU(3)$ flavor symmetry and in the limit of a very heavy c-quark. Long ago, there were already statements and suggestions in the literature that anticharm or antibeauty can be bound by chiral solitons in the case of a baryon number of $B = 1$ [40, 41] (so-called P-baryons). In [42], the mass differences of exotic baryons (Θ^+ and its analogs for anticharm and antibeauty) and nucleons were estimated in the flavor-symmetric limit for decay constants, $F_D = F_\pi$, in the chiral quark meson model. In [43], the antiflavor excitation energies were calculated in the rigid oscillator version [44] of the bound-state soliton model [45], for baryon numbers between 1 and 8. The rational map ansatz for multiskyrmions [46] was used as the starting configuration in the three-dimensional minimization $SU(3)$ program [47]. These energies were found to be close to 0.59 GeV for antistrangeness, 1.75 GeV for anticharm, and 4.95 GeV for antibeauty; in the last two cases, these energies are smaller than the masses of D- and B-mesons entering the Lagrangian [43]. The flavor symmetry-breaking in flavor decay constants ($F_D/F_\pi > 1$) plays an important role for these estimates. This was therefore a clear hint that such baryonic systems can be bound relative to strong interactions.

Similar results, in principle, follow from recent analysis within the bound-state soliton model [30] and within the diquark model [4]. The spectra of exotic states with heavy flavors have been estimated in different models, already after the discovery of the positive-strangeness pentaquark [48] (any baryon number), [49–53], and others. The possibility of the existence of nuclear matter fragments with positive strangeness was recently discussed in [54].

In this paper, we estimate the energies of ground states of multibaryons with baryon numbers up to approximately 30 with different (anti)flavors using a very transparent "rigid oscillator" model [44]. In the next section, we consider the properties of multiskyrmions that are required in calculating the energies of flavor excitations using the rational map approximation for $B > 1$ [46]. It is shown that the Θ^+ baryon is bound by nuclear systems, providing positive-strangeness multibaryons (Θ-hypernuclei), whose binding energy can reach several tens of MeV. The multiskyrmion configurations have some remarkable scaling properties, and, as a result, the flavor and antiflavor excitation energies are close to those for $B = 1$. The quantization scheme (a slightly modified rigid oscillator version [44]) is described in Section 3, where the flavor and antiflavor excitation energies are also calculated. The masses (binding energies) of ground states of positive-strangeness states (Θ-hypernuclei) are presented in Section 4, followed by those for anticharmed or antibeautiful states. The last section contains some conclusions and prospects.

2. PROPERTIES OF MULTISKYRMIONS

Here, we calculate the properties of multiskyrmion configurations necessary for calculation of the flavor excitation energies and hyperfine splitting constants that govern the $1/N_c$-corrections to the energies of the quantized states. As already noted, the details of baryon–baryon interactions do not enter the calculations explicitly, although their effect is implicit via the integral characteristics of the bound states of skyrmions shown in Tables 1 and 2.

The Lagrangian of the Skyrme model in its well-known form depends on parameters F_π, F_D, and e and can be written as [55, 56]

$$\begin{aligned}\mathscr{L} = {} & -\frac{F_\pi^2}{16}\mathrm{Tr}(l_\mu l^\mu) + \frac{1}{32e^2}\mathrm{Tr}[l_\mu, l_\nu]^2 \\ & + \frac{F_\pi^2 m_\pi^2}{16}\mathrm{Tr}(U + U^\dagger - 2) \\ & + \frac{F_D^2 m_D^2 - F_\pi^2 m_\pi^2}{24}\mathrm{Tr}(1 - \sqrt{3}\lambda_8)(U + U^\dagger - 2) \\ & + \frac{F_D^2 - F_\pi^2}{48}\mathrm{Tr}(1 - \sqrt{3}\lambda_8)(U l_\mu l^\mu + l_\mu l^\mu U^\dagger),\end{aligned} \tag{1}$$

where $U \in SU(3)$ is a unitary matrix incorporating chiral (meson) fields and $l_\mu = \partial_\mu U U^\dagger$. In this model, F_π is fixed at the physical value $F_\pi = 186$ MeV and m_D is the mass of the K-, D-, or B-meson. The ratios F_D/F_π are

Table 1. Static characteristics of multiskyrmions: moments of inertia and the Σ-term Γ, $\bar{\Gamma}$ in the SK4 variant of the model with $e = 4.12$ and for the SK6 variant of the model with $e' = 4.11$, in GeV^{-1}

B	Θ_I^{SK4}	$\Theta_F^{(0)SK4}$	Γ^{SK4}	$\bar{\Gamma}^{SK4}$	Θ_I^{SK6}	$\Theta_F^{(0)SK6}$	Γ^{SK6}	$\bar{\Gamma}^{SK6}$
1	5.56	2.05	4.80	14.9	5.13	2.28	6.08	15.8
2	11.5	4.18	9.35	22.0	9.26	4.94	14.0	24.7
3	14.4	6.34	14.0	27.0	12.7	7.35	20.7	30.4
4	16.8	8.27	18.0	31.0	15.2	8.93	24.5	33.7
5	23.5	10.8	23.8	35.0	18.7	11.8	32.8	38.3
6	25.4	13.1	29.0	38.0	21.7	14.1	39.3	41.6
7	28.9	14.7	32.3	44.0	23.9	15.4	42.5	43.4
8	33.4	17.4	38.9	47.0	27.2	18.5	51.6	46.9
9	37.8	20.6	46.3	47.5	30.2	21.1	59.1	49.7
10	41.4	23.0	52.0	50.0	32.9	23.5	65.8	51.9
11	45.2	25.6	58.5	52.4	35.8	26.1	73.6	54.3
12	48.5	28.0	64.1	54.6	38.4	28.3	79.9	56.2
13	52.1	30.5	70.2	56.8	41.2	30.8	87.1	58.1
14	56.1	33.6	78.2	58.9	44.3	34.0	96.9	60.5
15	59.8	36.3	85.1	60.9	47.1	36.7	105	62.4
16	63.2	38.9	91.5	62.8	49.7	39.3	112	64.1
17	66.2	41.2	96.8	64.6	52.1	41.3	118	65.4
18	70.3	44.5	106	66.4	55.2	44.8	129	67.5
19	73.9	47.4	113	68.2	58.0	47.8	138	69.2
20	77.5	50.4	121	69.9	60.8	50.8	147	70.8
21	80.9	53.2	128	71.5	63.5	53.6	156	72.4
22	84.3	56.0	136	73.1	66.1	56.4	164	73.8
23	88.0	59.2	144	74.7	69.0	59.7	174	75.4
24	91.3	62.0	151	76.2	71.6	62.5	183	76.7
25	94.7	64.9	159	77.6	74.2	65.4	192	78.0
26	98.2	68.1	168	79.1	77.0	68.7	202	79.4
27	102	71.1	176	80.5	79.7	71.7	211	80.8
28	105	74.3	185	81.9	82.5	75.1	222	82.2
32	118	86.4	217	87.2	93.0	87.4	260	86.9

known to be 1.22 and $2.28^{+1.4}_{-1.1}$ for kaons and D-mesons, respectively. The Skyrme parameter e is close to 4 in numerical fits of the hyperons spectra (see the discussion at the end of this section). In the variant of the model with a sixth-order term added to stabilize solitons, the contribution added to the Lagrangian density is [57–59]

$$L_6 = -\frac{c_6}{48}\mathrm{Tr}([l_\mu, l^\nu][l_\nu, l^\alpha][l_\alpha, l^\mu]), \tag{2}$$

where we introduce the coefficient 1/48 in the definition of the constant c_6 for further convenience. It is known that this term can be considered as an approximation to the exchange of the ω-meson in the limit as $m_\omega \longrightarrow \infty$ [57].[3] The flavor symmetry-breaking (FSB) in the Lagrangian is of the usual form and is sufficient to describe the mass splittings of the octet and decuplet

---

[3] In (2), we use one of several possible forms of the sixth-order term, all of which make the same contribution to the static mass of the $SU(2)$ solitons (see also the discussion in [57]). General consideration of higher order terms and the discussion of their role in establishing skyrmion properties can be found in [58].

Table 2. Static characteristics of multiskyrmions: moments of inertia and Σ-term, Γ, $\bar{\Gamma}$ for rescaled or nuclear variants of the model: $e = 3.00$ in the SK4 and $e' = 2.84$ in the SK6 variants, in GeV^{-1}

B	$\Theta_I^{\mathrm{SK4*}}$	$\Theta_F^{(0)\mathrm{SK4*}}$	$\Gamma^{\mathrm{SK4*}}$	$\bar{\Gamma}^{\mathrm{SK4*}}$	$\Theta_I^{\mathrm{SK6*}}$	$\Theta_F^{(0)\mathrm{SK6*}}$	$\Gamma^{\mathrm{SK6*}}$	$\bar{\Gamma}^{\mathrm{SK6*}}$
1	12.8	4.66	10.1	19.6	14.2	6.21	15.3	22.3
2	24.3	9.87	20.9	28.8	25.7	13.6	35.9	34.7
3	34.7	15.1	31.7	35.6	35.5	20.4	53.9	42.5
4	42.9	19.4	40.1	41.1	43.2	25.0	64.6	46.9
5	53.5	25.4	53.2	46.2	52.9	32.9	86.2	53.1
6	62.6	30.7	64.7	50.6	61.4	39.4	103	57.4
7	69.6	34.9	72.5	54.4	68.0	43.3	112	59.8
8	79.9	41.3	87.4	58.2	77.3	51.7	135	64.4
9	88.9	47.1	101	61.7	85.7	58.9	154	67.9
10	97.4	52.6	113	64.9	93.5	65.3	171	70.8
11	106	58.5	126	67.9	102	72.5	191	73.8
12	114	63.8	138	70.8	109	78.7	207	76.1
13	122	69.5	151	73.6	117	85.4	225	78.6
14	132	76.3	168	76.3	125	94.0	249	81.5
15	140	82.3	182	78.8	133	101	269	83.9
16	148	88.1	196	81.2	141	108	287	86.0
17	155	93.2	207	83.5	148	114	302	87.6
18	164	100	225	85.9	156	123	328	90.1
19	173	107	241	88.1	164	131	350	92.2
20	181	113	257	90.3	172	139	372	94.1
24	213	138	320	98.2	202	170	457	101
28	245	165	387	105	232	202	550	107
32	275	191	454	112	261	234	640	113

of baryons within the collective coordinate quantization approach [60]. A nice and useful feature of the Lagrangian in (1) and (2) is that it contains only the second power of the time derivative, which allows quantization to be performed without problems (see the next section).

The Wess–Zumino term, which is to be added to the action and which can be written as a five-dimensional differential form [56], plays an important role in the quantization procedure. It is given by

$$S^{WZ} = \frac{-iN_c}{240\pi^2}\int_{\Omega} d^5x\epsilon^{\mu\nu\lambda\rho\sigma}\mathrm{Tr}(l_\mu l_\nu l_\lambda l_\rho l_\sigma), \tag{3}$$

where Ω is a five-dimensional domain whose boundary is the four-dimensional space–time. Action (3) determines important topological properties of skyrmions, but it does not contribute to the static masses of classical configurations [21, 61]. Variation of this action can be represented as a well-defined contribution to the Lagrangian (an integral over four-dimensional space-time).

We begin our calculations with $U \in SU(2)$. The classical mass of $SU(2)$ solitons, in the most general case, depends on three profile functions: f, α, and β and is given by

$$M_{cl} = \int\left\{\frac{F_\pi^2}{8}[\mathbf{l}_1^2 + \mathbf{l}_2^2 + \mathbf{l}_3^2] + \frac{1}{2e^2}[[\mathbf{l}_1\mathbf{l}_2]^2 + [\mathbf{l}_2\mathbf{l}_3]^2 + [\mathbf{l}_3\mathbf{l}_1]^2] + \frac{1}{4}F_\pi^2 m_\pi^2(1 - c_f) + 2c_6(\mathbf{l}_1\mathbf{l}_2\mathbf{l}_3)^2\right\}d^3r, \tag{4}$$

where $\mathbf{l}_k$ are the $SU(2)$ chiral derivatives defined by $\vec{\partial} UU^\dagger = i\mathbf{l}_k\tau_k$, $k = 1, 2, 3$. The general parametrization of U_0 for an $SU(2)$ soliton used here is given by

$$U_0 = c_f + s_f\boldsymbol{\tau}\cdot\mathbf{n}$$

with

$$n_z = c_\alpha, \quad n_x = s_\alpha c_\beta, \quad n_y = s_\alpha s_\beta,$$

$$s_f = \sin f, \quad c_f = \cos f.$$

For the rational map ansatz, we here use the starting configurations [46]

$$n_x = \frac{2\mathrm{Re}R(\xi)}{1+|R(\xi)|^2}, \quad n_y = \frac{2\mathrm{Im}R(\xi)}{1+|R(\xi)|^2}, \\ n_z = \frac{1-|R(\xi)|^2}{1+|R(\xi)|^2}, \tag{5}$$

where $R(\xi)$ is a ratio of polynomials of the maximal power B in the variable

$$\xi = \tan(\theta/2)\exp(i\phi),$$

with θ and ϕ being polar and azimuthal angles defining the direction of the radius vector $\mathbf{r}$. An important assumption is that the vector $\mathbf{n}$ depends on angular variables but is independent of r, whereas the profile $f(r)$ depends on the distance from the soliton center only. The explicit form of $R(\xi)$ is given in [46, 62] for different values of B. Within the rational map approximation, all characteristics of multiskyrmions that we need (including the mass and moments of inertia) depend on two quantities given by integrals over angular variables,

$$\mathcal{N} = \frac{1}{8\pi}\int r^2(\partial_i n_k)^2 d\Omega, \\ \mathcal{I} = \frac{1}{8\pi}\int r^4[\vec{\partial} n_i \vec{\partial} n_k]^2 d\Omega, \tag{6}$$

which satisfy the inequality $\mathcal{I} \geq \mathcal{N}^2$ [46]. For the lowest-energy configuration, $\mathcal{N} = B$, $f(0) - f(\infty) = \pi$, and the value of $\mathcal{I}$ should be found by minimization of the map $S^2 \longrightarrow S^2$ [46]. The classical mass of the multiskyrmion then simplifies to

$$M_{cl} = 4\pi\int\left[\frac{F_\pi^2}{8}\left(f'^2 + 2B\frac{s_f^2}{r^2}\right) + \frac{s_f^2}{2e^2r^2} \right. \\ \left. \times\left(2f'^2B + s_f^2\frac{\mathcal{I}}{r^2}\right) + 4c_6\mathcal{I}f'^2\frac{s_f^4}{r^4} + \rho_{\mathrm{M.t.}}\right]r^2dr, \tag{7}$$

which should and can be easily minimized for definite B and $\mathcal{I}$. The mass term density is simple for the starting $SU(2)$ skyrmion,

$$\rho_{\mathrm{M.t.}} = F_\pi^2 m_\pi^2(1-c_f)/4.$$

The quantity λ can be introduced [59] that characterizes the relative weight of the sixth-order term as

$$\frac{\lambda}{(1-\lambda)^2} = c_6F_\pi^2e^4,$$

or

$$c_6 = \frac{\lambda}{F_\pi^2 e'^4}.$$

For the pure SK6 variant ($\lambda = 1$, $e \longrightarrow \infty$, and $e' = e\sqrt{1-\lambda}$ is fixed), there is the relation

$$c_6 = \frac{1}{F_\pi^2 e'^4}.$$

The "flavor" moment of inertia plays a very important role in the procedure of $SU(3)$ quantization [23, 61] (see formulas (16), (17), and (23) below). It defines the $SU(3)$ rotational energy

$$E_{\mathrm{rot}}(SU_3) = \Theta_F(\Omega_4^2 + \Omega_5^2 + \Omega_6^2 + \Omega_7^2)/2$$

with Ω_a, $a = 4, \ldots, 7$, being the angular velocities of rotation in the $SU(3)$ configuration space. For $SU(2)$ skyrmions as starting configurations and the rational map ansatz describing the classical field configurations, Θ_F is given by [63, 64]

$$\Theta_F = \frac{1}{8}\int(1-c_f)\left[F_D^2 + \frac{1}{e^2}\left(f'^2 + 2B\frac{s_f^2}{r^2}\right) \right. \\ \left. + 2c_6\frac{s_f^2}{r^2}\left(2Bf'^2 + \mathcal{I}\frac{s_f^2}{r^2}\right)\right]r^2dr. \tag{8}$$

It is simply related to $\Theta_F^{(0)}$ of the flavor symmetric case ($F_D = F_\pi$):

$$\Theta_F = \Theta_F^{(0)} + (F_D^2/F_\pi^2 - 1)\Gamma/4, \tag{9}$$

with Γ defined in Eq. (11) below.

The isotopic momenta of inertia are the components of the corresponding tensor of inertia presented and discussed in many papers (see, e.g., [23, 61, 63]). For the majority of multiskyrmions that we discuss, this tensor of inertia is close to the unit matrix multiplied by the isotopic moment of inertia:

$$\Theta_{ab} \approx \Theta_I\delta_{ab}, \quad \Theta_I = \Theta_{I,aa}/3.$$

This is exactly the case for $B = 1$ and, to within a good accuracy, for $B = 3$ and 7. Considerable deviations take place for the torus with $B = 2$; smaller ones for $B = 4$, 5, and 6; and, generally, deviations decrease with increasing B-number. In our estimates, we use a very simple expression obtained within the rational map approximation [63, 64]:

$$\Theta_I = \frac{4\pi}{3}\int s_f^2\left[\frac{F_\pi^2}{2} + \frac{2}{e^2}\left(f'^2 + B\frac{s_f^2}{r^2}\right) + 8c_6 B s_f^4 \frac{f'^2}{r^2}\right] r^2 dr. \tag{10}$$

At large enough baryon numbers, isotopic inertia (10) receives the leading contribution from the spherical envelope of the multiskyrmion where its mass is concentrated. The dimensions of this spherical bubble grow as $R_B \sim \sqrt{B}$ [63], and moments of inertia are roughly proportional to the baryon number.

The quantity Γ (or the Σ-term) determines the contribution of the mass term to the classical mass of solitons, and $\tilde{\Gamma}$ enters due to the presence of the FSB term proportional to the difference $F_D^2 - F_\pi^2$ in (1), the last term in (1). They define the potential in which the rigid oscillator moves and are given by

$$\begin{aligned}\Gamma &= \frac{F_\pi^2}{2}\int(1 - c_f)d^3 r,\\ \tilde{\Gamma} &= \frac{1}{4}\int c_f[(\vec{\partial} f)^2 + s_f^2(\vec{\partial} n_i)^2].\end{aligned} \tag{11}$$

The relation

$$\tilde{\Gamma} = 2(M_{cl}^{(2)}/F_\pi^2 - e^2\Theta_F^{\text{SK4}})$$

can also be established, where $M_{cl}^{(2)}$ is the second-order term contribution to the classical mass of the soliton and Θ_F^{SK4} is the Skyrme term contribution to the flavor moment of inertia. The calculated momenta of inertia Θ_F, Θ_I, Γ (or Σ-term), and $\tilde{\Gamma}$ for solitons with the baryon numbers up to 32 are presented in Tables 1 and 2. The Σ-term Γ receives the contribution from the bulk of the multiskyrmion, where $c_f \sim -1$, and therefore grows faster than the moment of inertia Θ_I. The flavor inertia Θ_F receives the contribution from the surface and the bulk of the multiskyrmion, and its behavior is intermediate between that of Γ and Θ_I.

For both variants of the model, SK4 and SK6, we calculated the static characteristics of multiskyrmions for two values of the only parameter of the model, the constant e (or e') for the SK6 variant, related to c_6 via

$$e' = \frac{1}{(F_\pi^2 c_6)^{1/4}}.$$

For the SK4 variant of the model and $e = 4.12$, the numbers given in Table 1 for $B = 1$–8 are obtained as a result of direct numerical energy minimization in three dimensions performed using the calculation algorithm developed in [47]. Therefore, they differ slightly from those obtained in the pure rational-map approximation. This difference is maximum for $B = 2$ and decreases with increasing B. In all other cases, we used the rational map approximation with values of the Morse function $\mathcal{F}$ given in [46, 62].

The second value of the constants, $e = 3.00$ and $e' = 2.84$, leads to the "nuclear variant" of the model, which allows a quite successful description of the mass splittings of nuclear isotopes for atomic (baryon) numbers between approximately 10 and 30 [65]. The static characteristics of multiskyrmions change considerably when the constants e or e' change by about 30% (see Table 2), because the dimensions of solitons scale as $1/F_\pi e$ and the isotopic mass splittings scale as $F_\pi e^3$. However, the flavor excitation energies change not crucially, even slightly for charm and beauty, according to the scale invariance of these quantities [63], as described in the next section.

3. FLAVOR AND ANTIFLAVOR EXCITATION ENERGIES

The $SU(3)$ effective action defined by (1), (3) leads to the collective Lagrangian obtained in [61]. To quantize the solitons in their $SU(3)$ configuration space, in the spirit of the bound-state approach to the description of strangeness proposed in [44, 45] and used in [43, 63], we consider the collective coordinate motion of the meson fields incorporated into the matrix U:

$$\begin{aligned}U(r, t) &= R(t)U_0(O(t)\mathbf{r})R^\dagger(t),\\ R(t) &= A(t)S(t),\end{aligned} \tag{12}$$

where U_0 is the $SU(2)$ soliton embedded into $SU(3)$ in the usual way (into the upper-left corner); $A(t) \in SU(2)$ describes $SU(2)$ rotations; $S(t) \in SU(3)$ describes rotations in the "strange," "charm," or "beauty" directions; and $O(t)$ describes rigid rotations in real space. In the quantization procedure of the rotator with the help of $SU(3)$ collective coordinates, the following definition of angular velocities in the $SU(3)$ configuration space is accepted [61]:

$$R^\dagger(t)\dot{R}(t) = -\frac{i}{2}\Omega_\alpha\lambda_\alpha. \tag{13}$$

Here, λ_α, $\alpha = 1, \ldots, 8$ are the $SU(3)$ Gell-Mann matrices. For the quantization method proposed in [44] and used here, parametrization (12) is more convenient and the components Ω_α can be expressed via collective coordinates introduced in (12).

For definiteness, we consider the extension of the (u, d) $SU(2)$ Skyrme model in the (u, d, s) direction, with D being the field of K-mesons, but it is clear that quite similar extensions can also be made in the directions of charm or bottom. Therefore,

$$S(t) = \exp(i\mathcal{D}(t)), \quad \mathcal{D}(t) = \sum_{a = 4, \dots, 7} D_a(t)\lambda_a, \quad (14)$$

where λ_a are the Gell-Mann matrices of the (u, d, s), (u, d, c), or (u, d, b) $SU(3)$ groups. The (u, d, c) and (u, d, b) $SU(3)$ groups are quite analogous to the (u, d, s) one. For the (u, d, c) group, a simple redefinition of hypercharge should be made. For the (u, d, s) group,

$$D_4 = \frac{K^+ + K^-}{\sqrt{2}}, \quad D_5 = \frac{i(K^+ - K^-)}{\sqrt{2}}, \text{ etc.}$$

For the (u, d, c) group,

$$D_4 = \frac{D^0 + \bar{D}^0}{\sqrt{2}}, \text{ etc.}$$

The angular velocities of the isospin rotations $\boldsymbol{\omega}$ are defined in the standard way [61]:

$$A^\dagger \dot{A} = -i\boldsymbol{\omega} \cdot \boldsymbol{\tau}/2.$$

Here, we do not consider the usual space rotations in detail, because the corresponding momenta of inertia for baryonic systems are much greater than the isospin momenta of inertia, and for the lowest possible values of the angular momentum J, the corresponding quantum correction is either exactly zero (for even B) or small. The field D is small in magnitude. In fact, it is on the order of $1/\sqrt{N_c}$ at least, where N_c is the number of colors in QCD (see Eq. (22)). Therefore, the expansion of the matrix S in D can be safely made.

The mass term of Lagrangian (1) can be calculated exactly, without expansion in powers of the field D, because the matrix S is given by [44]

$$S = 1 + i\mathcal{D}\sin d/d - \mathcal{D}^2(1 - \cos d)/d^2$$

with

$$\mathrm{Tr}\mathcal{D}^2 = 2d^2.$$

We find that

$$\Delta\mathcal{L}_M = -\frac{F_D^2 m_D^2 - F_\pi^2 m_\pi^2}{4}(1 - c_f)s_d^2. \quad (15)$$

This term can easily be expanded up to any order in d. The comparison of this expression with ΔL_M, within the collective coordinate approach of the quantization of $SU(2)$ solitons in the $SU(3)$ configuration space [23, 61], allows us to establish the relation

$$\sin^2 d = \sin^2 \nu,$$

where ν is the angle of the λ_4 rotation or the rotation into the strange (charm, beauty) direction. After some calculations, we find that the Lagrangian of the model, to the lowest order in the field D, can be written as

$$\begin{aligned} L = {} & -M_{cl, B} + 4\Theta_{F, B}\dot{D}^\dagger \dot{D} \\ & -\left[\Gamma_B\left(\frac{F_D^2}{F_\pi^2}m_D^2 - m_\pi^2\right) + \tilde{\Gamma}_B(F_D^2 - F_\pi^2)\right]D^\dagger D \quad (16) \\ & -i\frac{N_c B}{2}(D^\dagger \dot{D} - \dot{D}^\dagger D). \end{aligned}$$

Here and below, D is the doublet K^+, K^0 (D^0, D^-, or B^+, B^0):

$$d^2 = \mathrm{Tr}\mathcal{D}^2/2 = 2D^\dagger D.$$

We keep the standard notation for the moment of inertia of the rotation in the flavor direction Θ_F for Θ_c, Θ_b, or Θ_s [60, 61]; different notation is used in [44] (the index c denotes the charm quantum number, except in N_c). The contribution proportional to $\tilde{\Gamma}_B$ is suppressed by a small factor proportional to $(F_D^2 - F_\pi^2)/m_D^2$ in comparison to the term on the order of Γ and is more important for strangeness. The term proportional to $N_c B$ in (1) arises from the Wess–Zumino term in the action and is responsible for the difference in the excitation energies of strangeness and antistrangeness (flavor and antiflavor in the general case) [44, 45].

Following the canonical quantization procedure, the Hamiltonian of the system, including terms on the order of N_c^0, can be written as [44]

$$\begin{aligned} H_B = {} & M_{cl, B} + \frac{1}{4\Theta_{F, B}}\Pi^\dagger \Pi \\ & + \left[\Gamma_B \bar{m}_D^2 + \tilde{\Gamma}_B(F_D^2 - F_\pi^2) + \frac{N_c^2 B^2}{16\Theta_{F, B}}\right]D^\dagger D \quad (17) \\ & + i\frac{N_c B}{8\Theta_{F, B}}(D^\dagger \Pi - \Pi^\dagger D), \end{aligned}$$

where

$$\bar{m}_D^2 = (F_D^2/F_\pi^2)m_D^2 - m_\pi^2.$$

The momentum Π is canonically conjugate to variable D (see Eq. (18) below). Equation (17) describes an oscillator-type motion of the field D in the background formed by the (u, d) $SU(2)$ soliton. After diagonalization, which can be done explicitly following [44], the normal-ordered Hamiltonian can be written as

$$H_B = M_{cl,B} + \omega_{F,B}a^\dagger a + \bar{\omega}_{F,B}b^\dagger b + O(1/N_c), \quad (18)$$

where $a^\dagger$ and $b^\dagger$ are the operators of creation of the strangeness (i.e., antikaons) and antistrangeness (flavor and antiflavor) quantum number, and $\omega_{F,B}$ and $\bar{\omega}_{F,B}$ are the frequencies of flavor (antiflavor) excitations. D and Π are expressed in terms of a and b as [44]

$$\begin{aligned} D^i &= \frac{1}{\sqrt{N_c B\mu_{F,B}}}(b^i + a^{\dagger i}), \\ \Pi^i &= \frac{\sqrt{N_c B\mu_{F,B}}}{2i}(b^i - a^{\dagger i}), \end{aligned} \quad (19)$$

where

$$\mu_{F,B} = \left[1 + \frac{16[\bar{m}_D^2\Gamma_B + (F_D^2 - F_\pi^2)\tilde{\Gamma}_B]\Theta_{F,B}}{(N_c B)^2}\right]^{1/2} \quad (20)$$

is a slowly varying quantity. For a large mass m_D, it simplifies to

$$\mu_{F,B} \longrightarrow 4\bar{m}_D\frac{\sqrt{\Gamma_B\Theta_{F,B}}}{N_c B}. \quad (21)$$

Obviously, at large N_c, $\mu \sim N_c^0 \sim 1$, and the dependence on the B-number is also weak, because both Γ_B, $\Theta_{F,B} \sim N_c B$.[4] For the lowest states, the values of D are small,

$$|D| \sim [16\Gamma_B\Theta_{F,B}\bar{m}_D^2 + N_c^2B^2]^{-1/4}, \quad (22)$$

and increase as $(2|F| + 1)^{1/2}$ with increasing flavor number $|F|$. As follows from (22) [43, 44], deviations of the field D from the vacuum decrease with increasing mass m_D, as well as with an increasing number of colors N_c; this explains why the method works for any m_D, including charm and beauty quantum numbers.

The excitation frequencies ω and $\bar{\omega}$ are

$$\begin{aligned} \omega_{F,B} &= \frac{N_c B}{8\Theta_{F,B}}(\mu_{F,B} - 1), \\ \bar{\omega}_{F,B} &= \frac{N_c B}{8\Theta_{F,B}}(\mu_{F,B} + 1). \end{aligned} \quad (23)$$

The oscillation time can be estimated as

$$\tau_{\text{osc}} \sim \frac{\pi}{\omega_{F,B}} \sim \frac{2\pi(\Theta_B/\Gamma_B)^{1/2}}{m_D},$$

and, hence, it decreases with increasing m_D. As was observed in [43, 63], the difference

$$\bar{\omega}_{F,B} - \omega_{F,B} = \frac{N_c B}{4\Theta_{F,B}}$$

coincides, to the leading order in N_c, with the expression obtained in the collective coordinate approach [60, 61] (see the Appendix). At large m_D, using (21) for the difference $\omega_{F,1} - \omega_{F,B}$, we obtain ($N_c = 3$)

$$\begin{aligned} \bar{\omega}_{F,1} - \bar{\omega}_{F,B} \approx{}& \frac{\bar{m}_D}{2}\left[\left(\frac{\Gamma_1}{\Theta_{F,1}}\right)^{1/2} - \left(\frac{\Gamma_B}{\Theta_{F,B}}\right)^{1/2}\right] \\ &+ \frac{3}{8}\left(\frac{B}{\Theta_{F,B}} - \frac{1}{\Theta_{F,1}}\right). \end{aligned} \quad (24)$$

Obviously, at large m_D, the first term in (24) dominates and is positive if

$$\frac{\Gamma_1}{\Theta_{F,1}} \geq \frac{\Gamma_B}{\Theta_{F,B}}.$$

This is confirmed by the data in Table 1. We also note that the bracket in the first term in (24) is independent of the parameters of the model if the background $SU(2)$ soliton is calculated in the chirally symmetrical limit: both Γ and Θ scale as $1/F_\pi e^3$. In a realistic case where the physical pion mass is included in (1), there is some weak dependence on the parameters of the model.

The FSB in the flavor decay constants, i.e., the fact that $F_K/F_\pi \approx 1.22$ and $F_D/F_\pi = 2.28^{+1.4}_{-1.1}$, should be taken into account. In the Skyrme model, this fact leads to the increase of the flavor excitation frequencies, which changes the spectra of flavored (c, b) baryons and puts them in a better agreement with the data [40]. It also leads to some changes of the total binding energies of baryonic system [43]. This is partly due to the large contribution of the Skyrme term to the flavor moment of inertia Θ_F. We note that, in [44], the FSB in strangeness decay constant was not taken into account, and this led to underestimation of the strangeness excitation energies. Heavy flavors (c, b) have not been considered in these papers.

The addition of the term L_6 into starting Lagrangian (1) leads to modification of the flavored moment of inertia, according to the simple relation

$$\Theta_F = \Theta_F^{\text{kin}} + \Theta_F^{\text{SK4}} + \Theta_F^{\text{SK6}}.$$

However, in order to adequately take the symmetry-breaking terms into account, we have to express (in

---

[4] Strictly, at large B, $\Gamma_B \sim B^{3/2}$, as explained above. But, numerically, at $B < 30$, $\Gamma_B \sim B$, as can be seen in Tables 1 and 2.

some order of N_c^{-1}) the first set of coordinates (13) in terms of the collective coordinates $A(t)$ and $S(t)$ and substitute the result into $L_{\rm rot}$.

Terms on the order of N_c^{-1} in the Hamiltonian, which also depend on the angular velocities of rotations in the isospin and the usual space, are not crucial but important for numerical estimates of the spectra of baryonic systems. To calculate them, we should first obtain the Lagrangian of baryonic system including all the terms up to $O(1/N_c)$. The Lagrangian can be written in a compact form, slightly different from that in [44], as [42]

$$\begin{gathered} L \approx -M_{cl} + 2\Theta_{F,B}\Big[2\dot{D}^\dagger\dot{D}\Big(1-\frac{d^2}{3}\Big) \\ -\frac{4}{3}(D^\dagger\dot{D}\dot{D}^\dagger D - (D^\dagger\dot{D})^2 - (\dot{D}^\dagger D)^2) + (\boldsymbol{\omega}\cdot\boldsymbol{\beta})\Big] \\ +\frac{\Theta_{I,B}}{2}(\boldsymbol{\omega}-\boldsymbol{\beta})^2 - [\Gamma_B\tilde{m}_D^2 + (F_D^2 - F_\pi^2)\tilde{\Gamma}_B]D^\dagger D \qquad (25) \\ \times\Big(1-\frac{d^2}{3}\Big) + i\frac{N_cB}{2}\Big(1-\frac{d^2}{3}\Big)(\dot{D}^\dagger D - D^\dagger\dot{D}) \\ -\frac{N_cB}{2}\boldsymbol{\omega}D^\dagger\boldsymbol{\tau}D, \end{gathered}$$

where

$$d^2 = 2D^\dagger D$$

and

$$\boldsymbol{\beta} = -i(\dot{D}^\dagger\boldsymbol{\tau}D - D^\dagger\boldsymbol{\tau}\dot{D}). \qquad (26)$$

As we mentioned already, the role of the term L_6 reduces to the modification of the flavored inertia Θ_F in (25). It is a remarkable property of the starting Lagrangian including L_6 that only quadratic terms in Ω_a enter (25). To obtain this expression, we used the connection between components Ω_a and D, $\dot{D}$, ω_i,

$$\begin{gathered} \Omega_4^2 + \ldots + \Omega_7^2 = 8\dot{D}^\dagger\dot{D}\Big(1-\frac{d^2}{3}\Big) \\ -\frac{16}{3}(D^\dagger\dot{D}\dot{D}^\dagger D - (D^\dagger\dot{D})^2 - (\dot{D}^\dagger D)^2) + 4(\boldsymbol{\omega}\cdot\boldsymbol{\beta}), \end{gathered}$$

and the component Ω_8 that determines the WZW term contribution,

$$\Omega_8 = \sqrt{3}[i(1-d^2/3)(D^\dagger\dot{D} - \dot{D}^\dagger D) + \boldsymbol{\omega}D^\dagger\boldsymbol{\tau}D].$$

Taking the terms proportional to $1/N_c$ into account, we find that the canonical variable Π conjugate to D is

$$\begin{gathered} \Pi = \frac{\partial L}{\partial\dot{D}^\dagger} \\ = 4\Theta_{F,B}\Big[\dot{D}\Big(1-\frac{d^2}{3}\Big) - \frac{2}{3}D^\dagger\dot{D}D + \frac{4}{3}\dot{D}^\dagger DD\Big] \qquad (27) \\ + i(\Theta_{I,B} - 2\Theta_{F,B})\boldsymbol{\omega}\cdot\boldsymbol{\tau}D - i\Theta_{I,B}\boldsymbol{\beta}\cdot\boldsymbol{\tau}D \\ + i\frac{N_cB}{2}\Big(1-\frac{d^2}{3}\Big)D. \end{gathered}$$

From (25), the body-fixed isospin operator is

$$\begin{gathered} \mathbf{I}^{bf} = \frac{\partial L}{\partial\boldsymbol{\omega}} = \Theta_{I,B}\boldsymbol{\omega} + (2\Theta_{F,B} - \Theta_{I,B})\boldsymbol{\beta} \\ -\frac{N_cB}{2}D^\dagger\boldsymbol{\tau}D, \end{gathered} \qquad (28)$$

which can also be written as

$$\mathbf{I}^{bf} = \Theta_I\boldsymbol{\omega} + \Big(1-\frac{\Theta_I}{2\Theta_F}\Big)\mathbf{I}_F - \frac{N_cB\Theta_I}{4\Theta_F}D^\dagger\boldsymbol{\tau}D \qquad (29)$$

with the operator

$$\hat{\mathbf{I}}_F = \frac{i}{2}(D^\dagger\boldsymbol{\tau}\Pi - \Pi^\dagger\boldsymbol{\tau}D) = \frac{1}{2}(b^\dagger\boldsymbol{\tau}b - a^T\boldsymbol{\tau}a^{\dagger T}). \qquad (30)$$

Using the connection between Π, $\dot{D}$, and D given by (27) in the leading order, we obtain

$$\boldsymbol{\beta} \approx \frac{1}{2\Theta_F}\Big(\mathbf{I}_F + \frac{N_cB}{2}D^\dagger\boldsymbol{\tau}D\Big). \qquad (31)$$

For states with a definite flavor quantum number, we must make the substitution

$$D^\dagger\boldsymbol{\tau}D \longrightarrow -\frac{2\mathbf{I}_F}{N_cB\mu_F}$$

for flavor or

$$D^\dagger\boldsymbol{\tau}D \longrightarrow \frac{2\mathbf{I}_F}{N_cB\mu_F}$$

for antiflavor; for matrix elements of states with a definite flavor, we can then write

$$\mathbf{I}^{bf} = \Theta_{I,B}\boldsymbol{\omega} + c_{F,B}\mathbf{I}_F \qquad (32)$$

with

$$c_{F,B} = 1 - \frac{\Theta_{I,B}}{2\Theta_{F,B}\mu_{F,B}}(\mu_{F,B} - 1). \qquad (33)$$

We also used, within our approximation,

$$\Theta_{I,B}\boldsymbol{\beta} \approx (1 - c_{F,B})\mathbf{I}_F. \tag{34}$$

A relation similar to (32) also holds for antiflavor with

$$c_{\bar{F},B} = 1 - \frac{\Theta_{I,B}}{2\Theta_{F,B}\mu_{F,B}}(\mu_{F,B} + 1), \tag{35}$$

and it therefore differs from (33) by the change $\mu \longrightarrow -\mu$. Using the identities

$$-i\boldsymbol{\beta}\cdot\boldsymbol{\tau}D = 2D^{\dagger}D\dot{D} - (\dot{D}^{\dagger}D + D^{\dagger}\dot{D})D \tag{36}$$

and

$$\boldsymbol{\beta}^2 = 4D^{\dagger}D\dot{D}^{\dagger}\dot{D} - (\dot{D}^{\dagger}D + D^{\dagger}\dot{D})^2, \tag{37}$$

we find that the zero mode quantum corrections to the energies of skyrmions that scale with $1/N_c$ can be estimated [44] as

$$\begin{aligned}\Delta E_{1/N_c} &= \frac{1}{2\Theta_{I,B}}[c_{F,B}I_r(I_r+1) + (1-c_{F,B})I(I+1) \\ &\quad + (\bar{c}_{F,B} - c_{F,B})I_F(I_F+1)],\end{aligned} \tag{38}$$

where $I = I^{bf}$ is the value of the isospin of the baryon or baryon system, I_r is a quantity analogous to the "right" isospin I_r in the collective coordinate approach [61], and

$$\mathbf{I}_r = \mathbf{I}^{bf} - \mathbf{I}_F.$$

The hyperfine structure constants $c_{F,B}$ are given in (33), and $\bar{c}_{F,B}$ are defined by the relations

$$\begin{aligned}1 - \bar{c}_{F,B} &= \frac{\Theta_{I,B}}{\Theta_{F,B}(\mu_{F,B})^2}(\mu_{F,B} - 1), \\ 1 - \bar{c}_{F,B} &= -\frac{\Theta_{I,B}}{\Theta_{F,B}(\mu_{F,B})^2}(\mu_{F,B} + 1).\end{aligned} \tag{39}$$

For nucleons,

$$I = I_r = 1/2, \quad I_F = 0$$

and

$$\Delta E_{1/N_c}(N) = \frac{3}{8\Theta_{I,1}},$$

for the Δ-isobar,

$$I = I_r = 3/2, \quad I_F = 0,$$

and

$$\Delta E_{1/N_c}(\Delta) = \frac{15}{8\Theta_{I,1}},$$

as in the $SU(2)$ quantization scheme. The Δ-N mass splitting is described satisfactorily according to the values of Θ_I presented in Table 1.

As can be seen from Table 3, the flavor excitation energies somewhat decrease in the SK4 variant as the B-number increases from 1 to 7, but, further, these energies increase again and exceed the $B = 1$ value for $B \geq 20$. The last property can be connected, however, with specific character of the rational-map approximation (the quantity Γ increases faster than the flavored inertia Θ_F; see (24)), which becomes less realistic for larger values of B. Such behavior of the frequencies is important for conclusions about the possible existence of hypernuclei [66]. Table 3 is presented here for comparison with antiflavor excitation energies presented in Table 4. Generally, the rigid oscillator version of the bound-state model that we use here overestimates the flavor excitation energies. However, phenomenological consequences derived in [63, 66] for the binding energies of strange $S = -1$ hypernuclei are based mainly on the differences of these energies. The qualitative and, in some cases, quantitative agreement takes place between the data for binding energies of ground states of hypernuclei with atomic numbers between 5 and 20 and the results of calculations within the SK4 variant of the chiral soliton model, with the collective motion of solitons in the $SU(3)$ configuration space taken into account [66].

Another peculiarity of interest is that, for the rescaled variant of the model, the charm and beauty excitation energies are very close to those of the original variant (scaling property) but differ more substantially for strangeness, being greater by approximately 30–40 MeV. This somewhat unexpected behavior is explained by the fact that flavor excitation energies appear as a result of subtraction of two quantities that behave differently under rescaling (see (23)).

Similar to flavor energies, there is remarkable universality of antiflavor excitation energies for different baryon numbers, especially for anticharm and antibeauty: variations do not exceed a few percent. It follows from Table 4 that there is some decrease of the antiflavor excitation energies as B increases from 1; this effect is striking for the SK4 variant and especially for strangeness. Within the SK6 variant, the $B = 1$ energies for anticharm and antibeauty are slightly smaller than for $B \geq 2$.

For strangeness, $\bar{\omega}_s$ decreases with increasing B-number in most cases, as can be seen from Table 4 (except in the rescaled SK6 variant, where the $B = 1$ energy is slightly smaller than the $B = 2$ one), but it is always greater than the kaon mass, and, therefore, the

Table 3. Flavor excitation energies for strangeness, charm, and beauty, in GeV. $e = 4.12$ for the SK4 variant and $e' = 4.11$ for the SK6 variant. For rescaled variants (the numbers marked with *), $e = 3.00$ and $e' = 2.84$ for SK4 and SK6 variants, respectively. The ratio $F_D/F_\pi = 1.5$ for charm and $F_B/F_\pi = 2$ for beauty

B	ω_s^{SK4}	ω_c^{SK4}	ω_b^{SK4}	ω_s^{SK6}	ω_c^{SK6}	ω_b^{SK6}	$\omega_s^{\mathrm{SK4*}}$	$\omega_c^{\mathrm{SK4*}}$	$\omega_b^{\mathrm{SK4*}}$	$\omega_s^{\mathrm{SK6*}}$	$\omega_c^{\mathrm{SK6*}}$	$\omega_b^{\mathrm{SK6*}}$
1	0.307	1.54	4.80	0.336	1.61	4.93	0.345	1.55	4.77	0.375	1.62	4.89
2	0.298	1.52	4.77	0.346	1.64	4.98	0.339	1.54	4.75	0.386	1.66	4.95
3	0.293	1.51	4.76	0.342	1.64	4.98	0.336	1.54	4.74	0.385	1.66	4.95
4	0.285	1.50	4.74	0.328	1.62	4.95	0.330	1.52	4.72	0.377	1.64	4.93
5	0.290	1.51	4.75	0.334	1.63	4.96	0.334	1.53	4.74	0.380	1.65	4.94
6	0.290	1.51	4.76	0.332	1.63	4.96	0.334	1.54	4.74	0.379	1.65	4.94
7	0.285	1.50	4.74	0.324	1.62	4.95	0.331	1.53	4.73	0.374	1.64	4.93
8	0.290	1.51	4.76	0.329	1.63	4.96	0.335	1.54	4.75	0.377	1.65	4.94
9	0.292	1.52	4.77	0.331	1.63	4.97	0.336	1.54	4.76	0.378	1.65	4.94
10	0.293	1.52	4.78	0.331	1.63	4.97	0.337	1.55	4.76	0.378	1.65	4.94
11	0.295	1.53	4.79	0.332	1.63	4.97	0.338	1.55	4.77	0.378	1.65	4.95
12	0.295	1.53	4.79	0.331	1.63	4.97	0.338	1.55	4.77	0.378	1.65	4.95
13	0.296	1.53	4.79	0.332	1.63	4.98	0.339	1.55	4.77	0.378	1.65	4.95
14	0.300	1.54	4.80	0.335	1.64	4.98	0.342	1.56	4.79	0.379	1.65	4.95
15	0.301	1.54	4.81	0.336	1.64	4.99	0.343	1.56	4.79	0.380	1.66	4.95
16	0.302	1.54	4.81	0.336	1.64	4.99	0.343	1.56	4.79	0.380	1.66	4.96
17	0.302	1.54	4.81	0.335	1.64	4.99	0.343	1.56	4.79	0.379	1.66	4.95
20	0.308	1.56	4.84	0.340	1.65	5.00	0.347	1.58	4.81	0.382	1.66	4.96
24	0.312	1.57	4.85	0.343	1.66	5.01	0.351	1.58	4.83	0.384	1.66	4.97
28	0.316	1.58	4.87	0.347	1.66	5.02	0.354	1.59	4.85	0.385	1.67	4.98
32	0.319	1.59	4.88	0.349	1.67	5.02	0.356	1.60	4.86	0.386	1.67	4.98

state with positive strangeness can decay strongly into kaon and some final nucleus or nuclear fragments.

The heavy antiflavor excitation energies also reveal a notable scale independence; i.e., the values obtained with constant $e = 4.12$ and 3.00 (SK4 variant) shown in Tables 3 and 4 are close to each other within several percent, as well as the values for $e' = 4.11$ and 2.84 for the SK6 variant. This was actually expected from general arguments for large values of the FSB meson mass [43]. The change of numerical values of these energies is, however, important for conclusions concerning the binding energies of nuclear states with antiflavors. All excitation energies of antiflavors are smaller for rescaled variants, i.e., when the constants e or e' are decreased by about 30%. This seems natural because dimensions of multiskyrmions, which scale as $1/F_\pi e$, increase due to this change, and all energies become "softer." Such behavior occurs because antiflavor energies are the sum of two terms (see above (23)) that behave (roughly!) similarly under rescaling. Remarkably, the decrease of energies due to the rescaling is on the order of 100 MeV in all cases (e.g., for antistrangeness and $B = 1$, it is 119 MeV in the SK4 variant and 116 MeV in the SK6 variant) and slightly smaller for $\bar{c}$ (decrease due to rescaling about 100 MeV) and $\bar{b}$ (decrease by 110 MeV).

4. THE BINDING ENERGIES OF Θ^+-HYPERNUCLEI AND ANTICHARMED (ANTIBEAUTIFUL) HYPERNUCLEI

In view of sufficiently large values of antistrangeness excitation energies, one cannot talk about positive-strangeness hypernuclei that decay weakly, similarly to ordinary $S = -1$ hypernuclei. However, one can talk about Θ-hypernuclei where the Θ-hyperon is bound by several nucleons. A puzzling property of pentaquarks is their small width, $\Gamma_\Theta < \sim 10$ MeV according to experi-

Table 4. Antiflavor excitation energies for strangeness, charm, and beauty, as in Table 3. In the original variants of the model, $e = 4.12$ for the SK4 variant and $e' = 4.11$ for the SK6 variant. The numbers with * are for the rescaled variants of the model, $e = 3.0$ for the SK4 variant and $e' = 2.84$ for the SK6 variant. The ratio $F_D/F_\pi = 1.5$ for charm and $F_B/F_\pi = 2$ for beauty

B	$\bar{\omega}_s^{SK4}$	$\bar{\omega}_c^{SK4}$	$\bar{\omega}_b^{SK4}$	$\bar{\omega}_s^{SK6}$	$\bar{\omega}_c^{SK6}$	$\bar{\omega}_b^{SK6}$	$\bar{\omega}_s^{SK4*}$	$\bar{\omega}_c^{SK4*}$	$\bar{\omega}_b^{SK4*}$	$\bar{\omega}_s^{SK6*}$	$\bar{\omega}_c^{SK6*}$	$\bar{\omega}_b^{SK6*}$
1	0.591	1.75	4.94	0.584	1.79	5.04	0.472	1.65	4.83	0.468	1.69	4.93
2	0.571	1.72	4.90	0.571	1.80	5.08	0.459	1.63	4.81	0.470	1.72	4.99
3	0.564	1.71	4.89	0.569	1.80	5.07	0.455	1.63	4.80	0.468	1.72	4.99
4	0.567	1.71	4.87	0.580	1.80	5.06	0.454	1.62	4.78	0.468	1.71	4.97
5	0.558	1.71	4.88	0.571	1.80	5.07	0.452	1.62	4.80	0.466	1.71	4.98
6	0.555	1.71	4.88	0.571	1.80	5.07	0.451	1.62	4.80	0.465	1.71	4.98
7	0.559	1.71	4.88	0.578	1.80	5.06	0.451	1.62	4.79	0.466	1.71	4.97
8	0.553	1.71	4.89	0.571	1.80	5.07	0.450	1.63	4.80	0.465	1.71	4.98
9	0.550	1.71	4.90	0.569	1.80	5.07	0.450	1.63	4.81	0.465	1.71	4.98
10	0.549	1.71	4.90	0.569	1.80	5.07	0.450	1.63	4.82	0.465	1.71	4.98
11	0.547	1.71	4.90	0.567	1.80	5.08	0.450	1.63	4.82	0.464	1.71	4.98
12	0.547	1.72	4.91	0.568	1.80	5.08	0.450	1.63	4.82	0.464	1.71	4.98
13	0.546	1.72	4.91	0.567	1.80	5.08	0.450	1.64	4.83	0.464	1.71	4.99
14	0.543	1.72	4.92	0.564	1.80	5.08	0.450	1.64	4.84	0.464	1.72	4.99
15	0.542	1.72	4.92	0.563	1.80	5.08	0.450	1.64	4.84	0.464	1.72	4.99
16	0.541	1.72	4.93	0.562	1.80	5.08	0.450	1.64	4.85	0.464	1.72	4.99
17	0.542	1.72	4.93	0.564	1.80	5.09	0.450	1.64	4.85	0.464	1.72	4.99
18	0.540	1.72	4.93	0.561	1.81	5.09	0.451	1.65	4.85	0.464	1.72	5.00
19	0.539	1.73	4.94	0.559	1.81	5.09	0.451	1.65	4.86	0.464	1.72	5.00
20	0.538	1.73	4.94	0.558	1.81	5.09	0.451	1.65	4.86	0.464	1.72	5.00
24	0.536	1.73	4.96	0.555	1.81	5.10	0.452	1.66	4.88	0.463	1.72	5.00
28	0.533	1.74	4.97	0.552	1.81	5.10	0.453	1.67	4.89	0.463	1.72	5.01
32	0.532	1.74	4.98	0.550	1.81	5.11	0.453	1.67	4.90	0.463	1.73	5.01

ments where Θ^+ has been observed [1, 2], and probably even smaller, according to analyses of kaon–nucleon interaction data [67]. Possible explanations, from some numerical cancellation [24] and cancellation in a large-N_c expansion [68] to qualitative one in terms of the quark-model wavefunction [3, 4] and calculation using operator product expansion [69] have been proposed.[5] The width of nuclear bound states of Θ should be of the same order of magnitude as the width of Θ^+ itself or smaller; in addition to the smaller energy release, some suppression due to the Pauli blocking for the final nucleon from Θ decay can occur for heavier nuclei.

For anticharm and antibeauty, the excitation energies are smaller than the masses of the *D*- or *B*-meson, and it makes sense to consider the possibility of the existence of anticharmed or antibeauty hypernuclei that have a lifetime characteristic of weak interactions.

In the bound-state soliton model, and in its rigid oscillator version as well, the states predicted do not correspond a priori to definite $SU(3)$ or $SU(4)$ representations. They can be ascribed to definite irreducible $SU(3)$ representations as was shown in [43, 44]. Due to configuration mixing caused by flavor symmetry-breaking, each state with a definite value of flavor, *s*, *c*, or *b*, is some mixture of the components of several irreducible $SU(3)$ representations with a given value of F and isospin I, which is strictly conserved in our approach (unless manifestly isospin-violating terms are included into the Lagrangian). In the case of strange-

---

[5] In most variants of the explanation, it is difficult to expect a width of the Θ-hyperon on the order of 1 MeV, as obtained in [67]. Therefore, verification of the data analyzed in [67] seems to be of first priority.

ness, as calculations show (see, e.g., [27]), this mixture is usually dominated by the lowest irreducible $SU(3)$ representation, and admixtures do not exceed several percent. The situation changes for charm or beauty quantum numbers, where admixtures can have a weight comparable to the weight of the lowest configuration. However, we consider here the simplest possibility of one lowest irreducible representation, for rough estimates.

Let (p, q) characterize the irreducible $SU(3)$ representation to which the baryon system belongs. The quantization condition [61]

$$p + 2q = N_c B$$

for arbitrary N_c then changes to

$$p + 2q = N_c B + 3m,$$

where m is related to the number of additional quark–antiquark pairs $n_{q\bar{q}}$ present in the quantized states, $n_{q\bar{q}} \geq m$ [22, 70]. The nonexotic states with $m = 0$, or minimal states, have

$$p + 2q = 3B$$

($N_c = 3$ in what follows), and states with the lowest "right" isospin $I_r = p/2$ have

$$(p, q) = (0, 3B/2)$$

for even B and

$$(p, q) = (1, (3B-1)/2)$$

for odd B [22, 27]. For example, the state with $B = 1$, $|F| = 1$, $I = 0$, and $n_{q\bar{q}} = 0$ should belong to the octet of the (u, d, s) or (u, d, c) $SU(3)$ group, if $N_c = 3$ (see also [44]). For the first exotic states, the lowest possible irreducible $SU(3)$ representations (p, q) for each value of the baryon number B are defined by the relations

$$p + 2q = 3(B+1),$$

$$p = 1, \quad q = (3B+2)/2$$

for even B and

$$p = 0, \quad q = (3B+3)/2$$

for odd B. For example, we have $\overline{35}$, $\overline{80}$, $\overline{143}$, and $\overline{224}$-plets for $B = 2$, 4, 6, and 8, and $\overline{28}$, $\overline{55}$, and $\overline{91}$ plets for $B = 3$, 5, and 7.

Because we are interested in the lowest-energy states, we here discuss the baryonic systems with the lowest allowed angular momentum, i.e., $J = 0$, for $B =$ 4, 6, etc. and $J = 1/2$ for odd values of the B-number. There are some deviations from this simple law for the ground states of real nuclei, but, anyway, the correction to the energy of quantized states due to collective rotation of solitons is small and decreases with increasing B because the corresponding moment of inertia increases proportionally to B^2 [63, 64]. Moreover, the J-dependent correction to the energy may cancel in the differences of energies of flavored and flavorless states, and we therefore neglect these contributions in our rough estimates.

For the nonexotic states, we previously considered the energy difference between the state with flavor F belonging to the (p, q) irreducible representation and the ground state with $F = 0$ and the same angular momentum and (p, q) [66]. The situation is different for exotic states, because exotic and nonexotic states have different values of (p, q). The difference between $\bar{\omega}$ and ω,

$$\bar{\omega} - \omega = \frac{N_{c,B}}{4\Theta_{F,B}},$$

takes this distinction into account in the values of (p, q), as shown explicitly in Appendix.

For $B = 1, 3, 5, \ldots$, we have $I = I_r = 1/2$, $I_F = 0$ for the ground state, and therefore the correction

$$\Delta E_{1/N_c} = \frac{I(I+1)}{2\Theta_{I,B}} = \frac{3}{8\Theta_{I,B}}.$$

For the exotic antiflavored state, we have $I = 0$, $I_r = I_F = 1/2$, and the corrections are equal to

$$\Delta E_{1/N_c} = \frac{3\bar{c}_{F,B}}{8\Theta_{I,B}}.$$

For the difference of energies between exotic and nonexotic ground states, we obtain

$$\begin{aligned}\Delta E_{B,F} &= \bar{\omega}_{F,B} + \frac{3(\bar{c}_{\bar{F},B} - 1)}{8\Theta_{F,B}} \\ &= \bar{\omega}_{F,B} + \frac{3(\mu_{F,B} + 1)}{8\mu_{F,B}^2\Theta_{F,B}}.\end{aligned} \tag{40}$$

We note that the moment of inertia Θ_I does not enter the difference of energies (40).

For $B = 4, 6, \ldots$, the ground state has $I = I_r = I_F = 0$ (as for nucleus ^{4}He) and

$$\Delta E_{1/N_c} = 0.$$

For the first exotic states, $I = I_F = 1/2$, and we have a choice for I_r, $I_r = 0$ or 1. If

$$c_{\bar{F},B} = 1 - \frac{\Theta_{I,B}(\mu_{F,B}+1)}{2\Theta_{F,B}\mu_{F,B}} > 0,$$

we have $I_r = 0$, and if $c_{\bar{F},B} < 0$, we should take $I_r = 1$. In the first case, the correction to the energy of the state

$$\Delta E_{1/N_c} = \frac{3(1+\bar{c}_{\bar{F},B} - 2c_{\bar{F},B})}{8\Theta_{I,B}} = \frac{3(\mu_{F,B}+1)^2}{8\Theta_{F,B}\mu^2_{F,B})}.$$

For $B = 1$, the difference of the Θ_F and nucleon masses is

$$\begin{aligned}\Delta M_{\Theta_F N} &= \bar{\omega}_{F,1} - \frac{3(1-\bar{c}_{\bar{F},1})}{8\Theta_{I,1}} \\ &= \bar{\omega}_{F,1} + \frac{3(\mu_{F1}+1)}{8\mu^2_{F,1}\Theta_{F,1}}.\end{aligned} \qquad (41)$$

The difference in the masses of the Θ- and Λ-hyperons is also of interest and can be represented in the simple form

$$\begin{aligned}\Delta M_{\Theta_F\Lambda_F} &= \bar{\omega}_{F,1} - \omega_{F,1} + \frac{3(\bar{c}_{\bar{F},1} - \bar{c}_{F,1})}{8\Theta_{I,1}} \\ &= \frac{3(\mu_{F,1}+1)}{4\mu_{F,1}\Theta_{F,1}}.\end{aligned} \qquad (42)$$

The binding energy differences $\Delta\epsilon_{\bar{s},\bar{c},\bar{b}}$ are the changes of binding energies of the lowest baryon system with flavor $\bar{s}$, $\bar{c}$, or $\bar{b}$ and isospin $I = 0$ (for odd B) and $I = 1/2$ (for even B) in comparison with the usual u, d nuclei (when one nucleon is replaced by a Θ-hyperon). The classical masses of skyrmions are cancelled in such differences:

$$\Delta\epsilon_{B,F} = \Delta E_{\text{gr.st}}(B) - \Delta E(B,F) + \Delta M_{\Theta_F N}. \qquad (43)$$

It follows from (40) that, for an odd B-number, this change in the binding energy of the system is

$$\begin{aligned}\Delta\epsilon_{B,F} &= \bar{\omega}_{F,1} - \bar{\omega}_{F,B} + \frac{3(\mu_{F,1}+1)}{8\mu^2_{F,1}\Theta_{F,1}} \\ &\quad - \frac{3(\mu_{F,B}+1)}{8\mu^2_{F,B}\Theta_{F,B}}.\end{aligned} \qquad (44)$$

Evidently, in the limit of very heavy flavor, $\mu_F \longrightarrow \infty$,

$$\Delta\epsilon_{B,F} \longrightarrow \bar{\omega}_{F,1} - \bar{\omega}_{F,B}. \qquad (45)$$

For B-numbers 4, 6, …, we obtain

$$\begin{aligned}\Delta\epsilon_{B,F} &= \bar{\omega}_{F,1} - \bar{\omega}_{F,B} + \frac{3(\mu_{F,1}+1)}{8\mu^2_{F,1}\Theta_{F,1}} \\ &\quad - \frac{3(\mu_{F,B}+1)^2}{8\mu^2_{F,B}\Theta_{F,B}}.\end{aligned} \qquad (46)$$

In the limit of very heavy flavor, it follows from (46) that

$$\Delta\epsilon_{B,F} = \bar{\omega}_{F,1} - \bar{\omega}_{F,B} - \frac{3}{8\Theta_{F,B}}, \qquad (47)$$

and, hence, in comparison with the case of odd B-numbers, there is an additional contribution that decreases with increasing B-number (because inertia increases with B) from approximately 25 MeV for $B = 3$.

Formulas (44) and (46) allow us to perform numerical estimates for the binding energies of antiflavored states, using the results for frequencies and moments of inertia presented in previous tables.

Tables 5–7 show the binding energies of favored $J = 0$ states relative to the NN scattering state ($I = 1$, $J = 0$) for $B = 2$, which differ from (46) by added $1/\Theta_{I,B=2}$.

One should keep in mind that, for the SK4 model, the value of the Θ^+ mass is equal to 1588 MeV, which is approximately 150 MeV above the kaon–nucleon threshold. Therefore, the states with the largest binding energy shown in Table 5 are unstable relative to strong interactions. For the SK6 variant, $M_\Theta = 1566$ MeV and the binding energies are considerably smaller, by approximately 40–50 MeV in some cases (this is the main feature of the SK6 variant). For the rescaled variants, the difference between both variants is reduced considerably, but the binding energies are then underestimated.

From the phenomenological standpoint, we should describe the $B = 1$ states with the original variants of models, i.e., $e = 4.12$, $e' = 4.11$ and states with $10 < B = A < 30$, using rescaled variants, as is suggested by the results of [65]. This procedure gives the most optimistic values of $\Delta\epsilon_{S=+1}$, about 145 MeV for the SK4 variant and approximately 140 MeV for the SK6 variant. However, the uncertainty of this prediction is a few tens of MeV, at least.

For anticharm and antibeauty, there is considerable difference between the SK4 and SK6 variants (Tables 6, 7). The mass of the Θ_c-hyperon in the SK4 model is 2700 MeV and the mass of Θ_b is 5880 MeV, both well below the threshold for strong decay. For the SK6 variant, these masses are by 40 and 100 MeV greater, but also below the threshold. The SK6 variant is less attractive than the SK4 variant, mainly because the antiflavor excitation energies for $B = 1$ in the SK6 variant are smaller than for $B \geq 2$, which leads to repulsion for

Table 5. The binding energy differences and total binding energies of positive strangeness Θ^+-hypernuclei (in MeV) for the SK4 and SK6 variants of the model in rational-map approximation

B	$\Delta\epsilon^{SK4}$	ϵ^{SK4}	$\Delta\epsilon^{SK4}$	ϵ^{SK6}	$\Delta\epsilon^{SK4*}$	ϵ^{SK4*}	$\Delta\epsilon^{SK6*}$	ϵ^{SK6*}
2	47	47	75	75	25	25	17	17
3	67	76	45	53	26	34	4	12
4	20	49	−4	24	9	38	−8	20
5	81	108	47	74	30	57	6	33
6	56	88	24	56	20	52	−1	31
7	83	121	41	80	32	70	7	45
8	69	126	31	87	24	81	2	58
9	94	152	53	110	33	90	8	66
10	79	144	39	103	27	92	4	68
11	99	173	56	130	33	108	9	84
12	86	178	43	135	28	120	5	97
13	101	196	56	152	33	129	9	104
14	93	197	50	154	29	133	6	111
15	105	219	61	175	33	147	9	123
16	96	224	53	181	29	157	7	134
17	105	235	61	191	33	163	9	139
18	100	237	56	194	29	167	7	144
19	109	255	65	211	33	178	10	156
20	103	263	60	220	29	190	8	168
21	111	276	67	232	32	197	10	175
22	105	279	62	236	29	203	8	182
23	113	297	69	253	32	216	10	194
24	107	305	64	263	29	228	8	206
25	113	316	70	273	31	235	10	213
26	109	321	66	278	29	241	8	220
27	115	337	72	294	31	253	10	232
28	111	347	69	305	29	265	9	245
29	116	358	73	315	31	273	10	252
30	112	363	70	321	29	279	9	259
31	117	376	75	335	30	290	10	270
32	113	385	71	343	29	300	9	281

$B > 1$, in comparison with the more familiar SK4 model. Considerable decrease of binding energies for large B, greater than $B \sim 20$, may be connected with fact that the rational-map approximation becomes unrealistic for such large baryon numbers. The beauty decay constant F_b has not been measured yet, which introduces additional uncertainty in our predictions. Probably, the value $F_b/F_\pi = 1.8$ is the best for describing the Λ_b mass.

In Table 7, we present the binding energies of hypernuclei with anticharm and antibeauty quantum numbers for the rescaled SK4 and SK6 variants of the model.

Several specific features should be emphasized. The binding energies for the rescaled variants are in general

Table 6. The total binding energy differences and binding energies themselves (in MeV) for the antiflavored states, SK4 variant (first four columns), and SK6 variant (last four columns). $F_D/F_\pi = 1.5$, $F_B/F_\pi = 2$

B	$\Delta\epsilon_{\bar c}^{\mathrm{SK4}}$	$\epsilon_{\bar c}$	$\Delta\epsilon_{\bar b}^{\mathrm{SK4}}$	$\epsilon_{\bar b}$	$\Delta\epsilon_{\bar c}^{\mathrm{SK6}}$	$\epsilon_{\bar c}$	$\Delta\epsilon_{\bar b}^{\mathrm{SK6}}$	$\epsilon_{\bar b}$
2	61	61	90	90	56	56	44	44
3	38	46	49	57	–8	0	–36	–28
4	15	44	48	76	–29	–1	–36	–7
5	44	71	55	82	–5	22	–30	–3
6	27	59	43	75	–20	12	–39	–7
7	47	85	62	101	–5	34	–23	16
8	31	87	41	98	–17	40	–37	19
9	42	100	43	100	–6	51	–33	24
10	31	96	33	98	–15	50	–40	25
11	40	114	34	108	–7	68	–37	37
12	31	123	27	119	–15	78	–42	50
16	27	154	8	136	–15	113	–50	78
17	32	162	11	141	–10	120	–47	83
20	22	183	–7	154	–15	145	–57	104
24	19	217	–19	179	–16	182	–62	136
28	15	251	–31	205	–17	220	–68	169
32	12	283	–40	232	–18	254	–72	200

Table 7. The same as in Table 6, for the rescaled SK4 and SK6 variants of the model

B	$\Delta\epsilon_{\bar c}^{\mathrm{SK4*}}$	$\epsilon_{\bar c}$	$\Delta\epsilon_{\bar b}^{\mathrm{SK4*}}$	$\epsilon_{\bar b}$	$\Delta\epsilon_{\bar c}^{\mathrm{SK6*}}$	$\epsilon_{\bar c}$	$\Delta\epsilon_{\bar b}^{\mathrm{SK6*}}$	$\epsilon_{\bar b}$
2	36	36	54	54	–5	–5	–30	–30
3	24	32	35	43	–27	–19	–59	–51
4	19	48	44	72	–26	2	–45	–16
5	27	54	39	66	–22	5	–50	–23
6	18	50	31	63	–27	5	–52	–20
7	30	69	46	84	–17	22	–38	1
8	19	75	27	84	–24	32	–49	7
9	21	78	23	80	–21	36	–49	8
10	15	80	17	82	–25	40	–52	13
11	17	91	13	88	–22	52	–52	23
12	12	104	9	101	–25	67	–53	39
16	3	131	–12	115	–28	100	–61	66
17	6	136	–10	120	–26	104	–60	70
20	–4	156	–30	131	–31	130	–68	93
24	–10	188	–43	155	–33	166	–73	125
28	–17	220	–57	179	–35	202	–78	158
32	–21	251	–67	205	–37	235	–82	190

smaller than those for the original variants (Table 6), mainly due to the decrease in excitation energies for the $B = 1$ configuration (by approximately 100 MeV for the anticharm and 110 MeV for antibeauty). For greater B-numbers, this decrease is smaller. However, because the rescaled or nuclear variant is valid for sufficiently large baryon numbers, the binding energies can be greater than the values given in Tables 6 and 7, at least for B-numbers greater than approximately 10. This is similar to the situation with the strangeness quantum number (see Table 5 and its discussion).

5. CONCLUSIONS

The excitation energies of antiflavors are estimated within the bound-state version of the chiral soliton model in two different variants of the model, SK4 and SK6, and for two values of the model parameter (e or e'; see Tables 3 and 4). The bounds for the expected binding energies of hypernuclei are obtained in this way. These bounds are wide: variations of the total binding energy for the SK4 and SK6 models can reach 40–50 MeV. The difference between the original (baryon) variant and the rescaled (nuclear) variant is greater for strangeness and smaller for anticharm and antibeauty, where it is no greater than approximately 20–30 MeV for baryon numbers between 3 and approximately 20. If the logic is correct that the rescaled or nuclear variant of the model should be applied for sufficiently large B-numbers, beginning with $B \sim 10$, then we should expect the existence of weakly decaying hypernuclei with anticharm and antibeauty.

The properties of multiskyrmion configurations necessary for these numerical estimates have been calculated within the rational-map approximation [46], which provides remarkable scaling laws for the excitation energies of heavy antiflavors. This scaling property of heavy flavors (antiflavors) excitation energies, noted previously [43, 63] and confirmed in the present paper by numerical calculations, is fulfilled with good accuracy. The relative role of the quantum correction on the order of $1/N_c$ (hyperfine splitting) decreases with increasing baryon number as $1/B$, and, therefore, in addition to the $1/N_c$-expansion widely used and discussed in the literature, the $1/B$-expansion and arguments can be used to justify the chiral soliton approach at sufficiently large values of the baryon number.

Positive strangeness nuclear states are mostly bound relative to the decay into Θ^+ and nuclear fragments, and one can therefore talk about Θ^+ hypernuclei [54, 71]. The particular value of the binding energy depends on the variant of the model and is greater for the original SK4 variant (Table 5). The existence of deeply bound states is not excluded by our treatment, although the energy of the state is, in most cases, sufficient for the strong decay into kaon and residual nucleus or nuclear fragments.

The binding energies of the ground states of hypernuclei with heavy antiflavors ($\bar{c}$ or $\bar{b}$) shown in Tables 6 and 7 are more stable relative to variations of the model parameters (e or e'), but more sensitive to the model itself. Similarly to the case of antistrangeness, the binding energies for the SK6 variant of the model are systematically smaller than for the SK4 variant.

Within our approach, it is possible to obtain the spectra of excited states with greater values of isospin and angular momentum. The energy scale in the first case is given by $1/\Theta_I$ and in the second by $1/\Theta_J$, which is much smaller for large baryon numbers. Because $1/\Theta_I = 1/\Theta_J \approx 180$ MeV for $B = 1$ (see Table 1), it seems difficult, within the chiral soliton approach, to obtain such small spacing between the ground state and excited levels as derived, e.g., in [53] within the quark models.

Although we performed considerable numerical work, we feel that further refinements, improvements, and more precise calculations are necessary. For example, possible contributions on the order of $1/N_c$ to the flavor excitation energies mentioned, e.g., in [44], might change our conclusions. When the calculations for the present paper were finished, we became aware of papers [71, 72], where the possibility of the existence of antistrange Θ hypernuclei is discussed within more conventional approaches. The results obtained in [71, 72] qualitatively agree with ours.

ACKNOWLEDGMENTS

We thank V.A. Matveev and V.A. Rubakov for discussions and remarks. V.B.K. is indebted to Ya.I. Azimov and I.I. Strakovsky for useful e-mail discussions, and to M. Karliner, H. Walliser, and H. Weigel for numerous valuable discussions. The results of the present paper have been reported in part at the QFTHEP Conference, Peterhof, Russia, June 19–25, 2004, and the Symposium of London Mathematical Society, Durham, UK, August 2–12, 2004.

APPENDIX

Comparison of the Flavor and Antiflavor Excitation Energy Difference in the Rigid Rotator and Bound-State Models

Here, we show that the difference between flavor and antiflavor excitation energies given by (23) coincides with the difference of the $SU(3)$ rotation energies between exotic and nonexotic multiplets within the rigid rotator approach, in the leading-N_c approximation. The method used here is similar to that in [22] applied for arbitrary B-numbers and $N_c = 3$. The generalization to arbitrary N_c and N_F was recently made in [70]. For nonexotic multiplets, we have the quantization condition $p + 2q = N_cB$ [61]; we take $p = 1$ for odd B-numbers and $p = 0$ for even B. The contribution to the

$SU(3)$ rotation energy depending on the flavor moment of inertia, which is of interest here, is equal to [61]

$$\begin{gathered} E^{\mathrm{rot}}(SU_3) = \frac{1}{2\Theta_F} \\ \times [C_2(SU_3)(p, q) - I_r(I_r + 1) - N_c^2 B^2/12] \end{gathered} \qquad (48)$$

with

$$\begin{aligned} C_2(SU_3) &= \frac{p^2 + q^2 + pq}{3} + p + q \\ &= \frac{(p + 2q)^2 + 3p^2}{12} + \frac{p + 2q}{2} + \frac{p}{2}. \end{aligned}$$

The right isospin for the lowest nonexotic states is $I_r = p/2 = 0$ for even B (as for the nuclei ^{4}He, ^{12}C, ^{16}O, etc.) and $I_r = p/2 = 1/2$ for odd B (as for the isodoublets ^{3}H–^{3}He, ^{5}He–^{5}Li, etc.).

The lowest possible exotic irreducible $SU(3)$ representation (p, q) for each value of the baryon number B is defined by the relations

$$p' + 2q' = N_c B + 3m;$$

m coincides with the number of additional quark–antiquark pairs for several lowest values of p'. The difference of the $SU(3)$ rotation energies for exotic and nonexotic multiplets is given by

$$\begin{gathered} \Delta E^{\mathrm{rot}} = \frac{1}{2\Theta_{F,B}}[C_2(SU_3)' - C_2(SU_3) \\ - I'_r(I'_r + 1) + I_r(I_r + 1)]. \end{gathered} \qquad (49)$$

After simple transformations, it can be written as

$$\begin{gathered} \Delta E^{\mathrm{rot}} = \frac{1}{2\Theta_{F,B}}\left[\frac{m(2N_cB + 3m) + p'^2 - p^2)}{4}\right. \\ \left. + \frac{3m}{2} + \frac{p' - p}{2} + (I_r - I'_r)(I_r + I'_r + 1)\right]. \end{gathered} \qquad (50)$$

If $m = 1$, for the lowest irreducible $SU(3)$ representations, we have

$$p' = 1 \quad \text{and} \quad q' = (N_c B + 2)/2$$

for even B and

$$p' = 0 \quad \text{and} \quad q' = (N_c B + 3)/2$$

for odd B. We should keep in mind that the right isospin is given by

$$I'_r = \frac{p' + 1}{2} = I_r + 1$$

for $B = 2, 4, \ldots$ and

$$I'_r = \frac{p' + 1}{2} = I_r$$

for $B = 1, 3, 5, \ldots$. For charm or beauty, due to the large configuration mixing caused by large values of D- or B-meson masses present in the Lagrangian, such lowest irreducible representations are often not the main component of the mixed state ([51] may be of interest in this connection), but for strangeness, they are.

For even B ($m = 1$, $p = 0$, $p' = 1$), we have

$$\Delta E^{\mathrm{rot}} = \frac{1}{4\Theta_{F,B}}[N_c B + 2]. \qquad (51)$$

For odd B ($p = 1$, $p' = 0$), we obtain

$$\Delta E^{\mathrm{rot}} = \frac{1}{4\Theta_{F,B}}[N_c B + 3]. \qquad (52)$$

For $N_c = 3$ and $B = 1$, this coincides with well-known expression for the mass difference between the antidecuplet and the octet of baryons.

The leading-N_c contribution is the same as given by (23). For arbitrary m, the leading contribution is

$$\Delta E^{\mathrm{rot}} = \frac{m N_c B}{4\Theta_{F,B}}$$

for any multiplets with the final values of p' and I_r, including the values not considered here. It is worth noting that the correction to the leading contribution decreases not only with increasing N_c but also with increasing B (we recall that $\Theta_{F,B} \sim N_c B$). Therefore, convergence of both methods is better for larger values of B.

REFERENCES

1. T. Nakano *et al.* (LEPS Collab.), Phys. Rev. Lett. **91**, 012002 (2003); hep-ex/03010020; V. V. Barmin *et al.* (DIANA Collab.), Yad. Fiz. **66**, 1763 (2003) [Phys. At. Nucl. **66**, 1715 (2003)]; hep-ex/0304040.
2. S. Stepanyan *et al.* (CLAS Collab.), Phys. Rev. Lett. **91**, 252001 (2003); J. Barth *et al.* (SAPHIR Collab.), Phys. Lett. B **572**, 127 (2003); V. Kubarovsky and S. Stepanyan (CLAS Collab.), AIP Conf. Proc. **698**, 543 (2003); hep-ex/0307088; A. E. Asratyan, A. G. Dolgolenko, and M. A. Kubantsev, Yad. Fiz. **67**, 704 (2004) [Phys. At. Nucl. **67**, 682 (2004)]; V. Kubarovsky *et al.* (CLAS Collab.), Phys. Rev. Lett. **92**, 032001 (2004); A. Airapetian *et al.* (HERMES Collab.), Phys. Lett. B **585**, 213 (2004); R. Togoo *et al.*, Proc. Mongolian Acad. Sci. **4**, 2 (2003); A. Aleev *et al.* (SVD Collab.), submitted to Yad. Fiz.; hep-ex/0401024; M. Abdel-Bary *et al.* (COSY-TOF Collab.), hep-ex/0403011; S. Chekanov *et al.* (ZEUS Collab.), Phys. Lett. B **591**, 7 (2004); hep-ex/0403051; M. Barbi (for ZEUS and H1 Collab.), hep-ex/0407006.

3. M. Karliner and H. J. Lipkin, hep-ph/0307243; Phys. Lett. B **575**, 249 (2003); hep-ph/0307343; hep-ph/0401072.
4. R. Jaffe and F. Wilczek, hep-ph/0307341; Phys. Rev. Lett. **91**, 232003 (2003); hep-ph/0312369.
5. F. Close, *Summary Talk at the Baryon03 Conference*; hep-ph/0311087; AIP Conf. Proc. **717**, 919 (2004); hep-ph/0411396.
6. J. J. Dudek and F. E. Close, hep-ph/0311258; F. E. Close and J. J. Dudek, hep-ph/0401192.
7. K. Maltman, hep-ph/0408144; hep-ph/0412328.
8. J. Ping, D. Qing, F. Wang, and T. Goldman, hep-ph/0408176.
9. C. Alt *et al.* (NA49 Collab.), Phys. Rev. Lett. **92**, 042003 (2004); hep-ex/0310014.
10. H. G. Fischer and S. Wenig, hep-ex/0401014; Eur. Phys. J. C **37**, 133 (2004).
11. A. Aktas *et al.* (H1 Collab.), Phys. Lett. B **588**, 17 (2004); hep-ex/0403017.
12. M. I. Adamovich *et al.* (WA89 Collab.), hep-ex/0405042; U. Karshon (for ZEUS Collab.), hep-ex/0407004; I. Abt (for the HERA-B Collab.), hep-ex/0408048; B. Aubert (for the BABAR Collab.), hep-ex/0408064.
13. J. Pochodzalla, hep-ex/0406077.
14. V. D. Burkert, R. De Vita, S. Niccolai, and the CLAS Collab., nucl-ex/0408019; K. Hicks, hep-ph/0408001; hep-ex/0412048; V. D. Burkert, nucl-ex/0412033.
15. R. L. Jaffe, *Talk at the Topical Conference on Baryon Resonances* (Oxford, England, 1976), SLAC-PUB-1774; Phys. Rev. D **15**, 281 (1977).
16. H. Hogaasen and P. Sorba, Nucl. Phys. B **145**, 119 (1978); D. Strottman, Phys. Rev. D **20**, 748 (1979).
17. C. Roiesnel, Phys. Rev. D **20**, 1646 (1979).
18. A. V. Manohar, Nucl. Phys. B **248**, 19 (1984); M. Chemtob, Nucl. Phys. B **256**, 600 (1985).
19. M. Karliner and M. P. Mattis, Phys. Rev. D **34**, 1991 (1986).
20. L. C. Biedenharn and Y. Dothan, in *From SU(3) to Gravity (Ne'eman Festschrift)* (Cambridge Univ. Press, Cambridge, 1986).
21. M. Praszalowicz, *Talk at the Cracow Workshop on Skyrmions and Anomalies* (Mogilany, Poland, 1987).
22. V. B. Kopeliovich, NORDITA Preprint 90/55 NP (1990); Phys. Lett. B **259**, 234 (1991).
23. H. Walliser, Nucl. Phys. A **548**, 649 (1992); in *Proceedings of the Workshop on Baryons as Skyrme Solitons, Seigen, Germany, 1992*, Ed. by G. Holzwarth (World Sci., Singapore, 1992), p. 247.
24. D. Diakonov, V. Petrov, and M. Polyakov, Z. Phys. A **359**, 305 (1997).
25. H. Weigel, Eur. Phys. J. A **2**, 391 (1998).
26. R. L. Jaffe, hep-ph/0401187, v2; hep-ph/0405268.
27. V. B. Kopeliovich, B. Schwesinger, and B. E. Stern, Nucl. Phys. A **549**, 485 (1992).
28. D. Diakonov, V. Petrov, and M. Polyakov, hep-ph/0404212.
29. T. Cohen, Phys. Lett. B **581**, 175 (2004); hep-ph/0309111.
30. N. Itzhaki, I. R. Klebanov, P. Ouyang, and L. Rastelli, Nucl. Phys. B **684**, 264 (2004); I. Klebanov and P. Ouyang, hep-ph/0408251.
31. H. Walliser and V. B. Kopeliovich, Zh. Éksp. Teor. Fiz. **124**, 483 (2003) [JETP **97**, 433 (2003)]; hep-ph/0304058.
32. D. Borisyuk, M. Faber, and A. Kobushkin, hep-ph/0307370; Ukr. Phys. J. **49**, 944 (2004).
33. M. Praszalowicz, Phys. Lett. B **575**, 234 (2003); hep-ph/0308114.
34. B. Wu and B.-Q. Ma, hep-ph/0312041; hep-ph/0408121.
35. J. Ellis, M. Karliner, and M. Praszalowicz, J. High Energy Phys., 0405002 (2004); hep-ph/0401127.
36. G. Duplancic, H. Pasagic, and J. Trampetic, hep-ph/0404193; hep-ph/0405029; J. High Energy Phys., 0407027 (2004); B. J. Park, M. Rho, and D. P. Min, hep-ph/0405246; H. K. Lee and H. Y. Park, hep-ph/0406051.
37. H. Weigel, Eur. Phys. J. A **21**, 133 (2004); hep-ph/0404173; hep-ph/0405285.
38. B. K. Jennings and K. Maltman, Phys. Rev. D **69**, 094020 (2004); V. B. Kopeliovich, Usp. Fiz. Nauk **174**, 323 (2004) [Phys. Usp. **47**, 309 (2004)]; D. Diakonov, hep-ph/0406043; S. L. Zhu, hep-ph/0406204; M. Oka, hep-ph/0406211; Ya. I. Azimov and I. I. Strakovsky, hep-ph/0406312.
39. H. J. Lipkin, Phys. Lett. B **195**, 484 (1987).
40. D. O. Riska and N. N. Scoccola, Phys. Lett. B **299**, 338 (1993).
41. Y. Oh, B. Y. Park, and D. P. Min, Phys. Lett. B **331**, 362 (1994); Phys. Rev. D **50**, 3350 (1994).
42. V. B. Kopeliovich and M. S. Sriram, Phys. At. Nucl. **63**, 480 (2000); hep-ph/9809394.
43. V. B. Kopeliovich and W. J. Zakrzewski, Eur. Phys. J. C **18**, 369 (2000); Pis'ma Zh. Éksp. Teor. Fiz. **69**, 675 (1999) [JETP Lett. **69**, 721 (1999)]; hep-ph/9904386.
44. K. M. Westerberg and I. R. Klebanov, Phys. Rev. D **50**, 5834 (1994); **53**, 2804 (1996).
45. C. G. Callan and I. R. Klebanov, Nucl. Phys. B **262**, 365 (1985); N. Scoccola, H. Nadeau, M. Nowak, and M. Rho, Phys. Lett. B **201**, 425 (1988).
46. C. J. Houghton, N. S. Manton, and P. M. Sutcliffe, Nucl. Phys. B **510**, 507 (1998).
47. V. Kopeliovich, B. Schwesinger, and B. Stern, Pis'ma Zh. Éksp. Teor. Fiz. **62**, 477 (1995) [JETP Lett. **62**, 185 (1995)].
48. V. Kopeliovich, hep-ph/0310071; in *Proceedings of the Conference on Electroproduction of Strangeness on Nucleons and Nuclei, Sendai, Japan, 2003*, Ed. by K. Maeda, H. Tamura, S. N. Nakamura, and O. Hasimoto (World Sci., Singapore, 2004), p. 96.
49. K. Cheung, hep-ph/0308176; B. Wu and B.-Q. Ma, Phys. Rev. D **70**, 034025 (2004).
50. P.-Z. Huang *et al.*, hep-ph/0401191; I. Stewart, M. Wessling, and M. Wise, hep-ph/0402076.
51. P. Bicudo, hep-ph/0403295; P. Bicudo and G. M. Marques, Phys. Rev. D **69**, 011503(R) (2004).

52. S. Sasaki, Phys. Rev. Lett. **93**, 152001 (2004); T.-W. Chiu and T.-H. Hsieh, hep-ph/0404007; H. Kim and S. H. Lee, hep-ph/0404170.
53. K. Maltman, hep-ph/0408145; hep-ph/0412327.
54. G. A. Miller, nucl-th/0402099; Phys. Rev. C **70**, 022202(R) (2004).
55. T. H. R. Skyrme, Proc. R. Soc. London, Ser. A **260**, 127 (1961); Nucl. Phys. **31**, 556 (1962).
56. E. Witten, Nucl. Phys. B **223**, 422 (1983); **223**, 433 (1983).
57. A. Jackson *et al.*, Phys. Lett. B **154**, 101 (1985); A. Jackson, A. D. Jackson, and V. Pasquier, Nucl. Phys. A **432**, 567 (1985).
58. L. Marleau, Phys. Lett. B **235**, 141 (1990); Phys. Lett. B **244**, 580(E) (1990); Phys. Rev. D **45**, 1776 (1992); L. Marleau and J.-F. Rivard, Phys. Rev. D **63**, 036007 (2001).
59. I. Floratos and B. M. A. G. Piette, Phys. Rev. D **64**, 045009 (2001); J. Math. Phys. **42**, 5580 (2001).
60. B. Schwesinger and H. Weigel, Phys. Lett. B **267**, 438 (1991); H. Weigel, Int. J. Mod. Phys. A **11**, 2419 (1996).
61. E. Guadagnini, Nucl. Phys. B **236**, 35 (1984).
62. R. A. Battye and P. M. Sutcliffe, Rev. Math. Phys. **14**, 29 (2002).
63. V. B. Kopeliovich, Zh. Éksp. Teor. Fiz. **120**, 499 (2001) [JETP **93**, 435 (2001)]; J. Phys. G **28**, 103 (2002); Pis'ma Zh. Éksp. Teor. Fiz. **73**, 667 (2001) [JETP Lett. **73**, 587 (2001)].
64. A. M. Shunderuk, Yad. Fiz. **67**, 769 (2004) [Phys. At. Nucl. **67**, 748 (2004)].
65. V. B. Kopeliovich, A. M. Shunderuk, and G. K. Matushko, nucl-th/0404020; submitted to Yad. Fiz. (2005).
66. V. B. Kopeliovich, Zh. Éksp. Teor. Fiz. **123**, 891 (2003) [JETP **96**, 782 (2003)].
67. S. Nussinov, hep-ph/0307357; R. A. Arndt, I. I. Strakovsky, and R. L. Workman, Phys. Rev. C **68**, 042201(R) (2003); R. L. Workman *et al.*, nucl-th/0410110; W. R. Gibbs, nucl-th/0405024.
68. M. Praszalowicz, Phys. Lett. B **583**, 96 (2004); hep-ph/0311230.
69. B. L. Ioffe and A. G. Oganesian, Pis'ma Zh. Éksp. Teor. Fiz. **80**, 439 (2004) [JETP Lett. **80**, 386 (2004)]; hep-ph/0408152.
70. E. Jenkins and A. Manohar, hep-ph/0402024; Phys. Rev. D **70**, 034023 (2004).
71. D. Cabrera, Q. B. Li, V. K. Magas, *et al.*, nucl-th/0407007.
72. X. H. Zhong, Y. N. Tan, L. Li, and P. Z. Ning, nucl-th/0408046.

Journal of Experimental and Theoretical Physics, Vol. 100, No. 5, 2005, pp. 949–963.
Translated from Zhurnal Éksperimental'noĭ i Teoreticheskoĭ Fiziki, Vol. 127, No. 5, 2005, pp. 1075–1090.
Original Russian Text Copyright © 2005 by Belim.

ORDER, DISORDER, AND PHASE TRANSITIONS IN CONDENSED SYSTEMS

Effects of Long-Range Interaction on Critical and Multicritical Behavior of Compressible Disordered Systems

S. V. Belim
Omsk State University, pr. Mira 55, Omsk, 644077 Russia
e-mail: belim@univer.omsk.su

Received September 25, 2004

Abstract—A field-theoretic approach is applied to describe behavior of weakly disordered, isotropic elastic compressible systems with long-range interactions directly in the three-dimensional space for various values of the long-range interaction parameter a. A renormalization-group procedure is applied separately for $a > 2$ and $a \leq 2$ directly in the three-dimensional space. Renormalization-group equations are analyzed in the two-loop approximation, and critical and tricritical points are determined. It is shown that long-range effects are not important when $a \leq 2$, whereas they play a key role in the opposite case of $a > 2$. Critical exponents characterizing the system are obtained for various values of the long-range interaction parameter. Behavior of homogeneous and disordered systems characterized by two fluctuating order parameters is also described. *© 2005 Pleiades Publishing, Inc.*

1. INTRODUCTION

It is well known that critical behavior is determined by several parameters, including dimension, symmetry of the order parameter, and long-distance behavior of interaction. Of particular interest are systems with competing short- and long-range interactions. In conventional Ising-like systems, the coupling between fluctuations decays as $\exp(-r/r_0)$. For this reason, only nearest-neighbor interactions are taken into consideration, and systems of this type can be classified as short-range ones. When the coupling behaves as r^{-D-a}, where D is the space dimension, analysis cannot be restricted to nearest-neighbor interactions, and long-range effects must be taken into account.

It was shown in [1] that three types of critical behavior can be obtained by using ε expansion ($\varepsilon = 2a - D$), depending on the value of a. When $a \geq 2$, critical behavior is characterized by critical exponents similar to those of short-range systems; i.e., long-range order/effects are insignificant. When $a \leq D/2$, a strong effect of long-range interaction manifests itself in a phase transition characterized by a "standard" Gaussian fixed point with the critical exponents $\eta = 2 - a$, $\nu = 1/a$, and $\gamma = 1$. The correlation radius and susceptibility behave as

$$R_c \sim \tau^{-1/a}(\ln\tau^{-1})^{n'/a}, \quad \chi \sim \tau^{-1}(\ln\tau^{-1})^{n'}, \qquad (1)$$

where $\tau = |T - T_c|/T_c$ (T_c is the phase-transition temperature) and $n' = (n + 2)/(n + 8)$ (n is the order-parameter dimension. When $D/2 < a < 2$, long-range effects are weaker than in the "standard" regime. Therefore, the system exhibits non-Gaussian behavior characterized by the critical exponents $\eta = 2 - a + o(\varepsilon^2)$, $\nu = 1/a(1 + o(\varepsilon))$, and $\gamma = 1 + o(\varepsilon)$.

It was shown in [2] that long-range effects play an essential role in the critical behavior of a short-range system with $a \geq 2$ if the corresponding Fisher exponent η_{SR} is negative and $a < 2 - \eta_{SR}$.

The renormalization-group study of the critical behavior of one-dimensional systems developed in [3] by using expansion in terms of $1 - a > 0$ has shown that $1/\nu = 2(1 - a)^{1/2}$ in the limit of $a \longrightarrow 1$. The results of Monte Carlo simulations of Ising-like systems with long-range interactions reported in [4] for $D = 1$ and $D = 2$ largely agree with predictions of the renormalization-group analysis. However, certain details revealed in the simulations disagree with theoretical predictions. In particular, the value of ν obtained for one-dimensional systems in the case of $a = 1$ is much greater than that predicted by the renormalization-group analysis. Moreover, crossover to critical behavior characteristic of short-range systems is observed when $a > 3$ rather than 2 (as predicted by the theory). Monte Carlo simulations performed in [5] for $D = 2$ show that the crossover between long- and short-range critical behavior corresponds to $a = 1.75$, which also disagrees with the theory. The critical exponents obtained in that study are in good agreement with the results of the ε expansion for $a < 1.6$. The predictions obtained for larger values of the long-range interaction parameter substantially differ from those based on the renormalization-group analysis.

The discussion above suggests that critical exponents must be calculated directly in the three-dimensional space (without using ε expansion) in the framework of a field-theoretic approach, which is known to yield results in better agreement with experiment. In this paper, a field-theoretic analysis is performed to describe critical and multicritical behavior of Ising-like systems with long-range interactions. The effects of quenched disorder and elastic deformation on critical and multicritical behavior of long-range systems are also examined. The present analysis is restricted to systems with scalar order parameters (Ising-like systems), because the Harris criterion implies that effects of disorder are essential only for systems of this kind.

Elastic-strain–order-parameter coupling plays an important role in the behavior of compressible systems. It was shown in [6] that the critical behavior of an isotropic elastic solid modeled by a compressible lattice with quadratic striction is unstable with respect to the phonon–order-parameter coupling, and the system exhibits a weak first-order (nearly second-order) phase transition. Analysis becomes more complicated when elastic anisotropy is taken into account [7–10], but does not lead to qualitatively different results. Whereas the change in the type of phase transition induced by inhomogeneous deformation is a subtle effect due to fluctuations, external pressure is a much stronger factor that changes the sign of the effective constant of coupling between order parameters and the order of phase transition.

In structural transitions that do not involve piezoelectric effects in the paraphase, elastic strain plays the role of a secondary order parameter, and its fluctuations are not critical in most cases. In [11, 12], the general idea of phase transition in a system with an order parameter associated with nonfluctuating (additional) variables was used as a basis for analyses of the effect of quenched impurities on possible types of phase transitions using the lowest order ε expansion under various macroscopic constraints. Under the condition of constant stress, the phase trajectories leaving the neighborhood of the tricritical point of a disordered system were found to escape from the domain of stable second-order phase transition, and the transition was smeared out. In the absence of constant stress, the system did not exhibit tricritical behavior, second-order phase transitions were obtained, and the predicted crossover was analogous to that obtained in the lowest order ε expansion, i.e., the critical behavior was strongly changed by disorder when $n < 4$ and remained unchanged when $n > 4$. These results are quite obvious, because both self-coupling of order-parameter fluctuations and their coupling via the impurity field are described by closed renormalization-group equations in the lowest order perturbation theory. Vertices that represent coupling to additional variables must appear only in the next-order corrections to the theory and may drastically change the results.

It was shown in [11, 12] that elastic-strain–order-parameter coupling can lead to crossover in critical behavior and appearance of tricritical and tetracritical points in the phase diagram. Quenched disorder not only changes critical behavior, but also eliminates multicritical points [13].

This study also deals with systems whose phase diagrams contain bicritical and tetracritical points, i.e., points of intersection of two second-order transition lines with a first-order transition line and those where four second-order transition lines intersect, respectively. The behavior of a system in the neighborhood of a multicritical point is characterized by competing types of ordering. Whereas crossover from one order parameter to the other occurs at a bicritical point, ordering types can coexist in a mixed phase at a tetracritical point. Such systems can be described in terms of two order parameters that are transformed under different irreducible representations.

Quenched disorder changes the behavior of short-range systems near both bicritical and tetracritical points (see [14], where it was shown that order parameters are decoupled at a multicritical point in the case of delta-correlated disorder). In [15], it was revealed that elastic deformation induces change from bicritical to tetracritical behavior in homogeneous systems. In disordered systems [16], effects due to strain degrees of freedom lead to crossover in tetracritical behavior, while the type of multicritical behavior remains unchanged.

2. RENORMALIZATION-GROUP ANALYSIS

In a general model that takes into account both short- and long-range interactions, the Fourier transform $v(q)$ of the coupling between critical fluctuations can be written as the following function of $|q|$:

$$v(|q|) = v_0 + j_2|q|^2 + j_a|q|^a + w(|q|), \qquad (2)$$

where $w(q)/q^{\max(a,\,2)} \longrightarrow 0$ as $q \longrightarrow 0$.

For an Ising-like system near the critical point, a Hamiltonian including elastic strain can be written as

$$\begin{aligned} H_0 = {} & \frac{1}{2}\int d^D q(\tau_0 + j_a q^a + j_2 q^2) S_q S_{-q} \\ & + \frac{1}{2}\int d^D q \Delta\tau_q S_q S_{-q} \\ & + u_0 \int d^D q_1 d^D q_2 d^D q_3 S_{q1} S_{q2} S_{q3} S_{-q1-q2-q3} \\ & + a_3 \int d^D q_1 d^D q_2 y_{q1} S_{q2} S_{-q1-q2} \\ & + \frac{a_3^{(0)}}{\Omega} y_0 \int d^D q S_q S_{-q} + \frac{1}{2} a_1 \int d^D q y_q y_{-q} \\ & + \frac{1}{2}\frac{a_1^{(0)}}{\Omega} y_0^2 + \int d^D q h_q y_q + \frac{h_0}{\Omega} y_0, \end{aligned} \qquad (3)$$

where S_q is a fluctuating order parameter, u_0 is a positive constant, $\tau_0 \sim |T - T_c|/T_c$ (T_c is the phase-transition temperature), a is the long-range interaction parameter, the parameter j_a characterizes the relative strength of long-range interactions, the parameter j_2 characterizes the relative strength of short-range interactions, $\Delta\tau_q$ is a random impurity field (e.g., random temperature), a_1 and a_2 are the elastic constants of a crystal, and a_3 is the quadratic striction constant. The coupling between the impurity field and the nonfluctuating order parameter

$$y(x) = \sum_{\alpha=1}^{3} u_{\alpha\alpha}(x),$$

where $u_{\alpha\beta}$ is the strain tensor, is described by introducing the random field h_q thermodynamically conjugate to $u_{\alpha\alpha}(x)$. In (3), integration is performed in the terms depending on the nonfluctuating variables that are not coupled to the order parameter S_q, and the y_0 terms (describing homogeneous deformation) are separated. It was shown in [6] that this separation is necessary because the inhomogeneous deformations represented by y_q are responsible for exchange of acoustic phonons and for long-range effects that are absent under homogeneous deformation.

In the framework of the ε expansion with $\varepsilon = 2a - D$, if $a < 2$, then the term $j_a q^a$ transforms into $j_a q'^a$ with $q' = qb$ under a renormalization group transformation with scaling parameter b (see [1]). The coefficient of q^2 decreases as b^{a-2}, while the coefficient of S^4 scales with b^{2a-D}. Thus, long-range interaction changes the critical dimension, and the Gaussian fixed point plays a dominant role when $D > 2a$, because the S^4 term vanishes as $b \longrightarrow \infty$. Since the term $j_2 q^2$ is negligible when $a < 2$, the system exhibits Gaussian critical behavior when $a \le D/2$. When $D/2 < a < 2$, non-Gaussian critical behavior depending on the long-range interaction parameter is observed.

When $a \ge 2$, the term $j_2 q^2$ transforms into $j_2 q'^2$ with $q' = qb$ under a renormalization group transformation with scaling parameter b. The coefficient of q^a decreases as b^{2-a} while the coefficient of S^4 scales with b^{4-D}; i.e., the critical dimension is 4, as in systems without long-range interactions. The term $j_a q^a$ is negligible when $a \ge 2$.

When the impurity concentration is low, the random fields $\Delta\tau_q$, h_q, and h_0 can be modeled by using a Gaussian distribution function:

$$\begin{aligned}P[\Delta\tau, h, h_0] = A\exp\Big[&-\frac{1}{8b_1}\int\Delta\tau_q^2 d^D q \\ &-\frac{1}{8b_2}\int h_q^2 d^D q - \frac{1}{8b_3}\int h_0 d^D q \\ &-\frac{1}{4b_4}\int\Delta\tau_q h_q d^D q - \frac{1}{4b_5}\int\Delta\tau_q h_0 d^D q\Big],\end{aligned} \tag{4}$$

where A is a normalization factor and b_i denote a positive constant proportional to the concentration of quenched impurities.

Using the standard replica trick to average over the random impurity field, one obtains the effective Hamiltonian

$$\begin{aligned}H_R = {}& \frac{1}{2}\int d^D q(\tau_0 + j_a q^a + j_2 q^2)\sum_{a=1}^{m} S_q^a S_{-q}^a \\ &-\frac{\delta_0}{2}\sum_{a,b=1}^{m}\int d^D q_1 d^D q_2 d^D q_3 S_{q1}^a S_{q2}^a S_{q3}^b S_{-q1-q2-q3}^b \\ &+u_0\sum_{a=1}^{m}\int d^D q_1 d^D q_2 d^D q_3 S_{q1}^a S_{q2}^a S_{q3}^a S_{-q1-q2-q3}^a \\ &+g_0\sum_{a=1}^{m}\int d^D q_1 d^D q_2 y_{q1}^a S_{q2}^a S_{-q1-q2}^a \\ &+\frac{g_0^{(0)}}{\Omega}\sum_{a=1}^{m} y_0^a\int d^D q S_q^a S_{-q}^a \\ &+\frac{1}{2}\lambda\int d^D q y_q y_{-q} + \frac{1}{2}\frac{\lambda_0}{\Omega}y_0^2,\end{aligned} \tag{5}$$

where the positive constant parameters δ_0, g_0, $g_0^{(0)}$, λ, and λ_0 can be expressed in terms of a_i and b_i. The characteristics of the original system can be calculated by analytic continuation as $m \longrightarrow 0$.

Define an effective Hamiltonian depending only on the strongly fluctuating order parameter S by the relation

$$\exp\{-H[S]\} = B\int\exp\{-H_R[S, y]\}\prod dy_q. \tag{6}$$

If an experiment is carried out at constant volume, then y_0 is a constant and integration in (6) is performed over inhomogeneous deformations, whereas homogeneous deformations do not contribute to the effective Hamiltonian. At constant pressure, the Hamiltonian contains the additional term $P\Omega$, volume is represented in terms of the strain tensor components as

$$\Omega = \Omega_0\left[1 + \sum_{\alpha=1} u_{\alpha\alpha} + \sum_{\alpha\ne\beta} u_{\alpha\alpha}u_{\beta\beta} + O(u^3)\right], \tag{7}$$

and integration over homogeneous deformations is also performed in (6). It was noted in [8] that the quadratic terms in (7) can be important at high pressures and for crystals with significant striction effects. The resulting Hamiltonian is

$$\begin{aligned} H &= \frac{1}{2}\int d^D q(\tau_0 + j_a q^a + j_2 q^2)\sum_{a=1}^{m} S_q^a S_{-q}^a \\ &+ v_0 \sum_{a=1}^{m} \int d^D q_1 d^D q_2 d^D q_3 S^a_{q1} S^a_{q2} S^a_{q3} S^a_{-q1-q2-q3} \\ &- \frac{\delta}{2}\sum_{a,b=1}^{m} \int d^D q_1 d^D q_2 d^D q_3 \\ &\times S^a_{q1} S^a_{q2} S^b_{q3} S^b_{-q1-q2-q3} \\ &+ \frac{1}{2\Omega}(z_0 - w_0)\sum_{a=1}^{m} \int d^D q_1 d^D q_2 S^a_{q1} S^a_{-q1} S^a_{q2} S^a_{-q2}, \end{aligned} \tag{8}$$

$$z_0 = \frac{g_0^2}{\lambda}, \quad w_0 = \frac{g_0^{(0)2}}{\lambda_0}, \quad v_0 = w_0 - \frac{z_0}{2}.$$

The effective coupling constant $v_0 = u_0 - z_0/2$, which arises in the Hamiltonian owing to the striction effects determined by g_0, can have positive and negative values. Therefore, the Hamiltonian can be used to describe both first- and second-order phase transitions. When $v_0 = 0$, the system exhibits tricritical behavior. Furthermore, the effective interaction determined by the difference $z_0 - w_0$ in (8) can also lead to a change in phase-transition order. This representation of the effective Hamiltonian entails the existence of a higher order critical point where tricritical curves intersect when $v_0 = 0$ and $z_0 = w_0$ [17]. Note that Hamiltonian (8) is isomorphic to the Hamiltonian of the disordered Ising model with long-range interactions under the tricritical condition $z_0 = w_0$.

The behavior of the system near critical and tricritical points is determined by the values of the effective charges at the renormalization-group fixed point. When $a \geq 2$, the renormalization-group relations are

$$y_q^{(0)} = Z_1 y_q, \quad y_0^{(0)} = Z_0 y_0, \quad S_q^{(0)} = Z^{1/2} S_q,$$

$$\begin{gathered} \tau_0 = b^3 \tau Z_\tau, \quad w_0 = b^{4-D} u Z_u, \quad \delta_0 = b^{4-D}\delta Z_\delta, \\ g_0 = b^{2-D/2} g Z_g, \quad g_0^{(0)} = b^{2-D/2} g^{(0)} Z_g^{(0)}, \end{gathered} \tag{9}$$

$$j_0^{(1)} = b^{2-a} j^{(1)} Z_{j1}, \quad j_0^{(1)} = j_a/j_2.$$

The scaling parameter b is introduced to change to dimensionless quantities. It is obvious that the renormalization-group transformations of the effective charges and the corresponding values of fixed points are similar to those in the absence of long-range interactions.

When $a < 2$, the renormalization-group procedure is defined by the relations

$$\begin{gathered} y_q^{(0)} = Z_1 y_q, \quad y_0^{(0)} = Z_0 y_0, \quad S_q^{(0)} = Z^{1/2} S_q, \\ \tau_0 = b^a \tau Z_\tau, \quad u_0 = b^{2a-D} u Z_u, \\ \delta_0 = b^{2a-D}\delta Z_\delta, \quad g_0 = b^{a-D/2} g Z_g, \\ g_0^{(0)} = b^{a-D/2} g^{(0)} Z_g^{(0)}, \\ j_0 = b^{a-2} j Z_j, \quad j_0 = j_2/j_a. \end{gathered} \tag{10}$$

Since the effective charges λ and λ_0 are associated with the nonfluctuating order parameter y, they remain invariant under the renormalization-group transformations:

$$\lambda_R = \lambda, \quad \lambda_{0R} = \lambda_0. \tag{11}$$

Then, the Feynman diagram technique with the propagator $G(q) = 1/(\tau + |q|^a)$ is used to calculate the two-point vertices $\Gamma_\tau^{(2)}$, $\Gamma_\lambda^{(2)}$, and $\Gamma_{\lambda 0}^{(2)}$; the four-point vertices $\Gamma_u^{(4)}$ and $\Gamma_\delta^{(4)}$; and the nested two-point vertices $\Gamma_g^{(2,1)}$, $\Gamma_{g0}^{(2,1)}$, and $\Gamma_t^{(2,1)}$.

The appropriate Z-factors are determined by regularity conditions for the renormalized vertices written as the normalization conditions

$$\begin{gathered} Z\frac{\partial}{\partial k^2}\Gamma^{(2)}(k)\Big|_{k^2=0} = 1, \\ Z^2\Gamma_u^{(4)}\Big|_{k^2=0} = b^{2a-D} u, \\ Z^2\Gamma_\delta^{(4)}\Big|_{k^2=0} = b^{4-D}\delta, \\ Z_1 Z\Gamma_g^{(2,1)}\Big|_{k^2=0} = b^{2-D/2} g, \\ Z_0 Z\Gamma_{g0}^{(2,1)}\Big|_{k^2=0} = b^{2-D/2} g^{(0)}, \\ Z_1\Gamma_\lambda^{(2)}\Big|_{k^2=0} = b^{-D}\lambda, \\ Z_0\Gamma_{\lambda 0}^{(2)}\Big|_{k^2=0} = b^{-D}\lambda_0, \\ Z\Gamma_t^{(2,1)}\Big|_{k^a=0} = b^{2-D/2} t, \\ Z\Gamma_j 1^{(2,1)}\Big|_{k^2=0} = b^{2-a} j \end{gathered} \tag{12}$$

for $a \geq 2$ and

$$
\begin{aligned}
& Z\frac{\partial}{\partial k^2}\Gamma^{(2)}(k)\big|_{k^2=0} = 1,\\
& Z^2\Gamma_u^{(4)}\big|_{k^2=0} = b^{2a-D}u,\\
& Z^2\Gamma_\delta^{(4)}\big|_{k^2=0} = b^{2a-D}\delta,\\
& Z_1 Z\Gamma_g^{(2,1)}\big|_{k^2=0} = b^{a-D/2}g,\\
& Z_0 Z\Gamma_{g0}^{(2,1)}\big|_{k^2=0} = b^{a-D/2}g^{(0)},\\
& Z_1\Gamma_\lambda^{(2)}\big|_{k^2=0} = b^{-D}\lambda,\\
& Z_0\Gamma_{\lambda 0}^{(2)}\big|_{k^2=0} = b^{-D}\lambda_0,\\
& Z\Gamma_t^{(2,1)}\big|_{k^a=0} = b^{a-D/2}t,\\
& Z\Gamma_j^{(2,1)}\big|_{k^2=0} = b^{a-2}j
\end{aligned}
\tag{13}
$$

for $a < 2$.

The renormalization-group equations are analyzed in the two-loop approximation. The next step in the field-theoretic approach is the calculation of the scaling functions β and γ in the renormalization-group differential equation

$$
\begin{aligned}
& \left[b\frac{\partial}{\partial b} + \beta_u\frac{\partial}{\partial u} + \beta_\delta\frac{\partial}{\partial \delta} + \beta_j\frac{\partial}{\partial j}\right.\\
& \left. + \beta_g\frac{\partial}{\partial g} + \beta_{g0}\frac{\partial}{\partial g^{(0)}} - \gamma_\varphi\frac{n}{2}b\frac{\partial \ln Z_\varphi}{\partial b} - \gamma_\tau\tau\frac{\partial}{\partial \tau}\right]\\
& \times\Gamma^{(m)}(q;\tau, u, \delta, g, g^{(0)}, b) = 0.
\end{aligned}
\tag{14}
$$

For the effective interaction vertices defined as

$$v_1 = vJ_0,\quad v_2 = \delta J_0\quad v_3 = zJ_0,\quad v_4 = wJ_0, \tag{15}$$

one has functions β and γ for $a \geq 2$ that are similar to those obtained for short-range systems in [13], and

$$
\begin{aligned}
\beta_{j1} = & -(2-a)j^{(1)}\left[1 - 24v_1 + 8v_2 - 4v_3 + 2v_4\right.\\
& + 576\left(2\tilde{J}_1\big|_{a=2} - 1 - \frac{2}{3}\tilde{G}\big|_{a=2}\right)v_1^2\\
& - 120\left(2\tilde{J}_1\big|_{a=2} - 1 - \frac{8}{5}\tilde{G}\big|_{a=2}\right)v_1v_2\\
& \left. + 96\left(2\tilde{J}_1\big|_{a=2} - 1 - \frac{2}{3}\tilde{G}\big|_{a=2}\right)v_2^2\right].
\end{aligned}
\tag{16}
$$

For $a < 2$,

$$
\begin{aligned}
\beta_1 = & -(2a-D)v_1\left[1 - 36v_1 + 24v_2 + 1728\left(2\tilde{J}_1 - 1 - \frac{2}{9}\tilde{G}\right)v_1^2\right.\\
& \left. - 2304\left(2\tilde{J}_1 - 1 - \frac{1}{6}\tilde{G}\right)v_1v_2 + 672\left(2\tilde{J}_1 - 1 - \frac{2}{3}\tilde{G}\right)v_2^2\right],\\
\beta_2 = & -(2a-D)v_2\left[1 - 24v_1 + 8v_2 + 576\left(2\tilde{J}_1 - 1 - \frac{2}{3}\tilde{G}\right)v_1^2\right.\\
& \left. - 1152\left(2\tilde{J}_1 - 1 - \frac{1}{3}\tilde{G}\right)v_1v_2 + 352\left(2\tilde{J}_1 - 1 - \frac{1}{22}\tilde{G}\right)v_2^2\right],\\
\beta_3 = & -(2a-D)v_3\left[1 - 24v_1 + 16v_2 - 2v_3 + 576\left(2\tilde{J}_1 - 1 - \frac{2}{3}\tilde{G}\right)v_1^2\right.\\
& \left. - 120\left(2\tilde{J}_1 - 1 - \frac{8}{5}\tilde{G}\right)v_1v_2 + 96\left(2\tilde{J}_1 - 1 - \frac{2}{3}\tilde{G}\right)v_2^2\right],\\
\beta_4 = & -(2a-D)v_4\left[1 - 24v_1 + 8v_2 - 4v_3 + 2v_4 + 576\left(2\tilde{J}_1 - 1 - \frac{2}{3}\tilde{G}\right)v_1^2\right.\\
& \left. - 120\left(2\tilde{J}_1 - 1 - \frac{8}{5}\tilde{G}\right)v_1v_2 + 96\left(2\tilde{J}_1 - 1 - \frac{2}{3}\tilde{G}\right)v_2^2\right],
\end{aligned}
$$

$$\beta_j = -(a-2)j\Big[1 - 24v_1 + 8v_2 - 4v_3 + 2v_4 + 576\Big(2\tilde{J}_1 - 1 - \frac{2}{3}\tilde{G}\Big)v_1^2$$

$$- 120\Big(2\tilde{J}_1 - 1 - \frac{8}{5}\tilde{G}\Big)v_1v_2 + 96\Big(2\tilde{J}_1 - 1 - \frac{2}{3}\tilde{G}\Big)v_2^2\Big], \tag{17}$$

$$\gamma_t = (2a-D)\Big[-12v_1 + 4v_2 - 2v_3 + 2v_4 + 288\Big(2\tilde{J}_1 - 1 - \frac{1}{3}\tilde{G}\Big)v_1^2$$

$$- 192\Big(2\tilde{J}_1 - 1 - \frac{2}{3}\tilde{G}\Big)v_1v_2 + 32\Big(2\tilde{J}_1 - 1 - \frac{1}{2}\tilde{G}\Big)v_2^2\Big],$$

$$\gamma_\varphi = (2a-D)64\tilde{G}(3v_1^2 - 3v_1v_2 + v_2^2),$$

$$J_1 = \int \frac{d^Dqd^Dp}{(1+|q|^a)^2(1+|p|^a)(1+|q^2+p^2+2pq|^{a/2})},$$

$$J_0 = \int \frac{d^Dq}{(1+|q|^a)^2},$$

$$G = -\frac{\partial}{\partial|k|^a}\int \frac{d^Dqd^Dp}{(1+|q^2+k^2+2kq|^a)(1+|p|^a)(1+|q^2+p^2+2pq|^{a/2})}\bigg|_{k=0},$$

$$\tilde{J}_1 = \frac{J_1}{J_0^2}, \quad \tilde{G} = \frac{G}{J_0^2}.$$

When $a \le D/2$, the integrals J_0, J_1, and G are divergent. Finite expressions are obtained by introducing a cutoff parameter Λ and taking the limits of J_1/J_0^2 and G/J_0^2 as $\Lambda \longrightarrow \infty$. The integrals are performed numerically, and a sequence of J_1/J_0^2 and G/J_0^2 corresponding to various values of Λ is calculated and extrapolated to infinity.

The required physical information was extracted from the resulting expressions by applying the Padé–Borel method extended to the four-parameter case. The appropriate direct and inverse Borel transforms have the form

$$f(v_1, v_2, v_3, v_4) = \sum_{i_1, i_2, i_3, i_4} c_{i_1, i_2, i_3, i_4} v_1^{i_1} v_2^{i_2} v_3^{i_3} v_4^{i_4}$$

$$= \int_0^\infty e^{-t}F(v_1t, v_2t, v_3t, v_4t)dt, \tag{18}$$

$$F(v_1, v_2, v_3, v_4)$$

$$= \sum_{i_1, i_2, i_3, i_4} \frac{c_{i_1, i_2, i_3, i_4}}{(i_1 + i_2 + i_3 + i_4)!} v_1^{i_1} v_2^{i_2} v_3^{i_3} v_4^{i_4}. \tag{19}$$

To obtain an analytic continuation of the Borel transform of a function, a series in an auxiliary variable θ is introduced:

$$\tilde{F}(v_1, v_2, v_3, v_4, \theta) = \sum_{k=0}^{\infty} \theta^k$$

$$\times \sum_{i_1, i_2, i_3, i_4} \frac{c_{i_1, \dots, i_4}}{k!} v_1^{i_1} v_2^{i_2} v_3^{i_3} v_4^{i_4} \delta_{i_1 + i_2 + i_3 + i_4, k}. \tag{20}$$

The Padé approximant $[L/M]$ is applied to this series at $\theta = 1$. The [2/1] approximant is used to calculate the β functions in the two-loop approximation.

The critical behavior is completely determined by the stable fixed points defined by the condition

$$\beta_i(v_1^*, v_2^*, v_3^*, v_4^*, j^*) = 0 \quad (i = 1, 2, 3, 4, j). \tag{21}$$

The requirement of stability of a fixed point reduces to the condition that the eigenvalues b_i of the matrix

$$B_{i,j} = \frac{\partial \beta_i(v_1^*, v_2^*, v_3^*, v_4^*, j^*)}{\partial v_j} \tag{22}$$

are positive.

When $a \ge 2$, the stable fixed points coincide with those of short-range systems [13], because $j^{(1)*} = 0$ for all of these fixed points. The zero value of the effective charge characterizing the relative contribution of long-

Table 1. Fixed points and eigenvalues of the stability matrix for homogeneous systems

N	v_1^*	v_2^*	v_3^*	v_4^*	j	b_1	b_2	b_3	b_4	b_5
$a = 1.6$										
1.1	0.01597	0	0	0	0	0.32	–0.48	–0.62	–0.62	0.87
1.2	0.01597	0	0.30968	0	0	0.87	–0.48	0.62	0.62	0.16
1.3	0.01597	0	0.30968	0.30968	0	0.87	–0.48	0.62	–0.62	0.32
1.4	0	0	0.5	0	0	–1	–1	1	1	0.4
1.5	0	0	0.5	0.5	0	–1	–1	1	–1	0.4
1.6	–0.22762	0.59481	0	0	0	45.30	32.57	–0.12	–0.12	0.08
$a = 1.7$										
2.1	0.02049	0	0	0	0	0.23	–0.34	–0.53	–0.53	0.70
2.2	0.02049	0	0.26650	0	0	0.70	–0.34	0.53	0.53	0.12
2.3	0.02049	0	0.26650	0.26650	0	0.70	–0.34	0.53	–0.53	0.23
2.4	0	0	0.5	0	0	–1	–1	1	1	0.3
2.5	0	0	0.5	0.5	0	–1	–1	1	–1	0.3
2.6	–0.04523	0.27489	0	0	0	13.24	3.92	–0.17	–0.17	0.08
$a = 1.8$										
3.1	0.02323	0	0	0	0	0.15	–0.22	–0.49	–0.49	0.63
3.2	0.02323	0	0.24540	0	0	0.63	–0.22	0.49	0.49	0.08
3.3	0.02323	0	0.24540	0.24540	0	0.63	–0.22	0.49	–0.49	0.15
3.4	0	0	0.5	0	0	–1	–1	1	1	0.2
3.5	0	0	0.5	0.5	0	–1	–1	1	–1	0.2
3.6	0.06419	0.04688	0	0	0	0.63*	0.63*	–0.12	–0.12	0.08
3.7	0.06419	0.04688	0.06610	0	0	0.63*	0.63*	0.12	0.12	0.09
3.8	0.06419	0.04688	0.06610	0.06610	0	0.63*	0.63*	0.12	–0.12	0.08
$a = 1.9$										
4.1	0.04207	0	0	0	0	0.06	–0.18	–0.18	–0.18	0.68
4.2	0.04435	0	0.09519	0	0	0.68	–0.18	0.19	0.18	0.04
4.3	0.04435	0	0.09519	0.09519	0	0.68	–0.18	0.19	–0.19	0.06
4.4	0	0	0.5	0	0	–1	–1	1	1	0.1
4.5	0	0	0.5	0.5	0	–1	–1	1	–1	0.1
4.6	0.06656	0.04082	0	0	0	0.56*	0.56*	–0.12	–0.12	0.04
4.7	0.06656	0.04082	0.06572	0	0	0.56*	0.56*	0.12	0.12	0.05
4.8	0.06656	0.04082	0.06572	0.06572	0	0.56*	0.56*	0.12	–0.12	0.04

range interactions implies that the critical behavior of the system is dominated by short-range interactions.

The stable fixed points of the RG transformation, the eigenvalues of the fixed-point stability matrix, and the critical exponents for $1.5 < a \leq 1.9$ are listed in Table 1. When $0 < a < 1.5$, the only fixed point is the stable Gaussian one, $v^* = 0$. When $a = 1.5$, the values of the effective charges cannot be determined at the fixed point, because β is zero for $D = 3$. However, these values are not required since $\gamma_t = \gamma_\varphi = 0$ in this case.

An analysis of the fixed points and the eigenvalues of the stability matrix shows that short-range effects are not essential for systems with $a < 2$, whereas long-range interactions play a dominant role, because the relative strength of short-range interactions is $j^* = 0$ and the stability of the system with respect to j is determined by $b_5 > 0$.

The critical behavior of homogeneous "rigid" systems (fixed points 1.1, 2.1, 3.1, and 4.1) becomes similar to Gaussian behavior as a approaches $a = 1.5$ from

Table 2. Critical exponents

N	ν	α	η	γ	z
$a = 1.6$					
1.1	0.69736	–0.09208	0.40394	1.11303	2.00018
1.2	0.88948	–0.66844	0.40394	1.41966	2.00018
1.3	0.69736	–0.09208	0.40394	1.11303	2.00018
1.4	1.25	–1.75	0.4	2	2
1.5	0.625	0.125	0.4	1	2
$a = 1.7$					
2.1	0.66745	–0.00235	0.30486	1.13142	2.00078
2.2	0.83065	–0.49195	0.30486	1.40807	2.00078
2.3	0.66745	–0.00235	0.30486	1.13142	2.00078
2.4	1.17647	–1.52941	0.3	2	2
2.5	0.58823	0.23531	0.3	1	2
$a = 1.8$					
3.1	0.63634	0.09098	0.20746	1.14116	2.00153
3.2	0.78291	–0.34873	0.20746	1.40399	2.00153
3.3	0.63634	0.09098	0.20746	1.14116	2.00153
3.4	1.11111	–1.33333	0.2	2	2
3.5	0.55556	0.33333	0.2	1	2
3.6	0.73279	–0.19837	0.25098	1.28540	2.11225
3.7	0.75776	–0.27328	0.25098	1.32919	2.11225
3.8	0.73279	–0.19837	0.25098	1.28540	2.11225
$a = 1.9$					
4.1	0.65268	0.04196	0.11342	1.23179	2.00663
4.2	0.75143	–0.25429	0.11342	1.41814	2.00663
4.3	0.65268	0.04196	0.11342	1.23179	2.00663
4.4	1.05263	–1.15789	0.1	2	2
4.5	0.52632	0.42104	0.1	1	2
4.6	0.70679	–0.12037	0.13441	1.31979	2.12385
4.7	0.72133	–0.72133	0.13441	1.34695	2.12385
4.8	0.70679	–0.12037	0.13441	1.31979	2.12385

above. Since the eigenvalues b_2, b_3, and b_4 of the stability matrix are negative, the critical behavior of homogeneous "rigid" systems is unstable with respect to both dilution with quenched impurities and elastic deformation.

Homogeneous compressible systems with $1.5 < a < 2.0$ exhibit qualitatively similar critical behavior. The fixed points corresponding to constant deformation (1.2, 2.2, 3.2, and 4.2) are stable. For compressible systems at constant pressure and volume, the tricritical fixed points are 1.3, 2.3, 3.3, 4.3 and 1.4, 2.4, 3.4, 4.4, respectively. Points 1.5, 2.5, 3.5, and 4.5 are fourth-order ones (intersections of two tricritical lines), which are unstable with respect to dilution with quenched impurities.

Disordered "rigid" systems (fixed points 1.6, 2.6, 3.6, and 4.6) have stable fixed points in the physical region (v_1^*, $v_2^* > 0$) only if $a \geq 1.8$. Calculations show that the stable fixed points of three-dimensional systems are characterized by negative values of v_1^* if $1.6 \leq a < 1.8$, which points to a change from second- to first-order phase transition [18]. These fixed points are unstable with respect to elastic deformation.

Disordered compressible systems with $1.8 \leq a < 2.0$ exhibit specific critical behavior (fixed points 3.7 and

4.7). Fixed points 3.8 and 4.8 are the tricritical ones corresponding to $v_3^* = v_4^*$. Tricritical behavior corresponding to $v_1^* = 0$ cannot be observed since there does not exist any fixed point corresponding to physical values of the effective charges. Therefore, the phase diagram does not contain fourth-order critical points.

The exponent ν characterizing the growth of the correlation radius near the critical point ($R_c \sim |T - T_c|^{-\nu}$) is determined by the relation

$$\nu = 1/a(1 + \gamma_t(v_1^*, v_2^*, v_3^*, v_4^*))^{-1}.$$

The Fisher exponent η describing the behavior of the correlation function near the critical point in the wave-vector space ($G \sim k^{2+\eta}$) is determined by the scaling function γ_φ:

$$\eta = 2 - a + \gamma_\varphi(v_1^*, v_2^*, v_3^*, v_4^*).$$

The remaining critical exponents can be found from the scaling relations.

The values of the critical exponents for the fixed points listed in Table 1 are presented in Table 2.

3. CRITICAL DYNAMICS

Relaxational dynamics of spin systems near the critical temperature can be described by a Langevin-type equation for the order parameter:

$$\frac{\partial S}{\partial t} = -\lambda_0 \frac{\delta H}{\delta S} + \eta + \lambda_0 h, \qquad (23)$$

where λ_0 is a kinetic coefficient, $\eta(x, t)$ is a Gaussian random force (representing the effect of a heat reservoir) defined by the probability distribution

$$P_\eta = A_\eta \exp[-(4\lambda_0)^{-1} \int d^d x dt \eta^2(x, t)] \qquad (24)$$

with a normalization factor A_η, and h is an external field thermodynamically conjugate to the order parameter. The temporal correlation function $G(x, t)$ of the order-parameter field can be found by solving Eq. (23) with $H[S, \Delta\tau]$ given by Hamiltonian (3) for $S[\eta, h, \Delta\tau]$, averaging the result over P_η and $P[\Delta\tau, h, h_0]$, and retaining the component linear in $h(0)$:

$$G(x, t) = \frac{\delta}{\delta h(0)}[\langle S(x, t)\rangle]_{\mathrm{imp}}\Big|_{h=0}, \qquad (25)$$

where

$$[\langle S(x, t)\rangle]_{\mathrm{imp}} = B^{-1}\int D\{\eta\}\prod d\Delta\tau_q S(x, t) P_\eta P_\Delta \tau, \qquad (26)$$

$$B = \int D\{\eta\}\prod d\Delta\tau_q P_\eta P_\Delta \tau. \qquad (27)$$

Instead of dealing with the correlation function, it is reasonable to invoke the Feynman diagram technique and represent the corresponding vertex $\Gamma^{(2)}(k, \omega)$ in the two-loop approximation.

The dynamic critical exponent z characterizing critical slowing-down of relaxation is determined by substituting the dynamic scaling function $\gamma_\lambda(v_1, v_2, v_3, v_4)$:

$$z = 2 + \gamma_\lambda(v_1^*, v_2^*, v_3^*, v_4^*),$$

$$\gamma_\lambda = (2a - D)\Big[-4D'_1 - 532\Big(D'_2 - \frac{4}{9}\tilde{G}\Big)v_1^2 + 288\Big(D'_3 + \frac{1}{3}D'_1 - \frac{1}{3}\tilde{G}\Big)v_1 v_2 - 16(D'_4 + D'_5 + 4D'_1 - \tilde{G})v_2^2\Big],$$

$$D'_1 = \frac{1}{J_0}\frac{\partial D_1}{\partial(-i\omega/\lambda)}\bigg|_{k=0,\,\omega=0},$$

$$D_1 = \int \frac{d^D q}{1 + |q|^a - i\omega/\lambda},$$

$$D'_i = \frac{1}{J_0^2}\frac{\partial D_i}{\partial(-i\omega/\lambda)}\bigg|_{k=0,\,\omega=0} \quad (i = 2, \ldots, 5), \qquad (28)$$

$$D_2 = \frac{3}{4}\int \frac{d^D q d^D p}{(1 + |q|^a)(1 + |p|^a)(3 + |q|^a + |p|^a + |p + q|^a - i\omega/\lambda)},$$

$$D_3 = \frac{3}{4}\int \frac{d^D q d^D p}{2(1 + |q|^a - i\omega/\lambda)(1 + |p|^a)(2 + |q|^a + |p + q|^a)},$$

$$D_4 = \int \frac{d^D q d^D p}{(1 + |q|^a - i\omega/\lambda)(1 + |p|^a - i\omega/\lambda)(1 + |p + q|^a - i\omega/\lambda)},$$

$$D_5 = \int d^D q d^D p \left[\frac{1}{(1+|q|^a - i\omega/\lambda)^2 (1+|p+q|^a - i\omega/\lambda)} - \frac{1}{(1+|q|^a - i\omega/\lambda)^2 (1+|p|^a - i\omega/\lambda)}\right].$$

The summation of the asymptotic power series expansion of $\gamma_\lambda(v_1, v_2, v_3, v_4)$ is performed by using the Padé–Borel technique. The dynamic and static scaling exponents are shown in Table 2.

4. MULTICRITICAL BEHAVIOR

By applying the replica trick, the Hamiltonian of a disordered compressible system with long-range interactions characterized by two order parameters is represented as

$$\begin{aligned}
H_0 = {} & \frac{1}{2}\int d^D q(\tau_1 + q^a)\sum_{a=1}^{m}\Phi_q^a\Phi_{-q}^a \\
& + \frac{1}{2}\int d^D q(\tau_2 + q^a)\sum_{a=1}^{m}\Psi_q^a\Psi_{-q}^a \\
& + u_{01}\int d^D q_1 d^D q_2 d^D q_3 \sum_{a,b=1}^{m}(\Phi_{q1}^a\Phi_{q2}^a)(\Phi_{q3}^b\Phi^b_{-q1-q2-q3}) \\
& + u_{02}\int d^D q_1 d^D q_2 d^D q_3 \sum_{a,b=1}^{m}(\Psi_{q1}^a\Psi_{q2}^a)(\Psi_{q3}^b\Psi^b_{-q-q2-q3}) \\
& + 2u_{03}\int d^D q_1 d^D q_2 d^D q_3 \sum_{a,b=1}^{m}(\Phi_{q1}^a\Phi_{q2}^a)(\Psi_{q3}^b\Psi^b_{-q1-q2-q3}) \\
& - \frac{\delta_{01}}{2}\int d^D q_1 d^D q_2 d^D q_3 \sum_{a=1}^{m}(\Phi_{q1}^a\Phi_{q2}^a)(\Phi_{q3}^a\Phi^a_{-q-q2-q3}) \\
& - \frac{\delta_{02}}{2}\int d^D q_1 d^D q_2 d^D q_3 \sum_{a=1}^{m}(\Psi_{q1}^a\Psi_{q2}^a)(\Psi_{q3}^a\Psi^a_{-q1-q2-q3}) \\
& - \delta_{03}\int d^D q_1 d^D q_2 d^D q_3 \sum_{a=1}^{m}(\Phi_{q1}^a\Phi_{q2}^a)(\Psi_{q3}^a\Psi^a_{-q1-q2-q3}) \\
& + g_1\int d^D q_1 d^D q_2 y_{q1}\sum_{a=1}^{m}\Phi_{q2}^a\Phi^a_{-q1-q2} \\
& + g_2\int d^D q_1 d^D q_2 y_{q1}\sum_{a=1}^{m}\Psi_{q2}^a\Psi^a_{-q1-q2} \\
& + \frac{g_1^0}{\Omega}y_0\int d^D q\sum_{a=1}^{m}\Phi_q^a\Phi_{-q}^a + \frac{g_2^0}{\Omega}y_0\int d^D q\sum_{a=1}^{m}\Psi_q^a\Psi_{-q}^a \\
& + 2\beta\int d^D q y_q y_{-q} + 2\frac{\beta_0}{\Omega}y_0^2,
\end{aligned} \tag{29}$$

where Φ and Ψ are m-dimensional fluctuating order parameters, u_{01} and u_{02} are positive constants, $\tau_1 \sim |T - T_{c1}|/T_{c1}$, $\tau_2 \sim |T - T_{c2}|/T_{c2}$ (T_{c1} and T_{c2} are the phase-transition temperatures corresponding to the first and second order parameters, respectively),

$$y(x) = \sum_{\alpha=1}^{3} u_{\alpha\alpha}(x)$$

($u_{\alpha\beta}$ is the strain tensor), g_1 and g_2 are the quadratic striction constants, β is an elastic constant of a crystal, and D is the space dimension. The characteristics of the original system can be calculated by analytic continuation as $m \longrightarrow 0$. The nonnegative constants δ_{01}, δ_{02}, and δ_{03} characterize the coupling between critical fluctuations via the impurity field. Since the coupling between the impurity field and elastic strain is linear, averaging over the impurity field leads to overdetermination of δ_{01}, δ_{02}, and δ_{03}. In this expression for the Hamiltonian, integration is performed in the terms depending on the nonfluctuating variables that are not coupled to the order parameter. As in the case of a single order parameter, the y_0 terms (describing homogeneous deformation) are separated in (29).

Define an effective Hamiltonian depending only on the strongly fluctuating order parameters Φ and Ψ by the relation

$$\begin{aligned}
& \exp\{-H[\Phi, \Psi]\} \\
& = B\int \exp\{-H_0[\Phi, \Psi, y]\}\prod dy_q.
\end{aligned} \tag{30}$$

Then,

$$\begin{aligned}
H = {} & \frac{1}{2}\int d^D q(\tau_1 + q^2)\sum_{a=1}^{m}\Phi_q^a\Phi_{-q}^a \\
& + \frac{1}{2}\int d^D q(\tau_2 + q^2)\sum_{a=1}^{m}\Psi_q^a\Psi_{-q}^a \\
& + v_{01}\int d^D q_1 d^D q_2 d^D q_3 \sum_{a,b=1}^{m}(\Phi_{q1}^a\Phi_{q2}^a)(\Phi_{q3}^b\Phi^b_{-q1-q2-q3}) \\
& + v_{02}\int d^D q_1 d^D q_2 d^D q_3 \sum_{a,b=1}^{m}(\Psi_{q1}^a\Psi_{q2}^a)(\Psi_{q3}^b\Psi^b_{-q1-q2-q3}) \\
& + 2v_{03}\int d^D q_1 d^D q_2 d^D q_3 \sum_{a,b=1}^{m}(\Phi_{q1}^a\Phi_{q2}^a)(\Psi_{q3}^b\Psi^b_{-q1-q2-q3})
\end{aligned}$$

$$-\frac{\delta_{01}}{2}\int d^Dq_1d^Dq_2d^Dq_3\sum_{a=1}^{m}(\Phi^a_{q1}\Phi^a_{q2})(\Phi^a_{q3}\Phi^a_{-q1-q2-q3})$$

$$-\frac{\delta_{02}}{2}\int d^Dq_1d^Dq_2d^Dq_3\sum_{a=1}^{m}(\Psi^a_{q1}\Psi^a_{q2})(\Psi^a_{q3}\Psi^a_{-q1-q2-q3}) \qquad (31)$$

$$-\delta_{03}\int d^Dq_1d^Dq_2d^Dq_3\sum_{a=1}^{m}(\Phi^a_{q1}\Phi^a_{q2})(\Psi^a_{q3}\Psi^a_{-q1-q2-q3})$$

$$+\frac{z_1^2-w_1^2}{2}\int d^Dq_1d^Dq_2\sum_{a,b=1}^{m}(\Phi^a_{q1}\Phi^a_{-q1})(\Phi^b_{q2}\Phi^b_{-q2})$$

$$+\frac{z_2^2-w_2^2}{2}\int d^Dq_1d^Dq_2\sum_{a=1}^{m}(\Psi^a_{q1}\Psi^a_{-q1})(\Psi^a_{q2}\Psi^a_{-q2})$$

$$+(z_1z_2-w_1w_2)\int d^Dq_1d^Dq_2$$

$$\times\sum_{a,b=1}^{m}(\Phi^a_{q1}\Phi^a_{-q1})(\Psi^b_{q2}\Psi^b_{-q2}),$$

$$v_{01}=u_{01}-\frac{z_1^2}{2},\quad v_{02}=u_{02}-\frac{z_2^2}{2},\quad v_{03}=u_{03}-\frac{z_1z_2}{2},$$

$$z_1=\frac{g_1}{\sqrt{\beta}},\quad z_2=\frac{g_2}{\sqrt{\beta}},\quad w_1=\frac{g_1^0}{\sqrt{\beta_0}},\quad w_2=\frac{g_2^0}{\sqrt{\beta_0}}.$$

This Hamiltonian admits a wide diversity of multicritical points. The conditions for bicritical and tetracritical behavior are

$$\left(v_3+\frac{1}{2}(z_1z_2-w_1w_2-\delta_3)\right)^2$$

$$>\left(v_1+\frac{1}{2}(z_1^2-w_1^2-\delta_1)\right)$$

$$\times\left(v_2+\frac{1}{2}(z_2^2-w_2^2-\delta_2)\right),$$

and

$$\left(v_3+\frac{1}{2}(z_1z_2-w_1w_2-\delta_3)\right)^2$$

$$<\left(v_1+\frac{1}{2}(z_1^2-w_1^2-\delta_1)\right)$$

$$\times\left(v_2+\frac{1}{2}(z_2^2-w_2^2-\delta_2)\right),$$

respectively. Moreover, even higher order multicritical points can exist, owing to striction effects.

The functions β and γ in the renormalization-group equation for the renormalized vertices u_1, u_2, u_3, δ_1, δ_2, δ_3, g_1, g_2, $g_1^{(0)}$, and $g_2^{(0)}$ (or for the complex-valued vertices z_1, z_2, w_1, w_2, v_1, v_2, v_3, δ_1, δ_2, and δ_3, which are better suited for analyzing multicritical behavior) are calculated by a standard method based on the Feynman diagram technique and a renormalization procedure. As a result, the following expressions for β functions are obtained in the two-loop approximation:

$$\beta_{v1}=-v_1+36v_1^2+4v_3^2-24v_1\delta_1$$

$$-1728\left(2\tilde{J}-1-\frac{2}{9}\tilde{G}\right)v_1^3$$

$$-192\left(2\tilde{J}-1-\frac{2}{9}\tilde{G}\right)v_1v_3^2-64(2\tilde{J}-1)v_3^3$$

$$+96\left(2\tilde{J}-1-\frac{2}{3}\tilde{G}\right)v_1v_3\delta_3$$

$$+32(2\tilde{J}-1)v_3^2\delta_3+2304\left(2\tilde{J}-1-\frac{1}{6}\tilde{G}\right)v_1^2\delta_1$$

$$-672\left(2\tilde{J}-1-\frac{2}{3}\tilde{G}\right)v_1\delta_1^2+16(2\tilde{J}-1)v_3^2\delta_1,$$

$$\beta_{v2}=-v_2+36v_2^2+4v_3^2-24v_2\delta_2$$

$$-1728\left(2\tilde{J}-1-\frac{2}{9}\tilde{G}\right)v_2^3$$

$$-192\left(2\tilde{J}-1-\frac{2}{9}\tilde{G}\right)v_2v_3^2-64(2\tilde{J}-1)v_3^3$$

$$+96\left(2\tilde{J}-1-\frac{2}{3}\tilde{G}\right)v_2v_3\delta_3+32(2\tilde{J}-1)v_3^2\delta_3$$

$$+2304\left(2\tilde{J}-1-\frac{1}{6}\tilde{G}\right)v_2^2\delta_2$$

$$-672\left(2\tilde{J}-1-\frac{2}{3}\tilde{G}\right)v_2\delta_2^2+16(2\tilde{J}-1)v_3^2\delta_2,$$

$$\beta_{v3}=-v_3+16v_3^2+12v_1v_3+12v_2v_3-4v_3\delta_1$$

$$-4v_3\delta_2-16v_3\delta_3-320\left(2\tilde{J}-1-\frac{2}{5}\tilde{G}\right)v_3^3$$

$$
\begin{aligned}
&-288\left(2\tilde{J}-1-\frac{2}{3}\tilde{G}\right)v_1^2v_3\\
&-288\left(2\tilde{J}-1-\frac{2}{3}\tilde{G}\right)v_2^2v_3\\
&-576(2\tilde{J}-1)v_1v_3^2-576(2\tilde{J}-1)v_2v_3^2\\
&+448\left(2\tilde{J}-1-\frac{2}{7}\tilde{G}\right)v_3^2\delta_3\\
&+192(2\tilde{J}-1)v_3^2\delta_1+192(2\tilde{J}-1)v_3^2\delta_2\\
&-48\left(2\tilde{J}-1-\frac{2}{3}\tilde{G}\right)v_3\delta_1^2\\
&-48\left(2\tilde{J}-1-\frac{2}{3}\tilde{G}\right)v_3\delta_2^2\\
&+432\left(2\tilde{J}-1-\frac{2}{3}\tilde{G}\right)v_1v_3\delta_1\\
&+432\left(2\tilde{J}-1-\frac{2}{3}\tilde{G}\right)v_2v_3\delta_2\\
&+576(2\tilde{J}-1)v_1v_3\delta_3+576(2\tilde{J}-1)v_2v_3\delta_3\\
&-192(2\tilde{J}-1)v_3\delta_3^2\\
&-192(2\tilde{J}-1)v_3\delta_1\delta_3-192(2\tilde{J}-1)v_3\delta_2\delta_3,\\
\beta_{\delta 1} &= -\delta_1+16\delta_1^2-24v_1\delta_1-8v_3\delta_3\\
&-352\left(2\tilde{J}-1-\frac{1}{22}\tilde{G}\right)\delta_1^3+128(2\tilde{J}-1)v_3^2\delta_3\\
&-192(2\tilde{J}-1)v_3\delta_3^2-1152\left(2\tilde{J}-1-\frac{1}{3}\tilde{G}\right)v_1\delta_1^2\\
&+576\left(2\tilde{J}-1-\frac{2}{3}\tilde{G}\right)v_1^2\delta_1\\
&+64(2\tilde{J}-1-2\tilde{G})v_3^2\delta_1\\
&-192\left(2\tilde{J}-1-\frac{2}{3}\tilde{G}\right)v_3\delta_1\delta_3,\\
\beta_{\delta 2} &= -\delta_2+16\delta_2^2-24v_2\delta_2-8v_3\delta_3\\
&-352\left(2\tilde{J}-1-\frac{1}{22}\tilde{G}\right)\delta_2^3+128(2\tilde{J}-1)v_3^2\delta_3\\
&-192(2\tilde{J}-1)v_3\delta_3^2-1152\left(2\tilde{J}-1-\frac{1}{3}\tilde{G}\right)v_2\delta_2^2\\
&+576\left(2\tilde{J}-1-\frac{2}{3}\tilde{G}\right)v_2^2\delta_2\\
&+64(2\tilde{J}-1-2\tilde{G})v_3^2\delta_2\\
&-192\left(2\tilde{J}-1-\frac{2}{3}\tilde{G}\right)v_3\delta_2\delta_3,\\
\beta_{\delta 3} &= -\delta_3+8\delta_3^2+12v_1\delta_3+12v_2\delta_3+4v_3\delta_1\\
&+4v_3\delta_2+4\delta_1\delta_3+4\delta_2\delta_3\\
&-64(2\tilde{J}-1)\delta_3^3+288(2\tilde{J}-1)v_1\delta_3^2\\
&+288(2\tilde{J}-1)v_2\delta_3^2+288(2\tilde{J}-1)v_1^2\delta_3\\
&+288(2\tilde{J}-1)v_2^2\delta_3+48\left(2\tilde{J}-1-\frac{2}{3}\tilde{G}\right)\delta_1^2\delta_3\\
&+48\left(2\tilde{J}-1-\frac{2}{3}\tilde{G}\right)\delta_2^2\delta_3\\
&+96(2\tilde{J}-1)\delta_1\delta_3^2+96(2\tilde{J}-1)\delta_2\delta_3^2\\
&+64(2\tilde{J}-1)v_3^2\delta_1+64(2\tilde{J}-1)v_3^2\delta_2\\
&-32(2\tilde{J}-1)v_3\delta_1^2-32(2\tilde{J}-1)v_3\delta_2^2\\
&+64(2\tilde{J}-1-2\tilde{G})v_3^2\delta_3-192(2\tilde{J}-1-2\tilde{G})v_3\delta_3^2\\
&-288\left(2\tilde{J}-1-\frac{2}{3}\tilde{G}\right)v_1\delta_1\delta_3\\
&-288\left(2\tilde{J}-1-\frac{2}{3}\tilde{G}\right)v_2\delta_2\delta_3\\
&-128(2\tilde{J}-1)v_3\delta_1\delta_3-128(2\tilde{J}-1)v_3\delta_2\delta_3,\\
\beta_{z1} &= -z_1+24v_1z_1+2z_1^3-16\delta_1z_1-4\delta_3z_2\\
&+2z_1z_2^2+4v_3z_2-576\left(2\tilde{J}-1-\frac{2}{3}\tilde{G}\right)v_1^2z_1\\
&-32(2\tilde{J}-1)v_3^2z_1-16(2\tilde{J}-1-\tilde{G})v_3^2z_2\\
&+120\left(2\tilde{J}-1-\frac{8}{5}\tilde{G}\right)v_1z_1\delta_1
\end{aligned}
\tag{32}
$$

$$-32\left(2\tilde{J}-1-\frac{2}{3}\tilde{G}\right)z_1\delta_1^2-16(2\tilde{J}-1)z_1\delta_3^2$$

$$-32(2\tilde{J}-1)z_2\delta_3^2$$

$$+128(2\tilde{J}-1-5\tilde{G})v_3z_1\delta_3+128(2\tilde{J}-1-5\tilde{G})v_3z_2\delta_3,$$

$$\beta_{z2} = -z_2+24v_2z_2+2z_2^3-16\delta_2z_2-4\delta_3z_1$$

$$+2z_2z_1^2+4v_3z_1-576\left(2\tilde{J}-1-\frac{2}{3}\tilde{G}\right)v_2^2z_2$$

$$-32(2\tilde{J}-1)v_3^2z_2-16(2\tilde{J}-1-\tilde{G})v_3^2z_1$$

$$+120\left(2\tilde{J}-1-\frac{8}{5}\tilde{G}\right)v_2z_2\delta_2$$

$$-32\left(2\tilde{J}-1-\frac{2}{3}\tilde{G}\right)z_2\delta_2^2-16(2\tilde{J}-1)z_2\delta_3^2$$

$$-32(2\tilde{J}-1)z_1\delta_3^2+128(2\tilde{J}-1-5\tilde{G})v_3z_2\delta_3$$

$$+128(2\tilde{J}-1-5\tilde{G})v_3z_1\delta_3,$$

$$\beta_{w1} = -w_1+24v_1w_1+2z_1^2w_1-2w_1^3-16\delta_1w_1$$

$$-4\delta_3w_2+2w_1z_2^2$$

$$+4v_3w_2-576\left(2\tilde{J}-1-\frac{2}{3}\tilde{G}\right)v_1^2w_1$$

$$-32(2\tilde{J}-1)v_3^2w_1-16(2\tilde{J}-1-\tilde{G})v_3^2w_2$$

$$+120\left(2\tilde{J}-1-\frac{8}{5}\tilde{G}\right)v_1w_1\delta_1$$

$$-32\left(2\tilde{J}-1-\frac{2}{3}\tilde{G}\right)w_1\delta_1^2-16(2\tilde{J}-1)w_1\delta_3^2$$

$$-32(2\tilde{J}-1)w_2\delta_3^2$$

$$+128(2\tilde{J}-1-5\tilde{G})v_3w_1\delta_3$$

$$+128(2\tilde{J}-1-5\tilde{G})v_3w_2\delta_3,$$

$$\beta_{w2} = -w_2+24v_2w_2+2z_2^2w_2-2w_2^3-16\delta_2w_2$$

$$-4\delta_3w_1+2w_2z_1^2$$

$$+4v_3w_1-576\left(2\tilde{J}-1-\frac{2}{3}\tilde{G}\right)v_2^2w_2$$

$$-32(2\tilde{J}-1)v_3^2w_2-16(2\tilde{J}-1-\tilde{G})v_3^2w_1$$

$$+120\left(2\tilde{J}-1-\frac{8}{5}\tilde{G}\right)v_1w_2\delta_1$$

$$-32\left(2\tilde{J}-1-\frac{2}{3}\tilde{G}\right)w_2\delta_1^2-16(2\tilde{J}-1)w_2\delta_3^2$$

$$-32(2\tilde{J}-1)w_1\delta_3^2+128(2\tilde{J}-1-5\tilde{G})v_3w_2\delta_3$$

$$+128(2\tilde{J}-1-5\tilde{G})v_3w_1\delta_3.$$

The summation of these asymptotic expressions was performed by applying the Padé–Borel method extended to the case of many parameters.

The resulting system of summed β functions has a wide diversity of fixed points lying in the physical region of vertices $v_i \ge 0$, $\delta_i \ge 0$ ($i = 1, 2, 3$). A complete analysis of the fixed points corresponding to the critical behavior of a system characterized by a single order parameter is presented above. Tables 3 and 4 show the fixed points associated with multicritical behavior of homogeneous and disordered compressible systems, respectively. Table 3 also shows the values of the parameter

$$p = \left(v_3+\frac{1}{2}(z_1z_2-w_1w_2-\delta_3)\right)^2$$

$$-\left(v_1+\frac{1}{2}(z_1^2-w_1^2-\delta_1)\right)$$

$$\times\left(v_2+\frac{1}{2}(z_2^2-w_2^2-\delta_2)\right),$$

which is defined so that $p > 0$ and $p \le 0$ correspond to bicritical and tetracritical behavior, respectively.

An analysis of the fixed points of homogeneous compressible systems with long-range interactions and their stability leads to certain conclusions. When $1.5 < a \le 2.0$, tetracritical behavior is observed ($p < 0$) if the striction constants characterizing the coupling between the fluctuating order parameters and strain degrees of freedom have opposite signs. Systems with striction constants having like signs do not have stable fixed points, i.e., exhibit first-order phase transitions. The stable tetracritical fixed points corresponding to $1.6 < a < 2.0$ (2.1, 3.1, 4.1) are characterized by zero effective charges w_1^* and w_2^*, which implies that these tetracritical points are observed at constant volume. For $a = 1.6$, the effective charges have finite values (fixed point 1.1). This may be explained by the fact that the "rigid" system exhibits tetracritical and bicritical behavior when $a = 1.6$ and $1.6 < a < 2.0$, respectively. The phase diagram of an elastic substance may contain

Table 3. Fixed points and eigenvalues of the stability matrix for homogeneous systems

N	v_1^*, v_2^*, v_3^*	z_1^*, z_2^*	w_1^*, w_2^*	b_1, b_2, b_3	b_4, b_5	b_6, b_7	p
$a = 1.6$							
1.1	0.027427	0.224319	0.111301	0.157	1.118	1.798	–0.002092
	0.027427	–0.224319	–0.111301	0.738	0.138	0.256	
	0.026699			0.919			
1.2	0.027427	0.224319	0.224319	0.157	1.118	–1.050	–0.000039
	0.027427	–0.224319	–0.224319	0.738	0.138	–1.188	
	0.026699			0.919			
$a = 1.7$							
2.1	0.031287	0.248013	0	0.113	1.675	2.546	–0.003849
	0.031287	–0.248013	0	0.629	0.095	0.041	
	0.031334			0.809			
2.2	0.031287	0.248013	0.248013	0.113	1.675	–1.580	0.000039
	0.031287	–0.248013	–0.248013	0.629	0.095	–1.675	
	0.031334			0.809			
$a = 1.8$							
3.1	0.033682	0.266919	0	0.090	1.831	2.980	–0.004802
	0.033682	–0.266919	0	0.571	0.104	0.115	
	0.034575			0.753			
3.2	0.033682	0.266919	0.266919	0.090	1.831	–1.954	0.000061
	0.033682	–0.266919	–0.266919	0.571	0.104	–2.079	
	0.034575			0.753			
$a = 1.9$							
4.1	0.035842	0.297071	0	0.069	2.079	3.765	–0.079943
	0.035842	–0.297071	0	0.505	0.125	0.049	
	0.039202			0.702			
4.2	0.035842	0.297071	0.297071	0.069	2.079	–1.954	0.000252
	0.035842	–0.297071	–0.297071	0.505	0.125	–2.079	
	0.039202			0.702			

critical points of even higher orders. In particular, fixed points 1.2, 2.2, 3.2, and 4.2 correspond to $z_1 = w_1$ and $z_2 = w_2$, i.e., are the intersections of two tricritical lines associated with fourth-order critical points. These fixed points are not stable in the framework of the approximation adopted here. However, a complete analysis of their stability can be performed by retaining the cubic functions of strain degrees of freedom in the original Hamiltonian.

Table 4 demonstrates that the fixed points of a disordered "rigid" system lie in an unphysical region (δ_1, $\delta_2 < 0$). Furthermore, the stable fixed points have large values for which the theory employed here is inapplicable. This suggests that all fixed points lying in the physical region of effective-charge values are unstable; i.e., the phase diagram does not contain multicritical points. Therefore, calculation of fixed points for compressible disordered system is pointless, because the correspond-

Table 4. Fixed points and eigenvalues of the stability matrix for disordered systems

N	v_1^*, v_2^*, v_3^*	δ_1^*, δ_2^*, δ_3^*	b_1, b_2, b_3	b_4, b_5, b_6
		$a = 1.6$		
1.3	0	–0.630515	11.225	22.854
		–0.630515	15.069	22.854
		–3.713534	15.069	17.439
		$a = 1.7$		
2.3	0	–0.320512	2.239	11.106
		–0.320512	2.239	11.116
		–1.932190	5.197	9.250
		$a = 1.8$		
3.3	0	–0.256437	2.068	8.642
		–0.256437	2.068	8.642
		–1.545749	3.890	7.441
		$a = 1.9$		
4.3	0	–0.223270	1.224	3.149
		–0.223270	1.338	7.349
		–0.790114	1.338	7.349

ing effective charges v_i and δ_i have similar values; i.e., they also lie in an unphysical region. Thus, multicritical points are smeared out by quenched disorder.

5. CONCLUSIONS

Calculations performed directly in the three-dimensional space show that long-range effects are insignificant when $a \geq 2$. Homogeneous compressible and rigid systems with $1.5 < a < 2.0$ exhibit non-Gaussian critical behavior, which strongly depends on the value of a. Non-Gaussian critical behavior is also characteristic of disordered compressible and "rigid" systems with $1.8 \leq a < 2$. Disordered systems with $1.5 < a < 1.8$ exhibit first-order phase transitions. When $a < 1.5$, all systems considered here have Gaussian fixed points with corresponding critical exponents.

For homogeneous systems characterized by two fluctuating order parameters, long-range effects induce crossover in multicritical behavior. However, multicritical behavior is eliminated by introducing quenched disorder.

ACKNOWLEDGMENTS

This work was supported by the Russian Foundation for Basic Research, project no. 04-02-16002.

REFERENCES

1. M. E. Fisher, S.-K. Ma, and B. G. Nickel, Phys. Rev. Lett. **29**, 917 (1972).
2. H. K. Janssen, Phys. Rev. E **58**, R2673 (1998).
3. J. M. Kosterliz, Phys. Rev. Lett. **37**, 1577 (1976).
4. E. Bayong and H. T. Deep, Phys. Rev. B **59**, 11919 (1999).
5. E. Luijten and H. W. J. Blöte, Phys. Rev. B **56**, 8945 (1997).
6. A. I. Larkin and S. A. Pikin, Zh. Éksp. Teor. Fiz. **56**, 1664 (1969) [Sov. Phys. JETP **29**, 891 (1969)].
7. D. J. Bergman and B. I. Halperin, Phys. Rev. B **13**, 2145 (1976).
8. M. A. de Moura, T. C. Lubensky, Y. Imry, and A. Aharony, Phys. Rev. B **13**, 2176 (1976).
9. D. E. Khmel'nitskiĭ and V. L. Shneerson, Zh. Éksp. Teor. Fiz. **69**, 1100 (1975) [Sov. Phys. JETP **42**, 560 (1975)].
10. I. F. Lyuksyutov, Zh. Éksp. Teor. Fiz. **73**, 734 (1977) [Sov. Phys. JETP **46**, 383 (1977)].
11. V. M. Laptev and Yu. N. Skryabin, Phys. Status Solidi B **91**, K143 (1979).
12. Y. N. Skryabin and A. V. Shchanov, Phys. Lett. A **234**, 147 (1997).
13. S. V. Belim and V. V. Prudnikov, Fiz. Tverd. Tela (St. Petersburg) **45**, 1299 (2001) [Phys. Solid State **43**, 1353 (2001)].
14. V. V. Prudnikov, P. V. Prudnikov, and A. A. Fedorenko, Fiz. Tverd. Tela (St. Petersburg) **42**, 158 (2000) [Phys. Solid State **42**, 165 (2000)].
15. S. V. Belim, Pis'ma Zh. Éksp. Teor. Fiz. **75**, 547 (2002) [JETP Lett. **75**, 457 (2002)].
16. S. V. Belim, Pis'ma Zh. Éksp. Teor. Fiz. **76**, 118 (2002) [JETP Lett. **76**, 107 (2002)].
17. Y. Imry, Phys. Rev. Lett. **33**, 1304 (1974).
18. Yu. A. Izyumov and V. N. Syromyatnikov, *Phase Transitions and Symmetry of Crystals* (Nauka, Moscow, 1984) [in Russian].

Translated by A. Betev

Journal of Experimental and Theoretical Physics, Vol. 100, No. 5, 2005, pp. 964–970.
Translated from Zhurnal Éksperimental'noĭ i Teoreticheskoĭ Fiziki, Vol. 127, No. 5, 2005, pp. 1091–1098.
Original Russian Text Copyright © 2005 by Kolpakova, Czarnecki.

ORDER, DISORDER, AND PHASE TRANSITIONS IN CONDENSED SYSTEMS

Nonergodic State of Relaxation Ferroelectric $Cd_2Nb_2O_7$ in a Constant Electric Field

N. N. Kolpakova[a],* **and P. Czarnecki**[b]
[a]Ioffe Physicotechnical Institute, Russian Academy of Sciences, St. Petersburg, 194021 Russia
[b]Institute of Physics, A. Mickiewicz University, 61-614 Poznan, Poland
*e-mail: kolpakova@mail.ioffe.ru; nadia@hoth.amu.edu.pl

Received October 8, 2004

Abstract—The temperature dependence of the residual polarization of the nonergodic relaxation state (NERS) obtained from the measurements of pyroelectric current during zero-field heating (ZFH) in the temperature interval from 10 to 295 K is investigated for the $Cd_2Nb_2O_7$ relaxation system in two cases: (1) after sample cooling in a constant electric field E (FC) from $T = 295$ K to a preset temperature, which is much lower than the "freezing" temperature of the relaxation state ($T_f \approx 182$ K), field removal, and subsequent cooling in zero field (ZFC) to $T = 10$ K and (2) after ZFC from $T = 295$ K to the same temperature below T_f, application of the same field, and FC to $T = 10$ K. The behavior of the $P_r^{FC}(T)$ and $P_r^{ZFC}(T)$ dependences is analyzed. In the field $E < 2$ kV/cm, the P_r^{ZFC} curves as functions of $1/T$ have a broad low-intensity peak in the region $T \approx T_f$, which vanishes in stronger fields, when the $P_r^{FC}(1/T)$ curves intersect at $T \approx T_f$ and have no anomalies. The difference in the behavior of $P_r^{ZFC}(T)$ and $P_r^{FC}(T)$ indicates the difference in the nature of NERS formed during ZFC and FC of the system upon a transition through T_f. In the ZFC mode, NERS exhibits glasslike behavior; in the FC regime, features of the ferroelectric behavior even in the weak field. Analogous variations of $P_r^{ZFC}(T)$ and $P_r^{FC}(T)$ in a classical ferroelectric KDP are also given for comparison. © *2005 Pleiades Publishing, Inc.*

1. INTRODUCTION

The nature of the nonergodic relaxation state (NERS) emerging below the freezing point T_f of the ergodic relaxation state (ERS) in relaxation ferroelectrics, has become the object of intense experimental and theoretical investigations [1–11]. The following two main concepts are proposed: (1) a state of the dipole-glass type, which is formed as a result of random interactions between polar nanoclusters in the presence of random fields [1–7], or (2) a frustrated ferroelectric divided into nanodomains under the action of random electric fields [8–11]. At the same time, it was shown that the dielectric response of a relaxation ferroelectric in a strong constant and strong varying electric fields is controlled by the motion of ferroelectric domain walls both in NERS and in ERS [10, 11]. On the other hand, in the vicinity of the temperature T_m ($T_m > T_f$) corresponding to the peak of the dielectric response of the relaxation system, the coexistence of polar phases of different origin is detected (reorientable polar clusters with glasslike "freezing" of polarization and nanodomains with a temperature-independent behavior of polarization, which are fixed as a result of the pinning effect [12]). The contradictory interpretation of the origin of NERS and ERS in the region $T \longrightarrow T_f^+$ may be due to the fact that the dielectric response of relaxation ferroelectrics was studied by different researchers under different conditions. The main drawbacks of these studies, which complicate the interpretation of the results on the basis of a unified approach, include the measurement of static or dynamic permittivity, temperature scanning for a fixed or scanned constant electric field, arbitrariness in the choice of weak and strong dc and ac electric fields in the measurements, and arbitrariness in the choice of cooling or heating conditions in zero field or in a constant field (ZFC or ZFH and FC or FH, respectively), etc. [1–5, 8–11]. Although each of these factors makes it possible to reveal peculiarities in the behavior of a nonergodic system, neither of these factors clarifies the reason for different manifestation of NERS properties under different measuring conditions. Consequently, to answer the basic question about the origin of NERS in a relaxation ferroelectric, new experiments are required to study the properties of such systems. In this study, we consider for the first time the temperature dependence of residual polarization P_r obtained from measurements of pyroelectric current upon zero-field heating (ZFH) in a temperature range from 10 to 295 K for the $Cd_2Nb_2O_7$ relaxation system as an example in two cases: (i) after FC from room temperature to a preset temperature below T_f, removal of the constant field, and subsequent ZFC to $T = 10$ K; and (ii) after ZFC from room temperature to the same temperature below T_f, application of the same field, and FC to 10 K ($P_r^{FC}(T)$ and $P_r^{ZFC}(T)$, respectively). Such a sequence of field application and removal during cooling was not used earlier for studying either spin or dipole glasses, or relaxation ferroelectrics. Usually, to investigate the glasslike nature of NERS in relaxation systems, one needs to analyze the dielectric and polarization responses in the FC or ZFC regime to a preset temperature, which is much lower than T_f, followed by FH or ZFH from this temperature to room temperature [3, 5, 9]. Here, the measurements are made under the same condition, i.e., in the ZFH regime from $T = 10$ K to room temperature ($T \gg T_f$). The static polarization determined from the pyroelectric current may serve as a universal characteristic of the metastable NERS of a relaxation ferroelectric in an external electric field since the temperature dependences of the polarization of a cluster system and a system with a long-range ferroelectric order are different [7, 13]. In spite of the obviousness of this fact, systematic studies of the $P_r(T)$ dependence in relaxation systems under different thermal and electrical measuring conditions have not been carried out so far [2, 3, 5, 14]. New experiments proposed in this study for analyzing $P_r(T)$ show that the formation of glass and ferroelectric properties of the NERS is predetermined in the course of ZFC or FC (even in a weak field) of a nonequilibrium system upon a transition via T_f.

Our experiments were made with pyrochlorine $Cd_2Nb_2O_7$ (CN) ($Fd3m - O_h^7$), which is a unique example of an undiluted system with relaxation behavior [15, 16] (in contrast to mixed perovskites of the PMN–$PbMg_{1/3}Nb_{2/3}O_3$ and PLZT–$Pb_{1-x}La_x(Zr_yTi_{1-y})O_3$ ($Pm3m - O_h^1$) type. The relaxation properties of CN are determined by orientation disordering of O–Cd–O dipoles in the $(CdO_8)^{n-}$ sublattice, which exhibits a rhombohedral local symmetry $D_{3d} - \bar{3}m$ [15]. The high cubic symmetry of the system on the whole and the rhombohedral local symmetry of the $(CdO_8)^{n-}$ sublattice make it possible to carry out analysis of the dielectric behavior of this relaxation ferroelectric using the well-known models of spin and dipole glasses [17] and relaxation systems [4, 6, 7, 18]. However, the behavior of CN is much more complicated as compared to perovskites of the PMN type. In the temperature range from 300 to 4 K, the following states develop in this material successively: the relaxation state covering the para- and ferroelectric phases, ferroelastic state (below $T_s = 205$ K), the ferroelectric state (below $T_C = 196$ K), the state with an incommensurate–modulated structure ($T_{inc} = 85$ K, $T_{com} = 46$ K), and a state of the dipole glass type (below $T_g \approx 18$ K) [19]. The reasons for the formation of disordered states of various origins and their interrelation with the ferroelectric state in this compound have been studied insufficiently. The relaxation state in pyrochlorine, as well as relaxation ferroelectrics with the perovskite structure), is characterized by dielectric dispersion in a wide frequency range in the temperature region corresponding to the permittivity peak, $T_m \approx 190$ K ($T_m < T_C < T_s$), and subsequent freezing of the ERS at $T_f \approx 183$ K [15, 16].

2. EXPERIMENTAL TECHNIQUE

The experiments were performed on a monocrystalline plate of the $(111)_{cub}$ type, which was preliminarily annealed at $T = 353$ K for 4 h to reduce internal stresses. The powder X-ray diffraction method revealed that it has the pyrochlorine structure; no admixtures of other phases were detected. Silver-paste electrodes were deposited on the parallel surfaces of the plate. After the removal of a constant field E, the sample was first short-circuited for removing the residual surface charge. Sample cooling (FC and ZFC) always began from $T = 295$ K (i.e., from the temperature high enough for “erasing” the effects of previous measurements). Pyroelectric current was measured during ZFH from 10 to 295 K using a programmed Keithley-6514 high-sensitivity electrometer under slow heating at a rate of 1.5 K/min. The $P_r(T)$ curves for the value of the constant field were obtained by integrating the temperature dependence of the pyroelectric current. The error in the measurements of pyroelectric current (and, hence, polarization) did not exceed 0.05%. This enabled us to detect weak changes in the polarization of the relaxation system both in the region of T_f and in the paraelectric phase ($T > T_f$). Temperature was stabilized within ±0.05 K.

3. RESULTS AND DISCUSSION

Figures 1 and 2 show the typical $P_r^{ZFC}(T)$ and $P_r^{FC}(T)$ curves for pyrochlorine CN after cooling to $T = 120$ K and $T = 145$ K ($T \ll T_f$), respectively. The $P_r^{ZFC}(T)$ and $P_r^{FC}(T)$ curves for a normal classical ferroelectric KDP cooled to a temperature much lower than T_C are also shown for comparison (Fig. 2d). The polarization had not been studied previously under conditions of our experiments not only for relaxation systems, but neither for normal ferroelectrics. For this reason, we will first illustrate peculiarities in the behavior of polarization using KDP as an example, which show that the proposed method makes it possible to study disordered and nonequilibrium states of polar systems (polarization processes in polydomain ferroelectrics, relaxation oscillators with a nanodomain structure, and spin and dipole glasses).

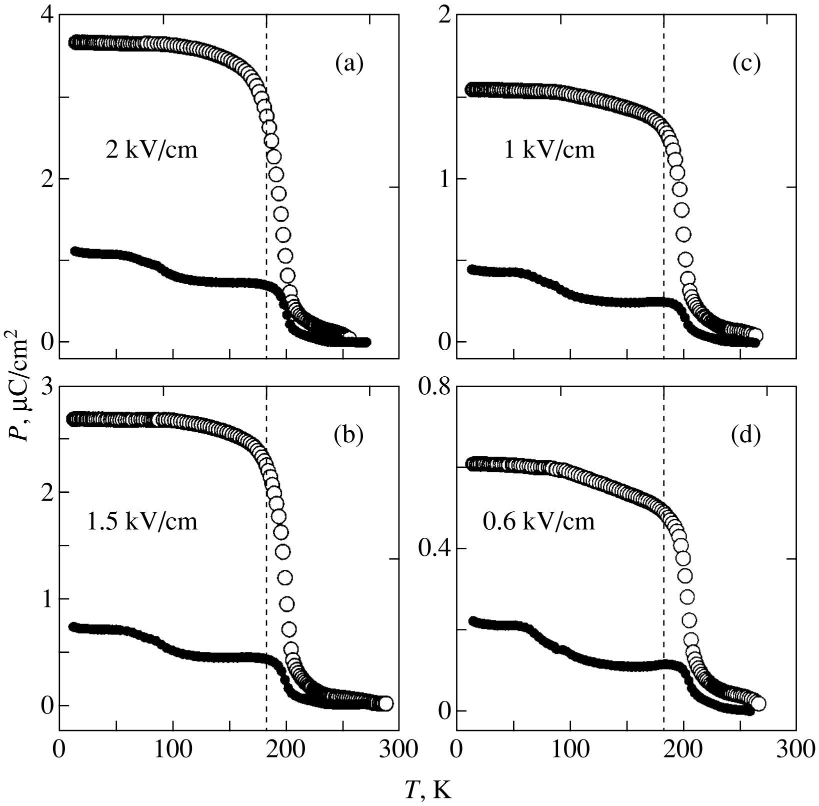

Fig. 1. Temperature dependence of the residual polarization in a pyrochlorine $Cd_2Nb_2O_7$ (CN) single crystal obtained from the ZFH measurements of pyroelectric current after cooling in the FC (○) and ZFC (●) modes from $T = 295$ K to $T = 120$ K, followed by further cooling under the same conditions to $T = 10$ K for several values of the constant electric field. The heating rate is 1.5 K/min. The dashed line indicates the freezing temperature T_f corresponding to the transition from the ERS to the NERS.

In the FC mode (2 kV/cm), the KDP sample cooled from room temperature to $T = 75$ K exhibits below T_C a monodomain ferroelectric state with the polarization oriented along the applied field ($T_C \approx 123$ K and $E_{\rm coer} \approx 200$ V/cm in KDP [13]). After the removal of the constant field and subsequent cooling in the ZFC mode to $T = 10$ K, the ferroelectric remains in the "frozen" monodomain state. In the ZFC from room temperature to the same temperature below T_C, the ferroelectric is in a polydomain state. After application of the same field at 75 K and subsequent cooling in the FC regime to $T = 10$ K, the ferroelectric passes to a monodomain state with the polarization oriented along the field. When the sample is heated in zero field from 10 to 295 K, the variation of $P_r^{FC}(T)$ corresponds to the monodomain state of the ferroelectric. The behavior of the $P_r^{ZFC}(T)$ curve is different. At low temperatures, the variation of $P_r^{ZFC}(T)$ corresponds to the monodomain state, while the polarization being measured is determined by the contribution of the polarization of the monodomain and polydomain states as we approach $T^- \approx 75$ K and above this temperature. The latter is a disordered state as regards the orientation of polarization in individual domains relative to the direction of the polarization of the monodomain state. As a result, the total value of $P_r^{ZFC}(T)$ in the normal ferroelectric is smaller than $P_r^{FC}(T)$.

In cooling of pyrochlorine CN in the ZFC and FC modes ($E < 3$ kV/cm) from room temperature to $T = 120$ K or $T = 145$ K, the frozen state of the relaxation system below T_f is a polydomain state. As other relaxation ferroelectrics, polar nanoregions "nucleate" in pyrochlorine long before T_f (approximately, in the region of $T \approx 270$ K) [20]. In the FC mode, the polarization of nanodomains acquires a component in the direction of the applied field. After the removal of the field at $T \ll T_f$ and subsequent cooling of the system in the ZFC mode to $T = 10$ K, this state is preserved. In the case of ZFC of the system to the same temperature below T_f, application of the same field, and subsequent FC to $T = 10$ K, the polarization of frozen nanodomains also acquires a component in the direction of the applied field, but this component is weaker. This is due to the fact that the NERS is characterized by a very wide spectrum of the relaxation time distribution from 10^{-12} s to macroscopic values [3, 5, 8]. In view of this feature of the nonergodic state, as well as the contribution of nonpolarized frozen nanodomains in the region

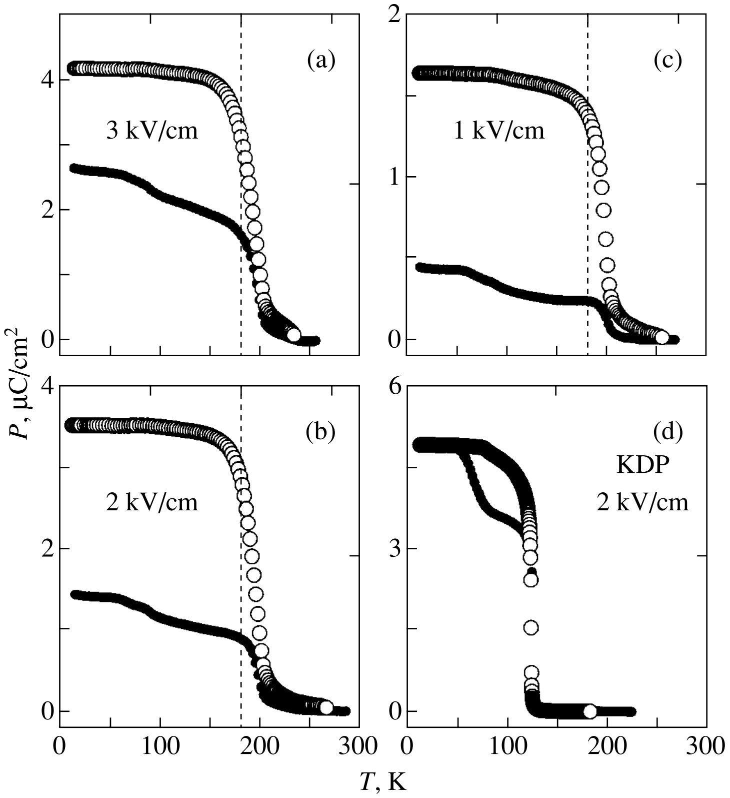

Fig. 2. (a, b, c) Temperature dependence $P(T)$ obtained from the ZFH measurements in pyrochlorine CN after cooling in the FC (○) and ZFC (●) modes from $T = 295$ K to $T = 145$ K, followed by further cooling under the same conditions to $T = 10$ K for several values of the constant electric field, and (d) the same for a KDP single crystal after cooling under the same conditions from $T = 295$ K to $T = 75$ K followed by cooling to $T = 10$ K. Gold electrodes are deposited on the KDP sample.

of $T^- \approx 120$ K (or 145 K) and above this temperature, polarization $P_r^{ZFC}(T)$ differs substantially from $P_r^{FC}(T)$ both in magnitude and in the temperature variation upon sample heating from $T = 10$ K to $T = 295$ K in zero field (see Figs. 1 and 2).

In contrast to KDP, pyrochlorine CN exhibits strong splitting between the ZFH static polarization after FC (ZFH/FC) and after ZFC (ZFH/ZFC) of the system ($\Delta P_r = P_r^{FC} - P_r^{ZFC}$). In fields up to 2 kV/cm, the splitting remains virtually unchanged in the entire temperature range from 10 K to T_f ($T_f \approx 182$ K for the sample under investigation). This means that the state of the system below T_f is completely frozen and nonergodic. Equally strong splitting between the FC and FH/ZFC static permittivities (Δε) as well as between the FC and FH/ZFC polarizations (ΔP) was observed earlier in orientation glasses [17] and relaxation ferroelectrics [3, 5, 8]. The observed splitting is a fundamental property of glass systems and, hence, a reliable argument in favor of the glasslike nature of the NERS in CN (at least in a field of $E < 2$ kV/cm).

In stronger fields ($E > 2$ kV/cm), the splitting between $P_r^{ZFC}(T)$ and $P_r^{FC}(T)$ becomes smaller as we approach T_f^- (see Figs. 1a, 2a, and 2b). As the temperature increases further, the values of P_r^{FC}, P_r^{ZFC}, and ΔP_r decrease rapidly as T^- approaches 200 K and not T_f^-. It should be noted that, with the generally accepted sequence of application and removal of the field in glasses and relaxation systems, the values of ΔP and Δε rapidly decrease as we approach T_f^- and vanish above this temperature [3, 5, 8]. Above $T = 200$ K, the polarization in pyrochlorine CN becomes low and slowly approaches zero at $T \sim 270$ K; here, the value of P_r^{FC} is always greater than P_r^{ZFC} and increases with the field. The "protracted tail" of the polarization implies the presence in the ERS of polar clusters that remain nonergodic up to high temperatures [3]. Another feature of our results is that the behavior of $P_r^{FC}(T)$ and $P_r^{ZFC}(T)$ in the region of 200 K and above matches the behavior of the local order parameter q in pyrochlorine CN [20] as well as in the PMN and PLZT compounds [12]. At the same time, the behavior of the FC and FH/ZFC static permittivity and polarization obtained for the PMN and PLZT compounds in the generally accepted sequence of field application and removal does not

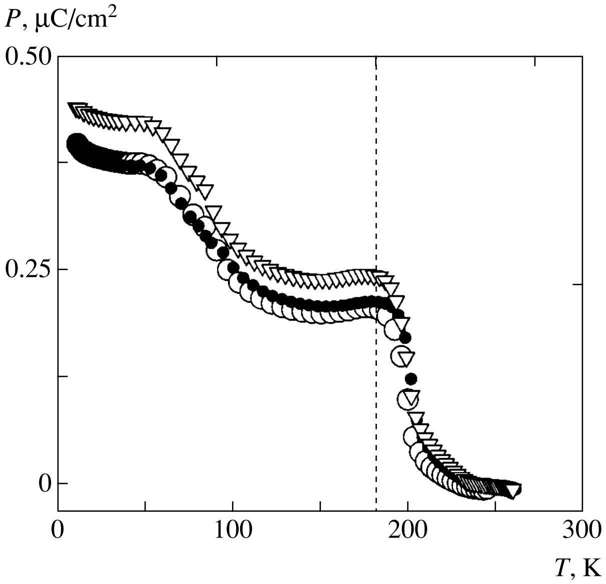

Fig. 3. Temperature dependence $P(T)$ obtained from the ZFH measurements in pyrochlorine CN after cooling in the ZFC mode to $T = 120$ K, followed by further cooling in the FC mode to $T = 10$ K in a field of 1 kV/cm for several values of heating rate: 1.5 (upper curve), 0.5, and 0.2 K/min (lower curve). The low-intensity broad peak in the region of T_f is due to the contribution from the polarization of nanodomains with long relaxation times corresponding to the laboratory scale.

match the behavior of the local order parameter q [2, 5, 12, 14]. Identical behavior of $P_r^{FC}(T)$ and $P_r^{ZFC}(T)$ after cooling to $T = 120$ K and 145 K indicates the thermal stability of the frozen state and the dependence of the properties of this state only on its polarization (either $E \neq 0$ as we pass through T_f, or field E is applied at $T \ll T_f$).

Since the normal ferroelectric and relaxation ferroelectric states develop in pyrochlorine simultaneously below T_C (198 K for the sample studied here [21]) [15, 16, 19], it should be borne in mind that both states may contribute to the polarization being measured. Analysis of the dielectric data obtained by different methods shows that the relaxation contribution dominates (at least in fields $E < 4$ kV/cm). This follows above all from the large difference between the values of P_r^{FC} and P_r^{ZFC}, which is typical of the NERS of a relaxation system (see Figs. 1 and 2). Small values of $P_r^{FC} \approx 1.54$ μC/cm^2 and $P_r^{ZFC} \approx 0.45$ μC/cm^2 (at 20 K) for $E = 1$ kV/cm and $P_r^{FC} \approx 0.61$ μC/cm^2 and $P_r^{ZFC} \approx 0.22$ μC/cm^2 (at 20 K) for $E = 0.6$ kV/cm in a weak field are rather typical of relaxation systems [5, 14]. It can be observed for comparison that $P_r^{FC} = P_r^{ZFC} \approx 5$ μC/cm^2 in KDP at $T = 20$ K in a field of 2 kV/cm (see Fig. 2d). In pyrochlorine CN in a field of 3 kV/cm, the value of $P_r^{FC} \approx 4.24$ μC/cm^2 and $P_r^{ZFC} \approx 2.7$ μC/cm^2 are comparable to the polarization in a normal ferroelectric, but the splitting between them ($\Delta P_r \approx 1.54$ μC/cm^2) is still significant (see Fig. 2a). Since the dielectric hysteresis loops in pyrochlorine CN as well as in other relaxation systems are strongly extended, a large difference appears between the coercive field and the saturated polarization field ($E_{\text{coer}} \approx 2.5$ kV/cm and $E_s \approx 10$ kV/cm for the sample at $T = 120$ K). It is also known that a field exceeding 4 kV/cm is required for switching ferroelectric domains in pyrochlorine CN [22].

The modes of cooling a relaxation system in a constant electric field used in this study have made it possible for the first time to discover a broad low-intensity peak on the temperature dependence of P_r^{ZFC} ($\Delta T \approx 40$ K) in the vicinity of T_f (see Figs. 1b, 1c, 1d, 2c, and 3). The height of the $\Delta P_{\max}$ peak exceeds the polarization value on the gently sloping part of the curve only by 3–5% (in the interval from 120 to 150 K), but is two orders of magnitude higher than the accuracy in polarization measurements. For this reason, the existence of a peak in the vicinity of T_f cannot be ignored. The slow decrease in the total polarization P_r^{ZFC} at $T \longrightarrow T_f^-$ is direct evidence of the presence of frozen nanodomains with various macroscopic relaxation times.

The height and position of the $\Delta P_{\max}$ peak do not change upon an increase in the field to 2 kV/cm (see Figs. 1 and 2) as well as upon an order-of-magnitude decrease in the heating rate (Fig. 3). In fields higher than 2 kV/cm, the temperature dependence of P_r^{ZFC} becomes monotonic; instead of the peak in the region of T_f, a kink is observed, which vanishes with a further increase in the field (see Figs. 2a and 2b). These facts also indicate that the origin of the peak on the $P_r^{ZFC}(T)$ curves is associated with intrinsic properties of a nonergodic relaxation state with a glasslike behavior, for which the characteristic relaxation times are comparable with the time of the experiment (7600 s, which corresponds to a frequency of 0.13 mHz). Glass properties of the NERS are manifested until a stronger field ($E > 2$ kV/cm) induces a change in this state.

Anomalies at $T_{\text{inc}} \approx 85$ K and $T_{\text{com}} \approx 50$ K correspond to a phase transition in pyrochlorine [19]. It should be noted that the behavior of $P_r^{FC}(T)$, $P_r^{ZFC}(T)$, and ΔP in the vicinity of T_{com} does not exhibit any noticeable pinning effects typical of incommensurate modulated structures [23]. Probably, the nonergodicity of the frozen state plays a decisive role in the behavior of the system down to low temperatures (i.e., below the phase-transition temperature at $T_{\text{com}} < T_{\text{inc}}$).

For a system with cubic symmetry and rhombohedral distortions (e.g., CN), total static polarization along vector **E** due to reorientable clusters has the form [7]

$$P_t = P_{cl}\tanh\frac{EP_{cl}L^3}{3kT} = P_{cl}\tanh\frac{EA}{T}, \qquad (1)$$

where P_{cl} is the effective polarization of the cluster, L is the cluster size, kT is the thermal energy, k is the Boltzmann constant, and $A = P_{cl}L^3/3k$. Since the polarization in measured in the ZFH mode after the removal of the field ($E \longrightarrow 0$), which corresponds to the condition $EA/T \ll 1$, relation (1) can be written in the form

$$P_t \propto 1/T, \qquad (2)$$

which can be directly used for $P_r^{ZFC}(T)$ and $P_r^{FC}(T)$. The corresponding curves display basically different behavior of polarization after ZFC and FC of the system passing through T_f even in a weak field (Fig. 4). In the region of $T = 200$ K, the $P_r^{ZFC}(1/T)$ curves coincide, but these curves diverge as we approach T_f^+ and have a broad peak in a weak field or a kink in a field $E \geq 2$ kV/cm for $T \sim T_f$ (Fig. 4a). The curves $P_r^{ZFC}(1/T)$ diverge weakly in a field $E < 2$ kV/cm in the entire temperature range; the curves intersect at $T \sim T_f$ and display no anomalies (Fig. 4b). In a field $E \geq 2$ kV/cm, the curves are noticeably displaced to a lower temperature, indicating that the behavior of the polarization no longer corresponds to a cluster system (in contrast to P_r^{ZFC} in the same fields). Moreover, this result implies that a relatively weak field creates premises for the formation of long-range ferroelectric order and, hence, the formation of a nonhomogeneous glasslike NERS in the course of FC of the system to a temperature below T_f. In this connection, to characterize NERS, we analyzed the behavior of $P_r^{FC}(T)$ using the well-known relation for spontaneous polarization in a normal ferroelectric [13]:

$$P_s^2 \propto (T_C - T).$$

Below T_f, a linear variation of $(P_r^{FC})^2$ with temperature is observed for $E \geq 2$ kV/cm (see the inset to Fig. 4); in other words, if the system is cooled in the FC mode, the ergodic relaxation state passes to the ferroelectric state. If $E < 1.5$ kV/cm, the temperature dependence of $(P_r^{FC})^2$ becomes nonlinear, the departure from linearity being the smaller, the stronger the field. The latter statement means that, in the course of system cooling in the FC mode in a weak field, regions with long-range ferroelectric ordering are formed in a glasslike NERS.

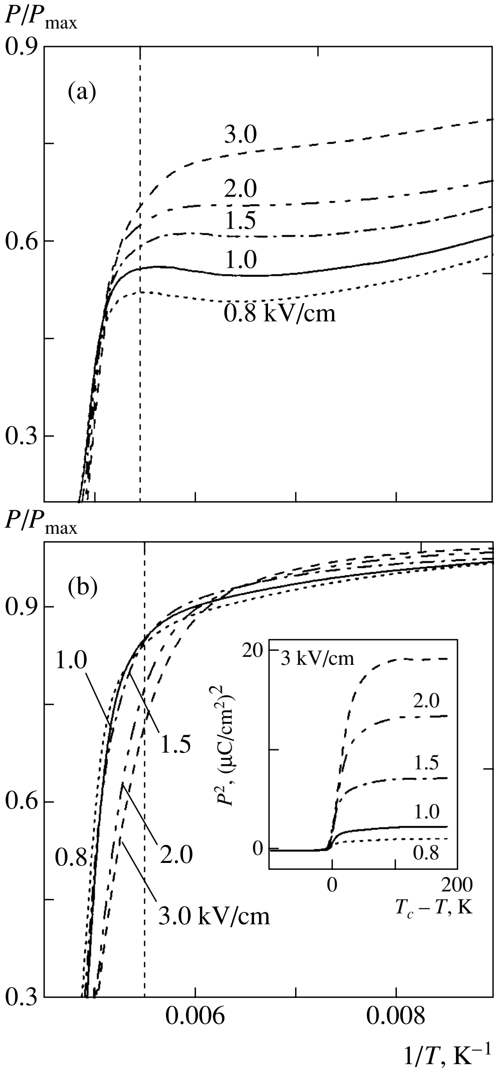

Fig. 4. Reduced polarization P/P_{max} obtained from (a) ZFC and (b) FC measurements in pyrochlorine CN versus the reciprocal temperature for several values of the constant field; P_{max} corresponds to polarization at 10 K for each field value.

4. CONCLUSIONS

To determine the nature of NERS in relaxation ferroelectrics, the residual polarization $P_r(T)$ of a undiluted high-symmetry relaxation pyrochlorine ($Cd_2Nb_2O_7$) system is analyzed for the first time during heating in the ZFH mode from $T = 10$ K to $T = 295$ K after two different modes of cooling in the FC mode from $T \gg T_f$ to 10 K. Analysis of the temperature and field dependences $P_r^{FC}(T)$, $P_r^{ZFC}(T)$, and ΔP is carried out taking into account the ideas concerning the features of orientation glasses and relaxation ferroelectrics with glasslike behavior. It is shown that the factor of the external constant electric field plays the key role in the formation of the properties of the nonergodic state when the system passes through the freezing temperature T_f (i.e., $E = 0$ or $E \neq 0$). This result is of fundamental importance for the physics of relaxation ferroelectricity since it clarifies the reason and conditions for ambiguous manifestations of (glass or ferroelectric) properties of NERS in relaxation systems. The difference in the behavior of polarizations $P_r^{FC}(T, E)$ and $P_r^{ZFC}(T, E)$ can also be used for revealing the glass or ferroelectric nature of NERS in relaxation systems of any type, including the model relaxation ferroelectric PMN.

ACKNOWLEDGMENTS

This study was supported by the Russian Foundation for Basic Research (project no. 04-02-16126) and KBN (Poland) (grant no. P03B 04722).

REFERENCES

1. D. Viehland, M. Wuttig, and L. E. Cross, Ferroelectrics **120**, 71 (1991).
2. D. Viehland, J. F. Li, S. J. Jang, *et al.*, Phys. Rev. B **46**, 8003 (1992).
3. D. Viehland, J. F. Li, S. J. Jang, *et al.*, Phys. Rev. B **46**, 8013 (1992).
4. V. Bobnar, Z. Kutnjak, R. Pirc, *et al.*, Phys. Rev. Lett. **84**, 5892 (2000).
5. A. Levstik, Z. Kutnjak, C. Filipič, *et al.*, Phys. Rev. B **57**, 11204 (1998).
6. R. Pirc, R. Blinc, and Z. Kutnjak, Phys. Rev. B **65**, 214101 (2002).
7. A. J. Bell, J. Phys.: Condens. Matter **5**, 8773 (1993).
8. V. Westphal, W. Kleemann, and M. D. Glinchuk, Phys. Rev. Lett. **68**, 847 (1992).
9. R. Sommer, N. K. Yushin, and J. J. van der Klink, Phys. Rev. B **48**, 13230 (1993).
10. A. E. Glazounov, A. K. Tagantsev, and A. J. Bell, Phys. Rev. B **53**, 11281 (1996).
11. A. K. Tagantsev and A. E. Glazounov, Phys. Rev. B **57**, 18 (1998).
12. R. Blinc, J. Dolinšek, A. Gregorovič, *et al.*, Phys. Rev. Lett. **83**, 424 (1999).
13. F. Jona and G. Shirane, *Ferroelectric Crystals* (Pergamon, Oxford, 1962).
14. R. Farhi, M. El Marssi, J.-L. Dellis, *et al.*, Ferroelectrics **176**, 99 (1996).
15. N. N. Kolpakova, P. P. Syrnikov, A. O. Lebedev, *et al.*, J. Appl. Phys. **90**, 6332 (2001).
16. N. N. Kolpakova, P. Czarnecki, W. Nawrocik, *et al.*, Zh. Éksp. Teor. Fiz. **121**, 462 (2002) [JETP **94**, 395 (2002)].
17. K. Binder and A. P. Young, Rev. Mod. Phys. **58**, 801 (1986).
18. D. Viehland, S. J. Jang, L. E. Cross, *et al.*, J. Appl. Phys. **69**, 414 (1991).
19. N. N. Kolpakova, I. L. Shul'pina, M. P. Shcheglov, *et al.*, Ferroelectrics **240**, 265 (2000).
20. N. N. Kolpakova, Zh. Éksp. Teor. Fiz. **123**, 607 (2003) [JETP **96**, 538 (2003)].
21. N. N. Kolpakova, P. Czarnecki, W. Nawrocik, *et al.*, Ferroelectrics **302**, 233 (2004).
22. Z.-G. Ye, N. N. Kolpakova, J.-P. Rivera, *et al.*, Ferroelectrics **124**, 275 (1991).
23. K. Hamano, Y. Ikeda, T. Fujimoto, *et al.*, J. Phys. Soc. Jpn. **49**, 2278 (1980).

Translated by N. Wadhwa

Journal of Experimental and Theoretical Physics, Vol. 100, No. 5, 2005, pp. 971–976.
Translated from Zhurnal Éksperimental'noĭ i Teoreticheskoĭ Fiziki, Vol. 127, No. 5, 2005, pp. 1099–1105.
Original Russian Text Copyright © 2005 by El'kin, Tsiok, Khvostantsev, Brazhkin.

ORDER, DISORDER, AND PHASE TRANSITIONS IN CONDENSED SYSTEMS

Precise In Situ Study of the Kinetics of Pressure-Induced Phase Transition in CaF_2 Including Initial Transformation Stages

F. S. El'kin, O. B. Tsiok, L. G. Khvostantsev, and V. V. Brazhkin
Vereshchagin Institute of High-Pressure Physics, Russian Academy of Sciences, Troitsk, Moscow oblast, 142190 Russia
e-mail: tsiok@hppi.troitsk.ru

Received November 12, 2004

Abstract—The kinetics of room-temperature phase transition in fluorite (CaF_2) single crystals under hydrostatic pressure up to 9 GPa was studied in situ by means of strain gauge compressibility measurements. Initial stages of the pressure-induced first-order phase transition kinetics (corresponding to less than 1% content of the new phase) were studied for the first time. In a broad range of concentrations of the new phase (5–20%), the transformation kinetics is well described within the framework of the classical Kolmogorov–Avrami–Mehl–Johnson model. The laws governing the initial and late stages of the transformation are more complicated and do not conform to the classical model. The initial stages involve avalanche growth in the nucleation rate corresponding to giant values of the Avrami exponent ($n \approx 20$). At large concentrations of the new phase (above 30%), the transformation rate significantly decreases (saturation) as a result of the formation of a rigid cellular structure of the new phase. © *2005 Pleiades Publishing, Inc.*

1. INTRODUCTION

Phase transformations in solids can be conditionally subdivided into two types with respect to the transition kinetics. Transformations of the diffusion type involve nucleation as a result of fluctuations and the subsequent growth of nuclei by means of diffusion, while martensite transformations imply a coherent conversion of one lattice into another by means of shear distortions [1]. This simplified classification is by no means exhaustive, since many of the polymorphous phase transformations caused by compression can hardly be classified into one of the two types. This is especially difficult in the case of pressure-induced phase transformations involving large relative volume changes, which take place at temperatures significantly below the melting point, in particular, at room temperature. Under such conditions, the diffusion mobility of atoms at low temperatures is "frozen" to a considerable degree, while a coherent martensite transformation in most cases is impossible. As a result, phase transformations proceed according to a mixed type of kinetics, the laws of which have almost not been investigated [2]. Since the overwhelming majority of polymorphous phase transformations take place under conditions of strong compression, the study of mechanisms and kinetics of such transitions is among basic problems of the physics of condensed media.

Previous investigations of the kinetics of pressure-induced phase transformations were carried out in most cases using X-ray diffraction measurements at elevated temperatures. The experimental data were obtained either by ex situ measurements on quenched samples [3] or from in situ experiments using high-brightness X-ray (predominantly synchrotron) radiation [4–7]. As a rule, the transition kinetics was studied for phase transformations of the diffusion type involving large volume changes, such as α-$GeO_2 \longrightarrow \beta$-$GeO_2$ [3], graphite $\longrightarrow$ diamond [4, 5], hexagonal BN $\longrightarrow$ cubic BN [6], and some others [7]. Theoretical analysis of the kinetic curves was usually performed in terms of the Kolmogorov–Avrami–Mehl–Johnson (KAMJ) model [8–10]. Strictly speaking, this approach was developed for the description of transformations with small volume changes between isotropic phases with zero shear moduli, so that applicability of the KAMJ model to description of the pressure-induced polymorphous phase transformations with large volume changes is rather questionable. The main parameter in this model—the Avrami exponent n—is determined by the conditions of nucleation and growth and may vary, depending on the particular mechanism, from 0.3 to 4 [1]. The values of n formally calculated for most of the phase transitions studied fall within $n \approx 1$–2 [3–7], which corresponds to one- or two-dimensional growth of preexisting nuclei.

It should be noted that X-ray diffraction (XRD) is characterized by a relatively high threshold (i.e., low sensitivity) for the detection of a newly formed structural modification, and this method provides insufficient accuracy from the standpoint of kinetic investigations. A minimum content of the new phase detectable by XRD is on the level of several percent, which limits the possibility of using this method for the investigation of early stages of crystal nucleation and growth. However, these initial stages of phase transformations are

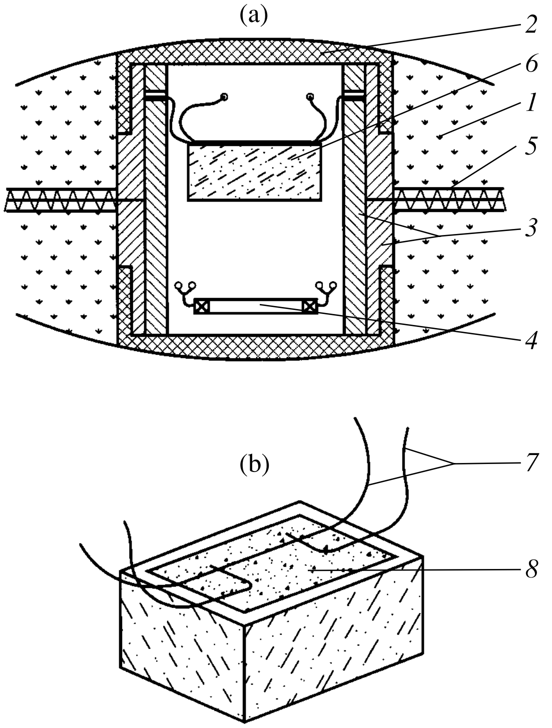

Fig. 1. Schematic diagram of (a) the high-pressure cell and (b) a sample with strain gauge: (*1*) gasket (pipestone); (*2*) lid (brass); (*3*) ampule case (Teflon); (*4*) pressure sensor (manganine); (*5*) output signal leads; (*6*) sample with bonded strain gauge; (*7*) current and potential leads (constantan wire 20 μm in diameter); (*8*) strain gauge base (paper of glass composite).

usually most important for assessing the applicability of various theoretical models.

In this study, the phase transition kinetics was studied using a strain gauge technique developed for measuring the compressibility of solids under a hydrostatic pressure of up to 9 GPa [11]. This technique allows the compressibility to be determined under conditions of large volume variations (up to 30%). The strain gauge method was successfully used for the investigation of compressibility of crystalline and amorphous solids and compacted powders [11–14]. Being comparable to XRD in absolute accuracy of volume measurements (in crystals), the strain gauge technique has a relative sensitivity several orders of magnitude higher than that of XRD. Using the proposed method, it is possible to monitor the fraction of a new phase in the sample in the course of transformation and to study the phase transition kinetics in situ at high pressures. The new phase can be detected at a threshold content of 0.03%. The strain gage technique offers high temporal resolution and ensures high-precision monitoring of the pressure in a broad temperature range (from 300 to 700 K [15]).

The aim of this study was to measure the kinetics of a pressure-induced first-order phase transition by means of the strain gauge technique in an ideal hydrostatic medium at room temperature. The compressibility measurements were performed in a broad range of concentrations of the new phase, including initial stages of the transformation.

The experiments were performed on fluorite (CaF_2) single crystals. According to published data, fluorite exhibits a room-temperature phase transition at 8 GPa with a significant (8.3%) relative volume change, whereby the low-pressure α-CaF_2 phase with an intrinsic cubic structure converts into a high-pressure γ phase with an orthorhombic structure of the α-$PbCl_2$ type [16].

2. EXPERIMENTAL

Singe crystal CaF_2 samples had the shape of parallelepipeds with dimensions of $2 \times 2.5 \times 3.5$ mm, with a strain gage bonded to one (preliminarily polished) face. The strain gauge technology and the method of compressibility measurement in solids under pressure are described elsewhere [11, 15].

Since fluorite crystals are characterized by perfect octahedral cleavage, the samples were cut so that their faces corresponded to cubic crystallographic planes. This orientation decreases the probability of strain gauge detachment and sample fracture as a result of the phase transformation.

High pressures were produced using an apparatus of the "toroid" type, comprising an ampule with a working volume of about 0.3 cm^3 filled with a hydrostatic medium, in which a pressure of up to 9 GPa could be created [17]. The high-pressure cell design is schematically depicted in Fig. 1.

The medium transmitting pressure to the sample was a mixture of methyl and ethyl alcohol (4 : 1), which is known to retain hydrostatic properties at pressures up to 10 GPa. The pressure was measured with the aid of a manganine-based sensor calibrated with respect to phase transitions in various reference substances. The reproducibility of pressure measurements in various experiments was on the order of 0.01 GPa. The measuring scheme ensured a pressure sensitivity of 0.001 GPa. In the course of loading the high-pressure cell, the rate of pressure variation in the ampule was 0.18 GPa/min.

The optimum experimental procedure was established during preliminary measurements of the fluorite crystal volume V as a function of the pressure p and time t (Fig. 2). The results of these measurements agree well with the published XRD data (Fig. 2a) [18].

Let us consider the results of preliminary measurements in more detail. In the first experiment (Fig. 2, curve *1*), the pressure was continuously increased at a rate of 0.18 GPa/min. The sample volume $V(p)$ began to drop sharply at 8.01 ± 0.01 GPa. This pressure corresponds to the onset of the α–γ phase transformation in fluorite, in agreement with published data [19]. At this time, the loading was interrupted and the pressure exhibited only a slight increase due to relaxation. After keeping the sample for 3 min in this state, whereby the

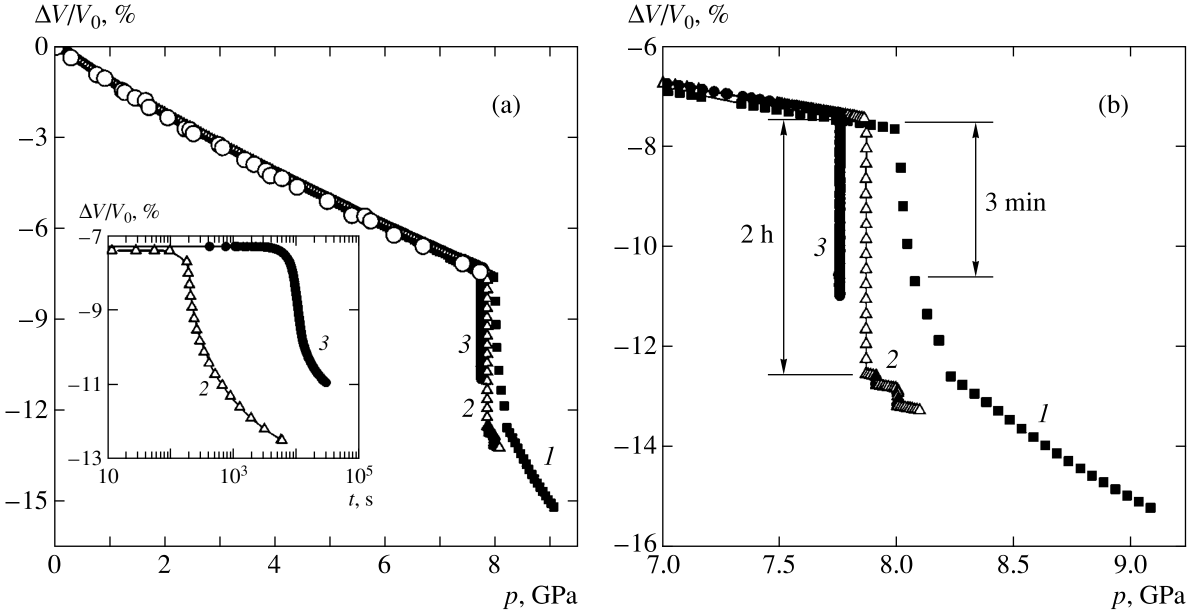

Fig. 2. (a) Plots of the relative volume change versus pressure in fluorite crystals under isothermal compression at T = 290 K: (*1*) pressure increased at a constant rate of 0.18 GPa/min; (*2*, 3) pressure kept constant at 7.87 and 7.76 GPa, respectively. Open circles reproduce XRD data from [18]. The inset shows the relative volume variation with time in the vicinity of the phase transition. (b) The region of phase transition on a greater scale (with characteristics transition times for kinetic curves *1* and *2*).

phase transition proceeded at a very slow rate, the loading was continued (Fig. 2b).

The second experiment showed that the phase transformation might start at a pressure below 8.01 GPa, which required a definite exposure at a fixed pressure (Fig. 2, curve *2*). In this experiment, the pressure was also increased at a rate of 0.18 GPa/min, but the loading was terminated on reaching a pressure of 7.82 GPa, after which the growth of pressure continued due to relaxation processes. Within approximately 200 s, the pressure in the ampule stabilized at a level of 7.87 GPa. Then, the pressure was maintained at this level to within ±0.001–0.002 GPa for 2 h, and the time variation of the volume was monitored. When the rate of the volume change significantly decreased, the pressure was given a stepwise increment, but this only slightly accelerated the transformation. Curve *3* in Fig. 2 was obtained at a fixed pressure of 7.76 GPa. As can be seen, curves *2* and *3* are significantly different, although the difference between pressures at which these measurements were performed is only slightly above 0.1 GPa. Thus, a relatively small change in the pressure at which the sample was kept leads to a significant modification of the phase transition kinetics.

Taking into account the results of preliminary experiments, we adopted the following scheme of measurements. In each experimental run, the pressure was increased at a preset rate and the sample volume was monitored. When the desired pressure level was reached, the load was rapidly controlled so as to compensate the relaxation processes in the high-pressure cell and maintain the pressure at a constant level, with an insignificant spike (below 0.005 GPa) within the first several seconds. Then, the pressure was fixed and the sample volume variation with time was monitored. This very procedure was used to obtain curve *3* in Fig. 2.

3. RESULTS AND DISCUSSION

The main series of experiments was carried out using the procedure described above. The phase transition in fluorite was studied at several fixed pressures in the interval 7.76 GPa ≤ p ≤ 8.01 GPa. The characteristic shape of the curves of sample volume versus time (on a logarithmic scale) is presented in the inset to Fig. 2a.

The kinetic data were analyzed in terms of the Avrami coordinates (ln[–ln(1 – x)] versus ln$t$), where $x(t)$ is the fraction of a new phase formed for the time t as a result of the phase transformation at a constant pressure p. The new phase fraction was defined as

$$x(t) = [\tilde{V}_p(t) - \tilde{V}_p]/\Delta\tilde{V}_{\text{trans}},$$

where $\tilde{V} = \Delta V/V_0$ is the relative volume change upon compression; V_0 is the sample volume at atmospheric pressure; $\tilde{V}_p$ is the volume before the transition onset ($\tilde{V}_p(0) = \tilde{V}_p$, because the sample immediately before the transition consists entirely of the old phase); and $\Delta\tilde{V}_{\text{trans}}$ = 8.3% is the total change in the volume as a result of the transition [19]. The Avrami coordinates make the kinetic curves highly illustrative, since the

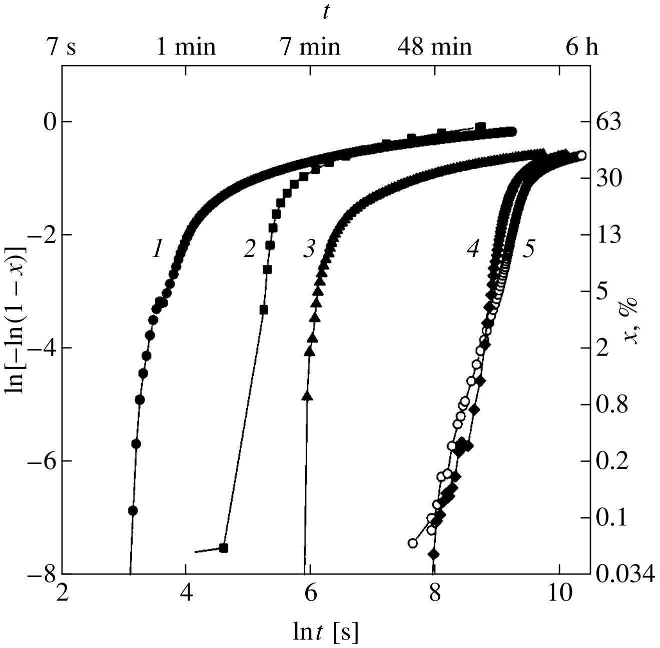

Fig. 3. Phase transformation kinetics in fluorite crystals at $T = 290$ K plotted in the Avrami coordinates at various pressure parameters $\Delta p = 8.01 - p$ [GPa]: (*1*) 0.09; (*2*) 0.14; (*3*) 0.17; (*4*, *5*) 0.25 GPa.

slope of the curve plotted in these coordinates is equal to the Avrami exponent n.

In representing data using the Avrami coordinates, a certain difficulty is encountered in selecting the point $t = 0$, which significantly influences the position and shape of the kinetic curves. We measured the time starting at the moment (t_0) when the pressure was fixed. This choice would certainly be optimum if it were possible to bring the system instantaneously to any point on the phase plane (without prehistory). Actually, the pressure could be varied only at a finite rate on the order of 0.18 GPa/min. Approaching a given point of measurement at a finite rate implies a prehistory ($\Delta t \neq 0$) with respect to a selected moment (t_0) of termination of the pressure growth. Therefore, it is necessary to fit the time t_0 in the adopted model to a certain time t_0 in a real experiment. In plotting the curves in Figs. 2 and 3, we used the assumption that $t_0 = 0$, which can be justified by the following estimates.

Consider a time interval between the moment when the pressure was fixed and the moment when a detectable fraction of the new phase (0.03%) was observed in the two extreme cases (i.e., in the experiments with minimum and maximum fixed pressures). For the phase transformation monitored at the minimum fixed pressure (7.76 GPa), this interval was about 2500 s, while at the maximum fixed pressure (8.01 GPa) it was about 20 s. The time of pressure increase from minimum to maximum at a constant rate of 0.18 GPa/min is 50 s. Taking this into account, we may ascertain that the transition kinetics in our experiments is determined primarily by the pressure and is weakly influenced by the prehistory, except for the curve obtained at a maximum pressure of 7.92 GPa.

Since the phase transformation onset under a continuous increase in pressure was observed at 8.01 GPa, whereas the kinetics was studied at fixed pressures $p <$ 8.01 GPa, it is convenient to introduce the pressure difference $\Delta p = 8.01 - p$ [GPa]. The kinetic curves of the α–γ phase transformation in CaF_2 at various Δp were plotted in the Avrami coordinates as depicted in Fig. 3. As can be seen from these data, all curves exhibit similar behavior. The only essential difference is the time shift, which significantly depends on Δp. Indeed, by varying this parameter, it was possible to obtain kinetic curves with phase transformation rates differing by several orders of magnitude.

It should be noted that all kinetic curves show anomalies in the region of $x = 5\%$ and exhibit bending in the region of $x = 20$–30%. These points separate the kinetic curves into three parts with different average slopes.

According to classical KAMJ theory, kinetic curves in the Avrami coordinates must appear as straight lines with a constant slope (Avrami exponent $n \leq 4$) without bending points. The limiting case $n = 4$ corresponds to three-dimensional growth of nuclei at a constant nucleation rate. Linear plots with $n \leq 4$ are usually observed for the kinetics of crystallization in metallic glasses at atmospheric pressure, which is accompanied by a negligibly small change in volume [20–22]. Lu and Wang [23] observed nonlinear behavior of the transition kinetics whereby the slope reached a maximum level of $n = 5$. This maximum value ($n = 5$) was explained by the fact that the phase transformation proceeded with increasing nucleation rate.

A significant difference of our investigation from those mentioned above consists in that the phase transformation in CaF_2 is accompanied by a large relative change in volume ($\Delta V = 8.3\%$) and takes place sufficiently far from the state of phase equilibrium. This implies that, at the onset of phase transition, a considerable amount of elastic energy is accumulated in the crystal.

Let us consider separately the different parts of the kinetic curves (Fig. 3). The initial parts have average slopes significantly dependent on Δp. The smaller this pressure difference, the greater the average slope. At a minimum value of $\Delta p = 0.09$ GPa, the initial part of the kinetic curve has a maximum slope with an Avrami exponent of $n \approx 20$. On the contrary, the curve for a maximum value of $\Delta p = 0.25$ GPa has a minimum slope of the initial part: $n \approx 4$. The value of $n \approx 20$ is significantly greater than the limiting Avrami exponent ($n = 4$) possible according to the classical theory. This discrepancy can be explained only by assuming that the phase transformation in the initial stage proceeds with avalanche growth in the nucleation rate. Note also that the curves in Fig. 3 corresponding to $\Delta p = 0.08$ GPa and (to a certain extent) $\Delta p = 0.14$ GPa exhibit uncertainties related to the aforementioned selection of the starting point t_0. However, allowance for a certain prehistory in compression with realistic times of $t_0 \sim 10–10^2$ s does not change the conclusion concerning giant values of the Avrami exponent n in the initial part of the kinetic curve.

In the middle parts of the kinetic curves ($5\% \le x \le 20–30\%$), the difference in n values for the kinetic curves obtained under various conditions is not as large ($n \approx 3–5$). Here, the trend in the average slope is opposite of that in the first part of the kinetic curves: the average n value increases with the parameter Δp. It should be noted that the Avrami exponents determined for the middle parts of the kinetic curves show the best agreement with the classical theory.

In the third part (beginning with $x = 20–30\%$), all curves exhibit a smooth decrease in the differential slope (down to $n \approx 0.1$) with time. It should be noted that all curves approach the same envelope and the transformation slows down so that the final content of the high-pressure phase never exceeded 63%.

The above features of the phase transformation kinetics can be explained assuming that there exists a certain geometric factor influencing the course of the phase transition. This hypothesis is confirmed by the fact that all the kinetic curves exhibit anomalies corresponding to the same fractions of the new phase ($x \approx$ 5% and 20–30%).

The nature of this geometric factor can be rationalized as follows. Fluorite crystals have easy slip panes corresponding to the cleavage planes. The nuclei of the new phase formed at some structural defects induce the slip along these planes. During growth, the nuclei cause the formation of new defects and, hence, further nucleation predominantly along such planes, which results in increasing nucleation rate. Thus, the new phase initially forms layers along the easy slip planes. These layers intersect with one another to form a three-dimensional fractal cellular structure in space. We believe that, in the initial stage of the phase transformation, nucleation proceeds primarily according to the shear mechanism. In the vicinity of pressures at which the crystal lattice is close to instability, the nucleation process acquires an avalanche character, which is manifested by the giant slopes of the initial parts of the kinetic curves.

The appearance of a considerable amount of the new phase in the form of a cellular framework may change the "local pressure" at which the old phase occurs, thus slowing down the transformation. The walls of the cells composed of the new phase bound the regions containing the old phase and grow at the expense of matter supplied from these regions. Since the phase transformation is accompanied by a significant (>8%) change in volume, the regions of the old phase bounded by shells of the new phase are characterized by a local decrease in pressure. The external pressure produced by the ambient medium is not transferred via the cellular framework to the old phase.

The hypothesis concerning the cellular structure is also confirmed by the fact that the phase transformation rate is subject to a decrease at approximately the same content of the new phase ($x \approx 20–30\%$) at various values of Δp. As Δp increases, the cells grow in size and acquire thicker walls and vice versa. Indirect evidence for this hypothesis is provided by the results of visual examination of the samples with an optical microscope after termination of the kinetic measurements. Although fluorite samples exhibit reverse transformation upon unloading, the traces of cellular structure formed in the course of the pressure-induced phase transformation were observed both in the bulk and on the surface of crystals. The samples initially appeared as transparent single crystals; after experiments in a high-pressure cell, they displayed regions capable of refracting and scattering light. The higher the pressure at which the phase transition took place, the lower the sample transparency after such experiments. Indeed, the sample subjected to phase transformation at the minimum pressure ($\Delta p = 0.25$ GPa) was most transparent and displayed clearly distinguishable cluster boundaries in the volume of the crystal.

4. CONCLUSIONS

Investigation of the pressure-induced polymorphous phase transformation in CaF_2 single crystals by means of the strain gauge technique revealed three sequential stages, which can be distinguished in the curves of phase transition kinetics.

The first stage (corresponding to a new phase content $x < 5\%$) is probably related to the formation of nuclei via the shear mechanism and is accompanied by avalanche growth in the nucleation rate. The average slopes of the corresponding parts of the kinetic curves are strongly dependent on the pressure and may reach giant values corresponding to the Avrami exponents $n \approx$ 10–20.

The parts of the curves corresponding to the second stage of the phase transformation ($5\% < x < 20–30\%$) exhibit approximately equal slopes ($n \approx 3–5$) weakly dependent on the pressure. This stage of the phase transition kinetics is most adequately described by the classical Kolmogorov–Avrami–Mehl–Johnson theory.

The third part of the phase transition kinetics ($x >$ 20–30%) exhibits a slow "saturation" character, with the kinetic curves attaining the same envelope. This stage of the transformation is probably related to the formation of a cellular framework of the new phase, with a local decrease in the pressure.

These features are related to a large change in volume accompanying the given phase transformation and to the fact that the transformation proceeds far from a state of phase equilibrium. The data obtained in this study refer to the phase transformation only at one temperature ($T \approx 290$ K). At higher temperatures, additional channels of the elastic energy relaxation may appear and significantly influence the course of the phase transformation (especially in the first and third stages), which requires its own experimental investigation.

REFERENCES

1. J. W. Christian, *The Theory of Transformations in Metals and Alloys* (Pergamon, Oxford, 1975), Part 1.
2. V. V. Brazhkin, A. G. Lyapin, R. N. Voloshin, *et al.*, Phys. Rev. Lett. **90**, 145503 (2003).
3. N. S. Brar and H. H. Schloessin, High Temp. High Press. **13**, 313 (1981).
4. V. L. Solozhenko, V. Z. Turkevich, O. O. Kurakevich, *et al.*, J. Phys. Chem. B **106**, 6634 (2002).
5. V. Z. Turkevich, T. Okada, W. Utsumi, *et al.*, Diamond Relat. Mater. **11**, 1769 (2002).
6. V. L. Solozhenko and V. Z. Turkevich, Diamond Relat. Mater. **7**, 43 (1998).
7. E. F. Skelton, S. B. Qadri, W. T. Elam, *et al.*, in *Solid State Physics under Pressure*, Ed. by S. Minomura (KTK Sci., Tokyo, 1985), p. 329.
8. A. N. Kolmogorov, Izv. Akad. Nauk SSSR, Ser. Mat. **1**, 335 (1937).
9. M. Avrami, J. Chem. Phys. **7**, 1103 (1939); **8**, 212 (1940); **9**, 177 (1941).
10. W. A. Johnson and R. T. Mehl, Trans. Metal. Soc. AIME **135**, 416 (1939).
11. O. B. Tsiok, V. V. Bredikhin, V. A. Sidorov, and L. G. Khvostantsev, High Press. Res. **10**, 523 (1992).
12. O. B. Tsiok, V. V. Brazhkin, A. G. Lyapin, and L. G. Khvostantsev, Phys. Rev. Lett. **80**, 999 (1998).
13. O. B. Tsiok, V. A. Sidorov, V. V. Bredikhin, *et al.*, Phys. Rev. B **51**, 12127 (1995).
14. F. S. El'kin, V. V. Brazhkin, L. G. Khvostantsev, *et al.*, Pis'ma Zh. Éksp. Teor. Fiz. **75**, 413 (2002) [JETP Lett. **75**, 342 (2002)].
15. F. S. El'kin, O. B. Tsiok, L. G. Khvostantsev, *et al.*, Prib. Tekh. Éksp., No. 1, 112 (2003) [Instrum. Exp. Tech. **46**, 101 (2003)].
16. E. Yu. Tonkov, *Phase Diagrams of the Compounds at High Pressures* (Nauka, Moscow, 1983), p. 218 [in Russian].
17. L. G. Khvostantsev, L. F. Vereshchagin, and A. P. Novikov, High Temp. High Press. **9**, 637 (1977).
18. R. J. Angel, J. Phys.: Condens. Matter **5**, L141 (1993).
19. D. P. Dandekar and J. S. Jamieson, Trans. Am. Crystallogr. Assoc. **5**, 19 (1969).
20. K. F. Kelton and J. C. Holzer, Phys. Rev. B **37**, 3940 (1988).
21. A. Nazareth and G. C. Hadjipanayis, Phys. Rev. B **40**, 5441 (1989).
22. Haixing Zheng and J. D. Mackenzie, Phys. Rev. B **43**, 3048 (1991).
23. K. Lu and J. T. Wang, J. Non-Cryst. Solids **117/118**, 716 (1990).

Translated by P. Pozdeev

Journal of Experimental and Theoretical Physics, Vol. 100, No. 5, 2005, pp. 977–982.
Translated from Zhurnal Éksperimental'noĭ i Teoreticheskoĭ Fiziki, Vol. 127, No. 5, 2005, pp. 1106–1112.
Original Russian Text Copyright © 2005 by Farutin, Marchenko.

ORDER, DISORDER, AND PHASE TRANSITIONS IN CONDENSED SYSTEMS

On the Theory of Spin Exchange Structures

A. M. Farutin and V. I. Marchenko
Kapitza Institute for Physical Problems, Russian Academy of Sciences, Moscow, 119334 Russia
e-mail: farutin@kapitza.ras.ru

Received December 16, 2004

Abstract—All possible types of spin ordering manifested in spin–spin correlation functions are determined. Some general characteristics of arbitrary spin structures predicted by macroscopic theory are examined, including energy associated with inhomogeneity, anisotropy, and energy in external fields. *© 2005 Pleiades Publishing, Inc.*

1. INTRODUCTION

Andreev and Grishchuk showed in [1] that spin ordering of special type can arise in condensed matter when exchange coupling is much stronger than relativistic effects. In this case, the average microscopic spin density

$$\mathbf{S}(\mathbf{r}) = \langle \hat{\mathbf{S}}(\mathbf{r}) \rangle \tag{1}$$

vanishes, and spontaneous breaking of spin rotation symmetry of the exchange Hamiltonian manifests itself by anisotropy of the spin–spin correlation function

$$S_{\alpha\beta}(\mathbf{r}_1, \mathbf{r}_2) = \langle \hat{S}_\alpha(\mathbf{r}_1) \hat{S}_\beta(\mathbf{r}_2) \rangle. \tag{2}$$

This state is not magnetic, because invariance under time reversal is preserved. However, many characteristics of the spin ordering are similar to those of normal exchange magnets [2] (low-frequency spin waves, magnetic resonance, susceptibility, etc.).

In principle, more complicated states may exist in which spontaneous breaking of spin exchange symmetry and invariance under time reversal is manifested only in multiple-spin correlation functions. The nonmagnetic phases for which only even correlation functions do not vanish are called spin nematics [1]. In the case a nonzero odd correlation function, such as the triple-spin correlation function

$$S_{\alpha\beta\gamma}(\mathbf{r}_1, \mathbf{r}_2, \mathbf{r}_3) = \langle \hat{S}_\alpha(\mathbf{r}_1) \hat{S}_\beta(\mathbf{r}_2) \hat{S}_\gamma(\mathbf{r}_3) \rangle, \tag{3}$$

the state is magnetic, because it is not invariant under time reversal. Phases characterized by odd spin correlation functions are called tensor magnets [3, 4]. They substantially differ from both normal magnets and spin nematics. These phases always have a low spin density due to relativistic effects. Recently, several materials were found in which extremely weak spontaneous sublattice magnetization is observed. Barzykin and Gorkov [5] suggested to detect tensor magnetic ordering in these materials by measuring elastic neutron scattering in an external magnetic field.

In [1, 3, 4], examples of tensor ordering were discussed, but the properties of the spin order parameter under crystallographic group transformations were not analyzed. In [6], the Landau theory of second-order phase transitions was applied to analyze spin nematic phases characterized by spin–spin correlation functions resulting from second-order phase transitions in crystals with tetragonal symmetry.

In this study, we determine all possible types of tensor spin ordering, relying on the general ideas of the theory of spin exchange symmetry [2]. As in the case of a normal magnet, this can be done without analyzing phase transitions. We also discuss some special properties of tensor spin ordering predicted by macroscopic theory.

2. EXCHANGE SYMMETRY

The symmetry of a spin exchange state is determined its symmetry under classical crystallographic transformations, their combinations with spin-space rotations and time reversal (interpreted as spin-space inversion), and spin rotations. Both spin density (1) and all spin correlation functions must be invariant under these operations.

Pure spin transformations of the last type obviously constitute a symmetry group equivalent to a point group [7]. We denote these spin symmetry groups by adding the superscript *s* to the symbols representing the corresponding space point groups. For example, $C^s_{\infty v}$, C^s_s, and E^s correspond to collinear, coplanar, and noncollinear noncoplanar magnets, respectively.

The construction of exchange symmetry groups for normal magnets is based on the following observation [2]. In the general case, microscopic spin density can be expressed as

$$\mathbf{S}(\mathbf{r}) = f_a^{(1)}\mathbf{a} + f_b^{(1)}\mathbf{b} + f_c^{(1)}\mathbf{c}, \tag{4}$$

where the mutually orthogonal unit vectors **a**, **b**, and **c** make up a basis in the spin space, i.e., change sign under time reversal. The parenthesized superscript of a real function f is the rank of the spin tensor under consideration. The spin density squared,

$$\mathbf{S}^2 = (f_a^{(1)})^2 + (f_b^{(1)})^2 + (f_c^{(1)})^2 \tag{5}$$

is invariant under both spin-space rotations and time reversal. As a state variable, it must be invariant under all transformations in the crystal symmetry group G.

In the case of a collinear magnet, the functions f are linearly dependent. For example, a basis can be selected in the spin space so that $f_\alpha^{(1)} = f_b^{(1)} = 0$, and the corresponding $f_c^{(1)}$ transforms under a one-dimensional representation. For a coplanar magnet, $f_c^{(1)}$ can be set to zero, and the corresponding linearly independent $f_a^{(1)}$ and $f_b^{(1)}$ transform under similar one-dimensional representations, or under different one-dimensional representations, or under a two-dimensional representation. The three linearly independent functions corresponding to a general noncollinear magnet transform under similar or different one-dimensional representations, or under a one-dimensional representation for one of them and a two-dimensional representation for the remaining two, or under a three-dimensional representation.

For these magnets with $C_{\infty v}^s$, C_s^s, and E^s symmetries, a prescribed spin density determines the symmetry of a state, and no analysis of correlation functions is required.

However, in the case of minimal breaking of the symmetry of the exchange Hamiltonian, when invariance under spin-space rotations is preserved and only invariance under time reversal is lost, the order parameter is the three-point correlation function

$$S_{\alpha\beta\gamma}(\mathbf{r}_1, \mathbf{r}_2, \mathbf{r}_3) = f^{(3-)}(\mathbf{r}_1, \mathbf{r}_2, \mathbf{r}_3)E_{\alpha\beta\gamma}. \tag{6}$$

The minus in the superscript of f refers to the antisymmetric part of the spin tensor, and the isotropic tensor $E_{\alpha\beta\gamma}$ is

$$\begin{aligned} E_{\alpha\beta\gamma} &= a_\alpha b_\beta c_\gamma + b_\alpha c_\beta a_\gamma + c_\alpha a_\beta b_\gamma \\ &\quad - b_\alpha a_\beta c_\gamma - a_\alpha c_\beta b_\gamma - c_\alpha b_\beta a_\gamma. \end{aligned}$$

It differs from the Levi-Civita symbol $e_{\alpha\beta\gamma}$ by the factor

$$\nu = \mathbf{a}\cdot[\mathbf{b}\times\mathbf{c}], \tag{7}$$

which changes sign under time reversal. The invariance of convolutions $S_{\alpha\beta\gamma}S_{\alpha\beta\gamma}$ under the group G implies that $f^{(3-)}$ transforms only under a one-dimensional representation. The corresponding material is a scalar magnet [3]. Both exchange and magnetic symmetries of this state are determined by the symmetry of $\nu f^{(3-)}$. The corresponding magnetic crystal symmetry obviously coincides with the crystal group G.

Isotropic quantity (7) is also nonzero for noncollinear noncoplanar magnets, for which all functions f in spin density (1) are linearly independent. We naturally call this quantity *magnetic chirality.* Dzyaloshinskiĭ [8] noted that domain walls of special kind can exist in such phases. States that differ by the sign of (7) cannot be transformed into one another by any spin-space rotation. Thus, the boundary between them has its structure determined by exchange interactions and therefore has an atomic thickness, in contrast to the domain-wall thickness in normal magnets determined by competing exchange and relativistic effects.

The phase with the highest chiral spin symmetry $\mathbf{D}_{\infty h}^s$ is called *axial spin nematic* [1] and is characterized by the anisotropic part of the spin–spin correlation function,

$$S_{\alpha\beta} = \frac{f_1^{(2)}}{\sqrt{6}}(3c_\alpha c_\beta - \delta_{\alpha\beta}), \tag{8}$$

where $f_1^{(2)}$ is a function of $\mathbf{r}_1$ and $\mathbf{r}_2$. By virtue of the invariance of the convolutions $S_{\alpha\beta}S_{\alpha\beta}$ and $S_{\alpha\beta}S_{\beta\gamma}S_{\alpha\beta}$ under the group G, the function $f_1^{(2)}$ is totally invariant (identity representation).

Tensor magnets with symmetry $\mathbf{D}_\infty^s$ are characterized by magnetic chirality (6) and spin–spin correlations (8) with $f^{(3-)}$ and $f_1^{(2)}$ that transform under the same or different one-dimensional representations.

The spin–spin correlation function for group $\mathbf{C}_{\infty h}^s$ magnets contains both (8) and

$$f_c^{(2-)}(a_\alpha b_\beta - b_\alpha a_\beta), \tag{9}$$

which is antisymmetric with respect to spin indices [1]. An analysis of the invariance of nonmagnetic spin convolutions shows that $f_1^{(2)}$ is again totally invariant, while $f_c^{(2-)}$ transforms under a one-dimensional representation. In this case, the role of order parameter is played by the pseudovector **P**, which is dual to the antisymmetric part of the spin–spin correlation function in the spin space,

$$\mathbf{P} = f_c^{(2-)}[\mathbf{a}\times\mathbf{b}]. \tag{10}$$

In addition to the spin–spin correlation function characterizing the case of $\mathbf{C}_{\infty h}^s$ (with similar selection rules for f), the group $\mathbf{C}_\infty^s$ admits the vector

$$\mathbf{S} = f_c^{(1)}\mathbf{c}, \tag{11}$$

where f transforms under a one-dimensional representation. This phase obviously has a magnetic chirality.

Under the finite groups, let us define the orientation of the basis vectors in the spin space as follows. Under the $\mathbf{T}^s$, $\mathbf{T}_d^s$, $\mathbf{T}_h^s$, $\mathbf{Y}^s$, and $\mathbf{Y}_h^s$ groups, the vectors **a**, **b**, and **c** are aligned with the three mutually orthogonal second-order axes; under the $\mathbf{O}^s$ and $\mathbf{O}_h^s$ groups, they are aligned with the fourth-order axes. Under the axial spin groups, the vector **c** is aligned with the principal axis. Under the $\mathbf{D}_n^s$, $\mathbf{D}_{nh}^s$, and $\mathbf{D}_{nd}^s$ groups, the vector **a** is aligned with one of the U_2^s axes. Under the $\mathbf{C}_{nv}^s$ group, the vector **a** lies in the symmetry plane σ_v^s. Under the $\mathbf{C}_n^s$, $\mathbf{C}_{nh}^s$, and $\mathbf{S}_{2n}^s$ groups, the vector **a** is arbitrarily oriented. Under the $\mathbf{C}_i^s$ group, the entire basis is arbitrarily oriented.

Under the $\mathbf{C}_i^s$ group, when exchange symmetry is lost completely while invariance under time reversal holds, it is reasonable to consider the antisymmetric part of the spin–spin correlation function, whose general form is

$$S^{(-)}_{\alpha\beta} = (f_a^{(2-)}a_\gamma + f_b^{(2-)}b_\gamma + f_c^{(2-)}c_\gamma)E_{\alpha\beta\gamma}. \tag{12}$$

Note that $\mathbf{C}_i^s$ does not admit linear dependence between the functions f. Invariance of the convolution $S^{(-)}_{\alpha\beta}S^{(-)}_{\alpha\beta}$ implies that the sum

$$(f_a^{(2-)})^2 + (f_b^{(2-)})^2 + (f_c^{(2-)})^2$$

is invariant under group G transformations. Thus, the functions f transform under the representations selected by rules similar to those for magnets. However, the additional requirement of invariance of $S^{(-)}_{\alpha\beta}S^{(-)}_{\beta\gamma}S^{(-)}_{\alpha\gamma}$ implies invariance of the product $f_a^{(2-)}f_b^{(2-)}f_c^{(2-)}$, which substantially reduces the number of possible types of ordering.

The groups $\mathbf{C}_n^s$ and $\mathbf{C}_{nv}^s$ with $n > 1$ admit collinear magnetism (11). Under the $\mathbf{C}_n^s$ groups, spin ordering is characterized by magnetic chirality. Therefore, the spin–spin correlation function contains antisymmetric part (9). Under $\mathbf{C}_2^s$, the correlation function $S_{\alpha\beta}$ contains the additional terms

$$\frac{f_2^{(2)}}{\sqrt{2}}(a_\alpha a_\beta - b_\alpha b_\beta) + \frac{f_3^{(2)}}{\sqrt{2}}(a_\alpha b_\beta + b_\alpha a_\beta). \tag{13}$$

An analysis of spin–spin convolutions shows that $f_2^{(2)}$ and $f_3^{(2)}$ transform either under identical or different one-dimensional representations or under a single two-dimensional one. Under $\mathbf{C}_{2v}^s$, (13) contains only the first term, which transforms under the identity representation.

Representations under the $\mathbf{C}_n^s$ and $\mathbf{C}_{nv}^s$ groups with $n > 2$ are selected by rules similar to those for $n = 2$, except that n-spin correlators are anisotropic. Instead of the pair of tensors in (13), rank n spin tensors must be used. They can be represented as

$$\{(a+ib)^n + (a-ib)^n\}, \quad i\{(a+ib)^n - (a-ib)^n\}.$$

Hereinafter, expressions in curly brackets imply obvious combinations of spin indices.

The $\mathbf{C}_{nh}^s$ structures differ from $\mathbf{C}_n^s$ structures only by the absence of magnetic vector (11).

Under the $\mathbf{S}_{2n}^s$ groups, the magnetic vector is also forbidden, but the spin–spin correlation function contains antisymmetric part (9). Axial anisotropy is associated with a correlation function of order $n + 3$. There exist the tensors $E_{\alpha\beta\gamma} * \{(a+ib)^n + (a-ib)^n\}$ and $iE_{\alpha\beta\gamma} * \{(a+ib)^n - (a-ib)^n\}$, where the asterisk denotes a tensor product. The corresponding amplitudes also admit one- and two-dimensional representations.

Under the $\mathbf{D}_n^s$ groups, the loss of invariance under time reversal implies the existence of nonzero triple-spin correlations (6).

Under $\mathbf{D}_2^s$, anisotropy in the spin space is described by the spin–spin correlation function

$$S_{\alpha\beta} = \frac{f_1^{(2)}}{\sqrt{6}}(3c_\alpha c_\beta - \delta_{\alpha\beta}) + \frac{f_2^{(2)}}{\sqrt{2}}(a_\alpha a_\beta - b_\alpha b_\beta). \tag{14}$$

The invariance of all possible spin convolutions implies that the functions $(f_1^{(2)})^2 + (f_2^{(2)})^2$ and $(f_1^{(2)})^3 - 3f_1^{(2)}(f_2^{(2)})^2$ must be invariant. Under any space group G, $f_1^{(2)}$ transforms under the identity representation and $f_2^{(2)}$ transforms under a one-dimensional representation. However, two-dimensional representations may also be admissible in certain cases. In particular, crystals of the rhombohedral and hexagonal systems admit representations with $\mathbf{k} = 0$, which keep invariant the polynomial

$$(f_1^{(2)})^3 - 3f_1^{(2)}(f_2^{(2)})^2 = \mathrm{Re}(f_1^{(2)} + if_2^{(2)})^3.$$

An example of such representation in any space group of crystal class C_3 is the representation under which the x and y vector components transform.

A simple analysis shows that the groups with higher order principal axes, as well as tetrahedral groups, admit spin correlation functions defined by a single tensor or two tensors of different rank whose amplitudes transform only under one-dimensional representations of G. The corresponding tensor order parameters are

$\mathbf{D}_n^s : E_{\alpha\beta\gamma}, \{(a + ib)^n + (a - ib)^n\};$

$\mathbf{D}_{nh}^s : \{(a + ib)^n + (a - ib)^n\};$

$\mathbf{D}_{nd}^s : E_{\alpha\beta\gamma} * \{(a + ib)^n + (a - ib)^n\};$

$\mathbf{T}^s : E_{\alpha\beta\gamma}, T_{\alpha\beta\gamma};$

$\mathbf{T}_d^s : T_{\alpha\beta\gamma};$

$\mathbf{T}_h^s : E_{\alpha\beta\gamma} * T_{\delta\eta\mu}.$

Here, $T_{\alpha\beta\gamma}$ is the tetrahedral tensor

$$\{abc\} = a_\alpha b_\beta c_\gamma + b_\alpha c_\beta a_\gamma$$
$$+ c_\alpha a_\beta b_\gamma + b_\alpha a_\beta c_\gamma + a_\alpha c_\beta b_\gamma + c_\alpha b_\beta a_\gamma.$$

The octahedral group $\mathbf{O}^s$ of spin symmetry admits triple spin correlations (6). The amplitude $f^{(3-)}$ transforms under a one-dimensional representation. Anisotropy in the spin space corresponds to a four-spin correlation function of the form $f^{(4)}O_{\alpha\beta\gamma\delta}$, where $O_{\alpha\beta\gamma\delta}$ is the totally symmetric traceless tensor

$$O_{\alpha\beta\gamma\delta} = a_\alpha a_\beta a_\gamma a_\delta + b_\alpha b_\beta b_\gamma b_\delta + c_\alpha c_\beta c_\gamma c_\delta - \frac{1}{5}I^{(4)}_{\alpha\beta\gamma\delta}$$

with cubic symmetry. Here, $I^{(4)}$ is the spherically symmetric rank four tensor

$$I_{\alpha\beta\gamma\delta} = \delta_{\alpha\beta}\delta_{\gamma\delta} + \delta_{\alpha\gamma}\delta_{\beta\delta} + \delta_{\alpha\delta}\delta_{\beta\gamma}.$$

The amplitude $f^{(4)}$ must be invariant under G, because the convolution $O_{\alpha\beta\gamma\delta}O_{\alpha\beta\mu\nu}O_{\gamma\delta\mu\nu}$ does not vanish.

Under the cubic $\mathbf{O}_h^s$ group, the order parameter is $O_{\alpha\beta\gamma\delta}$.

The icosahedral group $\mathbf{Y}^s$ admits triple-spin correlations (6), and spin-space anisotropy is associated with a six-spin correlation function of the form $f^{(6)}Y_{\alpha\beta\gamma\delta\eta\mu}$, where the tensor Y has the icosahedral symmetry. The tensor Y is the only order parameter under $\mathbf{Y}_h^s$. The symmetric traceless rank six tensor with icosahedral symmetry has the form

$$Y = \Big\{(c + \phi a)^6 + (c - \phi a)^6 + (a + \phi b)^6 + (a - \phi b)^6$$
$$+ (b + \phi c)^6 + (b - \phi c)^6 - \frac{2(1 + \phi^2)^3}{35}I^{(6)}\Big\},$$

where $\mathbf{c} + \phi\mathbf{a}$, $\mathbf{c} - \phi\mathbf{a}$, $\mathbf{a} + \phi\mathbf{b}$, $\mathbf{a} - \phi\mathbf{b}$, $\mathbf{b} + \phi\mathbf{c}$, and $\mathbf{b} - \phi\mathbf{c}$ are the position vectors of the six vertices of an icosahedron none of which is diametrically opposite to another. The icosahedron is inserted in the standard manner in a cube with edges of length 2 aligned with the basis vectors $\mathbf{a}$, $\mathbf{b}$, and $\mathbf{c}$. The number ϕ is $(\sqrt{5} - 1)/2$. The symmetric rank six tensor

$$I^{(6)}_{\alpha\beta\gamma\delta\eta\mu} = \delta_{\alpha\beta}I^{(4)}_{\gamma\delta\mu\nu} + \delta_{\alpha\gamma}I^{(4)}_{\beta\delta\mu\nu}$$
$$+ \delta_{\alpha\delta}I^{(4)}_{\beta\gamma\mu\nu} + \delta_{\alpha\mu}I^{(4)}_{\beta\gamma\delta\nu} + \delta_{\alpha\nu}I^{(4)}_{\beta\gamma\delta\mu}$$

is spherically symmetric.

Under both icosahedral spin groups, the function $f^{(6)}$ is invariant under G, because the convolution $Y_{\alpha\beta\gamma\delta\eta\mu}Y_{\alpha\beta\gamma\varepsilon\zeta\xi}Y_{\delta\eta\mu\varepsilon\zeta\xi}$ does not vanish.

Note that the tetrahedral, cubic, and icosahedral tensors are presented in different form in the theory of non-uniaxial nematic liquid crystals (e.g., see [9]).

3. LIFSHITZ INVARIANTS

A homogeneous state of spin ordering is unstable if its symmetry admits Lifshitz invariants, which have the form of convolutions of polynomials of a_α, b_β, and c_γ with the spatial derivatives $\partial_i a_\alpha$, $\partial_i b_\beta$, and $\partial_i c_\gamma$. Since the convolution of two basis vectors is either 0 or 1, these invariants reduce to sums of terms of the form $\tilde{a}_\alpha\partial_i\tilde{b}_a$, where $\tilde{\mathbf{a}}$ and $\tilde{\mathbf{b}}$ are basis vectors.

Under an infinitesimal spin-space rotation to an angle $\delta\boldsymbol{\theta}$, an arbitrary vector $\tilde{\mathbf{a}}$ changes by

$$\delta\tilde{\mathbf{a}} = \delta\boldsymbol{\theta} \times \tilde{\mathbf{a}}. \quad (15)$$

Therefore, the part of energy that is linear in gradients reduces to $L_{i\alpha}\theta_{i\alpha}$, where the matrix $L_{i\alpha}$ is a vector in the orbital space and a pseudovector in the spin space, and

$$\theta_{i\alpha} = \frac{\delta\theta_\alpha}{dx_i}. \quad (16)$$

By analogy with elasticity theory, $\theta_{i\alpha}$ should be called angular distortion (or orientational strain). The distortion $\theta_{i\alpha}$ is a pseudovector in the spin space, because it is obvious from (15) that $\delta\boldsymbol{\theta}$ is a spin pseudovector (invariant under time reversal).

The matrix $L_{i\alpha}$ is a characteristic of a spin system. Since it is independent of spatial gradients, it must have the symmetry of a homogeneous spin state. It is obvious that $L_{i\alpha}$ does not vanish only under finite spin symmetry groups and only in the cases when the antisymmetric part of the spin–spin correlation function does not vanish. Note also that the functions $f^{(2-)}$ must transform under the vector representation of G.

4. ENERGY OF ORIENTATIONAL STRAIN

In any axial spin phase with weakly nonuniform orientation of order parameter, the exchange energy has the standard form

$$\frac{1}{2}\Lambda_{ij}\partial_i\mathbf{c}\partial_j\mathbf{c}, \tag{17}$$

where the tensor Λ is invariant under G.

In the general case, the exchange energy is a quadratic function of the gradients of the angles of spin rotation of the form

$$\frac{1}{2}\Lambda_{ij\alpha\beta}\theta_{i\alpha}\theta_{j\beta}, \tag{18}$$

where the tensor Λ is symmetric in the orbital space and symmetric in the spin space. It is obvious that Λ is invariant under the exchange symmetry group of the state in question.

Under the tetrahedral, cubic, and icosahedral spin symmetry groups, $\Lambda_{ij\alpha\beta}$ reduces to the simple form

$$\Lambda_{ij}^{(0)}\delta_{\alpha\beta}, \tag{19}$$

where the spatial tensor $\Lambda_{ij}^{(0)}$ is invariant under G. The corresponding contribution is obviously contained in the energy associated with inhomogeneity of any spin ordering.

The groups $\mathbf{D}_n^s$, $\mathbf{D}_{nh}^s$, and $\mathbf{D}_{nd}^s$ with $n > 2$ admit an additional term

$$\Lambda_{ij}^{(1)}c_\alpha c_\beta, \tag{20}$$

where the tensor $\Lambda_{ij}^{(1)}$ is also invariant under G. This is also true for $\mathbf{C}_n^s$, $\mathbf{C}_{nv}^s$, $\mathbf{C}_{nh}^s$, and $\mathbf{S}_{2n}^s$ with $n > 2$ when the n- or $(n + 3)$-spin correlation function is determined by a single function of coordinates that transforms under a one-dimensional representation of G.

In the remaining nonaxial spin orderings, as well as in noncollinear magnets [2], a special analysis is required to determine Λ in each particular case.

5. RELATIVISTIC ANISOTROPY EFFECTS

Relativistic spin-orbit and magnetic dipole–dipole effects result in dependence of the energy of a crystal on the orientation of spin structures relative to the crystallographic axes.

By analogy with the theory of second-order phase transitions, the laws of transformation of the functions f^n under elements of G should be extended to the spin vector and tensors. Then the role of order parameter in antiferromagnets will be played by antiferromagnetic unit vectors $\mathbf{l}_i$ [2]. Only when magnetization $\mathbf{M}$ does not vanish, it should be treated as an order parameter instead of the unit vector $\mathbf{M}/|\mathbf{M}|$, because magnetization is contained in Maxwell's equations. In phases with tensor spin structures, the role of order parameters is played by tensors with amplitudes constant in space (see above). In particular, when correlation function (6) does not vanish, the order parameter can be defined as the unit chirality ν, which changes sign both under time reversal and under certain crystal transformations (in accordance with the law of transformation of $f^{(3-)}(\mathbf{r}_1, \mathbf{r}_2, \mathbf{r}_3)$).

In normal magnets, the energy associated with anisotropy can be expanded in terms of magnetic-vector components, with the fine structure constant α as an expansion parameter. In collinear magnets, the first term in the expansion, e.g., for a uniaxial crystal, can be written as $\beta^{[2]}l_z^2$. The anisotropic coefficient $\beta^{[2]}$ scales with α^2 times the volume density of exchange energy. Hereinafter, the superscript in brackets is the exponent of a power of the fine structure constant. The next term in the expansion for a uniaxial crystal is $\beta^{[4]}l_z^4$, where the coefficient $\beta^{[4]}$ has the order of α^4. Generally, the expansion of the energy of a collinear magnet contains only even powers n of components of the magnetic vector, and the corresponding coefficients scale with α^n. The energy of anisotropy of noncollinear coplanar magnets (spin structures with two vectors) has an analogous form. For noncollinear noncoplanar magnets, the energy may contain spin-orbit terms of special form. In particular, for the so-called disordered antiferromagnet, the role of the order parameter is played by three spin vectors S_x^α, S_y^β, and S_z^γ, where the subscripts indicate that they transform under a vector representation in the orbital space. In addition to the standard relativistic terms

$$\beta_1^{[2]}(S_i^i)^2 + \beta_2^{[2]}S_i^kS_k^i \tag{21}$$

(see [2]), we should also include the additional term

$$\beta_3^{[2]}\nu S_i^i. \tag{22}$$

On a microscopic level, this term is due to exchange and spin-orbit interactions and scales with α^2, as do the terms in (21). Note that this anomalous term is obviously small as compared to the standard ones (21) near the point of second-order transition to the paramagnetic state, when all components of the order parameter vanish.

These considerations suggest a general rule for the relativistic terms in the expansion in terms of an arbitrary spin order parameter: relativistic invariants with even and odd number n of spin indices scale with α^n and α^{n+1}, respectively.

Since all spin order parameters enumerated above are such that spin convolutions of their powers cannot yield anisotropic or nonaxial tensors of lower rank, anisotropy effects, as well as the orientational effects of magnetic and electric fields and uniform deformations of the crystal, are fully manifested only in relatively high order terms in the expansions in terms of the fine structure constant and external perturbation amplitudes.

Consider two examples: a $\mathbf{T}_d^s$ tetrahedral tensor magnet and an $\mathbf{O}_h^s$ cubic spin nematic in the exchange crystal class $\mathbf{D}_{2h}$.

In both cases, the first terms of the expansion of the anisotropy energy have the form $\beta_1 S_{zzzz} + \beta_2 S_{xxxx} + \beta_3 S_{yyyy} + \beta_4 S_{xxyy} + \beta_5 S_{yyzz} + \beta_6 S_{zzxx}$, where the cubically symmetric tensor S is $O_{\alpha\beta\gamma\delta}$ in the latter case and $S_{\alpha\beta\gamma\delta} = T_{\alpha\beta\mu}T_{\mu\gamma\delta}$ in the former. Note that the anisotropy arises in fourth-order terms in the fine structure constant (rather than in second-order terms, as in crystal class $\mathbf{D}_{2h}$ magnets).

In external magnetic field, the anisotropy of spin ordering corresponds to exchange-coupling terms proportional to $S_{\alpha\beta\gamma\delta}H_\alpha H_\beta H_\gamma H_\delta$ and in mixed exchange–relativistic terms

$$\eta_1 S_{\alpha\beta xx}H_\alpha H_\beta + \eta_2 S_{\alpha\beta yy}H_\alpha H_\beta + \eta_3 S_{\alpha\beta zz}H_\alpha H_\beta.$$

In the tetrahedral case, when f^3 transforms under the identity representation, energy contains anomalous terms: an exchange one proportional to $T_{\alpha\beta\gamma}H_\alpha H_\beta H_\gamma$ and exchange–relativistic one of the form

$$\zeta_1 T_{\alpha xx}H_\alpha + \zeta_2 T_{\alpha yy}H_\alpha + \zeta_3 T_{\alpha zz}H_\alpha.$$

As shown by Dzyaloshinskiĭ and Man'ko [10], terms of this type can arise for noncollinear noncoplanar magnets.

ACKNOWLEDGMENTS

We thank A.F. Andreev, L.A. Mel'nikovskii, L.A. Prozorova, and A.I. Smirnov for helpful discussions. This work was supported by the Russian Foundation for Basic Research, project no. 04-02-17294 and under the Presidential Program for Support of Scientific Schools.

REFERENCES

1. A. F. Andreev and I. A. Grishchuk, Zh. Éksp. Teor. Fiz. **87**, 467 (1984) [Sov. Phys. JETP **60**, 267 (1984)].
2. A. F. Andreev and V. I. Marchenko, Usp. Fiz. Nauk **130**, 39 (1980) [Sov. Phys. Usp. **23**, 21 (1980)].
3. V. I. Marchenko, Pis'ma Zh. Éksp. Teor. Fiz. **48**, 387 (1988) [JETP Lett. **48**, 427 (1988)].
4. V. I. Marchenko, Pis'ma Zh. Éksp. Teor. Fiz. **59**, 590 (1994) [JETP Lett. **59**, 618 (1994)].
5. V. Barzykin and L. P. Gorkov, Phys. Rev. Lett. **70**, 2479 (1993).
6. V. Barzykin, L. P. Gorkov, and A. V. Sokol, Europhys. Lett. **15**, 869 (1991).
7. L. D. Landau and E. M. Lifshitz, *Course of Theoretical Physics*, Vol. 3: *Quantum Mechanics: Non-Relativistic Theory*, 3rd ed. (Nauka, Moscow, 1974; Pergamon, New York, 1977).
8. I. E. Dzyaloshinskiĭ, Pis'ma Zh. Éksp. Teor. Fiz. **25**, 442 (1977) [JETP Lett. **25**, 414 (1977)].
9. L. G. Fel, Phys. Rev. E **52**, 2692 (1995).
10. I. E. Dzyaloshinskiĭ and V. I. Man'ko, Zh. Éksp. Teor. Fiz. **46**, 1352 (1964) [Sov. Phys. JETP **19**, 915 (1964)].

Translated by A. Betev

Journal of Experimental and Theoretical Physics, Vol. 100, No. 5, 2005, pp. 983–991.
Translated from Zhurnal Éksperimental’noĭ i Teoreticheskoĭ Fiziki, Vol. 127, No. 5, 2005, pp. 1113–1122.

The Electronic Structure and Optical and Magnetooptical Properties of the $CaCo_2$ Compound Synthesized at a High Pressure: Experiment and Theory

M. M. Kirillova[a], M. V. Magnitskaya[b], A. A. Makhnev[a], I. D. Lobov[a], L. V. Nomerovannaya[a], A. V. Tsvyashchenko[b], and L. N. Fomicheva[b]
[a]*Institute of Metal Physics, Ural Division, Russian Academy of Sciences,*
ul. S. Kovalevskoĭ 18, Yekaterinburg, 620219 Russia
[b]*Vereshchagin Institute of High-Pressure Physics, Russian Academy of Sciences,*
Troitsk, Moscow oblast, 142190 Russia
e-mail: kirillova@imp.uran.ru
Received November 24, 2004

Abstract—The optical properties (the real ε_1 and imaginary ε_2 permittivity parts, optical conductivity σ, and reflectivity R) of the new ferromagnetic compound $CaCo_2$ in the Laves cubic phase (C15) synthesized at a pressure of 8.0 GPa were studied over the spectral range $\hbar\omega$ = 0.2–9 eV. The field and spectral ($\hbar\omega$ = 0.5–4.2 eV) dependences of the equatorial Kerr effect were determined. The electronic structure and optical characteristics of $CaCo_2$ were calculated using the electron density functional theory by the linearized augmented-plane-wave method. The main band structure parameters of the compound were determined. The experimental and theoretical $\sigma(\omega)$ and $R(\omega)$ dependences were in satisfactory agreement with each other. The formation of the main absorption bands was found to be caused by the $(p,d \longrightarrow d,p)$-type electronic transitions related to the cobalt and calcium atoms. The exchange splitting of the 3d band of $CaCo_2$ was estimated, $2\Delta_{exc} \sim (1–1.3)$ eV. © *2005 Pleiades Publishing, Inc.*

1. INTRODUCTION

Synthesis under high-pressure conditions is extensively used to prepare new materials with unusual properties. For instance, experiments on synthesis of intermetallic compounds combining alkali and alkaline-earth metals on the one hand and magnetic 3d metals on the other have successfully been performed in recent years [1–3]. Interest in these compounds stems from the observation that Group I and II elements manifest the properties of transition d metals in them. They are also of interest in relation to geophysical problems, namely, for checking the hypothesis of the composition of the Earth’s core, which supposedly contains, along with iron family metals, light elements, in particular, potassium and calcium.

Recently, the new compounds $CaCo_2$ and $Ca(Fe_{1-x}Ni_x)_2$ have for the first time been obtained at a pressure of 8 GPa [2, 3]. The compounds crystallize in the cubic Laves phase C15 ($MgCu_2$ lattice). These substances broaden the current concepts of the class of magnetic alkaline-earth metal compounds, very few representatives of which are known. Importantly, these metastable high-pressure phases remain intact under normal conditions for a long time (the stablest of them, $CaCo_2$, can be kept for several months). According to the experimental data [2–4], $CaCo_2$ is a ferromagnet with a magnetic moment of $3.5\mu_B$ at T = 4.2 K per formula unit (the magnetic moment of $CaCo_2$ samples studied in [4] was $3.1\mu_B$/formula unit). The compound has a high Curie temperature (T_C = 528 K), which slightly decreases as the pressure grows (dT_C/dP = –14.5 K/GPa; T_C = 430 K at 7.5 GPa). Hyperfine magnetic field was measured in [4] by the NMR method to obtain H_{hf} = 15.7 T. The compound has a high compressibility and a low calculated density n_0 = 5.21 g/cm^3. First-principle calculations of the electronic structure of $CaCo_2$ were reported in [2, 3].

It follows from the data obtained earlier [2–4] that the electronic and magnetic properties of $CaCo_2$ are fairly unusual (see Section 2). We therefore continued studies of the electronic structure of this compound by metal optics methods. We deemed it interesting to compare information about the electronic structure obtained by optical measurements with the experimental and theoretical data reported earlier. Although certain special features of the substance (its metastable character and the high content of calcium susceptible to oxidation) might impede the preparation of high-quality surfaces, we made an attempt to measure the following optical characteristics: reflectivity R, Kerr effect, and diagonal σ_{xx} and off-diagonal σ_{xy} components of the optical conductivity tensor $\hat{\sigma}$. The purpose of this work was also to theoretically calculate the energy band structure of $CaCo_2$ and the frequency dependence of its interband optical conductivity to relate the special features of absorption to the electronic states of the substance and estimate the exchange splitting of the d band.

2. SAMPLES AND PROCEDURE FOR MEASUREMENTS

The $CaCo_2$ compound was synthesized from the initial mixture of components in a high-pressure chamber of the Toroid type at a 8.0 GPa pressure and under heating to the melting point. Heating was effected by current passage through the sample placed within a tube made of a potassium chloride single crystal. A description of the synthesis and the X-ray structure data on the high-pressure phase can be found in [2]. At normal pressure, $CaCo_2$ is not a stable phase. For this reason, we repeatedly performed phase analyses of the samples directly prior to optical measurements. A study of the crystal structure of $CaCo_2$ (five samples from different series) performed by X-ray diffraction on a DRON-ZM unit using Co K_α radiation showed that the Laves cubic phase C15 was retained in them.

Mirror sample surfaces for optical and magnetooptical measurements were prepared with a diamond paste, grain size smaller than 1 μm; toluene was used as a wetting liquid. After polishing, the surface was purified in an ultrasonic bath filled with toluene. Typical sample sizes were $(4–7) \times (3–5) \times (2–3)\ \mathrm{mm}^3$.

The refractive $n(\omega)$ and absorption $k(\omega)$ indexes (ω is the cyclic light wave frequency) were measured by the Bitti ellipsometry method over the wavelength range $\lambda = (0.25–6.0)\ \mu\mathrm{m}$ on an automated spectrometer with a single reflection from the sample and light incidence angles $\varphi = 67°–75°$. The error in the optical constants did not exceed 3%.

The reflectivity R at a $\varphi = 12°$ light incidence angle was measured on a VYF-2 vacuum spectrometer over the spectrum range $\hbar\omega = (4.5–9)$ eV. The optical constants n and k and the real $\varepsilon_{1,xx}$ and imaginary $\varepsilon_{2,xx}$ parts of the diagonal permittivity tensor components in this region were obtained from the reflectivity $R(\omega)$ values over the whole spectral range studied using the Kramers–Kronig equations as described in [5]. The $R(\omega)$ values in the high-energy region ($E > 9$ eV) were approximated by the ω^{-4} dependence.

The equatorial Kerr effect (δ_p) odd with respect to magnetization describes relative changes in reflected light intensity $\Delta I/I_0$ at equatorial (perpendicular to the plane of light incidence) sample magnetization and the p-polarization of the incident light wave. This effect was measured at $\lambda = (0.3–2.4)\ \mu\mathrm{m}$ using the modulation technique on a magnetooptical spectrometer. The field dependence of the equatorial Kerr effect was studied in fields $H \le 9$ kOe.

The depth of light penetration into the substance under study $\delta_0 = c/\omega k$ increases from 26.5 nm in the near ultraviolet range to 200 nm in the middle IR range, which corresponds to 36 to 270 atomic layers, respectively. This allows the optical and magnetooptical characteristics obtained to be treated as the volume properties of the substance.

We considered optical and magnetooptical properties measured at room temperature and atmospheric pressure for one of the five samples synthesized (No. 2109; further referred to as sample 1) with single-phase crystalline structure C15. This sample was also used to study the temperature dependence of electrical resistance $\rho(T)$ ($T = 78–290$ K). The optical constant n, k, and δ_p-effect values for single-phase samples from other synthesis series were close to those obtained for sample 1 and are not discussed below.

3. CALCULATIONS OF THE ELECTRONIC AND OPTICAL PROPERTIES OF $CaCo_2$

3.1. Computational Procedure

The electronic structure and optical properties of $CaCo_2$ were calculated using electron density functional theory [6] and the WIEN2k package [7]. In this package, the linear augmented-plane-wave method with a crystalline potential having the full lattice symmetry (FP-LAPW) is implemented. The calculations were performed for the paramagnetic and ferromagnetic states. The generalized gradient approximation to the exchange-correlation potential was used; the 3s and 3p Ca and Co states were included into the basis set as local orbitals. The optical spectra were calculated for the theoretical lattice parameter 7.261 Å (the experimental value is $a = 7.412$ Å) on a set of 1140 **k** points in the 1/48 irreducible Brillouin zone part. Estimates of some electronic structure characteristics (partial charges, magnetic moments, band widths, etc.) were obtained in the geometry of a quasi-atomic sphere by the generalized ASA-LMTO method [8].

Let us briefly describe the procedure for calculating optical properties. The imaginary permittivity part $\varepsilon_2(\omega)$ can be represented as the sum of the interband and intraband contributions, $\varepsilon_2(\omega) = \varepsilon_2^{\mathrm{inter}}(\omega) + \varepsilon_2^{\mathrm{intra}}(\omega)$. The Drude contribution determined by the intraband motion of electrons is written as

$$\varepsilon_2^{\mathrm{intra}}(\omega) = \frac{\gamma}{\omega}\frac{\omega_p^2}{\omega^2 + \gamma^2}. \qquad (1)$$

The plasma frequency in (1) was determined by summing over the Fermi surface,

$$\omega_p^2 = \frac{4\pi e^2}{3V_{\text{cell}}}\sum_{n,\mathbf{k}}|\mathbf{v}_n^{\mathbf{k}}|^2\delta(E_n^{\mathbf{k}} - E_{\text{F}}). \quad (2)$$

Here, e is the charge of the electron, V_{cell} is the unit cell volume, and $\mathbf{v}_n^{\mathbf{k}} = dE_n^{\mathbf{k}}/d\mathbf{k}$ is the velocity of the electron in the state $|n, \mathbf{k}\rangle$. The relaxation frequency $\gamma = 1/\tau$ related to scattering by phonons can be approximately estimated from the equation

$$\gamma = \rho_0\omega_p^2/4\pi, \quad (3)$$

where ρ_0 is the specific electrical resistance at a temperature above the Debye temperature.

The contribution $\varepsilon_2^{\text{inter}}(\omega)$ determined by interband electronic transitions is calculated by the equation

$$\varepsilon_2^{\text{inter}}(\omega) = \frac{e^2}{3\pi m^2\omega^2}\sum_{n\neq n'}\int_{BZ} d\mathbf{k}|\mathbf{M}_{nn'}^{k}|^2 \times\theta(E_{n'}^{k} - E_{\text{F}})\theta(E_{\text{F}} - E_n^{\mathbf{k}})\delta(E_{n'}^{\mathbf{k}} - E_n^{\mathbf{k}} - \hbar\omega), \quad (4)$$

where θ is a step function and $\mathbf{M}_{nn'}^{\mathbf{k}}$ denotes the matrix elements of interband optical transitions which can, in the dipole approximation, be written via the momentum operator $\mathbf{p}$,

$$\mathbf{M}_{nn'}^{\mathbf{k}} = \langle n'\mathbf{k}|\mathbf{p}\cdot\mathbf{e}|n\mathbf{k}\rangle \quad (5)$$

($\mathbf{e}$ is the polarization vector of the electromagnetic wave). Equations (1)–(5) were used to calculate the optical conductivity $\text{Re}\sigma(\omega) = \omega\varepsilon_2(\omega)/4\pi$.

The real part $\varepsilon_1(\omega)$ was calculated from $\varepsilon_2(\omega)$ using the Kramers–Kronig equation

$$\varepsilon_1(\omega) = 1 + \frac{2}{\pi}\int d\omega'\frac{\omega'\varepsilon_2(\omega')}{\omega'^2 - \omega^2}. \quad (6)$$

After this, the reflectivity can be determined as

$$R(\omega) = \left|\frac{\sqrt{\varepsilon(\omega)} - 1}{\sqrt{\varepsilon(\omega) + 1}}\right|^2. \quad (7)$$

3.2. The Electronic Structure of $CaCo_2$

Our calculations showed, in complete agreement with LMTO calculations [2, 3], that $CaCo_2$ is a ferrimagnet with the cobalt sublattice moment $\mu_{\text{Co}} = 1.55\mu_{\text{B}}$ and the oppositely directed induced moment on calcium $\mu_{\text{Ca}} = -0.38\mu_{\text{B}}$. Such a ferrimagnetic ordering is typical of Laves cubic phases AB_2 and is observed in neutron diffraction experiments. The calculated magnetic moment per $CaCo_2$ formula unit is $2.72\mu_{\text{B}}$, which is slightly smaller than the experimental moment. The value obtained is closer to the magnetic moment of pure cobalt ($\mu_{\text{Co}} = 1.71\mu_{\text{B}}$) than the values for the other cobalt compounds with nonmagnetic elements (where, as a rule, $\mu_{\text{Co}} \leq 1\mu_{\text{B}}$).

The electronic configuration of the calcium atom in $CaCo_2$ at normal pressure $P \approx 0$, when the compound is metastable, is $4sp^{1.1}3d^{0.9}$. The Ca atom has $z = 12$ nearest neighbors (Co atoms) at distances $d_{NN} \approx 3.07$ Å. The pure FCC calcium metal is also characterized by $z = 12$, but the interatomic distance in it is 3.94 Å. The d_{NN} distance in pure calcium becomes equal to 3.07 Å under approximately twofold uniform mechanical compression attained at $P \sim 30$ GPa. The number of d electrons n_d per atom in FCC calcium then increases from 0.5 to 0.9, that is, equal to that in $CaCo_2$. The specified pressure value and the corresponding occupation number $n_d \approx 1$ correspond to the final stage of “continuous *s*–*d* transition” in calcium. This term usually denotes gradual electron transfer from the *s* to *d* band caused by compression. In terms of the *s*–*d* transition concept, n_d is treated as a universal parameter, which, within certain limits, allows the chemical bond, crystal structure, and other properties of alkali and alkaline-earth metals to be predicted.

According to this picture, the chemical compression of the electron shell in $CaCo_2$ results in electron transfer into the empty *d* band of calcium instead of filling the *d* subband of cobalt with “spin down.” As a result, the numbers of *d* electrons on cobalt with spin up and spin down are 4.6 and 3.0, respectively, which is close to those for pure HCP cobalt (4.7 and 2.9). This explains the high value of the observed magnetic moment of $CaCo_2$. Also note that the very possibility of preparing the compound under consideration by applying high pressure has a simple explanation within the framework of the Midema model of alloy formation (see references in [3]), according to which an increase in the number of *d* electrons in a simple metal is a factor that favors the formation of its compounds with transition metals.

The energy bands $E_n(\mathbf{k})$ and density-of-state curves $N(E)$ for electrons with spins directed along ($\uparrow$) and oppositely to ($\downarrow$) the spontaneous magnetization direction are shown in Fig. 1. The partial densities of the *s*, *p*, and *d* states of the cobalt and calcium atoms in the C15 lattice are given in Figs. 2a and 2b. Distinguishing the bands originating from different atoms and different angular momenta *l* shows that the 3*d* cobalt states predominate in the density of states $N(E)$ below and directly above the Fermi level E_{F}, whereas the main contribution above 2 eV is made by the 3*d* states of calcium. The total density of states $N(E)$ (Fig. 1c) exhibits two peaks of free *d* bands of Ca, N_1 and N_2. The contribution of the *d* electrons of Ca to the total density of states at the Fermi level $N(E_{\text{F}})$ is comparable to the con-

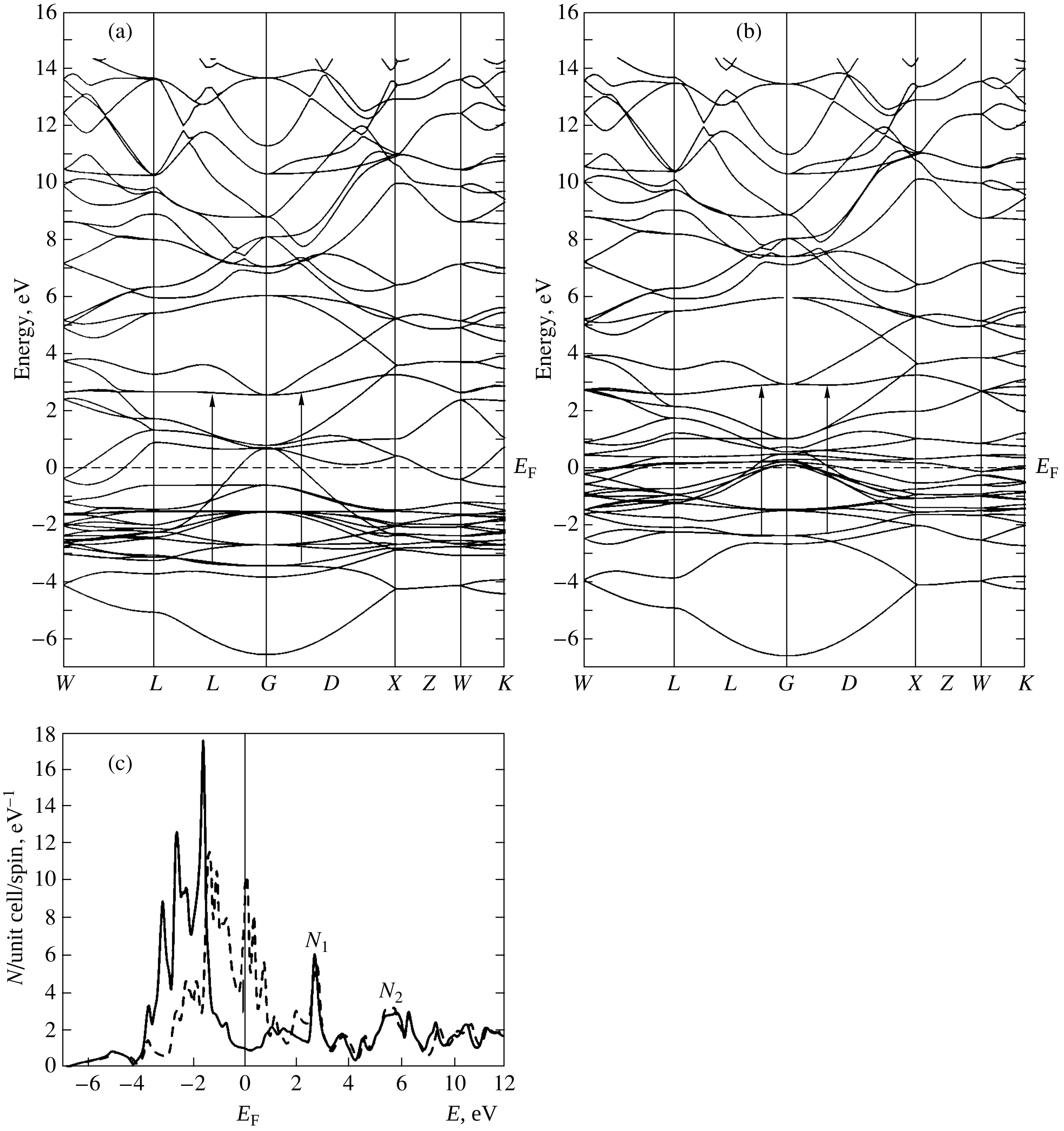

Fig. 1. Energy bands of ferromagnetic $CaCo_2$ with spin directions (a) along and (b) opposite to spontaneous magnetization and (c) density of states $N(E)$ for subbands with spins up (solid line) and down (dashed line).

tribution of the *s* and *p* states of atoms of both types; the contribution of the *d* states of Co is larger by more than an order of magnitude (see Fig. 2).

It follows from our calculations that the 3*d* band of calcium in $CaCo_2$ is very broad (estimates in the ASA approximation give 11.2 eV for spin-up electrons and 11.4 eV for spins-down electrons). For cobalt, the width of the $3d_\downarrow$ subband is 3.8 eV and that of the $3d_\uparrow$ subband, only 3.2 eV. As a result, the total width of the *d* band in $CaCo_2$ covers the interval of 15.8 eV, whereas the width of its occupied part does not exceed 3.8 eV. The large width of the *d* band of $CaCo_2$ is related to hybridization between the *s*, *p*, and *d* states of the Ca and Co atoms, as follows from the shape of the $N_j(E)$ partial curves in Fig. 2. Hybridization also determines the form of the *d* band of Ca in $CaCo_2$: neither in width nor in shape does it resemble the *d* band of pure calcium subjected to twofold compression.

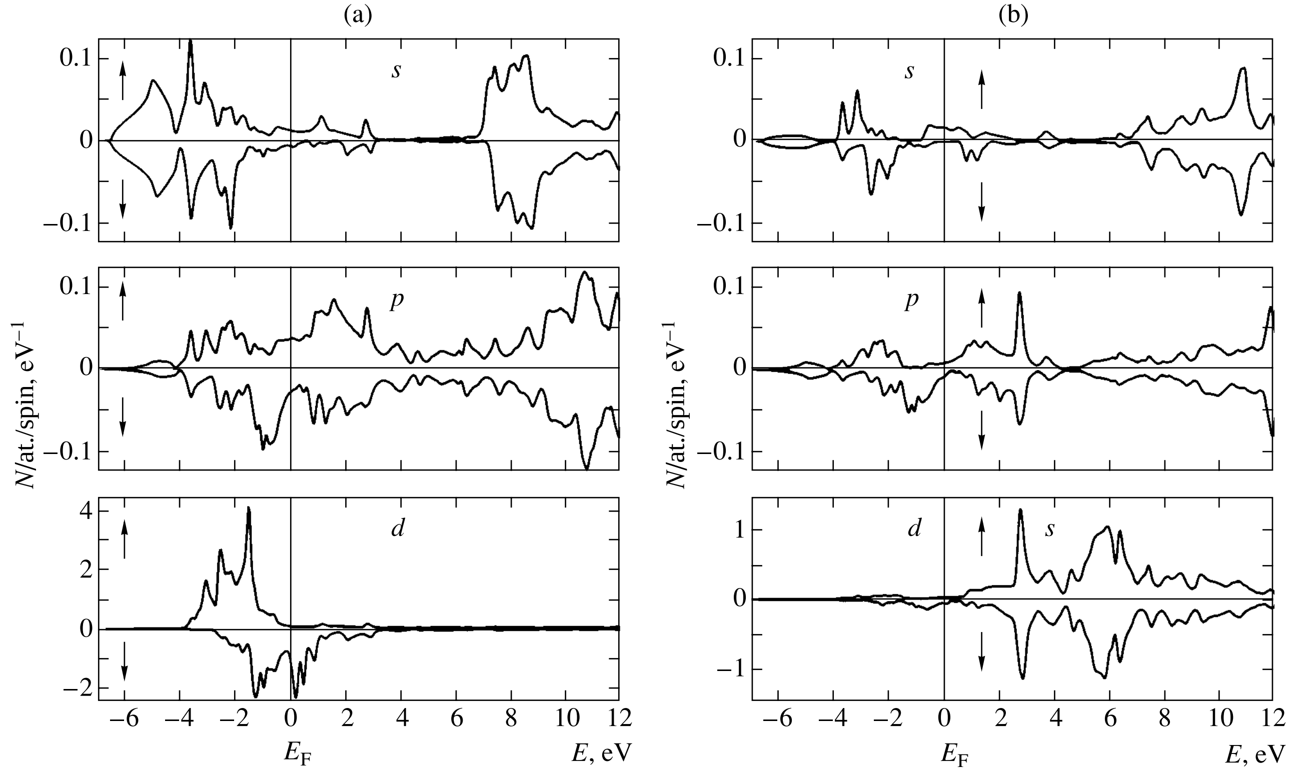

Fig. 2. Partial electronic state densities $N_n(E)$ for the s, p, and d bands in $CaCo_2$ on (a) cobalt and (b) calcium atoms. Arrows denote the directions of spins.

The calculations show that the exchange splitting of the 3d band of Co is $2\Delta_{exc} \sim 1.36$ eV. The magnetic moment of Co atoms determines the spin separation of the whole 3d band in $CaCo_2$. The shift of the spin-polarized bands in the spectrum of Ca is an order of magnitude smaller and directed oppositely (that is, the magnetic moment of the Ca atom is negative).

4. RESULTS AND DISCUSSION

4.1. A Comparison of the Experimental and Theoretical Re$\sigma_{xx}(\omega)$ *and* $R(\omega)$ *Dependences*

Let us consider the optical properties of $CaCo_2$. The form of the frequency dispersion of optical conductivity is evidence that the mechanism of interband light absorption plays a determining role over the spectral range studied ($\hbar\omega = 0.2$–9 eV).

It is known that the overall picture of interband absorption in a ferromagnet is created by the superposition of electron transitions in both spin subsystems, $\mathrm{Re}\sigma_{xx}(\omega) = \mathrm{Re}\sigma_{xx\uparrow} + \mathrm{Re}\sigma_{xx\downarrow}$. Fundamentally new special features of optical conductivity are only expected at the frequencies $\hbar\omega \sim 2|\xi|$ as a result of spin–orbit coupling of bands with oppositely directed spins (ξ is the spin–orbit band splitting parameter) [9]. Our experiments, however, did not cover the low-frequency IR spectral range, where these effects could be observed.

The experimental optical conductivity Re$\sigma_{xx}(\omega)$ curve for $CaCo_2$ is shown in Fig. 3. Note the wide band a with a maximum at 1.1 eV and the peculiar dou-

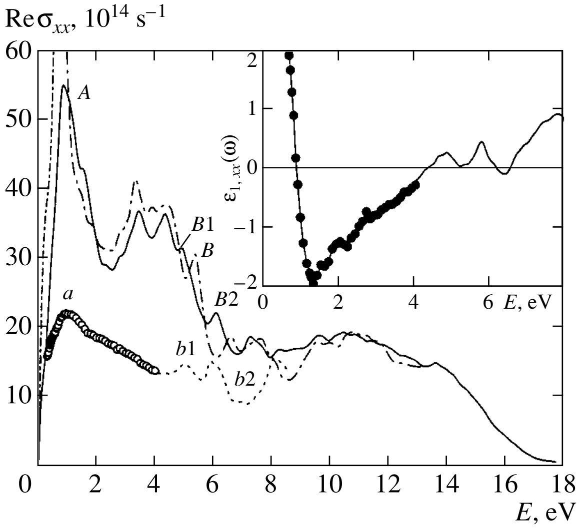

Fig. 3. Dissipative part of the diagonal component of the conductivity tensor Re$\sigma_{xx}(\omega)$ for $CaCo_2$. Experiment: ○, ellipsometry, and dashed curve, calculations from $R(\omega)$ by the Kramers–Kronig equations. Calculated Re$\sigma_{xx}(\omega)$ curves for the paramagnetic (dot-and-dash line) and ferromagnetic (solid line) states. The real permittivity part $\varepsilon_{1,xx}(\omega)$ is shown in the inset: ●, ellipsometry, and solid line, calculations from $R(\omega)$ by the Kramers–Kronig equations.

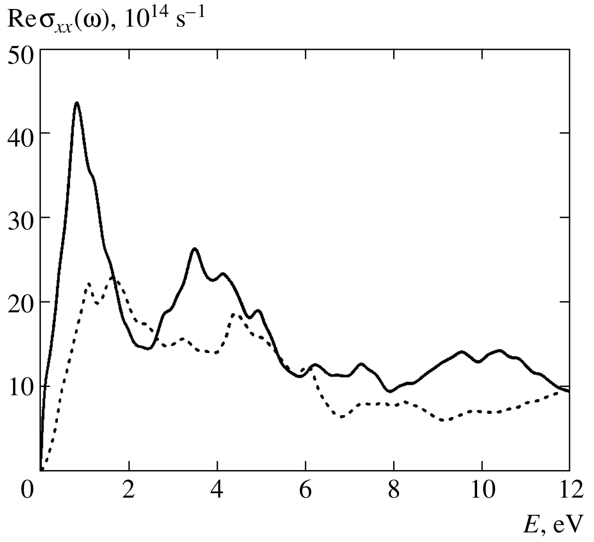

Fig. 4. Calculated partial contributions to optical conductivity of spins: $\mathrm{Re}\sigma_{xx}\uparrow$ (dashed line) and $\mathrm{Re}\sigma_{xx}\downarrow$ (solid line).

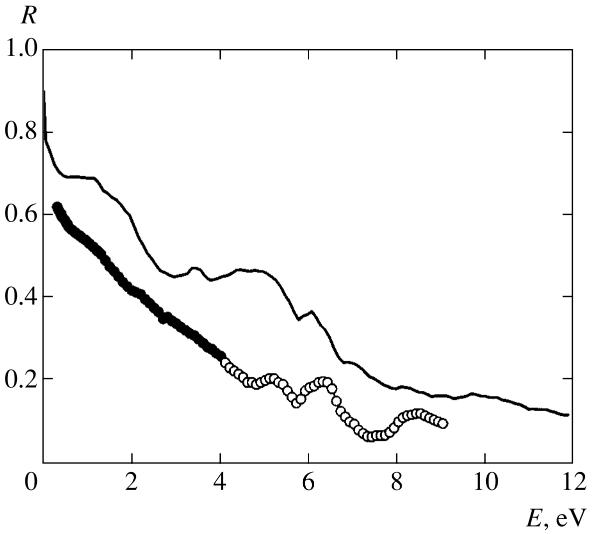

Fig. 5. Experimental reflectivity versus theoretical $R(\omega)$ curve (solid line) obtained for the ferromagnetic state. Experiment: ●, ellipsometry, and ○, measurements of $R(\omega)$ at $\varphi = 12°$.

ble structure *b*1–*b*2 with maxima at photon energies of 5 and 6 eV, respectively. An analysis of the partial contributions to interband conductivity allows the nature of these bands to be explained by direct electron transitions between particular energy band pairs. For instance, for the states with spins up, the major contribution to the formation of band *a* is made by transitions between the bands 23 $\longrightarrow$ 24, which intersect E_F in the *W*–*L* Brillouin zone direction (Van Hove singularity of the $\nabla E_n(\mathbf{k}) = \nabla E_{n'}(\mathbf{k})$ type). Electron transitions between the other pairs of bands (20, 21 $\longrightarrow$ 23, 22 $\longrightarrow$ 24) are less intense. In the system of bands with spins down, ten energy bands intersect the Fermi level. A series of electron transitions between the planar $d_\downarrow$ bands situated in the vicinity of the Fermi level (the (11–21) $\longrightarrow$ (19–25) transitions) make the most substantial overall contribution to the formation of the specified optical absorption band (Fig. 4). It follows that the amplitude and spectral profile of band *a* are determined by ($p,d \longrightarrow d,p$)-type interband transitions, that is, transitions between bands originating from the atomic *d* states of Co and Ca and, as a result of hybridization (see Fig. 2), containing substantial admixtures of *p* states. Optical conductivity calculations (Fig. 4) show that the contributions $\sigma_\downarrow$ and $\sigma_\uparrow$ of spin-polarized bands are comparable in magnitude at photon energies $E = (1.4–2.5)$ eV and $E = (4.3–6)$ eV. In the other spectral regions, electron transitions in the system with spins down predominate.

Next, let us consider the double structure observed in the ultraviolet spectral range with maxima at $\hbar\omega_1 = 5$ eV and $\hbar\omega_2 = 6$ eV (Fig. 3). It is noteworthy that the theoretical optical conductivity curve of ferromagnetic $\mathrm{CaCo_2}$ contains similar peaks *B*1 and *B*2, whereas only the intermediate peak *B* is clearly seen for the paramagnetic compound phase. An analysis of the partial contributions to interband conductivity leads us to conclude that the predominant contribution to the formation of the *B*1 (*b*1) and *B*2 (*b*2) structures is made by transitions between planar *d*-type bands 4 $\longrightarrow$ 28 in subsystems with spins up and down. These transitions are marked by vertical arrows in Figs. 1a and 1b. It follows that the splitting of peak *B* into two structures is caused by the mutual separation of the cobalt 3*d* band in the ferromagnetic phase caused by exchange interaction. The final states of the specified electron transitions are the calcium *d* bands (hybridized with the *p* states of Ca and Co). These bands form a narrow intense peak N_1 of the density of states $N(E)$ (Fig. 1c). Ignoring the exchange splitting of the free 3*d* band of Ca, we can estimate the exchange splitting of the 3*d* band in $\mathrm{CaCo_2}$ from the experimental optical data, $2\Delta_{\mathrm{exc}}^{3d} \sim 1$ eV. Interestingly, the exchange splitting of the 3*d* band in pure cobalt metal has a similar value, $2\Delta_{\mathrm{exc}}^{3d} \sim 1.5$ eV [10, 11].

The conclusion can be drawn that, on the whole, the total $\mathrm{Re}\sigma_{xx}(\omega)^{\mathrm{theor}}$ curve for the ferromagnetic state of $\mathrm{CaCo_2}$ well reproduces the energy positions of both the first absorption band at 1.1 eV and the double structure in the ultraviolet spectral range (5 and 6 eV). In the intermediate optical spectrum region, the experimental $\mathrm{Re}\sigma_{xx}$ curve has a smoother frequency dependence compared with the calculated curve. Possibly, the superposition of the partial contributions to optical conductivity of a large number of electron transitions with different excited state lifetimes causes spectral "smoothing." Smoothing of the $\mathrm{Re}\sigma_{xx}$ spectrum can also be caused by an experimental factor (the presence of small roughness that remains on mirror sample surfaces after polishing).

A comparison of the theoretical and experimental reflectivity curves $R(\omega)$ over the spectral range $\hbar\omega$ = 0.2–9 eV (Fig. 5) shows satisfactory agreement in the dispersion of the functions, which, however, have different values, especially at low frequencies. The calculations of $R(\omega)$ were performed with the inclusion of the intraband (Drude) contribution, which was determined from the calculated plasma frequency of conduction electrons $\hbar\omega_p$ = 3.82 eV and relaxation frequency $\hbar\gamma$ = 2 eV. The Drude rise in optical conductivity as the photon energy decreased down to $\hbar\omega \sim 0.2$ eV was not, however, observed experimentally for $CaCo_2$. In addition, positive real permittivities $\varepsilon_{1,xx}$ (see inset to Fig. 3) were observed at IR frequencies. It follows that the Drude contribution to the optical characteristics in the near IR spectral range is small and masked by a more substantial contribution of low-energy interband absorption. The available optical data are insufficient for estimating the plasma ω_p and relaxation γ frequencies of free carriers in $CaCo_2$. Measurements of the temperature dependence of electrical resistance $\rho(T)$ are evidence of the metallic conductivity type of $CaCo_2$. The specific resistance is high, $\rho_{290\,K}$ = 264 μΩ cm and $\rho_{78\,K}$ = 149 μΩ cm. The special features of the optical and electric properties of $CaCo_2$ described above are, in our view, caused by both the special features of the electronic structure of the compound and strong scattering of electrons by structural defects present in the strained metastable compound. In addition, the presence of a certain amount of microvoids at the skin-layer depth in the sample retained after the removal of pressure-transferring medium residuals can favor an increase in electrical resistance and a decrease in intraband conduction.

4.2. Magnetooptical Characteristics

Let us turn to the magnetooptical characteristics of $CaCo_2$. The response of a magnetized medium to the action of the electric field of a light wave results in the appearance of off-diagonal components in the optical conductivity tensor $\hat{\sigma}$. The source of gyrotropy, which manifests itself in the form of magnetooptical effects, is spin–orbit coupling, which removes the degeneracy of bands and modifies the wave functions of electrons. If *p*-polarized light falls on an optically isotropic magnetized medium (the *z* axis direction is $\mathbf{z} \parallel \mathbf{M}$, where $\mathbf{M}$ is the magnetization vector), the equatorial Kerr effect is described by the equation [12, 13]

$$\delta_p = -4\mathrm{Im}\frac{i\sigma_{xy}\tan\varphi}{\sigma_{xx}(1 - 4\pi i\sigma_{xx}/\omega - \tan^2\varphi)}, \qquad (8)$$

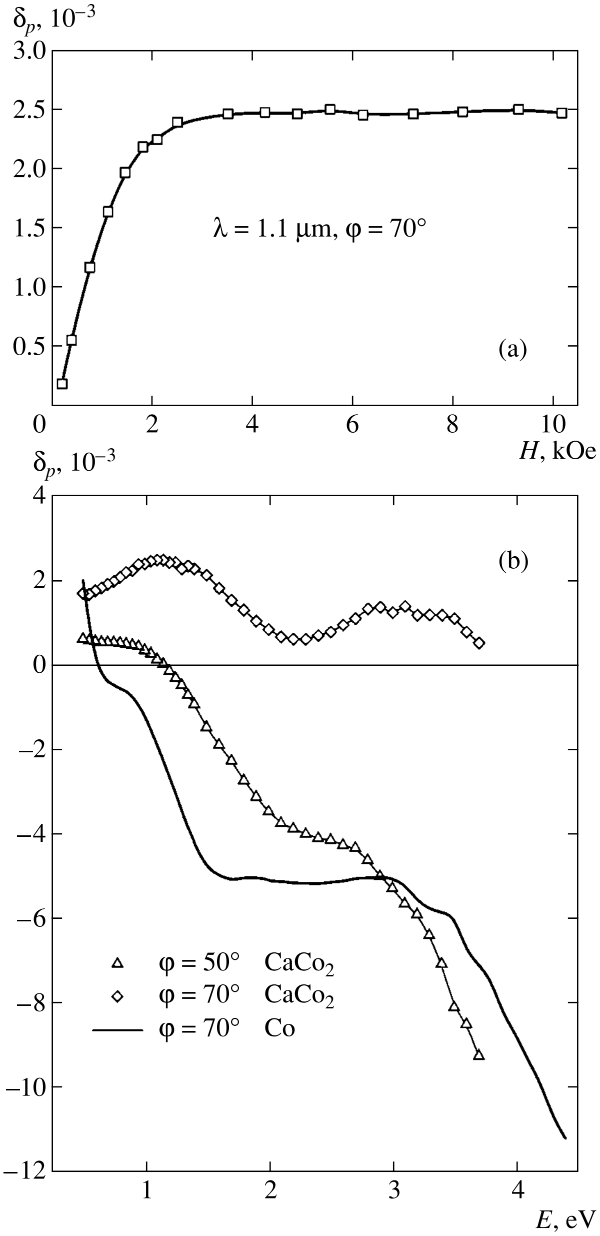

Fig. 6. (a) Field dependence of the δ_p effect in $CaCo_2$ and (b) spectral dependences of the δ_p effect for $CaCo_2$ at two light incidence angles (φ = 50° and 70°) and for HCP cobalt (φ = 70°).

where φ is the light incidence angle. It follows that the effect value is determined by both the diagonal σ_{xx} and off-diagonal σ_{xy} optical conductivity tensor components. The field dependence of the equatorial Kerr effect $\delta_p(H)$ is shown in Fig. 6a. This dependence characterizes sample magnetization in magnetic field $\mathbf{H}$ parallel to the plane of the sample. Measurements were taken at wavelength λ = 1.1 μm and φ = 70°. Sample saturation was observed at $H \sim 6$ kOe. The spectral dependence of the δ_p effect in $CaCo_2$ is shown in Fig. 6b. The equatorial Kerr effect curve (φ = 50°) passes through zero at E = 1.15 eV. The effect value then increases as the photon energy grows. At a φ = 70° light incidence angle, the dispersion of the equatorial

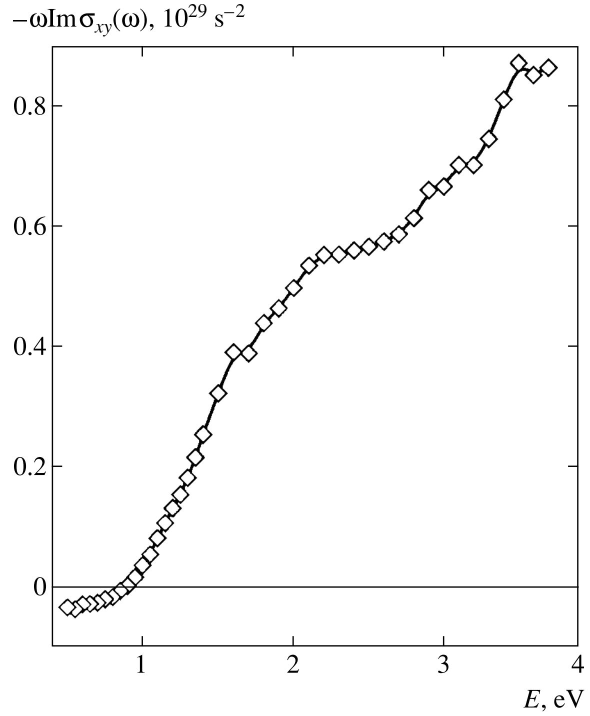

Fig. 7. Dissipative part of the off-diagonal conductivity tensor component $\omega\mathrm{Im}\sigma_{xy}(\omega)$ for the $CaCo_2$ compound.

Kerr effect is quite different: a maximum is observed in the spectral range $\hbar\omega = 0.8$–1.6 eV and in the region of 3 eV. Close to 1 eV, the δ_p value in $CaCo_2$ is more than twice as large as the absolute equatorial Kerr effect value in pure cobalt. The effect, however, weakens fourfold at 3 eV. Also note that the sign of the equatorial Kerr effect in $CaCo_2$ in the visible and UV spectral ranges is opposite to that observed in HCP cobalt.

We used the equatorial Kerr effect values obtained at two light incidence angles and our optical data to calculate the real and imaginary parts of the off-diagonal component of the tensor of optical conductivity of $CaCo_2$ $\sigma_{xy} = \sigma_{1,xy} - i\sigma_{2,xy}$. The calculations were performed with (8). The imaginary off-diagonal conductivity part $\omega\mathrm{Im}\sigma_{xy}$ is shown in Fig. 7. We see that the magnetooptical activity of the compound tends to increase as the photon energy increases in the spectral region $\hbar\omega = (1$–$4)$ eV. In the optical range studied, the magnitude and sign of this function are directly related to the character of the spin polarization of electrons participating in interband excitation processes. In a crude approximation at $\hbar\omega \ll 2|\xi|$, the $\omega\mathrm{Im}\sigma_{xy}(\omega)$ value, which characterizes the magnetoabsorption of the substance, is proportional to the difference $\mathrm{Re}\sigma_{xx\uparrow} - \mathrm{Re}\sigma_{xx\downarrow}$ [10]. This function should be calculated theoretically to gain understanding of the microscopic nature of magnetoabsorption in compounds comprising transition and alkaline-earth metals.

5. CONCLUSIONS

For the first time, we studied the optical and magnetooptical properties of the intermetallic ferromagnetic compound $CaCo_2$, which is formed only at a high pressure of about 8 GPa and remains metastable after pressure is removed. So far as we know, high-pressure intermetallic phases have not been studied by metal optics methods thus far. The compound has the metallic conduction type, which is substantiated by first-principles electronic structure calculations.

According to our calculations, the d band in $CaCo_2$ is very broad ($W_d = 15.8$ eV) because it is formed from the almost occupied 3d band of Co and the almost unoccupied 3d band of Ca. The large width of the d band and substantial s, p, d hybridization of the electronic states of Ca and Co in the $MgCu_2$ lattice cause intense electron transitions of the $(p,d \longrightarrow d,p)$ type over a wide photon energy range, including the near vacuum ultraviolet spectral range. This is substantiated by the form of optical spectra. The calculated optical conductivity $\mathrm{Re}\sigma_{xx}(\omega)$ and reflectivity $R(\omega)$ functions satisfactorily reproduce the main spectral features of the experimental curves.

The compound is characterized by a high magnetic moment value close to that for pure Co metal. The exchange splitting of the 3d band of $CaCo_2$ obtained from the calculated and experimental optical data is $2\Delta_{\mathrm{exc}} \sim (1$–$1.3)$ eV, which is also close to the exchange splitting of the 3d band of pure Co ($2\Delta_{\mathrm{exc}} \sim 1.5$ eV). On the whole, the conclusion can be drawn that the data of optical measurements and first-principle calculation results give a mutually consistent description of the electronic structure of $CaCo_2$.

ACKNOWLEDGMENTS

The authors are deeply indebted to E.G. Maksimov and Yu.A. Uspenskiĭ for fruitful discussions of the theoretical results. We also thank V.A. Sazonova for obtaining the X-ray diffraction patterns, A.V. Luk'yanov for help with experimental data processing according to the Kramers–Kronig equations, and V.P. Dyakin for measuring the electrical conductivity of the sample.

This work was financially supported by the Russian Foundation for Basic Research (project no. 04-02-16061), Dutch–Russian grant no. 047.016.005, and the program "Physics and Mechanics of Strongly Compressed Matter: Internal Structure of the Earth and Planets" of the Russian Academy of Sciences. Theoretical calculations were performed at the Supercomputer Center of the Russian Academy of Sciences.

REFERENCES

1. L. J. Parker, T. Atou, and J. V. Badding, Science **273**, 95 (1996).

2. A. V. Tsvyashchenko, L. N. Fomicheva, M. V. Magnitskaya, *et al.*, Pis'ma Zh. Éksp. Teor. Fiz. **68**, 864 (1998) [JETP Lett. **68**, 908 (1998)].
3. A. V. Tsvyashchenko, L. N. Fomicheva, M. V. Magnitskaya, *et al.*, Phys. Met. Metallogr. **93** (Suppl. 1), S59 (2002).
4. N. Nakamura, A. Nakahara, M. Shiga, *et al.*, Phys. Status Solidi B **241**, 352 (2002).
5. V. M. Maevskiĭ, A. V. Druzhinin, M. M. Kirillova, *et al.*, Available from VINITI, No. 5151-81 (Moscow), p. 39.
6. W. Kohn, Usp. Fiz. Nauk **172**, 336 (2002).
7. P. Blaha, K. Schwarz, G. K. H. Madsen, *et al.*, *WIEN2k, An Augmented Plane Wave + Local Orbitals Program for Calculating Crystal Properties* (K. Schwarz, Tech. Univ. Wien, Austria, 2001), ISBN 3-9501031-1-2.
8. S. Yu. Savrasov and D. Yu. Savrasov, Phys. Rev. B **46**, 12181 (1992).
9. Yu. A. Uspenskiĭ and S. V. Khalilov, Fiz. Met. Metalloved. **66**, 1097 (1988).
10. Yu. A. Uspenskiĭ and S. V. Khalilov, Zh. Éksp. Teor. Fiz. **95**, 1022 (1989) [Sov. Phys. JETP **68**, 588 (1989)].
11. S. V. Halilov and Yu. A. Uspenskii, J. Phys.: Condens. Matter **2**, 6137 (1990).
12. G. S. Krinchik, *Physics of Magnetic Phenomena* (Mosk. Gos. Univ., Moscow, 1985) [in Russian].
13. G. A. Bolotin and V. M. Maevskiĭ, Fiz. Met. Metalloved. **30**, 475 (1970).

Translated by V. Sipachev

Journal of Experimental and Theoretical Physics, Vol. 100, No. 5, 2005, pp. 992–997.
Translated from Zhurnal Éksperimental'noĭ i Teoreticheskoĭ Fiziki, Vol. 127, No. 5, 2005, pp. 1123–1129.
Original Russian Text Copyright © 2005 by Larionov.

ELECTRONIC PROPERTIES OF SOLIDS

The Magnetic Properties of Weakly Doped Layered Copper Oxides: Relaxation Function in the Model of Strongly Correlated Charge Carriers

I. A. Larionov
Kazan State University, ul. Kremlevskaya 18, Kazan, 420008 Tatarstan, Russia
e-mail: Igor.Larionov@ksu.ru

Received December 3, 2004

Abstract—The method of projection operators is applied to the two-dimensional model of strongly correlated charge carriers to explain the magnetic properties of weakly doped layered cuprates in the paramagnetic state. The theory explains the observed special features of the behavior of the imaginary part of the dynamic spin susceptibility averaged over the Brillouin zone over wide temperature and frequency ranges. © *2005 Pleiades Publishing, Inc.*

The magnetic properties of layered high-T_C cuprate superconductors remain to be the focus of attention of experimental and theoretical researchers [1]. Among the unusual properties revealed by inelastic neutron scattering, the behavior of the imaginary part of the dynamic spin susceptibility $\chi''(\omega, T)$ averaged over the Brillouin zone can be mentioned. This property exhibits universal behavior in wide temperature and frequency ranges $\omega \sim 10$ meV (the so-called ω/T scaling) and approximately follows the law

$$\chi''(\omega, T) = \int\chi''(\mathbf{q}, \omega, T)d^2q \approx I(|\omega|, 0)f(\omega/T), \qquad (1)$$

where

$$I(|\omega|, 0) = \chi''(\omega, T \longrightarrow 0). \qquad (2)$$

Such behavior was observed for a wide class of weakly doped layered high-T_C cuprates, including $La_{1.95}Ba_{0.05}CuO_4$ [2], $La_{1.98}Sr_{0.02}CuO_4$ [3], $La_{1.96}Sr_{0.04}CuO_4$ [4, 5], $YBa_2Cu_{2.9}Zn_{0.1}O_{6.6}$ [6], and even in the normal phase of $YBa_2Cu_3O_{6+x}$ superconducting samples with $T_C = 53$ K [7]. Similar behavior was also observed in nuclear magnetic/quadrupole resonance (NMR/NQR) measurements [8] at substantially lower frequencies $\omega \approx 2\pi \times 34$ MHz $(= 1.4 \times 10^{-4}$ meV). Aeppli *et al.* [9] also observed universal behavior in the almost optimally doped $La_{1.86}Sr_{0.14}CuO_4$ compound ($T_C = 35$ K).

In this work, we show that the $\chi''(\omega, T)$ dependences observed in the paramagnetic phase can be explained by applying the Zwanzig–Mori method of projection operators [10, 11] to the *t*–*J* model, which, according to Anderson [12], is most promising for describing the electronic properties of high-T_C cuprates [13]. The relaxation function method is used widely to describe the properties of spin nonequilibrium systems [14, 15]. It is, in particular, applied to analyze neutron scattering [16, 17] and magnetic relaxation [18] data.

We will concentrate on one compound, the most completely studied, $La_{1.96}Sr_{0.04}CuO_4$. It has the simplest structure among high-T_C cuprates (one current-carrying CuO_2 plane). Other weakly doped high-T_C compounds with a more complex chemical composition should exhibit similar behavior. Their analysis, however, requires more detailed knowledge of their electronic properties. Also note that an attempt to explain ω/T scaling was made recently [19], but the approximation used in [19] had a free parameter adjusted by comparing with the experimental $\chi''(\omega, T)$ values. Another more serious shortcoming of this theory was the use of a temperature-independent correlation length parameter, which only corresponded to experimental data at $T \lesssim 400$ K. At the same time, the method of exact diagonalization for small clusters of size of about 20 atoms that was employed in [19] only gives correct results at temperatures above 500 K. In this work, we show that the experimental $\chi''(\omega, T)$ dependences can be explained by determining static characteristics and obtaining dynamic values without adjustment parameters.

The Hamiltonian of the *t*–*J* model has the form

$$H_{t-J} = \sum_{i, j, \sigma} t_{ij}X_i^{\sigma 0}X_j^{0\sigma} + J\sum_{i>j}\left(\mathbf{S}_i \cdot \mathbf{S}_j - \frac{1}{4}n_in_j\right). \qquad (3)$$

Here, $\mathbf{S}_i$ is the operator of spin 1/2 on site i, $X_i^{\sigma 0}$ $(X_i^{0\sigma})$ is the Hubbard operator of creation (annihilation) or

1063-7761/05/10005-0992$26.00 © 2005 Pleiades Publishing, Inc.

particles with spin σ, the t_{ij} hopping integrals between the nearest neighbors describe the motion of particles in the two-dimensional lattice, and J is the superexchange antiferromagnetic coupling constant. In terms of Hubbard operators, the spin and density (n_i) operators have the form

$$S_i^{\sigma} = X_i^{\sigma\bar{\sigma}}, \quad S_i^z = \frac{1}{2}\sum_{\sigma}\sigma X_i^{\sigma\sigma}, \tag{4}$$

$$n_i = \sum_{\sigma} X_i^{\sigma\sigma} \quad (\sigma = -\bar{\sigma}) \tag{5}$$

with the standard normalization

$$X_i^{00} + X_i^{++} + X_i^{--} = 1. \tag{6}$$

The theory will be formulated following Mori [11]. The evolution of a dynamic variable, for instance, $S_{\mathbf{k}}^z(\tau)$, obeys the equation

$$\dot{S}_{\mathbf{k}}^z(\tau) \equiv \frac{dS_{\mathbf{k}}^z(\tau)}{d\tau} = iLS_{\mathbf{k}}^z(\tau). \tag{7}$$

Generally, L is the Liouville operator, and, in the language of quantum mechanics, $iLS_{\mathbf{k}}^z(\tau)$ corresponds to the commutator with Hamiltonian (3). The $S_{\mathbf{k}}^z(\tau)$ operators can be decomposed into components with respect to $S_{\mathbf{k}}^z \equiv S_{\mathbf{k}}^z(\tau = 0)$,

$$S_{\mathbf{k}}^z(\tau) = R(\mathbf{k}, \tau)S_{\mathbf{k}}^z + (1 - \mathcal{P}_0)S_{\mathbf{k}}^z(\tau), \tag{8}$$

where

$$R(\mathbf{k}, \tau)S_{\mathbf{k}}^z = \mathcal{P}_0 S_{\mathbf{k}}^z(\tau), \tag{9}$$

$\mathcal{P}_0$ is the linear Hermitian projection operator,

$$R(\mathbf{k}, \tau) \equiv (S_{\mathbf{k}}^z(\tau), (S_{-\mathbf{k}}^z)^*)(S_{\mathbf{k}}^z, (S_{-\mathbf{k}}^z)^*)^{-1} \tag{10}$$

is the relaxation function, and

$$\begin{aligned}(S_{\mathbf{k}}^z(\tau), (S_{-\mathbf{k}}^z)^*) &\equiv k_B T \int_0^{1/k_B T} d\varrho \\ &\times \langle e^{\varrho H} S_{\mathbf{k}}^z(\tau) e^{-\varrho H} (S_{-\mathbf{k}}^z)^* \rangle.\end{aligned} \tag{11}$$

The angle brackets denote thermodynamic averaging. The ω and J values will be given in either energy (eV), or temperature (K), or frequency (Hz) units. The Planck constant $\hbar$ will therefore be omitted in equations.

Further, a set of $f_0(\tau), f_1(\tau), \ldots, f_j(\tau), \ldots$ values determined by the equations

$$\begin{aligned}f_j(\tau) \equiv \exp(iL_j\tau) f_j \equiv \exp(iL_j\tau) iL_j f_{j-1} \\ (j \geq 1),\end{aligned} \tag{12}$$

can conveniently be introduced. Here,

$$\begin{aligned}f_0(\tau) &\equiv S_{\mathbf{k}}^z(\tau), \\ L_j &\equiv (1 - \mathcal{P}_{j-1})L_{j-1} \quad (L_0 = L), \\ \Delta_j^2 &\equiv (f_j, f_j^*)(f_{j-1}, f_{j-1}^*)^{-1},\end{aligned} \tag{13}$$

and $\{f_j\}$ is a set of orthogonal values. The use of a larger number of f_j gives a more accurate description of the $S_{\mathbf{k}}^z(\tau)$ operator. Applying the evolution operator $\exp(iL_n\tau)$ to the last set value, f_n, we obtain the $f_n(\tau)$ function called nth-order random force [11], which acts on the $S_{\mathbf{k}}^z(\tau)$ variable and is responsible for its fluctuations.

Applying the Laplace transform to the relaxation function

$$R^L(\mathbf{k}, s) = \int_0^{\infty} d\tau e^{-s\tau} R(\mathbf{k}, \tau), \tag{14}$$

we can construct the representation for $R^L(\mathbf{k}, s)$ in the form of an infinite fraction [11]. Lovesey and Meserve [20] truncated this fraction at the third step,

$$R(\mathbf{k}, s) = 1/\{s + \Delta_{1\mathbf{k}}^2/[s + \Delta_{2\mathbf{k}}^2/(s + 1/\tau_{\mathbf{k}})]\}. \tag{15}$$

They introduced the characteristic time

$$\tau_{\mathbf{k}} = \sqrt{\frac{2}{\pi\Delta_{2\mathbf{k}}^2}}. \tag{16}$$

Their approximation was based on the weak sensitivity of the $S_{\mathbf{k}}^z(\tau)$ operator to the character of random forces of higher orders. They demonstrated close agreement with the calculations performed by other authors and experimental data on neutron scattering in the paramagnetic phase of systems of arbitrary dimensions described by the Heisenberg Hamiltonian at both high temperatures and temperatures slightly higher than the Neél temperature T_N ($T \gtrsim T_N$).

The $\Delta_{j\mathbf{k}}^2$ values are related to the moments $\langle \omega_{\mathbf{k}}^n \rangle$ of the relaxation function

$$\langle \omega_{\mathbf{k}}^n \rangle = \frac{1}{i^n}\left[\frac{d^n R(\mathbf{k}, \tau)}{d\tau^n}\right]_{\tau = 0}, \tag{17}$$

as follows:

$$\Delta_{1\mathbf{k}}^2 = \langle \omega_{\mathbf{k}}^2 \rangle, \quad \Delta_{2\mathbf{k}}^2 = \frac{\langle \omega_{\mathbf{k}}^4 \rangle}{\langle \omega_{\mathbf{k}}^2 \rangle} - \langle \omega_{\mathbf{k}}^2 \rangle. \tag{18}$$

The odd moments are equal to zero, $\langle \omega_{\mathbf{k}}^{2m+1} \rangle = 0$.

The cross section of the magnetic scattering of neutrons gives information about the dynamic structure factor $S(\mathbf{k}, \omega)$, which is the Fourier transform of the spin–spin correlation function over the spatial and time variables. The structure factor is related to the imaginary part of the dynamic spin susceptibility $\chi''(\mathbf{k}, \omega)$ as

$$S(\mathbf{k}, \omega) = \frac{\chi''(\mathbf{k}, \omega)}{1 - \exp(-\omega/k_B T)}. \tag{19}$$

In the approximation that we use, it has the form [20]

$$\begin{aligned} &S(\mathbf{k}, \omega) \\ &= \frac{2\omega\chi(\mathbf{k})\tau_{\mathbf{k}}\Delta_{1\mathbf{k}}^2\Delta_{2\mathbf{k}}^2/[1 - \exp(-\omega/k_B T)]}{[\omega\tau_{\mathbf{k}}(\omega^2 - \Delta_{1\mathbf{k}}^2 - \Delta_{2\mathbf{k}}^2)]^2 + (\omega^2 - \Delta_{1\mathbf{k}}^2)^2}. \end{aligned} \tag{20}$$

The procedure for deriving analytic equations for the second and fourth relaxation function moments,

$$\begin{aligned} \langle\omega_{\mathbf{k}}^2\rangle &= \frac{i\langle[\dot{S}_{\mathbf{k}}^z, S_{-\mathbf{k}}^z]\rangle}{\chi(\mathbf{k})} \\ &= -\frac{(8Jc_1 - 4t_{\mathrm{eff}}pI_1)(1 - \gamma_{\mathbf{k}})}{\chi(\mathbf{k})} \end{aligned} \tag{21}$$

and

$$\langle\omega_{\mathbf{k}}^4\rangle = \frac{i\langle[\ddot{S}_{\mathbf{k}}^z, \dot{S}_{-\mathbf{k}}^z]\rangle}{\chi(\mathbf{k})}, \tag{22}$$

was described in [21]. Here, [… , …] is the commutator. The final equation for $\langle\omega_{\mathbf{k}}^4\rangle$ was obtained using the procedure for the decoupling of thermodynamic averages of four operators into pair correlation functions (mode–mode decoupling). The explicit form of the $\langle\omega_{\mathbf{k}}^4\rangle$ values is not given here because the corresponding equations are too cumbersome. We can only note that $\langle\omega_{\mathbf{k}\to 0}^2\rangle \sim k^2$ and $\langle\omega_{\mathbf{k}\to 0}^4\rangle \sim k^2$ at small $\mathbf{k}$.

The analytic equation for the static spin susceptibility $\chi(\mathbf{k})$ in (20) will be taken from [22],

$$\chi(\mathbf{k}) = \frac{4|c_1|}{Jg_-(g_+ + \gamma_{\mathbf{k}})}, \tag{23}$$

where

$$\gamma_{\mathbf{k}} = \frac{1}{z}\sum_{\boldsymbol{\rho}} \exp(i\mathbf{k} \cdot \boldsymbol{\rho}) = \frac{1}{2}(\cos k_x a + \cos k_y a), \tag{24}$$

and $z = 4$ is the number of nearest neighbors in a square lattice. The g_+ parameter is related to the antiferromagnetic correlation length ξ as

$$\frac{\xi}{a} = \frac{1}{2\sqrt{g_+ - 1}} \approx \frac{J\sqrt{g_-}}{k_B T}\exp\left(\frac{2\pi\rho_S}{k_B T}\right), \tag{25}$$

where ρ_S is the spin stiffness and $a = 3.79$ Å is the lattice constant. Following [23, 24], the correlation length in weakly doped samples and at low temperatures will be described using the equation

$$\xi_{\mathrm{eff}}^{-1} = \xi_0^{-1} + \xi^{-1} \tag{26}$$

for the effective correlation length. Here, the ξ value, unlike that used in [4, 5], depends on the concentration of charge carriers (holes) [22], and ξ_0 is determined from the best fit to the experimental data [5]. We assume that

$$\xi_0 = a/n\delta, \tag{27}$$

which corresponds to the picture of dynamic domain walls (stripes), where the $n \approx 2$ value best fits the mean distance between holes along domain walls. In (21) and (23),

$$c_1 = \frac{1}{z}\sum_{\rho}\langle S_i^z S_{i+\rho}^z\rangle \tag{28}$$

is the spin–spin correlation function.

The amplitude of hopping (the "fermionic" correlation function) between the nearest neighbors is given by the equation

$$T_1 = pI_1 = -\frac{1}{z}\sum_{\rho}\langle X_i^{\sigma 0} X_{i+\rho}^{0\sigma}\rangle = p\sum_{\mathbf{k}}\gamma_{\mathbf{k}} f_{\mathbf{k}}^h, \tag{29}$$

where

$$f_{\mathbf{k}}^h = [\exp(-E_{\mathbf{k}} + \mu)/k_B T + 1]^{-1} \tag{30}$$

is the Fermi distribution function,

$$p = (1 + \delta)/2 \tag{31}$$

is the factor of band narrowing because of electron correlations, and the mean number δ of doped holes per copper site, which can be identified with the nominal content x of strontium atoms, and the chemical potential μ are related by the equation

$$\delta = p\sum_{\mathbf{k}} f_{\mathbf{k}}^h. \tag{32}$$

The dielectric–metal transition will be described using the following equation for the effective hopping integral:

$$t_{\mathrm{eff}} = \delta J/0.3, \tag{33}$$

which is renormalized by electronic and antiferromagnetic correlations (see [12, 21, 23–25]). The spectrum of elementary excitations has the form

$$E_{\mathbf{k}} = 4t_{\mathrm{eff}}\gamma_{\mathbf{k}}. \tag{34}$$

All calculations were performed for $J = 0.12$ eV = 1393 K, $\delta \equiv x = 0.04$, $c_1 = 0.11057$, $g_- = 4.037$, and $2\pi\rho_S/J = 0.345$.

It follows that the determination of static characteristics, primarily the correlation length, whose concen-

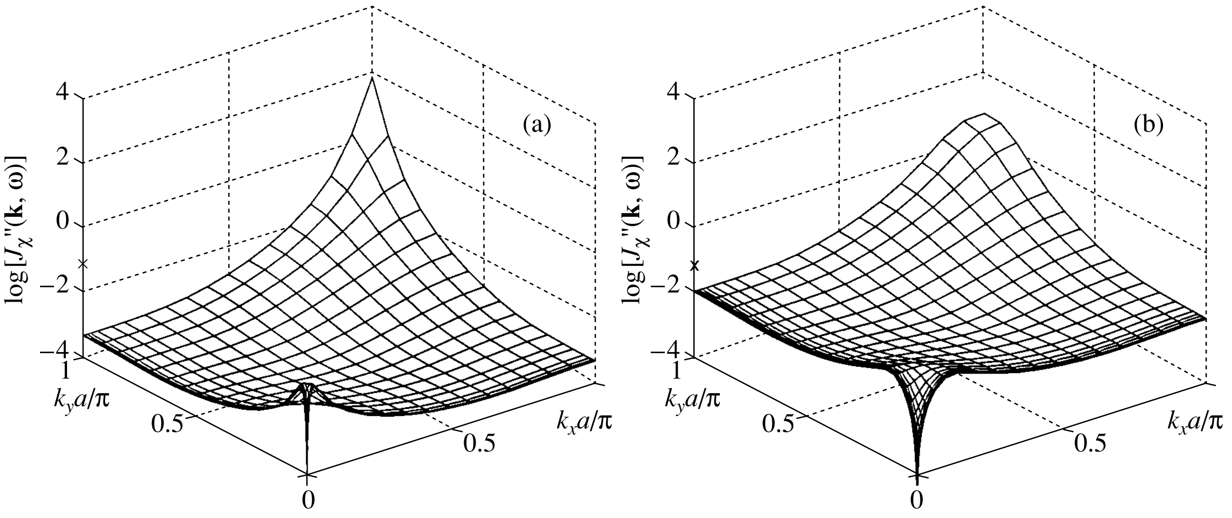

Fig. 1. Calculated imaginary part of the dynamic spin susceptibility $\chi''(\mathbf{k}, \omega)$ as a function of the wavevector at (a) $T = 100$ K and $\omega = 2$ meV and (b) $T = 150$ K and $\omega = 45$ meV for $La_{1.96}Sr_{0.04}CuO_4$. The cross on the vertical axis corresponds to $\chi''(\mathbf{k}, \omega)$ at the local maximum at small $q \sim 0$.

tration and temperature dependences in the region of weakly doped high-T_C cuprate compositions is still not completely understood (it is unclear whether one-dimensional walls (stripes) or other more exotic phases are formed) allows us to obtain dynamic values without adjustment parameters.

The calculated imaginary part of the dynamic spin susceptibility $\chi''(\mathbf{k}, \omega)$ is shown in Fig. 1 as a function of the wavevector. We see that, over wide temperature and frequency ranges, the major contribution to the value

$$\int \chi''(\mathbf{q}, \omega, T)d^2q \tag{35}$$

is made by the $\mathbf{q} \sim \mathbf{Q} = (\pi, \pi)$ values, whereas the contribution of $\mathbf{q} \sim 0$ only amounts to less than 1%; that is, it is negligibly small.

The normalized and averaged imaginary susceptibility part as a function of the ratio between frequency and temperature is shown in Fig. 2.

Systematic deviations of the calculated curves at high temperatures and low frequencies $\omega \lesssim 10$ meV from the experimental data and the observed deviations from universal behavior at $\omega \lesssim 3$ meV already mentioned in experimental works [3, 5] can be caused by both intensity loss in neutron scattering experiments and possible theory shortcomings originating from the approximations made. To check the theory, let us consider the NQR data and calculated spin-lattice relaxation rates for copper nuclei at $\omega \approx 2\pi \times 34$ MHz = 1.6 mK = 1.4×10^{-4} meV.

Note from the outset that we cannot exclude the possibility that the kinetic relaxation stage begins soon (high frequencies) after the system is disturbed from equilibrium, and its complete description requires knowledge of the one-particle distribution function. In our case, we used the three-pole (Markovian) approximation to relaxation function (15). This can be the reason for theoretical curve deviations from the experimental neutron scattering data at temperatures $T > \omega$. The discrepancies between theory and experiment would then increase as ω grows, whereas Fig. 2 shows that the discrepancies increase as ω decreases.

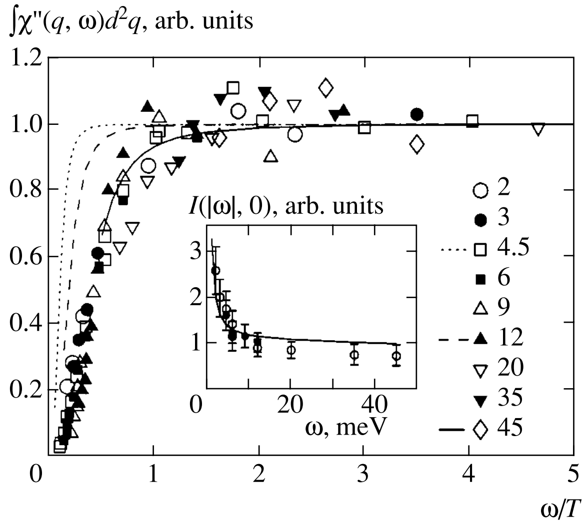

Fig. 2. Averaged imaginary part of the dynamic spin susceptibility as a function of the ratio between frequency and temperature for $La_{1.96}Sr_{0.04}CuO_4$ normalized by its value at large ω/T. Symbols are the experimental data from [4, 5] at various ω values specified in meV at the corresponding symbols. The dotted, dashed, and solid lines are the calculation results at $\omega = 4.5$, 12, and 45 meV, respectively. The scale of the experimental data in the inset (open circles) is adjusted to obtain the best fit to the theoretical curve.

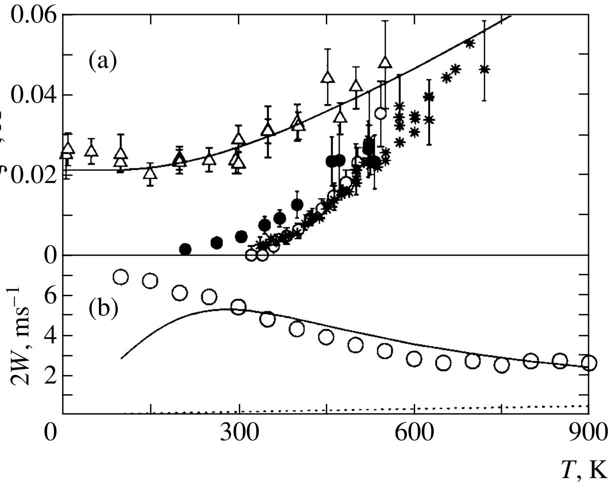

Fig. 3. Temperature dependences of (a) inverse correlation length (the solid line corresponds to the best fit to the experimental data for $x = 0.04$ (triangles); open circles, stars, and solid circles correspond to the experimental data on La_2CuO_4 [4, 5]) and (b) rate $2W = {}^{63}(1/T_1)$ of spin-lattice relaxation on ^{63}Cu nuclei lying in the CuO_2 plane (open circles are from [8]). The solid line corresponds to calculations without adjustment parameters, the dotted line is the contribution of spin diffusion.

The rate of spin-lattice relaxation in NMR/NQR experiments ($\omega \ll T, J$) is the dynamic structure factor $S(\mathbf{k}, \omega)$ averaged over the Brillouin zone with weight factor $^{\alpha}F(\mathbf{k})$ [26], which depends on the wavevector,

$$^{\alpha}(1/T_1) = \frac{1}{\pi}\sum_{\mathbf{k}} {}^{\alpha}F(\mathbf{k})^2 S(\mathbf{k}, \omega). \qquad (36)$$

The magnetic form factor of interest to us, $^{\alpha}F(\mathbf{k})$ for copper ^{63}Cu nuclei, has the form

$$^{63}F(\mathbf{k})^2 = (A_{ab} + 4\gamma_{\mathbf{k}}B)^2, \qquad (37)$$

where A_{ab} and B are the constants of the intrinsic and transferred hyperfine interaction, respectively. The quantization axis of the electric field gradient coincides with crystallographic axis c perpendicular to the CuO_2 plane. The CuO_2 plane is in turn determined by axes a and b. Following [27], we use the values $A_{ab} = 1.7 \times 10^{-7}$ eV and $B = 4 \times 10^{-7}$ eV.

The temperature dependences of the inverse correlation length and spin-lattice relaxation rate on ^{63}Cu nuclei lying in the CuO_2 plane are shown in Fig. 3. According to Fig. 3 and Eqs. (20) and (36), the spin-lattice relaxation rate and its temperature dependence are determined by the temperature dependence of the correlation length and the k_BT value, in agreement with [27]. At low temperatures at which $\xi_{\text{eff}} \approx$ const, the spin-lattice relaxation rate is, as it must be, proportional to the temperature, $1/T_1 \propto T$. At high temperatures, the correlation length in the sample with $x = 0.04$ behaves as in the undoped La_2CuO_4 compound (see Fig. 3) and the $^{63}(1/T_1)$ value is independent of the concentration of charge carriers [8]. It follows that our result is in agreement with the concept of an almost antiferromagnetic Fermi liquid (e.g., see [27]), a determining role played by the correlation length in the temperature and concentration dependences of the spin-lattice relaxation rate $1/T_1$, and the major contribution of wavevectors $\mathbf{q} \approx \mathbf{Q} = (\pi, \pi)$ to the $^{63}(1/T_1)$ value.

The contribution of spin diffusion to the $^{63}(1/T_1)$ value is shown by a dotted line in Fig. 3. We see that this contribution is small. At long times (low frequencies), it is sufficient to know several first moments of the distribution function to describe the system. This stage is known as the hydrodynamic relaxation stage. It follows from the theory of linear response and hydrodynamic approach that the dynamic structure factor at small $\mathbf{q}$ and ω has the form [16]

$$S(\mathbf{q} \sim 0, \omega \sim 0) \approx \frac{2\chi_S}{1 - \exp(-\omega/k_BT)} \frac{\omega D\mathbf{q}^2}{\omega^2 + (D\mathbf{q}^2)^2}, \qquad (38)$$

where $\chi_S \equiv \chi(\mathbf{k} = 0)$ and

$$D = \lim_{k \to 0} \frac{1}{k^2} \sqrt{\frac{\pi}{2} \frac{\langle \omega_{\mathbf{k}}^2 \rangle^3}{\langle \omega_{\mathbf{k}}^4 \rangle}} \approx 2.55 Ja^2 \qquad (39)$$

is the spin diffusion coefficient. The result obtained by the method that we use (Eq. (20) in the limit $k \longrightarrow 0$) is in agreement with (38). At low temperatures ($T < J$) and a very low frequency ω, the contribution of spin diffusion

$$(1/T_1)_{\text{diff}} \propto \ln(\text{const} \cdot J/\omega) \qquad (40)$$

is almost unnoticeable in NMR experiments as the frequency is varied because of the giant superexchange antiferromagnetic coupling value, $J \approx 1.8 \times 10^8$ MHz.

The deviations of the theoretical curve from the experimental $^{63}(1/T_1)$ values at low temperatures can be caused by inaccurate determination of the concentration of strontium atoms. Indeed, it is known that the spin-lattice relaxation rate $^{63}(1/T_1)$ and correlation length ξ are very sensitive to the concentration of strontium in the region of weakly doped compositions.

To summarize, the use of the method of projection operators and the two-dimensional t–J model allow us to explain the magnetic properties of weakly doped layered cuprates in the paramagnetic state. The theory explains the observed special features of the behavior of the imaginary part of the dynamic spin susceptibility averaged over the Brillouin zone over wide temperature and frequency ranges from $\omega \approx 10^{-4}$ meV (NMR) to

$\omega \approx 50$ meV (inelastic neutron scattering). At the same time, some deviation of the calculation results from the experimental data shows that the problem requires more detailed theoretical and experimental studies.

ACKNOWLEDGMENTS

This work was financially supported by INTAS (grant no. 01-0654), and a joint grant from the Civil Research and Development Foundation (USA) and the Ministry of Science and Education of the Russian Federation (no. Y1-P-07-19).

REFERENCES

1. M. A. Kastner, R. J. Birgeneau, G. Shirane, and Y. Endoh, Rev. Mod. Phys. **70**, 897 (1998).
2. S. M. Hayden, G. Aeppli, H. Mook, *et al.*, Phys. Rev. Lett. **66**, 821 (1991).
3. M. Matsuda, R. J. Birgeneau, Y. Endoh, *et al.*, J. Phys. Soc. Jpn. **62**, 1702 (1993).
4. B. Keimer, R. J. Birgeneau, A. Cassanho, *et al.*, Phys. Rev. Lett. **67**, 1930 (1991).
5. B. Keimer, N. Belk, R. J. Birgeneau, *et al.*, Phys. Rev. B **46**, 14034 (1992).
6. K. Kakurai, S. Shamoto, T. Kiyokura, *et al.*, Phys. Rev. B **48**, 3485 (1993).
7. R. J. Birgeneau, R. W. Erwin, P. M. Gehring, *et al.*, Z. Phys. B **87**, 15 (1992); B. J. Sternlieb, G. Shirane, J. M. Tranquada, *et al.*, Phys. Rev. B **47**, 5320 (1993).
8. T. Imai, C. P. Slichter, K. Yoshimura, and K. Kosuge, Phys. Rev. Lett. **70**, 1002 (1993).
9. G. Aeppli, T. E. Mason, S. M. Hayden, *et al.*, Science **278**, 1432 (1997).
10. R. Zwanzig, Phys. Rev. **124**, 983 (1961); R. Zwanzig, K. S. J. Nordholm, and W. C. Mitchell, Phys. Rev. A **5**, 2680 (1972).
11. H. Mori, Prog. Theor. Phys. **33**, 423 (1965); **34**, 399 (1965).
12. P. W. Anderson, Science **235**, 1196 (1987); G. Baskaran, Z. Zou, and P. W. Anderson, Solid State Commun. **63**, 973 (1987).
13. Yu. A. Izyumov, Usp. Fiz. Nauk **167**, 465 (1997) [Phys. Usp. **40**, 445 (1997)]; **169**, 225 (1999) [Phys. Usp. **42**, 215 (1999)].
14. U. Balucani, M. H. Lee, and V. Tognetti, Phys. Rep. **373**, 409 (2003).
15. D. N. Zubarev, *Nonequilibrium Statistical Thermodynamics* (Nauka, Moscow, 1971; Consultants Bureau, New York, 1974); R. Zwanzig, Annu. Rev. Phys. Chem. **16**, 67 (1965).
16. D. Forster, *Hydrodynamic Fluctuations, Broken Symmetry, and Correlation Functions* (Benjamin, Reading, MA, 1975; Atomizdat, Moscow, 1980); P. Kopietz, Phys. Rev. B **57**, 7829 (1998).
17. W. Marshall and R. D. Lowde, Rep. Prog. Phys. **31**, 705 (1968).
18. I. V. Aleksandrov, *Theory of Magnetic Relaxation. Relaxation in Liquids and Solid Nonmetallic Paramagnets* (Nauka, Moscow, 1975) [in Russian].
19. P. Prelovsek, I. Sega, and J. Bonca, Phys. Rev. Lett. **92**, 027002 (2004).
20. S. W. Lovesey and R. A. Meserve, J. Phys. C **6**, 79 (1973).
21. I. A. Larionov, Phys. Rev. B **69**, 214525 (2004); cond-mat/0401514.
22. A. Yu. Zavidonov and D. Brinkmann, Phys. Rev. B **58**, 12486 (1998).
23. A. Yu. Zavidonov, I. A. Larionov, and D. Brinkmann, Phys. Rev. B **61**, 15462 (2000).
24. A. Yu. Zavidonov and D. Brinkmann, Phys. Rev. B **63**, 132506 (2001).
25. N. M. Plakida, R. Hayn, and J.-L. Richard, Phys. Rev. B **51**, 16599 (1995).
26. F. Mila and T. M. Rice, Physica C (Amsterdam) **157**, 561 (1989); B. S. Shastry, Phys. Rev. Lett. **63**, 1288 (1989).
27. Y. Zha, V. Barzykin, and D. Pines, Phys. Rev. B **54**, 7561 (1996).

Translated by V. Sipachev

Journal of Experimental and Theoretical Physics, Vol. 100, No. 5, 2005, pp. 998–1004.
Translated from Zhurnal Éksperimental'noĭ i Teoreticheskoĭ Fiziki, Vol. 127, No. 5, 2005, pp. 1130–1137.
Original Russian Text Copyright © 2005 by Bonch-Bruevich, Vartanyan, Przhibel'skiĭ, Smirnov, Khromov.

Nonradiative Transition to the Ground State and Superelastic Scattering of Exited Atoms upon Impact on the Surface of Wide-Bandgap Dielectrics

A. M. Bonch-Bruevich, T. A. Vartanyan*, S. G. Przhibel'skiĭ,
V. N. Smirnov, and V. V. Khromov
Vavilov Optical Institute, State Scientific Center of the Russian Federation, St. Petersburg, 199034 Russia
**e-mail: tigran@jamnet.spb.su*

Received October 5, 2004

Abstract—The impact of excited cesium atoms on sapphire and glass surfaces have been experimentally studied. It is established that the probability of electron excitation quenching upon impact of an atom on the dielectric surface is close to unity. The velocity distribution of unexcited atoms upon scattering from the surface has been determined using the time-of-flight technique. The kinetic energies of most of these atoms are several tens of times greater than the energy of thermal motion of the excited atoms impinging on the surface. Conversion of the internal energy of atoms into their kinetic energy is explained in terms of nonradiative electron transitions with simultaneous excitation of lattice vibrations in the dielectric crystal. This mechanism of atomic excitation quenching near the dielectric surface explains the significant difference between the energies of atoms upon superelastic scattering and upon photodesorption from an adsorbed state. *© 2005 Pleiades Publishing, Inc.*

1. INTRODUCTION

The conversion of the energy of electron excitations in atoms and molecules into other forms plays a key role in the kinetics of gas discharge, laser plasma, heterogeneous catalysis, and some other phenomena. Owing to considerable effort devoted to investigations into these phenomena, extensive information has been gained concerning the energy conversion processes occurring in the gas phase, and models have been developed for their interpretation [1–5]. An example is offered by the process of resonance excitation quenching ($3P_{1/2,\,3/2}$) in sodium atoms occurring in the atmosphere of molecular gases (NO, C_2H_4, etc.). This process is exhaustively characterized with respect to both the total excitation quenching cross sections and the distribution of energy over translational, vibrational, and rotational degrees of freedom [3–5]. Modern theoretical methods provide a qualitative explanation of the experimental results.

The impact of excited atoms on solid surfaces are still insufficiently studied because of considerable experimental difficulties encountered in such investigations. Experimental data are available only for the probabilities of quenching of metastable states in atoms and molecules upon impact on the surface of some dielectrics and metals [5]. At the same time, neither has a theory been developed for the description of processes involved in the impact of an excited atom on the dielectric surface, nor mechanisms suggested explaining relaxation of the electron excitation energy between the degrees of freedom of the systems involved in this interaction.

We have studied the process of conversion of the electron excitation energy of incident cesium atoms into the kinetic energy of unexcited scattered atoms upon impact of the excited atoms on the surface of glass or sapphire. The kinetic energies of part of the scattered atoms exceed the initial values, which implies that superelastic scattering takes place. Possible approaches to theoretical description of this phenomenon are discussed.

2. EXPERIMENTAL METHODS AND RESULTS

Below we report on the results of direct experimental observation of the process of the energy of electron excitation being converted into kinetic energy upon impact of excited atoms on the surface of a solid. Cesium atoms were excited using intense resonance radiation immediately before impact on the dielectric surface. The excess kinetic energy of scattered atoms, acquired as a result of quenching of the electron excitation, was measured using the time-of-flight (TOF) technique.

The experiments were carried out at room temperature in a 60-mm-long glass cylindrical cell with flat windows made of glass or sapphire, filled with saturated cesium vapor. Since the room-temperature saturated cesium vapor pressure (1.6×10^{-6} Torr) is sufficiently low, interatomic collisions in the gas phase can be ignored.

The cell with cesium vapor (Fig. 1) was exposed to radiation of a cw distributed-feedback semiconductor laser (SDL-5712) with an output power of 40–60 mW, tuned to the central frequency of the atomic line of cesium (λ = 852.1 nm). The probing laser beam was incident perpendicular to the cell axis (i.e., parallel to the windows), passed through the cell at a fixed distance (7–10 mm) from one of the windows, and was detected by a photodiode with a broadband amplifier. Variations in the laser beam intensity related to changes in the light absorption by vapor in the cell were recorded by a storage oscillograph (S8-17). These changes were induced by pulsed radiation of a tunable dye solution laser generating in the wavelength range 820–860 nm, at an output power of 10^4–10^5 W/cm^2 and a spectral linewidth on the order of 10 cm^{-1}. The dye laser beam was directed at a sliding angle relative to the inner surface of one of the cell windows and produced excitation of cesium atoms immediately before their impact on the window surface. The laser pulses were synchronized with the oscillograph sweep. The sensitivity in this scheme was limited by the frequency noise of the probing semiconductor laser and amounted (in terms of the minimum detectable change in the number of absorbing atoms in the laser beam path) to approximately 10^5 atoms. In these estimations, we assumed the resonance absorption cross section to be $\sigma = 3 \times 10^{-12}$ cm^2, which corresponds to the Doppler broadening of the atomic line near room temperature. The signal-to-noise ratio in these experiments was about 5–6. The data presented below were obtained by averaging over oscillograms accumulated in the course of experiments.

Figure 2 (curve *1*) shows a typical oscillogram of pulses reflecting a change in the optical absorption in the cell for the pulsed laser radiation tuned in the region of 830–840 nm without exciting cesium vapor in the cell. A change in the intensity of laser radiation transmitted through the cell had a sign corresponding to an increase in the coefficient of absorption. It is natural to attribute this change to an increase in the number of absorbing species as a result of the action of pulsed dye laser radiation upon atoms desorbed from the cell window (this photodesorption signal is analogous to that described in [6]). Once we know the time of appearance of the response signal measured relative to the dye laser pulse (sweep start) and the distance from the cell window to the probing beam, the average velocity and energy of the photodesorbed atoms can be evaluated. This energy was about 0.03–0.04 eV, in good agreement with the data obtained previously for the photodesorption of sodium [6] and cesium [7] atoms from a sapphire surface.

An analogous oscillogram (Fig. 2, curve *2*) was obtained for the dye laser radiation tuned in resonance with an electron transition in cesium atom (λ = 852.1 nm). As can be seen, the photodesorption signal changed only in amplitude (because of a decrease in the output power upon tuning to a longer wavelength) and a new signal of the same sign (corresponding to an increase in the absorption) appeared closer to the sweep start. We thoroughly checked that both signals were observed only for the probing laser frequency tuned exactly to the atomic transition frequency, thus providing unambiguous evidence for an increase in the concentration of cesium atoms in the observation region. The two signals exhibited characteristic dependences on the exciting laser power. The photodesorption signal was proportional to this power [6, 7] and completely disappeared when the dye laser intensity decreased by a factor of 5–10 (the signal amplitude fell below the noise of the detection scheme). In contrast, the first (in time of appearance) signal almost did not decrease in amplitude but somewhat changed in shape (Fig. 2,

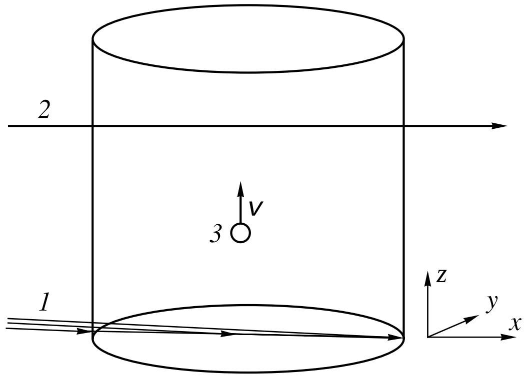

Fig. 1. Schematic diagram of the geometry of excitation of atoms approaching the surface and registration of atoms upon scattering: (*1*) exciting laser beam; (*2*) probing laser beam; (*3*) scattered atom moving away from the surface.

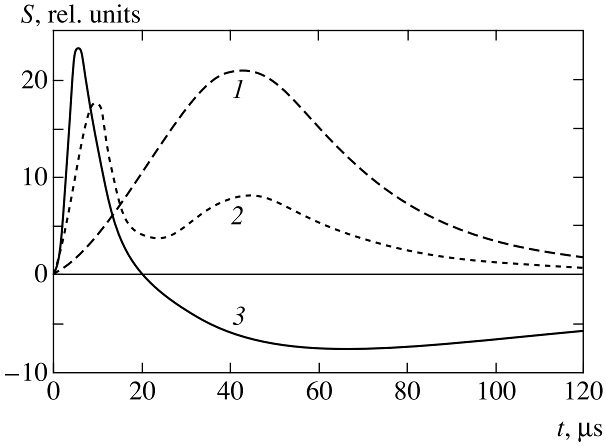

Fig. 2. Typical TOF spectra of atoms scattered from the surface of a sapphire window: (*1*) photodesorption induced by the dye laser detuned relative to the atomic line (λ = 840 nm), (*2*) superelastic scattering and photodesorption observed for the dye laser tuned in resonance with the free atoms (λ = 852.1 nm); (*3*) superelastic scattering observed when the excitation intensity was decreased to one-tenth of the level corresponding to curve *2*.

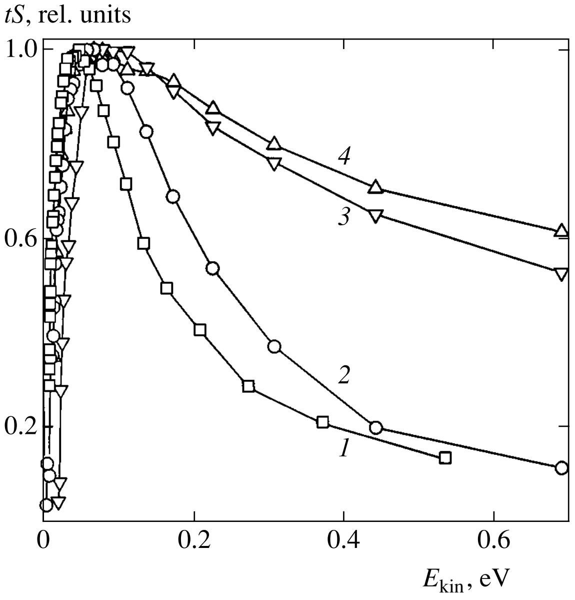

Fig. 3. Distribution of emitted atoms with respect to kinetic energies $E_{\rm kin}$ in the case of photodesorption (*1, 2*) and (*3, 4*) superelastic scattering from (*1, 4*) glass and (*2, 3*) sapphire.

curve *3*). The independence of the first signal amplitude of the dye laser power (within a certain interval) is naturally explained by saturation of the atomic line (in the range of the probing laser power intensities) and is evidence for this signal being related to the excitation of atoms in the cell volume.

The shape of the signal represented by curve *3* in Fig. 2 corresponds to what was expected. Indeed, being excited by the resonance laser radiation, a certain part of the atoms from the immediate vicinity of the window reaches the surface in the excited state. Upon impact on the surface and quenching of the electron excitation, such atoms are reflected from the surface with velocities exceeding the equilibrium values and overtake previously scattered unexcited atoms, thus increasing the density of particles in the observation region. Naturally, the absence of the contribution of these atoms to the equilibrium scattered fraction is manifested by a decrease in the corresponding density of atoms in the registration region below the equilibrium level. Thus, the action of the exciting laser radiation is equivalent to the simultaneous appearance of a source of high-energy atoms and an equal (in the number of emitted particles) negative source of atoms with equilibrium thermal distribution of velocities. Both these sources can be considered instantaneous, since the lifetime of the excited atomic state is on the same order of magnitude as the excitation pulse duration. For this reason, impacts of the excited atoms on the surface take place only within a period of time on the order of the duration of the excitation pulse. The latter value is about 25 ns, which is much shorter than the characteristic times of flight from the surface to the region of observation.

Using the results of measurements of the relative number of superelastically scattered atoms, it is possible to judge the probability of quenching of excited atoms on the surface. Indeed, the maximum flux of excited atoms to the surface amounts to half of the equilibrium flux $(1/4)N\text{v}$, where N is the concentration of atoms in the cell volume and v is the average velocity of thermal atoms in the cell. The saturated cesium vapor pressure at room temperature is 1.6×10^{-6} Torr, which corresponds to $N = 5 \times 10^{10}$ cm^{-3}. Then, the average velocity is estimated at $\text{v} = 2.2 \times 10^4$ cm/s. Thus, at a probability of quenching equal to unity, the maximum flux of scattered atoms is 2.8×10^{14} cm^{-2} s^{-1} (under conditions of saturated atomic transition). Once the probing and exciting laser beam diameters and the distance between these beams are known, it is possible to evaluate the number of atoms reaching the observation region after the action of the excitation laser pulse. This value is 4×10^6, in good agreement with the results of observations. This agreement confirms the above assumption that the probability of quenching of the electron excitation upon impact of an excited atom on the surface is close to unity.

The angular distribution of scattered atoms was determined from the decrease in amplitude of the signal of superelastically scattered atoms observed when the window was scanned with the exciting laser beam from the center to the periphery. These angular characteristics agree well (within the experimental accuracy) with the cosine distribution of the scattering angle according to the Lambert law. However, subsequent investigation of the surface of glass and sapphire windows using a high-precision profilometer showed that these materials even after deep grinding and fine polishing retain surface roughnesses with average heights of 1.8–2.4 nm for glass and 4–6 nm for sapphire. The lateral roughness size was 0.2–0.5 μm, and the proportion of flat terraces parallel to the window plane was negligibly small. In this context, the results of measurements of the angular characteristics of superelastic scattering are probably related to the surface roughness profile, rather than reflect the true angular profile of the atomic scattering process.

Figure 3 shows the TOF spectra reconstructed so as to demonstrate the distribution of scattered atoms with respect to their energies. For this purpose, the atomic velocities and the corresponding kinetic energies were determined using the times of flight to the observation region, and the signal intensity was multiplied by the flight time t in order to take into account nonuniform distortion of the scale on the passage from TOF to energy distribution. The negative parts of distributions corresponding to the lack of atoms with kinetic energies on the order of 10^{-2} eV are not depicted in Fig. 3. We also do not present the high-energy part of the spectrum, since the leading front of the experimental pulses reflecting a change in absorption of the probing laser beam is significantly distorted by a background signal related to the action of exciting laser radiation on the photodetector. Nevertheless, the reconstructed spectra show that the characteristic kinetic energy of scattered atoms accounts for a considerable part of the electron excitation energy (1.45 eV) and is several tens of times greater than the average thermal energy of atoms. The average kinetic energy of the scattered atoms is also much greater than the average kinetic energy of photodesorbed atoms. At the same time, a difference between the energy distributions of atoms scattered from glass and sapphire is rather small.

3. MECHANISM OF ENERGY CONVERSION NEAR THE SURFACE

In order to explain the phenomenon of superelastic scattering, it is necessary first to establish the mechanism responsible for almost complete quenching of the electron excitation of atoms during their interaction with the surface. The excitation energy (1.45 eV) is too small to be transferred to electrons of wide-bandgap dielectrics such as sapphire and glass. On the other hand, this energy is large compared to the energies of optical phonons in these materials. Therefore, processes of single-quantum excitation of dielectrics by incident atoms cannot be effective.

The electron excitation can be transferred to a dielectric by means of multiphonon processes. However, sequential excitation of a large number of phonons during the impact of an atom on a wall is low probable. Transformation of the nuclear vibrations of a dielectric from lower to highly excited energy states in a single event is possible under certain special conditions. Below we demonstrate the possibility of an effective multiphonon process by which the energy of electron excitation of an atom is converted into its kinetic energy and into the energy of vibrations of the dielectric crystal lattice.

Correct description of the interaction of excited atoms with the near-surface region of dielectrics is still an extremely complicated problem even for numerical model simulations. Let us assume that only a very near region of the dielectric is involved into the process of energy transfer from the incident atom to substrate. Nuclei occupying the crystal lattice sites in this region form, together with the incident atom, a quasi-closed dynamical system (collision complex) in which the energy conversion takes place. Upon transfer of the atomic excitation energy from the atom to this complex, the energy of lattice vibrations can be further transferred to the bulk of dielectric, but this will not influence the emission of the scattered atom.

This concept of such complexes was used previously [6] for explaining some features of the photodesorption of alkali metal atoms adsorbed on the surface of transparent dielectrics. According to estimates [6] a complex may involve several dozen (about forty) nuclei. It should be noted that the diameter of cesium atom is several times (approximately threefold) greater than the distance between adjacent lattice sites in the dielectric.

Thus, we have reduced the initial, insufficiently studied problem to a situation quite well studied in molecular physics—the problem of luminescence quenching during collisions of atoms with molecules and the photodetachment of atoms from molecules. As is known, the atomic luminescence quenching in collisions of atoms with small molecules is related to a nonadiabatic transition in the region of intersection (crossover) of their terms. This transition may lead to the excitation of strong nuclear vibrations in the molecule and to the conversion of a considerable part of its internal energy into the kinetic energy of the atom [3–5]. As will be shown below, the presence of a large number of nuclei in the complex makes the nonadiabatic process in the case under consideration somewhat different from that involved in collisions of atoms with small molecules. This difference requires special consideration.

The mechanism of conversion of the energy of atomic electron excitation into the motion of nuclei in the complex is as follows. A potential energy of the complex is the sum of the energy of deformation of the electron orbitals of the atom near the surface, the energy of interaction between the atomic nucleus and the dielectric, and the energy of displacements of the equilibrium lattice site positions caused by the atom. Naturally, the potential energy of the complex as a function of the distance z from the atom to the surface is different for various electron states. The total energy of the complex is given by the sum of the above potential energy and the energy of nuclear motions in the complex. In what follows, by terms is meant the differences of the total energy of the complex and the kinetic energies of atoms as functions of z.

As was noted above, a necessary condition for the effective energy transfer from electron excitations to nuclear motions is the intersection of terms. We have no grounds to assume that intersections are possible between terms corresponding to equal energies of the lattice vibrations. However, such intersections are possible if the energies of vibrations in the states corresponding to various terms are significantly different. In particular, a term corresponding to the state of excited atom and small lattice vibrations may intersect with a term corresponding to the state of unexcited atom and strong lattice vibrations. In this case, effective transitions from the first to the second state become possible.

The condition of intersecting terms is necessary but not sufficient for providing the effective energy transfer from electron excitations to the nuclear motions in the complex. The efficiency of the process involving strong changes in the nuclear motions is determined by the transition matrix element dependent on the overlap of the wavefunctions of nuclear motions in the initial and final states. Generally speaking, this overlap is expo-

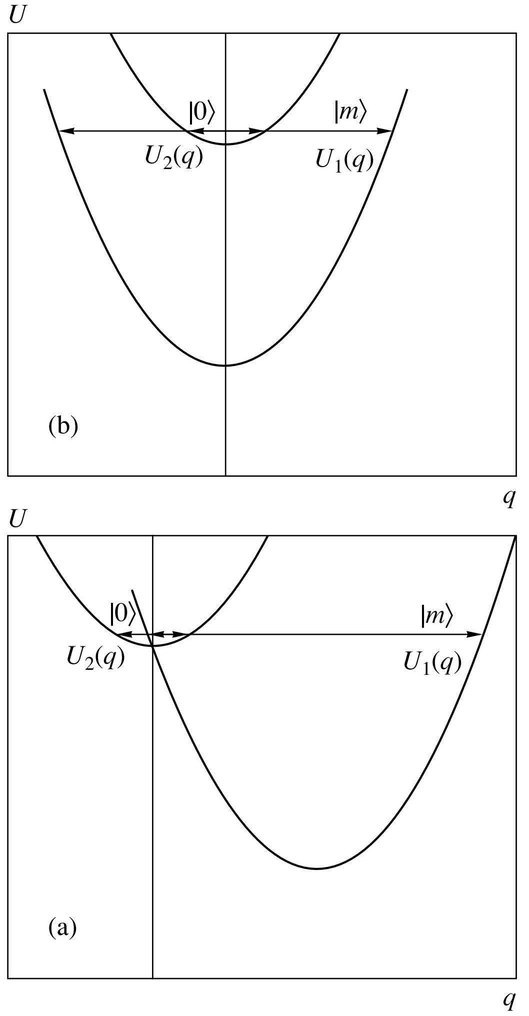

Fig. 4. Schematic diagram of potential energies for one of the normal modes: $U_1(q)$ corresponds to the ground state, and $U_2(q)$, to the excited state of an atom: (a) the potentials of inactive modes exhibit only a vertical shift upon a change of the electron state; (b) the overlap of vibrational wavefunctions of the active modes is most significant for the intersection of terms in the region of the bottom of the excited state.

nentially small if the initial and final states of nuclear vibrations are significantly different (as in the case mentioned above). However, significant overlap is also possible between the wavefunctions of weak and strong nuclear vibrations. This is illustrated by the following considerations.

An atom adiabatically slowly approaching the surface does not excite vibrations of the nuclei, but induces their displacements dependent on the electron state of the atom. The nuclear motions in the complex are conveniently described using the normal mode representation. Ignoring the Dushinski effect [8], we assume that the normal modes of the complex are independent of the atomic electron state. Then, each normal coordinate q of the complex corresponds to two potential energies: $U_1(q)$ for the ground state and $U_2(q)$ for the excited state (Fig. 4). The overlap of the wavefunctions of vibrations in the upper and lower electron states determines the efficiency of the transition between these states. When the atom is far from the surface ($z \longrightarrow \infty$), the $U_2(q)$ potential appears exactly as $U_1(q)$ displaced along the vertical axis. The transitions between such states are generally impossible. As the atom approaches the surface to a finite distance z, the $U_1(q)$ and $U_2(q)$ potentials are displaced and deformed differently, so that the overlap integral becomes nonzero. In the case of superelastic scattering of an excited atom, the initial oscillator state of the normal mode q is the ground state of vibrations in the $U_2(q)$ potential. According to the Franck–Condon principle, the most effective transition to the excited vibrational state in the $U_1(q)$ potential takes place when the $U_1(q)$ curve intersects with $U_2(q)$ in the vicinity of its minimum. A quantitative estimate of the overlap integral can be obtained by assuming that both potentials are described by identical quadratic functions. Then, the degree of overlap, as a function of the point of intersection, exhibits a sharp maximum [8] and reaches a value of $(2\pi m)^{-1/2}$, where m is the number of the final vibrational state of transition in the $U_1(q)$ potential. Assuming that the characteristic frequencies of normal modes in the complex fall within the IR absorption range of dielectrics and taking the electron transition energy to be about 1 eV, we obtain $m \sim 10$ and, hence, the degree of overlap can be sufficiently large.

It is necessary to pay attention to two circumstances. First, the amplitudes of nuclear vibrations in the complex in the case of strong excitation of normal modes are small because the excitation energy in most part of these modes is distributed more or less uniformly between lattice sites. This fact justifies the assumption of small displacements in our analysis. Second, it is possible that not all normal modes will provide for the required intersection of parabolas when the atom moves along the z axis. We believe that this intersection for a certain part of modes is observed at various positions of the atom relative to the surface. The modes for which the intersection takes place will be referred to as active.

The efficiency of the nonadiabatic transition is determined by the factors considered above and by the operator of transition between electron states. In the formalism of adiabatic states [8], this operator is related to the motion of atoms and is determined by the atomic momentum and by the dependence of the electron wavefunction on z. An equivalent but clear description of the nonadiabatic coupling can be obtained in a diabatic basis taking into account some approximate symmetry. In our case, the neglect of the dependence of the surface potential on the lateral coordinates leads to approximate axial symmetry and possible classification of electron states with respect to the normal projection of the orbital momentum. Then, the transition between intersecting terms Σ and Π is naturally related to the electric fields (not necessarily stationary, if the lattice vibrations are taken into account), which are tangent to the surface and can be significant at the dielectric surface. Quantitative evaluation of the probability of quenching requires detailed information (not available at present) about the potential of interaction between the atom and the surface. However, taking into account the fact that the excitation quenching cross sections for some atoms in collisions with molecules reach gaskinetic values [1], we may conclude that the above mechanism of nonadiabatic transitions can provide for the experimentally observed unit probability of the electron excitation quenching upon impact of an excited atom on the surface.

The above analysis shows that the quenching of atomic electron excitation at a dielectric surface may effectively proceed via the transfer of a part of internal atomic energy to the motion of nuclei in the dielectric lattice so that the atom retains its kinetic energy (according to the Franck–Condon principle) acquired on approach to the surface.

4. DISCUSSION OF RESULTS

Based on the proposed mechanism of nonradiative quenching of the electron excitation of an atom at a dielectric wall, the process of superelastic impact of the atom on the dielectric surface can be described as follows.

Excited atoms moving to the surface via an excited term can be deactivated in the events of internal energy transfer to the active modes. The probability of a single deactivation event is rather small, but each excited atom approaching the surface repeatedly encounters the possibility of such deactivation. For this reason, atoms exhibit complete deactivation despite the small probability of single event. Since various energies are transferred in different events, scattered atoms possess various kinetic energies (see Fig. 3).

Owing to the action of the attractive surface potential, the impinging atom acquires a significant kinetic energy. During a nonadiabatic transition, only the electron excitation energy is transferred to a collision complex comprising atom and substrate, while the kinetic energy of the impinging atom is not involved in the interaction. As a result, the atom (occurring in the ground state upon excitation quenching) is reflected upon the elastic impact on the wall. The reflected atom moves with a kinetic energy equal to that at the point of nonadiabatic transition minus the energy of binding in the ground state potential. If the depth of the excited potential at the point of nonadiabatic transition is significantly greater than the depth of the ground-state potential, the reflected atom may acquire a significant kinetic energy.

The mechanism of photodesorption of adatoms from a dielectric surface is essentially the same as the mechanism of superelastic scattering, but the course of the former process is different because of dissimilar initial conditions. Indeed, the adsorbed atom occurs initially in the ground electron state, the vibrations of nuclei at the lattice sites are not excited, and the equilibrium positions of these sites are displaced relative to those in the absence of adatoms. Upon absorption of a photon by the adatom, the system passes to another term on which the nuclei at the lattice sites initially occur in the same positions (according to the Franck–Condon principle) and then begin to move because the excited term has a different configuration of lattice sites. Similar to the case of superelastic scattering, most effectively excited are the normal modes for which the equilibrium positions are significantly displaced. The excited adatom also starts moving at the bottom of the upper term, but it is most probably involved in a nonadiabatic transition to the ground state of the unexcited term and in most cases remains bound to the surface (the quantum yield of photodesorption is small). The energy of the absorbed photon uniformly distributes over all degrees of freedom of the adsorption complex. For this reason, desorption events take place only in relatively rare cases determined by the statistics of distribution of the total energy of this complex over the nuclei, whereby a considerable part of the electron excitation energy is transferred to the energy of motion of the adatom, rather than to energy of nuclear vibrations at the lattice sites. This leads to the well-known features of photodesorption such as the Maxwell distribution of velocities of the desorbed atoms (see Figs. 2 and 3) and the dependence of the effective “temperature” of the adsorption complex on the photon energy. The most probable event is deactivation with the transition of the adatom to the ground state [6]. This is accompanied by the photoinduced diffusion of adatoms observed previously [9].

Thus, the main factor responsible for the difference in the kinetic energies of atoms upon photodesorption and second-order impact is related to a significant kinetic energy possessed by atoms in the latter case at the moment of nonadiabatic transition. This difference is also manifested in the energy distribution of scattered atoms. In the case of photodesorption, the width of the Maxwell distribution is determined by a fraction of the photon energy per oscillator in the adsorption complex and is on the order of 0.05 eV. For the second-order impact, the width of the energy distribution is determined by variation of the difference between the kinetic energies of atoms in the excited and ground state at the point of nonadiabatic transition, which is significantly greater than the former value.

We will not dwell here on the dependence of the velocity of scattered atoms on the energy losses during the impact of unexcited atoms on a dielectric. Although these losses can be relatively large (according to [10], the energy accommodation coefficient may exceed 0.75) and noticeably influence the velocity spectrum, this factor cannot substantially change the significant difference in the energies of photodesorbed atoms and those upon superelastic scattering.

The proposed description of the second-order impact of atoms on a dielectric surface can readily be presented in a theoretical form. However, presentation of such a theory is hardly expedient, since the description of experimental energy spectra of scattered atoms would require detailed information about the interactions of particles in the collision complex. Unfortunately, not much data are available even on the interactions of atoms with dielectrics.

ACKNOWLEDGMENTS

This study was supported in part by the Russian Foundation for Basic Research (project no. 01-02-17016), the Presidential Program of Support for Leading Scientific Schools in Russia (project no. NSh-270.2003.2), and the International Scientific-Technological Center (grant no. 2679).

REFERENCES

1. E. E. Nikitin, *Theory of Elementary Atomic-Molecular Reactions* (Khimiya, Moscow, 1971), Part 1 [in Russian].
2. B. M. Smirnov, *Excited Atoms* (Énergoizdat, Moscow, 1982) [in Russian].
3. P. Boschwina, W. Meyer, I. V. Hertel, and W. Reiland, J. Chem. Phys. **75**, 5438 (1981).
4. I. A. Silver, N. C. Blais, and E. H. Kwei, J. Chem. Phys. **71**, 3412 (1979).
5. I. V. Hertel and W. Reiland, J. Chem. Phys. **74**, 6757 (1981).
6. A. M. Bonch-Bruevich, T. A. Vartanyan, A. V. Gorlanov, *et al.*, Zh. Éksp. Teor. Fiz. **97**, 1077 (1990) [Sov. Phys. JETP **70**, 604 (1990)].
7. A. M. Bonch-Bruevich, T. A. Vartanyan, Yu. N. Maksimov, *et al.*, Zh. Éksp. Teor. Fiz. **112**, 362 (1997) [JETP **85**, 200 (1997)].
8. É. S. Medvedev and V. I. Osherov, *Theory of Nonradiative Transitions in Polyatomic Molecules* (Nauka, Moscow, 1983) [in Russian].
9. A. M. Bonch-Bruevich, T. A. Vartanyan, S. G. Przhibel'skiĭ, and V. V. Khromov, Opt. Spektrosk. **95**, 830 (2003) [Opt. Spectrosc. **95**, 777 (2003)].
10. A. M. Bonch-Bruevich, T. A. Vartanyan, S. G. Przhibel'skiĭ, *et al.*, Opt. Spektrosk. **95**, 885 (2003) [Opt. Spectrosc. **95**, 827 (2003)].

Translated by P. Pozdeev